The B-spline K-matrix Method in Atomic Physics

Luca Argenti

June 23, 2008

Abstract

In the course of this thesis the B-spline K-matrix method, a theoretical technique capable of reproducing the single ionization continuum of atoms, was developed. Two systems were addressed in particular: helium and boron, as representatives of two- and three-active-electron atoms.

Some of the findings presented here resulted in original contributions to the scientific literature. Total and partial photoionization cross sections and asymmetry parameters of the fundamental helium state were examined up to the sixth ionization threshold, yielding the first *ab initio* reproduction of the first intruder state effects below N=4 threshold, the first reproduction of dipole asymmetry parameters below N=6 threshold and of nondipole anisotropy parameter γ below N=2 threshold.

Most of the material presented here relies on the multiple basis implementation of the B-spline K-matrix method which allows the reproduction of almost arbitrarily excited metastable satellites below a prescribed threshold. The new technique, when used to investigate helium triplet states, yielded the most accurate and extensive existing characterization of triplet metastable states up to the fifth ionization threshold. Within more than 1700 natural and unnatural S, P and D doubly excited states, eleven intruder states were discovered, entirely unknown before.

At least two experimental groups, at ELETTRA in Trieste and at BESSY II in Berlin, are recently tackling the problem of measuring the metastable 2^3S helium photoionization cross section. We therefore undertook a parallel theoretical investigation of the photoionization process of both the fundamental and the excited ^{3}S helium states. The latter prelude to the future investigation of the radiative decay of doubly excited states and already revealed interesting peculiar features.

To this purpose, we devised an extension of the K-matrix method to treat the atom-radiation interaction non perturbatively.

A general three electron package has been developed and applied to study boron resonances. Specific formulas were derived to obtain arbitrary tensorial one-particle and scalar two-particle matrix elements between three electron states on *non-orthogonal* basis as required for an efficient exploitation of B-splines.

A detailed study of the B-spline effective completeness led to a general result which assure that B-spline based methods are well conditioned for a large class of knot grids.

Contents

Introduction

Since Hertz's discovery of the photoelectric effect in 1887 [1] and its proper explanation by Einstein in 1905 [2], photofragmentation processes proved to be among the most prolific means of investigation of atomic and molecular system dynamics.

In 1928 Compton and Boyce [3], and Kruger [4], two years later, found in the arc spectrum of helium the first evidence of a doubly excited state, assigning the 320.392 Å line to the $(2p^2)^3\mathrm{P}^e \rightarrow (2s2p)^3\mathrm{P}^o$ radiative decay.

The experimental practice made a considerable step forward when, in 1963, Madden and Codling [5] showed that synchrotron radiation is a useful X-ray source for spectroscopic purposes: they succeeded in measuring the first resonant profile in the photoionization spectrum of helium. Dedicated beamlines for atomic and molecular photoelectron spectroscopy experiments are now available at synchrotron laboratories all around the world: the Advanced Light Source at Berkeley [6], ELETTRA ring in Trieste [7], BESSY II in Berlin [8], Photon Factory in Tsukuba [9], SOLEIL near Paris [10], the Advanced Photon Source near Chicago [11], Synchrotron Radiation Source at Daresbury [12] and Max-Lab in Lund [13], just to mention the most relevant.

Despite its simplicity, helium, the smallest atom with electronic correlation, has been one of the most studied systems because of its almost inexhaustible manifold phenomenology, progressively disclosing as new, more refined experimental techniques became available.

Many characteristic Fano profiles were already clearly visible in the total photoionization cross section collected in 1963 by Madden and Codling [5]. Twenty years after, the first partial differential cross sections were measured [14] and, in the early nineties, the energy resolution dropped sharply through $\sim$ 5 meV [15] to $\sim$ 2 meV [16] when Domke *et al* observed for the first time the elusive $(2p, nd)$ $^1\mathrm{P}^o$ autoionizing Rydberg series below N=2 threshold. In the same period, the first detailed spectra of dipole anisotropy parameters also appeared [17]. By 1996, in new observations of helium doubly excited states, the unprecedented $\sim$ 1 meV resolution was achieved [18, 19].

At higher energies, the regular pattern of autoionizing multiplets were found to be perturbed by intruder states from series converging to high lying thresholds [20–22]. In the neighborhood of double photoionization threshold, myriad intruder states accumulates until roughly between $N \sim 8$ and $N \sim 13$ thresholds, any regularity is virtually lost [23–26]

New scaling laws for the amplitudes of the resonant character of partial cross

sections approaching the double photoionization limit soundly reflect the predictions of the most modern development of the semiclassical theory of the quantum three charged body problem [27, 28].

Beyond being an exemplary quantum analog of a classically chaotic system near the double ionization threshold, low lying doubly excited states have continued to yield new discoveries. A lot of attention has been devoted in particular to the radiative decay and to the relativistic effects on doubly excited states autoionization. In 2000, Gorczyca *et al* [29] demonstrated that both radiative decay and spin-orbit interaction had to be considered to account for the observed features of the photoionization spectrum in the immediate neighborhood of $N = 2$ threshold. In 2001 Penent *et al* eventually observed the radiative decay of triplet doubly excited states in the photoionization of the helium atom in its ground state [30]. The branching ratio between autoionization and radiative decay was measured only few years ago [31].

Measurements of photoionization spectra of metastable states are now affordable: preliminary results on the first resonant features in 2^3S He spectrum have recently been presented [32] and closer investigations are on schedule [33, 34].

Many new measurements on doubly excited states with symmetry which cannot be reached in ordinary photoionization experiments have recently been made accessible through the application of external electric [35–37] and magnetic fields [38,39].

Finally, sizable non dipole effects were found at unexpectedly low energies even in a target as small as helium [40].

All of these experimental findings represented in the past, and are often today, challenges to ever more accurate and reliable theories. The multiple basis B-spline K-matrix method developed in this thesis is one of them. It succeeded in providing original reproductions of some of the observations outlined above, often unveiling previously unknown details. Moreover, as discussed at length in the following chapters, it has unique features that makes it particularly fit to deal naturally with those processes which involves highly excited Rydberg series below prescribed thresholds, like the radiative cascades originating from doubly excited states.

Chapter 1

B-spline K-matrix method

1.1 Outline of photoionization observables

In atomic photoionization experiments, the gaseous target is introduced through a thin nozzle into a vacuum chamber where it intersects a photon beam. Upon photon absorption, the atom generally undergoes manifold transformations where two or more fragments, electrons, photons, ions, excited neutral states, result.

Let consider the exemplary case of helium in its fundamental state, illuminated with X-rays in the energy range between 24.6 eV and 79 eV, corresponding to single and double helium ionization thresholds respectively. With the absorption of one photon, helium may readily eject one electron (single photonionization - SPI), possibly leaving the parent ion in an excited state if $E_\gamma > 65.4$ eV (He^+ excitation threshold), or it may be temporarily trapped in a metastable state where, to a crude approximation, both the electrons are excited out of the fundamental level into outer bound orbitals (double photoexcitation - DPE). Such doubly excited states (DES) most often decay through autoionization (AI): one electron is eventually captured in a low-lying bound state of the parent ion releasing to the other electron enough energy to escape the atom. Since direct SPI and resonant AI result in the same final states, they give rise to characteristic interference figures in the photoionization spectra, known as Fano profiles [41].

If a metastable state is sufficiently long lived, the radiative decay (RD) may become a competitive or even dominant relaxation mechanism. The metastable state can even decay radiatively to a state of lower energy which itself lies in the continuum (radiative autoionization - RAI). In such case, one electron and one photon are ejected simultaneously.

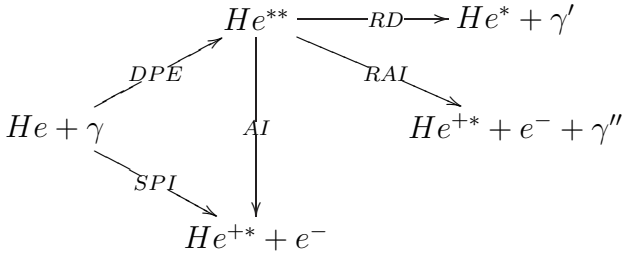

As all these processes depend strongly on the energy, polarization and intensity of the incident radiation, a stringent control on these light parameters is crucial. Modern X-ray beams for atomic and molecular photoionization experiments consist of monochromatized, strongly polarized synchrotron radiation produced through dedicated beamlines with energy resolutions ranging from few tenths to few meV. For example, PLEIADES beamline at SOLEIL [10] provides 20000-100000 resolving power between 35 eV and 1 keV, beam intensities from higher orders lower than 0.5%, and almost arbitrary polarizations: linear with arbitrary tilt, circular and elliptical.

To measure the total photoionization cross section (TCS), it is sufficient to collect directly all the ions produced [42]. To obtain partial cross sections and angular distribution parameters, instead, the photoelectrons are collected by time-of-flight spectrometers [43] along specific directions with small angular acceptances, e.g. 3°-6°. If the photoelectron has left the parent ion in the state α, its energy is found about $E_\gamma - E_\alpha$, where the energy of the impinging photon is narrowly peaked about E_γ. The ratio between the probability per unit of time that a photoelectron with energy $E_\gamma - E_\alpha$ is collected along the direction Ω with a solid angle acceptance $d\Omega$, and the total numeral photon flux density Φ_γ, defines the differential partial cross section $d\sigma_\alpha/d\Omega$

$$\frac{d\sigma_\alpha}{d\Omega} \equiv \frac{dP(E_\gamma - E_\alpha)}{dt d\Omega \Phi_\gamma}. \tag{1.1}$$

In order to compare with the experiment, we can use the quantum mechanical theoretical expression analogous to 1.1 provided by perturbation theory. To the lowest order, the partial differential photoionization cross section is proportional to the square module of the matrix element of a suitable transition operator between the initial and final state of the atom:

$$\frac{d\sigma_\alpha}{d\Omega} = \frac{(2\pi)^2}{c\omega_\gamma} |\langle \psi^-_{\alpha\vec{k}} | \vec{\epsilon} \cdot \sum_{i=1}^{n} e^{i\vec{k}_\gamma \cdot \vec{r}_i} \vec{p}_i | \phi_0 \rangle|^2. \tag{1.2}$$

The initial state ϕ_0 is clearly that of the target atom when injected into the reaction chamber. From the discussion above it is clear that the final state lies in the continuum: the photoelectron is asymptotically free, therefore its kinetic energy may vary by arbitrarily small amounts. Since all the measuring devices are macroscopic, they select a final state which is a broad, almost monochromatic photoelectron wavepacket, times a parent ion state in a definite energy level α, and which may be approximated, in a time independent approach, with a plane wave (actually a Coulomb wave) for the photoelectron, suitably coupled to the parent ion in the state α, plus a linear combination of incoming spherical waves in all the degenerate channels (incoming boundary conditions). Such states, indicated with the symbol $\psi^-_{\alpha\vec{k}}$ (α collects all the quantum numbers beyond the asymptotic photoelectron linear momentum, included the photoelectron spin projection), are also said to be controlled in the future: in a time dependent approach, any L^2 energy convolution of such states yields a wave packet which in the far future has

indeed a nonvanishing component in channel α only, since after leaving the atom, the photoelectron wavepacket eventually *is* an outgoing wave.

In the photoionization of strongly localized states at energies up to few hundreds eV, the exponential factor in equation 1.2 may be confidently approximated with 1 (dipole approximation). In this case the transition operator is a true rank one tensor. As a consequence the well known dipole selection rules apply and only a small number of final continuum manifolds with definite symmetry need to be calculated. Moreover, when the parent ion orientation is not measured, the angular distribution of the photoelectron is entirely described with a single parameter, $\beta_\alpha(E)$, ranging from -1 to 2:

$$\frac{d\sigma_{\alpha\vec{k}}}{d\Omega} = \frac{\sigma_\alpha(E)}{4\pi}\left\{1 + \beta_\alpha \cdot \frac{3\cos^2\theta - 1}{2}\right\} \tag{1.3}$$

where $\sigma_\alpha(E)$ is the integral cross section for channel alpha (see appendix B for the definition of symbols)

$$\sigma_\alpha(E) = \frac{\pi}{3\,c\,\omega_\gamma(2L_0+1)} \sum_{L\ell_\alpha} \left|\langle\phi_0\|\hat{V}_1^0\|\psi^{-\Gamma}_{\alpha E\ell_\alpha}\rangle\right|^2 . \tag{1.4}$$

For linearly polarized radiation, θ is the angle between the electron linear momentum and the light polarization axis. For circularly polarized radiation, equation 1.3 still holds, but θ is the angle between the electron and photon linear momenta. The expression of β for linearly polarized light is

$$\beta_\alpha = \left\{ \sum_{LL'} \sum_{\ell_\alpha \ell'_\alpha} \sqrt{30}\Pi_{\ell_\alpha LL'} C^{\ell'_\alpha 0}_{\ell_\alpha 0\, 20} (-)^{L_\alpha+\ell_\alpha+L+L'+L_0} \begin{Bmatrix} L' & 2 & L \\ \ell_\alpha & L_\alpha & \ell'_\alpha \end{Bmatrix} \begin{Bmatrix} 1 & 2 & 1 \\ L' & L_0 & L \end{Bmatrix} \times \right.$$
$$\left. \times\ \langle\phi_0\|\hat{V}_1^0\|\bar{\psi}^{(-)\Gamma}_{\alpha E\ell_\alpha}\rangle\langle\phi_0\|\hat{V}_1^0\|\bar{\psi}^{(-)\Gamma'}_{\alpha E\ell'_\alpha}\rangle^* \right\} \Bigg/ \left\{ \sum_{L\ell_\alpha} \left|\langle\phi_0\|\hat{V}_1^0\|\psi^{(-)\Gamma}_{\alpha E\ell_\alpha}\rangle\right|^2 \right\} . \tag{1.5}$$

As these formula shows, the theoretical reproduction of the experimentally observable quantities can be reduced to the calculation of matrix elements between bound and continuum atomic states with definite spherical symmetry and fulfilling appropriate boundary conditions.

The theory of electromagnetic transitions, and the scattering theory needed to deal with atomic states in the continuum and to compute photoionization parameters is covered in detail in the appendices A and B. The present chapter describes how to obtain numerically the accurate atomic states in the continuum needed for a positive comparison with modern experiments.

1.2 The close coupling equations

The eigenfunction of a $N+1$-electron system at energies below the double ionization threshold, where at most one electron can leave the system, can be written as a

linear combination of one electron orbitals suitably coupled to a complete set of bound N-electron states, plus a residual $N+1$ L^2 localized electron function:

$$\Psi_j^\Gamma(\mathbf{X}_{N+1}) = \mathcal{A}\sum_i \bar{\Phi}_i^\Gamma(\mathbf{X}_N;\hat{r}_{N+1}\sigma_{N+1})\frac{1}{r_{N+1}}F_{ij}^\Gamma(r_{N+1}) + \sum_i \chi_i^\Gamma(\mathbf{X}_{N+1})b_{ij}^\Gamma. \quad (1.6)$$

where $\mathcal{A}$ is the usual antisymmetrizer $\mathcal{A} = \frac{1}{N!}\sum_{\mathcal{P}\in\mathcal{S}_N}(-1)^{\mathrm{sgn}\mathcal{P}}\mathcal{P}$, $\mathbf{X}_N$ is a shorthand for the collection of spatial and spin variables for the first N electrons, and r_{N+1}, $\vec{r}_{N+1}$ and σ_{N+1} are the radius, direction and spin projection of the $N+1$-th electron. The channel functions $\bar{\Phi}_i^\Gamma$ are defined as parent ion (or atom) N-electron eigenstates with well defined angular momentum, spin and parity, coupled with the $N+1$-th electron spin-angular functions so to realize a specific total symmetry identified by parity, angular momentum, spin and their projections onto an axis, collectively indicated with Γ (we restrict the discussion to light systems, where the electrostatic approximation is justified - i.e. no magnetic interactions or other relativistic effects are taken into account). The χ_i^Γ's are also referred to as pseudostate channel, localized channel, or correlation functions.

At each energy E there are as many linearly independent solutions Ψ_j^Γ as the number of $\bar{\Phi}_i^\Gamma$ whose threshold E_j, the energy of the corresponding N-electron bound state, is lower than E. The expansion coefficients b_{ij}^Γ and the radial functions F_{ij}^Γ are such that Ψ_j^Γ is an eigenfunction of the total N-electron hamiltonian:

$$H\Psi_j^\Gamma = E\Psi_j^\Gamma. \quad (1.7)$$

Equation 1.7 can be projected onto the χ_i^Γ, integrating over all the spin and radial variables, and onto the $\bar{\Phi}_j^\Gamma$, integrating over all the variables except the $N+1$-th radius. The b_{ij}^Γ are eventually eliminated, yielding a system of integrodifferential equations known as the close coupling equations

$$\left[-\frac{1}{2}\frac{d^2}{dr^2} + \frac{\ell_i(\ell_i+1)}{2r^2} - \frac{Z-N}{r} - \epsilon_i\right]F_{ij}^\Gamma(r) - \\ - \sum_m \left\{V_{im}^\Gamma(r)F_{mj}^\Gamma(r) + \int\left[K_{im}^\Gamma(r,r') + X_{im}^\Gamma(r,r')\right]F_{mj}^\Gamma(r')dr'\right\} = 0 \quad (1.8)$$

where ℓ_i is the $N+1$-th electron orbital angular momentum in the i-th channel $\bar{\Phi}_i^\Gamma$, and $\epsilon_i = E - E_i$ is the asymptotic $N+1$-th electron energy, negative for closed channels, positive for open channels. $V_{ij}^\Gamma(r)$ is the local direct potential, while $K_{ij}^\Gamma(r,r')$ and $X_{ij}^\Gamma(r,r')$ are the nonlocal exchange and correlation potentials. The

explicit expressions of these potentials are

$$V_{ij}^{\Gamma}(r,r') = N \langle\bar{\Phi}_i^{\Gamma}|\frac{1}{r_{N\,N+1}} - \frac{1}{r_{N+1}}|\bar{\Phi}_j^{\Gamma}\rangle|_{r\equiv r_N, r'\equiv r_{N+1}} \tag{1.9}$$

$$\begin{aligned} K_{ij}^{\Gamma}(r,r') = N \; & \langle\bar{\Phi}_i^{\Gamma}(\mathbf{X}_{N-1}, r'\Omega_N\sigma_N;\Omega_{N+1}\sigma_{N+1})|(H-E) \\ & |\bar{\Phi}_j^{\Gamma}(\mathbf{X}_{N-1}, r\Omega_{N+1}\sigma_{N+1};\Omega_N\sigma_N)\rangle \end{aligned} \tag{1.10}$$

$$X_{ij}^{\Gamma}(r,r') = -\tfrac{N+1}{N} \langle\bar{\Phi}_i^{\Gamma}|(H-E)G_o^{\chi}(E;r,r')(H-E)|\bar{\Phi}_j^{\Gamma}\rangle \tag{1.11}$$

$$\text{where} \qquad G_o^{\chi}(E;r,r') = \sum_i \frac{|\chi_i\rangle\langle\chi_i|}{E-E_i^{\chi}}$$

To solve practical scattering or photoionization problems, the close coupling expansion 1.6, which in principle lead to exact solutions, must be truncated to a finite set of channels $\bar{\Phi}_i^{\Gamma}$ and correlation functions χ_i^{Γ}. Moreover, a prescription to get a complete set of linearly independent solutions at each energy must be given, and these solutions must be labeled according to the boundary conditions they fulfill. Many techniques accomplishing these tasks in different ways have been proposed.

A class of methods, reviewed by Nesbet [44], define functionals of the F_{ij}^{Γ}'s which are stationary about the exact solutions satisfying prescribed asymptotic conditions [45,46]. Among these variational methods, Kohn's [47] and Schwinger's [48] are perhaps the most popular.

The most widely used technique in the late twenty years, the R-matrix method, was introduced by Wigner and Eisenbud [49–51] in connection to the study of nuclear reactions, but encountered a considerable success also in the atomic and molecular physics community. For a review of the R-matrix method applied to atomic and molecular scattering problems see [52].

In the R-matrix approach, the configuration space is partitioned into two regions, one where all the $N+1$ electrons are confined within a prescribed radius a from the scattering centre, and one where only N electrons are confined within $r < a$, while $r_{N+1} > a$. The boundary radius a must be chosen so that the nonlocal exchange and correlation potential, which decay exponentially with r, are negligible, and the local direct potential has reached its asymptotic multipolar form. The close coupling expansion is truncated to a finite number of channels and the N-electron scatterer function and the $N+1$-electron correlation functions are expanded on finite basis within $r_i < a$. In this scheme, to any linear combination of incoming $N+1$-th electron wave components at the boundary $r = a$ there corresponds a unique set of outgoing components which defines the scattering properties of the system within a. The effects of the inner region on the electron scattering are entirely defined through a suitable hermitian Green function whose spectral decomposition is obtained with a single diagonalization of the total hamiltonian restricted to the inner region, modified with the addition of the Bloch operator [53] (which restores the hamiltonian hermiticity, broken by the truncation of the space to a set of functions which do not vanish at the boundary). The diagonalization,

which is the most time-consuming step, is performed just once, and essentially provides the solution of the scattering problem at any energy. The R-matrix method is therefore very efficient.

A completely different approach to scattering problems consists in the regularization of the asymptotic non-L^2 component of the wave functions by seeking the solutions to a similar problem where the radial coordinates are scaled by a phase factor (complex scaling) [54]:

$$r \rightarrow re^{\imath\theta}. \tag{1.12}$$

The θ-independent (complex) eigenvalues of the scaled hamiltonian are directly the position of the system resonances. The complex scaling methods yielded initially unclear results because of the sensibility of observables upon the angle θ when the rotation was performed about the origin and basis functions with noncompact support were used. A significant improvement in the complex scaling technique was obtained with the introduction of exterior complex scaling (ECS) [55, 56], where the radius acquires a phase factor only after a prescribed boundary r_0:

$$r \rightarrow r\theta(r_0 - r) + [r_0 + (r - r_0)e^{\imath\theta}]\theta(r - r_0) \tag{1.13}$$

With the inclusion of B-splines, ECS proved to be particularly successful not only in the characterization of metastable states [24] but more appealingly in yielding typical scattering observables like differential photoionization cross sections, not necessarily restricted only to single fragmentation processes. In 2004, Horner *et al* [57] obtained essentially exact results for the triply differential cross section of helium double photoionization. Today, ECS is among the most promising methods available.

The close coupling expansion 1.6 can be exploited directly in the solution of the time dependent Schrödinger equation [58]. In the case of photoionization the initial bound state is propagated under the influence of an external potential until the cross section can be extracted from the amplitude of the outgoing components of the wavefunction [59]. Smart implementations of such "brute force" methods seems to be the most appropriate to face the sophisticated photofragmentation processes made possible by today fs free electron laser facilities, but are clearly unfit to seek metastable states.

1.3 K-matrix

Formally a configuration interaction in the continuum, on the line of a pioneering paper by Fano [41], the L^2 K-matrix method [60, 61] follows the close coupling prescription: a complete set of stationary eigenfunctions of the hamiltonian $\psi^{\mathcal{P}}_{\alpha E}$ in the continuum, are approximated with a linear combination of partial wave channels $\phi_{\alpha E}$ (PWC's) plus a localized (or pseudostate) channel (LC):

$$\psi^{\mathcal{P}}_{\alpha E} = \phi_{\alpha E} + \sum_{\gamma} \sum\!\!\!\!\!\!\int d\epsilon\, \phi_{\gamma\epsilon} \frac{\mathcal{P}}{E - \epsilon} \mathbf{K}_{\gamma\epsilon,\alpha E} \tag{1.14}$$

where the index α runs over the open channels at energy E, while the index γ runs over all available channels (open and closed) including the LC.

Equation 1.14 echoes the Lippmann-Schwinger equation with the principal value Green function [62]

$$\psi^{\mathcal{P}}_{\alpha E} = \phi_{\alpha E} + G^{\mathcal{P}}_o(E) V \psi^{\mathcal{P}}_{\alpha E} \tag{1.15}$$

The Lippmann-Schwinger equation can indeed be cast in the form of equation 1.14, by defining the *off-shell* reaction matrix K as

$$K_{\gamma\epsilon,\alpha E} \equiv \langle \phi_{\alpha\epsilon} | V | \psi^{\mathcal{P}}_{\alpha E} \rangle. \tag{1.16}$$

The converse is actually not true as the unperturbed channels $\phi_{\alpha\epsilon}$ in 1.14 are generally defined in such a way that they are not orthogonal. In particular they are not the eigenchannels of an unperturbed hermitian operator. This is not a problem as the 1.14 should simply be looked at as a configuration interaction expansion, where the $\frac{\mathcal{P}}{E-\epsilon}$ factor allows $K_{\gamma\epsilon,\alpha E}$ to be regular in the first continuous energy index ϵ, and this is all what is required in order to solve the problem with standard numerical techniques. Moreover, we shall see in the following that the *on-shell* K-matrix, as computed from 1.14, still *is* the Cayley transform of the true scattering matrix of the physical problem (App. A).

A PWC function is defined as an $(N-1)-$electron bound parent state (atom or ion) Φ_{I_α} with well defined spin, parity, angular momentum and energy $I_\alpha \equiv (S_\alpha, \Pi_\alpha, L_\alpha, E_\alpha)$, coupled to a single particle state with definite angular momentum ℓ_α and asymptotic energy ϵ, to form an antisymmetric N electron state with definite spin S, parity Π, angular momentum L and projections Σ and M, which we shall indicate with the collective index $\Gamma \equiv (S, \Pi, L, \Sigma, M)$:

$$\phi^{\Gamma}_{\alpha E} = \mathcal{A} \sum_{\sigma_\alpha \sigma} C^{S\Sigma}_{S_\alpha \sigma_\alpha \, \frac{1}{2}\sigma} \sum_{m_\alpha m} C^{LM}_{L_\alpha m_\alpha \, \ell_\alpha m} \; \Phi^{\sigma_\alpha m_\alpha}_{I_\alpha} \otimes {}^2\varphi^{\Gamma,\sigma m}_{\alpha}. \tag{1.17}$$

The radial parts of the one particle orbitals $\varphi^{\Gamma}_{\alpha\epsilon}$ are defined so that the $\phi^{\Gamma}_{\alpha E}$ diagonalize the Hamiltonian within the (Γ, α) subspace:

$$\langle \phi^{\Gamma}_{\alpha E_\alpha + \epsilon} | \, \mathcal{H} \, | \phi^{\Gamma}_{\alpha E_\alpha + \epsilon'} \rangle = (E_\alpha + \epsilon) \; \delta(\epsilon - \epsilon'), \qquad \epsilon > 0, \tag{1.18}$$

$$\langle \phi^{\Gamma}_{\alpha E_\alpha + \epsilon_i} | \, \mathcal{H} \, | \phi^{\Gamma}_{\alpha E_\alpha + \epsilon_j} \rangle = (E_\alpha + \epsilon_i) \; \delta_{ij}, \qquad \epsilon_i, \epsilon_j < 0. \tag{1.19}$$

The partial wave channels normalized as

$$\langle \phi_{\alpha E} | \phi_{\alpha E'} \rangle = \delta(E - E') \tag{1.20}$$

have the following asymptotic behaviour

$$\phi_{\gamma E} \sim \sqrt{\frac{2k_\gamma}{\pi}} \, \Phi_\gamma \frac{e^{i\theta_\gamma(r)} - e^{-i\theta_\gamma(r)}}{2ik_\gamma r}, \quad \theta_\gamma(r) = k_\gamma r + \eta \log 2k_\gamma r - l_\gamma \pi/2 + \sigma_l + \delta_l \tag{1.21}$$

where Φ_γ is the parent ion function coupled to the spin and angular part of the $N+1$-th electron, $k_\gamma = \sqrt{2(E - E_\gamma)}$, $\eta = Z/k_\gamma$, σ_l is the Coulomb phaseshift and δ_l an additional phaseshift characteristic of the channel.

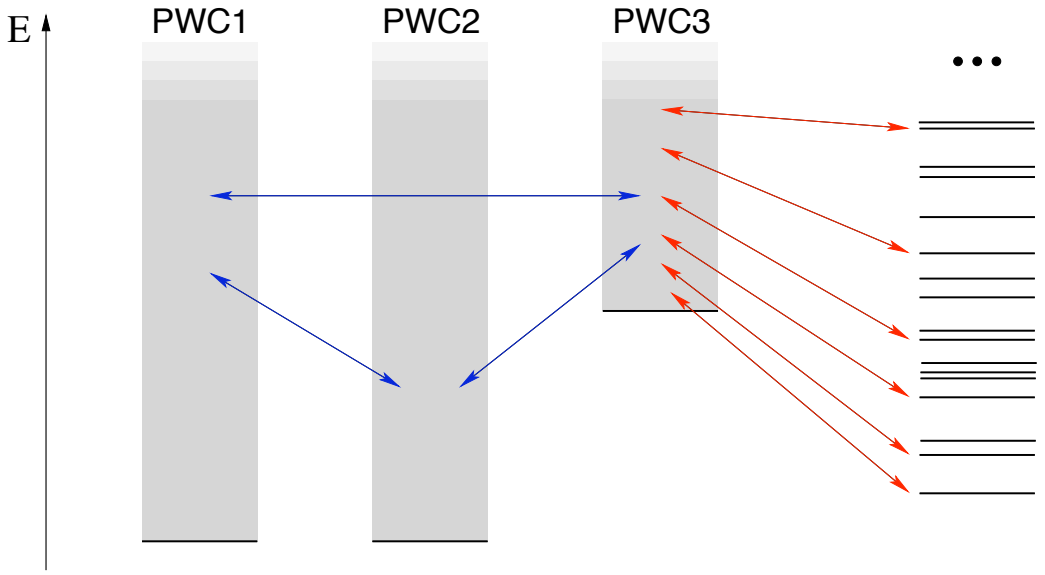

Figure 1.1: The K-matrix system of integral equations is a configuration interaction (CI) which includes the single ionization continuum. The set of continuum states in each partial wave channel is represented with a shadowed region above the channel threshold. The pile of levels on the right represent the pseudostate channel, comprising correlation functions as well as possible autoionizing states. All these channels interact with each other (arrows).

The localized channel comprises a large number of many-electron functions χ_i^Γ, with global symmetry Γ, built from localized orbitals, and which separately diagonalizes the Hamiltonian:

$$\langle \chi_i^\Gamma | \chi_j^\Gamma \rangle = \delta_{ij}, \qquad \langle \chi_i^\Gamma | H | \chi_j^\Gamma \rangle = \delta_{ij} E_i^\Gamma, \qquad \chi_i^\Gamma = \sum_j \Big[\bigwedge_k \varphi_{k_j} \Big]^\Gamma_{\mathbf{LS}} \, c_j^i \tag{1.22}$$

Equation (1.14) may be solved for the off-shell reaction K-matrix functions by requiring $\psi^{\mathcal{P}}_{\alpha E}$ to be an eigenfunction of the complete projected hamiltonian with eigenvalue E:

$$\langle \phi_{\beta E'} | \, E - \mathcal{H} \, | \psi^{\mathcal{P}}_{\alpha E} \rangle = 0 \quad \forall \, \beta, E'.$$

This leads to a system of integral equations for the off shell reaction matrix $\mathbf{K}$:

$$\mathbf{K}_{\beta E', \alpha E} - \sum_{\gamma \neq \beta} \sum\!\!\!\!\!\!\int d\epsilon \, \mathbf{V}_{\beta E', \gamma \epsilon}(E) \frac{\mathcal{P}}{E - \epsilon} \mathbf{K}_{\gamma \epsilon, \alpha E} = \mathbf{V}_{\beta E', \alpha E}(E)(1 - \delta_{\alpha\beta}) \tag{1.23}$$

where the effective potential $\mathbf{V}$ is defined as

$$\mathbf{V}_{\beta E', \alpha E} \equiv \langle \phi_{\beta E} | \, \mathcal{H} - E \, | \phi_{\alpha E} \rangle = \mathbf{H}_{\beta E', \alpha E} - E \, \mathbf{S}_{\beta E', \alpha E}$$

The K-matrix integral equations arise also in the minimization of a suitable functional through the Newton variational principle [62]. At each energy, where the scattering space is $n-$fold degenerate, n linearly independent coupled-channel functions $\psi^{\mathcal{P}}_{\alpha E}$ are obtained.

Consider now the following linear combinations of stationary wavefunctions

$$\boldsymbol{\psi}_E^{\pm} = \boldsymbol{\psi}_E^{\mathcal{P}} \left[\mathbf{1} \pm i\pi\mathbf{K}(E)\right]^{-1}$$

where $\boldsymbol{\psi}_E^{\pm} = (\psi_{1E}^{\pm}, \ldots, \psi_{nE}^{\pm})$ and $\mathbf{K}_{\alpha,\beta}(E) \equiv \mathbf{K}_{\alpha E,\beta E}$ is known as *on-shell* reactance matrix (see for example Newton §7.2.3 [62]). As $r \equiv r_{N+1} \to \infty$

$$\begin{aligned}
\psi_{\alpha E}^{\pm} &\sim \sum_{\beta}^{open} \Big\{\phi_{\beta E} + \sum_{\gamma}^{open} \iint d\epsilon \phi_{\gamma\epsilon} \frac{\mathcal{P}}{E-\epsilon} K_{\gamma\epsilon,\beta E}\Big\} [1 \pm i\pi K(E)]^{-1}_{\beta\alpha} = \\
&= \phi_{\alpha E} + \sum_{\beta\gamma}^{open} \iint d\epsilon \phi_{\gamma\epsilon} \frac{1}{E-\epsilon \pm i0^+} K_{\gamma\epsilon,\beta E} [1 \pm i\pi K(E)]^{-1}_{\beta\alpha} \qquad (1.24)
\end{aligned}$$

Replacing in the equation above the $\phi_{\gamma\epsilon}$ with their asymptotic behaviour 1.21, and closing the integrals with suitable circuits in the complex k plane, the following expression is obtained

$$\psi_{\alpha E}^{\pm} \sim \phi_{\alpha E} - \sum_{\gamma}^{open} \sqrt{\frac{2\pi}{k_\gamma}} \Phi_\gamma \frac{e^{\pm i\theta_\gamma(r)}}{r} \Big[\frac{K(E)}{1 \pm i\pi K(E)}\Big]_{\gamma\alpha} \qquad (1.25)$$

In $\psi_\alpha^{\pm}$ there are only outgoing (incoming) waves in all channels but α. In other terms $\boldsymbol{\psi}^{\pm}$ are recognized as the ordinary scattering solutions for wavepackets controlled in the past (future) (see appendix A). Since

$$\langle \boldsymbol{\psi}_E^{\pm} | \boldsymbol{\psi}_{E'}^{\pm} \rangle = \delta(E - E')\mathbf{1} \qquad (1.26)$$

the normalization of the stationary solutions is readily derived

$$\langle \boldsymbol{\psi}_E^{\mathcal{P}} | \boldsymbol{\psi}_{E'}^{\mathcal{P}} \rangle = \delta(E - E')(\mathbf{1} + \pi^2 K^2(E)). \qquad (1.27)$$

The scattering matrix, defined as

$$\langle \boldsymbol{\psi}_{E'}^{-} | \boldsymbol{\psi}_E^{+} \rangle = \delta(E - E')\mathbf{S}(E), \qquad (1.28)$$

therefore retains its familiar expression, as anticipated above:

$$\mathbf{S}(E) = \frac{\mathbf{1} - i\pi\mathbf{K}(E)}{\mathbf{1} + i\pi\mathbf{K}(E)}. \qquad (1.29)$$

The on-shell scattering matrix $\mathbf{S}$ is unitary. Moreover, since the systems of our interest are invariant under parity and time reversal, $\mathbf{S}$ is also symmetric [62]. As a consequence, the on-shell K-matrix is both symmetric and real.

For a correct asymptotic behaviour, the close coupling expansion might be restricted in principle to open channels only, but very poor results are then generally obtained as Feshback resonances, brought by closed channels, and most of the correlation would not be included. Closed PWC channels account for only a minor part of the correlation, because the close coupling expansion is both slow and incomplete: only bound states of the target are included. The convergence is greatly improved instead by the pseudostate or localized LC channel where the presence of true bound states and localized pseudo eigenstates quickly corrects those deficiencies. With a judicious choice of the localized channel, the close coupling expansion can be safely truncated beyond few closed thresholds above the energy of interest.

1.4 Discretization on an L^2 basis

Eq. 1.23 is an integral equation of the form

$$\sigma f(t) = \int_a^b K(t,s) f(s) ds + g(t) \tag{1.30}$$

in the unknown $f(t)$. The election procedure to solve these equations is through discretization:

$$\int_a^b y(s) ds = \sum_{j=1}^{N} w_j y(s_j). \tag{1.31}$$

where w_j are the weights and s_j the abscissas of a quadrature rule. Evaluating the equation at the quadrature points and defining f_i as $f(t_i)$, g_i as $g(t_i)$ and $\tilde{\mathsf{K}}_{ij} = K(t_i, s_j) w_j$, the integral equation is eventually reduced to

$$(\sigma \mathsf{1} - \tilde{\mathsf{K}}) \cdot \mathsf{f} = \mathsf{g}. \tag{1.32}$$

This is a linear system and can be solved applying the standard LU decomposition and back substitution algorithms. The solution is well-conditioned, unless sigma is very close to an eigenvalue of $\tilde{\mathsf{K}}$.

Now we can drive our attention to the details of our computational scheme which explicitly takes in to account the scattering nature of the physical problem underlying equation 1.23. There are many peculiarities that must be considered. First of all the unknown is a function of a number of channel indexes, the discrete channel identifier γ and an index within the channel which might be continuous, discrete or both. Continuous indexes formally vary in semi-infinite energy intervals starting at the corresponding channel thresholds.

The abscissas of the quadrature rule in the discretization of the continuum energy index of a specific partial wave channel are taken as the eigenvalues of the hamiltonian projected onto a finite approximation to that channel where a nourished set of B-splines-based one particle wavefunctions are coupled to the channel parent ion. Full details on the definition of this basis are given in section 1.6 and in appendix C.

Energy grids are consequently defined *a priori* and cannot be chosen at will to meet the needs of integral accuracy. The grid lacks in particular the lower limit of the continuum interval which must therefore be extrapolated. The kernel is formed by two distinct factors: an analytical part, which is the representation of the principal part resolvent $\langle \alpha\epsilon | G_0(E) = \frac{1}{E-\epsilon} \langle \alpha\epsilon |$, and a numerical part, that takes into account the energy matrix elements as well as the superposition between functions in different channels.

The Cauchy integral

$$\mathcal{I}(f, g; E) \equiv \int_a^b f(t) \frac{\mathcal{P}}{x - t} g(t) dt \tag{1.33}$$

can be reduced to

$$\mathcal{I}(f, g; x) \simeq \mathsf{f} \cdot \mathsf{P}(x) \mathsf{g}. \tag{1.34}$$

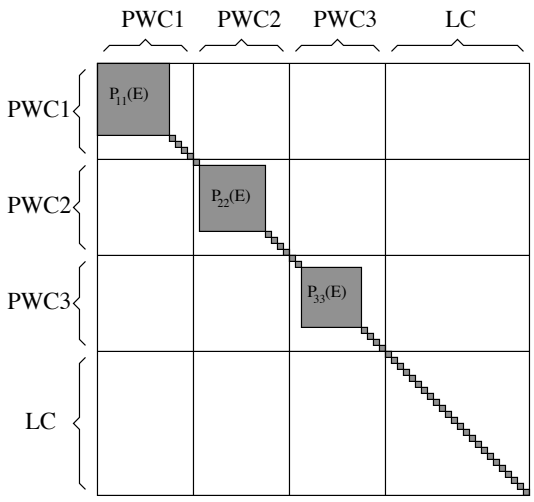

Figure 1.2: Structure of the integration matrix. The diagonal blocks are filled when B-spline interpolation is used, while they are band diagonal when the Lagrange interpolation is adopted.

where f and g are expanded on a set of characteristic functions χ

$$f(t) \simeq \sum_{i=1}^{n} \chi_i(t)\mathsf{f}_i, \quad \chi_i(t_j) = \delta_{ij},\ \mathsf{f}_i \equiv f(t_i). \tag{1.35}$$

and the principal part integration matrix is given by

$$\mathsf{P}_{ij}(x) \equiv \int_a^b \chi_i(t)\frac{\mathcal{P}}{x-t}\chi_j(t). \tag{1.36}$$

In eq. 1.23 there is an integration interval for each channel, so an integration matrix must be separately defined for each channel:

$$\mathsf{P}^{\gamma}_{ij}(E) \equiv \int_{E_\gamma}^{\infty} \chi^{\gamma}_i(\epsilon)\frac{\mathcal{P}}{E-\epsilon}\chi^{\gamma}_j(\epsilon). \tag{1.37}$$

The higher limit has to be truncated. Actually, the cut can be rather severe without significantly affecting the result and possibly improving the speed and stability of the method.

In equation 1.23, the discrete indexes do not need any integration:

$$\sum_i (E\mathsf{S}_{\beta E',\gamma i} - \mathsf{H}_{\beta E',\gamma i})\frac{1}{E-E_{\gamma i}}\mathsf{K}_{\gamma i,\alpha E}. \tag{1.38}$$

Discrete indexes corresponds to the pseudostates of the localized channel and to those discrete states in the partial wave channels whose energy is lower than the corresponding channel threshold. The discretized version of equations 1.23 is finally

$$\mathsf{K}_{\beta,\alpha E} - \sum_{\gamma\neq\beta} \mathsf{V}_{\beta\gamma}(E)\mathsf{G}^{\gamma}_{\mathsf{o}}(E)\mathsf{K}_{\gamma,\alpha E} = \sum_{i=1}^{n_\alpha} \mathsf{V}_{\beta,\alpha\epsilon_i}(E)\chi^{\alpha}_i(E). \tag{1.39}$$

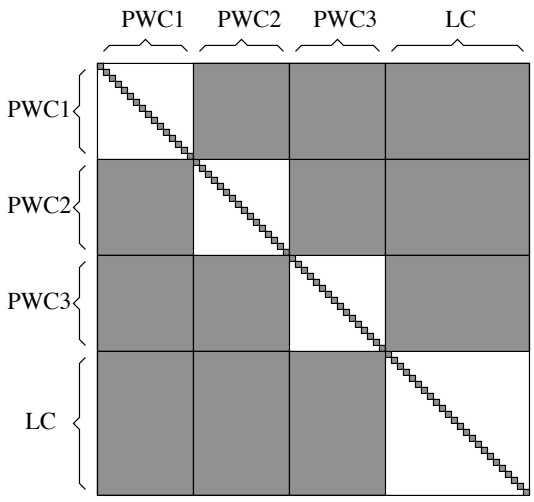

Figure 1.3: Structure of **H** and **S** matrices adapted to the K-matrix algorithm.

or

$$\sum_{\gamma\neq\beta}\left[\delta_{\beta\gamma}\mathsf{1}-\mathsf{V}_{\beta\gamma}(E)\mathsf{G}^{\gamma}_{\mathsf{o}}(E)\right]\mathsf{K}_{\gamma,\alpha E}=\mathsf{V}_{\beta,\alpha E}(E) \tag{1.40}$$

Diagonal blocks of V are explicitly excluded on the left hand side of equation 1.40, while the α block in the interpolation on the right hand side should be zero.

The *on-shell* K-matrix is obtained from the *off-shell* K-matrix again through interpolation:

$$K_{\alpha\beta}(E)=\sum_{i=1}^{n_\alpha}\chi_i^\alpha(E)K_{\alpha\epsilon_i,\beta E} \tag{1.41}$$

Since the *on-shell* K-matrix should be real and symmetric, and the interpolation above does not yield symmetry by construction, the symmetry check on K(E) is a good test on the calculation consistency. Actually, in almost all the calculations carried out in this thesis, the average absolute error $K_{ij}-K_{ji}$ was smaller than 10^{-12} times the average $K_{ij}+K_{ji}$.

Finally, the scattering matrix obtained through the Cayley transform of $K(E)$ is still not the scattering matrix of the physical process, as even if $K(E)$ were zero, the partial wave channels still account for phase shifts δ_α which affects the scattering matrix. The physical scattering matrix $S_p(E)$ may thus be written as

$$S_p=e^{i\Delta}\frac{1-i\pi K}{1+i\pi K}e^{i\Delta}, \tag{1.42}$$

where Δ is a diagonal matrix: $\Delta_{\alpha\alpha}=\delta_\alpha$. Conversely, the "physical" K-matrix can be written as

$$K_p=-\frac{1}{\pi}\frac{\sin\Delta-\pi\cos\Delta\,K}{\cos\Delta+\pi\sin\Delta\,K} \tag{1.43}$$

As implemented now, the LU factorisation must be carried out at each single energy without regard to previously computed points. This makes the present implementation of the K-matrix method somewhat lengthy when compared to

other methods, where the heavy calculation is performed just once. Hopefully, there is plenty of space for substantial optimization, because most of the time the solution changes smoothly and may therefore be predicted and refined on the basis of the the solutions obtained at neighboring energies. If applicable, such propagation of the solution might well improve the speed of the method by some orders of magnitude.

A similar discretization method was exploited in 1970 by Reinhardt and Szabo [63] to determine the elastic electon-atom scattering phase shift and extended shortly after to the inelastic case [64, 65]. Many different L^2 methods have been proposed in the literature for the case of a single open channel; few authors extended them to the multichannel case making use of some basic results of scattering theory [66–75] as we do.

The L^2 K-matrix method has already been applied successfully to a number of problems in atomic physics [74, 76–79]. In section 1.6 and in appendix C we shall discuss a particular basis, the B-spline basis, and its advantages over other functional spaces.

1.5 Basis Conditioning

As put forth in the previous section, to solve equations (1.18) and (1.19), the Hamiltonian is diagonalized with the radial part of one particle states φ_α in (1.17) projected on a B-spline basis. In the case of two electron systems, the parent ion functions have just one electron. The PWC basis is therefore reduced in order to be orthogonal to the target, and to avoid redundancy between different PWC channels.

Some of the eigenvalues fall below the parent ion energy and approximate the first terms of a Rydberg series. Eigenfunctions corresponding to energies above that of the parent ion approximate continuum wave functions. The radial part of the corresponding $\varphi_{\alpha\epsilon}$ is fitted with a "shifted" spherical Coulomb function of the same energy in the radial region where asymptotic behaviour is eventually reached and B-spline knots are still thick enough to faithfully reproduce oscillations. By this procedure, both the partial wave shift $\delta_{\alpha E}$ and the normalization factor are determined. The fitting also sort out the states without a correct asymptotic behaviour: irregular wavepackets with too large energies for their oscillations to be representable by the available splines. As described in detail in the next section, in our case the knot spacing rises rapidly beyond a certain radius R_2, where the calculated oscillating wave functions fade. If R_2 is large enough, this fictitious behaviour does not affect the inter-channel interaction.

Look at the expressions of the potentials $V^\Gamma_{ij}(r)$, $K^\Gamma_{ij}(r,r')$ and $X^\Gamma_{ij}(r,r')$ in 1.8 as $r \to \infty$: the two nonlocal potentials die out as fast as the functions adopted to represent the bound parent ion states and the correlation functions. Indeed, in definition 1.12, r can be recognized as the argument of one of these functions. Since bound and correlation functions have exponential tails or even, in some numerical approximations, compact supports, their influence is negligible beyond

a characteristic distance R_1

$V_{ij}^{\Gamma}(r)$ gives rise instead to multipolar potential at large distances:

$$V_{ij}^{\Gamma}(r) = \sum_{\ell} \frac{a_{ij\ell}^{\Gamma}}{r^{\ell+1}}, r \geq R_1 \tag{1.44}$$

The multipoles[1] range from the maximum between $|\ell_i - \ell_j|$ and $|L_i - L_j|$ and the minimum between $\ell_i + \ell_j$ and $L_i + L_j$, where ℓ_i and L_i are respectively the orbital angular momentum of the $N+1$-th electron and the angular momentum of the parent ion in the i-th partial wave channel. Moreover $\ell \geq 1$, the monopole contribution having been explicitly removed already in the definition 1.12, and the parity of ℓ must be simultaneously equal to that of $\ell_i - \ell_j$ and $L_i - L_j$. The dipole term, $\ell = 1$, gives rise, in second order, to a relatively long range attractive polarization potential

$$V(r) \to -\frac{\alpha}{2r^4} \tag{1.45}$$

which might not be negligible at distances R_2 as large as 100 au, depending on the polarization of the parent ion states, particularly at low energies.

The entire K-matrix method actually relies on the hypothesis that all the partial wave channels are totally decoupled after R_2. This assumption has eventually to be validated either by the convergence of results with increasing R_2 or by a positive comparison with experimental results.

In our experience, roughly half of the eigenstates, those with higher energies, are not reliable and can be rejected. A knots spacing of 0.75 au below R_2 yields a hundred reliable PWC continuum states over an energy interval of roughly 2.5 au above parent-ion energy. In the case of He, such a wide energy is required to reach the highest ionization thresholds from the fundamental $1s$ state of He^+ but is much beyond needs for those PWC's corresponding to excited He^+ states. In practice all the PWC's states with energies higher than 0.25 au above the double photoionization threshold are removed. These high lying states, irrespective of wether they are good representations of monoenergetic functions or not, *do* superpose to the true eigenfunctions at lower energies, but their contribution is effectively recovered through the LC. The overall effect of this selection is to reduce substantially the total dimension of the linear system which has eventually to be solved. In the $3s\varphi_{p\epsilon}$ channel, for example, we retain 32 Rydberg states and 60 continuum states out of a basis with original dimension of 274.

Finally all Rydberg-type orbitals are also removed and the resulting set of the PWC functions is the Conditioned Partial Wave Channel (CPWC). In the calculation of the $^1P^o$ manifold, examined in chapter 2, 9 open channels and 16 closed channels, all those up to N=5 threshold, are included: $1, 2, 3, 4, 5s\,\varphi_p$, $2, 3, 4, 5p\,\varphi_{s,d}$, $3, 4, 5d\,\varphi_{p,f}$, $4, 5f\,\varphi_{d,g}$ and $5g\,\varphi_{f,i}$. The highest nine closed channels could have been

[1]
$$a_{ij\ell}^{\Gamma} = \frac{\sqrt{4\pi}\Pi_{l_i}}{\Pi_\ell}(-)^{\mathcal{N}+\mathcal{N}_j} C_{l_i 0\,\ell 0}^{\ell_j 0} \begin{Bmatrix} L_i & l_i & L \\ l_j & L_j & \ell \end{Bmatrix} \langle \Phi_i \| \mathcal{O}_\ell \| \Phi_j \rangle, \quad \mathcal{O}_{\ell m} \equiv \sum_{i=1}^{N} r_i^\ell Y_{\ell m}(\hat{r}_i)$$

omitted but their inclusion do not increase much the total size and allows to use the same basis to investigate the energy interval below N = 5 threshold.

The LC functions should be conditioned as well since they superposes greatly with all partial wave channels. The possible arbitrariness of the final solution would otherwise yields numerical instability and the appearance of pathological, unphysical results. This is particularly true in the case of two electron systems where the full-CI limit is easily reached. To eliminate the redundancy, the projector over all CPWC is diagonalized over the localized two electron basis LC. Most of the projector spectrum is nearly zero but its final part rises steeply to 1.

The subspace with eigenvalues which differ from 1 less than a small threshold (10^{-2}) is removed. The remains define the reduced localized channel (RLC). In our case the total LC space has dimension 4826 (full-CI space spawned by 31 s, 30 p, 29 d, 28 f, 27 g, 27 h, 27 i orbitals). By the above procedure 222 functions are left out and consequently the LC set reduces to a RLC with 4604 functions effectively linearly independent on all the CPWC functions.

To complete the conditioning, the RLC and the set of all the Rydberg states from the PWC's are merged. The Hamiltonian is diagonalized on the merged basis to form the final Conditioned Localized Channel (CLC). The CLC states of highest energy do not contribute significantly to the final result and may be left out. In our example the complete CLC basis has 5371 terms, 4500 of which are retained in the final calculation. The overall dimension of the CLC plus the CPWC's is 6000, which is substantially smaller than the original total size of 9731.

We conclude this section mentioning a possible further improvement of the conditioning protocol, which is both substantial and peculiar to the K-matrix. The two parameters that limit the accuracy of K-matrix results are the extensions of the quantization boxes for parent ion and correlation states R_1, for continuum states R_2, and for Rydberg satellites R_3. As we shall see, R_3 can be chosen easily to be very large, as it can be reached with a quadratic increase of B-spline knots positions. R_2 must be sufficiently larger than R_1 for multipolar energy terms to be negligible, and R_1 must be large enough to accomodate all the required parent ions. Since the continuous wave represented within $r \leq R_2$ must have a uniform quality, the B-spline knot spacing must also be uniform (the asymptotic spacing is independent on R_2, and it is coarsly defined by the energy difference between the first single and the double ionization threshold. In the case of helium $\Delta E = 2$ au).

Now imagine that we wanted to reach the $20th$ threshold in ^{1}S helium within the "monodimensional" s approximation, where only $ns\epsilon_s$ channels are taken into account. The energy of the lowest bound state in each partial wave channel spectrum (suitably orthogonalized to the channels with lower thresholds) , with dominant configuration ns^2, is given with good approximation by the following Rydberg series [80]:

$$E_n = -\frac{3.3142}{(n + 0.0597)^2}. \tag{1.46}$$

To reach the 20-th threshold, we must be able to represent all those states whose energy fall below this threshold, corresponding to $n \leq 26$. To properly accomodate

the 26−th orbital, R_1 must be of the order of 700 au, and $R_2 \sim 1000$ au or even larger. To properly represent the oscillations of the most energetic waves near the double photoionization threshold, an asymptotic knot spacing within $r \leq R_2$ of ≤ 1au is required. This means that each single partial wave channel counts some thousands functions, and the problem is already almost untractable. Nevertheless, the diagonalization of a single partial wave channel would not be untractable at all. It would yield a large number of good states in the continuum, much denser in the energy interval of interest than is required for an accurate interpolation of matrix elements. The solution is thus already at hand: we select a small number of nonconsecutive states in the continuum, recovering a pwc dimension which is essentially invariant with respect to R_1 and R_2. What's more, since the single photoionization thresholds accumulate at the double photoionization threshold, the energy gap above thresholds is eventually small, and could possibly be represented by just two or three points. Most of the channels may thus yield some tens of Rydberg states and few states in the continuum. The conditioned problem would therefore be reduced to a perfectly affordable effective dimension of just two or three thousands terms.

1.6 B-splines

The use of B-splines as basis functions for quantum mechanical calculations dates back to the early eighties [81], but it was after publication of "A Practical Guide to Splines" by deBoor [82] that B-splines was recognized as a powerful tool for atomic physics calculations [83] particularly to reproduce those processes which involve the ionization continuum [84] and highly excited, or diffuse states [85]. Fully developed atomic packages, entirely based on B-splines, are now available [86–88]. More recently, successful B-splines approaches to molecules have also been developed [89–91].

A broad survey of B-splines applications to atomic and molecular physics was given by Bachau *et al* [92]. For a recent review covering the applications of B-splines to Hartree-Fock and Dirac-Fock calculations see [93]. In appendix C the definitions, main properties and an indepth analysis of B-splines effective completeness are given. In the present section a brief survey of the most original exploitments of B-spline properties peculiar to this thesis will be given.

1.6.1 Flexibility

The most crucial issue when using B-splines is probably knot collocation. Indeed, for a sufficiently regular function of one real variable f, n knots $t_1, \ldots, t_n$ can be chosen so that the approximation error of f by the spline space \$ of order k corresponding to $\mathbf{t}$ is dominated by [82]

$$\min_{\tilde{f}\in\$} \max_x |f(x) - \tilde{f}(x)| \leq \mathrm{const}_k n^{-k} \left(\int_a^b |D^k f|^{1/k} dx \right)^k . \tag{1.47}$$

If $D^k f$ is not uniformly distributed on f's domain, the error 1.47 can be substantially smaller than that obtained with an evenly spaced grid of knots.

Bound states of either charged and neutral systems have exponential tails which are suitably represented with exponentially increasing set of knots [92]. At small radii, instead, it is useful to allow for a fully free optimization of knot positions. In this way the convergence of observables as a function of the number of knots is surprisingly fast. We found the SCF energy minimization through the free optimization of an assigned number of knots to suitably serve this purpose. In table 1.1 an example of the this convergence for the fundamental helium state energy as a function of the number of knots for B-splines of order 7 is shown. In appendix C more examples are given.

n	E
3	-2.857 091 391
4	-2.861 502 991
5	-2.861 628 353
6	-2.861 678 169
7	-2.861 679 299
8	-2.861 679 879
9	-2.861 679 974
10	-2.861 679 984
11	-2.861 679 992
12	-2.861 679 993 4
13	-2.861 679 994 526
14	-2.861 679 995 332
∞	-2.861 679 995

Table 1.1: Hartree-Fock energies of the Helium atom obtained on B-spline basis with order $k = 7$, defined by fully optimized grids with 3 to 14 knots.

As anticipated in section 2, continuum states for charged parent ions and for neutral parent atoms (electron-atom scattering, negative ion photodetachment) have an oscillatory character as $r \to \infty$

$$\phi_l(r) \propto \frac{1}{kr} \sin(kr + Z/k \log(2kr) - l\pi/2 + \sigma_l + \delta_l). \tag{1.48}$$

In this case, an asymptotically evenly spaced set of knots represents the oscillatory function with uniform accuracy. The interval between two consecutive knots should be sufficiently narrow to ensure a good representation of the shifted Coulomb waves in the whole energy interval of interest. In practice, a spacing of 0.75 au assures an energy interval of roughly 2.5 au above threshold.

In the discretized K-matrix method, matrix elements with one or two continuum indexes are interpolated between values at adjacent energies. A sufficiently thick energy grid is therefore required. Moreover, at large distances from the nucleus, a multipolar potential may still be strong, in particular when the parent ion is highly

polarizable. It is thus essential that the set of evenly spaced knots reaches a large radius R. In all the calculations presented in this thesis we adopted $R \sim 250$ au.

Rydberg states for charged parent ions accumulates on the limiting zero energy state $\phi_l^{E=0}$ [94]:

$$\phi_l^{E=0}(r) = \sqrt{r} J_{2l+1}(\sqrt{8r}). \tag{1.49}$$

Asymptotically

$$\phi_l^{E=0} = \frac{r^{1/4}}{\sqrt{\pi}} \cos\left(\sqrt{8r} - l\pi - \frac{3}{4}\pi\right), \quad r \to \infty \tag{1.50}$$

Because of the square root of r in the argument of a periodic function, a quadratically increasing set of knots assures that in the oscillating part of the wave function the number of knots per half-wave is roughly constant. In table 1.6.1 some hydrogen eigenvalues of s states with principal quantum number n up to the 220-th are reported with the absolute error with respect to the exact $1/2n^2$ Rydberg series. The original B-spline basis is built on a grid with 1375 knots of order $k = 7$. All reported eigenvalues are computed with fantastic precision. Once the total number

n	Energy	Error
1	-0. 499 999 999 999 972	2.8 [-14]
2	-0. 124 999 999 999 986	1.4 [-14]
3	-0. 055 555 555 555 545	1.1 [-14]
4	-0. 031 249 999 999 991	9.3 [-15]
...	...	...
218	-0. 000 010 520 999 916	2.4 [-17]
219	-0. 000 010 425 137 091	3.3 [-17]
220	-0. 000 010 330 578 512	3.1 [-17]

n of Rydberg states we are interested in is established, the set of knots can be more readily completed after $r \simeq n^2$ adding an exponentially increasing set of knots to the quadratic set (beyond the largest classical turning point there are no more oscillations). In figure 1.4 the hydrogen s Rydberg state with $n = 225$ is shown.

1.6.2 Efficiency

In a scattering atomic system, all the dynamical regimes surveyed thus far, each one neatly represented with a specific set of knots, interact and must be represented simultaneously. The use of many *independent* B-spline basis is not viable: when knots do not coincide, non-zero conditions for integrals get tricky, and many different integral tables are required. Moreover this is a perfect recipe to destroy non-singularity of superposition matrix, whose regularization introduces all sort of

Figure 1.4: $225s$ hydrogen orbital: $r\phi_{225s}(r)$. B-splines allow full representation to machine accuracy of hugely excited states with economical basis.

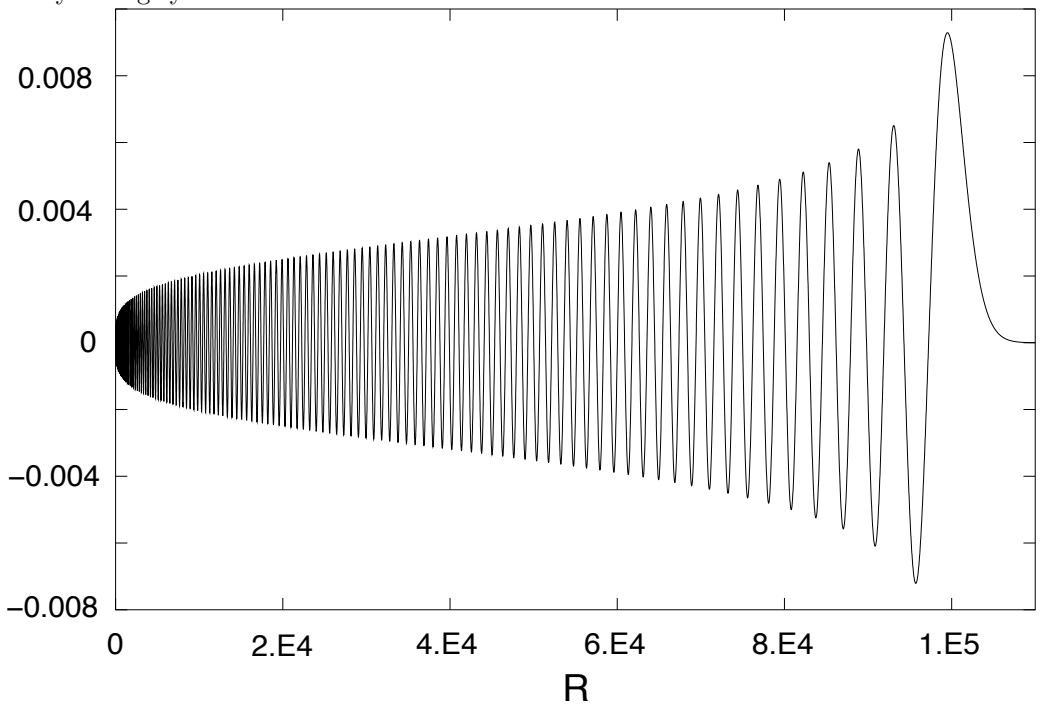

anomalous oscillations in residual basis functions. So the question arises whether a common and efficient B-spline basis can be chosen exhibiting all the desired properties. A trivial solution would be to choose the basis for the "most demanding" character, say continuum states. In this approach it is difficult to get a concise basis for short range correlation and target states. What is suitable for one electron in the continuum is much much beyond needs for two electrons of comparable energy, at least as long as the double ionization is not concerned. The resulting CI for parent ions and neutrals would be unnecessarily huge, possibly unmanageable.

An alternative way is suggested by a property of B-splines as trivial as remarkable: given a knot grid I, the B-splines defined by a sub set $J \subset I$ are all linear combinations of those defined on the larger set. Therefore we can merge all the knot sets and extract in a clear way an optimal subset for all kinds of function characters. Such procedure, though, can still be improved because with the merging many intervals appear which are far too small to actually enrich the functional space: there is no point in having occasional 0.1 au intervals (good for keV electrons ...) at dozens au from the nucleus.

The general procedure we devised consists instead in three steps:

1. Choose an optimal basis for short range wavefunctions, up to a certain distance R_1;

2. Define a suitable basis for the continuum by prolonging the previous basis with its tangent with an assigned slope up to a given distance R_2 where the non monopolar potential terms are assumed to be negligible;

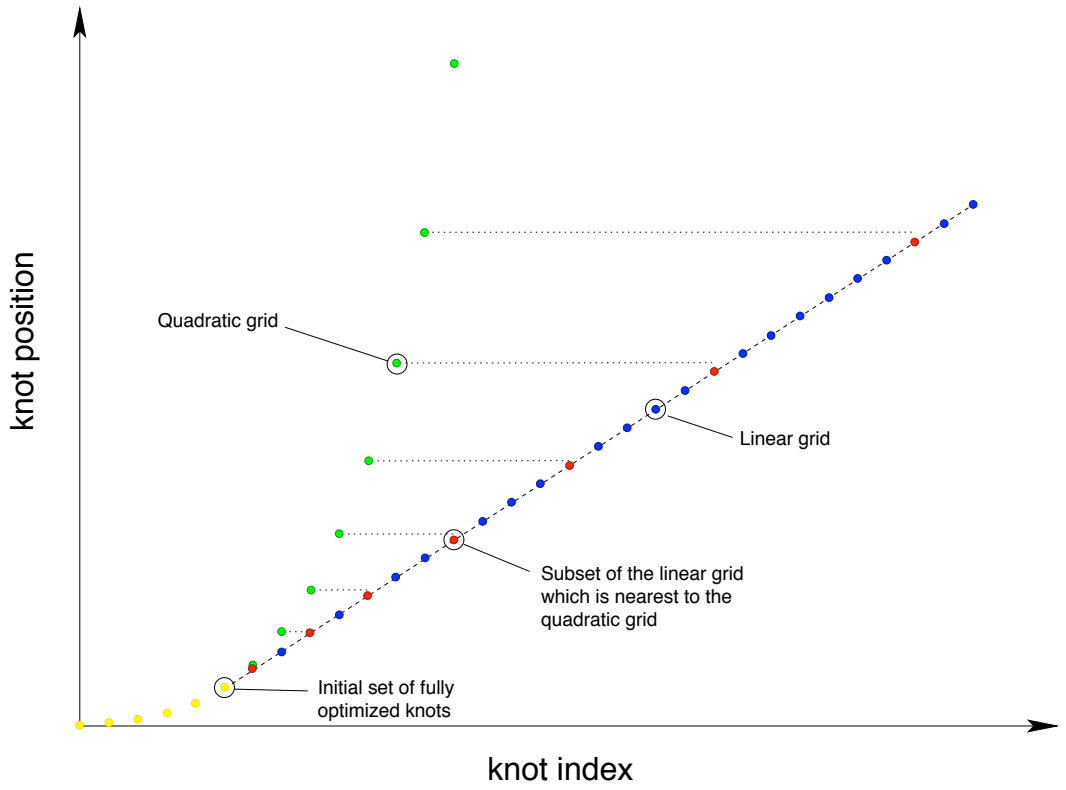

Figure 1.5: Set of knots involved in the merging procedure to produce an efficient common grid. An initial set of knots (yellow) is established through free optimization (see text for details). It is prolonged with a quadratically (green) and linearly (blue) increasing set of knots. A subset (red) is sought in the latter in order to reproduce the former with a minimal error.

3. Replace the knots in the short range basis with the nearest knots in the corresponding continuum basis: at very small radii the knots coincides, while at higher radii they differ by small amounts which are generally irrelevant to the basis performance;

4. Complete the largest set of knots with those widely spaced knots needed to represent as much long range satellites as needed, up to a third distance R_3.

As a result, a relatively small basis is obtained, and optimal basis for every behaviour can be easily extracted from it. In figure 1.5 the various sets of knots involved in the merging process are represented.

As a final remark, we stress the fact that the continuum wave functions have a bad behaviour beyond the limit radius where the knot spacing rises rapidly : they oscillates a bit with odd frequencies and rapidly die out. These solutions are nevertheless perfectly fit to K-matrix method because contributions to energy matrix elements among continua and between continua and large satellites comes mainly from short range interactions. This means that with K-matrix, the quantization box for satellites can be much larger (by order of magnitudes!) than the quantization box for the continuum.

1.7 Resonance characterization

We seek resonances as poles of the scattering matrix $\mathbf{S}(E)$ (1.29) in the lower half of the complex energy plane [49, 95–97]. The problem can be reduced to find the poles of the $\mathbf{S}(E)$ determinant:

$$\det \mathbf{S}(E) = \exp\left\{ 2i \sum_{j}^{open} \varphi_j(E) \right\} \tag{1.51}$$

where the eigenphases $\varphi_j(E)$ are related to the real eigenvalues $\lambda_j(E)$ of $\mathbf{K}(E)$ matrix through $\varphi_j(E) = -\arctan[\pi\lambda_j(E)]$. The determinant is unimodular on the real axis and clearly have the same poles of $\mathbf{S}(E)$ which consequently appear as a well known Breit-Wigner phase factors:

$$e^{2i\varphi_j(E)} = \frac{E - E_j - i\Gamma_j/2}{E - E_j + i\Gamma_j/2}, \qquad \varphi_j = \arctan\left[2(E - E_j)/\Gamma_j\right] + \frac{\pi}{2} \tag{1.52}$$

where E_j and Γ_j are respectively energy and width of the jth resonance .

For a not too large energy interval comprising N_{res} resonances, $\det \mathbf{S}(E)$ may be written in the form of product of a smooth background phase factor and N_{res} resonance phase factors (This property of the total phaseshift was recognized some thirty years ago [98]):

$$\det \mathbf{S}(E) = \exp\left(2i \sum_{p=1}^{N_{res}} \varphi_p(E) + 2i\varphi_{bg}(E) \right).$$

To find the resonance positions it is sufficient to add up the eigenphases from the scattering matrix and fit the result with a linear combination of arcotangent functions plus a smooth polynomial background. This procedure must be applied separately for each isolated group of resonances. Figure 1.6 illustrates the fitting procedure. Total phaseshift, divided by π, around an isolated doubly excited states multiplet in $^1\mathrm{P}^o$ helium manifold below N=5 threshold is reported as a function of energy together with its derivative (scaled to fit in the plot), which represents the density of states. The fitting function (nine resonance terms plus a polynomial background of fourth degree) is superposed to the phase shift as a thicker line. The corresponding resonance parameters are reported in table 1.2 (The outer principal quantum number n in the classification of resonances is chosen to match that by Rost *et al* [99]).

In figure 1.7 a more spectacular example of autoionizing multiplet series is reported: the $^3\mathrm{D}^e$ helium manifold below N=5 threshold.

Huge resonances with widths comparable to or larger than the intermultiplet distance may be missed because they cannot be distinguished from a polynomial background in a small interval. A technique to circumvent this is to subtract progressively the narrower fitted resonances and to repeat the fitting procedure on the residual spectrum.

Figure 1.6: Total phaseshift and state density for an isolated multiplet in the $^1P^o$ helium manifold below N=5 ionization threshold.

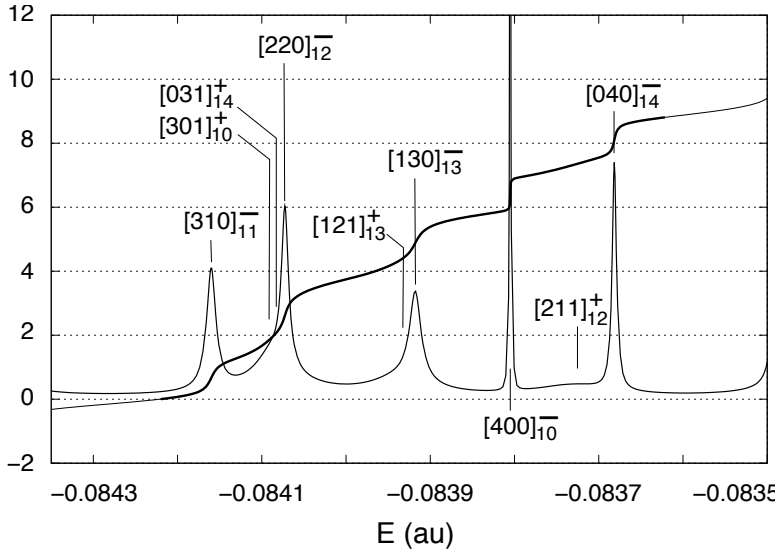

Table 1.2: Parameters of a selected group of $^1P^o$ helium resonances below N=5 ionization threshold, corresponding to the peaks shown in figure 1.6.

$[N_1N_2m]^A$	E (au)	$\Gamma/2$ (au)
$[031]^+_{14}$	-0. 084 080	6.79[-5]
	-0. 084 092	6.29[-5][a]
$[121]^+_{13}$	-0. 083 935	4.19[-5]
	-0. 083 966	5.68[-5][a]
$[211]^+_{12}$	-0. 083 729	5.76[-5]
	-0. 083 737	5.97[-5][a]
$[301]^+_{10}$	-0. 084 087	2.38[-5]
	-0. 084 103	2.48[-5][a]
$[040]^-_{14}$	-0. 083 682	2.76[-6]
	-0. 083 678	2.87[-6][a]
$[130]^-_{13}$	-0. 083 918	7.79[-6]
	-0. 083 919	7.60[-6][a]
$[220]^-_{12}$	-0. 084 073	4.76[-6]
	-0. 084 079	5.84[-6][a]
$[310]^-_{11}$	-0. 084 160	6.37[-6]
	-0. 084 169	5.77[-6][a]
$[400]^-_{10}$	-0. 083 805	3.77[-7]
	-0. 083 820	3.21[-7][a]

[a][Rost *et al* (1997)] [99]

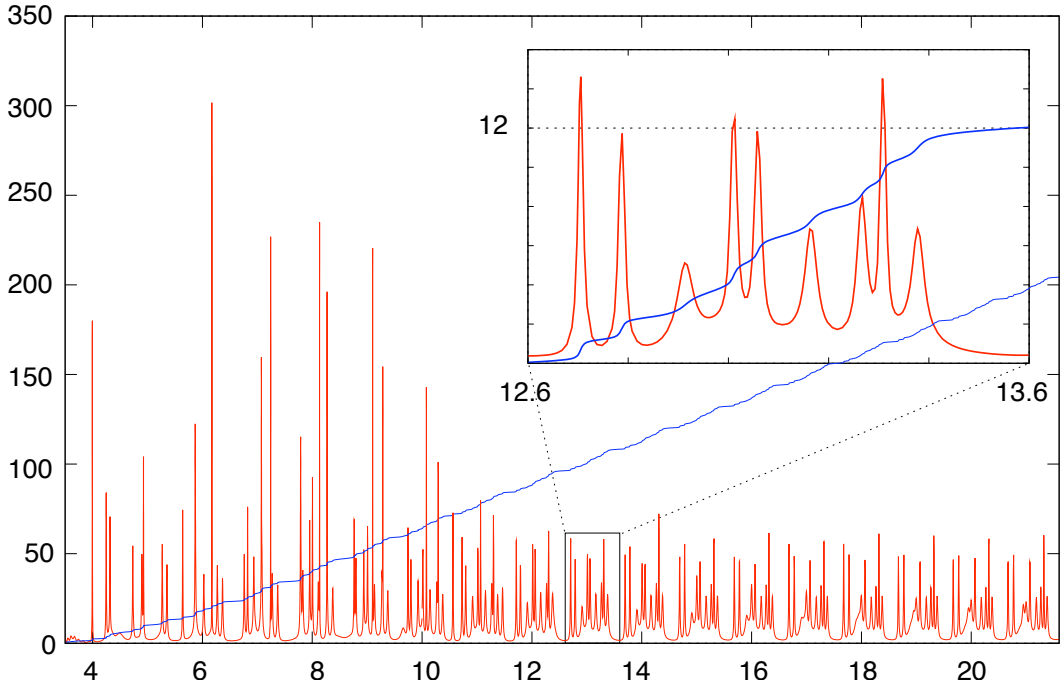

Figure 1.7: $^3\mathrm{D}^e$ helium total phaseshift divided by π (blue) and state density (red) below N=5 threshold as a function of the effective principal quantum number n^*. In the asymptotic region each multiplet is formed by twelve resonances, corresponding to the degeneracy of the N=5 $^3\mathrm{D}^e$ threshold: $5s\mathcal{W}_d$, $5p\mathcal{W}_p$, $5p\mathcal{W}_f$, and $5\ell\mathcal{W}_{\ell-2,\ell,\ell+2}$ for $\ell = 2, 3, 4$. The excursion of the total phaseshift in the interval of one effective quantum number reproduces closely this number as the inset shows. The nine narrower resonances are clearly visible as Lorentz peaks in the density of states, that is the derivative of ϕ_{tot}/π with respect to n^* (The resonances in the inset has actually been scaled for clarity). As shown in the text, for autoionizing Rydberg resonances the density of states per unit of effective quantum number can be seen as the number of revolutions performed by an electron temporarily captured when scattering off the parent ion.

The derivative of the δ_{sum}/π represents the density of states in the continuum

$$\rho = \frac{1}{\pi}\frac{d\delta}{dE}. \tag{1.53}$$

As first observed by Eisenbud [100], the derivative of the phase shift is proportional to the time delay of an electron scattering off the parent ion

$$\tau = 2\hbar\frac{d\delta}{dE} = h\rho(E). \tag{1.54}$$

The first equation in 1.54 is often referred to as the Wigner-Eisenbud relation [101]. For a recent review of time delay in quantum scattering, see De Carvalho *et al* [102]. In the specific case of photoionization, the long range Coulomb interaction between the parent ion and the leaving photoelectron gives rise to infinitely many metastable states below each ionization threshold, arranged in multiplets. The multiplet series eventually stabilizes in a periodic pattern (that is the derivative of total phaseshift with respect to the effective quantum number $n^* \equiv [2(E_{thr} - E)]^{-1/2}$ converges to a periodic function of n^*). The characteristic period of a specific orbit is $T =$

$h/\Delta E$ where $\Delta E \sim 1/n^{*3}$ is the distance between two consecutive corresponding resonances. Consequently, the number of revolutions N_{rev} of a wavepacket captured in a metastable state around the energy E is

$$N_{rev} = \tau/T = n^{*3}\rho(E) = \rho(n^*) \tag{1.55}$$

As the density of states $\rho(n^*)$ is periodic, the impinging electron follows essentially homothetic trajectories at corresponding energies ($n_2^* = n_1^* + k$ with $k = 1, 2, 3, \ldots$), with characteristic sizes rising as n^{*2}, and periods rising as n^{*3}, analogously to the third Kepler's law. In the case shown in figure 1.7, the impinging electron may perform tens to hundreds revolutions before leaving the ion.

1.8 Radiative K-matrix

This section is devoted to the treatment of atom and radiation on equal ground. We are not presently interested in high intensity fields but to single photon processes where the branching ratios of fluorescence channels might be comparable to those of autoionization channels. In this case the ion yield spectrum, what is often actually measured in photoionization experiments, ceases to reproduce the absorption cross section, while the fluorescence yield spectrum grows complementarily. One expects also to find larger resonances and a qualitative modification of spectra: as the incident photon energy approaches a given photoionization threshold, the autoionization width gets narrower while the fluorescence width converges to a finite value and eventually dominates giving rise to a complete superposition of autoionizing states.

This idea has already be exploited by a number of authors. General theoretical formulation of the so called radiation damping can be found in [103–105]. The first application to the radiative decay on an isolated resonance have been presented by Berrington and coworkers in 1990 [106]. In 1995 Robicheaux, Gorczyca, Pindzola and Badnell described in detail the inclusion of radiation damping in the close coupling equations with the "pole approximation", obtained neglecting the channel-channel interaction through emission and absorption of virtual photons.

In the same way we defined a partial wave channel (see eq. 1.17), we can define a fluorescence channel, coupling to a bound state ϕ_a a photon with definite spherical symmetry j, electric ($\lambda = +$) or magnetic ($\lambda = -$) character, and energy ω (see appendix B for definitions)

$$|\phi^{\Gamma}_{aj\lambda E}\rangle = \sum_{m_a\mu} C^{LM}_{Lam_a,j\mu}\ \phi_{Lam_aS\sigma} \otimes b^{(\lambda)\dagger}_{\omega j\mu}|-\rangle. \tag{1.56}$$

As long as the electronic spin is a constant of motion, we can couple the angular momentum of the field to the orbital angular momentum of the electrons. Moreover, when the A field is taken as uniform, the A^2 term in the hamiltonian can be neglected, and the fluorescence channels do not require any prediagonalization:

$$\langle \phi^{\Gamma}_{aj\lambda\omega} | H | \phi^{\Gamma}_{aj\lambda\omega'} \rangle = (E_a + \omega)\, \delta(\omega - \omega') \tag{1.57}$$

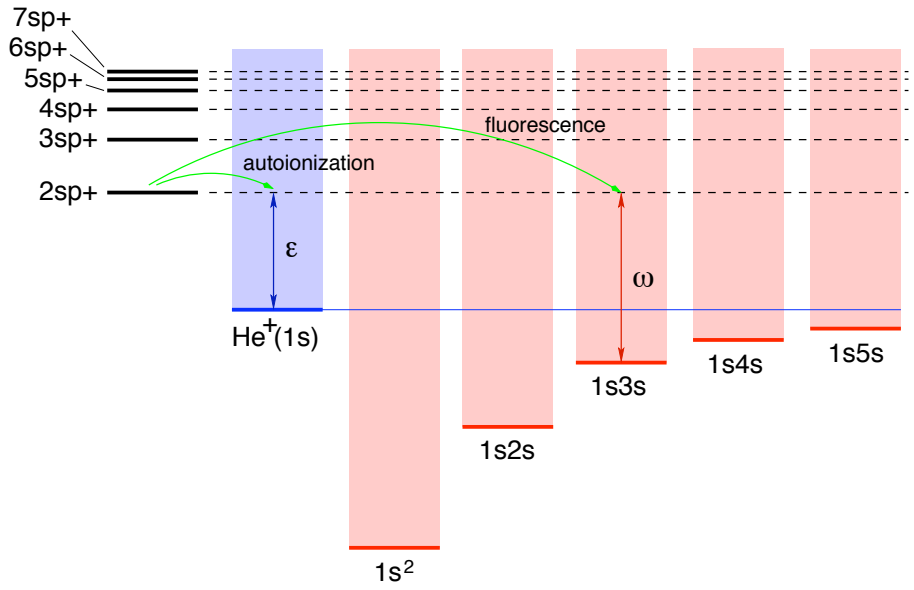

Figure 1.8: Schematic representation of autoionization and fluorescence decay channels

The close coupling autoionization wave functions are seeked then in the following form

$$|\Psi^{\wp}_{\alpha E}\rangle = |\phi_{\alpha E}\rangle + \sum_{\gamma} \sum\!\!\!\!\!\!\int d\epsilon |\phi_{\gamma\epsilon}\rangle \frac{\wp}{E-\epsilon} K_{\gamma\epsilon;\alpha E} + \sum_{d} \int^{\Omega_d} d\omega |d \otimes \omega\rangle \frac{\wp}{E - E_d - \omega} K_{d\omega;\alpha E} \tag{1.58}$$

where in $|d \otimes \omega\rangle$ the bound state d is coupled to a dipole photon to form a state with the same symmetry of autoionization channels $|\phi_{\alpha E}\rangle$. The ultraviolet cutoffs Ω_d have been introduced to regularize the integrals and can be chosen in such a way that they do not appear in the final, considerably simplified equations. A similar expression holds for the fluorescence channels

$$|\Psi^{\wp}_{a\omega}\rangle = |a \otimes \omega\rangle + \sum_{\gamma} \sum\!\!\!\!\!\!\int d\epsilon |\phi_{\gamma\epsilon}\rangle \frac{\wp}{E-\epsilon} K_{\gamma\epsilon;a\omega} + \sum_{d} \int^{\Omega_d} d\omega' |d \otimes \omega'\rangle \frac{\wp}{E - E_d - \omega'} K_{d\omega';a\omega} \tag{1.59}$$

where it is understood that $E = E_a + \omega$. These equations are transformed into a system of coupled integral equations through passages analogous to those followed in the previous sections. All the details and definitions of symbols are given in appendix E. The final system of equations for the components on autoionization

channels is very similar to the conventional K-matrix equation:

$$[1 - \mathsf{VP}(E)]\mathsf{K}_{\bullet,\alpha E} = \mathsf{V}(E)_{\bullet,\alpha E} \tag{1.60}$$

$$[1 - \mathsf{VP}(E)]\mathsf{K}_{\bullet,a\omega} = C\omega^{1/2}\nabla_{\bullet,a} \tag{1.61}$$

Actually, the K matrix between matter channels remains *unchanged* with respect to the case where the fluorescence channels are completely omitted. This remains thus the only time-consuming step. The components on the fluorescence channels are given in terms of the former solutions by

$$\mathsf{K}_{b\omega,\alpha E} = C\omega^{1/2}\left\{\nabla_{b,\alpha E} + \nabla_{b,\bullet}\mathsf{P}(E)\mathsf{K}_{\bullet,\alpha E}\right\} \tag{1.62}$$

$$\mathsf{K}_{b\omega',a\omega} = C\omega'^{1/2}\nabla_{b,\bullet}\mathsf{P}(E)\mathsf{K}_{\bullet,a\omega} \tag{1.63}$$

The on-shell K-matrix is manifestly symmetric. Even if the matter K-matrix is left unchanged, the transition matrices $\mathsf{T}^{\pm}$ *do* change, and so does the scattering matrix S as well as all the resonance widths.

In the case of just one discrete state i coupled to a fluorescence channel $a \otimes \omega$ a simple calculation leads to the following expression for the radiative linewidth:

$$\Gamma(E) = 2\pi C^2(E - E_a)|\nabla_{a,i}|^2$$

which coincides with the well known radiative decay rate of i. In appendix E, this method is applied, as an example, to the radiative decay of an autoionizing state.

Chapter 2

Singlet helium photoionization

2.1 Introduction

Despite the apparent simplicity of the helium system, its photoionization spectrum displays a richness of details that has begun to be fully appreciated only in the last two decades. The N-th ion threshold is announced by a resonance multiplet series with $(2N-1)$ terms which, for small N ($N \lesssim 7$) [23], can be labelled according to a set of approximate quantum numbers. When in a doubly excited state the outer electron is so far away from the nucleus that its effects on the inner electron can be approximated by a constant electric field, the available configurations of the inner electron are adequately labeled with the Stark quantum numbers N_1, N_2 and m [107]. A set of Stark quantum numbers therefore identify an asymptotic Rydberg series of doubly excited states with assigned inner electron principal quantum number $N = N_1 + N_2 + |m| + 1$, total spin, angular momentum, and parity. A single term in a series is identified with an additional index n for the principal quantum number of the outer electron: $[N_1 N_2 m]_n$. A further symbol $A = +/-/0$, originating in the molecular approximation scheme, is generally also specified (for further details on the many almost equivalent classification schemes of doubly excited states, see appendix F).

When many interacting doubly excited states with different N occur in the same energy interval, though, these approximate quantum numbers loose their meaning. This happens already below the N=4 threshold where, in the $^1P^o$ symmetry, the first intruder state, $[031]^+_5$, appears. As the energy rises, the increasing number of intruder states perturb the regularity of the photoionization spectrum [22, 24, 108] until, beyond N=9, it is virtually lost [23–25, 109].

Much theoretical work has been dedicated to the detailed study of anomalies above N = 4 threshold [21–24, 99, 108, 110]. Nevertheless, not earlier than a couple of years ago (2006), the aforementioned very first anomaly in the photoionization spectrum of helium was still only experimentally resolved [21]. This is because the $[031]^+_5$ perturber, which falls just ~ 10 meV below the $N = 4$ threshold, affects the underlying autoionizing Rydberg series in a region where the principal quantum number n of the outer electron is so large, $n \geq 14$, to seriously challenge ordinary R-

matrix programs, where all satellites are constrained within the quantization box. With the present implementation of the multiple-base B-spline K-matrix method instead, highly excited autoionizing Rydberg states are easily obtained with high accuracy, as far as only the outer electron is concerned. In the next section we discuss the first *ab initio* reproduction [111] of the experimental results mentioned above.

In dipole approximation, the angular distribution of any specific photoionization cross section (either total or partial) of helium is entirely described by a single dipole anisotropy parameter β. As far as we know, the first and only measurements of the partial cross sections asymmetry parameters β_N below N=6 are reported as preliminary data by Jiang and Püttner in Jiang PhD thesis [112]. A theoretical investigation of the photoionization spectrum under N=5 and N=6 thresholds was therefore undertaken [113] in order to reproduce their experimental findings. In sections 2.3 and 2.4 we discuss those results. We find a good agreement with all the available published data and a semi-quantitative agreement with Jiang and Püttner's β_N^6's.

When non dipolar interaction terms between the atom and the incident radiation field are taken into account, the many multipolar amplitudes resulting in the same final quantum state give rise to interference effects that alter the photoelectron dipolar angular distribution (see appendix B). To measure these effects in helium at low energies is particularly challenging as helium is much smaller than the employed radiation wavelength and they are consequently also small. In proximity of resonance features of both dipolar and quadrupolar electric (the leading non dipolar) cross sections, though, the latter may even become dominant, resulting in a sizable peak in the backward-forward photoelectron anisotropy, provided that the resolution is sufficiently high to resolve those resonances. The first successful measurement of this interference effect has been performed in 2002 by Krassig *et al* [114], but have not been reproduced yet with an *ab initio* calculation. In section 2.5 a set of such calculations is presented. A good quantitative agreement is found, with the exception of the immediate neighborhood of the dipolar Fano profile minimum, where the simulated nondipole anisotropy parameter is found to depend strongly on the experimental energy resolution.

2.2 $[031]_5^+$, the first intruder state

Let summarize briefly what is expected below the N = 4 threshold. The $^1P^o$ resonances accumulating at threshold are classified in seven series with different parabolic quantum numbers $[N_1N_2m]^A$ [99, 115]:

$$[021]^+,\ [111]^+,\ [201]^+,\ [030]^-,\ [120]^-,\ [210]^-,\ [300]^-.$$

The nine-fold degenerate underlying continuum where these resonances are embedded can be partitioned itself within the parabolic quantum number scheme:

- N = 1: $[000]^-$

- N = 2: $[001]^+$, $[010]^-$, $[100]^-$
- N = 3: $[011]^+$, $[101]^+$, $[020]^-$, $[110]^-$, $[200]^-$.

It is customary to define the reduced resonance width $\bar{\Gamma}$ and the quantum defect μ as

$$\bar{\Gamma}_n \equiv \Gamma_n \cdot (n^*)^3, \qquad n^* = 1/\sqrt{2(E_{thr} - E_n)}, \qquad \mu_n = n - n^*.$$

Within each series, $\bar{\Gamma}_n$ and μ_n are expected to converge to a limit characteristic of that series [94]

$$\bar{\Gamma}_n^{[N_1 N_2 m]^A} \longrightarrow \bar{\Gamma}_\infty^{[N_1 N_2 m]^A}, \qquad \mu_n^{[N_1 N_2 m]^A} \longrightarrow \mu_\infty^{[N_1 N_2 m]^A}.$$

In figure 2.1 the logarithm of reduced widths $\overline{\Gamma}$ of resonances below N = 4 threshold are reported as functions of the effective quantum number n^*, together with the available results by Rost *et al* [99] which reach $n^* = 11 \div 12$ (if not otherwise stated, all values are in atomic units and nuclear mass is considered infinite).

If we ignore for a while the deep quenching of $[021]^+$ series around $n^* \sim 14-15$, it is easy to discern three classes of series according to their asymptotic reduced widths

- I class: $[021]^+$, $[111]^+$, $[201]^+$, $\log_{10}\bar{\Gamma}_\infty \sim -0.5 \div -1.5$
- II class: $[030]^-$, $[120]^-$, $[210]^-$, $\log_{10}\bar{\Gamma}_\infty \sim -2.0 \div -2.5$
- III class: $[300]^-$, $\log_{10}\bar{\Gamma}_\infty \sim -4.0$

This is to be expected on the basis of propensity rules for non-radiative transitions [99] which describe three decay mechanisms of decreasing efficiency: a) $\Delta N_2 = -1$, b) $\Delta m = -1$, c) $\Delta N_1 \neq 0$.

Besides autoionization, doubly excited states may decay also through emission of radiation. The main mechanism is the radiative decay of the inner electron with principal quantum number N, to a lower state with principal quantum number N−1. To a first approximation, which improves as the outer electron is more excited, it is possible to estimate a lower limit to the radiative lifetime. It can be easily checked [116] that, considering the radiative lifetimes of the p inner electron orbitals, which have the shortest lifetimes, the lower limits for the radiative resonance width $\Gamma_{r,lim}$ range from $2,4 \cdot 10^{-7}$ au for N = 2 to $9.3 \cdot 10^{-9}$ au for N = 6. As already evidenced by Rubensson *et al* [117], the radiative decay mechanism cannot be neglected if one wants to make a proper comparison with the latest most accurate measurements on doubly excited states below the N = 2 threshold made possible by today experimental standards. The importance of the radiative decay changes much according to which energy interval is considered. Between the N = 3 and N = 4 threshold, just the narrowest $[300]^-$ series might be seriously broadened below $n = 30$. It is worth to mention that $\Gamma_{r,lim}$ generally overestimates the true radiative width since in doubly excited states the inner electron

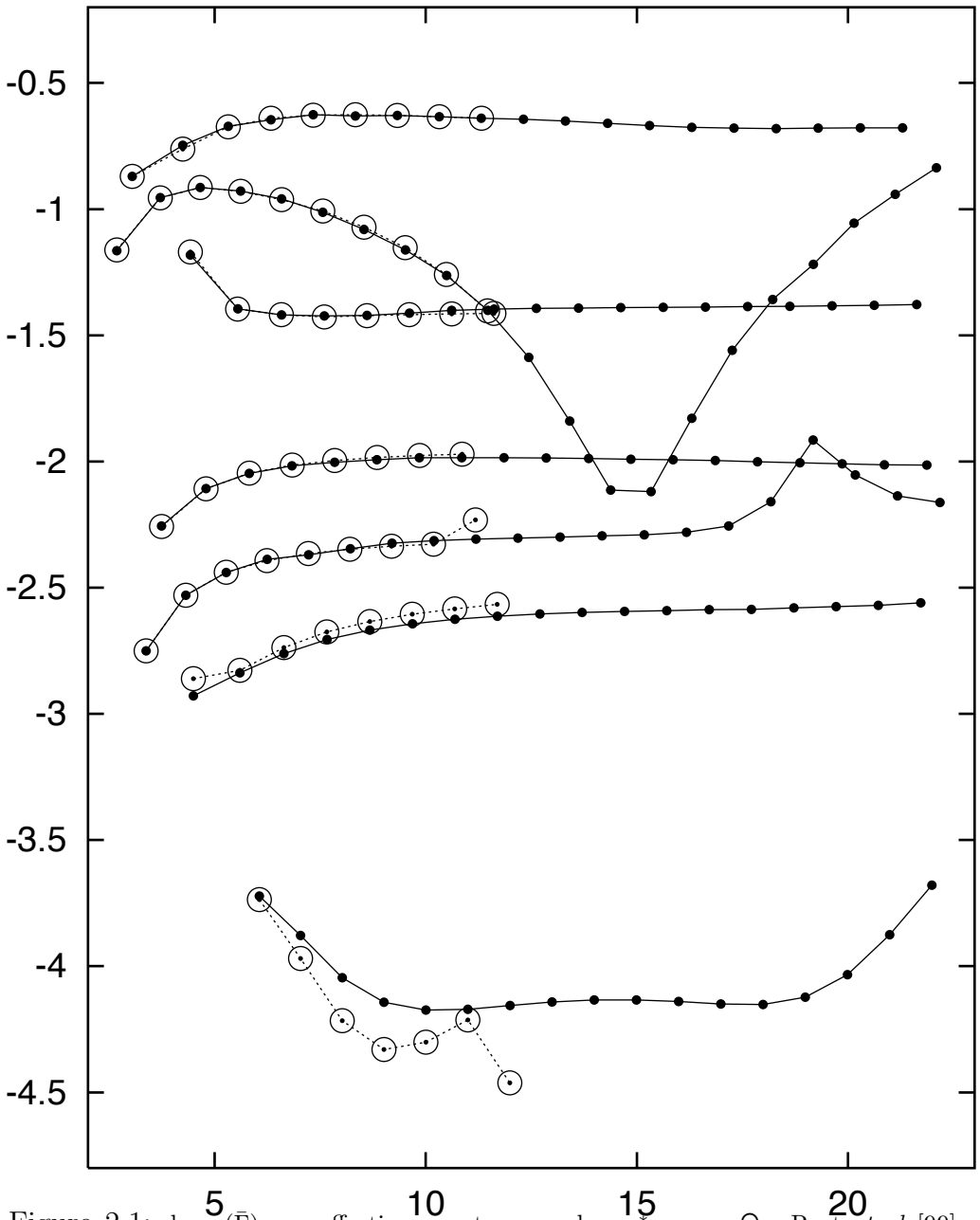

Figure 2.1: $\log_{10}(\bar{\Gamma})$ vs. effective quantum number n^*. ·····○ , Rost *et al* [99]; ——● , present work. The series, in decreasing order of width between $n^* = 5$ and $n^* = 10$, are $[111]^+$, $[021]^+$, $[201]^+$, $[120]^-$, $[030]^-$, $[210]^-$ and $[300]^-$.

has not a well defined angular momentum and its lifetime is enhanced by its non-p components, as already predicted theoretically [118, 119] and recently confirmed experimentally [120].

Resonance parameters for $[300]^-$ series cannot consequently be compared to experiment (were it available) since the radiative lifetime of inner $4p$ orbital ($\Gamma_{rad} \simeq 3.1 \cdot 10^{-8}$ au) is comparable to or shorter than the autoionization life-time. With the last three terms of the series, the reduced width begin to rise. This is most probably the symptom of an incipient loss of accuracy in the representation of Rydberg satellites, which hopefully compromises only this series even if further investigation may be required to confirm this.

At this point it's worth to mention that the same calculations were performed with a slightly larger localized basis set, which extended up to 70 au instead of 60 au, and no significant differences were observed. This means that within the energy interval examined in this article, all configurations with both electrons located beyond 60 au can be safely neglected.

The accord between the present resonance parameters and those published by Rost *et al* [99] is generally very good with few exceptions. The series computed by Rost *et al* begin probably to loose reliability in correspondence of the last term, as is apparent in $[030]^-$ and $[300]^-$ series. Moreover $[210]^-$ series has a slightly larger reduced width than that computed in the present paper. Their resonance parameters for $[210]^-$ series are actually in better agreement with those we obtained in a preliminary calculation where the maximum orbital angular momentum was equal to 4 instead of 6. It's plausible that in Rost *et al* results, part of the correlation in higher terms was lacking.

Finally, there is a relatively high discrepancy between $[300]^-$ series, but since widths by Rost *et al* have been published with only a couple of significant figures, their values are probably affected by a large uncertainty.

Once the general frame has been outlined, the interesting characteristic of this energy interval is clearly the anomalous behaviour of $[021]^+$ and $[030]^-$ series. A plot of $\log_{10}\overline{\Gamma}$ *versus* quantum defect is reported in figure 2.2. Five series, those indicated with letters b, c, d, f and g, converge rapidly to their limiting values, approaching μ_∞ from higher μ values. The $[021]^+_n$ series, indicated with the letter a, drifts toward higher quantum defects and suffer a strong quenching which reaches its maximum in correspondence of $n = 16 \div 17$. Finally $[030]^-_n$ series, indicated with the letter e, approaches its limiting quantum defect from below and experiences a clear spike in reduced width between $n = 20$ and $n = 24$ which corresponds to an opposite shoulder in the larger [021]+ series.

This phenomenology can be clarified if we join together the effects on the two irregular series in a total quantum defect and reduced width

$$\mu_n = \mu_n^{[021]^+} + \mu_n^{[030]^-}, \qquad \bar{\Gamma}_n = \bar{\Gamma}_n^{[021]^+} + \bar{\Gamma}_n^{[030]^-}.$$

In figure 2.3 μ_n and $\bar{\Gamma}_n$ are plotted as functions of the averaged energy of corresponding terms in the two series: $E_n = (E_n^{[021]^+} + E_n^{[030]^-})/2$. The collective quantum defect undergoes the characteristic increase due to the presence of an

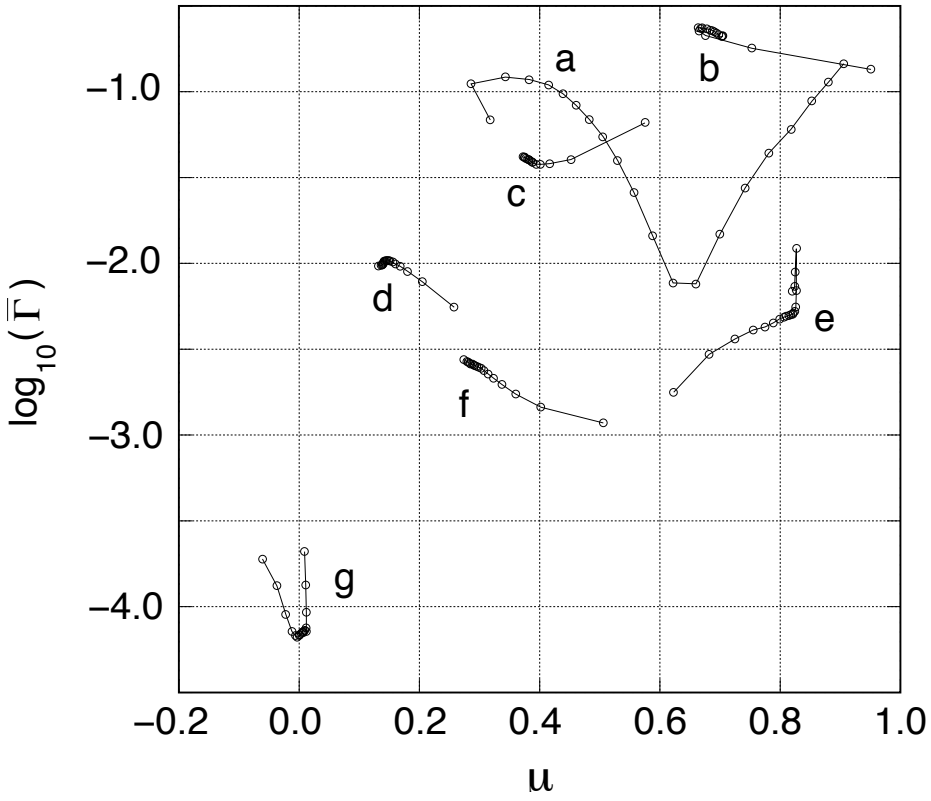

Figure 2.2: The seven series of $^1P^o$ doubly excited states below the N= 4 threshold in a plot of $log_{10}(\bar{\Gamma})$ vs. quantum defect μ (μ has been freely translated by integers for the sake of clarity). a) $[021]_n^+$, b) $[111]_n^+$, c) $[201]_n^+$, d) $[120]_n^-$, e) $[030]_n^-$, f) $[210]_n^-$, g) $[300]_n^-$. The two series $[021]^+$ and $[030]^-$ display an anomalous behaviour. This results is explained with the hypothesis of the $[031]_5^+$ satellite being an intruder state in this energy range.

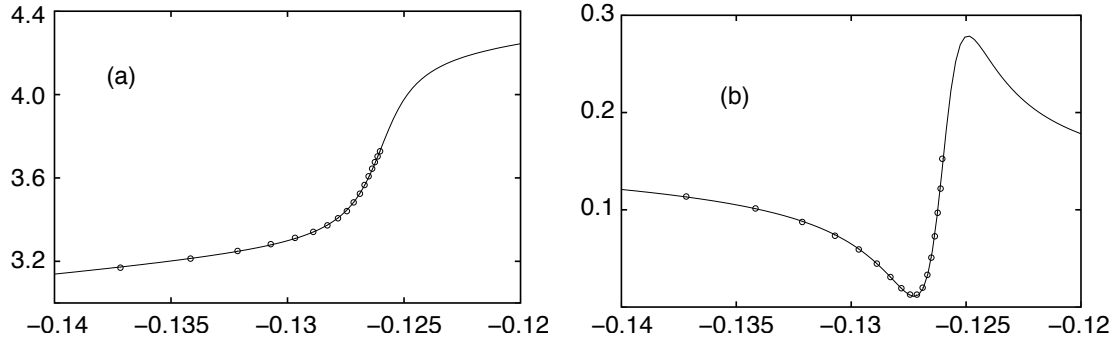

Figure 2.3: Compound quantum defect μ_n (a) (pure number) and reduced width $\bar{\Gamma}_n$ (b) (au) in proximity of the $[031]_5^+$ intruder state. On x-axis, energy in atomic units is reported. See text for more details.

Table 2.1: $[031]_5^+$ pseudo-resonance parameters.

E_0(au)	γ(au)	q	F^2	μ_0	μ_1	$\bar{\Gamma}_0$	$\bar{\Gamma}_1$
-0.1260	0.0012	-1.10	0.12	3.75	0.011	0.13	-0.001

intruder state which is known as $[031]_5^+$ [99, 121], the first term of a series with N = 5.

A similar phenomenon below N = 4 threshold has been already discussed for the simpler case of S doubly excited states [122, 123] where what is identified with the $(N, k)_5 = (5, 4)_5$ intruder state interacts with the $(4, 3)_n$ series leaving the other Rydberg series unaffected according to propensity rules. In that case the quantum defect jump occurs at around $0.004au$ below threshold, four times the distance of the present $[031]_5^+$ pseudo-resonance and is therefore much easier to be identified.

A first hint of experimental evidence of the $[031]_5^+$ intruder state has been suggested by Domke [20] and later confirmed by Püttner *et al* [21] in a high resolution experiment (2 meV) performed at the Advanced Light Source in Berkeley.

The anomalies are consistent with non-radiative propensity rules since the $[021]^+$ and $[030]^-$ resonances are actually the only ones which may be coupled with the $[031]_5^+$ intruder state. The two series act as an underlying continuum where the intruder state dissolves. Moreover, the intruder state couples the two series. When the $[021]^+$ series, which experiences a large μ drift, reaches the corresponding term in $[030]^-$ series, the two series mixes and a limited exchange of decay width is observed. This may explain the spike in $[030]^-$ and the corresponding shoulder in $[021]^+$ reduced width.

The continuous line in figure 2.3a is a least square fit to the points with the 4-parameter function

$$\mu = \mu_0 + \mu_1\epsilon + \frac{1}{\pi}\arctan(\epsilon), \quad \epsilon \equiv \frac{E - E_0}{\gamma}$$

a simple two parameter resonant profile and a linear background lead to a remarkable agreement with all seventeen points. Other four parameters are needed to fit the total reduced width in figure 2.3b, which is known to be modulated by a Fano shape [94] (resonance energy and width are taken from the previous fitting to keep the number of free parameters to a minimum)

$$\bar{\Gamma} = \left[\frac{(q-\epsilon)^2}{1+\epsilon^2} - 1\right] F^2 + \bar{\Gamma}_0 + \bar{\Gamma}_1\epsilon.$$

In table 2.1 the optimal values of the eight fitting parameters are reported. If this interpretation is correct, the effects of $[031]_5^+$ pseudo-resonance should be visible even across threshold. Unfortunately it was not possible to confirm this point since, in an interval of few tenth of eV above each threshold, our method exhibits oscillating results which are usually quenched in the otherwise more interesting higher part of the energy interval between two thresholds.

Table 2.2: $[021]^+$ (upper values) and $[030]^-$ (lower values) resonance parameters for $n = 12, 13$. The highest values in Rost *et al* classification [99] are reported for comparison. ($[-n] \equiv 10^{-n}$).

n	-E (au)	Γ (au)	E (eV)	Γ (eV)	μ	$\bar{\Gamma}(au)$
Rost *et al*	0.1295425	4.78[-5]				
12	0.1295400	4.72[-5]	75.47825	1.28[-3]	1.506	5.46[-2]
	0.1298115	4.58[-6]	75.47087	1.25[-4]	1.806	4.86[-3]
Rost *et al*	0.1298231	4.46[-6]				
Rost *et al*	0.1288034	2.62[-5]				
13	0.1288005	2.63[-5]	75.49837	7.15[-4]	1.530	3.97[-2]
	0.1289940	3.51[-6]	75.49311	9.56[-5]	1.811	4.92[-3]
Rost *et al*	0.1290039	4.2 [-6]				

Püttner *et al* [21] were drawn to similar conclusions by looking at the principal $[021]^+$ series without considering the contribution of $[030]^-$ series.

In table 2.2 we compare the resonance parameters of the $n = 12, 13$ terms in the two perturbed series with the highest values available in the paper of Rost *et al* [99]. An excellent agreement is found, as also figure 2.1 shows. In the same paper, the authors published also the parameters related to the $[031]_5^+$ resonance which, according to their calculation, should fall at -0.12640 au and have a width of $2.2[-3]$ au. These values are fictitious since there is no such thing as a single pole with dominant N=5 character. The intruder $[031]_5^+$ state is rather smoothly distributed over the two perturbed Rydberg series as it has been pointed out later by the same authors [21]. As a consequence, the two perturbed series are actually expected to exhibit a mixed $[021]^+/[030]^-/[031]^+$ character.

Partial photoionization cross sections to the $2s$ and $2p$ He^+ states were measured for the first time by Woodruff and Samson [14] up to N= 5 ionization threshold by measuring the yield of fluorescence photons in the decay of residual parent ion to fundamental $1s$ state ($2s$ state decays radiatively thanks to collisions). By means of a cylindrical electrostatic energy analyser, Zubek *et a* [124] succeeded in selecting $n = 2$ and $n = 3$ ionic yields below N= 4 threshold. Domke *et al* [15, 19, 20] published many results of total photoionization yield with an energy resolution $\Delta E \leq 6$ meV. The total cross section measure with the highest resolution, $\Delta E \leq 2$ meV, has been published by Püttner *et al* [21]. Absolute partial cross sections can be found in a paper by Menzel *et al* [125]. In 2003 Harries *et al* [126] published the first measures of $\sigma_{n\ell}$, the partial cross sections resolved both in principal and in angular quantum numbers. For a thorough review of the experimental determination of the asymmetry parameter prior to 1991 see Zubek *et al* [17]. For more recent results see [125].

On the theoretical side a number of authors investigated the energy interval below N= 4 ionization threshold [22, 78, 108, 127–130], unfortunately without reproducing its features in the neighborhood of threshold.

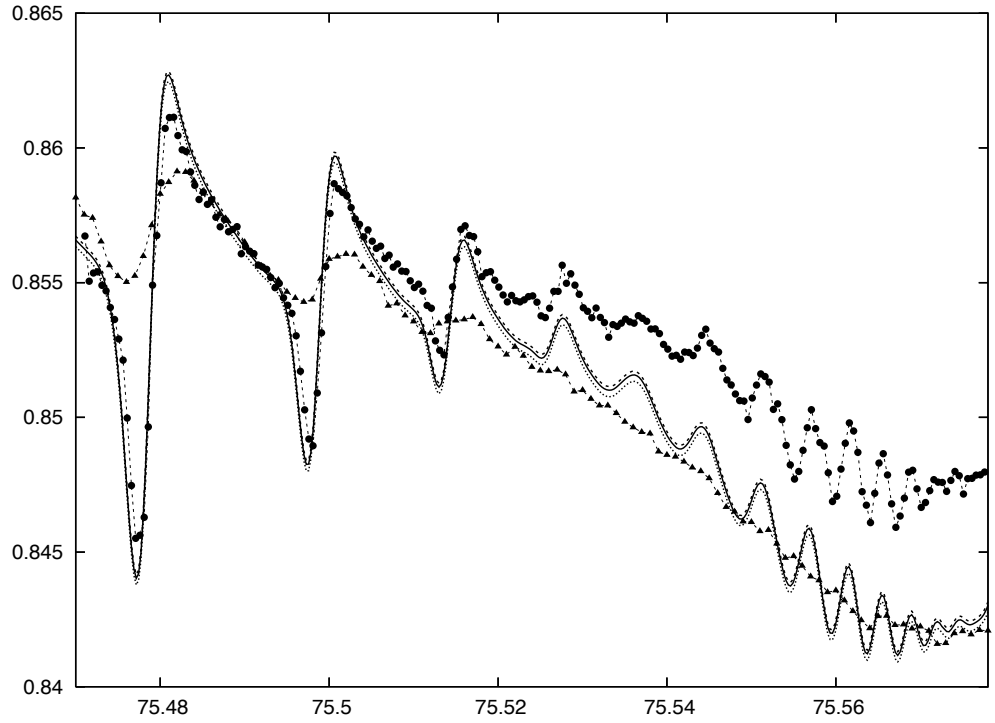

Figure 2.4: Total photoionization cross sections of Helium below N= 4 threshold in the energy window where the effects of $[031]_5^+$ appear. Cross sections is given in Mb. On the x axis the photon energy in eV is reported. Theoretical predictions: ——velocity gauge, ·····acceleration gauge, - - - -length gauge. Experimental data: - - - -●- - - -Püttner *et al* (1999) [21], - - - -▲- - - -Domke *et al* (1996) [19].

In figure 2.4 we have compared our theoretical prediction of total cross section, through the well known expression (see appendix B for the definition of symbols)

$$\sigma = \sum_{\alpha} \sigma_{\alpha}, \quad \sigma_{\alpha} = \frac{\pi}{3\, c\, \omega_{\gamma}(2L_0+1)} \sum_{L\ell_{\alpha}} \left| \langle \phi_0 \| \hat{V}_1^0 \| \psi_{\alpha E \ell_{\alpha}}^{(-)\Gamma} \rangle \right|^2 . \tag{2.1}$$

in the neighborhood of the resonance quenching caused by the $[031]_5^+$ intruder state with the experimental results by Püttner *et al* (1999) [21] and Domke *et al* (1996) [19]. Theoretical data have been convoluted with a gaussian resolution function, FWHM= 2.36 meV. The small rounded peak that appears in the last 2 meV of each spectrum is a boundary effect of the convolution algorithm and can be safely ignored. The intruder state manifests itself in cross sections and asymmetry parameter as a clear change of character between 75.47 eV and 75.58 eV.

Our and experimental data are in substantial agreement. There is actually a small inconsistency between baselines of the two experimental data set. Our theoretical prediction reproduces the oscillating details of the high resolution data by Püttner *et al* [21] and follows faithfully the baseline of the 6 meV resolution data by Domke *et al* [19]. Experimental data, which are given in arbitrary units, have been scaled and shifted in energy to fit our theoretical prediction. Photon

energies in experimental data sets by Domke and Püttner have been lowered by 9 meV and 5 meV respectively.

All our calculations compare favorably with experimental and theoretical results cited thus far. Every cross section and asymmetry parameter has been calculated in length, velocity and acceleration gauges. The excellent gauge accord, the three being almost indistinguishable, certifies both convergence and accuracy of our computation. Further results in this energy window on partial photoionization cross sections and asymmetry parameters are reported in appendix L.

2.3 Below N=5 threshold

Many experiments have been devoted to the energy interval below N=5 threshold to find total cross section [14,15,20,131], partial cross sections [17,110,124,125,131, 132], total [17] and partial [125,131] dipole asymmetry parameters. In some cases, resonance parameters have been extracted from experimental results [15,20]. In the following we will compare mainly to the measurements by Domke *et al* [20] with a photon beam of FWHM 5.4 meV for the total cross section, to the measurements by Menzel *et al* [131] with 12 meV FWHM resolution for the β_n and σ_n, and to the more recent σ_n measurements by Jiang and Püttner [110] obtained with a resolution of 6 meV FWHM.

On the theoretical side, a large number of techniques have been applied. Resonance parameters are generally determined by means of complex rotation. Here we will refer to the review by Rost, Schulz, Domke and Kaindl [99] for both doubly excited states classification schemes and comparison of resonance parameters. In the calculation of total and partial cross sections and asymmetry parameters, R-matrix method has been the favored one. See in particular the papers by Schneider, Liu and Rost [108], by van der Hart and Greene [22], where a B-spline basis has been adopted, and to references cited therein.

All the calculations were carried out with a maximum orbital angular momentum $\ell_{max} = 6$, obtaining $E(1^1S^e) = -2.903\,642\,673$ au for the energy of the ground state (accurate electrostatic limit $-2.903\,724\,377$ au [133]) in good agreement with the estimated limit for $\ell_{max} = 6$ of $-2.903\,643\,88$ au [134]. The Rydberg constant used for the binary system $^4He^+$ - e^- is $R_{^4He^+} = \frac{M_{^4He^+}}{M_{^4He}} R_h = 13.603828(12)$ eV.

The energy scale is given by the experimental first ionization potential of helium plus the theoretical excitation energy with respect to the ground state of He^+.

Since parent He^+ states are built in a finite size box, energies of states with different angular momenta differ by tiny amounts. N=5 threshold energy ranges from $-0.\ 079\ 999\ 942$ au for $5s$ level to $-0.\ 079\ 999\ 999$ au for $5g$ level. N=6 threshold energies ranges from $-0.\ 055\ 555\ 235$ au for $6s$ level to $-0.\ 055\ 555\ 553$ au for $6h$ level. An average over all angular momenta is taken as reference: $E^5_{av} = -0.\ 079\ 999\ 977$ au, $E^6_{av} = -0.\ 055\ 555\ 410$ au. These discrepancies are much smaller than the estimated errors upon the calculated energies of the two electron states.

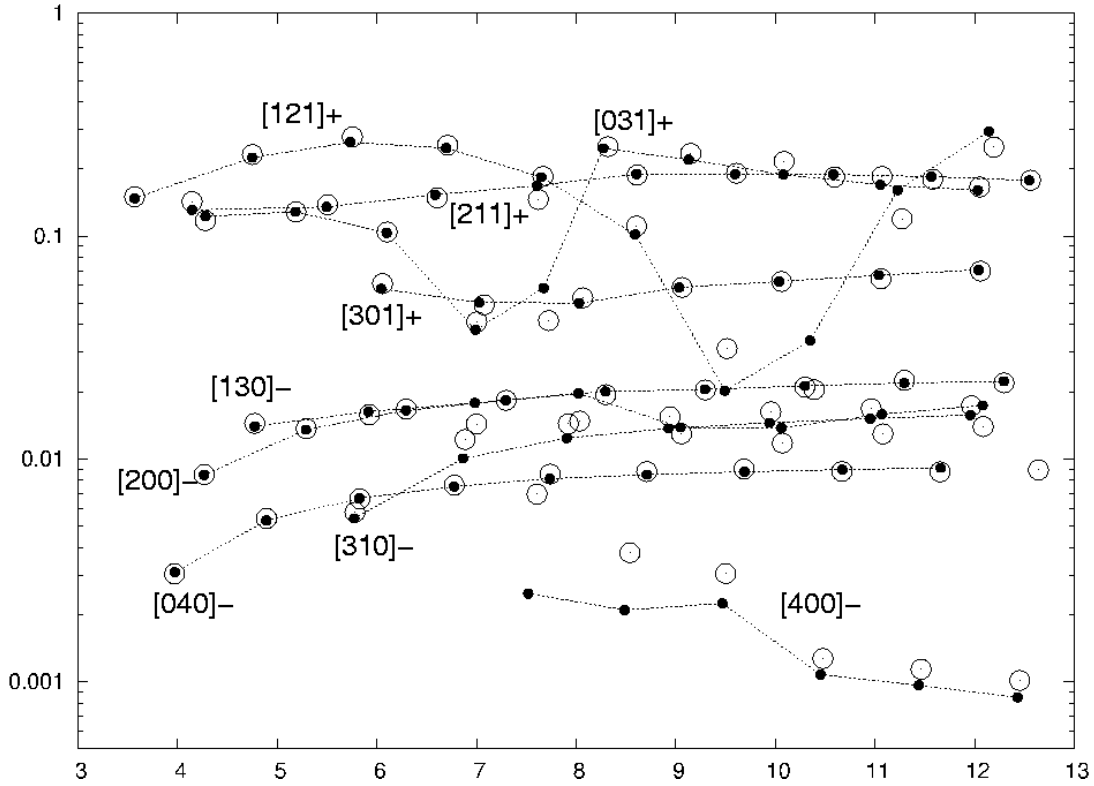

Figure 2.5: Log of the reduced width $\bar{\Gamma}$ *versus* the effective principal quantum number n^* of the 9 series in the N=4-N=5 interval. • - Rost *et al* ; ∘ - present results.

Resonances. In figure 2.5 our theoretical results are compared with those by Rost *et al* [99] in a reduced width, $\bar{\Gamma} = \Gamma \cdot (n^*)^3$, *vs* effective principal quantum number n^* plot. There is an excellent agreement for [211]+, $[301]^+$, $[130]^-$ and $[040]^-$ series which all display a regular behavior.

As is well known, two intruder states formally belonging to two series converging to the higher N=6 threshold fall in this energy interval, the $[041]^+$ state which causes the modulation of $[031]^+$ series, and the $[131]^+$ state, which causes the $[121]^+$ series quenching (see [99] for more details). Also for these two perturbed series there is still a fairly good agreement.

The $[200]^-$ and $[310]^-$ series differ slightly in our and in Rost treatment. In our calculations the two series come closer a couple of terms earlier than in Rost results but remains more separated in width, while those calculated by Rost yield almost indistinguishable doublets.

An inferior agreement is found in the narrowest $[400]^-$ series. Extremely narrow series are more difficult to be determined numerically and absolute differences are actually much amplified in a logarithmic scale, so that at the moment we cannot conclude if these differences are due to a different representation of system dynamics or rather to the width determining algorithm.

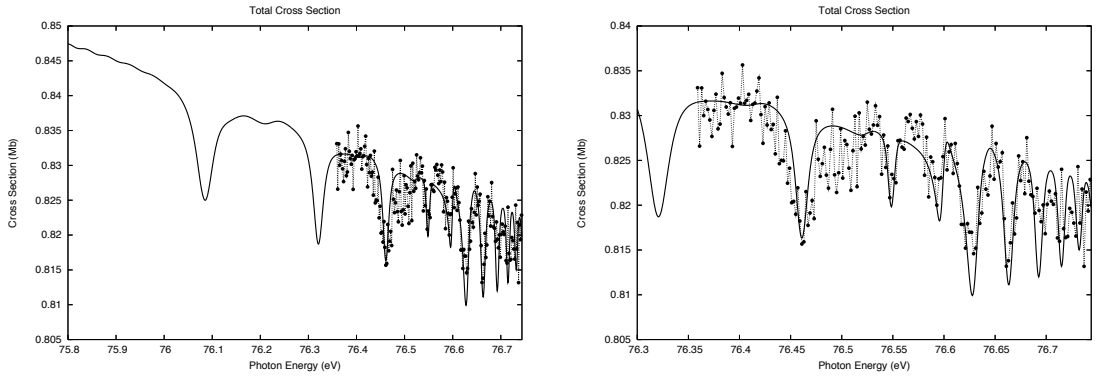

Figure 2.6: Total cross sections below N=5 threshold compared with measurements by Menzel *et al* ($\bullet\cdots\bullet$) [125]. Experimental results have been scaled by a factor 1.048.

Cross sections. In figure 2.6 the original total cross sections is compared with experimental data by Menzel *et al* [125, 131] scaled with a factor 1.048.

In figure 2.7, our theoretical partial cross sections have been compared with data by Menzel *et al* [125, 131] and by Jiang *et al* [110]. Data by Jiang are on an arbitrary scale so a suitable factor has been applied. As for the total cross section, a scale factor has been applied even to partial cross sections: 1.062 (n=1), 0.905 (n=2), 1.0 (n=3,4). It is interesting here to observe that almost identical scaling factors (1.05 for σ_{tot}, 1.06 for σ_1, 0.915 for σ_2, 1.0 for $\sigma_{3,4}$) have been applied by the same author in their original experimental/theoretical paper [131] in order to compare the experimental data with the computed ones. In reporting the experimental data for $\sigma_{3,4}$, an energy shift of -3 meV and $+2$ meV has been applied to Jiang and Menzel data respectively. All partial cross sections have been convoluted with a FWHM = 6 meV gaussian. All experimental and theoretical data agree very well. Menzel data have a much smaller dispersion than those by Jiang, but the energy resolution is slightly smaller. Very good agreement is found with Jiang data even for the height of the narrowest peaks.

Asymmetry parameters. In dipole approximation, the angular distribution of electrons emitted in the photoionization of an unoriented system by a linearly polarized incident light is general [135] and completely described by means of a single asymmetry parameter β

$$\frac{d\sigma}{d\Omega} = \frac{\sigma}{4\pi}\left[1 + \beta\ (3\cos^2\theta - 1)/2\right] \tag{2.2}$$

where θ is the angle between the momentum of the ejected electron and the light polarization axis. Expressions like (2.2) hold for partial and total cross sections $\sigma_{n\ell}$, σ_n and σ_{tot} with weighted asymmetry parameters:

$$\beta_n = \sum_\ell \sigma_{n\ell}\beta_{n\ell}/\sigma_n, \qquad \beta_{tot} = \sum_n \sigma_n\beta_n/\sigma$$

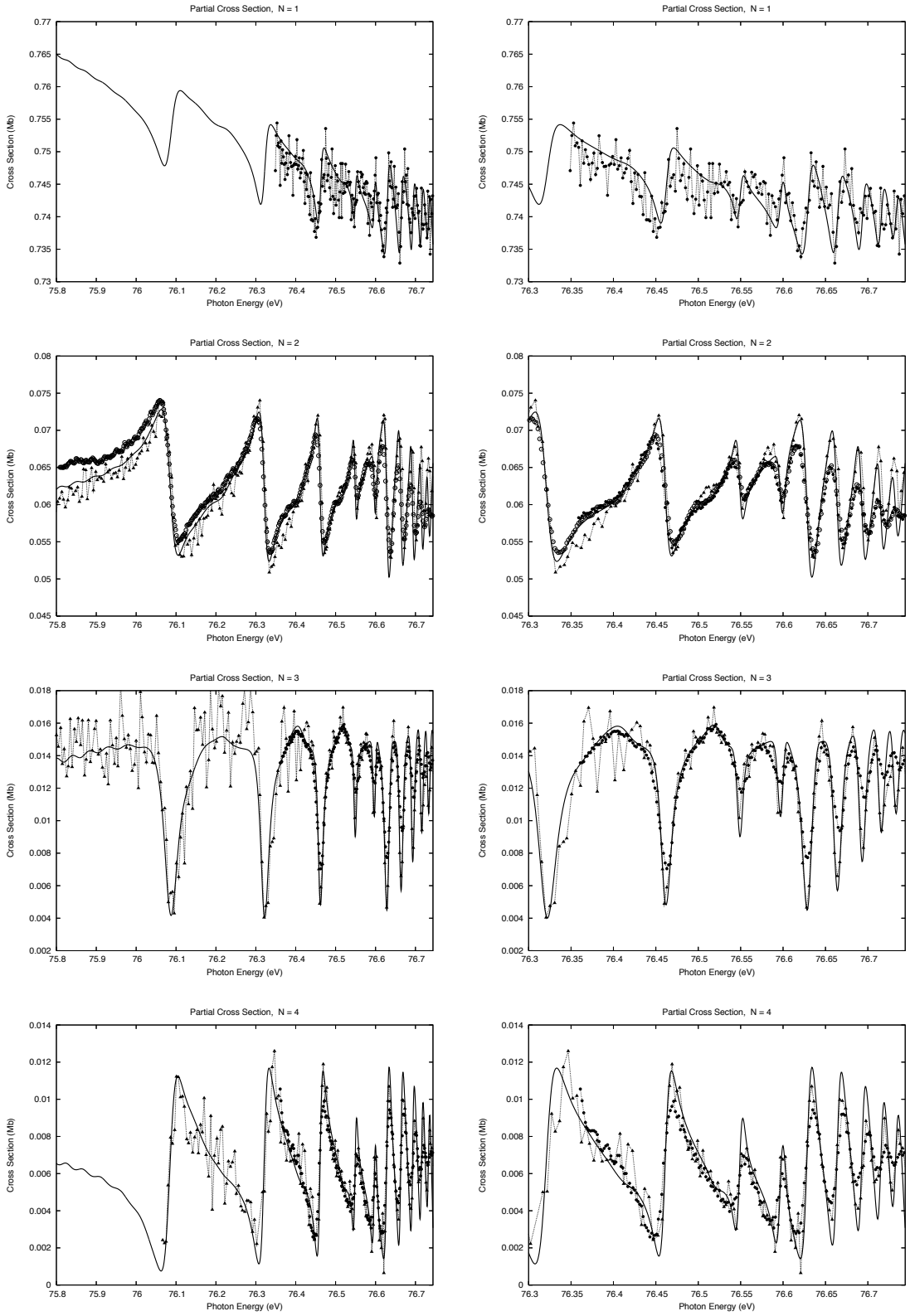

Figure 2.7: Partial cross sections σ_n below N=5 He^+ excitation threshold compared with data by Menzel *et al* $\bullet\cdots\bullet$, $\circ\cdots\circ$ [125] and by Jiang *et al* $\blacktriangle\cdots\blacktriangle$ [110].

Calculation and measurement of the beta parameters is well known to be much more demanding than that of partial cross sections. In figure 2.8 the β_n parameters, convoluted with a 12 meV FWHM gaussian, have been compared with experimental data by Menzel [125] and Jiang [110]. There is a good agreement in the resonant features of all plots. The largest absolute disagreement between the two experiments ($\Delta\beta_2 \simeq 0.1$)and between theory and experiment ($\Delta\beta_2 \simeq 0.25$) is found for β_2. The data of Menzel are actually much more pronounced also in resonant features so that, by chance, they are reproduced with good approximations by twice our theoretical prediction. The absolute agreement is good in β_3 with Jiang data and in β_4 with Menzel data.

2.4 Below N=6 threshold

Cross sections. For cross sections, the agreement with available data is better than among resonances: here minor peaks in the theoretical predictions are not found in the experimental picture, but all main features are reasonably reproduced.

In figure 2.10 the partial cross sections σ_n are compared with the experimental results by Jiang *et al* [110]. The theoretical results are convoluted with 10 meV (σ_{tot}) and 6 meV (σ_n) FWHM gaussian for a ready comparison with the cited experimental literature. In figure 2.9 a linear background ($= -0.034\cdot(E-77.1\,\mathrm{eV})$) has been subtracted to the total cross section for a clearer comparison with data by Domke *et al* [20]. The original cross section has a negative slope similar to σ_1 which is the dominant contribution. Experimental $\sigma_{2,3,4}$ have been shifted by 15 meV at lower energies for a closer comparison with our theoretical prediction. The two dominant peaks at 76.9 eV and at 77.05 eV as well as the first four peaks in the group between 77.13 eV and 77.4 eV show a good correspondence. The last peaks are instead progressively more out of phase with a disagreement in the position of the last cumulative peak by roughly 15 meV. A problem of energy scale convention might be the origin of this discrepancy. Experimental σ_5 data are available in the energy window between 77.15 eV and N=6 threshold. With an energy shift of 8 meV downward, a remarkable agreement between several of the higher energy peaks is obtained.

Dipole Asymmetry Parameters. As far as we know, theoretical partial cross section asymmetry parameters below N=6 threshold have not yet been published and their experimental measurements appeared only in Jiang PhD dissertation (freely available online [112]). In figure 2.11 our theoretical predictions are compared with existing measurements. β agreement is pretty good in absolute value and some resonant features are clearly recognizable. Experimental β_2 data lies between 0.41 and 0.51 while our theoretical prediction lies between 0.46 and 0.54 which results in an average difference of 0.04 which is relatively small. A clear correspondence between peak at 77.0 eV, valley at 77.08 eV and peak at 77.15 eV can be seen. Experimental and theoretical β_3 differ on average by ~ 0.1 units, and there is still a correspondence between three features analogous to those ob-

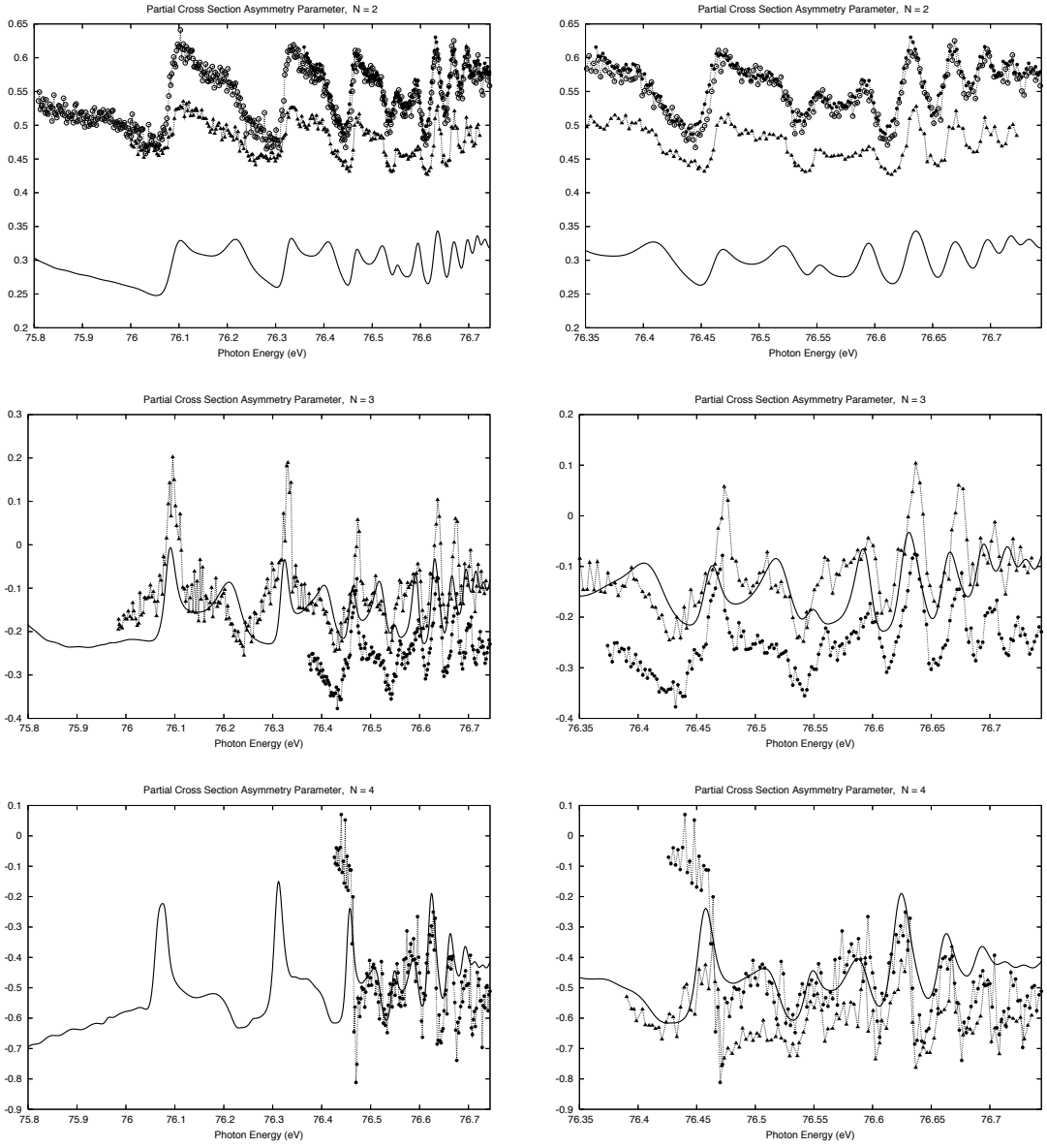

Figure 2.8: Asymmetry parameters below N=5 threshold compared with data by Menzel *et al* $\bullet\cdots\bullet$, *circ* $\cdots\circ$ [125] and Jiang *et al* $\blacktriangle\cdots\blacktriangle$ [110].

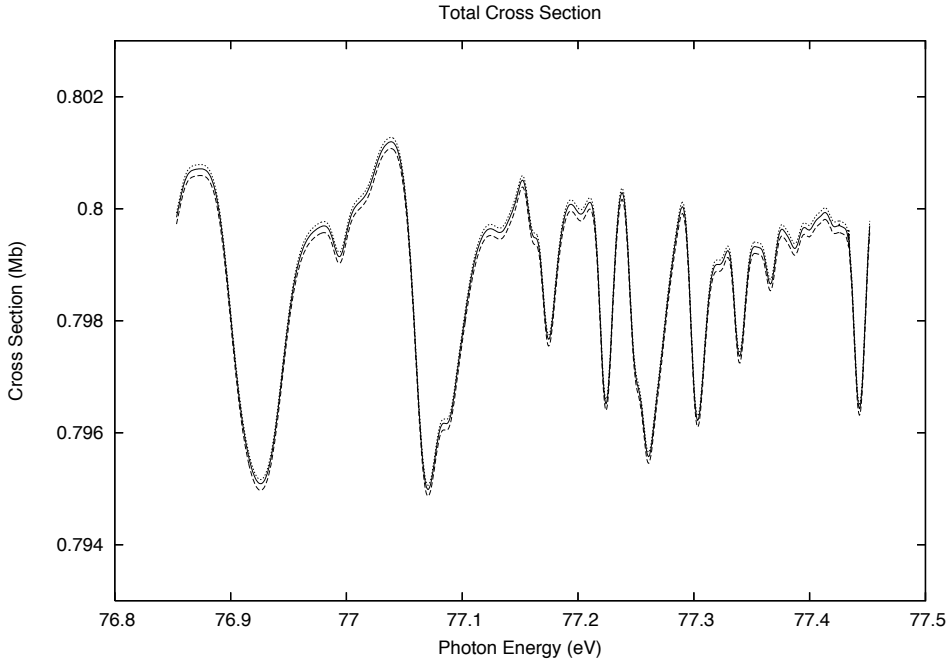

Figure 2.9: Total cross sections below N=6 threshold. Baseline has been subtracted for a better comparison with experimental data by Domke.

served in β_2. It should be noted that modulations in theoretical and experimental quantity are of comparable amplitude. In β_4 a difference of ~ 0.15 units between theory and experiment is found. A steep peak at ~ 77.8 eV is the most remarkable feature common to both experimental and theoretical data. Other correspondences are difficult to ascertain. There are no experimental data for a comparison with β_5. With the present knowledge, the predictive value of our plot should be limited to the most evident features, that is a definitely negative average value, large variations of angular distribution (β changes by as much as 0.7 units with this convolution width) and most probably a narrow peak at 76.9 eV, a broader peak between 77.0 and 77.1 eV and two valleys after them.

2.5 Non dipole effects

As shown in appendix B, magnetic dipole and electric quadrupole transitions give rise to a peculiar photoelectron angular distribution fully described by two additional parameters γ and δ, beyond the dipole anisotropy parameter β:

$$\frac{\partial\sigma^{\updownarrow}}{\partial\Omega} = \frac{\sigma}{4\pi}\left\{1 + \beta\cdot\frac{3\cos^2\theta - 1}{2} + (\delta + \gamma\cos^2\theta)\times\sin\theta\cos\phi\right\} \tag{2.3}$$

Non dipole transition amplitudes are typically two order of magnitudes ($\sim 1/c$) smaller than dipole amplitudes. Their contribution to the total cross section is therefore usually negligible. The alteration of the angular distribution may instead be sizable and even macroscopic, specifically near non-dipole resonant transitions or

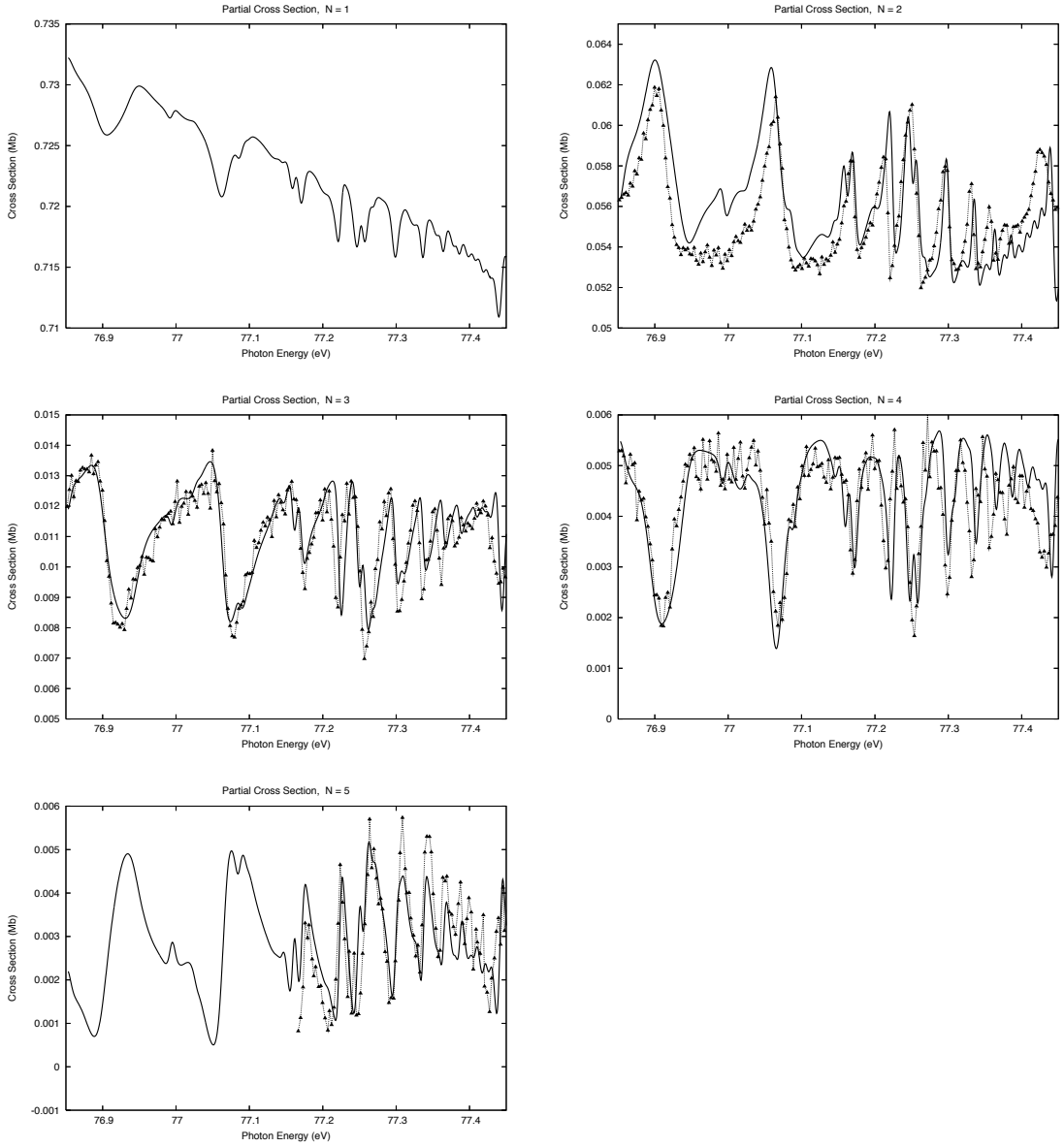

Figure 2.10: Partial cross sections below N=6 threshold. Comparison is made with experimental results by Jiang *et al* [110] where available.

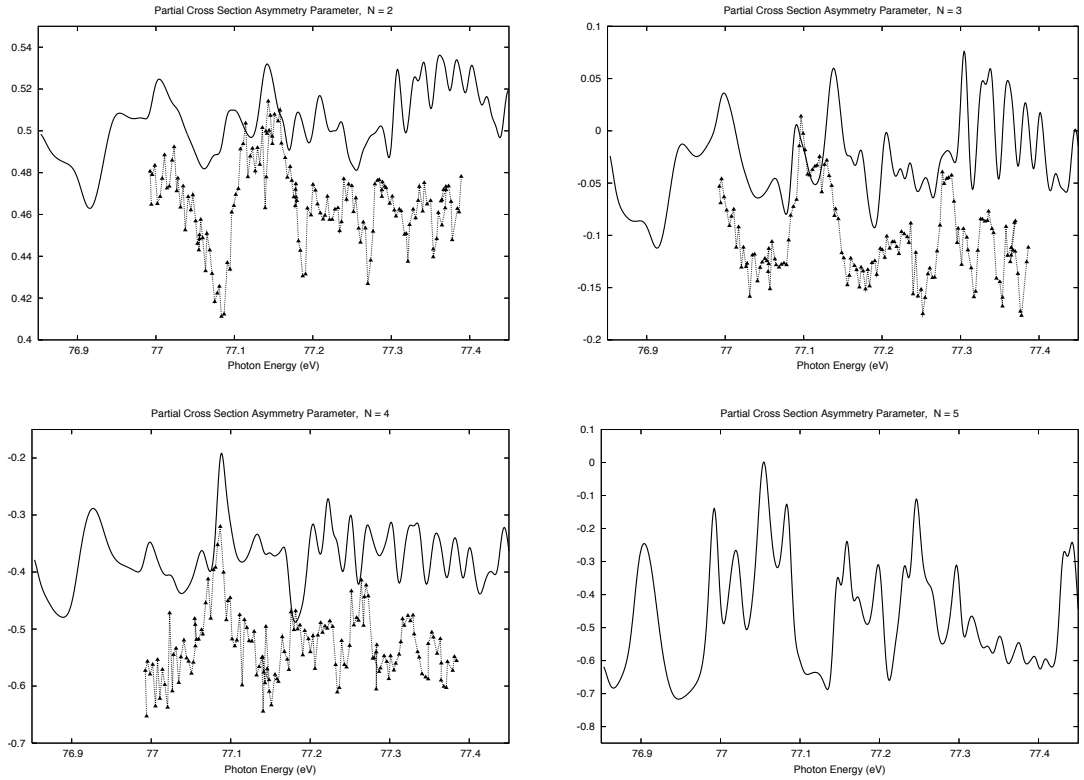

Figure 2.11: Partial cross section asymmetry parameters below N=6 threshold. Experimental data ▲ ··· ▲ are taken from Jiang PhD dissertation.

for very diffuse systems. The most striking effect is a forward-backward anisotropy. At large energies this phenomenon, also known as retardation effect, appears as a structureless drag in the forward direction, simply due to the photon momentum transfer to the ejected electron [136].

The backward-forward anisotropy results in a net electronic current [137, 138] which has been suggested to be in connection with selective diffusive separation of chemical elements in stars under radiation pressures [139].

Low energy nondipole effects are expected in very diffuse systems. In 1986 Leuchs *et al* [140] indeed observed the interference between quadrupole and dipole transitions in low-energy (2 eV) photoionization from a sodium rydberg state.

Later, evidences of low-energy non-dipole effects were found even in small systems, thanks to the resonant character of quadrupolar transitions. Martin *et al* [141] measured the E1-E2 interference in Cadmium, with values which are 0.5% of the dipole cross section for photon energies as low as 13 eV.

In rare gases in particular, the anisotropy is very large [142,143]. Dolmatov and Manson [144] observed it in Ne and Ar at energies as low as few tens of eV, and found it to be comparable to or even larger than nondipole terms from hundreds to thousands of eV. A large number of similar experimental results have been gathered since [145–151]

The nondipole effects in helium are much less pronounced than in the heavier atoms. The first observation of a backward-forward asymmetry, due to the dipole-forbidden $1s^2{}^1\mathrm{S}\rightarrow 2p^2{}^1\mathrm{D}_2$ resonance below N=2 threshold, was made few years ago (2002) by Krässig, Kanter *et al* [40, 114].

We are not aware of any *ab initio* calculation of the γ resonant profile: the existing theoretical predictions are based on simple models with few parameters. In the following we report the results of a fully *ab initio* calculation of the γ parameter. The analytical expression for γ when a linearly polarized incident radiation is assumed and when both the initial atomic state and the final parent ion state are S states is the following:

$$\gamma_\alpha = -9\sqrt{2}\frac{Re\left(\langle\phi_0\|\hat{V}_1^0\|\bar{\psi}_{\alpha Ep}^{(-)P}\rangle\langle\phi_0\|\hat{V}_2^1\|\bar{\psi}_{\alpha Ed}^{(-)D}\rangle^*\right)}{\left|\langle\phi_0\|\hat{V}_1^0\|\psi_{\alpha Ep}^{(-)P}\rangle\right|^2}, \tag{2.4}$$

see appendix B for the derivation.

In figure 2.12 all the involved quantities are reported: the dipole cross section (red curve), the electric quadrupole cross section (blue curve, amplified by a factor 10^5), and the "interference cross section" $\gamma\sigma$, as it appear in equation 2.3 (green curve, amplified by a factor 10^3).

Some considerations on few details are to be drawn here. First of all, the expressions given above for the γ anisotropy parameter is only valid when the dipole cross section is much larger than all the others. This is clearly not the case in the neighborhood of the minimum of the dipolar Fano profile (red curve in figure 2.12). Actually both the interference term and the dipolar cross section are zero there. In this case the appropriate expression for the gamma parameter simply makes use

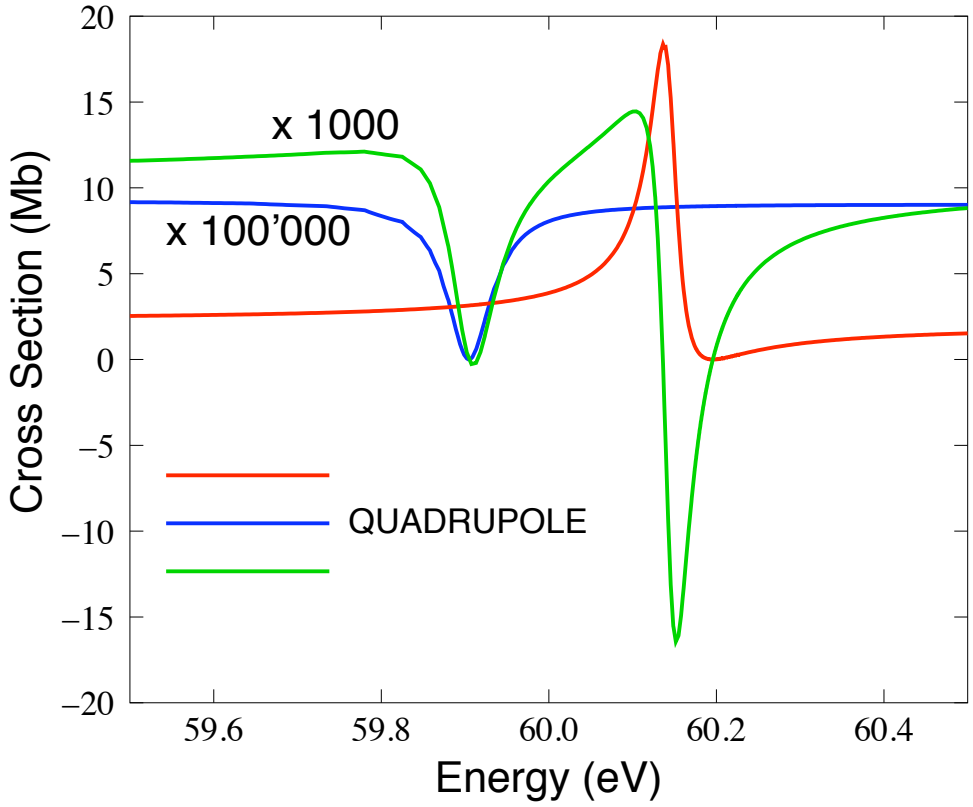

Figure 2.12: Cross sections involved in the calculation of the non dipole effects in the photoionization cross section of the helium fundamental singlet state near the first couple of $^1P^o$ and $^1D^e$ doubly excited states. The quadrupole channel total cross section (in blue) contribute negligibly to the total cross section as the ordinary dipole total cross section (in red) dominates by a factor 10^5. The angular distribution of the cross section instead is influenced by sizable amounts, depending on the interference term (in green) which is linear with respect to the quadrupole transition amplitude. The deviation from a dipole angular distribution is largest around the maximum of the quadrupole cross section, near the quadrupole resonance, and near the zero of the dipole cross section.

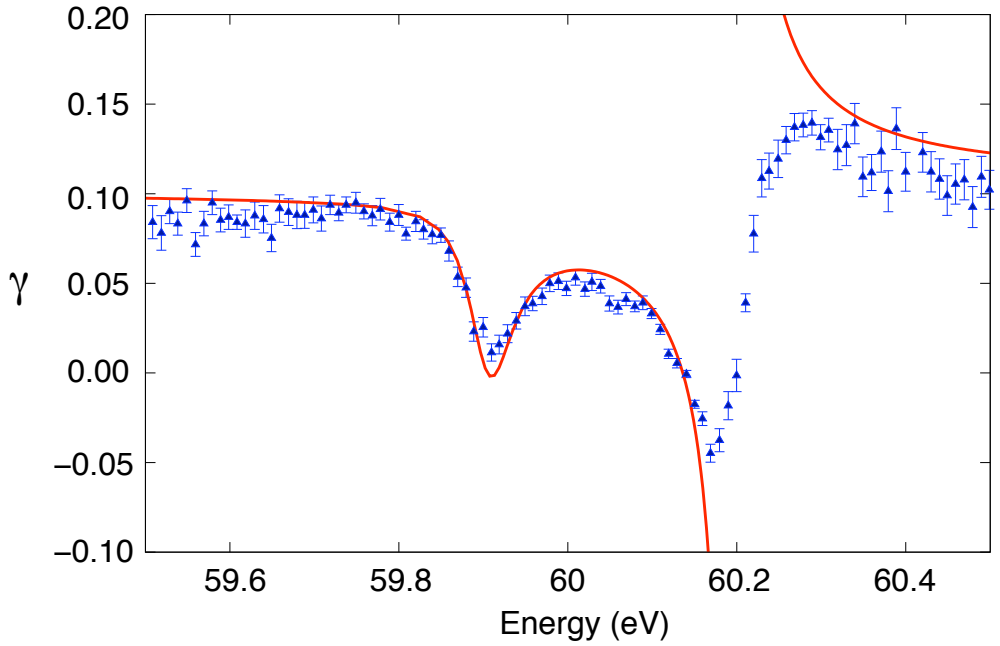

Figure 2.13: Comparison between the experimental and the unconvoluted theoretical γ factor. There is in general already a very good agreement with the most prominent exception of an energy interval of 0.1 eV across the dipole resonance. The experimental values are by Krassig *et al* [114]

of the total cross section, dipolar and quadrupolar, in the denominator of 2.4. In this way the γ parameter is well defined and regular in the whole energy interval. We shall see however that much more drastic regularization are required in order to compare positively with the experiment, performed with an energy resolution of some tens meV. In figure 2.13 the Krassig's experimental results are compared with our theoretical prediction. There is a remarkable quantitative agreement in the whole region except near the zero of the dipolar cross section. Clearly some further regularization is required. 20 meV FWHM experimental resolution are declared. In the upper panel of figure 2.14 we report the convoluted gamma factor with gaussian weight functions with FWHM=20, 30 and 40 meV. The experimental data far from 60.2 eV are in substantial agreement with all these resolutions, but the large positive and negative peaks do not still compensate. As the measurement is performed taking the ratio between two photoionization cross sections, though, the proper convolution procedure requires first that both the interference term and total cross section term be separately convoluted, and only then the ratio of the two to be taken. In this way we obtained the predictions reported in the lower panel in figure 2.14. A better agreement is then found, even if a significant discrepancy at $E \sim 60.25$ eV still persists.

In our opinion the structure induced in the γ parameter by the zeroes of the dipole cross section should be quietly recognized as the plain artifact of an unbecoming definition.

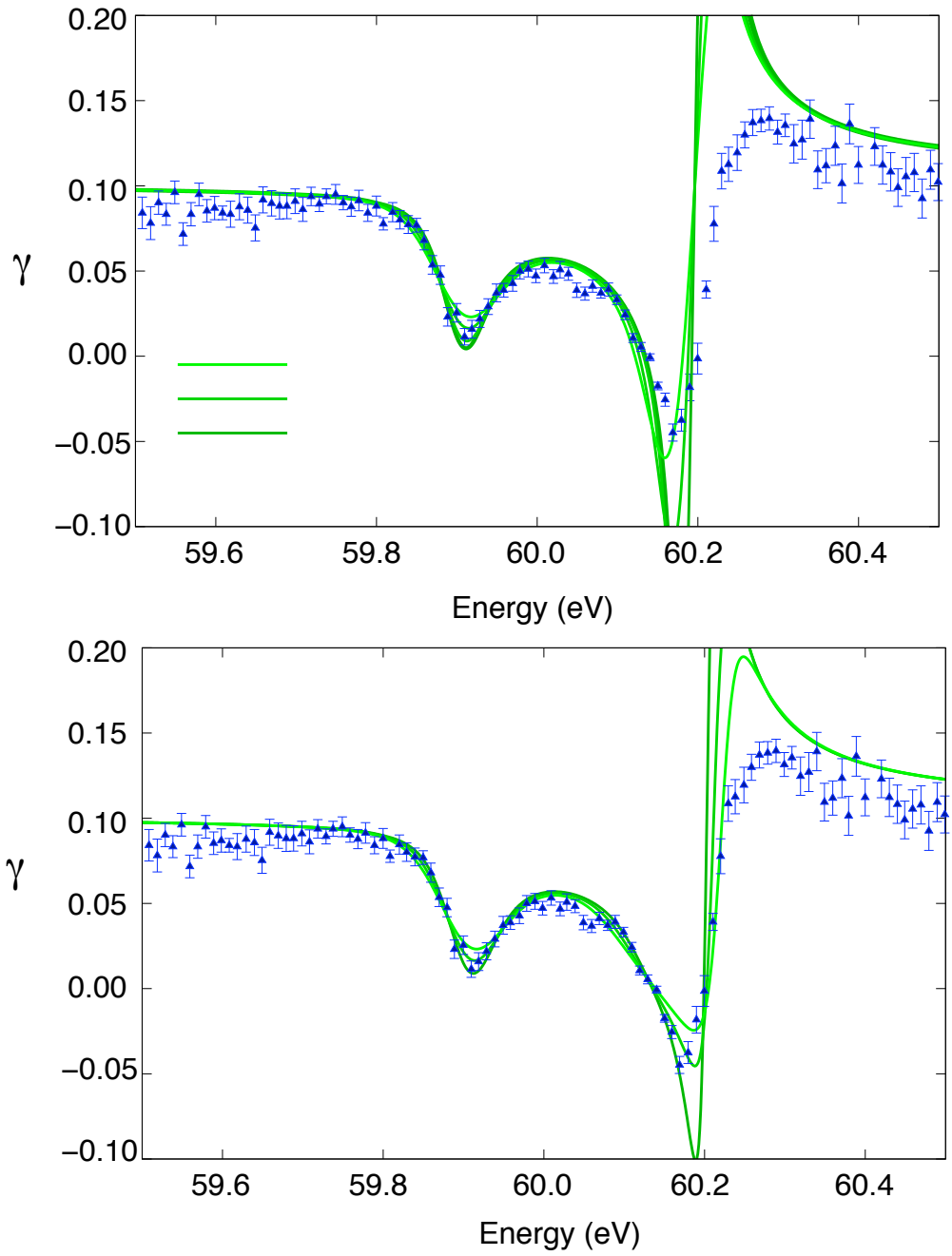

Figure 2.14: Upper panel: comparison between the experimental and the convoluted γ factor. The theoretical values are convoluted with gaussian functions with three different FWHM: 20, 30 and 40 meV. Even with the largest convolution width there is still a remarkable disagreement near the dipole resonance. This is partly due to the inapplicability of the convolution to the asymmetry parameter. Krassig *et al* [114] claim an experimental resolution of 20 meV. Lower panel: the experimental asymmetry parameter γ is obtained as the quotient of measurements with finite resolution. A better procedure to reproduce the experiment is thus to first convolute the product of matrix elements and then to employ them in the expression of the asymmetry parameter. This procedure brings the theoretical prediction nearest to the experiment, even if a good agreement is still lacking, particularly in the 100 meV interval above the dipole resonance.

Chapter 3

Helium triplet states

3.1 Introduction

The very first evidence of doubly excited states was the observation in 1928 by Compton and Boyce [3] and, two years later, by Kruger [4], of a triplet decay: the 320.392 Å line due to $(2p^2)^3\mathrm{P}^e \rightarrow (2s2p)^3\mathrm{P}^o$ transition in the arc spectrum of helium. Since then many experiments have been found involving the triplet doubly excited states of helium: in the energy spectrum of electrons emitted after bombardment with positively charged ions [152] or with electrons [153], during the relaxation of excited helium atom after decay of He^- negative ion resonances [154], and in beam foil experiments [155]. In 2000 Gorczyca *et al* [29] found that the electrostatic approximation cannot account for the anomalous behaviour in the photoionization cross section of helium close to N=2 threshold [117]: both radiative decay and the spin-orbit interaction between singlet and triplet doubly excited states have to be taken into account to fully explain the observations. The first direct evidence of the population of LS-forbidden triplet doubly excited states in the photoionization of fundamental helium followed soon [30], and later investigations confirmed those findings [119, 156, 157]. TDES are also produced through collisions of singlet doubly excited states with other gas particles, as evidenced by the enhancement of fluorescence decay of TDES as pressure is raised [31]. At BESSY II (Berlin), Mickat *et al* [158] measured the radiative decay of singly excited triplet Rydberg satellites. Coreno *et al* [159], at ELETTRA (Trieste), observed visible fluorescent emissions from $(2p7d)$ and $(2p8d)$ $^3\mathrm{D}^o$ states.

Information on triplet doubly excited states obtained in fluorescence decay studies, though, are necessarily incomplete. Since the experiment by Madden and Codling [5], photoionization with synchrotron radiation has been one of the most prolific means of investigation of atomic doubly excited states. Apparently the same technique could be used for triplets: the metastable fundamental $2^3\mathrm{S}$ state has a huge lifetime, $\sim 10^4 s$ [160], and it is produced with high efficiency by electric discharges in helium. Moreover, below N=2 threshold, $1s2s \rightarrow 2snp$ transitions are allowed already in the independent particle approximation, giving rise to very large resonant signals, well above the underlying $1s2s \rightarrow 1s\epsilon p$ direct ionization

background. Still the experiment proved in the past to be challenging. In the early seventies, Stebbings *et al* [161] succeeded in measuring the background absolute cross section, but no resonant features were observed. The required technology became available only quite recently. The three lowest ^{3}P resonances in 2^3S photoionization spectrum below N=2 threshold has eventually been observed, for the first time, at GASPHASE beamline of ELETTRA in Trieste [32].

As far as we know, the group in Trieste is recently (April 2008) trying to single out as much as a dozen of new resonances below N=2 threshold [33]. Moreover, a group at Bessy II in Berlin is designing the triplet spectrum investigation even beyond N=2 threshold [34].

We present here a detailed analysis of the photoionization of the metastable 2^3S state in dipole approximation [162] to provide a reliable guide for these new closer experimental investigations. Total cross section, partial cross sections and dipole asymmetry parameters are calculated up to N=5 threshold.

Photoionization of 2^3S has been examined before by several authors. Most of the calculations, though, are restricted below N=2 threshold [163–168], while some of those crossing the multichannel threshold did not get to the resonant region [169,170]. Only Sánchez and Martín [171] and Zhou and Lin [172] examined in some detail the resonant structure below N=3 threshold. At the best of our knowledge, the energy region beyond N=3 threshold has never been taken into account. In the present investigation, peaks assignment in photoionization spectra is performed whenever possible, and the role of $[040]_5^+$ intruder state below N=4 threshold is elucidated.

The accurate evaluation of photoionization cross sections may also be used to improve the parameters required to evaluate the depletion of 2^3S in compact, optically thick planetary nebulae, where the photoionization plays a significant role [173], and to compute the He^+ - e^- recombination rates needed to improve constraints on big bang nucleosynthesis models [174,175].

We also examine in great detail [176] the autoionization properties of helium triplet doubly excited states with $L \leq 2$ up to N=5 threshold. Various theoretical techniques have been employed to compute resonance parameters in the past, among which Feshbach projection method [177], many-body perturbation theory [178], stabilization method [179,180], and complex coordinate method [123, 181–184]. These investigations, though, focused, with few exceptions, on the first few resonances only, leaving a vast majority of the spectrum uncovered. Moreover many symmetries are not considered, and energies and widths are often hardly accurate. Due to the renewed experimental interest in autoionization and radiative decay of triplet doubly excited states, a comprehensive, accurate study of autoionizing triplet states seemed to be timely.

As shown in previous chapters, the B-spline K-matrix method provides reliable parameters for metastable multiplets in helium up to very high excitations of the external electron. As many as twenty autoionizing multiplets below each threshold from N=1 to N=5 in ^{3}S, $^3P^e$, $^3P^o$, $^3D^e$ and $^3D^o$ manifolds with strongly correlated CI wave functions (maximum orbital angular momentum $\ell_{max} = 8$) have been determined and separated in series, within the electrostatic, fixed nucleus

approximation.

For states with total angular momenta $L > 2$, relativistic effects cannot be neglected. In Rydberg states the main corrections in the LS coupling come from triplet-singlet mixing of same n,L,J states:

$$\Psi(n^3L_J) = \Psi_0(n^3L_J)\cos\theta + \Psi_0(n^1L_J)\sin\theta.$$

The mixing coefficients $\sin\theta$ are known from literature (see Table 11.11 in [185]) to be around ~ 0.0003, ~ 0.01 and ~ 0.5 for P, D and F states respectively, which correspond to a contribution to the norm of the states of $\sim 10^{-5}\%$, $\sim 0.01\%$ and $\sim 30\%$. For D states the singlet component is still far smaller than the dominant triplet, while for F states the two are almost equivalent. This is why the present work does not cover symmetries with $L > 2$.

The classification of most series and intruder states according to Stark/Lin $[N_1N_2m]^A$ quantum numbers was accomplished by a bold employment of the propensity rules. The corresponding decay paths through Stark channels are depicted by an effective graphical form.

A wealth of completely new dynamical features emerged in the process, among which nine clearly visible intruder states: $[040]_5^+$ $^3P^o$, $[031]_5^+$ $^3D^e$ and $[031]_5^+$ $^3P^e$ below N=4 threshold, $[050]_6^+$ and $[140]_6^+$ $^3P^o$, $[041]_6^+$ and $[131]_6^+$ $^3P^e$ and $[032]_6^+$ $^3D^o$ below N=5 threshold. Two other $^3D^e$ intruder states below N=5 threshold, most probably $[041]_6^+$ and $[131]_6^+$, are thought to cause the observed complex resonance pattern which could not be disentangled here. Moreover, interseries interactions alone give rise to many dramatic effects, as in the case of $^3D^e$ symmetry below N=3 threshold, which, being not mediated by any intruder state, indicate a failure of the Stark model.

The unabridged table set of all the Rydberg and resonance parameters, reported in appendix K, is presently in press on Atomic Data and Nuclear Data Tables [186]. Some representative excerpts are tabulated here below each ionization threshold in comparison with the best available data from literature. Whenever available, the most accurate and extensive data in literature are reported also as white circles in $\bar{\Gamma}$ vs n^* plots (see for example figure 3.3.a) along with our data, which are represented by black dots. Dots belonging to the same autoionizing series are connected by a continuous line.

3.2 Autoionization decay paths

As outlined in section 2.1, to a first approximation, the doubly excited helium states $[N_1N_2m]_n^A$ (see Rost *et al* [99] and appendix F) states decay to underlying channels according to three different mechanisms:

$$\begin{aligned} A) &\quad \Delta N_2 = -1 \\ B) &\quad \Delta m = -1 \\ C) &\quad \Delta N_1 \neq 0. \end{aligned}$$

whose efficiency follows the order $A > B > C$. Decay is enhanced (suppressed) for + (−) states. + states decaying by means of either A or B mechanism, with large widths ($\bar{\Gamma} \simeq 10^{-1} - 10^{0}$), are known as type I resonances, − states decaying through A or B mechanisms, with intermediate widths ($\bar{\Gamma} \simeq 10^{-3} - 10^{-2}$), form type II resonances, finally all states decaying through C mechanism, with the smallest widths ($\bar{\Gamma} \simeq 10^{-8} - 10^{-3}$), form type III resonances. As a rule of thumb, reduced widths of resonances are ordered according to the following *propensity rules*: $AI > BI > AII > BII > CIII$.

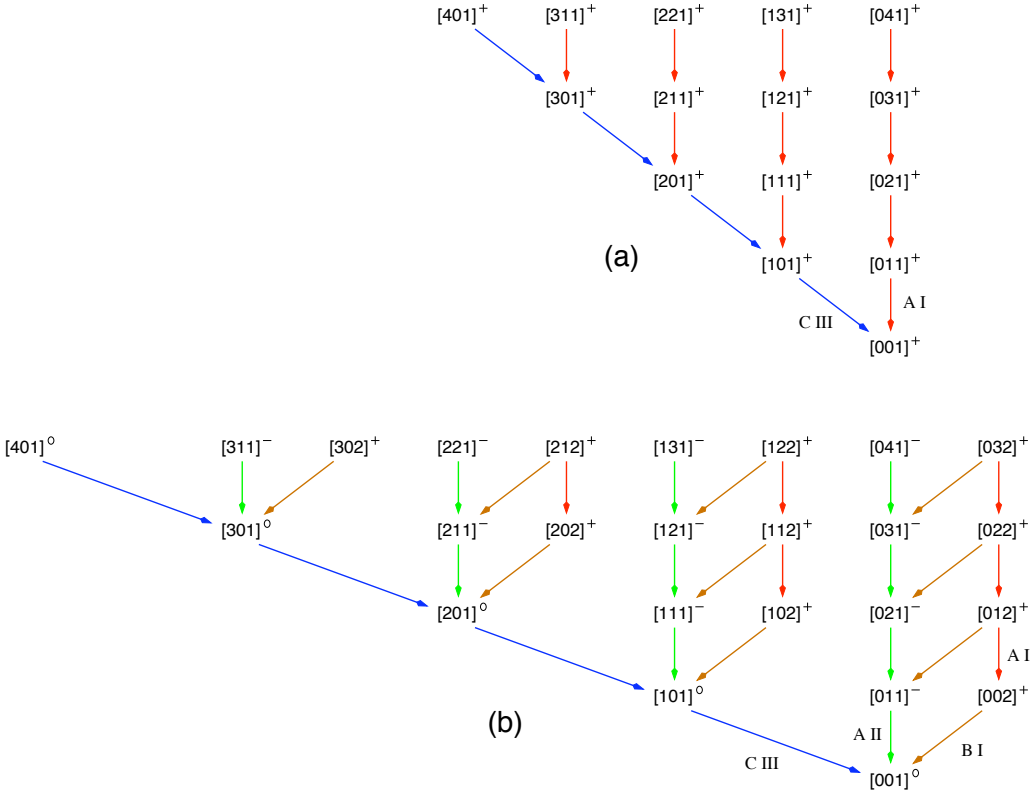

Figure 3.1: Autoionization decay paths of $^3P^e$ (a), and $^3D^o$ (b) doubly excited states of helium up to N=6 threshold. Channels are labelled with mixed Stark/Lin numbers $[N_1N_2m]^A$. Channels with the same threshold N (N= N_1+N_2+m+1) are on the same row. Next to an exemplary set of arrows, representing the relevant decay modes, the corresponding mechanisms are indicated. Similar arrows are understood to correspond to the same mechanism. See text for details.

In figures 3.1 and 3.2 the autoionization decay paths for helium unnatural and natural states respectively, with $L \leq 2$, are reported in detail. Please note that $CIII$ decay mode is reported only when the other more efficient mechanisms are unavailable. All decay paths are sections of a global $\{[N_1N_2m]\}$ lattice (Lin's A quantum number is undetermined because it depends on global $^{2S+1}L^{\pi}$ symmetry) which extends indefinitely along A, B and C edges. Each $[N_1N_2m]$ lattice point corresponds to infinite angular momenta $L = m, m+1, \cdots$ which give rise, for each term $[N_1N_2m]_n$, to a corresponding "rotor-like" series [187,188] . The lattice corner is [000] for natural and [001] for unnatural parity states respectively. Figures 3.1 and 3.2 will be used throughout.

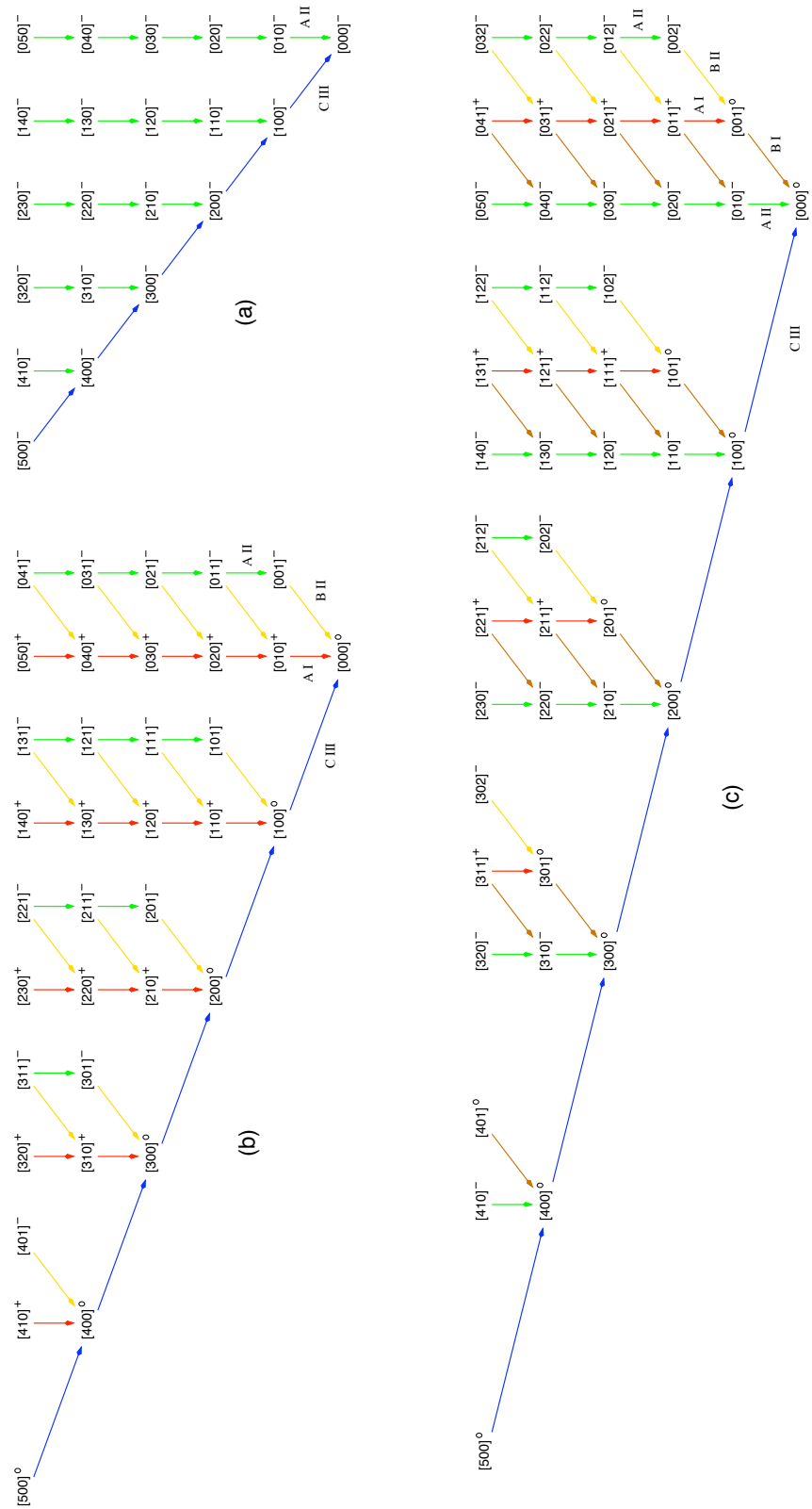

Figure 3.2: Autoionization decay paths of ^{3}S (a), ^{3}P^o (b), and ^{3}D^e (c) helium doubly excited states up to N=6 threshold. See figure 3.1 and text for details.

Following Lin [189], the energies of the lowest terms in series with the same global symmetry and converging to the same threshold, should be ordered according to the rule $A = +1 < A = -1 < A = 0$. Among those with the same A, the lowest has the highest K. At low energies, these criteria are useful to identify the character of intruder states and interpret most of the preeminent features of autoionizing series. From extensive calculations in singlet symmetry [22–25,108,109], though, it is well known that, as energy rises, the $[N_1N_2m]^A$ classification scheme as well as the propensity rules steadily loose their applicability. We will show with some length in the following that, as expected, also for the triplet manifold they are violated in a number of ways even between first and fifth ionization thresholds.

3.3 Computational details

Every PWC channel comprises roughly 275 functions, 30-34 of which lie below the parent ion energy. Those states which lie more than 0.5 au above the double ionization threshold are not used since they are effectively reproduced by the localized channel. In this way, depending on the parent ion energy, only 65 to 127 states above threshold are retained and form a set of conditioned PWC's with a substantial reduction of the space dimension (see chapter 1 for details on matrix conditioning).

In each manifold ${}^3\mathrm{L}^\pi$, the pseudo-state channel, which gives rise to autoionizing states, Rydberg states and short range correlation is built in few steps. First the full-CI space with suitable symmetry is constructed from 31 s, 30 p, 29 d, 28 f, 27 g, 27 h, 27 i, 27 j and 27 k orbitals. The dimensions of these spaces are reported on the second column in table 3.1 under LC label. To obtain accurate bound Rydberg states the full-CI LC is augmented with the PWC which has the lowest threshold. The corresponding dimension is reported on the fifth column in table 3.1 under BR label. To obtained the LC space to be used in K-matrix evaluation few more steps are required. The full-CI LC is first effectively orthogonalized to the whole conditioned PWC space, to avoid numerical singularities. The dimensions of orthogonalized LC spaces are reported on the third column in table 3.1 under LC_{ort} label. The orthogonalized space is finally augmented with all those PWC states which lie below their threshold. The corresponding dimensions are reported on the fourth column in table 3.1 under LC_{KM} label.

The number of PWC (open and closed) and the total dimension of their continuum parts are reported in table 3.1 on sixth and seventh column respectively. The last column specifies the total dimension of the linear systems which is to be solved in order to get the reaction K-matrix.

In table 3.2 the energies of He^+ parent ion states are reported. The difference with respect to the exact $-2/n^2$ electrostatic values is at least one order of magnitude smaller than the accuracy in the final two electron results.

We chose a pragmatic strategy to classify the autoionizing series . For high values of the effective principal quantum number $n^* \equiv 1/\sqrt{2(E_{threshold} - E)}$ all separate branches of the autoionizing multiplet series can be easily recognized in

Table 3.1: Block dimensions. See text for details.

$^3L^\pi$	LC	LC_{ort}	LC_{KM}	BR	N_{PWC}	PWC	TOT
^3S	3439	3303	3761	3685	15	1118	4879
$^3P^e$	3196	3100	3411	3442	10	703	4114
$^3P^o$	6284	6052	6819	6530	25	1827	8646
$^3D^e$	8439	8161	9099	8685	31	2240	11339
$^3D^o$	5354	5212	5698	5600	16	1117	6815

Table 3.2: Parent ion energies

	N=1	N=2	N=3
ℓ			
s	-1.999 999 989	-0.499 999 987	-0.222 222 197
p		-0.499 999 998	-0.222 222 216
d			-0.222 222 221

	N=4	N=5
ℓ		
s	-0.124 999 968	-0.079 999 942
p	-0.124 999 988	-0.079 999 966
d	-0.124 999 997	-0.079 999 984
f	-0.124 999 999	-0.079 999 994
g		-0.079 999 999

a $\bar{\Gamma}$ vs. n^* plot where each branch converge to a finite limit as $n^* \to \infty$. For most series, $\Delta n^* - 1$ and $\Delta\bar{\Gamma}$ between two adjacent terms are small and smooth, so that every series can be traced back to the first term. Autoionizing series can be labelled according to the asymptotic values of K and T approximate quantum numbers in Herrick classification scheme (see [99] and references therein for details). At the moment we do not have the possibility of determining the (K,T) character of resonances. We therefore assigned to each series an arbitrary letter and added the corresponding Herrick's labels when available in literature.

In $^3D^e$ symmetry, the first terms of the twelve autoionizing series converging to $N = 5$ threshold couldn't be separated solely on the basis of quantum defect and reduced width. Intruder states from higher thresholds are likely to cause strong mixing between satellites from different series. (K, T) resonance character might actually be meaningless here. In A series, some resonance widths are comparable to the intermultiplet distance and the fitting procedure failed to find them.

All our data are reported with a fixed number of figures, only part of which are likely to have reached convergence. The number of reliable figures for each result is to be estimated by comparison with other accurate calculations in literature, what is done in some detail in the following. All the photoionization cross section spectra (actually photoabsorption cross sections, as the fluorescence channels are not taken into account and the fluorescence decay may not be negligible at all) have been convoluted with a FWHM=5 meV gaussian kernel, corresponding to a reasonable experimental resolution.

3.4 Below N=1 threshold.

Within electrostatic approximation, the bound states below the first ionization threshold have natural parity and are arranged, in each symmetry, in single Rydberg series with dominant configuration $1sn\ell$ (Table 3.3).

In order to show the accuracy which is to be expected in the representation of Rydberg satellites, in table 3.3 the energies of the lowest ten Rydberg states for each natural symmetry treated here, ^3S, $^3P^o$ and $^3D^e$, are compared to the highly accurate results by Bürgers *et al* [123] and Drake *et al* [190], truncated to nine decimal figures. The other few ^3S states available in literature and the rest of our computed energies have been omitted for clarity (the full set of results is reported in appendix K) Discrepancies are perfectly tolerable, being of the order of $\sim 5 \times 10^{-8}$ au. In ^3S series, three minor points should be remarked. First, our $1s6s$ energy is lower than those by Bürgers *et al* and Drake *et al* by $4.7 \cdot 10^{-8}$ au, probably falling below the electrostatic limit. This might be due to round-off errors in our calculations. The energy level for $1s11s$ state published by Bürgers *et al* is clearly wrong due to a typing error in their original paper (compare with the $1s10s$ energy) . Finally, the uncertainty for the $1s15s$ state by Bürgers seems underestimated: the distance with our energy is roughly twice as large (but that again could be due to round-off error in our result). In $^3P^o$ symmetry, the general agreement is within few tens of billionth of atomic unit, with a remarkable, possibly

Table 3.3: ^{3}S, ^{3}P^o and ^{3}D^e Rydberg states energies (au) below N=1 threshold.

n	^{3}S	^{3}P^o	^{3}D^e
2	-2.175 229 311	-2.133 164 081	
	-2.175 229 378[b]	-2.133 164 192[b]	
	-2.175 229 378[a]		
3	-2.068 689 043	-2.058 081 046	-2.055 636 295
	-2.068 689 067[b]	-2.058 081 084[b]	-2.055 636 309[b]
	-2.068 689 067[a]		
4	-2.036 512 067	-2.032 324 332	-2.031 288 834
	-2.036 512 083[b]	-2.032 324 354[b]	-2.031 288 848[b]
	-2.036 512 083[a]		
5	-2.022 618 867	-2.020 551 187	-2.020 021 029
	-2.022 618 872[b]	-2.020 551 187[b]	-2.020 021 027[b]
	-2.022 618 872[a]		
6	-2.015 377 500	-2.014 207 991	-2.013 901 454
	-2.015 377 453[b]	-2.014 207 959[b]	-2.013 901 415[b]
	-2.015 377 453[a]		
7	-2.011 129 892	-2.010 404 944	-2.010 212 089
	-2.011 129 920[b]	-2.010 404 960[b]	-2.010 212 106[b]
	-2.011 129 920[a]		
8	-2.008 427 100	-2.007 946 990	-2.007 817 912
	-2.008 427 122[b]	-2.007 947 014[b]	-2.007 817 935[b]
	-2.008 427 122[a]		
9	-2.006 601 502	-2.006 267 248	-2.006 176 667
	-2.006 601 517[b]	-2.006 267 267[b]	-2.006 176 685[b]
	-2.006 601 516[a]		
10	-2.005 310 783	-2.005 068 790	-2.005 002 804
	-2.005 310 795[b]	-2.005 068 805[b]	-2.005 002 818[b]
	-2.005 310 794[a]		

[a])Bürgers, Wintgen and Rost (1995) [123]
[b])Drake and Yang (1992) [190]

fortuitous, $1s5p$ state where a discrepancy of only $5 \cdot 10^{-10}$ au is found. Similar considerations apply to $^3D^e$ symmetry.

Oscillator strengths. In table 3.4 some oscillator strengths in velocity gauge for $^3P^o \leftarrow ^3S^e$ and $^3D^e \leftarrow ^3P^o$ transitions between Rydberg states are compared with recent accurate data from literature [185]. A remarkably good agreement is found, with discrepancies of the order of 10^{-7}.

In table 3.5 the inner coherence of our data is examined by comparing the results obtained in length, velocity and acceleration gauges. Discrepancies between length and velocity gauges are of the order of one part in a million. For transitions which include the lowest states, disagreement with acceleration gauge is one or two order of magnitude larger. The accuracy in acceleration matrix elements is completely lost when almost degenerate initial and final states are considered. This is possibly due to the fact that acceleration matrix elements are so small (they need to be hugely amplified by $(\Delta E)^{-2}$ in order to be compared to velocity oscillator strengths) that their accuracy is badly sploiled by an absolute numerical error.

3.5 Below N=2 threshold.

Below N=2 threshold, unnatural parity states are prevented to autoionize in electrostatic approximation. Comparison with the most accurate calculation available for $^3P^e$ symmetry [191] evidences an agreement of 10^{-6} au for the fundamental state, and 10^{-7} au for the first excited states (Table 3.6). For $^3D^o$ symmetry the only reference we could found [178] has just five significant decimal digits, all in agreement with our result (Table 3.6).

Natural parity states, instead, may decay by autoionization. Most of the existing calculations for ^3S [123,178,184], $^3P^o$ [166,167,178,179,183,184,192–196] and $^3D^e$ [178,184,197] symmetries address this energy interval. In figures 3.3.a through 3.3.f, the three pairs of $\bar{\Gamma}$ vs n^* and μ vs n^* plots corresponding to ^3S, $^3P^o$ and $^3D^e$ symmetries are reported. All autoionizing series are regular: both reduced widths and quantum defects rapidly get to their limiting values. The close overlap of white circles (literature data: see [123] for ^3S states, and [184] for both $^3P^o$ and $^3D^e$ states) and black dots (present results) confirm a very good agreement.

In ^3S symmetry, for which the most accurate results are available, the disagreement in energy position is comparable to or (occasionally much) lower than 10^{-7} au. Resonance widths agree to all common digits (except at most ± 1 on the last one), which reach four digits in the best cases (Table 3.7). Looking at the second row from below in figure 3.2.a, we see that in ^3S symmetry two series are expected, one with intermediate width, labelled $[010]^-$, which decays through AII mechanism, and a narrow one, $[100]^-$, which decays through $CIII$ mechanism. By comparison with the actual $\bar{\Gamma}$ vs n^* plot, reported in figure 3.3.a, $[010]^-$ and $[100]^-$ can be recognized as A and B series respectively.

In $^3P^o$ symmetry, our calculations compares well with the best available data. In all three "branches" of the multiplet series, roughly six digits should be granted.

Table 3.4: Some oscillator strengths. The upper values are the present results ($\ell_{max} = 8$), the lower values are by Drake [185].

	2^3S	3^3S	4^3S	5^3S
2^3P^o	0. 539 087 0	-0. 208 536 4	-0. 031 720 9	-0. 011 340 9
	0. 539 086 1	-0. 208 535 9	-0. 031 720 8	-0. 011 340 9
3^3P^o	0. 064 460 8	0. 890 852 7	-0. 435 672 0	-0. 067 607 2
	0. 064 461 2	0. 890 851 3	-0. 435 671 1	-0. 067 607 3
4^3P^o	0. 025 768 8	0. 050 082 9	1. 215 264 8	-0. 668 300 2
	0. 025 768 9	0. 050 083 3	1. 215 263 0	-0. 668 300 3
5^3P^o	0. 012 490 4	0. 022 913 8	0. 044 229 8	1. 530 631 8
	0. 012 490 6	0. 022 914 1	0. 044 230 5	1. 530 628 7
6^3P^o	0. 006 982 3	0. 011 993 6	0. 021 630 5	0. 041 518 2
	0. 006 982 2	0. 011 993 3	0. 021 630 1	0. 041 517 7
7^3P^o	0. 004 298 9	0. 007 077 0	0. 011 775 0	0. 021 099 2
	0. 004 299 0	0. 007 077 2	0. 011 775 4	0. 021 100 3

	2^3P^o	3^3P^o	4^3P^o	5^3P^o
3^3D^e	0. 610 226 0	0. 112 099 3	-0. 036 959 0	-0. 006 900 9
	0. 610 225 2	0. 112 100 4	-0. 036 959 2	-0. 006 900 9
4^3D^e	0. 122 846 9	0. 477 595 0	0. 200 948 0	-0. 088 301 0
	0. 122 846 9	0. 477 593 8	0. 200 949 8	-0. 088 301 7
5^3D^e	0. 047 006 8	0. 124 552 7	0. 438 388 1	0. 280 056 2
	0. 047 007 1	0. 124 553 2	0. 438 388 8	0. 280 055 8
6^3D^e	0. 023 469 7	0. 053 009 9	0. 123 944 3	0. 429 449 8
	0. 023 469 2	0. 053 009 3	0. 123 941 4	0. 429 441 0
7^3D^e	0. 013 563 5	0. 028 158 0	0. 055 231 9	0. 125 233 2
	0. 013 563 8	0. 028 158 7	0. 055 233 2	0. 125 238 9
8^3D^e	0. 008 604 6	0. 016 981 0	0. 030 285 3	0. 057 057 4
	0. 008 604 7	0. 016 980 9	0. 030 285 3	0. 057 058 9

Table 3.5: Comparison of gauges for oscillator strengths between Rydberg states

		2^3S	3^3S	4^3S
	l	5. 390 873[-1]	-2. 085 364[-1]	-3. 172 095[-2]
2^3P^o	v	5. 390 870[-1]	-2. 085 364[-1]	-3. 172 093[-2]
	a	5. 390 702[-1]	-2. 085 392[-1]	-3. 172 130[-2]
	l	6. 446 079[-2]	8. 908 528[-1]	-4. 356 721[-1]
3^3P^o	v	6. 446 082[-2]	8. 908 527[-1]	-4. 356 720[-1]
	a	6. 446 146[-2]	8. 908 104[-1]	-4. 356 786[-1]
	l	2. 576 875[-2]	5. 008 291[-2]	1. 215 265[+0]
4^3P^o	v	2. 576 876[-2]	5. 008 293[-2]	1. 215 265[+0]
	a	2. 576 894[-2]	5. 008 394[-2]	1. 215 435[+0]
		11^3S	12^3S	13^3S
	l	2. 298 997[-2]	4. 293 775[-2]	3. 984 829[+0]
13^3P^o	v	2. 299 004[-2]	4. 293 780[-2]	3. 984 830[+0]
	a	2. 216 232[-2]	6. 717 708[-1]	4. 359 201[+2]
	l	1. 321 110[-2]	2. 361 594[-2]	4. 398 427[-2]
14^3P^o	v	1. 321 117[-2]	2. 361 600[-2]	4. 398 430[-2]
	a	1. 797 465[-3]	4. 967 529[-2]	1. 008 119[+0]
	l	8. 412 606[-3]	1. 357 805[-2]	2. 427 827[-2]
15^3P^o	v	8. 412 677[-3]	1. 357 812[-2]	2. 427 832[-2]
	a	4. 239 960[-5]	7. 208 423[-3]	8. 874 723[-2]
	l	5. 772 151[-3]	8. 651 026[-3]	1. 396 123[-2]
16^3P^o	v	5. 772 216[-3]	8. 651 086[-3]	1. 396 129[-2]
	a	6. 472 873[-5]	1. 222 488[-3]	1. 640 007[-2]

Table 3.6: $^3P^e$ and $^3D^o$ Rydberg states below N=2 threshold ($\ell_{max} = 8$).

n	$^3P^e$	$^3D^o$
2	-0. 710 499 239	
	-0. 710 500 155 678 334[b]	
	-0. 710 500[a]	
3	-0. 567 812 762	-0. 559 328 053
	-0. 567 812 898 725 3[b]	-0. 559 33[a]
	-0. 567 81[a]	
4	-0. 535 867 134	
	-0. 535 867 188 7[b]	
5	-0. 522 254 537	
	-0. 522 25(3)[b]	

[a]) Lindroth (1994) [178]
[b]) Goodson *et al* (1991) [191]

Table 3.7: $^3S^e$ resonances below N=2 threshold ($\ell_{max} = 8$).

	A			B	
n	E (au)	Γ (au)	n	E (au)	Γ (au)
3	-0. 602 577 486	6. 651[-6]	3	-0. 559 746 441	2. 606[-7]
	-0. 602 577 505[a]	6. 65 [-6]		-0. 559 746 626[a]	2. 60 [-7]
4	-0. 548 840 846	3. 095[-6]	4	-0. 532 505 270	1. 431[-7]
	-0. 548 840 858[a]	3. 094[-6]		-0. 532 505 349[a]	1. 44 [-7]
5	-0. 528 413 960	1. 542[-6]	5	-0. 520 549 113	8. 203[-8]
	-0. 528 413 972[a]	1. 542[-6]		-0. 520 549 199[a]	8. 2 [-8]
6	-0. 518 546 252	8. 569[-7]	6	-0. 514 180 007	5. 038[-8]
	-0. 518 546 375[a]	8. 56 [-7]		-0. 514 180 356[a]	5. 0 [-8]
7	-0. 513 046 289	5. 201[-7]	7	-0. 510 378 019	3. 284[-8]
	-0. 513 046 496[a]	5. 2 [-7]		-0. 510 378 174[a]	3. 2 [-8]
8	-0. 509 672 670	3. 377[-7]	8	-0. 507 925 053	2. 249[-8]
	-0. 509 672 798[a]	3. 38 [-7]		-0. 507 925 149[a]	2. 2 [-8]
9	-0. 507 455 981	2. 311[-7]	9	-0. 506 250 009	1. 603[-8]
	-0. 507 456 056[a]	2. 32 [-7]		-0. 506 250 079[a]	1. 6 [-8]
10	-0. 505 922 102	1. 649[-7]	10	-0. 505 055 287	1. 181[-8]
	-0. 505 922 151[a]	1. 64 [-7]		-0. 505 055 341[a]	1. 2 [-8]

[a]Bürgers, Wintgen and Rost (1995) [123]

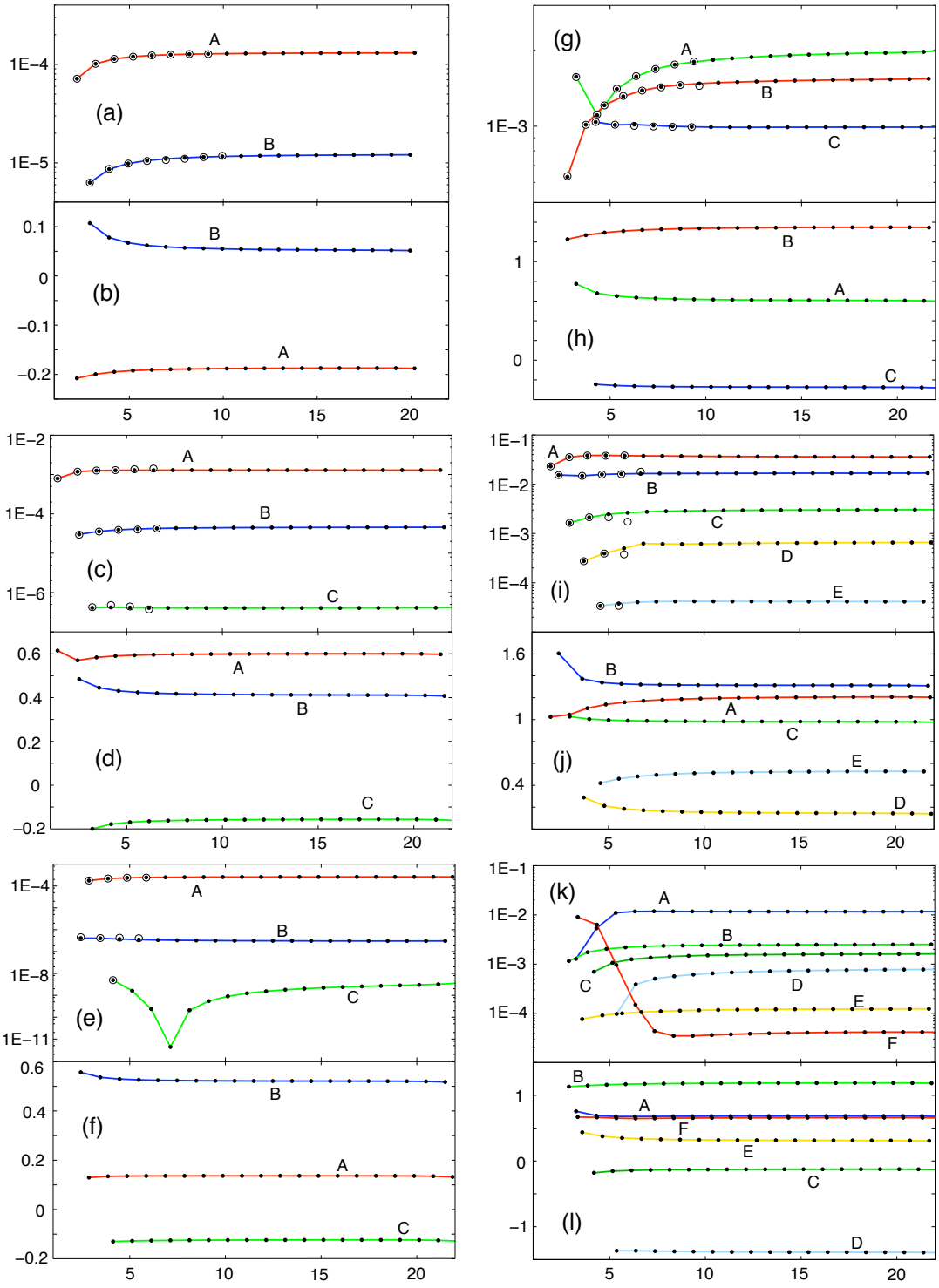

Figure 3.3: Reduced widths and quantum defects vs effective quantum number n^* for ^{3}S, ^{3}P^o and ^{3}D^e states below N=2 and N=3 thresholds. Below N=2 : a) $\bar{\Gamma}_{^3S}$, b) $\mu_{^3S}$, c) $\bar{\Gamma}_{^3P^o}$, d) $\mu_{^3P^o}$, e) $\bar{\Gamma}_{^3D^e}$, f) $\mu_{^3D^e}$. Below N=3 : g) $\bar{\Gamma}_{^3S}$, h) $\mu_{^3S}$, i) $\bar{\Gamma}_{^3P^o}$, j) $\mu_{^3P^o}$, k) $\bar{\Gamma}_{^3D^e}$, l) $\mu_{^3D^e}$. White circles are the most accurate data available in literature. See text for details.

Widths errors should be lower than one part over a hundred (Table 3.8).

Table 3.8: $^3P^o$ resonances below N=2 threshold ($\ell_{max} = 8$).

A $(K,T) = (1,0)$			B $(K,T) = (0,1)$			C $(K,T) = (-1,0)$		
n	E (au)	Γ (au)	n	E (au)	Γ (au)	n	E (au)	Γ (au)
2	-0. 760 490 639	2. 989[-4]						
	-0. 760 491	2. 998[-4]^a						
	-0. 760 492 4	2. 999[-4]^b						
	-0. 760 489	2. 99 [-4]^c						
3	-0. 584 671 760	8. 230[-5]	3	-0. 579 030 867	1. 895[-6]	3	-0. 548 844 002	1. 253[-8]
	-0. 584 672	8. 25 [-5]^a		-0. 579 030 6	1. 89 [-6]^a		-0. 548 844	— ^{a}
	-0. 584 672 3	8. 225[-5]^b		-0. 579 030 49	1. 894[-6]^b		-0. 548 844 35	— ^{b}
	-0. 584 671	8. 24 [-5]^c		-0. 579 030	1. 85 [-6]^c		-0. 548 841	1. 3 [-8]^c
4	-0. 542 837 034	3. 157[-5]	4	-0. 539 558 730	7. 979[-7]	4	-0. 528 638 225	5. 777[-9]
	-0. 542 837	3. 17 [-5]^a		-0. 539 558 7	8. 9 [-7]^a		-0. 528 638	— ^{a}
	-0. 542 837 25	3. 16 [-5]^b		-0. 539 558 785	7. 7 [-7]^b		-0. 528 638 41	— ^{b}
	-0. 542 837	3. 17 [-5]^c		-0. 539 558	7. 90 [-7]^c		-0. 528 637	6. 6 [-7]^c
5	-0. 525 711 793	1. 491[-5]	5	-0. 523 946 606	4. 126[-7]	5	-0. 518 709 909	3. 006[-9]
	-0. 525 711	— ^{a}		-0. 523 945	— ^{a}			
	-0. 525 71	— ^{b}		-0. 523 943 5	— ^{b}		-0. 518 693	— ^{b}
	-0. 525 711	1. 51 [-5]^c		-0. 523 946	4. 10 [-7]^c		-0. 518 708	3. 2 [-9]^c
6	-0. 517 107 078	8. 134[-6]	6	-0. 516 079 530	2. 385[-7]	6	-0. 513 155 641	1. 745[-9]
	-0. 517 105	7. 6 [-6]^b		-0. 516 077 5	— ^{b}		-0. 513 145	— ^{b}
	-0. 517 107	8. 6 [-6]^c		-0. 516 079	2. 3 [-7]^c		-0. 513 155	1. 6 [-9]^c
7	-0. 512 191 135	4. 904[-6]	7	-0. 511 547 658	1. 494[-7]			
	-0. 512 19	— ^{b}		-0. 511 551	— ^{b}			
	-0. 512 206	5. 4 [-6]^c		-0. 511 547	1. 5 [-7]^c			
8	-0. 509 123 755	3. 178[-6]						
	-0. 509 095	— ^{b}						

^{a} Kar and Ho (2006) [180], (2005) [179]; ^{b} Ho (1993) [183]; ^{c} Chen (1997) [184]

From figure 3.2.b we see that in $^3P^o$ symmetry three autoionizing series are expected: a large $[010]^+$ series, decaying with AI mechanism, a $[001]^-$ series with intermediate reduced width, decaying with BII mechanism, and a narrow $[100]^0$ series which should decay through $CIII$ mechanism only. Once again the predictions of the approximate asymptotic theory are confirmed as shown in figure 3.3.c, where the aforementioned series are readily recognized in A, B and C series respectively (the unfortunate coincidence of letters for series and mechanisms is accidental).

Similar considerations apply for $^3D^e$ symmetry (Table 3.9). The $^3D^e$ picture

Table 3.9: $^3D^e$ resonances below N=2 threshold. $[n] = 10^n$.

A $[N_1N_2m]^A = [001]^0$

n	E (au)	Γ (au)
3	-0.560 686	7.520[-6]
	-0.560 684	7.56 [-6][a]
4	-0.533 463	3.821[-6]
	-0.533 462	3.82 [-6][a]
5	-0.521 131	2.063[-6]
	-0.521 130	2.08 [-6][a]
6	-0.514 541	1.219[-6]
	-0.514 540	1.2 [-6][a]

B $[N_1N_2m]^A = [010]^-$

n	E (au)	Γ (au)
3	-0.583 784	2.838[-8]
	-0.583 784	3.12 [-8][a]
4	-0.541 679	9.778[-9]
	-0.541 679	1.0 [-8][a]
5	-0.525 019	4.184[-9]
	-0.525 018	4.8 [-9][a]
6	-0.516 688	2.151[-9]
	-0.516 687	2.5 [-9][a]

C $[N_1N_2m]^A = [100]^0$

n	E (au)	Γ (au)
4	-0.529 312	7.062[-11]
	-0.529 312	7. [-11][a]
5	-0.519 017	1.196[-11]
	-0.519 016	— [a]
6	-0.513 322	1.023[-12]
	-0.513 322	— [a]

[a])Chen (1997) [184]

is similar to $^3P^o$, but width ratios are even larger. The three $[001]^0$, $[010]^-$ and $[100]^0$ series predicted in figure 3.2.c are readily recognized as A, B and C series in 3.3.e plot. This last series actually display a curious dip around $n^* = 7$. Data used for comparison [184], also shown in table 3.9, unfortunately lack crucial points to confirm this. There are no reasons to suspect our data to be wrong. Still this "spontaneous quenching" is unusual, because there is no apparent cause for it: neither intruder states (which appear only above N=3 threshold) nor collisions among series (quantum defects are all well separated, see figure 3.3.f), where nearly degenerate states can "share" some of their width. It is worth to point out, though, that terms in C series are so narrow that they decay radiatively.

Photoionization cross sections Excitation cross sections are huge. The total cross section convoluted with a gaussian weight function with FWHM= 5 meV reaches 1 GB (see figure 3.4). The first three peaks, corresponding to $[010]^+_2$, $[010]^+_3$ and $[001]^-_3$ terms respectively, have actually been observed recently [32]. The reason why photoionization cross sections to doubly excited states below N=2 are so large is trivial: transitions from the dominant $1s2s$ configuration of the target state to the $2snp$ components shared by all $^3\mathrm{P}^o$ doubly excited states below N=2 are allowed.

At variance with the photoionization of the fundamental $1s^2\ 1^1\mathrm{S}$ helium state, it is well known that in the photoionization spectrum of metastable states many non-dominant series are relatively large [166, 171, 172, 198]. In particular Zhou *et al* [166, 172] claimed this to be an evidence of the inapplicability of propensity rules for radiative transitions [199, 200] to the photoionization of metastable states. Propensity rules as derived in [199] indeed rely on the hypothesis that the the electron motion is restricted around the so called "saddle point" $\vec{r}_1 = -\vec{r}_2$, a relevant configuration for symmetrically excited states $N = n$, what is clearly not the case for $1s2s$ metastable states. As a consequence the excitation of the vanishingly narrow $[100]^0$ series, which on account of propensity rules should be prohibited ($\Delta\nu = 2 \neq 0, \pm 1$), is as intense as the excitation of the largest $[010]^+$ series and both are less intense than $[001]^-$ peaks by a factor ~ 10.

In 1999 Rubensson *et al* [117] demonstrated that radiative decay must be taken into account for a proper interpretation of photoionization spectra, since fluorescence branching ratio can be non negligible or even dominant for many narrow doubly excited states. Also in the case of triplet doubly excited states, autoionization is the dominant channel for only one of the three triplet resonance series converging to N=2 threshold, while for the other two narrower series the radiative decay rapidly prevails [119]. According to table I in [119] the autoionization branching ratio for $[001]^-_n$ terms decreases from 80.8% for $n = 3$ to 11.4% for $n = 8$ with a corresponding complementary increase of the fluorescence branching ratio from 19.2% to 88.6%. $[100]^0_n$ terms behave similarly with autoionization branching ratios falling from 74.1% for $n = 3$ to 16.9% for $n = 8$. Absolute heights and widths not including the coupling to the spontaneous emission channel (see table 3.8) are therefore unreliable for most of the narrower resonances. Since the integrated cross section is nevertheless approximately preserved, our choice to present our calculations as photoabsorption spectra convoluted with a reasonable resolution is justified.

In an experiment with 5 meV resolution, a dozen multiplets should be visible as a collective peak, and for six or seven multiplets all peaks (the first two multiplets have actually only one and two peaks each) should be recognized. It must be emphasized, though, that because of the comparable concurrence of autoionization and radiative decay neither the ion yield nor the fluorescence spectrum are expected to provide the photoabsorption spectrum.

To conclude this paragraph we observe that in figure 3.4 all the three gauges are reported: length and velocity are indistinguishable, while acceleration, reported with a dashed line, can be barely recognized in the last plot.

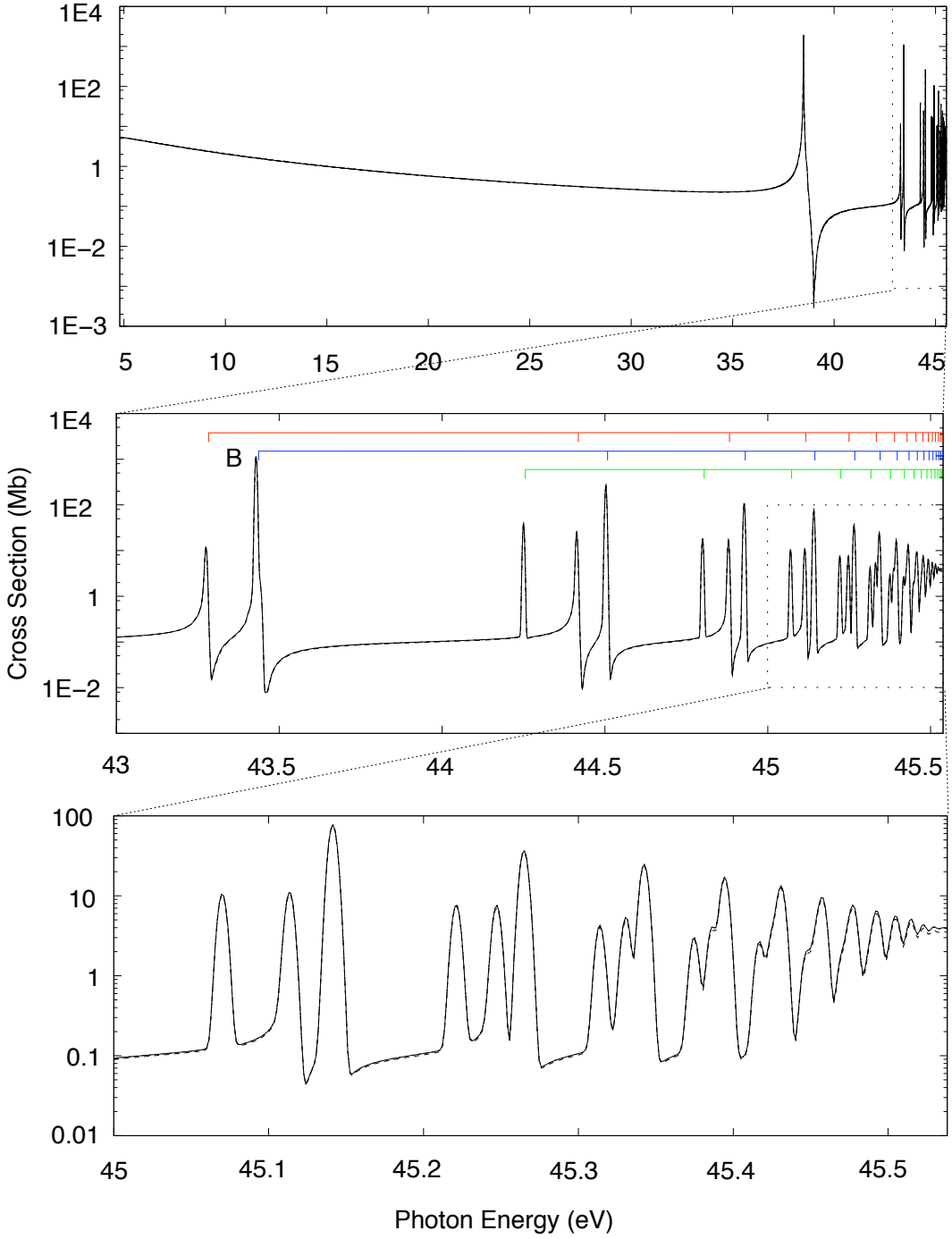

Figure 3.4: Total 2^3S helium photoionization cross section σ_{tot} below N=2 threshold. A) $[010]^+$, B) $[001]^-$, C) $[100]^0$.

3.6 Below N=3 threshold.

Below N=3 threshold all doubly excited states decay essentially through autoionization. In figures 3.3.g through 3.3.l and 3.8.a through 3.8.d the $\bar{\Gamma}/\mu$ vs n^* pairs for natural and unnatural states respectively are shown. No signatures of intruder states can be discerned: quantum defect series do not undergo any significant rise.

^{3}S resonances are in beautiful agreement with data by Bürgers *et al* [123], the most accurate available in literature. The worst energy level disagreement is $3.5 \cdot 10^{-6}$ au for the $n = 7$ term in A ($K = 0$) series. The $n = 7$ term has the worst agreement also in the other two series. In the other cases the disagreement is of the order of $1 \cdot 10^{-6}$ au. Resonance widths agree within few parts in a thousand, with the possible exceptions of those which in the literature are reported with less than four significant digits (Table 3.10).

The series assignment on the basis of propensity rules (see figure 3.2.a, third row from below) is the following: A is assigned to $[110]^-$, B to $[020]^-$, both decaying AII, C to $[200]^-$ decaying $CIII$. B is assigned to the channel with the largest K because of the smaller energy of its first term. Note how the three series cluster just below $n^* = 5$.

Most of ^{3}P^o literature data, by Ho [183], are in very good agreement with our results with the exception of the last few terms which are likely to be more accurate in the present work. See table 3.13 for a detailed comparison.

Please note that the original value E=-0.484 2805 Ry for the $n = 6$ term of C series reported in literature [183] is probably misprinted and should read instead E=-0.484 3805 Ry. In this way the agreement with our results (Table 3.13) improves by two order of magnitude and is consistent with the excellent agreement found for n=5 and n=6 terms in C series.

Here the pattern is standard (see figure 3.2.b): the two largest A and B series correspond to $[020]^+$ (highest K) and $[110]^+$ channels, decaying through the highly favoured AI mechanism. C is the $[011]^-$ series, it decays through both AII and BII mechanism. The narrower D is identified with $[101]^-$ series which decays BII only. Also D lowest term energy is higher than the energy of the lowest C, coherently with the lower K value of $[101]^-$. Finally E is assigned to $[200]^0$ which decays $CIII$.

For ^{3}D^e the comparison with the rather old results by Oberoi [177] (Table 3.11) show a good agreement for A and E series ($1 \cdot 10^{-5}$ au), a worst agreement for B and C series ($1 \cdot 10^{-4}$) au, and a remarkably bad agreement for F series ($2 \cdot 10^{-}3$ au). The strongest disagreement are in correspondence with the lowest states in each series, probably because Oberoi results are less accurate for the most correlated states.

Table 3.10: $^3S^e$ resonances below N=3 threshold ($\ell_{max} = 8$).

A ($K = 0$)			B ($K = 2$)			C ($K = -2$)		
n	E (au)	Γ (au)	n	E (au)	Γ (au)	n	E (au)	Γ (au)
4	-0. 270 283 422	4. 683[-5]	4	-0. 287 277 011	2. 963[-5]	4	-0. 249 964 424	1. 358[-5]
	-0. 270 283 614	4. 662[-5][a]		-0. 287 277 138	2. 983[-5][a]		-0. 249 964 616	1. 358[-5][a]
5	-0. 249 000 355	1. 371[-5]	5	-0. 258 133 940	1. 953[-5]	5	-0. 240 313 501	6. 965[-6]
	-0. 249 000 418	1. 380[-5][a]		-0. 258 133 976	1. 950[-5][a]		-0. 240 314 494	6. 98 [-6][a]
6	-0. 239 695 136	9. 167[-6]	6	-0. 244 807 143	1. 163[-5]	6	-0. 234 966 464	4. 133[-6]
	-0. 239 696 887	9. 200[-6][a]		-0. 244 807 489	1. 160[-5][a]		-0. 234 969 582	4. 084[-6][a]
7	-0. 234 565 599	6. 102[-6]	7	-0. 237 670 165	7. 124[-6]	7	-0. 231 690 681	2. 624[-6]
	-0. 234 569 038	6. 122[-6][a]		-0. 237 672 213	7. 156[-6][a]		-0. 231 692 116	2. 600[-6][a]
8	-0. 231 419 790	4. 201[-6]	8	-0. 233 432 364	4. 651[-6]	8	-0. 229 534 909	1. 768[-6]
	-0. 231 421 646	4. 200[-6][a]		-0. 233 433 327	4. 644[-6][a]		-0. 229 535 701	1. 760[-6][a]
9	-0. 229 344 766	2. 977[-6]	9	-0. 230 718 511	3. 168[-6]	9	-0. 228 040 350	1. 248[-6]
	-0. 229 345 782	2. 982[-6][a]		-0. 230 719 088	3. 156[-6][a]		-0. 228 040 873	1. 246[-6][a]
10	-0. 227 902 299	2. 175[-6]	10	-0. 228 879 603	2. 239[-6]	10	-0. 226 961 568	9. 153[-7]
	-0. 227 902 914	2. 182[-6][a]		-0. 228 880 000	2. 234[-6][a]		-0. 226 962	2. [-6][a]
11	-0. 226 858 396	1. 633[-6]	11	-0. 227 577 458	1. 634[-6]			
	-0. 226 859	2. [-6][a]		-0. 227 577 8	1. 6 [-6][a]			

[a]) Bürgers, Wintgen and Rost (1995) [123]

Table 3.11: $^3D^e$ resonances below N=3 threshold ($\ell_{max} = 8$).

A			B			C		
n	E (au)	Γ (au)	n	E (au)	Γ (au)	n	E (au)	Γ (au)
4	-0. 269 760 137	3. 740 [-5]	4	-0. 283 046 467	4. 890 [-5]	4	-0. 250 840 023	9. 559 [-6]
	-0. 269 76	— [a]		-0. 283 14	— [a]		-0. 250 72	— [a]
5	-0. 249 134 456	6. 642 [-5]	5	-0. 255 929 620	3. 056 [-5]			
	-0. 249 14	— [a]		-0. 255 94	— [a]			

D			E			F		
n	E (au)	Γ (au)	n	E (au)	Γ (au)	n	E (au)	Γ (au)
						3	-0. 325 326 889	7. 271 [-4]
							-0. 326 58	— [a]
			4	-0. 261 601 751	1. 684 [-6]	4	-0. 267 315 659	2. 458 [-4]
				-0. 261 62	— [a]		-0. 267 60	— [a]
5	-0. 239 589 052	6. 263 [-7]	5	-0. 245 602 301	9. 169 [-7]	5	-0. 248 816 197	7. 765 [-5]
	—	—		-0. 245 58	— [a]		-0. 248 88	— [a]

[a] Oberoi (1972) [177]

For $^3D^e$ the picture would be identically neat, were not for the formidable dive in the first part of F series (see table 15 in appendix K). F is asymptotically the narrowest series and should therefore be assigned $[200]^0$ label (see figure 3.2.c, third row from below). Still it starts with a reduced width well above all other series and reaches its limiting $\bar{\Gamma}$ value beyond the sixth term only. Looking at the corresponding μ plot a possible explanation is found: F resonances are almost degenerate with A resonances, corresponding to the largest $[011]^+$ series, the only channel which decays AI. Because of this, small departures from the asymptotic condition are sufficient to cause the strong mixing and the consequent width sharing observed here. Indeed this is an evidence of the shortcoming of the propensity rules based upon approximate model, making the assignment of the first two terms to A or F series a matter of taste. The other series are regular. E is probably $[002]^-$ which decays BII. The assignment of the remaining B, C and D series is uncertain.

The agreement between present and literature data in $^3P^e$ symmetry [178, 182, 201] are comparable to the $^3P^o$ case (Table 3.12): few millionths of au at worst for resonance positions, few thousandths for resonance widths. $^3P^e$ picture (figure 3.8.a) is interpreted plainly (see figure 3.1.a): A is the $[011]^+$ series which decays AI, and B is the $[101]^+$ series which decays $CIII$. Very good agreement is found with literature data by Ho and Bhatia [182].

Table 3.12: $^3P^e$ resonances below N=3 threshold ($\ell_{max} = 8$)

A			B		
n	E (au)	Γ (au)	n	E (au)	Γ (au)
2	-0. 336 083 896	4. 487[-3]			
	-0. 336 087 9	4. 489[-3] [a]			
3	-0. 271 555 941	1. 788[-3]	3	-0. 291 155 340	7. 399[-5]
	-0. 271 557 150	1. 789[-3] [a]		-0. 291 158 23	7. 40 [-5] [a]
4	-0. 250 930 988	8. 553[-4]	4	-0. 253 574 102	2. 350[-5]
	-0. 250 931 50	8. 55 [-4] [a]		-0. 253 574 650	2. 352[-5] [a]
5	-0. 240 959 065	4. 552[-4]	5	-0. 241 957 507	1. 444[-5]
	-0. 240 960	4. 5 [-4] [a]		-0. 241 958 3	1. 44 [-5] [a]
			6	-0. 235 890 571	9. 539[-6]
				-0. 235 894	8. 0 [-6] [a]

[a]) Ho and Bhatia (1993) [182]

$^3D^o$ (figure 3.8.c) does not correspond closely to the prediction of propensity rules (see figure 3.1.b). The three series $[002]^+$, $[011]^-$ and $[101]^0$ which decay BI, AII and $CIII$ respectively, should be well separated. A series is actually clearly recognized as the expected largest $[002]^+$ series and the low energy of its first term confirms this. B and C series, though, have comparable widths and even intersect around $n^* = 8$. On the basis of first term energy, B should be the $[001]^-$ series,

but in that case the AII mechanism would be asymptotically half as effective as the $CIII$ mechanism.

Table 3.13: $^3P^o$ resonances below N=3 threshold. $[n] = 10^n$.

A $[N_1N_2m]^A = [020]^+$

n	E (au)	Γ (au)
3	-0.350 370	2.982[-3]
	-0.350 38	2.99 [-3][a]
	-0.350 378	2.987[-3][b]
4	-0.279 4761	1.379[-3]
	-0.279 4776	1.374[-3][b]
5	-0.255 161	6.489[-4]
	-0.255 162	6.46 [-4][b]
6	-0.243 374	3.355[-4]
	-0.243 38	3.3 [-4][b]
7	-0.236 875	1.904[-4]
	-0.236 875	1.92 [-4][b]

B $[N_1N_2m]^A = [110]^+$

n	E (au)	Γ (au)
4	-0.309 375	1.121[-3]
	-0.309 38	1.12 [-3][a]
	-0.309 380	1.118[-3][b]
5	-0.260 2321	3.111[-4]
	-0.260 2339	3.100[-4][b]
6	-0.245 2337	1.556[-4]
	-0.245 2350	1.553[-4][b]
7	-0.237 754	8.867[-5]
	-0.237 757	8.74 [-5][b]
8	-0.233 430	5.514[-5]
	-0.233 401	6.0 [-5][b]

C $[N_1N_2m]^A = [011]^-$

n	E (au)	Γ (au)
4	-0.278 816 98	6.261[-5]
	-0.278 817 05	6.256[-5][b]
5	-0.253 5529	3.343[-5]
	-0.253 5529	3.345[-5][b]
6	-0.242 1895	1.964[-5]
	-0.242 1903	1.7 [-5][b†]
7	-0.236 0681	1.217[-5]
	-0.236 0682	8.0 [-6][b]

D $[N_1N_2m]^A = [101]^-$

n	E (au)	Γ (au)
4	-0.258 5246	5.367[-6]
	-0.258 5249	5.361[-6][b]
5	-0.244 0364	3.571[-6]
	-0.244 0367	3.57 [-6][b]
6	-0.237 0107	2.532[-6]
	-0.237 0131	1.916[-6][b]

E $[N_1N_2m]^A = [200]^0$

n	E (au)	Γ (au)
5	-0.246 0593	3.523[-7]
	-0.246 0597	3.512[-7][b]
6	-0.238 5110	2.223[-7]
	-0.238 5119	2. [-7][b]

[a])Lindroth (1994) [178]
[b])Ho (1993) [183]
[†] Changed value. See text for details.

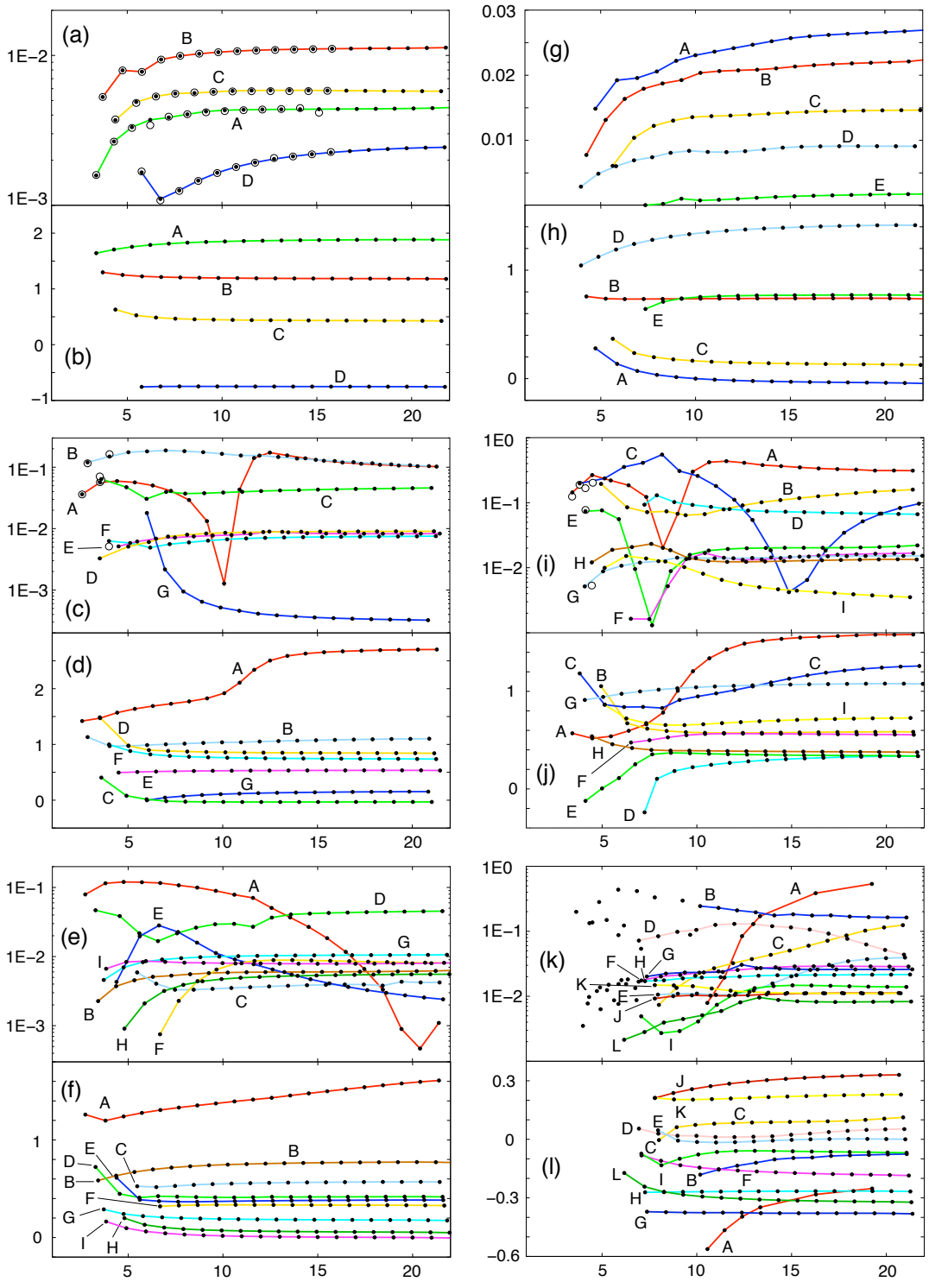

Figure 3.5: Reduced widths and quantum defects vs effective quantum number n^* for ^{3}S, ^{3}P^o and ^{3}D^e states below N=4 and N=5 thresholds. Below N=4 : a) $\bar{\Gamma}_{^3S}$, b) $\mu_{^3S}$, c) $\bar{\Gamma}_{^3P^o}$, d) $\mu_{^3P^o}$, e) $\bar{\Gamma}_{^3D^e}$, f) $\mu_{^3D^e}$. Below N=5 : g) $\bar{\Gamma}_{^3S}$, h) $\mu_{^3S}$, i) $\bar{\Gamma}_{^3P^o}$, j) $\mu_{^3P^o}$, k) $\bar{\Gamma}_{^3D^e}$, l) $\mu_{^3D^e}$. White circles are the most accurate data available in literature. See text for details.

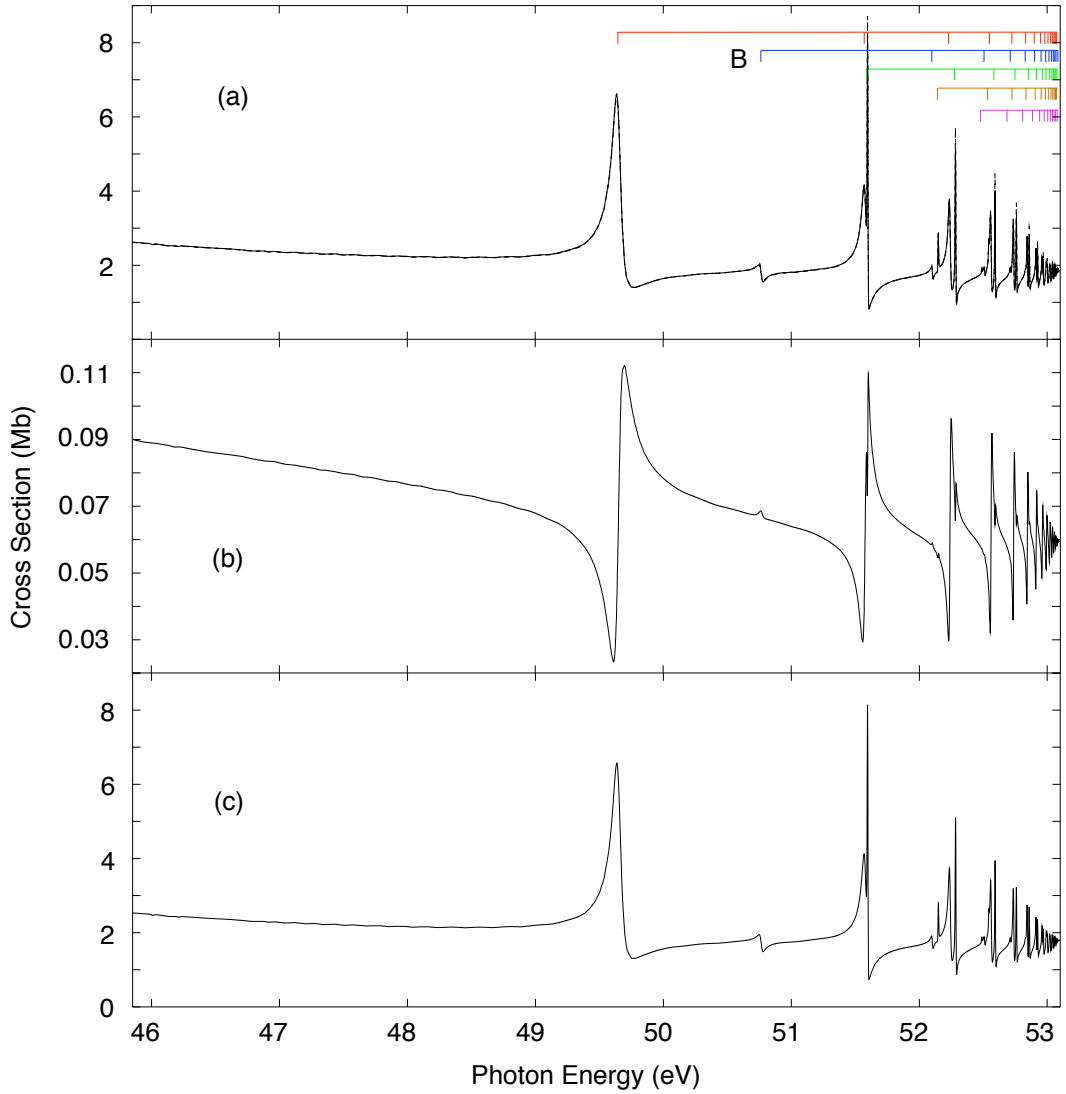

Figure 3.6: Total cross section σ_{tot} (a) and partial cross sections σ_1 (b) and σ_2 (c) below N=3 threshold. A) $[020]^+$, B) $[110]^+$, C) $[011]^-$, D) $[101]^-$, E) $[200]^0$.

Photoionization cross sections In figure 3.6.a the total cross section below N=3 threshold is reported in length, velocity and acceleration gauges. As before the gauge agreement is excellent. At this resolution, all resonances in the first complete multiplet, that between 52.45 eV and 52.65 eV, should be recognizable. The second term of $[011]^-$ series and the third term in $[020]^+$ series give rise to peaks in the total cross section of comparable intensity. The other three terms are smaller by roughly an order of magnitude. As expected, σ_2 is the largest partial cross section. In σ_1 $[020]^+$ series is actually dominant on the whole energy range (see figures 3.6.b and 3.7.b), $[011]^-$ series is ten times smaller, $[200]^0$ and $[110]^+$ series are barely visible and $[101]^-$ series cannot be recognized at all. In σ_2 (see figures 3.6.c and 3.7.c), which is roughly thirty times larger that σ_1, all five series are clearly visible and $[011]^-$ series is only slightly less intense than $[020]^+$ series.

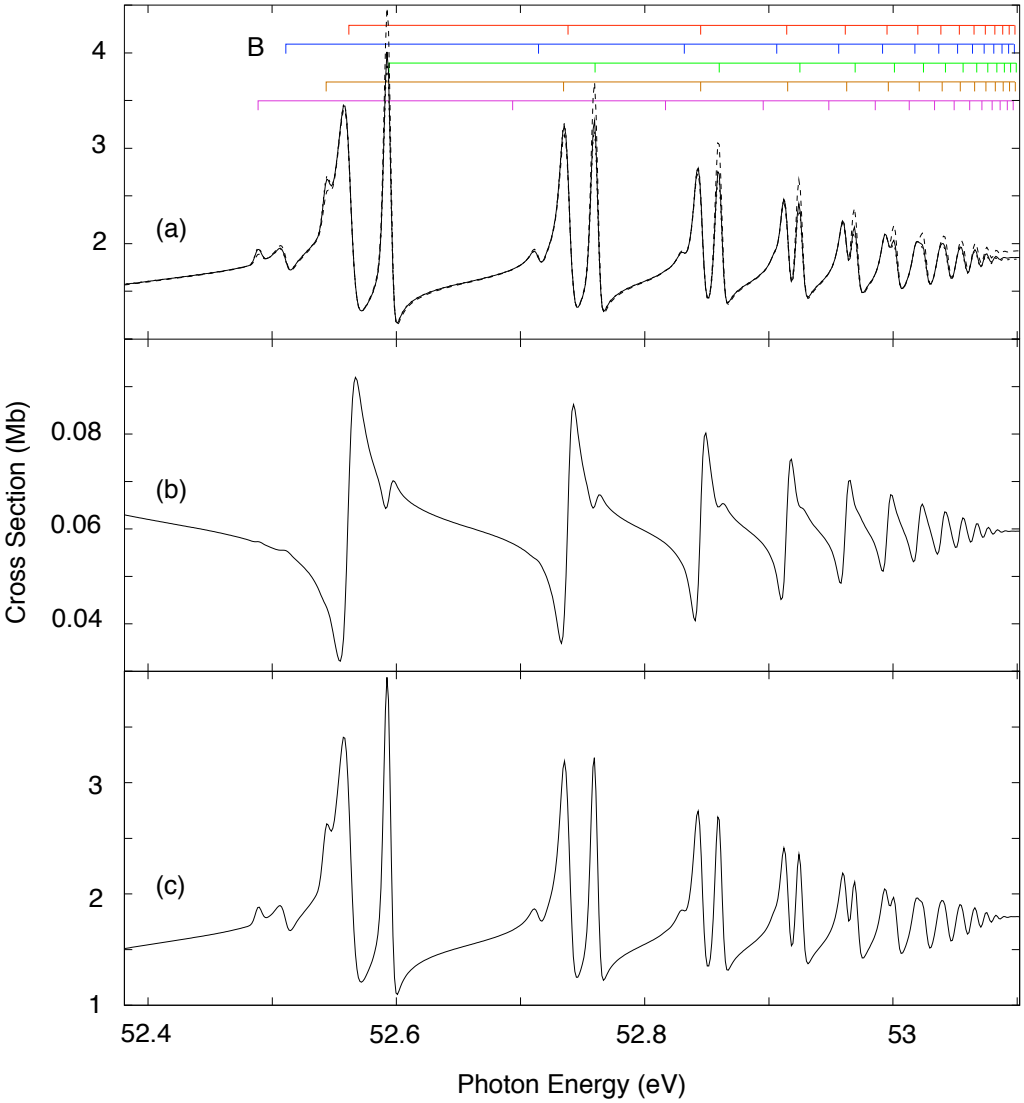

Figure 3.7: Details of total cross section σ_{tot} (a) and partial cross sections σ_1 (b) and σ_2 (c) below N=3 threshold. See figure 3.6 for label description.

In figure 3.6.a, in the non-resonant photon energy region between 46 and 49 eV, small oscillations can be seen. Such artifacts are found in all spectra immediately after the opening of a new parent ion excitation threshold. A similar disturbance appears also in the total phase-shift. These fictitious oscillations fade rapidly in both frequency and amplitude, getting completely negligible after a couple of effective quantum number units. In test calculations we have verified that enlarging the quantization box the oscillations get progressively smaller, leaving essentially unaltered the resonant structure and the average background. Given the excellent agreement of our resonance parameters with the best of those found in literature [176] and the excellent agreement among the three gauges, we concluded that the present calculation was already enough accurate to satisfactorily reproduce all the interesting phenomena in the energy region examined here.

3.7 Below N=4 threshold.

To account for accuracy of metastable states in this energy region, table 3.14 compares some ^{3}S states with accurate data by Bürgers *et al* [123]. Energy differences are of the order of 10^{-6} au, often much smaller than that, and resonance widths are in agreement within one part in a hundred or even a thousand. In figure 3.5.a, the whole set of results by Bürgers *et al* is plotted: even the available higher terms are shown to be in striking agreement with our data. All series have comparable reduced widths, the narrowest D is assigned tentatively to $[300]^-$ channel, decaying $CIII$ (see figure 3.2.a, fourth row from below), but the other three are too similar to be confidently assigned to the remaining $[210]^-$, $[120]^-$ and $[030]^-$ channels. Our calculation predicts a "collision" between B and D series to take place around $n^* = 6$. The same feature is clearly seen already in Bürgers data and therefore should be reliable.

The mestastable ^{3}P^o states below N=4 threshold reported in literature [181] are far less accurate than below lower thresholds: very good agreement is found within the discernible accuracy of available data. The large discrepancy for the D resonance is probably a shortcoming of literature data (Table 3.15). Moreover, in literature two series out of seven are not reported.

Table 3.14: $^3S^e$ resonances below N=4 threshold. $[n] = 10^n$.

A			B		
n	E (au)	Γ (au)	n	E (au)	Γ (au)
5	-0.169 3070	4.174[-5]	5	-0.161 480 68	1.041[-4]
	-0.169 3066	4.202[-5][a]		-0.161 480 66	1.040[-4][a]
6	-0.152 1222	3.366[-5]	6	-0.147 168 47	7.429[-5]
	-0.152 1220	3.360[-5][a]		-0.147 168 81	7.423[-5][a]
7	-0.143 1745	2.302[-5]	7	-0.139 996	4.045[-5]
	-0.143 1760	2.276[-5][a]		-0.139 998	4.035[-5][a]
8	-0.137 9605	1.551[-5]	8	-0.135 8564	3.005[-5]
	-0.137 9613	1.428[-5][a]		-0.135 8574	3.003[-5][a]
9	-0.134 6788	1.039[-5]	9	-0.133 2298	2.097[-5]
	-0.134 6795	1.051[-5][a]		-0.133 2304	2.101[-5][a]
10	-0.132 4903	7.421[-6]	10	-0.131 4566	1.505[-5]
	-0.132 4907	7.430[-6][a]		-0.131 4570	1.509[-5][a]

C			D $[N_1N_2m]^A = [300]^-$		
n	E (au)	Γ (au)	n	E (au)	Γ (au)
5	-0.151 176 48	4.434[-5]	5	-0.140 0872	8.689[-6]
	-0.151 176 42	4.482[-5][a]		-0.140 0885	8.818[-6][a]
6	-0.141 6904	2.983[-5]	6	-0.135 9726	3.585[-6]
	-0.141 6914	2.939[-5][a]		-0.135 9755	3.504[-6][a]
7	-0.136 7854	1.932[-5]	7	-0.133 3279	2.701[-6]
	-0.136 7871	1.924[-5][a]		-0.133 3292	2.680[-6][a]
8	-0.133 8106	1.304[-5]	8	-0.131 5331	2.183[-6]
	-0.133 8117	1.299[-5][a]		-0.131 5337	2.174[-6][a]
9	-0.131 8487	8.995[-6]	9	-0.130 2610	1.779[-6]
	-0.131 8492	9.080[-6][a]		-0.130 2614	1.772[-6][a]
10	-0.130 4807	6.559[-6]	10	-0.129 3271	1.453[-6]
	-0.130 4810	6.566[-6][a]		-0.129 3274	1.448[-6][a]

[a]) Bürgers, Wintgen and Rost (1995) [123]

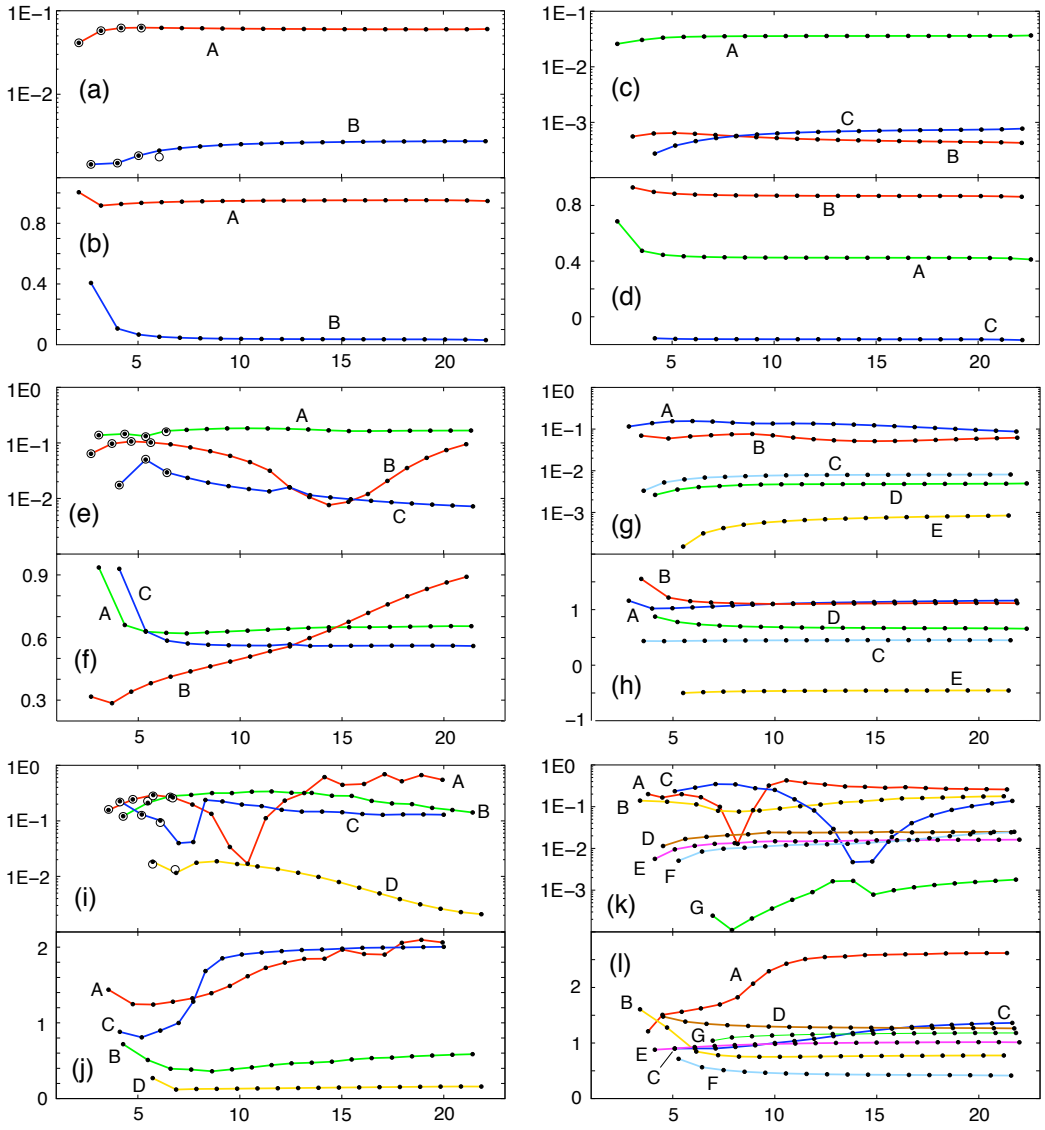

Figure 3.8: Reduced widths and quantum defects vs effective quantum number n^* for $^3P^e$ and $^3D^o$ states below N=3, N=4 and N=5 thresholds. Below N=3 : a) $\bar{\Gamma}_{^3P^e}$, b) $\mu_{^3P^e}$, c) $\bar{\Gamma}_{^3D^o}$, d) $\mu_{^3D^o}$. Below N=4 : e) $\bar{\Gamma}_{^3P^e}$, f) $\mu_{^3P^e}$, g) $\bar{\Gamma}_{^3D^o}$, h) $\mu_{^3D^o}$. Below N=5 : i) $\bar{\Gamma}_{^3P^e}$, j) $\mu_{^3P^e}$, k) $\bar{\Gamma}_{^3D^o}$, l) $\mu_{^3D^o}$. White circles are the most accurate data available in literature. See text for details

Table 3.15: $^3P^o$ resonances below N=4 threshold ($\ell_{max} = 8$).

A			B			C		
n	E (au)	Γ (au)	n	E (au)	Γ (au)	n	E (au)	Γ (au)
4	-0. 200 081 541	2. 106[-3]	4	-0. 185 761 841	5. 077[-3]	4	-0. 163 688 665	1. 380[-3]
	-0. 200 08	2. 1 [-3][a]		-0. 185 75	4. 9 [-3][a]		-0. 163 7	1. 34 [-3][a]
5	-0. 165 151 518	1. 285[-3]	5	-0. 155 787 599	2. 286[-3]			
	-0. 165 14	1. 3 [-3][a]		-0. 155 8	2. 5 [-3][a]			

D			E			F		
n	E (au)	Γ (au)	n	E (au)	Γ (au)	n	E (au)	Γ (au)
5	-0. 165 479 474	7. 553[-5]	5	-0. 149 636 646	5. 621[-5]	5	-0. 156 237 035	9. 798[-5]
	-0. 165 482	1. 63 [-3][a]		—	—		-0. 156 24	8. [-5][a]

G		
n	E (au)	Γ (au)
6	-0. 138 880 613	8. 298[-5]
	—	—

[a]Ho (1982) [181]

Below N=4 threshold, the first intruder states appear in $^3P^o$, $^3P^e$ and $^3D^e$ series. $^3P^o$ hosts the first intruder state of this survey. Theory predicts three "strong" channels, $[030]^+$, $[120]^+$ and $[210]^+$ which all decay AI (see figure 3.2.b, fourth row from below), and clearly correspond to A, B and C series collectively; three "intermediate" channels, $[021]^-$ (AII and BII), $[111]^-$ (AII and BII) and $[201]^-$ (BII), corresponding to the group formed by D, E and F series; and finally the narrowest channel $[300]^0$ ($CIII$) which corresponds to G series. The intruder state should be $[040]_5^+$, since it has the largest K among series converging to the higher N=5 threshold. It interacts exclusively with A series which therefore should correspond plainly to $[030]^+$ series. In figures 3.12.a and 3.12.b and in table 3.20 details of $[040]_5^+$ intruder state characterization are reported. Since the assignment of the remaining series would be questionable, it is not considered here. Once again there is an interaction between a narrow and a large series: the first term of G series collides with the third term of C series causing the former to be unusually large and the latter to quench slightly.

As below N=3 threshold, the only available data for $^3D^e$ states are due to Oberoi (1972) [177]. Rather large discrepancies with our results (Table 3.16) are found. Beyond ^3S states, $^3P^e$ states are those most accurately computed below N=4 threshold. Comparison with data by Ho and Bhatia [182] are generally within few millionths of au, with an isolated spike of $1.7 \cdot 10^{-5}$ au for the lowest metastable state in A series (Table 3.17).

In $^3D^e$ symmetry there is one intruder state, probably $[031]_5^+$ (see figure 3.2.c). It dissolves in A series, thus identified with $[021]^+$ channel (AI decay). $[111]^+$, the other large series in the multiplet, is recognized as D series. E series should correspond to the narrowest $[300]^0$ channel ($CIII$). D collides around its fourth term with E series, and around its ninth term with A series. All other series are regular. The detailed assignment to the remaining $[012]^-$, $[030]^-$, $[102]^-$, $[120]^-$, $[201]^0$ and $[210]^-$ channels is left unsettled. In figures 3.12.e and 3.12.f and table 3.20 details of $[031]_5^+$ intruder state characterization are reported. As a concluding remark, we observe that the quantum defect of A series rises by merely 0.4 units: it therefore lays half below and half above threshold. Unfortunately, as examined in greater detail in the following subsection, the low energy region in $^3D^e$ symmetry below N=5 threshold is particularly demanding: large series, like that the present perturber state belongs to, are often indistinguishable from a smooth background in the total phaseshift, so that a clear sign of $[031]_5^+$ intruder state cannot be recognized above threshold. Still it is true that total phaseshift baseline above N=4 threshold rises steadily in possible agreement with a low energy resonance with large width.

Table 3.16: $^3D^e$ resonances below N=4 threshold ($\ell_{max} = 8$).

A			B			C		
n	E (au)	Γ (au)	n	E (au)	Γ (au)	n	E (au)	Γ (au)
4	-0. 191 597 213	3. 850[-3]	4	-0. 167 875 236	5. 697[-5]	6	-0. 141 685 015	3. 595[-5]
	-0. 192 658	— [a]		—	— [a]		—	—
5	-0. 159 583 226	2. 088[-3]	5	-0. 151 230 011	4. 479[-5]			
	-0. 159 356	— [a]		-0. 151 200	—			

D			E			F		
n	E (au)	Γ (au)	n	E (au)	Γ (au)	n	E (au)	Γ (au)
4	-0. 171 555 467	1. 328[-3]	5	-0. 150 986 983	5. 089[-5]	7	-0. 136 205 239	2. 519[-6]
	-0. 171 518	— [a]		-0. 150 160	— [a]		—	—
5	-0. 149 126 704	4. 083[-4]						
	-0. 148 868	— [a]						

G			H			I		
n	E (au)	Γ (au)	n	E (au)	Γ (au)	n	E (au)	Γ (au)
4	-0. 161 297 966	8. 979[-5]	5	-0. 146 691 679	8. 190[-6]	4	-0. 158 979 138	1. 181[-4]
	-0. 161 104	— [a]		—	—		-0. 158 672	— [a]

[a] Oberoi (1972) [177]

Table 3.17: $^3P^e$ resonances below N=4 threshold ($\ell_{max} = 8$).

A			B			C		
n	E (au)	Γ (au)	n	E (au)	Γ (au)	n	E (au)	Γ (au)
4	-0. 178 240 156	4. 775[-3]	4	-0. 194 440 707	3. 296[-3]	4	-0. 155 172 439	2. 582[-4]
	-0. 178 257	4. 807[-3][a]		-0. 194 442	3. 305[-3][a]		-0. 155 177 6	2. 585[-4][a]
5	-0. 151 544 472	1. 776[-3]	5	-0. 161 234 044	1. 888[-3]	5	-0. 142 343 805	3. 229[-4]
	-0. 151 550	1. 766[-3][a]		-0. 161 223	1. 903[-3][a]		-0. 142 342	3. 285[-4][a]
6	-0. 142 327 804	8. 540[-4]	6	-0. 148 031 683	1. 053[-3]	6	-0. 137 150 797	1. 117[-4]
	-0. 142 341	8. 379[-4][a]		-0. 148 032	1. 05 [-3][a]		-0. 137 15	1. 1 [-4][a]
7	-0. 137 292 634	6. 339[-4]	7	-0. 140 836 221	5. 758[-4]			
	-0. 137 30	6. 12 [-4][a]		-0. 140 84	5. 7 [-4][a]			

[a])Ho and Bhatia (1993) [182]

In $^3P^e$ symmetry, the third and last intruder state below this threshold, probably $[031]^+_5$, is encountered. It interacts strongly (AI mechanism) with $[021]^+$ channel which is recognized in B series, the only one whose quantum defect rises steadily by a significant amount (see figure 3.8.f). As B series drifts through the resonant multiplet, it collides about $n^* = 12.5$ with the narrowest C series, which has $[201]^+$ character ($CIII$ mechanism). The remaining A series corresponds to the $[111]^+$ channel (AI mechanism), in accordance to the fact that its fundamental states has an higher energy than that of the first term in B series. The second term of C series is almost degenerate with the third term of A series. This circumstance is confirmed by the independent calculations by Ho and Bhatia [182] which beautifully agree with our data (see figure 3.8.e). Again this collision causes a small dip in A series and a small peak in C series.

At the best of our knowledge, no $^3D^o$ data are available for comparison below N=4 threshold.

$^3D^o$ symmetry (see figure 3.8.c) is regular. Its five A, B, C, D and E series are straightforwardly assigned to the $[012]^+$ (AI), $[102]^+$ (BI), $[021]^-$ (AII), $[111]^-$ (AII) and $[201]^0$ ($CIII$) channels respectively. A and B series are almost degenerate and intersects around $n^* = 10$. In that neighbourhood the two corresponding $\bar{\Gamma}$ series get slightly closer.

Photoionization cross sections Four main characteristic should be noted in photoionization spectrum: i) there is again a clearly dominating series: $[030]^+$ (see figures L.10 and 3.9), ii) between 55.5 eV and 55.75 eV a nice interference effect due to $[040]^+_5$ intruder state can be appreciated (see figure 3.9), iii) a mirroring behaviour between σ_1 and σ_2 is visible, iv) the largest resonant features in total cross section are one order of magnitude smaller than the background. The grey region (yellow in the on-line version) highlights the $[E_r - \Gamma_r : E_r + \Gamma_r]$ energy interval ($E_r = -0.128875(7)$ au $\iff$ $E_\gamma = 55.5675(2)$ eV, $\Gamma_r = 1.37(2)\,10^{-3}$ au $= 37.3(5)$ meV) where the intruder state dissolve in $[030]^+$ series, as described at length in [176]. The situation is very similar to that encountered below N=4 threshold in the photoionization of the fundamental $1s^2$ state [111].

3.8 Below N=5 threshold.

Below N=5 threshold the whole ^3S, $^3D^e$, $^3D^o$ symmetries and four series out of nine in $^3P^o$ symmetry are not as yet reported in literature.

In $^3S^e$ symmetry there are no signatures of intruder states. Except E series, which is recognized as the narrow $[400]^-$ series (see figure 3.5.g), the other four series, $[310]^-$, $[220]^-$, $[130]^-$ and $[040]^-$, with comparable reduced widths, are left unassigned. Please note that in this case the reduced widths are plotted on a linear scale (figure 3.5.g) A tiny collision between E and B series takes place around $n^* = 9.2$.

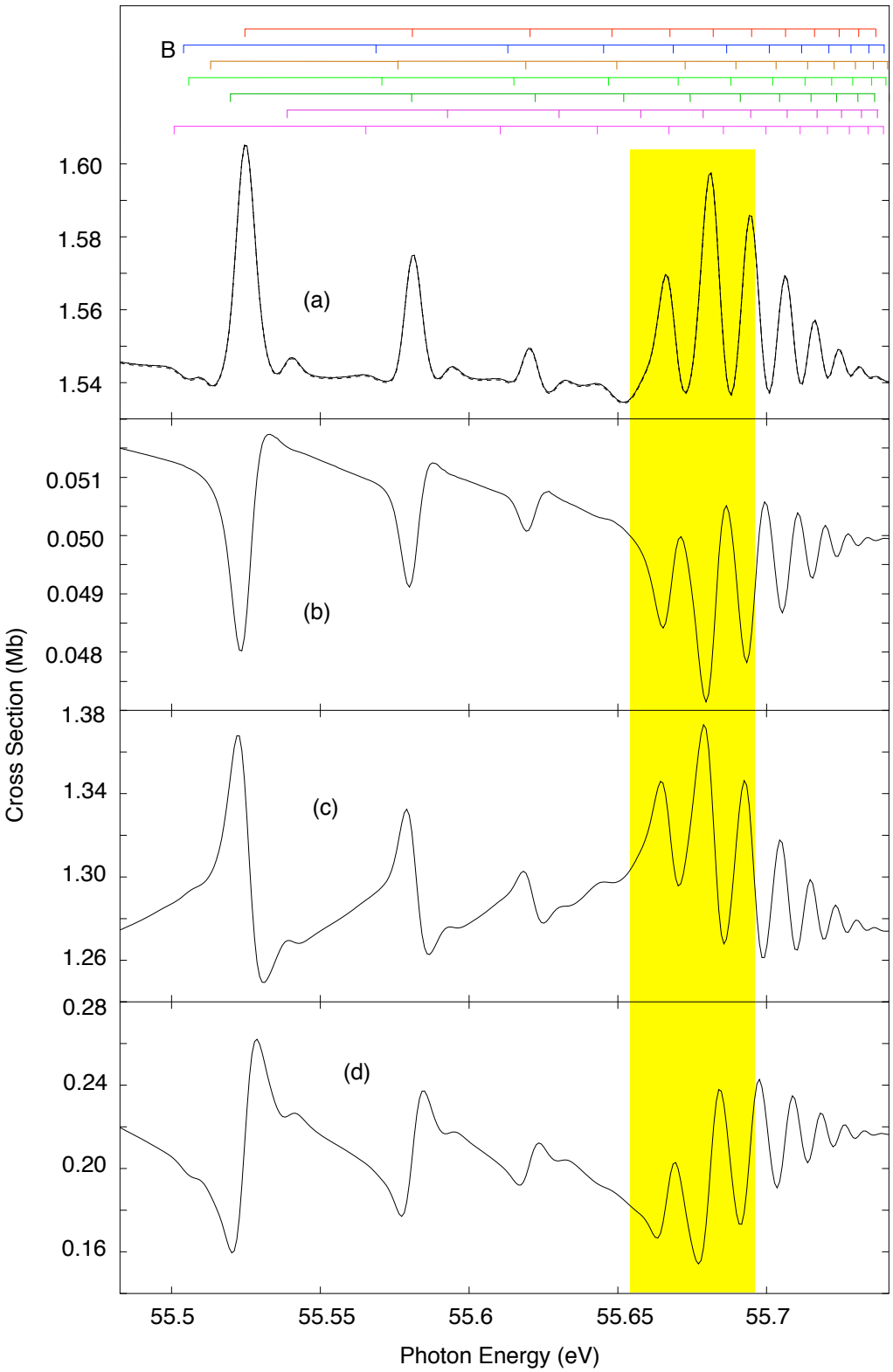

Figure 3.9: Details of the total and partial cross sections below N=4 threshold. σ_{tot} (a), σ_1 (b), σ_2 (c), σ_3 (d). See figure L.10 and text for label details.

Table 3.18: $^3P^o$ resonances below N=5 threshold ($\ell_{max} = 8$).

A			B			C		
n	E (au)	Γ (au)	n	E (au)	Γ (au)	n	E (au)	Γ (au)
4	-0. 122 504 611	3. 565[-3]	6	-0. 100 430 772	1. 609[-3]	5	-0. 114 321 608	3. 554[-3]
	-0. 122 75	3. 1 [-3][a]		—	—		-0. 114 35	3. 4 [-3][a]
5	-0. 104 893 779	2. 953[-3]						
	-0. 104 55	2. 2 [-3][a]						

D			E			F		
n	E (au)	Γ (au)	n	E (au)	Γ (au)	n	E (au)	Γ (au)
7	-0. 089 539 098	2. 456[-4]	4	-0. 109 415 996	1. 054[-3]	7	-0. 091 745 806	5. 923[-6]
	—	—		-0. 109 375	1. 1 [-3][a]		—	—

G			H			I		
n	E (au)	Γ (au)	n	E (au)	Γ (au)	n	E (au)	Γ (au)
5	-0. 109 915 045	7. 560[-5]	5	-0. 105 129 575	1. 361[-4]	6	-0. 098 954 598	7. 344[-5]
	-0. 109 465	2. 39 [-3][a]		-0. 105 125	6. [-5][a]		—	—

[a]Ho (1982) [181].

The most recent $^3P^o$ data [181] are 25 years old and are in rather poor agreement with our results with some large differences like in A resonance energies and G resonance width (Table 3.18).

We feel that no definitive conclusions can be drawn from this comparison: literature data may simply be unfit to certify the reliability of our $^3P^o$ calculation in this energy window. Two intruder states, probably $[050]_6^+$ and $[140]_6^+$, can be recognized. $[050]_6^+$ dissolves through AI mechanism in $[040]^+$ channel and falls at an energy lower than that of the second intruder state. This leads to assign $[040]^+$ character to A series. Analogously, C series is recognized as the $[130]^+$ channel. B and D series should correspond to $[220]^+$ and $[310]^+$ channels respectively and I series to the asymptotically narrowest $[400]^0$ channel. The other series cannot be assigned unequivocally. They collectively correspond to the remaining $[031]^-$, $[121]^-$, $[211]^-$ and $[301]^-$ channels which decay by either AII or BII mechanism. A remarkable violation of propensity rules is to be noted here: E and F channels, which should be left undisturbed by the intruder state, actually suffer a strong quenching in close correspondence to that in A series. The few available data for comparison, by Ho [181], date back to 1982 and are in poor agreement with ours.

In $^3D^e$ symmetry, at low energy, the regularity of resonance series is almost completely destroyed: those clearly discernible paths at high effective quantum numbers could not be confidently prolonged below n^* around 8 for most series, whose assignment is therefore particularly problematic. At least one, maybe two, intruder states fall here, probably $[041]_6^+$ and $[131]_6^+$ (see figure 3.5.k). A and C series are probably $[121]^+$ and $[031]^+$ channels respectively, while B series corresponds to the remaining "unperturbed" channel $[211]^+$ among those which decay through AI mechanism. The fitting procedure failed to localize as much as four terms of A series. This is because their reduced width is comparable to a whole $\Delta\mu = 1$ interval so that their effect on the total phaseshift could not be distinguished from the background. The effectiveness of the fitting procedure is compromised also by the large number of terms in each multiplet (12) which "hide" the largest ones. In the case of $^3P^e$ symmetry, where some series are even larger than in $^3D^e$ symmetry, all terms could actually be determined because multiplets are only fourfold.

Below N=5 threshold, the most accurate data available in literature for a comparison are for $^3P^e$ states (see table 3.19). The quantitative agreement of our results with those obtained by Ho and Bhatia [182] is less accurate: energy differences as large as 10^{-4} au are found. The deviations found, however, are small indeed and the resonance widths are still in good agreement, as the superposition of the two data sets in figure 3.8.i shows. The general features of autoionizing series should therefore be reliable. In $^3P^e$ two intruder states, probably $[041]_6^+$ and $[131]_6^+$ (those with predictably the lowest energies), can be observed (see figure 3.1.a and 3.8.i). $[041]_6^+$ dissolves in $[031]^+$ channel, which thus corresponds to C series, while $[131]_6^+$ dissolves in $[121]^+$ channel, recognized in A series. The remaining large B series is unaffected by intruder states and is therefore identified with the $[211]^+$ channel. Finally D series corresponds to the narrowest $[301]^+$ channel. The picture here is very neat: μ rises are independent and almost complete ($\Delta\mu = 1$), and there are no clear signs of collisions between series. The available literature data [182] are

Table 3.19: $^3P^e$ resonances below N=5 threshold. $[n] = 10^n$.

A $[N_1N_2m]^A = [121]^+$			B $[N_1N_2m]^A = [211]^+$		
n	E (au)	Γ (au)	n	E (au)	Γ (au)
6	-0.109 477	3.223[-3]	6	-0.107 285	1.547[-3]
	-0.109 463	3.122[-3][a]		-0.107 27	1.53 [-3][a]
7	-0.098 555	9.301[-4]	7	-0.096 589	1.275[-3]
	-0.098 602	9.06 [-4][a]		-0.096 641	1.374[-3][a]
8	-0.093 427	4.458[-4]	8	-0.091 459	9.695[-4]
	-0.093 44	4.1 [-4][a]		-0.091 51	9.4 [-4][a]

C $[N_1N_2m]^A = [031]^+$			D $[N_1N_2m]^A = [301]^+$		
n	E (au)	Γ (au)	n	E (au)	Γ (au)
6	-0.119 404	3.458[-3]			
	-0.119 30	3.54 [-3][a]			
7	-0.102 137	2.260[-3]	7	-0.095 236	9.778[-5]
	-0.102 096	2.269[-3][a]		-0.095 254	8.85 [-5][a]
8	-0.095 081	1.525[-3]	8	-0.090 562	3.545[-5]
	-0.095 134	1.48 [-3][a]		-0.090 725	4.2 [-5][a]
9	-0.091 069	8.713[-4]			
	-0.091 11	8.5 [-4][a]			

[a])Ho and Bhatia (1993) [182]

in encouragingly good agreement with our results.

In $^3D^o$ symmetry, A quantum defect rises by a whole unit; a corresponding Fano-profile is observed in the $\bar{\Gamma}$ plot (see figure 3.8.k). C quantum defect undergoes a smooth increase by a half unit while $\bar{\gamma}$ experiences a deep quenching. Running through the multiplet, C series collides with G series between ninth and tenth C term. As a consequence, G series, which is the smallest by at least an order of magnitude, spreads slightly in this region. From the discussion above we can conclude that there are two other intruder states in $^3D^o$ symmetry. We guess them to be $[032]_6^+$, interacting with $[022]^+$ channel, which corresponds to A series, and $[122]_6^+$, interacting with $[112]^+$ channel, which corresponds to C series (see figure 3.1.b). The remaining large non interacting B series corresponds to $[202]^+$ channel. G series is recognized as the narrowest $[301]^0$ channel. Finally the remaining $[031]^-$, $[121]^-$ and $[211]^-$ channels collectively correspond to D, E, F series but are otherwise left unassigned.

Photoionization cross sections and asymmetry parameters The spectrum here has a very peculiar behaviour. Looking at figure 3.10 and 3.11 there are two strong series: E with a first peak around 56.2 eV, and D, which is responsible for the last crest of peaks beginning at 56.75 eV. E series almost dies out after the fourth term. The first four terms are actually those which deviate most from the asymptotic behaviour in terms of quantum defect of the series [176]. It is thus possible that the lowest $[050]_6^+$ intruder state is responsible for this behaviour. From figures 3.10 and 3.11 mirroring of partial cross sections σ_N and $\sigma_{N'}$ with odd $N + N'$ and mimicking of those with even $N + N'$ is apparent.

3.9 Intruder states

Intruder states dissolve in the underlying resonance series much as metastable states dissolve in the underlying continua. Intruder state parameters can indeed be extracted from μ vs E and from $\bar{\Gamma}$ vs E plots in exactly the same way as resonance parameters are extracted from the total phaseshift and q and F parameters of their Fano profile are extracted from the scattering cross section. For those intruder states which interact with only a single autoionizing series to a good approximation, the following fitting formulas for the corresponding μ and $\bar{\Gamma}$ series can be adopted:

$$\mu(E) = \frac{1}{\pi}\arctan(\epsilon) + \frac{1}{2} + \mu_0 + \mu_1\,\epsilon \tag{3.1}$$

$$\bar{\Gamma}(E) = F\,\frac{q+\epsilon}{1+\epsilon^2} + \bar{\Gamma}_0 + \bar{\Gamma}_1\,\epsilon \tag{3.2}$$

where $\epsilon \equiv 2(E - E_0)/\Gamma$ and E_0, Γ, F, q, μ_0, μ_1, $\bar{\Gamma}_0$ and $\bar{\Gamma}_1$ are fitting parameters. To characterize an intruder state, quantum defect is fitted first so to determine its energy position E_0 and width Γ. In this way μ and $\bar{\Gamma}$ fits require four parameters each.

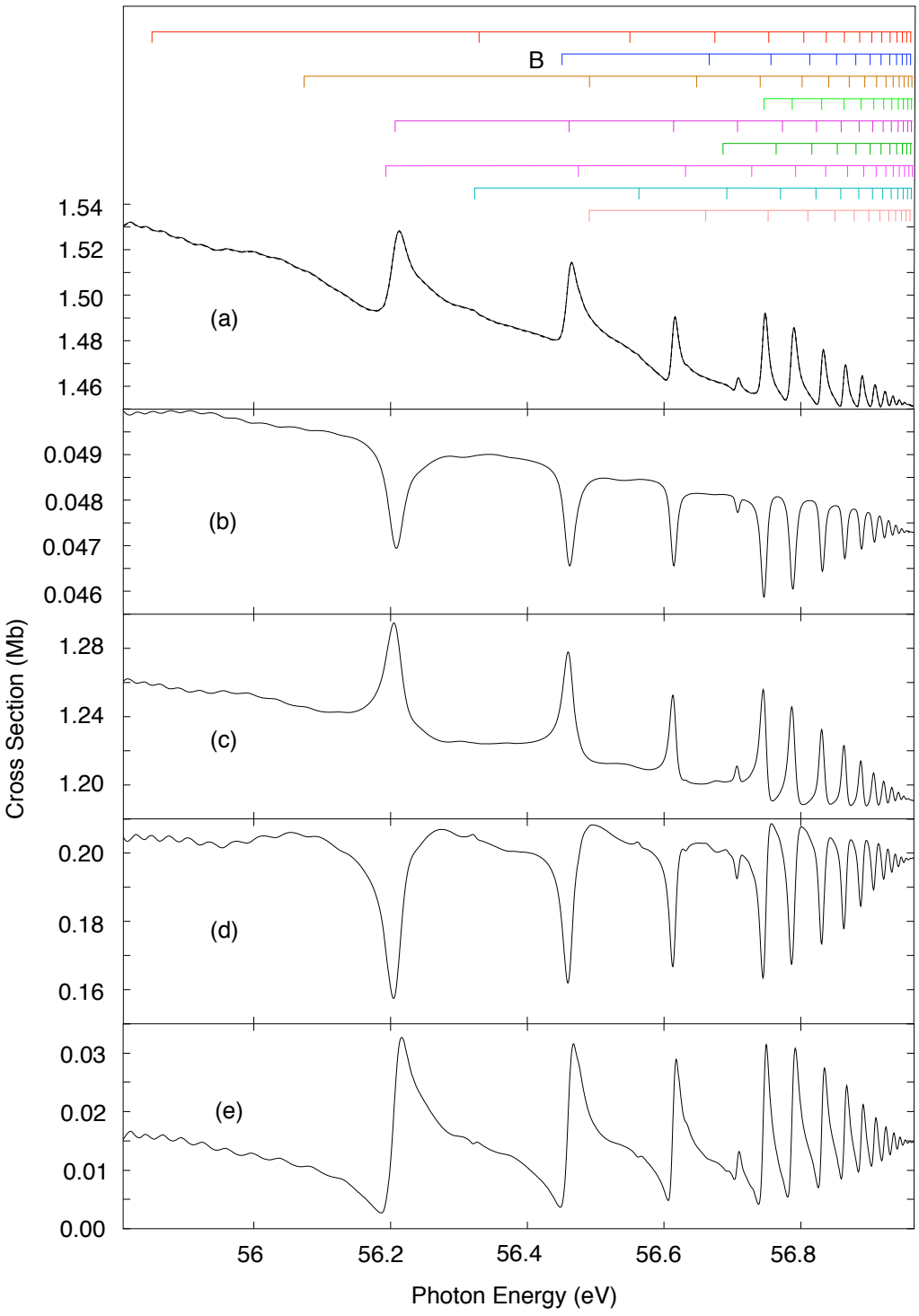

Figure 3.10: Total and partial cross sections below N=5 threshold. σ_{tot} (a), σ_1 (b), σ_2 (c), σ_3 (d), σ_4 (e). See text for label explanation.

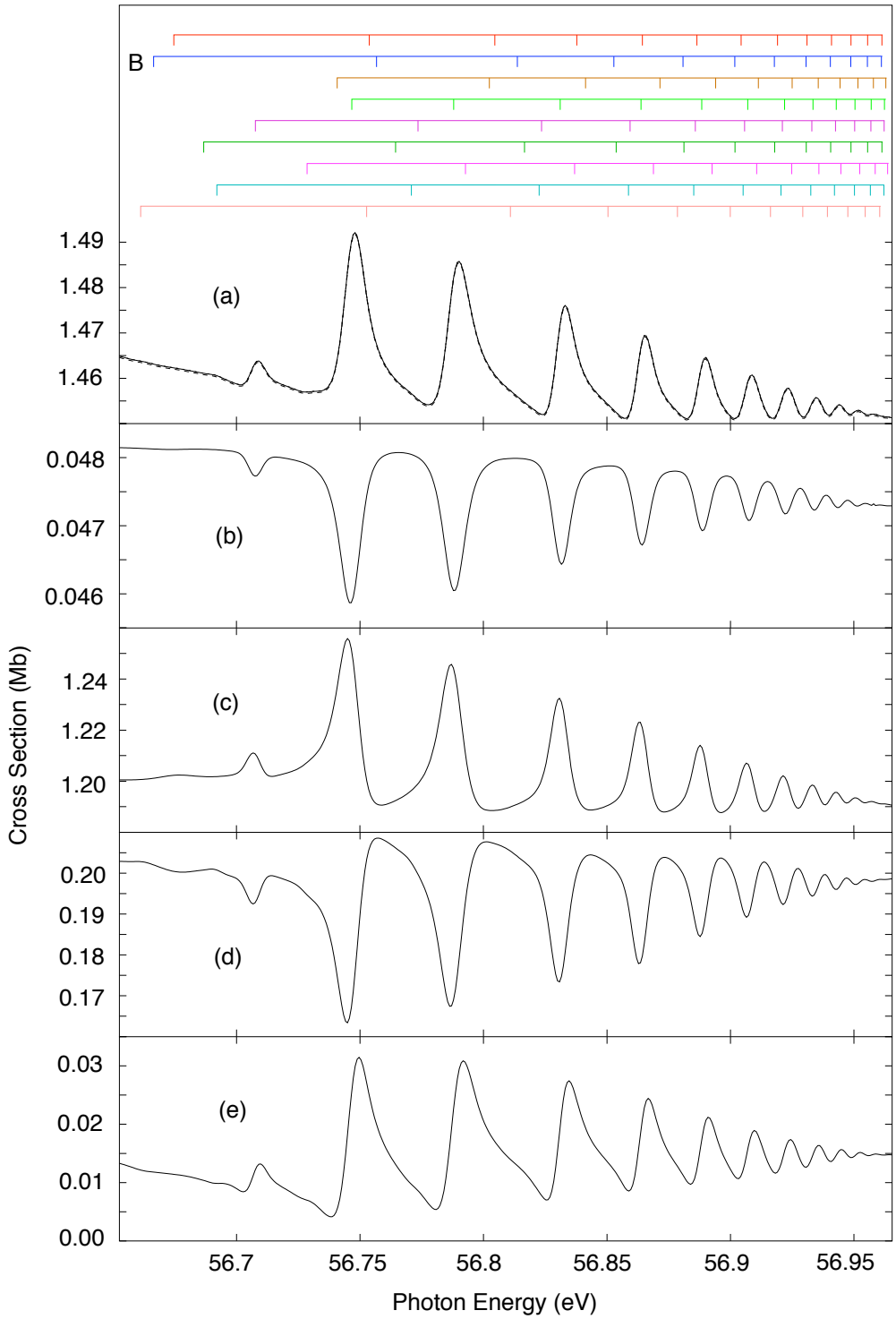

Figure 3.11: Details of the total and partial cross sections below N=5 threshold. σ_{tot} (a), σ_1 (b), σ_2 (c), σ_3 (d), σ_4 (e). See text for label explanation.

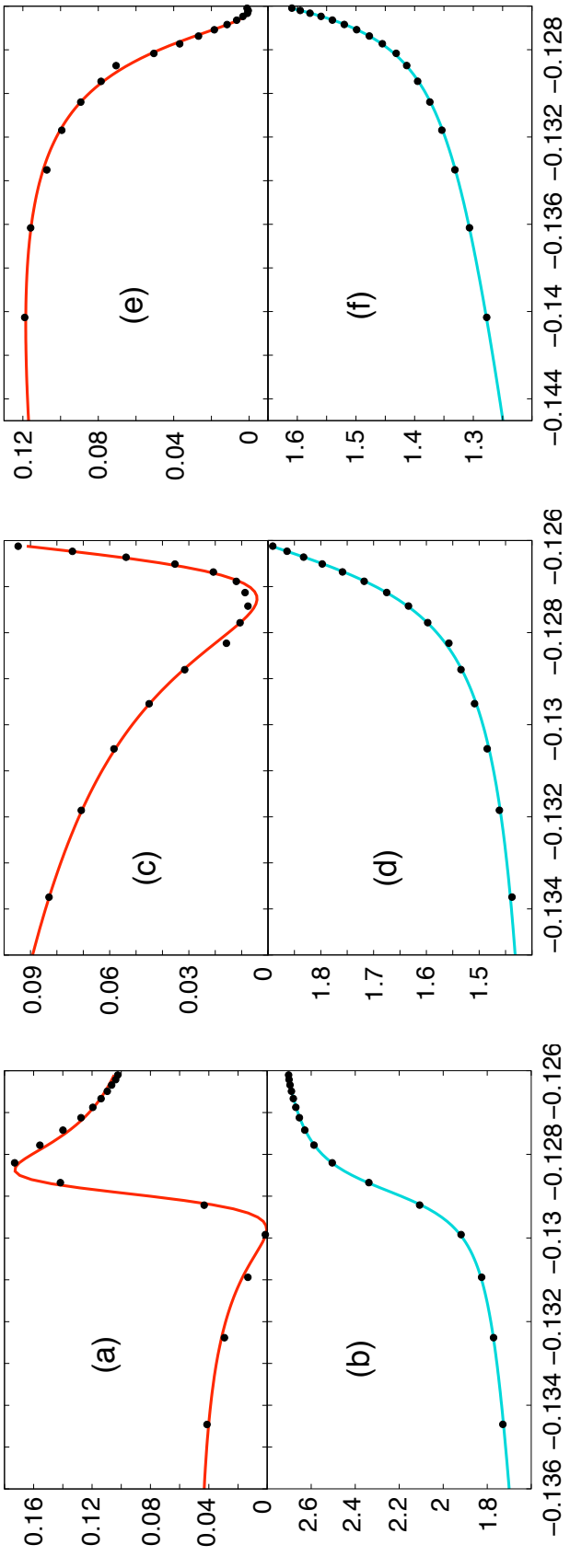

Figure 3.12: Intruder states below N=4 threshold. Effects of $[040]_5^+$ on a) $\bar{\Gamma}$ vs E and b) μ vs E for $[030]^+$ $^3\mathrm{P}^o$ series. Effects of $[031]_5^+$ on c) $\bar{\Gamma}$ vs E and d) μ vs E for $[021]^+$ $^3\mathrm{P}^e$ series. Effects of $[031]_5^+$ on e) $\bar{\Gamma}$ vs E and f) μ vs E for $[021]^+$ $^3\mathrm{D}^e$ series. Energy and reduced widths are in atomic units. See table 3.20 for fitting parameters and text for details.

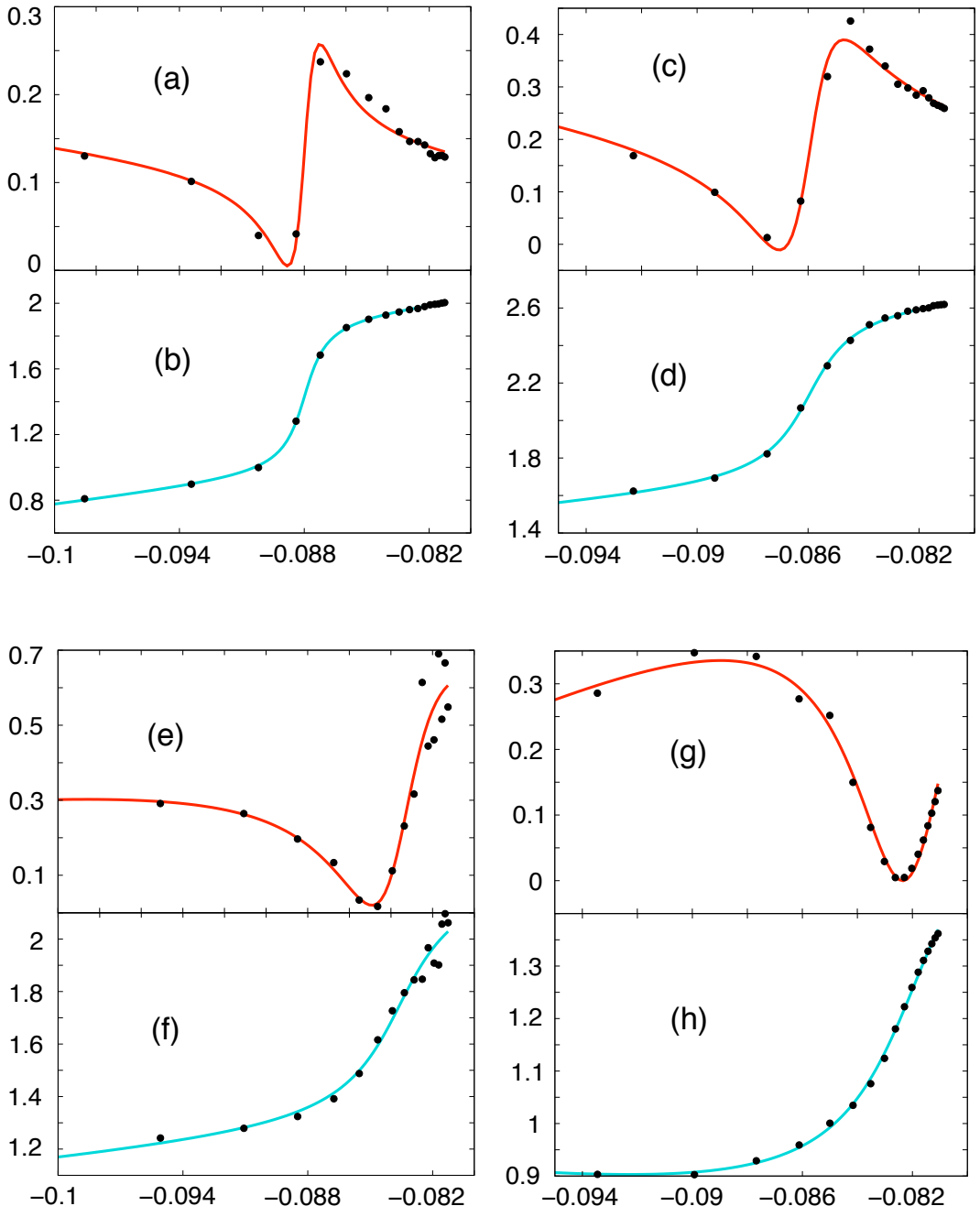

Figure 3.13: Intruder states below N=5 threshold. Effects of $[041]_6^+$ on a) $\bar{\Gamma}$ vs E and b) μ vs E for $[031]^+$ $^3P^e$ series. Effects of $[032]_6^+$ on c) $\bar{\Gamma}$ vs E and d) μ vs E for $[022]^+$ $^3D^o$ series. Effects of $[131]_6^+$ on e) $\bar{\Gamma}$ vs E and f) μ vs E for $[121]^+$ $^3P^e$ series. Effects of $[122]_6^+$ on g) $\bar{\Gamma}$ vs E and h) μ vs E for $[112]^+$ $^3D^o$ series. Energy and reduced widths are in atomic units. See table 3.20 for fitting parameters and text for details.

Table 3.20: Some intruder triplet states in helium. All values are in au. Standard deviation on the last digit is indicated in parenthesis. [n] is to be read 10^n.

$^{2S+1}L^{\pi}$	$[N_1N_2m]^A_n$	E	Γ	F	q
$^3P^o$	$[040]^+_5$	-0.128 875(7)	1.37(2) [-3]	0.165(5)	0.30(3)
$^3P^e$	$[031]^+_5$	-0.126 08(2)	2.4(6) [-3]	0.193(7)	-0.01(3)
$^3D^e$	$[031]^+_5$	-0.125 12(2)	2.63(9) [-3]	0.29(2)	-0.14(3)
$^3P^e$	$[041]^+_6$	-0.087 98(2)	1.57(4) [-3]	0.26(2)	0.06(6)
$^3D^o$	$[032]^+_6$	-0.085 696(3)	2.43(7) [-3]	0.42(2)	-0.08(4)
$^3P^e$	$[131]^+_6$	-0.0835(4)	4.3(6) [-3]	0.52(7)	-0.5(2)
$^3D^e$	$[122]^+_6$	-0.081 94(9)	4.7(1) [-3]	0.15(1)	-3.8(3)

Seven intruder states were parametrized quickly, while the two ^{3}P^o intruder states $[050]^+_6$ and $[140]^+_6$ below N=5 threshold interact with many series and overlap, so that a more sophisticated fit should be employed. The numerical values of the fitting parameters are reported in table 3.20. Figures 3.12 and 3.13 show how the elementary (3.1) and (3.2) models are able to reproduce closely the observed behaviour.

3.10 Photoionization of Rydberg satellites

In the photoionization of a Rydberg state, the oscillator strength concentrates on final autoionizing doubly excited states with similar excitation of the external electron, giving rise to a comb structure with vanishing contributions from the continuum. When properly normalized, the combs display auto-similarity, because almost all the oscillator strength is due to the transition of the inner electron only, while the outer electron is merely "shaken up".

In the very peculiar case of targets with the same principal quantum number of the external electron and of threshold, the spectrum is amplified. Intruder states can concentrate effectively the excitation on the group of DES where the intruder dissolves. This phenomenon is particularly evident for the $[040]^+_5$ state below N=4 threshold (left panel in figure 3.14). Two intruder states fall below N=5 threshold: $[050]^+_6$ and $[140]^+_6$. Apparently both give rise to an amplification in the photoionization spectrum of $1s5s$ Rydberg (right panel in figure 3.14), the former between n=6 and n=8, the latter beyond n=10. Cross sections are divided by n^{*3}. In this way the integrals on n^* axis is constant. The spectra are clearly autosimilar, small changes being attributable to the influence of intruder states still beyond $n = 20$.

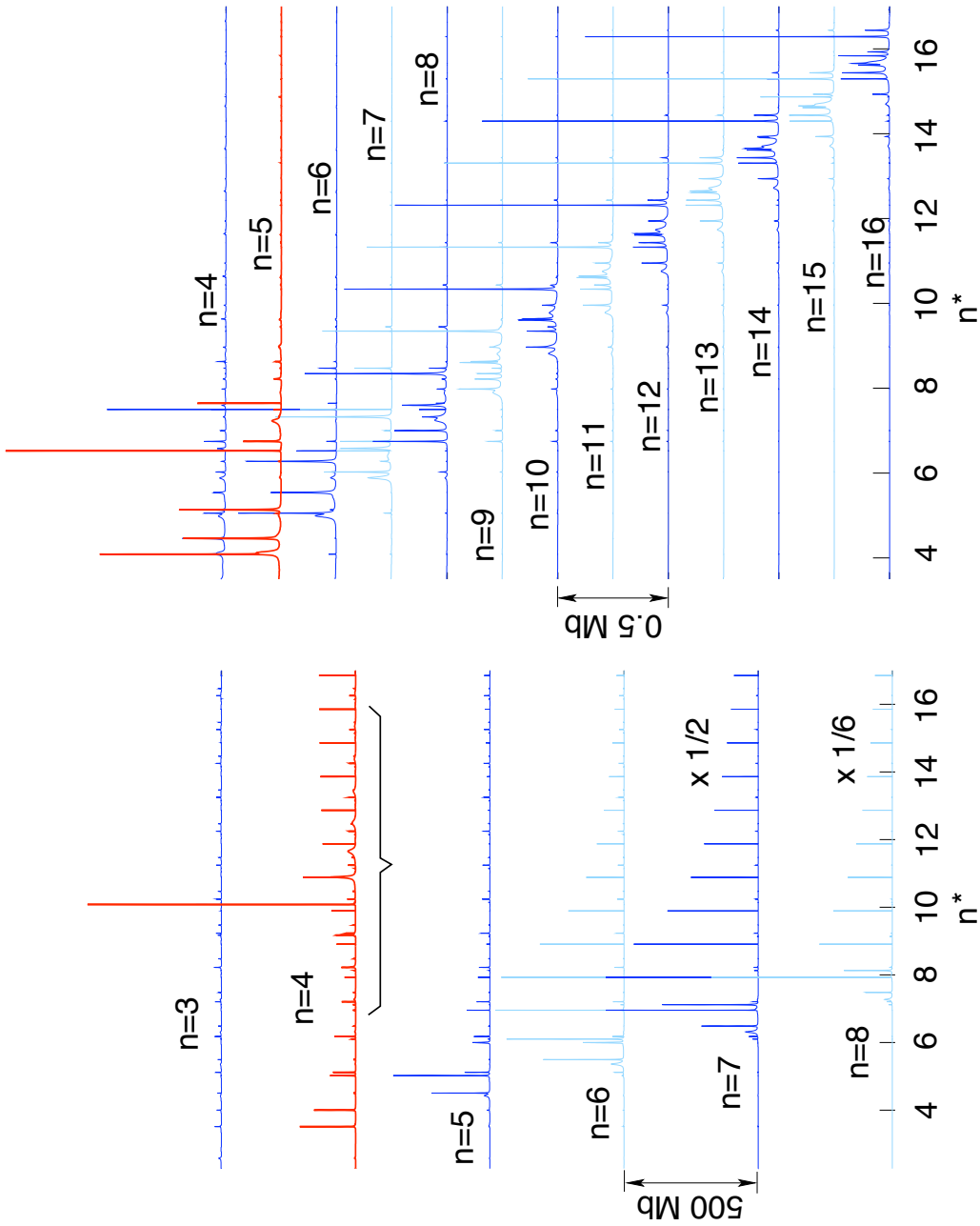

Figure 3.14: Total photoionization cross section spectra of the $1sns$ ^{3}S Rydberg series, below N=4 (left panel) and N=5 (right panel) thresholds. The latter are divided by n^{*3} in order to emphasize the autosimilarity between the terms in the series. See text for more details

3.11 Radiative decay of doubly excited states

The availability of a large number of Rydberg states leads naturally to the accurate treatment of radiative cascades in helium. In chapter 1 and in appendix B, the question of radiative decay of doubly excited states to a discrete as well as to a continuous state is considered in a general perspective, either with an extension of the K-matrix method to include the atom-radiation interaction non perturbatively, or with a two-photon approach. As we have not yet implemented those models, we will present here the much simpler situation of radiative decay of those doubly excited states which are bounded in electrostatic approximation: unnatural states below N=2 threshold.

These states decay to final states both below and above the ionization threshold. In the latter case, the doubly excited states decay simultaneously radiatively and by autoionization:

$$\mathrm{He}(2pnp\,^3P^e) \rightarrow \mathrm{He}^+(1s) + e^- + \gamma \tag{3.3}$$

$$\mathrm{He}(2pnd\,^3D^o) \rightarrow \mathrm{He}^+(1s) + e^- + \gamma \tag{3.4}$$

The state width due to the radiative decay is therefore written as

$$\Gamma_0 = \sum_i \Gamma_{i\leftarrow 0} + \sum_\alpha \int_{E_\alpha}^{E_0} dE\ \frac{d\Gamma_{\alpha\leftarrow 0}}{dE} \tag{3.5}$$

where (see appendix B for the definition of the transition operators)

$$\Gamma_{i\leftarrow 0} = \frac{\omega_{0,i}}{3\pi\hbar c^3}\ \frac{1}{2L_0+1}\ |\langle\phi_0\|\hat{V}_1^0\|\phi_i\rangle|^2 \tag{3.6}$$

$$\frac{d\Gamma_{\alpha\leftarrow 0}}{dE} = \frac{\omega}{3\hbar c^3}\ \frac{1}{2L_0+1}\ \sum_{L\ell_\alpha}^{ele}\left|\langle\phi_0\|\hat{V}_1^0\|\psi^{(-)\Gamma}_{\alpha E\ell_\alpha}\rangle\right|^2 \tag{3.7}$$

The non resonant radiative autoionization contribution to the lifetime of these states is comparable to that of the third less intense transition to a bound Rydberg state. See figures 3.16 and 3.15. The contribution from the resonant process is much smaller, being of the order of one part in a thousand for $2p^2\ ^3\mathrm{P}^e$, as shown in figure 3.17.

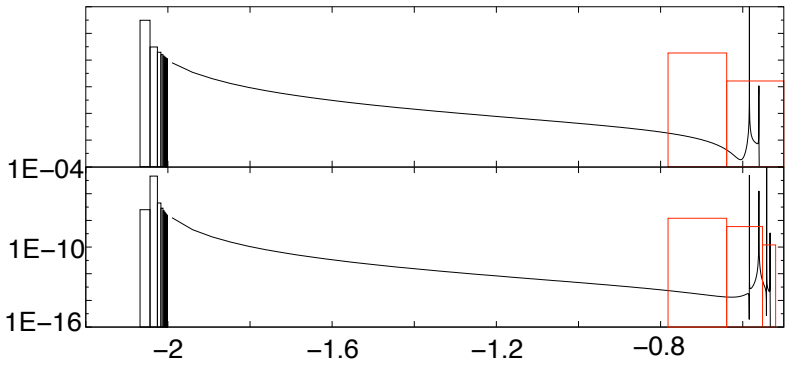

Figure 3.15: State radiative decay width density $\Gamma(E)$ as a function of energy (in au) for the first two $^3D^o$ doubly excited states below N=2 threshold to $^3D^e$ (black) and $^3P^e$ red symmetry.

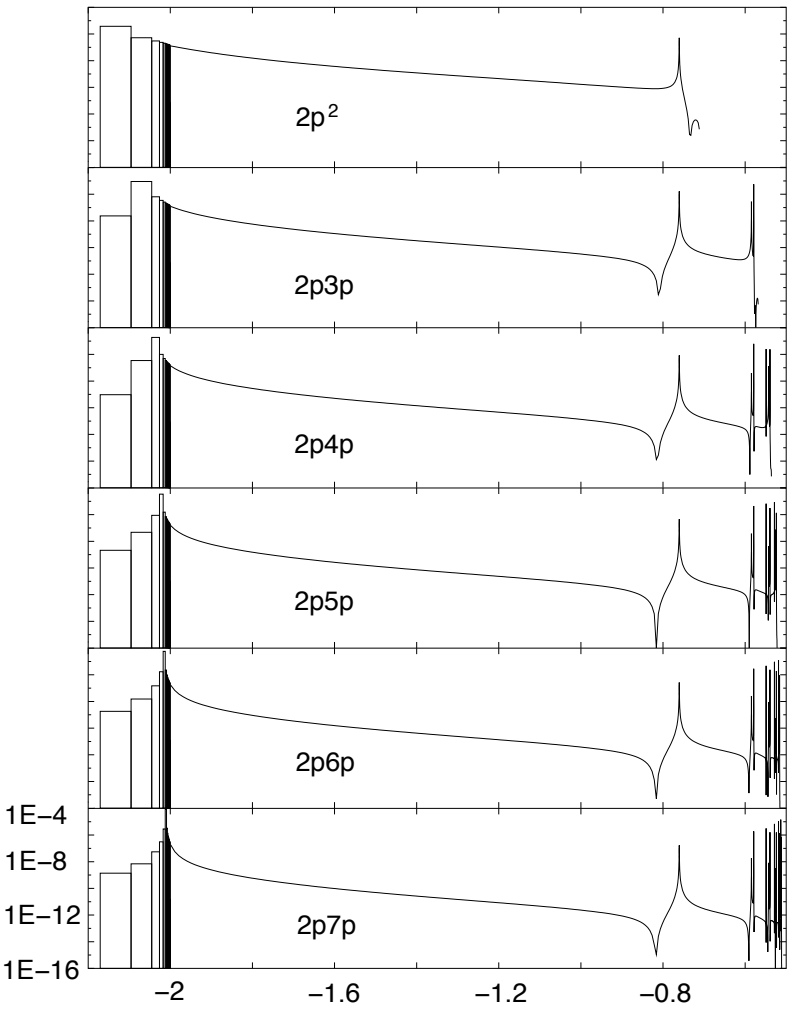

Figure 3.16: State radiative decay width density $\Gamma(E)$ as a function of energy (in au) for the first six $^3P^e$ doubly excited states below N=2 threshold to $^3P^o$ symmetry (the other final symmetries are not shown).

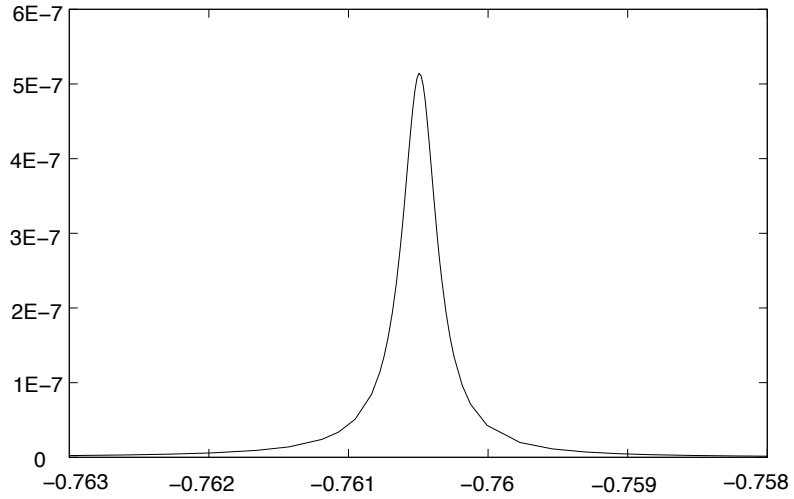

Figure 3.17: Detail of the state radiative decay width density $\Gamma(E)$ as a function of energy for the $2p^2\ {}^3\mathrm{P}^e$ doubly excited state to the ${}^3\mathrm{P}^o$ underlying continuum in a neighborhood of the $[010]_2^+$ resonance.

Chapter 4

Three electron systems

4.1 Separation of spin and spatial components

An N-electron wave function with well defined spin can be expanded on the set of antisymmetrized products of spin functions Θ_i^{NS} and a spatial function F:

$$\Phi = \mathcal{A}\Theta_i^{NS}F \tag{4.1}$$

where $\mathcal{A} = \frac{1}{N!}\sum_{\mathcal{P}}(-1)^{\mathrm{sgn}\mathcal{P}}\mathcal{P}$. It is well known that the Θ_i^{NS} form the basis for an irreducible representation of the symmetric group $\mathcal{S}_N$ [202]. Their indexes enumerate the group of different paths in the branching diagram which give rise to the right final spin [203]. The action of antisymmetrizer on 4.1 leads naturally to Wigner projectors onto the conjugate representation $\tilde{\alpha}$:

$$\mathcal{A}\Theta_i^{\alpha}F = \frac{1}{n_\alpha}\sum_j \Theta_j^{\alpha}\mathsf{W}_{ji}^{\tilde{\alpha}}F \tag{4.2}$$

where

$$\mathsf{W}_{ij}^{\alpha} \equiv \frac{n_\alpha}{N!}\sum_{\mathcal{P}}\mathsf{D}_{ij}^{\alpha *}(\mathcal{P})\mathcal{P}, \quad \mathsf{D}_{ij}^{\tilde{\alpha}}(\mathcal{P}) \equiv (-1)^{\mathcal{P}}\mathsf{D}_{ij}^{\alpha *}(\mathcal{P}) \tag{4.3}$$

Exploiting the properties of Wigner operators

$$\mathsf{W}_{ij}^{\alpha\dagger} = \mathsf{W}_{ji}^{\alpha}\ , \qquad \mathsf{W}_{ij}^{\alpha}\mathsf{W}_{kl}^{\beta} = \delta_{\alpha\beta}\delta_{jk}\mathsf{W}_{il}^{\alpha}, \tag{4.4}$$

the matrix element between such states of a spinless operator totally symmetric upon particle permutations can be written as

$$\langle\Phi'|\mathcal{O}|\Phi\rangle = \sum_{j'j}\langle\Theta_{j'}^{S}\mathsf{W}_{j'i'}^{\tilde{S}}F'|\mathcal{O}|\Theta_j^{S}\mathsf{W}_{ji}^{\tilde{S}}F\rangle \ = \ \langle F'|\mathcal{O}\mathsf{W}_{i'i}^{\tilde{S}}|F\rangle \tag{4.5}$$

Matrix elements can be written as a sum over the $(N+1)!$ permutations and the $N+1$ monoelectronic or $\binom{N}{2}$ bielectronic terms in the observable $\mathcal{O}$:

$$\langle\Phi'|\mathcal{O}|\Phi\rangle = \sum_n\sum_{\mathcal{P}}\mathsf{D}_{i'i}^{\tilde{S}*}(\mathcal{P})\langle F'|o_n\mathcal{P}|F\rangle \tag{4.6}$$

There are some features in this expression to be noted. First the spin coupling is fully accounted for in the irreducible representation factor D. This is also the case in the remarkable instance of a single photoionization channel, where a parent ion of well defined multiplicity is coupled to a free electron:

$$\begin{aligned}\Psi &= \mathcal{A}^{(N+1)}[\Phi \otimes \phi] = \\ &= \mathcal{A}^{(N+1)}[\mathcal{A}^{(N)}\Theta_i^{NS_\alpha} F \otimes {}^2\theta f] = \\ &= \mathcal{A}[\Theta_i^{NS_\alpha} \otimes {}^2\theta][F \otimes f] = \\ &= \mathcal{A}\Theta_{S_\alpha i}^{(N+1)S}[F \otimes f] = \\ &= \sum_j \Theta_j^{(N+1)S} \mathsf{W}_{j,S_\alpha i}^{(N+1)\tilde{S}}[F \otimes f]\end{aligned}$$

A true CI target requires the contributions of many spin coupling schemes, so that the wave function in that case has a slightly more complicated expression

$$\Psi = \sum_j \Theta_j^{(N+1)S} \sum_i C_i \mathsf{W}_{j,S_\alpha i}^{(N+1)\tilde{S}}[F_i \otimes f]$$

For two electron targets, though, both $\mathcal{S}_2$ irreducible representations are monodimensional and the indexes actually coincide with the target spin. The matrix element between singlet and triplet target channels in overall doublet multiplicity, for example, requires the set of $\mathsf{D}_{0,1}^{\{\tilde{2},1\}}(\mathcal{P})$ factors.

In atoms all angular integrations in 4.6 can be reduced to contractions of Clebsch-Gordan coefficients. Moreover, all the contractions over magnetic quantum numbers can be written in terms of products of $3nj$ symbols. For three electrons, eighteen different formulas are required for both one and two particle operators. They are derived in appendix G with the use of graphical techniques. In the case of more than three electrons, the number of different formulas rises prohibitively (96 monoelectronic and 144 bielectronic angular factors for four electrons) making derivation by hand exceedingly tedious. As explained at length in appendix G, this approach to compute matrix elements is useful only for non-orthogonal basis sets. When orthogonal basis sets are used instead, more concise and effective methods have been devised ages ago [204].

4.2 The LC refining algorithm

In three electron systems, the correlation space in the close coupling expansion 1.6 is typically two or three orders of magnitude larger than in the corresponding two electron cases, where the full-CI limit is easily reached. Basis sets with some millions of configurations are common. As we were more interested in inserting some correlation in the scattering wave functions, rather than getting very accurate results for few bound states, we decided to deal with the localized space swiftly by automatically selecting few thousands configurations out of the total space, among the most relevant to improve the energy region of interest.

The basis $\mathcal{B}$ that we seek is defined by the requirement that the variations of the lowest N energies E_i, through the addition of a configuration not included in $\mathcal{B}$, are all lower than a corresponding set of assigned thresholds ϵ_i. Conversely, the variation of at least one of the same set of energies is required to be larger than the corresponding ϵ_i when any configuration in $\mathcal{B}$ is removed.

$\mathcal{B}$ is not necessarily well defined, as many different basis might fulfill the stated requirement. We nevertheless are confident that if the configurations are built on SCF orbitals, a reasonable approximation of a useful $\mathcal{B}$ can be obtained through an iterative algorithm.

We proceed indeed as follows. In the first step, the energies of all the configurations are computed, and the hamiltonian is diagonalized on a certain number of those with the lowest energies, say 1000, which form $\mathcal{B}_1$, the first basis.

From this point, the algorithm proceeds iteratively. Let $\mathcal{B}_n$ be the basis at the n-th step, and H_n the hamiltonian matrix restricted to that basis. The contribution of all the configurations to the energy of the first N states is evaluated perturbatively according to the following formula

$$\Delta \mathrm{E}_i \equiv \frac{|\langle \phi_i | H - E_i | a \rangle|^2}{\epsilon_a - E_i} \tag{4.7}$$

which is the first non-zero perturbative contribution of the configuration a to the energy of the $i-th$ state. Only those configurations which contribute to at least one of the lowest N eigenvalues of H_n more than its prescribed threshold, are included in the next $\mathcal{B}_{n+1}$ basis.

The algorithm generally gets rapidly to a reasonable result, but then begins to oscillate including and rejecting just few almost irrelevant configurations, so that some stopping criterion has been included.

Helium negative ion As an example of the basis iterative refinement, we shall consider the case of He^-. In electrostatic approximation, the $^4P^o$ He^- manifold has one loosely bound state which lies ~ 77.52 meV below the 2^3S helium metastable state [205], with $1s2s2p$ dominant configuration. We have used a basis with maximum orbital angular momentum $\ell_{max} = 8$, roughly 30 orbitals in each angular momentum, and which reach the maximum radius of ~ 60 au. The total dimension is 1994764. In table 4.1 we have reported the energies obtained at each iterative step of the basis refinement. At the fourth step, the optimized basis grew to 12131 functions. The corresponding energy differs by merely ~ 0.128 meV from the literature value, that is two parts in a thousand of the total binding energy.

4.3 Boron

At the best of our knowledge, there is only one theoretical work on boron photoionization [206] by Kupliauskienė, published ten years ago, where the photoionization-excitation cross sections are calculated within a relaxed-orbital Hartree-Fock scheme.

Table 4.1: Convergence of the He^- $1s2s2p\ ^3P^o$ energy along the steps in iterative refinement of CI LC space. The reference space, generated by $31s$, $30p$, $29d$, $28f$, $27g$, $27h$, $27i$, $27j$ and $27k$ orbitals, has 1994764 functions. One threshold ϵ_1 has been set to 10^{-9}.

N	Dim	E (au)
0	1	-2.111 881 85
1	1000	-2.133 149 93
2	1187	-2.177 534 13
3	12143	-2.178 068 09
4	12131	-2.178 068 64
Reference [205]		-2.178 073 33

The author investigate only the energy interval 10 eV above threshold and completely omit resonances.

Here we present some preliminary results on Boron, where the inner $1s^2$ shell is approximated as a single-configuration frozen core, with the addition of a semiempirical polarization potential, as described in the following paragraph.

4.3.1 Polarizable core

For those processes where the energy of the photon is so low that only valence electrons can be excited, the inner electrons can tentatively be modeled with a frozen single determinant core. Such an approximation is actually too drastic as the long range dynamical correlation between the outer valence and the inner core electrons can be quite significant.

Long range correlation between valence electrons and core electrons can be partly taken in to account with a semiempirical polarization interaction term. The static polarization energy of a system of n equal point charges outside a polarizable sphere is

$$E_{pol} = -\frac{\alpha e^2}{2} \sum_{ij} \frac{\hat{r}_i \cdot \hat{r}_j}{r_i^2 r_j^2} \tag{4.8}$$

where the scalar polarizability α of the core ϕ_0 is given by

$$\alpha = 2 \sum_{i \neq 0} \frac{|\langle \phi_0 | \mu_0 | \phi_i \rangle|^2}{E_i - E_0} \tag{4.9}$$

where ϕ_i are excited states. The polarization term cannot be applied as it is because it is justified only for those configurations where the point charges are outside the polarizable charge distribution, and it is even badly divergent near the origin. The solution we adopted here is to attach to the polarization term, a regularizing factor. A good choice is the smooth step function $\mathcal{W}_6(r; r_o)$:

$$\mathcal{W}_6(r; r_o) = 1 - e^{-\left(\frac{r}{r_o}\right)^6} \tag{4.10}$$

where r_o is a cutoff radius. A useful effective polarization operator can thus be written as

$$H_{pol} = -\frac{\alpha}{2}\sum_i \frac{\mathcal{W}_6(r_i, r_o)}{r_i^4} - \alpha \sum_{i,j>i} \frac{\mathcal{W}_6^{1/2}(r_i, r_o)\mathcal{W}_6^{1/2}(r_j, r_o)}{r_i^2\, r_j^2} P_1(\Omega_{ij}) \tag{4.11}$$

where we have isolated the one body and the two body contributions. A different cutoff parameter r_o can be chosen for every orbital angular momentum, that is, if ϕ_ℓ is an orbital with well defined angular momentum ℓ, then:

$$\langle \vec{r}\,|\hat{\mathcal{W}}|\phi_\ell\rangle = \mathcal{W}_6(r; r_\ell)\phi_\ell(\vec{r}) \tag{4.12}$$

The whole set of cutoff parameters can be optimized to improve the single excitation spectrum of the ionic system with only one valence electron. No new formula are needed beyond those already implemented for the calculation of standard electrostatic hamiltonian. The monoelectronic polarization term can be dealt with most easily including its radial integral among the kinetic term and electron-nucleus term, while the two body term is analogous to the $\ell = 1$ multipole in the lagrange expansion of electron-electron repulsion, but its radial part is easier in that it factorizes in the product of two monoelectronic terms. A similar treatment has been adopted in many other context, see for example [207,208].

Parent ions All the states spawned by the configurations $1s^2 2\ell n\ell'$ with $n \leq 4$ are considered and the excitation energies with respect to the fundamental $1S^e$ state are compared with the available experimental data, thoroughly revised by Ryabtsev *et al* in a recent paper [209]. In each group, the first value is the nonrelativistic present calculation, while the underlying values are from the experiment. When more experimental values with different J coupling are available, the weighted average $\sum_J (2J+1)E_J / \sum_J (2J+1)$ is reported.

Partial wave channels In the following we report the effective potentials for the partial wave channels in all the symmetries involved in the photoionization of the fundamental state of boron: $^2S^e$, $^2P^e$, $^2P^o$ and $^2D^e$. The effective potentials are defined, on the line of the close coupling equations 1.8, as

$$V_i(r) = \frac{l(l+1)}{2r^2} - \frac{1}{r} - V_{ii}^{\Gamma}(r) - \int [K_{ii}^{\Gamma}(r, r') + X_{ii}^{\Gamma}(r, r')]dr' \tag{4.13}$$

The reduction of nonlocal potentials adopted above gives a reliable idea of these potentials only if they have diagonal predominance, but actually is otherwise arbitrary. On the abscissas of effective potentials plots, $\log(r+1)$ is reported. In appendix I the effective potentials are reported also for other symmetries.

In table 4.3 the energies we obtained for boron Rydberg states have been compared with those reported in a recent compilation of experimental data by Kramida and Ryabtsev (2007) [210].

Table 4.2: Energies of the B^+ parent ions.

Configuration	Term	E_{th} (au)	ΔE (au)	E_{th}-E_{exp}
$1s^2 2s^2$	$^1S^e$	-24.304444	0.000000	—
$1s^2 2s2p$	$^3P^o$	-24.134085	0.170359	
			0.170179	1.80[-4]
$1s^2 2s2p$	$^1P^o$	-23.969472	0.334972	
			0.334419	5.53[-4]
$1s^2 2p^2$	$^3P^e$	-23.853199	0.451245	
			0.450742	5.03[-4]
$1s^2 2p^2$	$^1D^e$	-23.837698	0.466746	
			0.466399	3.47[-4]
$1s^2 2p^2$	$^1S^e$	-23.722597	0.581847	
			0.581667	1.80[-4]
$1s^2 2s3s$	$^3S^e$	-23.712995	0.591449	
			0.591293	1.56[-4]
$1s^2 2s3s$	$^1S^e$	-23.677187	0.627257	
			0.627053	2.04[-4]
$1s^2 2s3p$	$^3P^o$	-23.648210	0.656234	
			0.656078	1.56[-4]
$1s^2 2s3p$	$^1P^o$	-23.647633	0.656811	
			0.656581	2.30[-4]
$1s^2 2s3d$	$^3D^e$	-23.617926	0.686518	
			0.686410	1.08[-4]
$1s^2 2s3d$	$^1D^e$	-23.599467	0.704977	
			0.704802	1.75[-4]
$1s^2 2s4s$	$^3S^e$	-23.546370	0.758074	
			0.757923	1.51[-4]
$1s^2 2s4s$	$^1S^e$	-23.539148	0.765296	
			0.765170	1.26[-4]
$1s^2 2s4p$	$^1P^o$	-23.526997	0.777447	
			0.777271	1.76[-4]
$1s^2 2s4p$	$^3P^o$	-23.522657	0.781787	
			0.781621	1.66[-4]
$1s^2 2s4d$	$^3D^e$	-23.511170	0.793274	
			0.793136	1.38[-4]
$1s^2 2s4f$	$^3F^o$	-23.507407	0.797037	
			0.796918	1.19[-4]
$1s^2 2s4f$	$^1F^o$	-23.507321	0.797123	
			0.797003	1.20[-4]
$1s^2 2s4d$	$^1D^e$	-23.504408	0.800036	
			0.799851	1.85[-4]

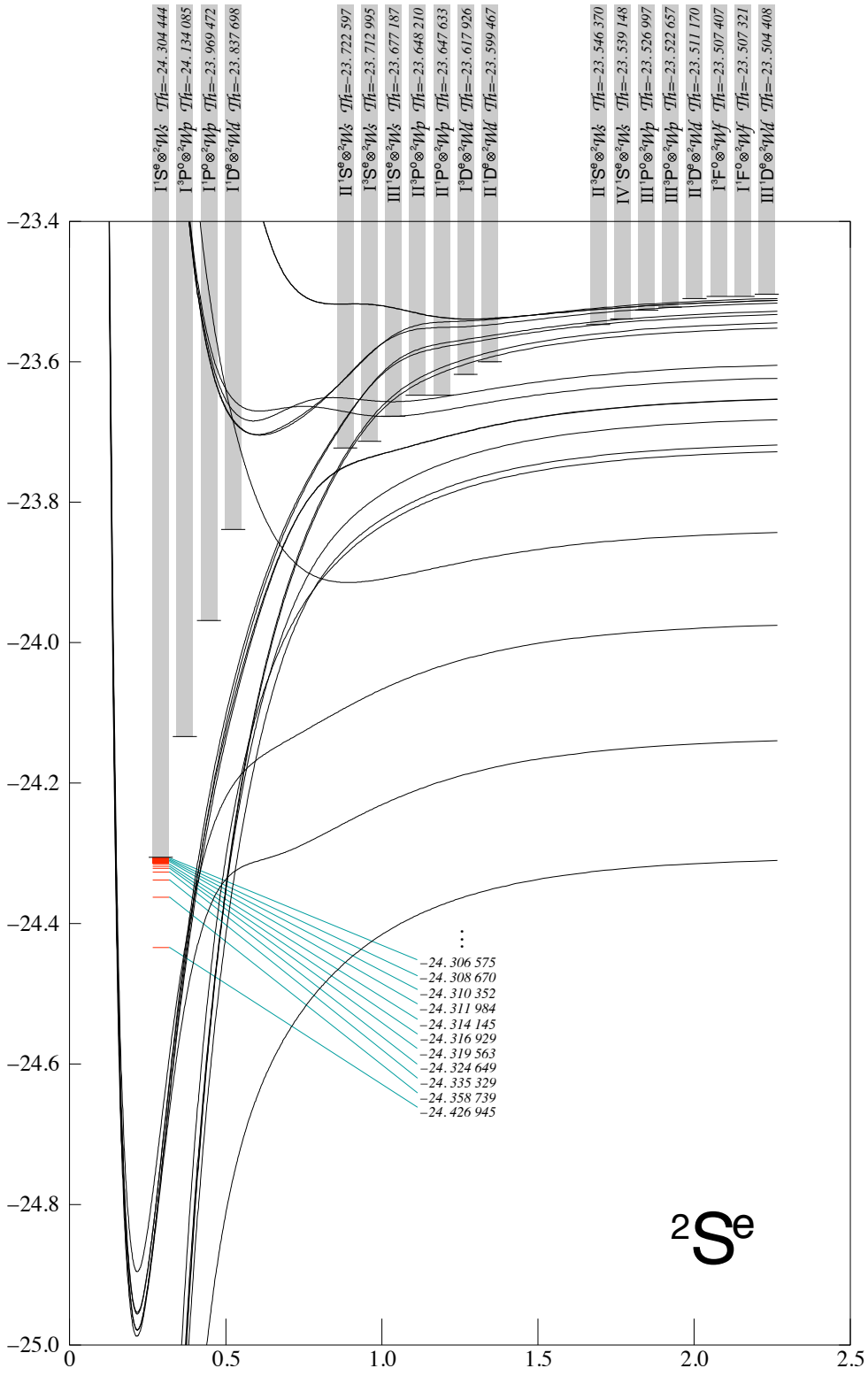
1¹S⊗²ns Th= -24.304 444
1³P°⊗²np Th= -24.134 085
1¹P°⊗²np Th= -23.969 472
1¹D⊗²nd Th= -23.837 698
2¹S⊗²ns Th= -23.722 597
1³S⊗²ns Th= -23.712 995
3¹S⊗²ns Th= -23.677 187
2³P°⊗²np Th= -23.648 210
2¹P°⊗²np Th= -23.647 633
1³D⊗²nd Th= -23.617 926
2¹D⊗²nd Th= -23.599 467
2³S⊗²ns Th= -23.546 370
4¹S⊗²ns Th= -23.539 148
3¹P°⊗²np Th= -23.526 997
3³P°⊗²np Th= -23.522 657
2³D⊗²nd Th= -23.511 170
1³F°⊗²nf Th= -23.507 407
1¹F°⊗²nf Th= -23.507 321
3¹D⊗²nd Th= -23.504 408
−23.4
−23.6
−23.8
−24.0
−24.2
−24.4
−24.6
−24.8
−25.0
0
0.5
1.0
1.5
2.0
2.5
−24.306 575
−24.308 670
−24.310 352
−24.311 984
−24.314 145
−24.316 929
−24.319 563
−24.324 649
−24.335 329
−24.358 739
−24.426 945
²Se

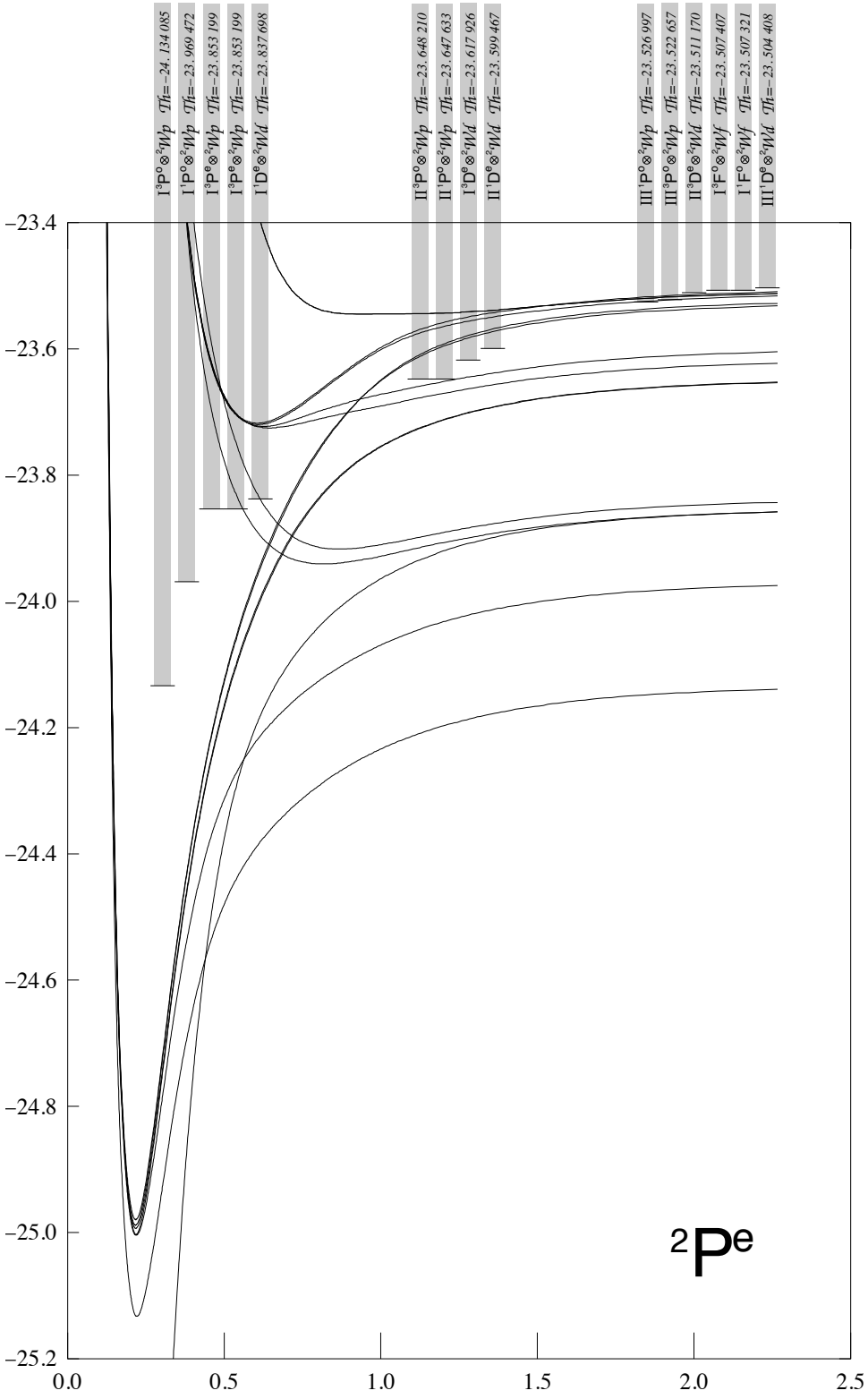
I 3P°⊗2Wp Th=−24.134085
I 1P°⊗2Wp Th=−23.969472
I 3P°⊗2Wp Th=−23.853199
I 3P°⊗2Wp Th=−23.853199
I 1D°⊗2Wd Th=−23.837698
II 3P°⊗2Wp Th=−23.648210
II 1P°⊗2Wp Th=−23.647633
I 3D°⊗2Wd Th=−23.617926
II 1D°⊗2Wd Th=−23.599467
III 1P°⊗2Wp Th=−23.526997
III 3P°⊗2Wp Th=−23.522657
II 3D°⊗2Wd Th=−23.511170
I 3F°⊗2Wf Th=−23.507407
I 1F°⊗2Wf Th=−23.507321
III 1D°⊗2Wd Th=−23.504408
−23.4
−23.6
−23.8
−24.0
−24.2
−24.4
−24.6
−24.8
−25.0
−25.2
0.0
0.5
1.0
1.5
2.0
2.5
2Pe

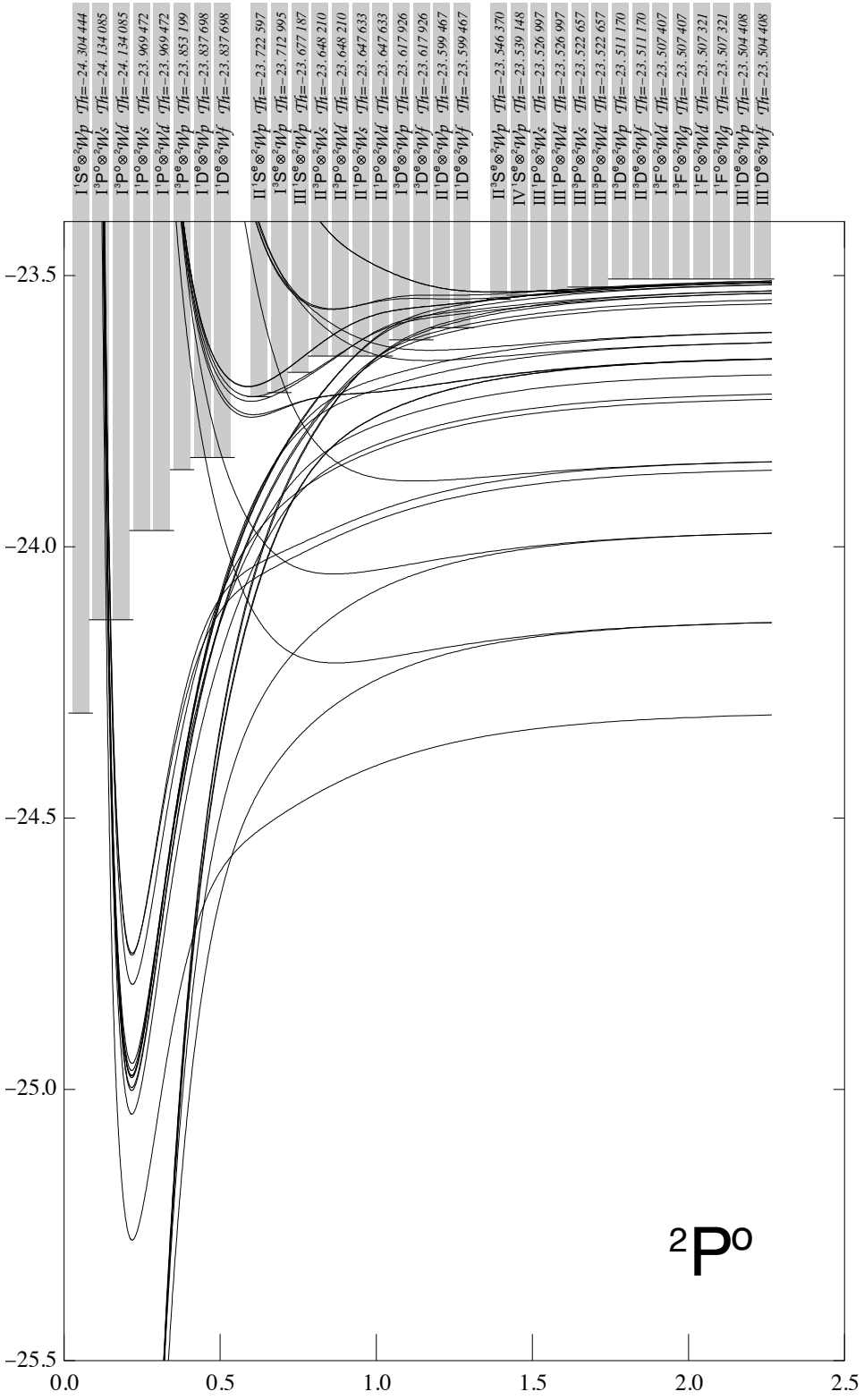
1 ¹S^e ⊗ ²₂Wp Th=−24. 304 444
1 ³P^o ⊗ ²₂Ws Th=−24. 134 085
1 ³P^o ⊗ ²₂Wd Th=−24. 134 085
1 ¹P^o ⊗ ²₂Ws Th=−23. 969 472
1 ¹P^o ⊗ ²₂Wd Th=−23. 969 472
1 ³P^e ⊗ ²₂Wp Th=−23. 853 199
1 ¹D^e ⊗ ²₂Wp Th=−23. 837 698
1 ¹D^e ⊗ ²₂Wf Th=−23. 837 698
II ¹S^e ⊗ ²₂Wp Th=−23. 722 597
1 ³S^e ⊗ ²₂Wp Th=−23. 712 995
III ¹S^e ⊗ ²₂Wp Th=−23. 677 187
II ³P^o ⊗ ²₂Ws Th=−23. 648 210
II ³P^o ⊗ ²₂Wd Th=−23. 648 210
II ¹P^o ⊗ ²₂Ws Th=−23. 647 633
II ¹P^o ⊗ ²₂Wd Th=−23. 647 633
I ³D^e ⊗ ²₂Wp Th=−23. 617 926
I ³D^e ⊗ ²₂Wf Th=−23. 617 926
II ¹D^e ⊗ ²₂Wp Th=−23. 599 467
II ¹D^e ⊗ ²₂Wf Th=−23. 599 467
II ³S^e ⊗ ²₂Wp Th=−23. 546 370
IV ¹S^e ⊗ ²₂Wp Th=−23. 539 148
III ¹P^o ⊗ ²₂Ws Th=−23. 526 997
III ¹P^o ⊗ ²₂Wd Th=−23. 526 997
III ³P^o ⊗ ²₂Ws Th=−23. 522 657
III ³P^o ⊗ ²₂Wd Th=−23. 522 657
II ³D^e ⊗ ²₂Wp Th=−23. 511 170
II ³D^e ⊗ ²₂Wf Th=−23. 511 170
1 ³F^o ⊗ ²₂Wd Th=−23. 507 407
1 ³F^o ⊗ ²₂Wg Th=−23. 507 407
1 ¹F^o ⊗ ²₂Wd Th=−23. 507 321
1 ¹F^o ⊗ ²₂Wg Th=−23. 507 321
III ¹D^e ⊗ ²₂Wp Th=−23. 504 408
III ¹D^e ⊗ ²₂Wf Th=−23. 504 408
−23.5
−24.0
−24.5
−25.0
−25.5
0.0
0.5
1.0
1.5
2.0
2.5
²P^o

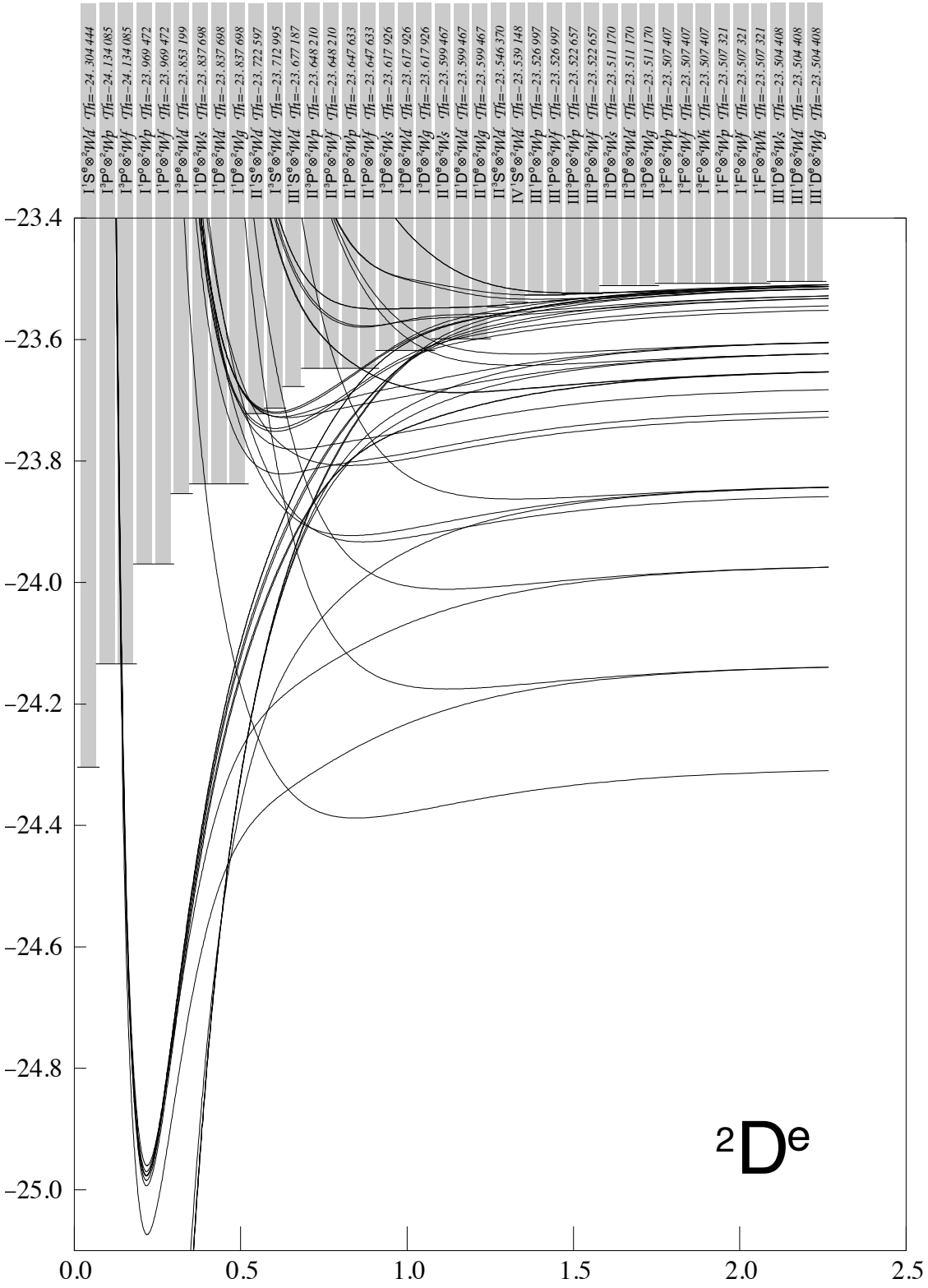
1¹S⁰⊗²Nd Th=-24.304 444
1³P⁰⊗²Np Th=-24.134 085
1³P⁰⊗²Nf Th=-24.134 085
1¹P⁰⊗²Np Th=-23.969 472
1¹P⁰⊗²Nf Th=-23.969 472
1³P⁰⊗²Nd Th=-23.853 199
1¹D⁰⊗²Ns Th=-23.837 698
1¹D⁰⊗²Nd Th=-23.837 698
1¹D⁰⊗²Ng Th=-23.837 698
1³S⁰⊗²Nd Th=-23.722 597
1³S⁰⊗²Nd Th=-23.712 995
1¹S⁰⊗²Nd Th=-23.677 187
1³P⁰⊗²Np Th=-23.648 210
1³P⁰⊗²Nf Th=-23.648 210
1¹P⁰⊗²Np Th=-23.647 633
1¹P⁰⊗²Nf Th=-23.647 633
1³D⁰⊗²Ns Th=-23.617 926
1³D⁰⊗²Nd Th=-23.617 926
1³D⁰⊗²Ng Th=-23.617 926
1¹D⁰⊗²Ns Th=-23.599 467
1¹D⁰⊗²Nd Th=-23.599 467
1¹D⁰⊗²Ng Th=-23.599 467
1³S⁰⊗²Nd Th=-23.546 370
2¹S⁰⊗²Nd Th=-23.539 148
1¹P⁰⊗²Np Th=-23.526 997
1¹P⁰⊗²Nf Th=-23.526 997
1³P⁰⊗²Np Th=-23.522 657
1³P⁰⊗²Nf Th=-23.522 657
1³D⁰⊗²Ns Th=-23.511 170
1³D⁰⊗²Nd Th=-23.511 170
1³D⁰⊗²Ng Th=-23.511 170
1³F⁰⊗²Np Th=-23.507 407
1³F⁰⊗²Nf Th=-23.507 407
1³F⁰⊗²Nh Th=-23.507 407
1¹F⁰⊗²Np Th=-23.507 321
1¹F⁰⊗²Nf Th=-23.507 321
1¹F⁰⊗²Nh Th=-23.507 321
1¹D⁰⊗²Ns Th=-23.504 408
1¹D⁰⊗²Nd Th=-23.504 408
1¹D⁰⊗²Ng Th=-23.504 408
−23.4
−23.6
−23.8
−24.0
−24.2
−24.4
−24.6
−24.8
−25.0
0.0
0.5
1.0
1.5
2.0
2.5
²Dᵉ

Table 4.3: Comparison of Boron doublet Rydberg energies above the fundamental $1s^2 2s^2 2p$ ^{3}2P^o state with the available experimental results, from NIST database [211].

^{2}S^e		^{2}P^o		^{2}D^e	
n	E (au)	n	E (au)	n	E (au)
1	0.182 4573	1	0.0003167	1	0.2186185
	0.182 4341		0.0000000(1/2)		0.2180522(3/2)
2	0.250 6678		0.0000695(3/2)		0.21805365(5/2)
	0.250 6448	2	0.2215425	2	0.2496244
3	0.274 0805		0.221491735(1/2)		0.249539695(3/2)
	0.274 0474		0.22149986(3/2)		0.249540475(5/2)
4	0.284 7712	3	0.2633221	3	0.2733841
	0.284 69		0.2632941(1/2)		0.2733501(3/2)
5	0.289 9053		0.26329701(3/2)		0.27335055(5/2)
	0.289 6036			4	0.2847294
6	0.292 5248	^{2}P^e			0.2847045(3/2)
	0.292 3163				0.28470525(5/2)
7	0.295 2722	n	E (au)	5	0.2909209
	0.295 2144				0.29090055(3/2)
8	0.297 4263	1	0.3313216		0.29090055(5/2)
	0.297 3928		0.3304385(1/2)	6	0.2946558
9	0.299 0569		0.3304916(3/2)		0.2946368(3/2)
	0.298 9382	2	0.3963435		0.29463695(5/2)
			0.3957615(1/2)	7	0.2970792
			0.3957855(3/2)		0.2970607(3/2)
		3	0.4336333		0.2970608(5/2)
			0.4348905(1/2)	8	0.2987843
			0.434909(3/2)		0.2987208(3/2,5/2)
		4	0.4501606	9	0.3003763
			0.4507195(3/2)		0.29990765(3/2,5/2)
		5	0.4585667		
			0.4587396(3/2)		

Table 4.4: Comparison of Boron quadruplet Rydberg energies above the fundamental $1s^2 2s^2 2p\ ^3\mathrm{2P}^o$ state with the available experimental results, from NIST database [211].

$^4\mathrm{S}^e$		$^4\mathrm{P}^e$		$^4\mathrm{D}^o$	
n	E (au)	n	E (au)	n	E (au)
1	0.3921041	1	0.1323976	1	0.4157530
	0.392755(3/2)		0.1315415(1/2)		0.4149585(3/2)
			0.131564(3/2)		0.414966(5/2)
$^4\mathrm{S}^o$			0.131593(5/2)		0.4149785(7/2)
				2	0.4424892
n	E (au)	$^4\mathrm{P}^o$			0.441696(3/2)
1	0.4439246				0.4417265(5/2)
	0.442437(3/2)	n	E (au)		0.441744(7/2)
		1	0.3527474	3	0.4545794
			0.3519015(1/2)		0.453837(7/2)
			0.3519351(3/2)		
			0.351994(5/2)		
		2	0.4193579		
			0.418561(5/2)		
			0.418577(3/2)		
			0.418585(1/2)		
		3	0.4217358		
			0.4209085(5/2)		

Resonances The data on boron resonances in literature are so scarce that no useful comparison can still be done. In figure 4.1 we simply reported the density of states in the four manifold required to compute the photoionization cross section of the Boron $1s^2 2s^2 2p$ fundamental state. The density of states is actually filtered through an arcotangent in order to fit into the plot.

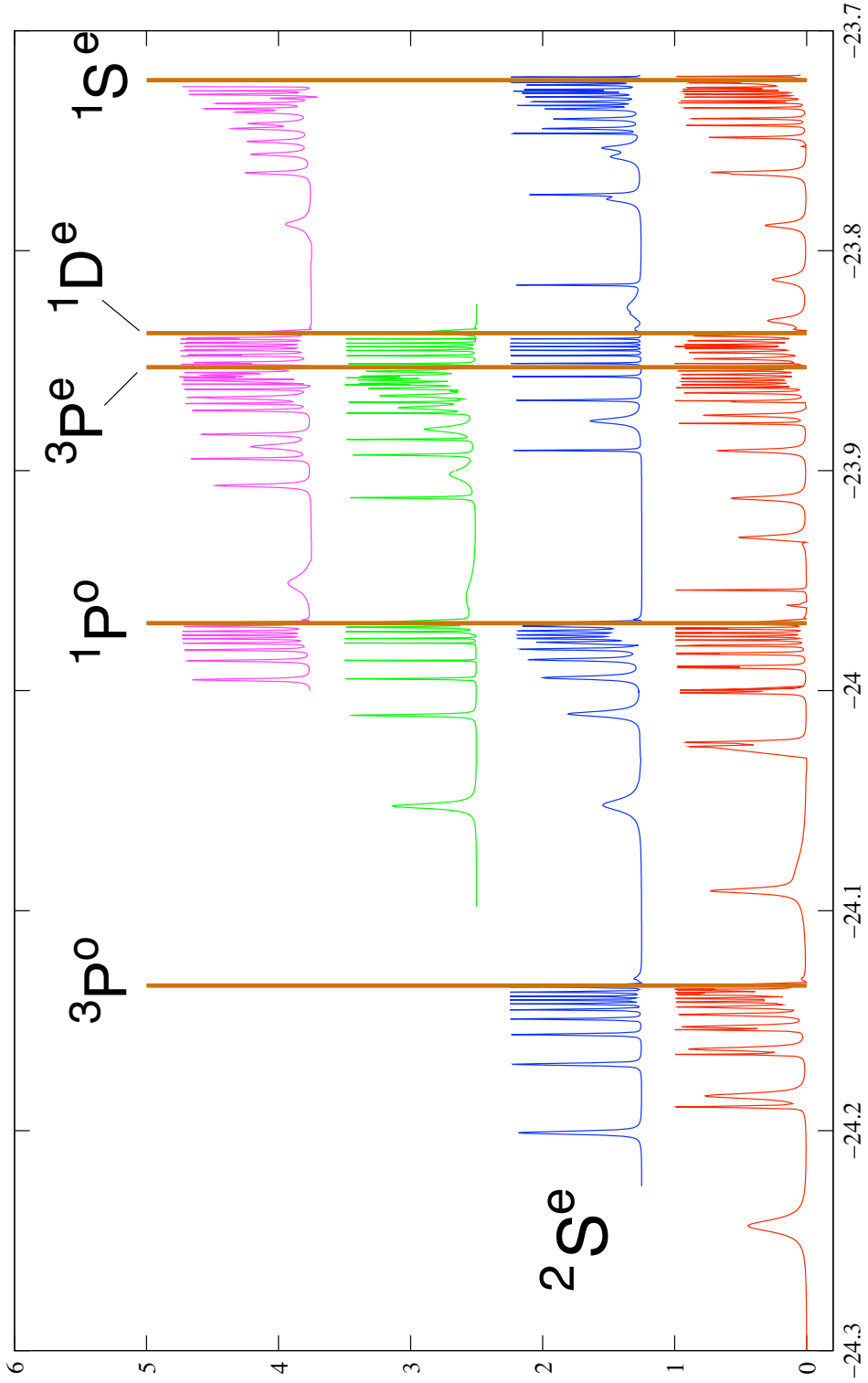

Figure 4.1: Arcotangent of the Boron atom density of states in $^2S^e$, $^2P^e$, $^2P^o$ and $^2D^e$ symmetry up to the sixth threshold.

Summary and Outlook

In this dissertation, a B-spline K-matrix technique was designed, implemented and applied to study the single ionization states of atomic systems with two and three active valence electrons. The new technique was applied to investigate relevant aspects of the photoionization spectrum of helium and of the resonant structure of both helium and boron.

On the procedural side the following main contributions were given.
An indepth investigation of effective completeness, the most remarkable property of B-splines, led to the assessment of a general result on the well conditioning of B-spline based methods, irrespective of the defining grid.

A protocol have been devised to build *a priori* knot grids capable of yielding arbitrarily highly excited autoionizing Rydberg states below specific thresholds, as it was recognized that, peculiar to the K-matrix method, the quantization boxes for the continuum and the metastable part of the wavefunction need not to coincide.

General formulas for three-electron matrix elements of arbitrary one and two particle operators, between states on non orthogonal orbital basis have been derived.

An extension to the K-matrix technique for the *ab initio* non perturbative treatment of the atom-radiation interaction has been devised.

A conditioning protocol for the K-matrix algorithm has been formulated and exploited, leading to a substantial reduction of the matrix dimensions.

A fitting method to determine resonance parameters from the total phase shift has been exploited in the fitting of resonance series themselves in order to define pseudo positions, widths and q parameters for intruder states.

On the applicative side, many original calculations were undertaken. The effects of $[031]_5^+\ ^1\mathrm{P}^o$, the first intruder $^1\mathrm{P}^o$ state in helium, on the photoionization spectrum measured in 1999 by Püttner *at al* [21] were reproduced for the first time with an *ab initio* calculation [111].

The dipole asymmetry parameters β_N below $N = 6$ threshold in the photoionization of helium were computed for the first time [113] in support to some preliminary results by Jiang *et al* (2006) [112].

A broad investigation on metastable helium triplet states up to the fifth ionization

threshold yielded the most extensive and accurate characterization of resonances in both natural and unnatural symmetries with $L \leq 2$ [186] now available. This was a very remarkable step forward since the data available in this domain were despairingly few, uneven and often inaccurate.

The autoionization paths of helium doubly excited states have been arranged in effective graphical schemes which exhibit the propensity rules for non radiative decay. Propensity rules was massively used to classify the aforementioned helium triplet doubly excited states and the eleven intruder states found there, none of which was known before [176]. Nine of these intruder states have been assigned a pseudo position, width, q and strength parameter.

In order to provide accurate photoionization spectra of the metastable 2^3S helium state for the interpretation of some late experiments which succeeded to reveal the resonant structure of its spectrum [32–34], we obtained total and partial cross sections and asymmetry parameters for the process up to the fifth ionization threshold [162].

As far as we know, no *ab initio* calculation of the non dipole forward-backward anisotropy parameter in the low energy photoionization spectrum of helium, measured by Krässig *et al* [114], are available yet. We therefore developed our general multipolar code to reproduce those results finding a substantial agreement with the experimental data.

The three-electron code was applied to the boron atom where the inner core was simulated with a semiempirical polarization potential in order to reproduce the B III excitation energies. Single ionization states were computed with the K-matrix method up to the sixth ionization threshold and the first few resonances in most of the doublet and quadruplet natural and unnatural symmetries up to $L = 2$ below each threshold were determined.

Many research lines can be pursued by means of the computational tools designed and developed in this thesis. Thanks to the native accurate treatment of highly excited Rydberg states allowed by the multiple B-spline basis K-matrix method, a natural future investigation is the non perturbative treatment of radiative cascades from doubly excited helium states. A considerable effort has been spent in the design and implementation of a general three active electron code, which is, nevertheless, yet largely unexploited. Finally, the general code for multiple matrix elements should allow closer investigation of nondipole effects.

Acknowledgements

It is a pleasure to thank the many people who helped me to complete this thesis.

First of all, I would like to thank Prof. Roberto Moccia: his challenging supervision and relentless guidance are crucial ingredients in all the results presented here.

In the late years Dr. Lorenzo Avaldi, Dr. Paola Bolognesi, Dr. Robert Richter and Dr. Ralph Püttner offered me useful glances on the photoionization processes from the unique perspective of the experimentalist.

A thank is due to Prof. Renato Colle: the investigation on B-spline effective completeness was undertaken when working on double photoionization problems; in the same period, some of the results collected during the PhD were eventually cast in their final form.

I wish to thank all my friends, which are too many to be listed here. Nevertheless I would like to mention, among them, Dr. Eugenio Paoloni. Three qualities, competence, helpfulness and cohabitation, fatally turned him into the favourite target of uncountable (answered) queries.

Finally I want to express my deep gratitude to Michele, my father, Giuliana, my mother and Mauro, my brother, for their unending support and care.

Appendix A

Scattering

Quantum scattering theory is treated in almost any QM textbook. We will give a swift survey of the subject, in order to get to the most relevant results used throughout this thesis. Full details can be found in [62, 212–214].

A.1 Time dependent theory

Given the following partition of the total hamiltonian H

$$H = H_0 + H', \tag{A.1}$$

we define the Green's functions of the Schrödinger equations corresponding to H and H_o as

$$(i\partial_t - H_0)G^{\pm}(t) = \delta(t), \quad (i\partial_t - H)\mathcal{G}^{\pm}(t) = \delta(t) \tag{A.2}$$

$$G^{\pm}(t) = \mathcal{G}^{\pm}(t) = 0 \quad \text{for} \quad \pm t < 0. \tag{A.3}$$

Formal solutions are readily found:

$$G^{\pm}(t) = \mp i\theta(\pm t)e^{-iH_0 t}, \qquad \mathcal{G}^{\pm}(t) = \mp i\theta(\pm t)e^{-iHt}. \tag{A.4}$$

The differential equations A.2 can be converted into an integral equation:

$$\begin{aligned} G^{\pm}(t-t') &= \int_{\infty}^{\infty} G^{\pm}(t-t'')(i\partial_{t''} - H)\mathcal{G}^{\pm}(t''-t')dt'' = \\ &= \int_{\infty}^{\infty} (i\partial_{t''} - H_0)G^{\pm}(t-t'')\mathcal{G}^{\pm}(t''-t')dt'' - \\ &- \int_{-\infty}^{\infty} G^{\pm}(t-t'')H'\mathcal{G}^{\pm}(t''-t')dt'' = \\ &= \mathcal{G}^{\pm}(t-t') - \int_{-\infty}^{\infty} G^{\pm}(t-t'')H'\mathcal{G}^{\pm}(t''-t')dt'' \end{aligned} \tag{A.5}$$

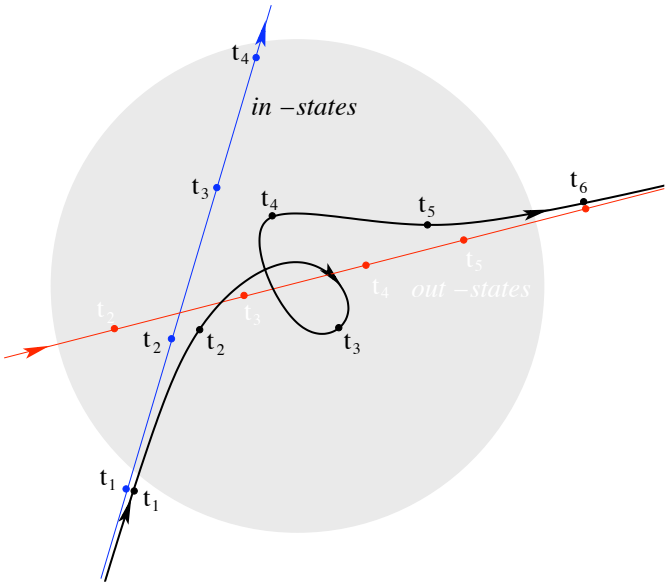

Figure A.1: Schematic representation of the *in* and *out* states in the classical scattering analogue. It is clear that in order for the *in* and *out* states to be well defined, they must correspond to unbound states of the total hamiltonian. Bound states have no such limits at all. This is true also for long range potential such as that between charged particles, in which case only the trajectory tangent is well defined.

or

$$\mathcal{G}^{\pm}(t-t') = G^{\pm}(t-t') + \int_{-\infty}^{\infty} G^{\pm}(t-t'')H'\mathcal{G}^{\pm}(t''-t')dt''. \tag{A.6}$$

$G^{\pm}(t)$ propagates forward (backward) in time, by an interval t, any state vector subject to an unperturbed evolution. The $\mathcal{G}$'s do just the same for the complete hamiltonian. Given the full dynamics of a state vector, we can define the two asymptotes for $t \to \pm\infty$

$$\psi_{in}(t) \equiv \lim_{t'\to-\infty} iG^{+}(t-t')\psi(t') \tag{A.7}$$

$$\psi_{out}(t) \equiv \lim_{t'\to+\infty} -iG^{-}(t-t')\psi(t'). \tag{A.8}$$

The two cases are represented schematically in figure A.1. The limiting procedure can be reversed

$$\psi(t) = \lim_{t'\to-\infty} i\mathcal{G}^{+}(t-t')\psi_{in}(t') = \lim_{t'\to+\infty} -i\mathcal{G}^{-}(t-t')\psi_{out}(t'); \tag{A.9}$$

from the identity

$$i\partial_{t'}[G^{+}(t-t')\psi(t')] = -\delta(t-t')\psi(t') + G^{+}(t-t')H'\psi(t') \tag{A.10}$$

and the definition (A.7), we get by integration

$$\psi(t) = \psi_{in}(t) + \int_{-\infty}^{\infty} dt' G^{+}(t-t') H' \psi(t'). \tag{A.11}$$

A similar equation holds with ψ_{out}:

$$\psi(t) = \psi_{out}(t) + \int_{-\infty}^{\infty} dt' G^{-}(t-t') H' \psi(t'). \tag{A.12}$$

These equations allow to label ψ with a complete set of expectation values of operators which commute with the unperturbed hamiltonian H: the expectation values of the corresponding *in* or *out* state:

$$\psi^{+}(\alpha, t) = \psi_{in}(\alpha, t) + \int_{-\infty}^{\infty} dt' G^{+}(t-t') H' \psi^{+}(\alpha, t') \tag{A.13}$$

$$\psi^{-}(\alpha, t) = \psi_{out}(\alpha, t) + \int_{-\infty}^{\infty} dt' G^{-}(t-t') H' \psi^{-}(\alpha, t'). \tag{A.14}$$

With similar passages it is possible to write ψ in terms of $\psi_{in/out}$ only:

$$\psi(t) = \psi_{in}(t) + \int_{-\infty}^{\infty} dt' \mathcal{G}^{+}(t-t') H' \psi_{in}(t'), \tag{A.15}$$

$$\psi(t) = \psi_{out}(t) + \int_{-\infty}^{\infty} dt' \mathcal{G}^{-}(t-t') H' \psi_{out}(t'). \tag{A.16}$$

The applications taking $\psi_{in}(t)$ and $\psi_{out}(t)$ in $\psi(t)$ are called Møller wave operators and are actually independent of t:

$$\psi^{\pm}(t) = \Omega^{(\pm)} \psi_{in/out}(t), \qquad \Omega^{(\pm)} = 1 \mp i \int_{-\infty}^{\infty} dt \mathcal{G}^{\pm}(-t) H' G^{\mp}(t), \tag{A.17}$$

moreover, thanks to the hermiticity of H',

$$\psi_{in/out}(t) = \Omega^{(\pm)\dagger} \psi(t). \tag{A.18}$$

We can use these expressions to express the *out* states in terms of the corresponding *in* states:

$$\psi_{out}(t) = \Omega^{(-)\dagger} \Omega^{(+)} \psi_{in}(t). \tag{A.19}$$

The scattering operator $S \equiv \Omega^{(-)\dagger}\Omega^{(+)}$ establishes the correspondence between the initial free wave packet, which is approaching the scattering event, and the final free wave packet, emerging from the collision. S commutes with the unperturbed hamiltonian

$$[S, H_0] = 0, \qquad S \equiv \Omega^{(-)\dagger}\Omega^{(+)}, \tag{A.20}$$

it is therefore a constant of motion

$$S_{\alpha\beta} = \langle\psi(\alpha, t)|S|\psi(\beta, t)\rangle \tag{A.21}$$

We can easily derive the relation

$$\psi_{in}(t) = S^\dagger\psi_{out}(t). \tag{A.22}$$

If the sets $\{\psi_{in}\}$ and $\{\psi_{out}\}$ are complete, S is unitary

$$S^\dagger S = SS^\dagger = 1. \tag{A.23}$$

The Cayley transform of S yields its hermitian representation, known as reactance operator or K-matrix [1]

$$K = -\frac{i}{\pi}\frac{1-S}{1+S}, \qquad S = \frac{1-i\pi K}{1+i\pi K}. \tag{A.24}$$

A.2 Time independent theory

The Fourier transform of the Green functions

$$G^\pm(z) = \int_{-\infty}^{\infty} dt e^{izt} G^\pm(t) \qquad \pm Im(z) > 0 \tag{A.25}$$

$$\mathcal{G}^\pm(z) = \int_{-\infty}^{\infty} dt e^{izt} \mathcal{G}^\pm(t), \qquad \pm Im(z) > 0 \tag{A.26}$$

yields a unique function on the whole complex plane, except on the real positive axis where it is discontinuous:

$$G(z) = \frac{1}{z - H_0}, \qquad \mathcal{G}(z) = \frac{1}{z - H}. \tag{A.27}$$

[1] our K-matrix is $-i/\pi$ times that generally defined in literature.

The two limits from above and from below are the regularized Fourier transform on the real axis of + and − operators respectively:

$$G^{\pm}(E) = \frac{1}{E - H_0 \pm i0^+}, \qquad \mathcal{G}^{\pm}(E) = \frac{1}{E - H \pm i0^+}. \tag{A.28}$$

The resolvent $G^{\pm}(E)$ have an hermitian and a skew-hermitian part

$$G^{\pm}(E) = G^{\mathcal{P}}(E) \mp i\pi\delta(E - H_0), \qquad G^{\mathcal{P}}(E) = \frac{\mathcal{P}}{E - H_0} \tag{A.29}$$

If we Fourier transform equation A.6 we obtain the operator version of the celebrated Lippmann-Schwinger equation [215]

$$\mathcal{G}^{\pm}(E) = G^{\pm}(E) + G^{\pm}(E)H'\mathcal{G}^{\pm}(E). \tag{A.30}$$

The Lippmann-Schwinger equation in terms of state vectors is obtained by Fourier transforming equations (A.13) and (A.14):

$$\psi^{+}_{\alpha E} = \phi_{\alpha E} + G^{+}(E)H'\psi^{+}_{\alpha E} \tag{A.31}$$

$$\psi^{-}_{\alpha E} = \phi_{\alpha E} + G^{-}(E)H'\psi^{-}_{\alpha E}, \tag{A.32}$$

where $\phi_{\alpha E}$ is an eigenfunction of H_0 and a of complete set of commuting operators with eigenvalues collectively indicated with α.

The so called standing wave solution, defined by

$$\psi^{\mathcal{P}}_{\alpha E} = \phi_{\alpha E} + G^{\mathcal{P}}(E)H'\psi^{\mathcal{P}}_{\alpha E}, \tag{A.33}$$

is of particular interest to the present thesis as the stationary Lippmann-Schwinger equation (A.33) leads to a set of K-matrix integral equations analogous to those already encountered in the first chapter. From $\psi^{\mathcal{P}}_{\alpha E}$ the solutions with incoming and outgoing asymptotic conditions are easily obtained. To see this, replace the partitioning

$$\psi^{\mathcal{P}}_{\alpha E} = \psi^{+}_{\alpha} + \Delta\psi_{\alpha E} \tag{A.34}$$

into (A.33), consider that $\psi^{+}_{\alpha E}$ itself obey the Lippmann-Schwinger equation and that $\delta(E - H_0)$ can be represented as

$$\delta(E - H_0) = \sum_{\alpha} |\phi_{\alpha E}\rangle\langle\phi_{\alpha E}|. \tag{A.35}$$

As a result

$$\Delta\psi_{\alpha E} = i\pi \sum_{\beta} \phi_{\beta E} T_{\beta\alpha}(E) + G^{\mathcal{P}}(E) H' \Delta\psi_{\alpha E} \tag{A.36}$$

where we have defined

$$T_{\beta\alpha}(E) = \langle \phi_{\alpha E} | H' | \psi^{+}_{\alpha E} \rangle. \tag{A.37}$$

$\Delta\psi_{\alpha E}$ must be consequently a linear combination of the $\psi^{\mathcal{P}}_{\beta E}$'s:

$$\Delta\psi_{\alpha E} = i\pi \sum_{\beta} \psi^{\mathcal{P}}_{\beta E} T_{\beta\alpha}(E), \tag{A.38}$$

finally

$$\psi^{+}_{\alpha E} = \psi^{\mathcal{P}}_{\alpha E} - i\pi \sum_{\beta} \psi^{\mathcal{P}}_{\beta E} T_{\beta\alpha}(E). \tag{A.39}$$

The same argument can be repeated, with trivial modifications, for the $\psi^{-}_{\alpha E}$ states:

$$\psi^{-}_{\alpha E} = \psi^{\mathcal{P}}_{\alpha E} + i\pi \sum_{\beta} \psi^{\mathcal{P}}_{\beta E}(E) T^{*}_{\alpha\beta}. \tag{A.40}$$

In other terms the $\psi^{\pm}$ are linear combinations of the $\psi^{\mathcal{P}}$.

Note that if the $\psi^{\pm}$ states are normalized according to

$$\langle \boldsymbol{\psi}^{\pm}_{E} | \boldsymbol{\psi}^{\pm}_{E'} \rangle = \delta(E - E') \cdot \mathbf{1} \tag{A.41}$$

then the corresponding stationary states are not orthogonal

$$\langle \boldsymbol{\psi}^{\mathcal{P}}_{E} | \boldsymbol{\psi}^{\mathcal{P}}_{E'} \rangle = \delta(E - E') \cdot (1 + \pi^2 \mathbf{K}^2(E)) \tag{A.42}$$

where $\mathbf{K}(E)$ is the *on shell* K-matrix, that is the Cayley transform of the unitary matrix which transforms the $\boldsymbol{\psi}^{+}_{E}$ states into the $\boldsymbol{\psi}^{-}_{E}$ states.

A.3 Transition rate

Under the influence of a perturbation potential, the free packets are scattered along states which would otherwise remain unpopulated. We shall briefly derive the generalized Fermi golden rule for the transition rate between unperturbed states.

Consider the following wavepacket controlled in the past

$$\psi_i(t) = \int d\gamma \, dE \, s(\gamma - \alpha) \, g(E - E_i) \, e^{-iEt} \, \psi^{+}_{\alpha E} \tag{A.43}$$

where the s and g functions are narrowly peaked around zero (in some meaningful sense: it does not really matter how the space of α quantum numbers is actually made up) and normalized L^2 to 1. $\psi^+_{\alpha E}$ can be written as

$$\psi^+_{\alpha E} = \psi_{\alpha E} + \int d\beta\, d\epsilon\, \psi_{\beta\epsilon} \frac{1}{E - \epsilon + i0^+} T_{\beta\epsilon,\alpha E} \tag{A.44}$$

Any unperturbed ray $\psi_{\beta E_f}$ outside the cone where ψ_i lies in the far past, gets progressively populated; the transition amplitude is

$$\begin{aligned} A_{f\leftarrow i}(t) &= \int d\alpha\, dE\, g(\alpha)\, g_\sigma(E - E_i)\, e^{-i(E-E_f)t}\, \langle \psi_{\beta E_f} | \psi^+_{\alpha E} \rangle = \\ &= \int d\alpha\, dE\, g(\alpha)\, g_\sigma(E - E_i)\, e^{-i(E-E_f)t}\, \frac{T_{\beta E_f,\alpha E}}{E - E_f + i0^+} \simeq \\ &\simeq T_{\beta E_f,\alpha E_i} \int d\alpha\, dE\, g(\alpha)\, g_\sigma(E - E_i)\, \frac{e^{-i(E-E_f)t}}{E - E_f + i0^+} = \\ &= T_{\beta E_f,\alpha E_i} \int dE\, g_\sigma(E - E_i)\, \frac{e^{-i(E-E_f)t}}{E - E_f + i0^+} \end{aligned} \tag{A.45}$$

The transition rate is

$$\begin{aligned} \mathcal{W}_{f\leftarrow i} \equiv \frac{d}{dt} |A_{f\leftarrow i}(t)|^2 \Big|_{t=0} &= -i |T_{\beta E_f,\alpha E_i}|^2 \times \\ \times \int dE\, dE'\, g(E - E_i)\, g(E' - E_i) &\frac{E - E'}{E - E_f + i0^+} \frac{1}{E' - E_f - i0^+} \end{aligned} \tag{A.46}$$

Exploiting the identity

$$\frac{\epsilon - \epsilon'}{(\epsilon' - i0^+)(\epsilon + i0^+)} = \frac{1}{\epsilon' - i0^+} - \frac{1}{\epsilon + i0^+} = \frac{\mathcal{P}}{\epsilon'} - \frac{\mathcal{P}}{\epsilon} + i\pi\delta(\epsilon) + i\pi\delta(\epsilon') \tag{A.47}$$

and the symmetry of the integral in (A.46), we get

$$\mathcal{W}_{f\leftarrow i} = 2\pi |T_{\beta E_f,\alpha E_i}|^2\, g(E_f - E_i). \tag{A.48}$$

In the limit of an initial wave packet with well definite energy, the distribution function can be replaced with a delta

$$\mathcal{W}_{f\leftarrow i} = 2\pi\, \delta(E_f - E_i)\, |T_{\beta E_f,\alpha E_i}|^2 \tag{A.49}$$

Moreover, for low energy electromagnetic transitions in light atoms, the perturbative approach yields very accurate results and the ψ^+ can be replaced usefully by the Born series

$$\mathcal{W}_{f\leftarrow i} = 2\pi\,\delta(E_f - E_i)\,|\langle\psi_{\beta E_f}|V\sum_{j=0}^{\infty}[G_0^+(E_i)V]^j|\psi_{\alpha E_i}\rangle|^2 \tag{A.50}$$

A.4 Scattering cross section

When both the initial and the final states are normalized as

$$\langle\psi_{\alpha\hat{\Omega}E}|\psi_{\beta\hat{\Omega}'E'}\rangle = \delta_{\alpha\beta}\delta(\hat{\Omega}-\hat{\Omega}')\delta(E-E') \tag{A.51}$$

the transition rate divided by the particle flux density associated with the incoming state is the cross section for the scattering of the incoming particles in an energy interval dE' and an angular sector $d\Omega'$:

$$\frac{\sigma_{\beta\hat{\Omega}'E'\leftarrow\alpha\hat{\Omega}E}}{dE'd\hat{\Omega}'} = \frac{\mathcal{W}_{\beta\hat{\Omega}'E'\leftarrow\alpha\hat{\Omega}E}}{\Phi_{\alpha E}} \tag{A.52}$$

$\Phi_{\alpha E}$ is readily derived as

$$\Phi_{\alpha E} = \frac{k^2}{(2\pi)^3}, \qquad k = \sqrt{2(E-E_\alpha)} \tag{A.53}$$

thus

$$\frac{\sigma_{\beta\hat{\Omega}'E'\leftarrow\alpha\hat{\Omega}E}}{dE'd\hat{\Omega}'} = \frac{(2\pi)^4}{k^2}\delta(E'-E)\,|T_{\beta\hat{\Omega}'E'\leftarrow\alpha\hat{\Omega}E}|^2 \tag{A.54}$$

or

$$\frac{\sigma_{\beta\hat{\Omega}'E\leftarrow\alpha\hat{\Omega}E}}{d\hat{\Omega}'} = \frac{(2\pi)^4}{k^2}\,|T_{\beta\hat{\Omega}'E'\leftarrow\alpha\hat{\Omega}E}|^2 \tag{A.55}$$

With the alternative normalization

$$\langle\psi_{\alpha\vec{k}}|\psi_{\beta\vec{k}'}\rangle = \delta_{\alpha\beta}\;\delta^{(3)}(\vec{k}-\vec{k}') \tag{A.56}$$

the cross section expression is instead

$$\frac{\sigma_{\beta\vec{k}'\leftarrow\alpha\vec{k}}}{d\hat{\Omega}'} = (2\pi)^4\;\frac{k'}{k}\;|T_{\beta\vec{k}'\leftarrow\alpha\vec{k}}|^2. \tag{A.57}$$

A.5 Partial wave expansion

The *on-shell* S matrix relative to the scattering of an electron off an atom or atomic ion, can be expanded in terms of matrix elements between states with definite spherical symmetry, where the S matrix itself is diagonal:

$$\begin{aligned} S_{\beta\hat{\Omega}'\sigma',\alpha\hat{\Omega}\sigma}(E) = \sum_{LMS\Sigma}\sum_{l_1m_1}\sum_{l_2m_2} & C^{LM}_{L_\beta M_\beta\, l_2m_2}C^{S\Sigma}_{S_\beta\Sigma_\beta\,\frac{1}{2}\sigma'}C^{LM}_{L_\alpha M_\alpha\, l_1m_1}C^{S\Sigma}_{S_\alpha\Sigma_\alpha\,\frac{1}{2}\sigma}\times \\ & \times Y_{l_2m_2}(\hat{\Omega}')\,Y^*_{l_1m_1}(\hat{\Omega})\,\bar{S}^{\Gamma}_{\beta l_2,\alpha l_1}(E) \end{aligned} \tag{A.58}$$

where

$$\bar{S}^{\Gamma}_{\beta l_2,\alpha l_1}(E) = e^{-i(\frac{l_2\pi}{2}-\sigma_{\eta_{l_2}}-\delta^{\Gamma}_{\beta l_2})} S^{\Gamma}_{\beta l_2,\alpha l_1}(E) e^{i(\frac{l_2\pi}{2}+\sigma_{\eta_{l_2}}+\delta^{\Gamma}_{\beta l_2})}. \tag{A.59}$$

The transition matrix is related to the *on-shell* scattering matrix through the following relation

$$S_{\beta\hat{\Omega}'\sigma',\alpha\hat{\Omega}\sigma}(E) = \delta_{\alpha\beta}\delta_{\sigma\sigma'}\delta(\hat{\Omega}'-\hat{\Omega}) - 2i\pi T_{\beta\hat{\Omega}'\sigma',\alpha\hat{\Omega}\sigma}(E). \tag{A.60}$$

If we define

$$M^{\Gamma}_{\beta l_2,\alpha l_1}(E) = \delta_{\alpha\beta}\delta_{l_2 l_1} - \bar{S}^{\Gamma}_{\beta l_2,\alpha l_1}(E) \tag{A.61}$$

we can find the following expansion for T

$$\begin{aligned} T_{\beta\hat{\Omega}'\sigma',\alpha\hat{\Omega}\sigma}(E) = \frac{1}{2i\pi} \sum_{LMS\Sigma} \sum_{l_1 m_1} \sum_{l_2 m_2} & C^{LM}_{L_\beta M_\beta\, l_2 m_2} C^{S\Sigma}_{S_\beta\Sigma_\beta\, \frac{1}{2}\sigma'} C^{LM}_{L_\alpha M_\alpha\, l_1 m_1} C^{S\Sigma}_{S_\alpha\Sigma_\alpha\, \frac{1}{2}\sigma} \times \\ & \times Y_{l_2 m_2}(\hat{\Omega}')\, Y^*_{l_1 m_1}(\hat{\Omega})\, M^{\Gamma}_{\beta l_2,\alpha l_1}(E) \end{aligned} \tag{A.62}$$

In order to get the scattering cross section we have to take the square module of (A.62). Major simplifications arise when an average over the initial and a sum over the final orientations is performed.

$$\begin{aligned} \frac{\sigma_{\beta\hat{\Omega}'E\leftarrow\alpha\hat{\Omega}E}}{d\hat{\Omega}'} = & \frac{(2\pi)^2}{k^2} \frac{1}{2\Pi^2_{S_\alpha L_\alpha}} \sum_{M_\alpha M_\beta} \sum_{\Sigma_\alpha\Sigma_\beta} \sum_{\sigma\sigma'} \sum_{LMS\Sigma} \sum_{l_1 m_1} \sum_{l_2 m_2} \sum_{L'M'S'\Sigma'} \sum_{l_3 m_3} \sum_{l_4 m_4} \times \\ & \times C^{S\Sigma}_{S_\beta\Sigma_\beta\, \frac{1}{2}\sigma'} C^{S\Sigma}_{S_\alpha\Sigma_\alpha\, \frac{1}{2}\sigma} C^{S'\Sigma'}_{S_\beta\Sigma_\beta\, \frac{1}{2}\sigma'} C^{S'\Sigma'}_{S_\alpha\Sigma_\alpha\, \frac{1}{2}\sigma} \times \\ & \times C^{LM}_{L_\beta M_\beta\, l_2 m_2} C^{LM}_{L_\alpha M_\alpha\, l_1 m_1} C^{L'M'}_{L_\beta M_\beta\, l_4 m_4} C^{L'M'}_{L_\alpha M_\alpha\, l_3 m_3} \times \\ & \times Y_{l_2 m_2}(\hat{\Omega}')\, Y^*_{l_4 m_4}(\hat{\Omega}')\, Y^*_{l_1 m_1}(\hat{\Omega})\, Y_{l_3 m_3}(\hat{\Omega})\, M^{\Gamma}_{\beta l_2,\alpha l_1}(E) M^{\Gamma'*}_{\beta l_4,\alpha l_3}(E) \end{aligned} \tag{A.63}$$

With ordinary algebraic techniques (see appendix G) most of the summations are replaced with closed formula. As a result, the differential cross section is expanded in terms of Legendre polynomials of the scattering angle

$$\begin{aligned} \frac{\sigma_{\beta\hat{\Omega}'E\leftarrow\alpha\hat{\Omega}E}}{d\hat{\Omega}'} = & \frac{1}{8k^2} \frac{1}{\Pi^2_{S_\alpha L_\alpha}} \sum_j (2j+1)\, P_j(\hat{\Omega}\cdot\hat{\Omega}') \sum_S (2S+1) \sum_{LL'} (2L+1)(2L'+1) \times \\ & \times \sum_{l_1 l_2 l_3 l_4} (-1)^{L_\alpha+L_\beta+l_1+l_2} \Pi_{l_3 l_4} C^{l_2 0}_{j'0\, l_4 0} C^{l_1 0}_{j0\, l_3 0} \begin{Bmatrix} L_\beta & l_2 & L \\ j & L' & l_4 \end{Bmatrix} \begin{Bmatrix} L_\alpha & l_1 & L \\ j & L' & l_3 \end{Bmatrix} \times \\ & \times M^{\Gamma}_{\beta l_2,\alpha l_1}(E) M^{\Gamma'*}_{\beta l_4,\alpha l_3}(E) \end{aligned} \tag{A.64}$$

The total cross section formula is drastically simpler in that only the $j = 0$ term survives:

$$\sigma_{\beta\leftarrow\alpha}(E) = \frac{\pi}{2k^2} \sum_{SL} \frac{(2S+1)(2L+1)}{(2S_\alpha+1)(2L_\alpha+1)} \sum_{l_1 l_2} |M^{\Gamma}_{\beta l_2,\alpha l_1}(E)|^2 \tag{A.65}$$

The total probability of scattering off a target alpha can be cast in the following form

$$\sigma_\alpha = \frac{4\pi}{k^2} \sum_{SL} \frac{(2S+1)(2L+1)}{2(2S_\alpha+1)(2L_\alpha+1)} \sum_\ell \left(\frac{\bar{S}_\Gamma^{1/2} - \bar{S}_\Gamma^{-1/2}}{2i} \right)^2_{\alpha\ell,\alpha\ell} \tag{A.66}$$

Finally, in the elastic scattering region off a totally symmetric target, the familiar expression

$$\sigma = \frac{4\pi}{k^2} \sum_\ell (2\ell+1) \sin^2 \delta_\ell. \tag{A.67}$$

is found.

Appendix B

Atom-radiation interaction

B.1 Field quantization

The interaction between radiation and matter in the non relativistic approximation is accounted for by the minimal coupling lagrangian[1]

$$L = \sum_i \frac{m_i}{2}\dot{r}_i^2 + \int \left(\frac{E^2 - B^2}{8\pi} + \frac{1}{c}\vec{A}\cdot\vec{j} - \rho\phi \right) d^3r \tag{B.1}$$

where the potential scalar and vector fields are defined by

$$\vec{E} = -\nabla\phi - \frac{1}{c}\partial_t\vec{A}, \qquad \vec{B} = \nabla\times\vec{A}. \tag{B.2}$$

The charge density ρ and the current density $\vec{j}$ for point charges are given by

$$\rho(\vec{r},t) = \sum_i q_i\delta^{(3)}(\vec{r}-\vec{r}_i(t)), \qquad \vec{j}(\vec{r},t) = \sum_i q_i\dot{\vec{r}}_i(t)\delta^{(3)}(\vec{r}-\vec{r}_i(t)). \tag{B.3}$$

The minimal action principle $\delta\int_{t_1}^{t_2} L(t)dt = 0$, equivalent to the Eulero Lagrange equations,

$$\frac{d}{dt}\partial_{\dot{\vec{r}}_i}L - \partial_{\vec{r}_i}L = 0, \qquad \frac{d}{dt}\partial_{\dot{\phi}}\mathcal{L} + \partial_{\vec{r}}\cdot\partial_{\partial_{\vec{r}}\phi}\mathcal{L} - \partial_\phi\mathcal{L} = 0 \tag{B.4}$$

where $\mathcal{L}$ is the lagrangian density, yields the correct equations of motion for both fields and particles. Assuming the Coulomb gauge ($\nabla\cdot\vec{A} = 0$), straightforward passages actually lead to the familiar Maxwell equations and Lorentz force

[1] Gauss system and atomic units ($e = 1$, $\hbar = 1$, $m_e = 1$, $\alpha = 1/c$) will be used throughout.

$$\nabla^2\phi = -4\pi\rho, \qquad \Box\,\vec{A} = -\frac{4\pi}{c}\vec{j}_\perp, \qquad m_i\ddot{\vec{r}}_i = q_i(\vec{E} + \frac{1}{c}\dot{\vec{r}}_i \times \vec{B}). \tag{B.5}$$

The Hamilton function corresponding to (B.1) is

$$H = \sum_i \vec{p}_i \cdot \dot{\vec{r}}_i + \int \left(\Pi_{\vec{A}} \cdot \dot{\vec{A}} + \Pi_\phi \dot{\phi}\right) d^3r - L \tag{B.6}$$

where the conjugate momenta to the lagrangian coordinates $\vec{r}_i$, $\vec{A}(\vec{r})$ and $\phi(\vec{r})$ are defined as

$$\vec{p}_i = \partial_{\dot{\vec{r}}_i} L = m_i\dot{\vec{r}}_i + \frac{q_i}{c}\vec{A}(\vec{r}_i, t), \quad \vec{\Pi}_{\vec{A}} = \partial_{\dot{\vec{A}}}\mathcal{L} = \frac{1}{4\pi c^2}\partial_t\vec{A}, \quad \vec{\Pi}_\phi = \partial_{\dot{\phi}}\mathcal{L} = 0. \tag{B.7}$$

The hamiltonian of an atomic system in the fixed nucleus approximation is readily derived

$$H = \sum_i \left\{\frac{1}{2}\left(\vec{p}_i - \alpha\vec{A}\right)^2 - \frac{Z}{r_i}\right\} + \sum_{i,j>i}\frac{1}{r_{ij}} + \frac{1}{8\pi}\int (E_\perp^2 + B^2) d^3r \tag{B.8}$$

Three separate energy terms are recognized: one for the electrons interacting through instantaneous Coulomb potentials, one for the free transverse field and one for the interaction between the transverse field and the electrons

$$H = H_{Mat} + H_{Rad} + H_{Rad-Mat} \tag{B.9}$$

$$H_{Mat} = \sum_i \left(\frac{p_i^2}{2m_i} - \frac{Z}{r_i}\right) + \sum_{i,j>i}\frac{1}{r_{ij}} \tag{B.10}$$

$$H_{Rad} = \frac{1}{8\pi}\int (E_\perp^2 + B^2) d^3r \tag{B.11}$$

$$H_{Rad-Mat} = -\alpha\sum_i \vec{A}(\vec{r}_i, t)\cdot\vec{p}_i + \frac{\alpha^2}{2}\sum_i A(\vec{r}_i, t)^2 \tag{B.12}$$

The habitual canonical quantization for the electron motion

$$[(\vec{r}_i)_\alpha, (\vec{p}_j)_\beta] = i\delta_{ij}\delta_{\alpha\beta} \tag{B.13}$$

can also be applied to the transverse field within any of those specific domains – bounded, unbounded; cubic, spherical, etc. – which embody in a natural way those

kinematic conditions which are frequently encountered in atomic physics. In order to get all of them at once we shall derive the general result .

Consider an arbitrary domain D and a complete basis of transverse field functions $\vec{U}_{\mu\lambda}$ satisfying the homogeneous Helmholtz equation

$$(\nabla^2 + k^2)\vec{U}_{\mu\lambda} = 0. \tag{B.14}$$

The $\vec{U}_{\mu\lambda}$ depend on a set of continuous μ and discrete λ parameters and are orthonormalized according to

$$\int_D d^3r \vec{U}_{\mu\lambda}(\vec{r})\vec{U}^*_{\mu'\lambda'}(\vec{r}) = \delta_{\lambda\lambda'}\delta(\mu - \mu'). \tag{B.15}$$

Thanks to eq. (B.14), the fields also obey the orthogonality condition

$$(k - k') \int_D d^3r \vec{U}_{\mu\lambda}(\vec{r})\vec{U}_{\mu'\lambda'}(\vec{r}) = 0 \tag{B.16}$$

The vector potential can be expanded on this basis:

$$\vec{A} = \sum\!\!\!\!\!\!\int_{\lambda} d\mu \left(A_{\lambda\mu} e^{-i\omega t}\vec{U}_{\mu\lambda} + A^*_{\lambda\mu} e^{i\omega t}\vec{U}^*_{\mu\lambda} \right) \tag{B.17}$$

The energy of the free radiation field can be cast in the form

$$H_{Rad} = \frac{1}{8\pi c^2} \int \left(\dot{\vec{A}} \cdot \dot{\vec{A}} - \vec{A} \cdot \ddot{\vec{A}} \right) d^3r \tag{B.18}$$

where we used the wave equation obeyed by the free field

$$\Box \vec{A} = 0 \tag{B.19}$$

and the following identity for transverse fields

$$\int d^3r (\nabla \times \vec{A}) \cdot (\nabla \times \vec{B}) = - \int d^3r \vec{A} \cdot \nabla^2 \vec{B} \tag{B.20}$$

Replacing (B.17) in (B.18) and exploiting eqns.(B.15-B.16), the following expression for the energy in terms of the independent parameters $A_{\lambda\mu}$ is readily obtained:

$$H_{Rad} = \sum\!\!\!\!\!\!\int_{\lambda} d\mu \frac{\omega^2}{4\pi c^2} \left(A_{\lambda\mu} A^*_{\lambda\mu} + A^*_{\lambda\mu} A_{\lambda\mu} \right). \tag{B.21}$$

If we define the conjugate canonical coordinates $Q_{\lambda\mu}$, $P_{\lambda\mu}$ as

$$Q_{\mu\lambda} = \frac{1}{\sqrt{4\pi c^2}}(A^*_{\mu\lambda} + A_{\mu\lambda}), \quad P_{\mu\lambda} = \frac{i\omega}{\sqrt{4\pi c^2}}(A^*_{\mu\lambda} - A_{\mu\lambda}) \tag{B.22}$$

the hamiltonian results in a sum of independent harmonic oscillators explicitly written in terms of the $Q_{\lambda\mu}$ and the $P_{\lambda\mu}$

$$H_{Rad} = \sum\!\!\!\!\!\!\int_{\lambda} d\mu \, \frac{1}{2} \, \left(P^2_{\lambda\mu} + \omega^2_{\mu\lambda} Q^2_{\lambda\mu} \right) \tag{B.23}$$

The canonical quantization now reads

$$[Q_{\lambda\mu}, P_{\lambda'\mu'}] = i\delta_{\lambda\lambda'}\delta(\mu - \mu'). \tag{B.24}$$

We can define the ladder operators as

$$\begin{array}{rl} b^\dagger_{\lambda\mu} & = \frac{1}{\sqrt{2\omega}} \left(\omega Q_{\lambda\mu} - i P_{\lambda\mu} \right) \\ b_{\lambda\mu} & = \frac{1}{\sqrt{2\omega}} \left(\omega Q_{\lambda\mu} + i P_{\lambda\mu} \right) \end{array} \tag{B.25}$$

$$[b_{\lambda\mu}, b_{\lambda',\mu'}] = 0, \qquad [b^\dagger_{\lambda\mu}, b^\dagger_{\lambda',\mu'}] = 0, \qquad [b_{\lambda\mu}, b^\dagger_{\lambda',\mu'}] = \delta_{\lambda\lambda'}\delta(\mu - \mu') \tag{B.26}$$

$b^\dagger_{\lambda\mu}$ and $b_{\lambda\mu}$ are interpreted respectively as the creator and destructor of a photon in the mode $(\lambda\mu)$ and are the quantum analogues of $A^*_{\lambda\mu}$ and $A_{\lambda\mu}$:

$$\sqrt{\frac{\omega}{2\pi c^2}} \, A^*_{\lambda\mu} \to b^\dagger_{\lambda\mu}, \quad \sqrt{\frac{\omega}{2\pi c^2}} \, A_{\lambda\mu} \to b_{\lambda\mu} \tag{B.27}$$

The fundamental state of the radiation space where no photons are present, the vacuum state $|-\rangle$, is normalized as

$$\langle - | - \rangle = 1 \tag{B.28}$$

In every mode, all the well known relations for the harmonic oscillator are valid

$$b^\dagger |n\rangle = \sqrt{n+1}|n+1\rangle, \qquad b|n\rangle = \sqrt{n}|n-1\rangle \tag{B.29}$$

$$H_{Rad} = \sum\!\!\!\!\!\!\int_{\lambda} d\mu\, \omega \left(b^{\dagger}_{\lambda\mu} b_{\lambda\mu} + \frac{1}{2} \right) \tag{B.30}$$

For bounded domains, where there are only discrete parameters, the radiation space is the tensor product of the spaces of multiple occupancy for every oscillator:

$$\mathcal{H} = \bigotimes_{\lambda} \mathcal{H}_{\lambda}, \qquad \mathcal{H}_{\lambda} = \bigoplus_{n=0}^{\infty} \frac{1}{\sqrt{n!}} b^{\dagger n}_{\lambda} |-\rangle \tag{B.31}$$

while for unbounded domains, the radiation states are properly defined as the superposition of one, two, ..., n photon states defined through L^2 functions $\phi^{(n)}(\mu_1\lambda_1, \mu_2\lambda_2, \ldots, \mu_n\lambda_n)$ with suitable restrictions on the ordering of parameters

$$|\phi\rangle = \sum\!\!\!\!\!\!\int_{\lambda} d\mu |\mu\lambda\rangle \phi^{(1)}(\mu\lambda) + \sum\!\!\!\!\!\!\int_{\lambda} \sum\!\!\!\!\!\!\int_{\lambda'} d\mu d\mu' |\mu\lambda \otimes \mu'\lambda'\rangle \phi^{(2)}(\mu\lambda, \mu'\lambda') + \ldots \tag{B.32}$$

The general expression for the quantized transverse vector potential in Heisemberg representation is obtained replacing the $A_{\lambda\mu}$ and $A^{\dagger}_{\lambda\mu}$ in eq. (B.17) by their quantum analogues from eq. (B.27). The transformation to the Schrödinger picture amounts simply to strip off the time factors:

$$\vec{A} = \sum\!\!\!\!\!\!\int_{\lambda} d\mu \sqrt{\frac{2\pi c}{k}} \left(\vec{U}_{\mu\lambda} b_{\mu\lambda} + \vec{U}^{*}_{\mu\lambda} b^{\dagger}_{\mu\lambda} \right) \tag{B.33}$$

We can now specialize equation (B.33), as anticipated, to the four most popular schemes in atomic physics: the cubic box with edge L and periodic boundary conditions, the spherical box of radius R and reflecting boundary conditions, and the unlimited domain in cartesian and spherical coordinates. The cartesian schemes are best suited for processes where the radiation field is populated mainly along a specific direction, as in the case of the photoionization with synchrotron radiation or in the interaction with lasers, while the spherical schemes are appropriate to describe photonic-atomic states with well defined $SO(3)$ symmetry, such as those encountered in the spontaneous decay.

Cubic box. In a cubic box with edge L and periodic boundary conditions, there are three denumerable parameters for the wave direction $\vec{k}$, $k_i = 2\pi n_i/L$, $n_i \in \mathbb{Z} \setminus \{0\}$, and one for its polarization λ in the plane orthogonal to $\vec{k}$

$$\vec{U}_{\vec{k}\lambda} = \frac{e^{i\vec{k}\cdot\vec{r}}}{L^{3/2}} \hat{\epsilon}_{\hat{k}\lambda}, \quad \vec{A} = \sum_{\vec{k},\lambda} \left(\frac{2\pi c}{L^3 k} \right)^{1/2} \left(\hat{\epsilon}_{\hat{k}\lambda} e^{i\vec{k}\cdot\vec{r}} b_{\vec{k}\lambda} + \hat{\epsilon}^{*}_{\hat{k}\lambda} e^{-i\vec{k}\cdot\vec{r}} b^{\dagger}_{\vec{k}\lambda} \right) \tag{B.34}$$

$$[b_{\vec{k}\lambda}, b^{\dagger}_{\vec{k}'\lambda'}] = \delta_{\vec{k}\vec{k}'} \delta_{\lambda\lambda'} \tag{B.35}$$

Unbounded domain in cartesian coordinates. with unbounded domains we have the freedom to choose the normalization of the basis functions

$$\vec{U}_{\vec{k}\lambda} = \frac{e^{i\vec{k}\cdot\vec{r}}}{\sqrt{(2\pi)^3}}\,\hat{\epsilon}_{\hat{k}\lambda}, \quad \vec{A} = \sum_{\lambda}\int d^3k \left(\frac{c}{4\pi^2 k}\right)^{1/2}\left(\hat{\epsilon}_{\hat{k}\lambda}e^{i\vec{k}\cdot\vec{r}}b_{\vec{k}\lambda} + \hat{\epsilon}^*_{\hat{k}\lambda}e^{-i\vec{k}\cdot\vec{r}}b^\dagger_{\vec{k}\lambda}\right) \tag{B.36}$$

$$[b_{\vec{k}\lambda}, b^\dagger_{\vec{k}'\lambda'}] = \delta^{(3)}(\vec{k}-\vec{k}')\delta_{\lambda\lambda'} \tag{B.37}$$

or

$$\vec{U}_{\omega\hat{k}\lambda} = \omega\frac{e^{i\vec{k}\cdot\vec{r}}}{\sqrt{(2\pi c)^3}}\,\hat{\epsilon}_{\hat{k}\lambda},$$
$$\vec{A} = \sum_{\lambda}\int d\hat{k}\,d\omega \left(\frac{\omega}{4\pi^2 c}\right)^{1/2}\left(\hat{\epsilon}_{\hat{k}\lambda}e^{i\vec{k}\cdot\vec{r}}b_{\omega\hat{k}\lambda} + \hat{\epsilon}^*_{\hat{k}\lambda}e^{-i\vec{k}\cdot\vec{r}}b^\dagger_{\omega\hat{k}\lambda}\right) \tag{B.38}$$

$$[b_{\omega\hat{k}\lambda}, b^\dagger_{\omega'\hat{k}'\lambda'}] = \delta(\omega-\omega')\delta(\hat{k}-\hat{k}')\delta_{\lambda\lambda'} \tag{B.39}$$

Spherical box. Four discrete parameters, $jm\lambda k_i$, classify the basis functions in a spherical box. j and m are the total angular momentum $j = 1, 2, 3, \ldots$ (there are no scalar photons) and its projection on a quantization axis $m = -j, -j+1, \ldots, j-1, j$, λ defines the polar $(+)$ or axial $(-)$ character of the transverse field, corresponding to electric and magnetic 2^j-poles respectively, finally the momenta k_i are chosen in such a way to fulfill the total reflection conditions at the boundary

$$\vec{U}_{ijm\lambda} = \sqrt{\frac{2k_i^2}{R}}\vec{\Theta}^{(\lambda)}_{k_ijm}, \quad \vec{A} = \sum_{ijm\lambda}\left(\frac{4\pi c k_i}{R}\right)^{1/2}\left\{\vec{\Theta}^{(\lambda)}_{k_ijm}b^{(\lambda)}_{k_ijm} + \vec{\Theta}^{(\lambda)*}_{k_ijm}b^{(\lambda)\dagger}_{k_ijm}\right\} \tag{B.40}$$

$$[b^{(\lambda)}_{k_ijm}, b^{(\lambda')\dagger}_{k_{i'}j'm'}] = \delta_{jj'}\delta_{mm'}\delta_{\lambda\lambda'}\delta_{ii'} \tag{B.41}$$

The electromagnetic multipoles $\vec{\Theta}^{(\lambda)}_{kjm}$ are defined as follows

$$\vec{\Theta}^{(+)}_{kjm} = \frac{\nabla\times\vec{\ell}\,u_{kjm}}{k\sqrt{j(j+1)}}, \qquad \vec{\Theta}^{(-)}_{kjm} = \frac{\vec{\ell}\,u_{kjm}}{\sqrt{j(j+1)}}; \qquad \vec{\Theta}^{(\pm)}_{kjm} = \nabla\times\frac{\vec{\Theta}^{(\mp)}_{kjm}}{k} \tag{B.42}$$

where

$$u_{klm} = j_l(kr)Y_{lm}(\theta,\phi) \tag{B.43}$$

The vector potential in (B.40) is actually approximated: we used the asymptotic approximation for the electric multipoles to obtain an explicit expression for the normalization coefficient; however this is perfectly acceptable as long as the $R \to \infty$ limit is taken in the final results.

Unbounded domain in spherical coordinates.

$$\vec{U}_{kjm\lambda} = \sqrt{\frac{2k^2}{\pi}}\vec{\Theta}^{(\lambda)}_{kjm}, \quad \vec{A} = \sum_{jm\lambda}\int \sqrt{4ck}\, dk\Big\{\vec{\Theta}^{(\lambda)}_{kjm} b^{(\lambda)}_{kjm} + \vec{\Theta}^{(\lambda)*}_{kjm} b^{(\lambda)\dagger}_{kjm}\Big\} \tag{B.44}$$

$$[b^{(\lambda)}_{kjm}, b^{(\lambda')\dagger}_{k'j'm'}] = \delta_{jj'}\delta_{mm'}\delta_{\lambda\lambda'}\delta(k-k') \tag{B.45}$$

Also in this case, other normalizations can be chosen; for example:

$$\vec{U}_{\omega jm\lambda} = \sqrt{\frac{2k^2}{\pi c}}\vec{\Theta}^{(\lambda)}_{kjm}, \quad \vec{A} = \sum_{jm\lambda}\int \sqrt{4\alpha\omega}\, d\omega\Big\{\vec{\Theta}^{(\lambda)}_{kjm} b^{(\lambda)}_{\omega jm} + \vec{\Theta}^{(\lambda)*}_{kjm} b^{(\lambda)\dagger}_{\omega jm}\Big\} \tag{B.46}$$

$$[b^{(\lambda)}_{\omega jm}, b^{(\lambda')\dagger}_{\omega' j'm'}] = \delta_{jj'}\delta_{mm'}\delta_{\lambda\lambda'}\delta(\omega-\omega') \tag{B.47}$$

Dipole approximation When all the relevant wavelengths in the atom-radiation interaction are much larger than the characteristic size of the atom, the field can be approximated with its value at the origin. This is usually called the dipole approximation: the magnetic multipoles are manifestly zero and since (see eq. 18 pag 148 in [216])

$$\nabla \times [\, r^l\, \vec{L}\, Y_{lm}(\theta,\phi)] = i(l+1)\sqrt{l(2l+1)}\, r^{l-1}\, \vec{Y}^{l-1}_{lm}(\theta,\phi)$$

only the electric dipole gives rise to a non vanishing contribution

$$\vec{\Theta}^{(\lambda)}_{kjm}(\vec{0}) = \delta_{\lambda +}\, \delta_{j\,1}\, \frac{i}{\sqrt{6\pi}}\, \vec{\epsilon}_{1m}.$$

It should be observed that the vector potential in dipole approximation does not coincide with the complete electric dipole component. The vector potential operator at the origin in spherical and cartesian unbounded domains are

$$A^\mu = i\sqrt{\frac{2\alpha}{3\pi}}\int \omega^{1/2} d\omega(\epsilon^\mu_1 b^{(+)}_{\omega 1\mu} - \epsilon^{\mu *}_1 b^{(+)\dagger}_{\omega 1\mu}) \tag{B.48}$$

$$\vec{A} = \sum_{\lambda} \int d^3k \left(\frac{c}{4\pi^2 k}\right)^{1/2} \left(\hat{\epsilon}_{\hat{k}\lambda} b_{\vec{k}\lambda} + \hat{\epsilon}^*_{\hat{k}\lambda} b^\dagger_{\vec{k}\lambda}\right). \tag{B.49}$$

Equation (B.48) clearly shows that at each wavelength there is essentially only one mode which interacts with the localized atom, while in (B.49) an integral over all the possible directions and a sum over all the polarizations remain. This is a marked advantage of the spherical over the cartesian scheme when computing matrix elements between states with definite $SO(3)$ global symmetry: it is much more straightforward to adopt spherical photons from the outset instead of dealing with irrelevant channels, which sooner or later must nevertheless be projected out.

B.2 Transition amplitudes and rates

The interaction term (B.12) causes the eigenstates of the decoupled hamiltonian to evolve. Matter-radiation interaction can indeed be seen as a scattering process between photons and charged particles, where photons may be emitted or absorbed. The transition rate from an initial state (of both matter and radiation) $|i\rangle$ to a final state $|f\rangle$ is therefore given plainly by the generalized Fermi golden rule (see appendix A on scattering)

$$W_{f\leftarrow i} = 2\pi\delta(E_f - E_i)\Big|\sum_{j=0}^{\infty}\langle f|V[G_0^+(E_i)V]^j|i\rangle\Big|^2 \tag{B.50}$$

The absorption of a single photon of well defined momentum and polarization is represented, in a cubic box, as the transition from the initial state $|i\rangle = |A\rangle \otimes |n\rangle$ to the final state $|f\rangle = |B\rangle \otimes |n-1\rangle$. The transition rate is proportional to the photon flux $\mathcal{F}$ and, to the lowest order approximation, is given by:

$$W_{f\leftarrow i} = \frac{4\pi^2}{c\omega}\delta(E_B - E_A - \omega)\mathcal{F}|\langle B|\hat{\epsilon}\cdot\sum_i e^{i\vec{k}\cdot\vec{r}_i}\vec{p}_i|A\rangle|^2 \tag{B.51}$$

The transition rate divided by the photon flux and integrated in the total final energy, yields the photoabsorption cross section:

$$\sigma_{f\leftarrow i} = \frac{4\pi^2}{c\omega}|\langle B|\hat{\epsilon}\cdot\sum_i e^{i\vec{k}\cdot\vec{r}_i}\vec{p}_i|A\rangle|^2 \tag{B.52}$$

When the final state lies in the single ionization continuum where a complete set of eigenfunctions $\psi^-_{\alpha,E\hat{k}_e\sigma}$ with the normalization condition

$$\langle\psi^-_{\alpha,E\hat{k}_e\sigma}|\psi^-_{\beta,E'\hat{k}'_e\sigma'}\rangle = \delta_{\alpha\beta}\delta(E-E')\delta(\Omega_k - \Omega'_k)\delta_{\sigma\sigma'}$$

are available, the expression (B.52) gives the partial differential cross section

$$\frac{d\sigma_{\alpha,E\hat{k}_e\sigma}}{d\Omega_{\hat{k}_e}} = \frac{(2\pi)^2}{c\omega_\gamma}|\langle\psi^-_{\alpha,E\hat{k}_e\sigma}|\vec{\epsilon}\cdot\sum_{i=1}^{n} e^{i\vec{k}_\gamma\cdot\vec{r}_i}\vec{p}_i|\phi_0\rangle|^2. \tag{B.53}$$

The very same results can be obtained in the unbound domain scheme, where the absorption of a single initial photon is considered, provided that the final result is properly normalized with respect to the photon flux density. The latter can be derived easily by taking the expectation value of the Pointing vector $\vec{S} = 1/4\pi\,\vec{E}\times\vec{B}$ on the single occupancy state $b^\dagger_{\vec{k}\lambda}|-\rangle$ and dividing the results by ω. This yields a finite value equal to $c/(2\pi)^3\,\hat{k}$. Cross sections are usually measured in barns: 1b= 10^{-28}m^2. Since 1au= $5.291772108\cdot10^{-11}$m, 1b is of the same order of magnitude of a nuclear section. Soft X-ray atomic photoionization cross sections of dipole allowed transitions are typically of the order of magnitude of 1Mb, while those for processes of second order in the field expansion around the origin (electric quadrupole, magnetic dipole) are of the order of 100b.

B.3 Driven Schrödinger equation

As we have seen, the photoionization of an atom can be seen as the collision of a photon with the atom where the photon disappears. The stationary wave function that properly describe the process is therefore

$$\Psi^+_{0\omega} = \phi_0\otimes\omega + \psi^+_{scat} \tag{B.54}$$

where in ψ^+_{scat} all radiative channels have only incoming components, while autoionization channels have only outgoing components. We can annihilate as usual the first member by applying the operator $(E-\mathcal{H})$ where $E = E_0+\omega$ and $\mathcal{H}$ is the total hamiltonian $\mathcal{H} = H + H_{Rad} + H'$:

$$(E - H - H_{Rad} - H')\psi^+_{scat} = H'\phi_0\otimes\omega \tag{B.55}$$

As long as radiative channels in the scattering function are completely neglected, we can write simply

$$(E_0+\omega-H)\psi^+_{scat} = H'\phi_0\otimes\omega \tag{B.56}$$

This is known as the driven Schrödinger equation.

B.4 Multipolar expansion

To cast the photoionization differential cross section (B.53)

$$\frac{\partial^2\sigma_{\alpha,E\hat{k}_e\sigma}}{\partial E\partial\Omega_{\hat{k}_e}} = \frac{(2\pi)^2}{c\omega_\gamma}|\langle\psi^-_{\alpha,E\hat{k}_e\sigma}|\vec{\epsilon}\cdot\sum_{i=1}^{n} e^{i\vec{k}_\gamma\cdot\vec{r}_i}\vec{p}_i|\phi_0\rangle|^2,$$

in a sum over cross products of transition matrix elements between irreducible representation of SO(3), both the radiation field and the matter wave have to be expanded in spherical waves:

$$e^{i\vec{k}\cdot\vec{r}} = 4\pi \sum_{J=0}^{\infty} i^J j_J(kr) \sum_{M=-J}^{J} Y_J^M(\hat{k}) Y_{JM}(\hat{r}). \tag{B.57}$$

where j_J is a spherical Bessel function. The interaction term becomes

$$e^{i\vec{k}\cdot\vec{r}}\vec{\epsilon}\cdot\vec{p} = 4\pi \sum_{J=0}^{\infty} i^J j_J(kr) \sum_{M\mu} Y_J^M(\hat{k}) \epsilon_1^\mu Y_{JM}(\hat{r}) p_{1\mu}. \tag{B.58}$$

With few passages we can couple the orbital angular momentum with the polarization vector

$$\begin{aligned}
\sum_{M\mu} Y_J^M(\hat{k}_\gamma)\epsilon_1^\mu Y_{JM}(\hat{r}) p_{1\mu} &= \sum_{M\mu} Y_J^M(\hat{k}_\gamma)\hat{e}_1^\mu \cdot \hat{\epsilon} \sum_{T\tau} C^{T\tau}_{JM\,1\mu} [Y_J(\hat{r}) \otimes p_1]_{T\tau} = \\
&= \sum_{T\tau} \hat{\epsilon}\cdot \left(\sum_{M\mu} C^{T\tau}_{JM\,1\mu} Y_J^M(\hat{k}_\gamma)\hat{e}_1^\mu \right) [Y_J(\hat{r}) \otimes p_1]_{T\tau} = \\
&= \sum_{T\tau} \left[\vec{\epsilon}\cdot \vec{Y}_T^{J\tau}(\hat{k}_\gamma)\right] \left[Y_J(\hat{r}) \otimes p_1\right]_{T\tau}
\end{aligned} \tag{B.59}$$

where we made use of the following definitions of tensor product and vector spherical harmonics

$$\{\mathfrak{M}_{J_1} \otimes \mathfrak{N}_{J_2}\}_{JM} \equiv \sum_{M_1 M_2} C^{JM}_{J_1 M_1\, J_2 M_2} \mathfrak{M}_{J_1 M_1} \mathfrak{N}_{J_2 M_2}, \tag{B.60}$$

$$\vec{Y}_T^{J\tau}(\theta,\phi) \equiv \sum_{M\mu} C^{T\tau}_{JM\,1\mu}\; Y_J^M(\theta,\phi)\; \vec{e}_1^{\,\mu}. \tag{B.61}$$

The multipolar expansion of the interaction term is then

$$V = \sum_{T=1}^{\infty} \sum_{\tau=-T}^{T} \sum_{J=T-1}^{T+1} 4\pi i^J\, \vec{\epsilon}\cdot \vec{Y}_T^{J\tau}(\hat{k}_\gamma) \sum_{i=1}^{N} j_J(k_\gamma\, r_i) \left[Y_J(\hat{r}_i) \otimes p_1^{(i)}\right]_{T\tau}. \tag{B.62}$$

The multipolar transition operator $\left[Y_J(\hat{r}_i)\otimes p_1^{(i)}\right]_{T\tau}$ has the parity of $J+1$. The true tensors, with $J = T \pm 1$, are the electric multipoles ET while the pseudo-tensors, with $J = T$, are the magnetic multipoles MT:

$$V^{(MT)} \equiv \sum_{\tau} 4\pi i^T \left(\vec{Y}_T^{T\tau}(\hat{k}_\gamma)\cdot\vec{\epsilon}\right) \sum_{i=1}^{N} j_T(k_\gamma r_i)\left[Y_T(\hat{r}_i)\otimes p_1^{(i)}\right]_{T\tau}, \tag{B.63}$$

$$\begin{aligned} V^{(ET)} \equiv \sum_{\tau} 4\pi \Big\{ & i^{T-1}\left(\vec{Y}_T^{T-1\,\tau}(\hat{k})\cdot\vec{\epsilon}\right) \sum_{i=1}^{N} j_{T-1}(k\,r_i)\left[Y_{T-1}(\hat{r}_i)\otimes p_1^{(i)}\right]_{T\tau} + \\ & i^{T+1}\left(\vec{Y}_T^{T+1\,\tau}(\hat{k})\cdot\vec{\epsilon}\right) \sum_{i=1}^{N} j_{T+1}(k\,r_i)\left[Y_{T+1}(\hat{r}_i)\otimes p_1^{(i)}\right]_{T\tau}\Big\}. \end{aligned} \tag{B.64}$$

The reduced matrix elements of the one-particle operators $j_J(kr)[Y_J(\hat{r})\otimes p_1]_{T\tau}$ can be formulated in terms of reduced matrix elements of $j_J(kr)\,p$:

$$\begin{aligned} &\langle f' Y_{\ell' m'}|j_J(k_\gamma r)[Y_J(\hat{r})\otimes p_1]_{T\tau}|fY_{\ell m}\rangle = \\ &= \sum_{\mu\nu}\langle f' Y_{\ell' m'}|j_J(k_\gamma r)Y_{J\mu}(\hat{r})p_{1\nu}|fY_{\ell m}\rangle C^{T\tau}_{J\mu\,1\nu} = \\ &= \sum_d \frac{\Pi_{Jd}}{\sqrt{4\pi}\Pi_{\ell'}} C^{\ell' 0}_{d0\,J0}\sum_{\mu\nu\delta} C^{T\tau}_{1\nu\,J\mu} C^{\ell' m'}_{d\delta\,J\mu}\langle f' Y_{d\delta}|j_J(k_\gamma r)p_{1\nu}|fY_{\ell m}\rangle = \\ &= \sum_d \frac{\Pi_J}{\sqrt{4\pi}\Pi_{\ell'}} C^{\ell' 0}_{d0\,J0}\langle f' Y_d\|j_J(k_\gamma r)p_1\|fY_\ell\rangle \sum_{\mu\nu\delta} C^{T\tau}_{1\nu\,J\mu} C^{\ell' m'}_{d\delta\,J\mu} C^{d\delta}_{\ell m\,1\nu} = \\ &= \frac{C^{\ell' m'}_{\ell m\,T\tau}}{\sqrt{2\ell'+1}}\sum_d \frac{\Pi_{JTd}}{\sqrt{4\pi}} \begin{Bmatrix} 1 & J & T \\ \ell' & \ell & d \end{Bmatrix} C^{\ell' 0}_{J0\,d0}\langle f' Y_d\|j_J(k_\gamma r)p_1\|fY_\ell\rangle(-)^{J+T+1}, \end{aligned} \tag{B.65}$$

where we used the relation

$$\sum_{\mu\nu\delta} C^{T\tau}_{1\nu\,J\mu} C^{\ell' m'}_{d\delta\,J\mu} C^{d\delta}_{\ell m\,1\nu} = (-)^{1+J+T}\Pi_{Td} C^{\ell' m'}_{T\tau\,\ell m} \begin{Bmatrix} 1 & J & T \\ \ell' & \ell & d \end{Bmatrix}, \tag{B.66}$$

therefore

$$\begin{aligned} \langle f' Y_{\ell'}\|j_J(k_\gamma r)[Y_J(\hat{r})\otimes p_1]_T\|fY_\ell\rangle = & \sum_d \frac{\Pi_{JTd}}{\sqrt{4\pi}} \begin{Bmatrix} 1 & J & T \\ \ell' & \ell & d \end{Bmatrix} C^{\ell' 0}_{J0\,d0} \\ & \langle f' Y_d\|j_J(k_\gamma r)p_1\|fY_\ell\rangle(-)^{J+T+1} \end{aligned} \tag{B.67}$$

In particular

$$\begin{aligned} \langle f' Y_{\ell'}\|j_0(k_\gamma r)[Y_0(\hat{r})\otimes p_1]_1\|fY_\ell\rangle &= \frac{1}{\sqrt{4\pi}}\langle f'\ell'\|j_0(k_\gamma r)p_1\|f\ell\rangle \\ \langle f' Y_{\ell'}\|j_2(k_\gamma r)[Y_2(\hat{r})\otimes p_1]_1\|fY_\ell\rangle &= \sqrt{\frac{15}{4\pi}}\sum_d \Pi_d C^{\ell' 0}_{20\,d0} \begin{Bmatrix} 2 & 1 & 1 \\ \ell & \ell' & d \end{Bmatrix} \times \\ & \quad \times \langle f' d\|j_2(k_\gamma r)p_1\|f\ell\rangle. \end{aligned} \tag{B.68}$$

$$\langle f'Y_{\ell'}\|j_1(k_\gamma r)[Y_1(\hat{r})\otimes p_1]_1\|fY_\ell\rangle = -\frac{3}{\sqrt{4\pi}}\sum_d \Pi_d\, C^{\ell'0}_{10\,d0}\begin{Bmatrix}1 & 1 & 1\\ \ell & \ell' & d\end{Bmatrix}\times \\ \times\langle f'd\|j_1(k_\gamma r)p_1\|f\ell\rangle. \tag{B.69}$$

$$\langle f'Y_{\ell'}\|j_1(k_\gamma r)[Y_1(\hat{r})\otimes p_1]_2\|fY_\ell\rangle = \sqrt{\frac{15}{4\pi}}\sum_d \Pi_d C^{\ell'0}_{10\,d0}\begin{Bmatrix}1 & 1 & 2\\ \ell & \ell' & d\end{Bmatrix}\times \\ \times\,\langle f'd\|j_1(k_\gamma r)p_1\|f\ell\rangle. \tag{B.70}$$

$$\langle f'Y_{\ell'}\|j_3(k_\gamma r)[Y_3(\hat{r})\otimes p_1]_2\|fY_\ell\rangle = \sqrt{\frac{35}{4\pi}}\sum_d \Pi_d C^{\ell'0}_{30\,d0}\begin{Bmatrix}3 & 1 & 2\\ \ell & \ell' & d\end{Bmatrix}\times \\ \times\,\langle f'd\|j_3(k_\gamma r)p_1\|f\ell\rangle.$$

If we define

$$V^J_{T\tau} = \sum_{i=1}^{N} v^J_{T\tau}(i), \qquad v^J_{T\tau}(i) = 4\pi i^J j_J(k_\gamma r_i)[Y_J(\hat{r}_i)\otimes p_1^{(i)}]_{T\tau}, \tag{B.71}$$

we can rewrite the total transition operator as

$$V = \sum_{T=1}^{\infty}\sum_{J=T-1}^{T+1}\sum_{\tau=-T}^{T}\left[\vec{\epsilon}\cdot\vec{Y}^{J\tau}_T(\hat{k}_\gamma)\right]\, V^J_{T\tau}. \tag{B.72}$$

In general

$$\langle\psi^{\Gamma'}|V|\psi^{\Gamma}\rangle = \sum_{T=1}^{\infty}\sum_{J=T-1}^{T+1}\sum_{\tau=-T}^{T}\left[\vec{\epsilon}\cdot\vec{Y}^{J\tau}_T(\hat{k}_\gamma)\right]\,\langle\psi^{\Gamma'}|V^J_{T\tau}|\psi^{\Gamma}\rangle = \\ = \sum_{T=1}^{\infty}\sum_{J=T-1}^{T+1}\underbrace{\left\{\sum_{\tau=-T}^{T}\frac{C^{L'M'}_{LM\,T\tau}}{\sqrt{2L'+1}}[\vec{\epsilon}\cdot\vec{Y}^{J\tau}_T(\hat{k}_\gamma)]\right\}}_{\text{KINEMATICS}}\times\underbrace{\langle\psi^{\Gamma'}\|V^J_T\|\psi^{\Gamma}\rangle}_{\text{DYNAMICS}} \tag{B.73}$$

where the kinematic term of a transition matrix element between atomic states with definite symmetry has been factored out.

In principle we should evaluate the integral $\langle f'Y_{\ell'}\|j_J(kr)p_1\|fY_\ell\rangle$ at each photon energy. Hopefully, for large wavelengths, few terms of the j_J Taylor series lead to converged results already:

$$j_J(z) = z^J\sum_\nu \frac{(-z^2)^\nu}{2^\nu\nu!(2J+2\nu+1)!!}, \tag{B.74}$$

$$\hat{v}^{J}_{T\tau} = \sum_{\nu=0}^{\infty} k_p^{J+2\nu}\ \hat{v}^{J\nu}_{T\tau}, \qquad \hat{v}^{J\nu}_{T\tau} = 4\pi i^J \frac{(-)^\nu \cdot r^{J+2\nu}}{2^\nu \nu!(2J+2\nu+1)!!}[Y_J(\hat{r}) \otimes p_1]_{T\tau}. \quad \text{(B.75)}$$

B.5 Expansion of the outgoing electron wave

The expansion we look for is

$$\psi^{-}_{\alpha;\vec{k}_e\,\sigma} = \sum_{\ell_\alpha} \sum_{m=-\ell_\alpha}^{\ell_\alpha} \sum_{\Gamma} C^{LM}_{L_\alpha m_\alpha\, \ell_\alpha m} C^{S\Sigma}_{S_\alpha \sigma_\alpha\, \frac{1}{2}\sigma}\, Y^*_{\ell_\alpha m}(\hat{k}_e)\, \bar{\psi}^{(-)\Gamma}_{\alpha E} \quad \text{(B.76)}$$

where Γ is a collective index for the symmetry $(LS\Pi, M\Sigma)$ and we have incorporated the phase shift factor in the wavefunction:

$$\bar{\psi}^{(-)\Gamma}_{\alpha E} = e^{i\left(\frac{\ell_\alpha \pi}{2} - \sigma_{\eta_{\ell_\alpha}} - \delta^{\Gamma}_{\alpha\ell_\alpha}\right)} \psi^{(-)\Gamma}_{\alpha E} \quad \text{(B.77)}$$

Asymptotically $(r_n \to \infty)$ $\psi^{-}_{\alpha;\vec{k}_e\,\sigma}$ is

$$\psi^{-}_{\alpha;\vec{k}_e\,\sigma} \propto \underbrace{\Phi_\alpha \cdot e^{i\vec{k}_e\cdot\vec{r}_n} \cdot {}^2\chi_\sigma(\zeta_n)}_{\text{plane wave in channel } \alpha} + \underbrace{\sum_{\gamma}^{open} \Phi_\gamma \cdot C_\gamma(\hat{r}_n, \zeta_n) \cdot \frac{e^{-ik_\gamma r_n}}{k_\gamma r_n}}_{\substack{\text{incoming spherical waves} \\ \text{in every open channel}}} \quad \text{(B.78)}$$

with the normalization

$$\langle \psi^{-}_{\alpha;\vec{k}_e\,\sigma} | \psi^{-}_{\beta;\vec{k}'_e\,\sigma'} \rangle = \delta_{\alpha\beta}\delta_{\sigma\sigma'}\delta(E-E')\delta(\hat{k}_e - \hat{k}'_e) \quad \text{(B.79)}$$

The complete expansion of the transition matrix element between a bound state ϕ_0 and a continuum state $\psi^{-}_{\alpha,\vec{k}_e\sigma}$ is

$$\langle \phi_0 | V | \psi^{-}_{\alpha,\vec{k}_e\sigma} \rangle = \sum_{T=1}^{\infty} \sum_{J=T-1}^{T+1} \sum_{\Gamma\ell_\alpha m} \left\{ \sum_{\tau=-T}^{T} C^{L_0 M_0}_{LM\,T\tau}\ \frac{\vec{\epsilon}\cdot\vec{Y}^{J\tau}_T(\hat{k}_\gamma)}{\sqrt{2L_0+1}} \right\} \times$$
$$\times \quad C^{LM}_{L_\alpha m_\alpha\, \ell_\alpha m}\ C^{S\Sigma}_{S_\alpha\sigma_\alpha\, \frac{1}{2}\sigma}\ Y^*_{\ell_\alpha m}(\hat{k}_e)\ \langle \phi_0 \| V^J_T \| \bar{\psi}^{(-)\Gamma}_{\alpha,E} \rangle. \quad \text{(B.80)}$$

B.6 Orientational Average

Most of the photoionization experiments are not designed to discriminate the target or the final fragments on the basis of their orientation (spin polarization, atomic magnetic quantum numbers, etc). In order to reproduce the experimental results, the differential cross section (B.53) must be averaged over the initial atomic and summed over the final atomic and electronic polarizations.

$$\frac{\partial\sigma_{\bar{\alpha},E\hat{k}_e}}{\partial\Omega_{\hat{k}_e}} = \frac{(2\pi)^2}{c\omega_\gamma(2S_0+1)(2L_0+1)} \sum_{\Sigma_0 M_0} \sum_{m_\alpha} \sum_{\sigma_\alpha\sigma} |\langle\phi_0|V|\psi^-_{\alpha,\vec{k}_e\sigma}\rangle|^2 \tag{B.81}$$

Through straightforward algebraic passages (which we spare to the inculpable reader), a final result is obtained which can be cast in several forms, for example

$$\begin{aligned}\frac{\partial\sigma_{\bar{\alpha},E\hat{k}_e}}{\partial\Omega_{\hat{k}_e}} = \frac{(2\pi)^2}{c\omega_\gamma} &\times \sum_{\ell_e m_e} Y_{\ell_e m_e}(\hat{k}_e) \times \\ &\times \sum_{TT'} \sum_{JJ'} \Big\{ \sum_{\tau\tau'} C^{T\tau}_{\ell_e m_e\, T'\tau'} \left[\vec{\epsilon}_\gamma \cdot \vec{Y}^{J\tau}_T(\hat{k}_\gamma)\right] \left[\vec{\epsilon}_\gamma \cdot Y^{J'\tau'}_{T'}(\hat{k}_\gamma)\right]^* \Big\} \times \\ &\times \sum_{\ell_\alpha\ell'_\alpha} \sum_{LL'} \frac{\Pi_{\ell_\alpha\ell_e LL'}}{\sqrt{4\pi}(2L_0+1)\Pi_T} C^{\ell'_\alpha 0}_{\ell_\alpha 0\,\ell_e 0} \begin{Bmatrix} L' & \ell_e & L \\ \ell_\alpha & L_\alpha & \ell'_\alpha \end{Bmatrix} \begin{Bmatrix} T & \ell_e & T' \\ L' & L_0 & L \end{Bmatrix} \times \\ &\times (-)^{L+L'+L_0+T'+L_\alpha+\ell_\alpha} \langle\phi_0\|V^J_T\|\bar{\psi}^{(-)\Gamma}_{\alpha E\ell_\alpha}\rangle \cdot \langle\phi_0\|V^{J'}_{T'}\|\bar{\psi}^{(-)\Gamma'}_{\alpha E\ell'_\alpha}\rangle^*. \end{aligned} \tag{B.82}$$

or

$$\begin{aligned}\frac{\partial\sigma_{\bar{\alpha},E\hat{k}_e}}{\partial\Omega_{\hat{k}_e}} = &\frac{(2\pi)^2}{c\omega_\gamma} \sum_{K\ell_e\ell_\gamma} \Big([\epsilon\otimes\epsilon]_K \cdot [Y_{\ell_e}(\hat{k}_e)\otimes Y_{\ell_\gamma}(\hat{k}_\gamma)]_K \Big) \sum_{TT'} \sum_{JJ'} \begin{Bmatrix} T & J & 1 \\ T' & J' & 1 \\ \ell_e & \ell_\alpha & K \end{Bmatrix} \times \\ &\times \sum_{LL'} \sum_{\ell_\alpha\ell'_\alpha} \frac{1}{4\pi} \Pi_{\ell_e\ell_\alpha\ell_\gamma JTT'LL'} C^{\ell'_\alpha 0}_{\ell_e 0\,\ell_\alpha 0} C^{J'0}_{\ell_\gamma 0\, J0} (-1)^{L_\alpha+\ell'_\alpha+L+L'+T+L_0} \times \\ &\times \begin{Bmatrix} \ell_\alpha & \ell_e & \ell'_\alpha \\ L' & L_\alpha & L \end{Bmatrix} \begin{Bmatrix} L_0 & T & L \\ \ell_e & L' & T' \end{Bmatrix} \langle\phi_0\|V^J_T\|\bar{\psi}^{(-)\Gamma}_{\alpha E\ell_\alpha}\rangle \langle\phi_0\|V^{J'}_{T'}\|\bar{\psi}^{(-)\Gamma'}_{\alpha E\ell'_\alpha}\rangle^*. \end{aligned} \tag{B.83}$$

These expressions can be easily specialized to simpler cases of our interest. The next sections will be dedicated to this task where for clarity the bar over initial and final state indexes will be dropped.[2]

[2]The bar over ψ is not an average: its possible absence indicates that two conjugate phase factors annihilated.

B.7 Integral cross sections

We get integral cross sections easily from differential cross sections integrating over $\hat{k}_e$

$$\sigma_{\alpha,E} = \int d\hat{\Omega}_{\hat{k}_e} \frac{\partial \sigma_{\alpha,E\hat{k}_e}}{\partial \Omega_{\hat{k}_e}}. \tag{B.84}$$

In the integration process, just the $\ell_e = 0$ term survives and the expression B.82 is greatly simplified:

$$\begin{aligned} \sigma_{\alpha,E} &= \frac{(2\pi)^2}{c\omega_\gamma} \sum_{JJ'T} \sum_{\tau} \frac{\left[\vec{\epsilon}\cdot \vec{Y}_T^{J\tau}(\hat{k}_\gamma)\right]\left[\vec{\epsilon}\cdot Y_T^{J'\tau}(\hat{k}_\gamma)\right]^*}{(2L_0+1)(2T+1)} \times \\ &\times \sum_{L\ell_\alpha} \langle \phi_0 \| V_T^J \| \psi_{\alpha E \ell_\alpha}^{(-)\Gamma} \rangle \langle \phi_0 \| V_T^{J'} \| \psi_{\alpha E \ell_\alpha}^{(-)\Gamma} \rangle^* \end{aligned} \tag{B.85}$$

We expect integral cross sections to be polarization independent. That this is the case can be easily proved if we remember that

$$\sum_{M=-J}^{J} |\vec{a}\cdot \vec{Y}_{JM}^{J+1}(\hat{n})|^2 = \frac{1}{8\pi}\{J|\vec{a}|^2 + (J+2)|\hat{n}\cdot\vec{a}|^2\} \tag{B.86}$$

$$\sum_{M=-J}^{J} |\vec{a}\cdot \vec{Y}_{JM}^{J}(\hat{n})|^2 = \frac{2J+1}{8\pi}\{|\vec{a}|^2 - |\hat{n}\cdot\vec{a}|^2\} \tag{B.87}$$

$$\sum_{M=-J}^{J} |\vec{a}\cdot \vec{Y}_{JM}^{J-1}(\hat{n})|^2 = \frac{1}{8\pi}\{(J+1)|\vec{a}|^2 + (J-1)|\hat{n}\cdot\vec{a}|^2\} \tag{B.88}$$

$$\sum_{M=-J}^{J} (\vec{a}\cdot \vec{Y}_{JM}^{J+1}(\hat{n}))^* (\vec{a}\cdot \vec{Y}_{JM}^{J-1}(\hat{n})) = \frac{\sqrt{J(J+1)}}{8\pi}\{|\vec{a}|^2 - 3|\hat{n}\cdot\vec{a}|^2\} \tag{B.89}$$

as a consequence

$$\begin{aligned} \sigma_{\alpha,E} = \Big\{ &\sum_{TL\ell_\alpha}^{ele} \left| \sqrt{\tfrac{T}{2T+1}} \langle \phi_0 \| V_T^{T+1} \| \psi_{\alpha E\ell_\alpha}^{(-)\Gamma} \rangle + \sqrt{\tfrac{T+1}{2T+1}} \langle \phi_0 \| V_T^{T-1} \| \psi_{\alpha E\ell_\alpha}^{(-)\Gamma} \rangle \right|^2 + \\ &\sum_{TL\ell_\alpha}^{mag} \left| \langle \phi_0 \| V_T^{T} \| \psi_{\alpha E\ell_\alpha}^{(-)\Gamma} \rangle \right|^2 \Big\} \frac{\pi}{2\,c\,\omega_\gamma (2L_0+1)}. \end{aligned} \tag{B.90}$$

In an expansion of V_T^J in powers of k_γ, the leading, constant term is purely dipolar. The next term scales as k_γ^2 and contains electric dipole, magnetic dipole and electric quadrupole contributions:

$$\sigma \simeq \sigma^{(E1;00,00)} + 2\sigma^{(E1;00,20)} + 2\sigma^{(E1;00,01)} + \sigma^{(M1;10,10)} + \sigma^{(E2;10,10)} \tag{B.91}$$

where we have adopted the notation $\sigma^{(XT;J\nu,J'\nu')}$.

Electric dipole d lowest order $(T = 1, J = 0)$**:**

$$\sigma^{d}_{E,\alpha} = \frac{\pi}{3\,c\,\omega_\gamma(2L_0+1)} \sum_{L\ell_\alpha}^{ele} \left| \langle \phi_0 \| \hat{V}^0_1 \| \psi^{(-)\Gamma}_{\alpha E \ell_\alpha} \rangle \right|^2 . \tag{B.92}$$

Pure magnetic dipole m $(T = 1, J = 1)$**:**

$$\sigma^{m}_{E,\alpha} = \frac{\pi}{2\,c\,\omega_\gamma(2L_0+1)} \sum_{L\ell_\alpha}^{mag} \left| \langle \phi_0 \| \hat{V}^1_1 \| \psi^{(-)\Gamma}_{\alpha E \ell_\alpha} \rangle \right|^2 . \tag{B.93}$$

Pure electric quadrupole Q lowest order $(T = 2, J = 1)$**:**

$$\sigma^{Q}_{E,\alpha} = \frac{3\pi}{10\,c\,\omega_\gamma(2L_0+1)} \sum_{L\ell_\alpha}^{ele} \left| \langle \phi_0 \| \hat{V}^1_2 \| \psi^{(-)\Gamma}_{\alpha E \ell_\alpha} \rangle \right|^2 . \tag{B.94}$$

In the frequent case where ϕ_0 is an S^e state we can write:

$$\sigma^{d}_{E,\alpha} = \frac{\pi}{3\,c\,\omega_\gamma} \sum_{\ell} \left| \langle \phi_0 \| \hat{V}^0_1 \| \psi^{(-)P^o}_{\alpha E \ell} \rangle \right|^2 . \tag{B.95}$$

$$\sigma^{m}_{E,\alpha} = \frac{\pi}{2\,c\,\omega_\gamma} \sum_{\ell} \left| \langle \phi_0 \| \hat{V}^1_1 \| \psi^{(-)P^e}_{\alpha E \ell} \rangle \right|^2 . \tag{B.96}$$

$$\sigma^{Q}_{E,\alpha} = \frac{3\pi}{10\,c\,\omega_\gamma} \sum_{\ell} \left| \langle \phi_0 \| \hat{V}^1_2 \| \psi^{(-)D^e}_{\alpha E \ell} \rangle \right|^2 . \tag{B.97}$$

To conclude this section we observe that for two electron systems, the magnetic contribution to the photoionization cross section of an S state is identically zero.

B.8 Dipole anisotropy parameter β

In this section we will derive the angular distribution of photoelectrons in the specific case of lowest order dipole approximation, $T = T' = 1$, $J = J' = 0$:

$$\begin{aligned} \frac{\partial \sigma_{\alpha, E\hat{k}_e}}{\partial \Omega_{\hat{k}_e}} = {} & \frac{(2\pi)^2}{c\omega_\gamma} \sum_{\ell_e m_e} Y_{\ell_e m_e}(\hat{k}_e) \frac{1}{4\pi} \sum_{\tau\tau'} C^{1\tau}_{\ell_e m_e\, 1\tau'}\ \epsilon^{\tau} \epsilon^{\tau' *} \times \\ & \times \sum_{\ell_\alpha \ell'_\alpha} \sum_{LL'} \frac{\Pi_{\ell_\alpha \ell_e L L'}}{\sqrt{4\pi}(2L_0+1)\Pi_1} C^{\ell'_\alpha 0}_{\ell_\alpha 0\, \ell_e 0} \begin{Bmatrix} L' & \ell_e & L \\ \ell_\alpha & L_\alpha & \ell'_\alpha \end{Bmatrix} \begin{Bmatrix} 1 & \ell_e & 1 \\ L' & L_0 & L \end{Bmatrix} \times \\ & \times\ (-)^{L+L'+L_0+1+L_\alpha+\ell_\alpha} \langle \phi_0 \| V^0_1 \| \bar{\psi}^{(-)\Gamma}_{\alpha E \ell_\alpha} \rangle \cdot \langle \phi_0 \| V^0_1 \| \bar{\psi}^{(-)\Gamma'}_{\alpha E \ell'_\alpha} \rangle^* . \end{aligned} \tag{B.98}$$

First of all note that ℓ_α and ℓ'_α must have the same parity, so ℓ_e is restricted to the values 0 and 2. We will consider only linear and circular polarization with $\hat{z}$ as quantization axis. In all these cases τ can assume only one value and the only m_e term which survives is 0. The angular distribution is thus given by the superposition of a constant term ($\ell_e = 0$) and a d_{z^2} term[3]:

$$\frac{\partial \sigma^d_{E,\alpha,\hat{k}_e}}{\partial \Omega_{\hat{k}_e}} = \frac{\sigma^d_{E,\alpha}}{4\pi} \left\{ 1 + \beta_\alpha \cdot \frac{3\cos^2\theta - 1}{2} \right\} \tag{B.99}$$

where β is the celebrated dipole anisotropy factor. β can assume only values between +2 and -1, since differential cross section is positive by construction. The total cross sections measurements are usually made at the magic angle $\mathrm{atan}(\sqrt{2}) \simeq 54^o\,44'\,8''$ where the differential cross section coincides with the averaged total cross section, irrespective to the β value. Thanks to the fact that all polarization dependence is gathered in a common geometrical factor, the anisotropy parameters for circularly and linearly polarized light are proportional to each other:

$$\beta^{\circlearrowleft} = \beta^{\circlearrowright} = -\frac{1}{2}\,\beta^{\updownarrow}. \tag{B.100}$$

Of course the angular distribution of a photoelectron with $\beta = 2$ produced with linearly polarized light differs from that of a photoelectron with $\beta = -1$ produced with circularly polarized light. In the two cases the $\hat{z}$ axis differ, for with linearly polarized light the beam propagates on the xy plane since $\hat{k}_\gamma$ has to be orthogonal to $\hat{\epsilon}_\gamma$, while for circularly polarized light the field rotates on xy plane and $\vec{k}_\gamma$ is parallel to the quantization axis. The geometry for linear and circular polarizations are depicted in figures B.1 and B.2. Finally, for an unpolarized laser beam, β is exactly

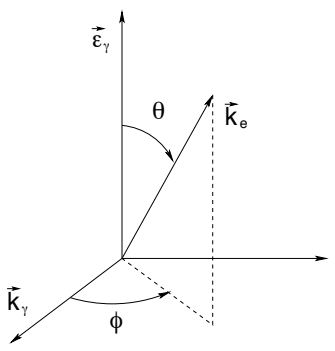

Figure B.1: Geometry of photoelectron angular distribution with linearly polarized light.

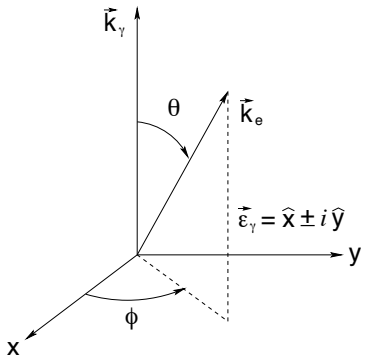

Figure B.2: Geometry of photoelectron angular distribution with circularly polarized light.

the same as in the case of circular polarization, since it's a statistic average of the

[3] $Y_{20}(\theta,\phi) = \sqrt{\frac{5}{4\pi}} \cdot \frac{3\cos^2\theta - 1}{2}$

two circular polarizations which are identical. It's an easy matter to demonstrate that the average of the two linear polarization angular distribution lead to the very same result.

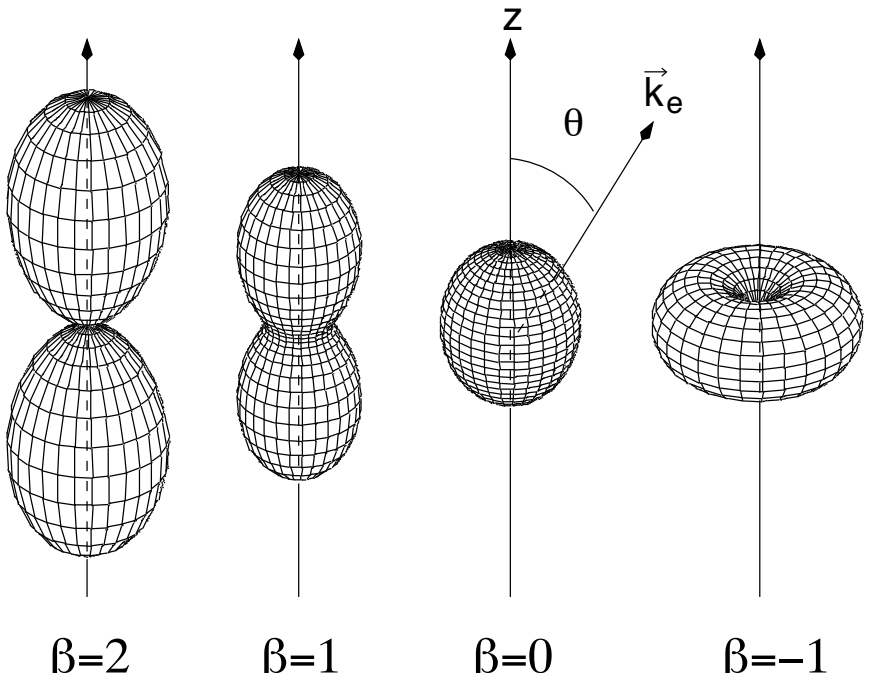

Figure B.3: Photoelectron angular distribution for different values of the dipole anisotropy parameter β. The arrows point parallel to the $\hat{z}$ axis.

The explicit form of β with linearly polarized laser is

$$\beta_\alpha^{\updownarrow} = \left\{ \sum_{LL'} \sum_{\ell_\alpha \ell'_\alpha} \sqrt{30}\Pi_{\ell_\alpha L L'} C^{\ell'_\alpha 0}_{\ell_\alpha 0\, 20} (-)^{L_\alpha+\ell_\alpha+L+L'+L_0} \begin{Bmatrix} L' & 2 & L \\ \ell_\alpha & L_\alpha & \ell'_\alpha \end{Bmatrix} \begin{Bmatrix} 1 & 2 & 1 \\ L' & L_0 & L \end{Bmatrix} \times \right.$$
$$\left. \times \langle \phi_0 \| \hat{V}_1^0 \| \bar{\psi}^{(-)\Gamma}_{\alpha E \ell_\alpha} \rangle \langle \phi_0 \| \hat{V}_1^0 \| \bar{\psi}^{(-)\Gamma'}_{\alpha E \ell'_\alpha} \rangle^* \right\} \Bigg/ \left\{ \sum_{L\ell_\alpha} \left| \langle \phi_0 \| \hat{V}_1^0 \| \psi^{(-)\Gamma}_{\alpha E \ell_\alpha} \rangle \right|^2 \right\} \quad \text{(B.101)}$$

the expression simplifies further if the photoionization of an S state is considered

$$\beta^{\updownarrow}_{\alpha \leftarrow S} = \frac{\sum_{\ell_\alpha \ell'_\alpha} \sqrt{30}\Pi_{\ell_\alpha} C^{\ell'_\alpha 0}_{\ell_\alpha 0\, 20} (-)^{L_\alpha+\ell_\alpha} \begin{Bmatrix} 1 & 2 & 1 \\ \ell_\alpha & L_\alpha & \ell'_\alpha \end{Bmatrix} \langle \phi_0 \| \hat{V}_1^0 \| \bar{\psi}^{(-)P}_{\alpha E \ell_\alpha} \rangle \langle \phi_0 \| \hat{V}_1^0 \| \bar{\psi}^{(-)P}_{\alpha E \ell'_\alpha} \rangle^*}{\sum_{\ell_\alpha} \left| \langle \phi_0 \| \hat{V}_1^0 \| \psi^{(-)P}_{\alpha E \ell_\alpha} \rangle \right|^2} \quad \text{(B.102)}$$

if the final state is an S target coupled to a p wave then we find the well known result $\beta^{\updownarrow} = 2$ and $\beta^{\circlearrowleft} = \beta^{\circlearrowright} = -1$. If a P parent ion is available, β has a structure due to interference between s and d outgoing spherical waves:

$$\beta_{P\leftarrow S} = \frac{|V_d|^2 - 2^{\frac{3}{2}} Re(V_s V_d^*)}{V_s^2 + V_d^2} \tag{B.103}$$

where we have defined $V_l \equiv \langle \phi_0 \| \hat{V}_1^0 \| \bar{\psi}_{\alpha E\ell}^{(-)P} \rangle$. When the target state has the exotic symmetry S^o, each parent ion state can be coupled to a single outgoing wave with the same angular momentum to give rise to a P^e state so the energy dependent matrix elements in the numerator and denominator of eq B.102 cancel with each other and an energy independent β factor results:

$$\beta = \sqrt{30}\Pi_\ell \, C^{\ell 0}_{\ell 0\, 20} \begin{Bmatrix} 1 & 2 & 1 \\ \ell & \ell & \ell \end{Bmatrix}. \tag{B.104}$$

Total cross section anisotropy parameter. The total differential cross section, where the parent ion state is arbitrary, is the sum of partial differential cross sections. It has the usual dipole angular dependence where the anisotropy factor is simply the weighted average of partial anisotropy factors:

$$\frac{\partial\sigma}{\partial\Omega} = \frac{\sigma}{4\pi}\Big(1 + \beta \cdot \frac{3\cos^2\theta - 1}{2}\Big), \qquad \beta = \sum_\alpha \frac{\sigma_\alpha}{\sigma}\beta_\alpha. \tag{B.105}$$

B.9 Beyond the dipole approximation

In dipole approximation the photoelectron angular distribution depends only on the angle between the electron momentum and the light polarization.
A macroscopic breakdown of the dipole approximation may be expected when the light wavelength is comparable to the target mean radius, for example with hard X-rays or with diffuse excited atomic states [140]. In other cases, nondipole corrections may not contribute significantly to the total cross section but may alter the photoelectron angular distribution through constructive and destructive interference with the dominant dipole amplitude. This effects must be taken in to account to properly interpret high precision measurements. Moreover, specific local feature like quadrupole and dipole resonances may cause significant departures from dipole approximation. When nondipole terms cannot be neglected, the cylindrical symmetry of the photoelectron angular distribution is broken and a dependence on the azimuthal angle is expected. In particular, when the lowest-order nondipole contribution to the differential cross section are taken into account, two nondipole anisotropy parameters arise:

$$\frac{\partial\sigma^{\updownarrow}}{\partial\Omega} = \frac{\sigma}{4\pi}\Big\{1 + \beta \cdot \frac{3\cos^2\theta - 1}{2} + (\delta + \gamma\cos^2\theta) \times \sin\theta\cos\phi\Big\} \tag{B.106}$$

$$\frac{\partial\sigma^{\circlearrowleft}}{\partial\Omega} = \frac{\sigma}{4\pi}\Big\{1 + \beta \cdot \frac{3\cos^2\theta - 1}{2} + (\delta + \gamma\cos^2\theta) \times \cos\theta\Big\} \tag{B.107}$$

The derivation of this result is somehow more lengthy than in dipole approximation but equally straightforward. The E1-E1 term is of course the same as before. We will consider only the lowest order contribution from the E1-E2 and E1-M1 interferences, since all other terms are of higher order in k_γ. For other derivations see Cooper [217–219] and Grum-Grzhimailo [220]

B.9.1 E1-E2

The geometric factor in eq (B.82) of the interference term between electric dipole and electric quadrupole ($T = 1$, $J = 0$, $T' = 2$, $J' = 1$ plus complex conjugate) is

$$\sum_{m_e} Y_{\ell_e m_e}(\hat{k}_e) \sum_{\tau\tau'} C^{1\tau}_{\ell_e m_e\, 2\tau'} \left[\vec{\epsilon}_\gamma \cdot \vec{Y}_1^{0\tau}(\hat{k}_\gamma)\right] \left[\vec{\epsilon}_\gamma \cdot Y_2^{1\tau'}(\hat{k}_\gamma)\right]^* \tag{B.108}$$

ℓ_e can only take on values 1 and 3, the value 2 being prohibited on ground of parity considerations (ℓ_α and ℓ'_α have to be of different parity because they are coupled to the same target state but give rise to two compound states reached from a same bound state by means of two transition operators of different parity).

Linear polarization For linear polarization (with reference to geometry in fig. B.1) (B.108) reduces to

$$\begin{aligned} \ell_e = 1 \quad &\Rightarrow \quad -\frac{3}{16\pi}\sqrt{\frac{3}{5\pi}}\,\sin\theta\,\cos\phi \\ \ell_e = 3 \quad &\Rightarrow \quad \frac{3}{16\pi}\sqrt{\frac{2}{5\pi}}\,(5\,\cos^2\theta\,-\,1)\,\sin\theta\,\cos\phi \end{aligned} \tag{B.109}$$

With linear polarization the interference term is thus:

$$\begin{aligned} \frac{\partial\sigma^{(E1-E2)\updownarrow}}{\partial\Omega} = &\frac{3}{8\sqrt{5}c\omega_\gamma}\frac{1}{2L_0+1}\cdot\sin\theta\cos\phi \quad \times \\ &\times \sum_{LL'}\sum_{\ell_\alpha\ell'_\alpha} \Pi_{\ell_\alpha LL'} \langle\phi_0\|\hat{V}_1^0\|\bar{\psi}^{(-)\Gamma}_{\alpha E\ell_\alpha}\rangle\langle\phi_0\|\hat{V}_2^1\|\bar{\psi}^{(-)\Gamma'}_{\alpha E\ell'_\alpha}\rangle^* (-)^{L_\alpha+\ell_\alpha+L+L'+L_o} \quad \times \\ &\times \left\{ -\sqrt{3}\,C^{\ell'_\alpha 0}_{\ell_\alpha 0\, 10} \begin{Bmatrix} L' & 1 & L \\ \ell_\alpha & L_\alpha & \ell'_\alpha \end{Bmatrix} \begin{Bmatrix} 1 & 1 & 2 \\ L' & L_o & L \end{Bmatrix} + \right. \\ &\left. + \sqrt{\frac{14}{3}}\,C^{\ell'_\alpha 0}_{\ell_\alpha 0\, 30} \begin{Bmatrix} L' & 3 & L \\ \ell_\alpha & L_\alpha & \ell'_\alpha \end{Bmatrix} \begin{Bmatrix} 1 & 3 & 2 \\ L' & L_o & L \end{Bmatrix} (5\cos^2\theta - 1) \right\}. \end{aligned} \tag{B.110}$$

So the general expressions for the nondipole anisotropy parameters are

$$\gamma_\alpha^{(E1-E2)\updownarrow} = \left\{ 3\sqrt{\frac{3\cdot 5\cdot 7}{2}} \sum_{LL'} \sum_{\ell_\alpha \ell'_\alpha} \Pi_{\ell_\alpha L L'} C^{\ell'_\alpha 0}_{\ell_\alpha 0\, 30} (-)^{L_\alpha+\ell_\alpha+L+L'+L_0} \times \right.$$
$$\left\{ \begin{matrix} L' & 3 & L \\ \ell_\alpha & L_\alpha & \ell'_\alpha \end{matrix} \right\} \left\{ \begin{matrix} 1 & 3 & 2 \\ L' & L_0 & L \end{matrix} \right\} \times$$
$$\left. \times \ \langle \phi_0 \| \hat{V}_1^0 \| \bar{\psi}^{(-)\Gamma}_{\alpha E \ell_\alpha} \rangle \langle \phi_0 \| \hat{V}_2^1 \| \bar{\psi}^{(-)\Gamma'}_{\alpha E \ell'_\alpha} \rangle^* \right\} \Bigg/ \left\{ \sum_{L\ell_\alpha} \left| \langle \phi_0 \| \hat{V}_1^0 \| \psi^{(-)\Gamma}_{\alpha E \ell_\alpha} \rangle \right|^2 \right\} + C.C. \quad \text{(B.111)}$$

$$\delta_\alpha^{(E1-E2)\updownarrow} = \left\{ -\frac{9}{\sqrt{5}} \sum_{LL'} \sum_{\ell_\alpha \ell'_\alpha} \Pi_{\ell_\alpha L L'} (-)^{L_\alpha+\ell_\alpha+L+L'+L_0} \times \right.$$
$$\langle \phi_0 \| \hat{V}_1^0 \| \bar{\psi}^{(-)\Gamma}_{\alpha E \ell_\alpha} \rangle \langle \phi_0 \| \hat{V}_2^1 \| \bar{\psi}^{(-)\Gamma'}_{\alpha E \ell'_\alpha} \rangle^* \times$$
$$\times \left[\sqrt{3}\, C^{\ell'_\alpha 0}_{\ell_\alpha 0\, 10} \left\{ \begin{matrix} L' & 1 & L \\ \ell_\alpha & L_\alpha & \ell'_\alpha \end{matrix} \right\} \left\{ \begin{matrix} 1 & 1 & 2 \\ L' & L_0 & L \end{matrix} \right\} + \right.$$
$$\left. \left. + \sqrt{\frac{14}{3}}\, C^{\ell'_\alpha 0}_{\ell_\alpha 0\, 30} \left\{ \begin{matrix} L' & 3 & L \\ \ell_\alpha & L_\alpha & \ell'_\alpha \end{matrix} \right\} \left\{ \begin{matrix} 1 & 3 & 2 \\ L' & L_0 & L \end{matrix} \right\} \right] \right\} \Bigg/$$
$$\Bigg/ \left\{ \sum_{L\ell_\alpha} \left| \langle \phi_0 \| \hat{V}_1^0 \| \psi^{(-)\Gamma}_{\alpha E \ell_\alpha} \rangle \right|^2 \right\} + C.C. \quad \text{(B.112)}$$

If L_0 is zero

$$\gamma_\alpha^{(E1-E2)\updownarrow} = \left\{ -3\sqrt{\frac{3\cdot 5\cdot 7}{2}} \sum_{\ell_\alpha \ell'_\alpha} \Pi_{\ell_\alpha}\, C^{\ell'_\alpha 0}_{\ell_\alpha 0\, 30} (-)^{L_\alpha+\ell_\alpha} \left\{ \begin{matrix} L' & 3 & L \\ \ell_\alpha & L_\alpha & \ell'_\alpha \end{matrix} \right\} \times \right.$$
$$\left. \times \ \langle \phi_0 \| \hat{V}_1^0 \| \bar{\psi}^{(-)\Gamma}_{\alpha E \ell_\alpha} \rangle \langle \phi_0 \| \hat{V}_2^1 \| \bar{\psi}^{(-)\Gamma'}_{\alpha E \ell'_\alpha} \rangle^* \right\} \Bigg/ \left\{ \sum_{\ell_\alpha} \left| \langle \phi_0 \| \hat{V}_1^0 \| \psi^{(-)\Gamma}_{\alpha E \ell_\alpha} \rangle \right|^2 \right\} + C.C. \quad \text{(B.113)}$$

$$\delta_\alpha^{(E1-E2)\updownarrow} = \left\{ \frac{9}{\sqrt{15}} \sum_{\ell_\alpha \ell'_\alpha} \Pi_{\ell_\alpha} (-)^{L_\alpha+\ell_\alpha} \langle \phi_0 \| \hat{V}_1^0 \| \bar{\psi}^{(-)\Gamma}_{\alpha E \ell_\alpha} \rangle \langle \phi_0 \| \hat{V}_2^1 \| \bar{\psi}^{(-)\Gamma'}_{\alpha E \ell'_\alpha} \rangle^* \times \right.$$
$$\times \left[3\, C^{\ell'_\alpha 0}_{\ell_\alpha 0\, 10} \left\{ \begin{matrix} L' & 1 & L \\ \ell_\alpha & L_\alpha & \ell'_\alpha \end{matrix} \right\} + \sqrt{14}\, C^{\ell'_\alpha 0}_{\ell_\alpha 0\, 30} \left\{ \begin{matrix} L' & 3 & L \\ \ell_\alpha & L_\alpha & \ell'_\alpha \end{matrix} \right\} \right] \left. \right\} \Bigg/$$
$$\Bigg/ \left\{ \sum_{\ell_\alpha} \left| \langle \phi_0 \| \hat{V}_1^0 \| \psi^{(-)\Gamma}_{\alpha E \ell_\alpha} \rangle \right|^2 \right\} + C.C. \quad \text{(B.114)}$$

Finally, if $L_\alpha = 0$ the only nonzero parameter is γ

$$\gamma_\alpha^{(E1-E2)\updownarrow} = -9\sqrt{2}\frac{Re\left(\langle\phi_0\|\hat{V}_1^0\|\bar{\psi}_{\alpha Ep}^{(-)P}\rangle\langle\phi_0\|\hat{V}_2^1\|\bar{\psi}_{\alpha Ed}^{(-)D}\rangle^*\right)}{\left|\langle\phi_0\|\hat{V}_1^0\|\psi_{\alpha Ep}^{(-)P}\rangle\right|^2} \tag{B.115}$$

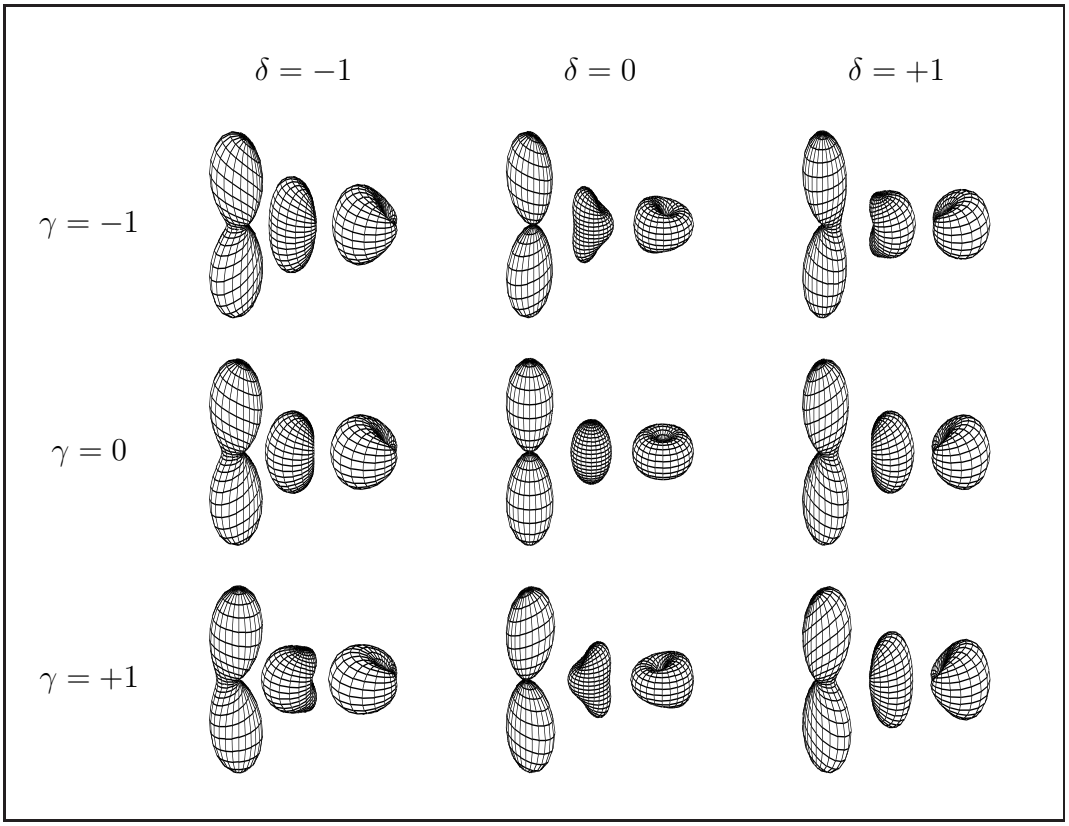

Figure B.4: Angular distribution with nondipole anisotropy with a linearly polarized laser beam.

Circular polarization for circular polarization (with reference to geometry in fig. B.2) (B.108) reduces to

$$\begin{aligned} \ell_e = 1 \quad &\Rightarrow \quad -\frac{3}{16\pi}\sqrt{\frac{3}{5\pi}}\cos\theta \\ \ell_e = 3 \quad &\Rightarrow \quad -\frac{3}{16\pi}\sqrt{\frac{1}{10\pi}}\,(5\,\cos^2\theta\,-\,3)\,\cos\theta. \end{aligned} \tag{B.116}$$

The interference term becomes

$$\frac{\partial\sigma^{(E1-E2)\circlearrowleft}}{\partial\Omega} = -\frac{\sqrt{3}}{8\sqrt{5}c\omega_\gamma}\frac{1}{2L_0+1}\cdot\cos\theta \quad \times$$
$$\times \sum_{LL'}\sum_{\ell_\alpha\ell'_\alpha}\Pi_{\ell_\alpha LL'}\langle\phi_0\|\hat{V}_1^0\|\bar{\psi}^{(-)\Gamma}_{\alpha E\ell_\alpha}\rangle\langle\phi_0\|\hat{V}_2^1\|\bar{\psi}^{(-)\Gamma'}_{\alpha E\ell'_\alpha}\rangle^*(-)^{L_\alpha+\ell_\alpha+L+L'+L_o} \quad \times$$
$$\times \left\{3\,C^{\ell'_\alpha 0}_{\ell_\alpha 0\,10}\begin{Bmatrix}L' & 1 & L\\ \ell_\alpha & L_\alpha & \ell'_\alpha\end{Bmatrix}\begin{Bmatrix}1 & 1 & 2\\ L' & L_o & L\end{Bmatrix}+\right.$$
$$\left.+\sqrt{\frac{7}{2}}\,C^{\ell'_\alpha 0}_{\ell_\alpha 0\,30}\begin{Bmatrix}L' & 3 & L\\ \ell_\alpha & L_\alpha & \ell'_\alpha\end{Bmatrix}\begin{Bmatrix}1 & 3 & 2\\ L' & L_o & L\end{Bmatrix}(5\cos^2\theta-3)\right\}+C.C. \tag{B.117}$$

So the general expressions for the nondipole anisotropy parameters are

$$\gamma_\alpha^{(E1-E2)\circlearrowleft} = \left\{-\frac{3}{2}\sqrt{\frac{3\cdot5\cdot7}{2}}\sum_{LL'}\sum_{\ell_\alpha\ell'_\alpha}\Pi_{\ell_\alpha LL'}\,C^{\ell'_\alpha 0}_{\ell_\alpha 0\,30}(-)^{L_\alpha+\ell_\alpha+L+L'+L_0}\times\right.$$
$$\begin{Bmatrix}L' & 3 & L\\ \ell_\alpha & L_\alpha & \ell'_\alpha\end{Bmatrix}\begin{Bmatrix}1 & 3 & 2\\ L' & L_0 & L\end{Bmatrix}\times$$
$$\left.\times\ \langle\phi_0\|\hat{V}_1^0\|\bar{\psi}^{(-)\Gamma}_{\alpha E\ell_\alpha}\rangle\langle\phi_0\|\hat{V}_2^1\|\bar{\psi}^{(-)\Gamma'}_{\alpha E\ell'_\alpha}\rangle^*\right\}\Bigg/\left\{\sum_{L\ell_\alpha}\left|\langle\phi_0\|\hat{V}_1^0\|\psi^{(-)\Gamma}_{\alpha E\ell_\alpha}\rangle\right|^2\right\}+C.C. \tag{B.118}$$

$$\delta_\alpha^{(E1-E2)\circlearrowleft} = \left\{-\frac{9}{2}\sqrt{\frac{3}{5}}\sum_{LL'}\sum_{\ell_\alpha\ell'_\alpha}\Pi_{\ell_\alpha LL'}(-)^{L_\alpha+\ell_\alpha+L+L'+L_0}\times\right.$$
$$\langle\phi_0\|\hat{V}_1^0\|\bar{\psi}^{(-)\Gamma}_{\alpha E\ell_\alpha}\rangle\langle\phi_0\|\hat{V}_2^1\|\bar{\psi}^{(-)\Gamma'}_{\alpha E\ell'_\alpha}\rangle^*\times$$
$$\times\left[C^{\ell'_\alpha 0}_{\ell_\alpha 0\,10}\begin{Bmatrix}L' & 1 & L\\ \ell_\alpha & L_\alpha & \ell'_\alpha\end{Bmatrix}\begin{Bmatrix}1 & 1 & 2\\ L' & L_0 & L\end{Bmatrix}-\right.$$
$$\left.\left.-\sqrt{\frac{7}{2}}\,C^{\ell'_\alpha 0}_{\ell_\alpha 0\,30}\begin{Bmatrix}L' & 3 & L\\ \ell_\alpha & L_\alpha & \ell'_\alpha\end{Bmatrix}\begin{Bmatrix}1 & 3 & 2\\ L' & L_0 & L\end{Bmatrix}\right]\right\}\Bigg/$$
$$\Bigg/\left\{\sum_{L\ell_\alpha}\left|\langle\phi_0\|\hat{V}_1^0\|\psi^{(-)\Gamma}_{\alpha E\ell_\alpha}\rangle\right|^2\right\}+C.C. \tag{B.119}$$

If $L_0 = 0$

$$\gamma_\alpha^{(E1-E2)\circlearrowleft} = \left\{\frac{3}{2}\sqrt{\frac{3\cdot5\cdot7}{2}}\sum_{\ell_\alpha\ell'_\alpha}\Pi_{\ell_\alpha}\,C^{\ell'_\alpha 0}_{\ell_\alpha 0\,30}(-)^{L_\alpha+\ell_\alpha}\begin{Bmatrix}2 & 3 & 1\\ \ell_\alpha & L_\alpha & \ell'_\alpha\end{Bmatrix}\times\right.$$
$$\left.\times\ \langle\phi_0\|\hat{V}_1^0\|\bar{\psi}^{(-)P}_{\alpha E\ell_\alpha}\rangle\langle\phi_0\|\hat{V}_2^1\|\bar{\psi}^{(-)D}_{\alpha E\ell'_\alpha}\rangle^*\right\}\Bigg/\left\{\sum_{\ell_\alpha}\left|\langle\phi_0\|\hat{V}_1^0\|\psi^{(-)P}_{\alpha E\ell_\alpha}\rangle\right|^2\right\}+C.C. \tag{B.120}$$

$$\delta_\alpha^{(E1-E2)\circlearrowleft} = \left\{ \frac{9}{2}\sqrt{\frac{3}{5}} \sum_{\ell_\alpha \ell'_\alpha} \Pi_{\ell_\alpha} (-)^{L_\alpha+\ell_\alpha} \langle \phi_0 \| \hat{V}_1^0 \| \bar{\psi}^{(-)P}_{\alpha E \ell_\alpha} \rangle \langle \phi_0 \| \hat{V}_2^1 \| \bar{\psi}^{(-)D}_{\alpha E \ell'_\alpha} \rangle^* \times \right.$$
$$\left. \times \left[C^{\ell'_\alpha 0}_{\ell_\alpha 0\, 10} \begin{Bmatrix} 2 & 1 & 1 \\ \ell_\alpha & L_\alpha & \ell'_\alpha \end{Bmatrix} - \sqrt{\frac{7}{2}}\, C^{\ell'_\alpha 0}_{\ell_\alpha 0\, 30} \begin{Bmatrix} 2 & 3 & 1 \\ \ell_\alpha & L_\alpha & \ell'_\alpha \end{Bmatrix} \right] \right\} \Bigg/$$
$$\Bigg/ \left\{ \sum_{\ell_\alpha} \left| \langle \phi_0 \| \hat{V}_1^0 \| \psi^{(-)P}_{\alpha E \ell_\alpha} \rangle \right|^2 \right\} + C.C. \quad \text{(B.121)}$$

Finally, if $L_\alpha = 0$

$$\delta_\alpha^{(E1-E2)\circlearrowleft} = -\frac{9}{2\sqrt{2}} \frac{\langle \phi_0 \| \hat{V}_2^1 \| \bar{\psi}^{(-)D}_{\alpha E \ell'_\alpha} \rangle}{\langle \phi_0 \| \hat{V}_1^0 \| \bar{\psi}^{(-)P}_{\alpha E \ell_\alpha} \rangle} + C.C. \quad \text{(B.122)}$$

$$\gamma_\alpha^{(E1-E2)\circlearrowleft} = +\frac{9}{2\sqrt{2}} \frac{\langle \phi_0 \| \hat{V}_2^1 \| \bar{\psi}^{(-)D}_{\alpha E \ell'_\alpha} \rangle}{\langle \phi_0 \| \hat{V}_1^0 \| \bar{\psi}^{(-)P}_{\alpha E \ell_\alpha} \rangle} + C.C. \quad \text{(B.123)}$$

(B.124)

That is, in this special case $\delta_\alpha^{\circlearrowleft}$ is the opposite of $\gamma_\alpha^{\circlearrowleft}$ and the angular distribution is:

$$\frac{\partial \sigma_\alpha^{\circlearrowleft}}{\partial \Omega} = \frac{\sigma}{4\pi} \left\{ 1 + \beta_\alpha^{\circlearrowleft} \cdot \frac{3\cos^2\theta - 1}{2} + \delta_\alpha^{\circlearrowleft} \sin^2\theta \cos\theta \right\} \quad \text{(B.125)}$$

which is exactly what we get if we take the average of two orthogonal linear polarization. In general, with unoriented targets the circular polarization gives rise to processes indistinguishable from those promoted by unpolarized light.

B.9.2 E1-M1

The geometric factor in eq (B.82) in this case is

$$\sum_{m_e} Y_{1 m_e}(\hat{k}_e) \sum_{\tau\tau'} C^{1\tau}_{1 m_e\, 1\tau'} \left[\vec{\epsilon} \cdot \vec{Y}_1^{0\tau}(\hat{k}_\gamma) \right] \left[\vec{\epsilon} \cdot Y_1^{1\tau'}(\hat{k}_\gamma) \right]^* \quad \text{(B.126)}$$

ℓ_e can take on only the value 1. Eq (B.126) for linear and circular polarization reduces to

$$\updownarrow \;\rightarrow\; \frac{3}{16\pi\sqrt{\pi}} \sin\theta\cos\phi \quad \text{(B.127)}$$

$$\circlearrowleft \;\rightarrow\; \frac{3}{16\pi\sqrt{\pi}} \cos\theta \quad \text{(B.128)}$$

This means that $\gamma^{(E1-M1)}$ is always zero while $\delta^{(E1-M1)}$ is the same in the two polarizations. The interference term is

$$\frac{\partial\sigma^{(E1-M1)}}{\partial\Omega} = -\frac{3}{4c\omega_\gamma}\frac{1}{2L_0+1}\cdot\sin\theta\cos\phi\sum_{LL'}\sum_{\ell_\alpha\ell'_\alpha}\Pi_{\ell_\alpha LL'}C^{\ell'_\alpha 0}_{\ell_\alpha 0\,10}\begin{Bmatrix}L' & 1 & L\\ \ell_\alpha & L_\alpha & \ell'_\alpha\end{Bmatrix}\begin{Bmatrix}1 & 1 & 1\\ L' & L_o & L\end{Bmatrix}\times$$
$$\times(-)^{L_\alpha+\ell_\alpha+L+L'+L_o}Re\left(\langle\phi_0\|\hat{V}^0_1\|\bar{\psi}^{(-)\Gamma}_{\alpha E\ell_\alpha}\rangle\langle\phi_0\|\hat{V}^1_1\|\bar{\psi}^{(-)\Gamma'}_{\alpha E\ell'_\alpha}\rangle^*\right) \tag{B.129}$$

and

$$\delta^{(E1-M1)}_\alpha = \left\{-9\sum_{LL'}\sum_{\ell_\alpha\ell'_\alpha}\Pi_{\ell_\alpha LL'}\,C^{\ell'_\alpha 0}_{\ell_\alpha 0\,10}(-)^{L_\alpha+\ell_\alpha+L+L'+L_0}\begin{Bmatrix}L' & 1 & L\\ \ell_\alpha & L_\alpha & \ell'_\alpha\end{Bmatrix}\begin{Bmatrix}1 & 1 & 1\\ L' & L_0 & L\end{Bmatrix}\times\right.$$
$$\left.\times\ Re\left(\langle\phi_0\|\hat{V}^0_1\|\bar{\psi}^{(-)\Gamma}_{\alpha E\ell_\alpha}\rangle\langle\phi_0\|\hat{V}^1_1\|\bar{\psi}^{(-)\Gamma'}_{\alpha E\ell'_\alpha}\rangle^*\right)\right\}\Bigg/\left\{\sum_{L\ell_\alpha}\left|\langle\phi_0\|\hat{V}^0_1\|\psi^{(-)\Gamma}_{\alpha E\ell_\alpha}\rangle\right|^2\right\} \tag{B.130}$$

If $L_0 = 0$

$$\delta^{(E1-M1)}_\alpha = \left\{9\sum_{\ell_\alpha\ell'_\alpha}\Pi_{\ell_\alpha}\,C^{\ell'_\alpha 0}_{\ell_\alpha 0\,10}(-)^{L_\alpha+\ell_\alpha}\begin{Bmatrix}1 & 1 & 1\\ \ell_\alpha & L_\alpha & \ell'_\alpha\end{Bmatrix}\times\right.$$
$$\left.\times\ Re\left(\langle\phi_0\|\hat{V}^0_1\|\bar{\psi}^{(-)\Gamma}_{\alpha E\ell_\alpha}\rangle\langle\phi_0\|\hat{V}^1_1\|\bar{\psi}^{(-)\Gamma'}_{\alpha E\ell'_\alpha}\rangle^*\right)\right\}\Bigg/\left\{\sum_{L\ell_\alpha}\left|\langle\phi_0\|\hat{V}^0_1\|\psi^{(-)\Gamma}_{\alpha E\ell_\alpha}\rangle\right|^2\right\} \tag{B.131}$$

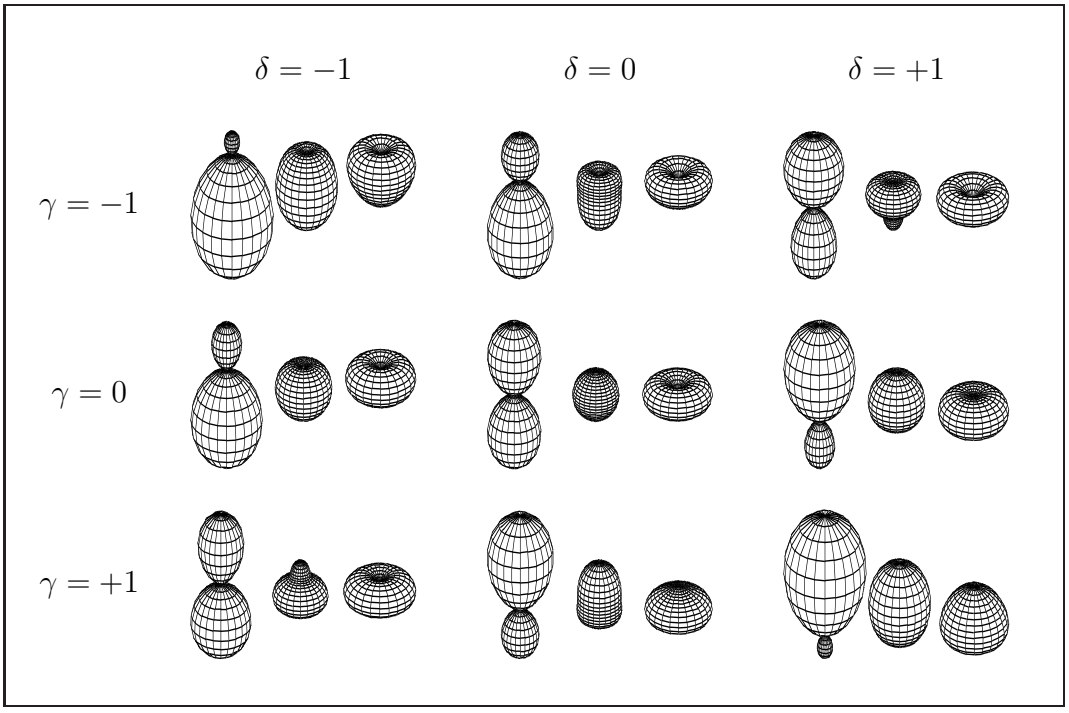

Figure B.5: Angular distribution with nondipole anisotropy with a circularly polarized laser beam.

B.10 Radiative decay

The spontaneous transition rate of an excited level with the emission of one photon irrespective to emission direction and polarization is given by the contribution of both discrete and continuum final states:

$$\Gamma_0 = \sum_i \Gamma_{i\leftarrow 0} + \sum_\alpha \int_{E_\alpha}^{E_0} dE \; \frac{d\Gamma_{\alpha\leftarrow 0}}{dE} \tag{B.132}$$

where, in our notations

$$\Gamma_{i\leftarrow 0} = \frac{\omega_{0,i}}{3\pi\hbar c^3} \; \frac{1}{2L_0+1} \; |\langle\phi_0\|\hat{V}_1^0\|\phi_i\rangle|^2 \tag{B.133}$$

$$\frac{d\Gamma_{\alpha\leftarrow 0}}{dE} = \frac{\omega}{3\hbar c^3} \; \frac{1}{2L_0+1} \; \sum_{L\ell_\alpha}^{ele} \left|\langle\phi_0\|\hat{V}_1^0\|\psi_{\alpha E\ell_\alpha}^{(-)\Gamma}\rangle\right|^2 \tag{B.134}$$

The radiative decay to the continuum may be enhanced by the presence of a resonance. This picture is schematically represented in figure B.6

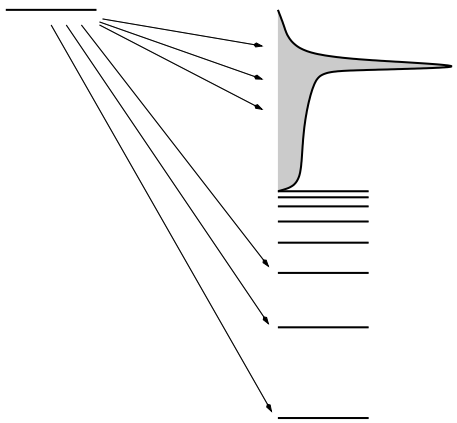

Figure B.6: Radiative decay of a discrete state to both discrete and scattering final states.

The spontaneous radiative decay rate in dipole approximation of an excited state to a final state with the emission of a single photon with arbitrary direction and polarization is easily derived as

$$\mathcal{W} = \frac{4\omega}{3c^3}|\langle B|\sum_i \vec{p}_i|A\rangle|^2 \tag{B.135}$$

B.11 Radiative transitions in the continuum

The treatment of simultaneous autoionization-fluorescence channels is problematic in a non perturbative approach. In the present section the lowest order perturbative

approach will therefore be followed. It is not uncommon that doubly excited states live so long that they can decay radiatively to other doubly excited states. When the initial doubly excited state is created in a photoionization experiment, we are dealing with a two photon process, for which the transition rate is given by

$$\mathcal{W} = 2\pi\delta(E+\omega-E_0-\omega_0)\left|\langle\psi^-_{\alpha E}\otimes\omega|VG_0^+(E_0+\omega_0)V|\phi_0\otimes\omega_0\rangle\right|^2 \tag{B.136}$$

The G_0^+ can be expanded on a complete set of intermediate states:

$$G_0^+(E) = \sum_{\Gamma'}\sum_{\gamma}\sum\!\!\!\!\!\!\int d\epsilon \frac{|\psi^{\Gamma'}_{\gamma\epsilon}\rangle\langle\psi^{\Gamma'}_{\gamma\epsilon}|}{E-\epsilon+i0^+} \tag{B.137}$$

(the asymptotic condition obeyed by the wavefunctions in the expansion is irrelevant). If we divide (B.136) by the incident photon flux and assume the unbounded domain in cartesian coordinates scheme with $\delta(\omega-\omega')$ normalization for the emitted photon, we obtain the following cross section

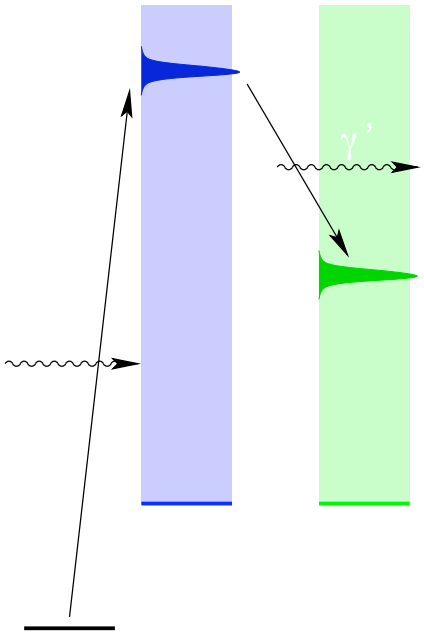

Figure B.7: Radiative decay between doubly excited states

$$\frac{d\sigma_{\Gamma\alpha\omega\leftarrow\phi_0\omega_0}}{d\omega_0 d\omega d\hat{\Omega}} = \alpha^4\frac{\omega}{\omega_0}\left|\sum_{\Gamma'\gamma}\sum\!\!\!\!\!\!\int d\epsilon \frac{\langle\psi^{\Gamma-}_{\alpha E_0+\omega_0-\omega}|\hat{\epsilon}^*_{\hat{k}\lambda}\cdot\vec{P}|\psi^{\Gamma'-}_{\gamma\epsilon}\rangle\langle\psi^{\Gamma'-}_{\gamma\epsilon}|\hat{\epsilon}_{\hat{k}_0\lambda_0}\cdot\vec{P}|\phi_0\rangle}{E_0+\omega_0-\epsilon+i0^+}\right|^2 \tag{B.138}$$

For an accurate evaluation of the two photon transition amplitude, the pole contribution must be considered separately from that of the principal part [221]. The

cross section can be averaged over the initial and summed over the final atomic polarizations if these are not measured in the experiment. To this purpose we can separate kinematics and dynamics as usual

$$\langle \psi^{\Gamma-}_{\alpha E_0+\omega_0-\omega} | \hat{\epsilon}^*_{\hat{k}\lambda} \cdot \vec{P} | \psi^{\Gamma'-}_{\gamma\epsilon} \rangle = \langle \psi^{\Gamma-}_{\alpha E_0+\omega_0-\omega} \| P_1 \| \psi^{\Gamma'-}_{\gamma\epsilon} \rangle \sum_{\mu} \frac{C^{LM}_{L'M'\,1\mu}}{\sqrt{2L+1}} \epsilon^{*\mu}_{\hat{k}\lambda} \quad \text{(B.139)}$$

$$\langle \psi^{\Gamma'-}_{\gamma\epsilon} | \hat{\epsilon}_{\hat{k}_0\lambda_0} \cdot \vec{P} | \phi_0 \rangle = \langle \psi^{\Gamma'-}_{\gamma\epsilon} \| P_1 \| \phi_0 \rangle \sum_{\mu_0} \frac{C^{L'M'}_{L_0M_0\,1\mu_0}}{\sqrt{2L'+1}} \epsilon^{\mu_0}_{\hat{k}_0\lambda_0} \quad \text{(B.140)}$$

The overall averaged expression can be written as a sum of terms, each having a geometric factor of the following form

$$\Pi^{-1}_{LLL'L''} \sum_{\substack{M_0MM'M'' \\ \mu\mu'\mu_0\mu'_0}} C^{LM}_{L'M'\,1\mu} C^{L'M'}_{L_0M_0\,1\mu_0} C^{LM}_{L''M''\,1\mu'} C^{L''M''}_{L'M''\,1\mu'_0} \epsilon^{\mu_0}_{\hat{k}_0\lambda_0} \epsilon^{\mu'_0 *}_{\hat{k}_0\lambda_0} \epsilon^{\mu *}_{\hat{k}\lambda} \epsilon^{\mu'}_{\hat{k}\lambda} \quad \text{(B.141)}$$

contraction of repeated Clebsh Gordan indexes can be performed with the help of graphical rules (see appendix G):

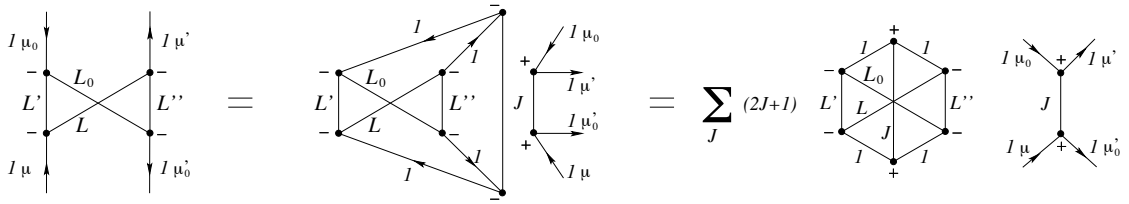

or, in algebraic terms

$$\sum_J \frac{2J+1}{3} \begin{Bmatrix} J & 1 & 1 \\ 1 & L_0 & L'' \\ 1 & L' & L \end{Bmatrix} \sum_{\nu} C^{1\mu_0}_{1\mu' J\nu} C^{1\mu'_0}_{1\mu J\nu} \quad \text{(B.142)}$$

We are left with the following contraction over magnetic quantum numbers which depends on the polarization of the two involved photons

$$\sum_{\nu\mu\mu'\mu_0\mu'_0} C^{1\mu_0}_{1\mu' J\nu} C^{1\mu'_0}_{1\mu J\nu} \epsilon^{\mu_0}_{\hat{k}_0\lambda_0} \epsilon^{\mu'_0 *}_{\hat{k}_0\lambda_0} \epsilon^{\mu *}_{\hat{k}\lambda} \epsilon^{\mu'}_{\hat{k}\lambda} \quad \text{(B.143)}$$

We shall consider the case of a linearly polarized incident light along the quantization axis $\hat{z}$: $\epsilon^{\mu_0}_{\hat{k}_0\lambda_0} = \delta_{\mu_0 0}$. In this case the expression (B.143) reduces to

$$F^{\lambda}_J \equiv \sum_{\mu} |C^{10}_{1\mu\, J-\mu} \epsilon^{\mu}_{\hat{k}\lambda}|^2, \qquad J = 0, 1, 2 \quad \text{(B.144)}$$

J runs over 0, 1 and 2 only, therefore the summation can easily be performed explicitly. The two possible polarization that are interesting in this arrangement are that orthogonal to the incident photon polarization, indicated with $\hat{\epsilon}_\perp$ and $\hat{\epsilon}_\theta \equiv \hat{k} \times \hat{\epsilon}_\perp$, as reported in figure B.11

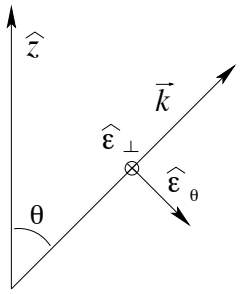

$\hat{\epsilon}_\perp$ and $\hat{\epsilon}_\theta$ (often indicated as $\hat{e}_\phi$ and $\hat{e}_\theta$) have the following expressions in terms of the spherical versors $\hat{e}_\mu$ (see [216] pag. 8 eq. 34)

$$\begin{aligned} \hat{\epsilon}_\perp &= \frac{i}{\sqrt{2}} \left(e^{i\phi}\, \hat{e}_{-1} + e^{-i\phi}\, \hat{e}_{+1} \right) \\ \hat{\epsilon}_\theta &= -\sin\theta\, \hat{e}_0 + \frac{\cos\theta}{\sqrt{2}} \left(e^{i\phi}\, \hat{e}_{-1} - e^{-i\phi}\, \hat{e}_{+1} \right) \end{aligned}$$

where

$$\hat{e}_{-1} = \frac{1}{\sqrt{2}} (\hat{e}_x - i\hat{e}_y), \qquad \hat{e}_0 = \hat{e}_z, \qquad \hat{e}_{+1} = -\frac{1}{\sqrt{2}} (\hat{e}_x + i\hat{e}_y) \tag{B.145}$$

The sum in B.144 with $\lambda = \perp, \theta$ is readily done and the result is

$$F_0^\perp = 0, \qquad F_1^\perp = \frac{1}{2}, \qquad F_2^\perp = \frac{3}{10}$$

$$F_0^\theta = \sin^2\theta, \qquad F_1^\theta = \frac{1 - \sin^2\theta}{2}, \qquad F_2^\theta = \frac{3 + \sin^2\theta}{10}$$

We define $M^{\Gamma'}_{\Gamma\alpha,\Gamma_0\phi_0}(\omega_0, \omega)$ as

$$M^{\Gamma'}_{\Gamma\alpha,\Gamma_0\phi_0}(\omega_0, \omega) = \alpha^2 \sqrt{\frac{\omega}{\omega_0}} \sum_\gamma \sum\!\!\!\!\!\!\int d\epsilon \frac{\langle \psi^{\Gamma-}_{\alpha E_0+\omega_0-\omega} \| P_1 \| \psi^{\Gamma'-}_{\gamma\epsilon} \rangle \langle \psi^{\Gamma'-}_{\gamma\epsilon} \| P_1 \| \phi_0 \rangle}{E_0 + \omega_0 - \epsilon + i0^+} \tag{B.146}$$

The complete expression for the cross section is then

$$\frac{d\sigma_{\Gamma\alpha\omega\leftarrow\phi_0\omega_0}}{d\omega_0 d\omega d\Omega} = \sum_{\Gamma'\Gamma''} M^{\Gamma'}_{\Gamma\alpha,\Gamma_0\phi_0}(\omega_0,\omega) M^{\Gamma''*}_{\Gamma\alpha,\Gamma_0\phi_0}(\omega_0,\omega) \times \tag{B.147}$$

$$\times \sum_J \frac{(2J+1)}{3(2L_0+1)} \begin{Bmatrix} J & 1 & 1 \\ 1 & L_0 & L'' \\ 1 & L' & L \end{Bmatrix} F_J^\lambda \tag{B.148}$$

When the initial state has $L_0 = 0$, this expression gets much simpler. Indeed

$$\begin{Bmatrix} J & 1 & 1 \\ 1 & 0 & L'' \\ 1 & L' & L \end{Bmatrix} = \delta_{L'1}\delta_{L''1}\frac{1}{3}\begin{Bmatrix} J & 1 & 1 \\ L & 1 & 1 \end{Bmatrix} \tag{B.149}$$

therefore we can write

$$\frac{d\sigma_{\Gamma\alpha\omega\leftarrow\phi_0\omega_0}}{d\omega_0 d\omega d\Omega} = |M_{\Gamma\alpha,\Gamma_0\phi_0}(\omega_0,\omega)|^2 \sum_J \frac{2J+1}{9}\begin{Bmatrix} J & 1 & 1 \\ L & 1 & 1 \end{Bmatrix} F_J^\lambda \tag{B.150}$$

The geometric term

$$\sum_J \frac{2J+1}{9}\begin{Bmatrix} J & 1 & 1 \\ L & 1 & 1 \end{Bmatrix} F_J^\lambda$$

can be summed up explicitly for the three allowed final angular momenta and for the two polarizations θ and $\perp$

	$L=0$	$L=1$	$L=2$
θ	$\frac{2}{27}\sin^2\theta$	$\frac{1}{18}\cos^2\theta$	$\frac{1}{90}(3+\sin^2\theta)$
$\perp$	0	$\frac{1}{18}$	$\frac{1}{30}$

It is to be noted that for each final angular momentum the two intensities with different polarization converge to the same value, as they should since for $\theta = 0$ the two polarizations are actually indistinguishable. Secondly, because of the averaging process, the emitted light has no polarization coherence, it is therefore no surprise that non vanishing intensities for any polarization can be detected. What we actually measure if we do not look at the final atomic state is the total cross section $d\sigma_{\omega\leftarrow\phi_0\omega_0}/d\omega_0 d\omega d\Omega$ due to all the possible final symmetries Γ and channels α

$$\frac{d\sigma_{\omega\leftarrow\phi_0\omega_0}}{d\omega_0 d\omega d\Omega} = \sum_\Gamma \frac{\sigma_{\Gamma\omega\leftarrow\phi_0\omega_0}}{d\omega_0 d\omega d\Omega}, \quad \text{where} \quad \frac{d\sigma_{\Gamma\omega\leftarrow\phi_0\omega_0}}{d\omega_0 d\omega d\Omega} = \sum_\alpha \frac{d\sigma_{\Gamma\alpha\omega\leftarrow\phi_0\omega_0}}{d\omega_0 d\omega d\Omega} \tag{B.151}$$

Hopefully we can extract the contributions from the three final angular momenta by simply measuring the total cross sections at $\theta = 0$ and at $\theta = \pi$ in the two polarization:

$$\sum_{\alpha} |M_{S\alpha,S\phi_0}(\omega_0,\omega)|^2 = -\frac{18}{11}\sigma(0) + \frac{27}{2}\sigma_\theta(\pi) + \frac{18}{11}\sigma_\perp(\pi) \quad \text{(B.152)}$$

$$\sum_{\alpha} |M_{P\alpha,S\phi_0}(\omega_0,\omega)|^2 = \frac{180}{11}\sigma(0) + \frac{18}{11}\sigma_\perp(\pi) \quad \text{(B.153)}$$

$$\sum_{\alpha} |M_{D\alpha,S\phi_0}(\omega_0,\omega)|^2 = \frac{30}{11}\sigma(0) - \frac{30}{11}\sigma_\perp(\pi) \quad \text{(B.154)}$$

B.12 Gauges

The transition matrix elements in dipole approximation can be computed in either of three difference gauges: length, velocity and acceleration. Since

$$[\,H,\vec{r}\,] = -i\vec{p} \quad \text{and} \quad [\,H,\vec{p}\,] = iZ\frac{\vec{r}}{r^3} \quad \text{(B.155)}$$

the matrix elements of $\vec{p}$, $\vec{r}$ and $\vec{r}/r^3$ between eigenstates of the hamiltonian are interrelated through the following identities

$$(E-E')\langle\psi\|R_1\|\psi'\rangle = -i\langle\psi\|P_1\|\psi'\rangle = \langle\psi\|A_1\|\psi'\rangle/(E-E') \quad \text{(B.156)}$$

where

$$\vec{R} = \sum_i \vec{r}_i \quad \vec{P} = \sum_i \vec{p}_i \quad \vec{A} = Z\sum_i \frac{\vec{r}_i}{r_i^3} \quad \text{(B.157)}$$

The identity B.156 is not satisfied for approximate eigenfunctions of the hamiltonian. As the three operators weight the wavefunctions in radically different ways, a best choice can be done in order to obtain the most reliable results. The acceleration gauge has usually great disadvantages over the first two, since it is exceptionally demanding near the nucleus, where the wave functions are highly correlated. For good results, large orbital angular momenta are required, even if length or velocity would give good results with much less correlated wavefunctions. When good acceleration matrix elements can nevertheless be obtained, like in helium, the radiative transitions between continuum states are well defined and regular at the outset, and this is an immense advantage over the other two gauges.

In our experience, the velocity gauge gives the most reliable matrix elements. It generally works when either acceleration or length gauges fail. Moreover it can be regularized straightforwardly to deal with radiative transitions in the continuum, in those cases where accurate wavefunctions are not available and the acceleration gauge yield inaccurate results. The regularization consists simply in computing the transition radial matrix elements up to a certain distance R_2 where the wavefunctions have reached their asymptotic behaviour:

$$\phi_l(r) \sim \cos(\delta) f_l(kr) + \sin(\delta) g_l(kr), \quad r \geq R_2 \quad \text{(B.158)}$$

$$\phi_{l'}(r) \sim \cos(\delta') f_{l'}(k'r) + \sin(\delta') g_{l'}(kr). \quad \text{(B.159)}$$

where f_l and g_l are respectively the regular and irregular radial solutions with angular momentum l pertinent to the problem. The integrand between regular and irregular Bessel functions in a semi-infinite domain can be regularized and integrated analytically

$$I_{11}(k,k',l,l';R_2) = \lim_{\lambda\to 0^+}\int_{R_2}^{\infty} f_l(kr)\frac{d}{dr}f_{l'}(k'r)e^{-\lambda r}r^2dr \quad \text{(B.160)}$$

$$I_{12}(k,k',l,l';R_2) = \lim_{\lambda\to 0^+}\int_{R_2}^{\infty} f_l(kr)\frac{d}{dr}g_{l'}(k'r)e^{-\lambda r}r^2dr \quad \text{(B.161)}$$

$$I_{21}(k,k',l,l';R_2) = \lim_{\lambda\to 0^+}\int_{R_2}^{\infty} g_l(kr)\frac{d}{dr}f_{l'}(k'r)e^{-\lambda r}r^2dr \quad \text{(B.162)}$$

$$I_{22}(k,k',l,l';R_2) = \lim_{\lambda\to 0^+}\int_{R_2}^{\infty} g_l(kr)\frac{d}{dr}g_{l'}(k'r)e^{-\lambda r}r^2dr \quad \text{(B.163)}$$

The correction to the integral computed on the $[0, R_2]$ interval is therefore of the form

$$\begin{bmatrix} \cos\delta & \sin\delta \end{bmatrix} \begin{bmatrix} I_{11}(k,k',l,l';R_2) & I_{12}(k,k',l,l';R_2) \\ I_{21}(k,k',l,l';R_2) & I_{22}(k,k',l,l';R_2) \end{bmatrix} \begin{bmatrix} \cos\delta' \\ \sin\delta' \end{bmatrix} \quad \text{(B.164)}$$

Nikolopoulos addressed the problem of transition matrix elements between states in the continuum in a recent paper, where he shows that a "surface contribution" can be computed in all the three gauges [222].

The length gauge is almost always as good as the velocity gauge, but it displays extremely bad behaviours for particular transitions when the wavefunctions are computed with the multiple B-spline K-matrix method: those between highly excited Rydberg states and continuum wave functions. In such cases, the bound states reaches beyond the radius where the oscillating part of the continuum wave function is dumped. Since the length gauge greatly emphasizes that region, a very bad agreement with the other two gauges is found, except near resonances, where the continuum is dominated again by a well represented far-reaching autoionizing Rydberg satellite. We insist that in these cases the velocity and acceleration gauges are in very good agreement. This problem is therefore characteristic of length gauge only.

Appendix C

B-Splines

B-splines were conceived by Isaac Jacob Schoenberg (1903-1990) during the second world war [223,224], but it was only after the publication of deBoor's book [82] that B-splines begun to be extensively adopted by the atomic and molecular community.

In this chapter we survey the definition and main properties of B-splines. We also present some original results and applications pertinent to this thesis. Specifically, a detailed characterization of the B-spline property known as *effective completeness*, and a closer look to SCF energy convergence on fully optimized sets of knots.

C.1 Definition and basic properties

The splines are defined as piecewise polynomials of order k (maximum degree $k-1$), $\mathcal{C}^\infty$ everywhere, except at a fixed set of knots $\{t_i\}$ where they are at least $\mathcal{C}^{k_i-2}$, with $k \geq k_i \geq 1$. $\nu_i = k - k_i + 1$ is called the knot multiplicity because the same spline basis can be obtained from a basis with $\sum_i \nu_i$ maximally regular knots in the limit where sets of ν_i contiguous knots coalesce to i-th knots. In other terms the spline space is specified by an order k and a non-decreasing set of knots. The total dimension of spline space is $n + k$, but if we specialize to the subset which is zero below the lowest and above the highest knots we are left with a space of dimension $n - k$. As a consequence every spline extends at least over k adjacent intervals ($k+1$ consecutive knots, when counted with their multiplicity). The $n-k$ independent splines restricted to k intervals, clearly a basis of the spline space, are commonly called B-splines.

$B_i^k(x)$, the i-th B-spline of order k, which extends from the knot t_i to the knot t_{i+k}, is defined iteratively, according to deBoor [82], as follows:

$$B_i^1(x) = \theta(x - t_i) \cdot \theta(t_{i+1} - x) \tag{C.1}$$

$$B_i^k(x) = \frac{x - t_i}{t_{i+k-1} - t_i} B_i^{k-1}(x) + \frac{t_{i+k} - x}{t_{i+k} - t_{i+1}} B_{i+1}^{k-1}(x). \tag{C.2}$$

In figure C.1, the iterative generation of B-splines on a uniform grid with 6 knots (the first and last knots are maximally degenerate) up to fifth order is shown. In

the following, unless otherwise stated, we shall refer to standard set of knots where the first and last breakpoints are maximally degenerate while the other are non degenerate:

$$t_1 = t_2 = \ldots = t_k \leq t_{k+1} \leq \ldots \leq t_{n-k} \leq t_{n-k+1} = t_{n-k+2} = \ldots = t_n$$

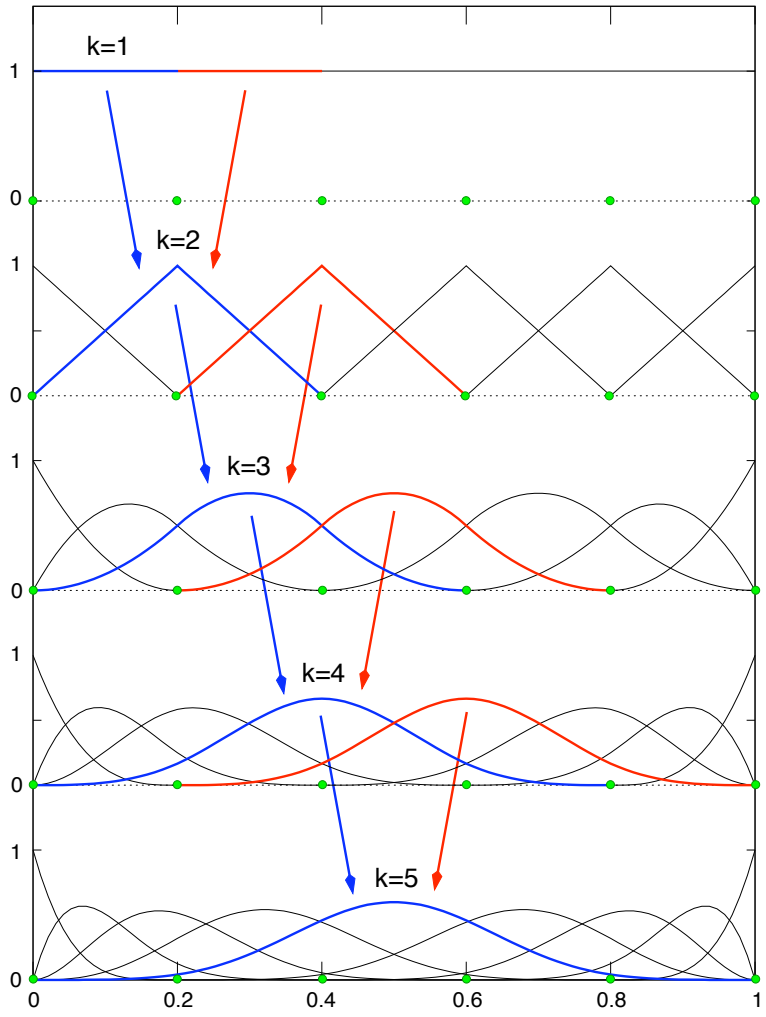

Figure C.1: Iterative generation of B-splines.

B-splines are invariant upon affine transformations: that is, if

$$\text{if} \quad x \to x' = a\,x + b, \quad t_i \to t'_i = a\,t_i + b \quad \text{then} \quad B_i^{k\prime}(x') = B_i^k(x). \tag{C.3}$$

This property is proven easily by induction from the iterative definition C.1 C.2:

$$\begin{aligned} B_i^{1\prime}(x') &= \theta(x' - t'_i) \cdot \theta(t'_{i+1} - x') = & \text{(C.4)} \\ &= \theta(a\,x - a\,t_i) \cdot \theta(a\,t_{i+1} - a\,x) = & \text{(C.5)} \\ &= \theta(x - t_i) \cdot \theta(t_{i+1} - x) = B_i^1(x); & \text{(C.6)} \end{aligned}$$

moreover the rational factors in C.2 are manifestly invariant upon affine transformations, so the thesis follows immediately. If an operator kernel has well defined scaling properties upon affine transformations:

$$o(x,y) \to o(x',y') = f(a,b)o(x,y) \tag{C.7}$$

so is for the matrix elements of the corresponding operator:

$$\begin{aligned} \langle B'_i|\mathcal{O}|B'_j\rangle &= \int dx'dy' B'_i(x')o(x',y')B'_j(y') && \text{(C.8)} \\ &= a^2 f(a,b)\int dxdy B_i(x)o(x,y)B_j(y) = && \text{(C.9)} \\ &= a^2 f(a,b)\langle B_i|\mathcal{O}|B_j\rangle && \text{(C.10)} \end{aligned}$$

For the identity operator, in particular, $f(a,b) = 1/a$ ($o(x,y) = \delta(x-y)$) and

$$\langle B'_i|B'_j\rangle = a\langle B_i|B_j\rangle \tag{C.11}$$

It is useful therefore to define the L^2-normalized B-splines as

$$\bar{B}_i(x) \equiv B_i(x)/\sqrt{\langle B_i|B_i\rangle} \tag{C.12}$$

The superposition matrix between L^2 normalized B-splines is itself invariant upon affine transformations. As a consequence, since B-splines are defined locally (that is a B-splines depends on the positions of knots within its support only), the superposition matrix for a grid with a smoothly changing knot spacing is "almost the same" as that for an evenly spaced set of knots. The exact meaning of this statement will be precised later in this appendix. To avoid a cumbersome notation, we shall everywhere omit the bar and assume that all the B-splines are L^2-normalized unless otherwise stated.

The advantages of B-splines are manifold [92]. Since the support D_i of the i-th B-spline is formed by k consecutive intervals, the integrals between two B-splines and a local operator are zero unless their indices differ less than the order k:

$$\langle B_i|O|B_j\rangle = \int_{D_i\cap D_j} B_i(x)o(x)B_j(x)dx. \tag{C.13}$$

As a consequence, matrices are sparse and often (not always, because we consider polyelectronic functions) band-diagonal. On uniform grids, matrices of translationally invariant operators, that is with kernel $o(x,y) = o(x-y)$, are Toeplitz:

$$\langle B_i|O|B_j\rangle = \langle B_{i+n}|O|B_{j+n}\rangle. \tag{C.14}$$

If an hermitian operator O is both local and translationally invariant, like the identity and the kinetic energy, its matrix on a uniform grid is Toeplitz and banded, in other terms it is defined by just k numbers.

B-splines are positive: expansion coefficients of represented functions are akin to the functions themselves. Without rapid oscillations of coefficients, the cancellation errors are kept at minimum. In particular [82], if $f = \sum_i B_i c_i$

$$\left| c_i - \frac{M+m}{2} \right| \leq D_k \frac{M-m}{2}, \quad m = \min_{x\in[a,b]} f(x),\ M = \max_{x\in[a,b]} f(x) \tag{C.15}$$

where D_k is a constant that depends only on k and not on the particular partition of the $[a, b]$ interval: At any point, the evaluation of a linear combination of B-splines

k	2	3	4	5	6
D_k	1	3	5.5680...	12.0886...	22.7869...

requires the evaluation of k basis functions only. With Gauss-type integration technique, matrix elements of operators with polynomial kernels are exact. The error ϵ in the approximation of a $\mathcal{C}^k$ function f with B-splines, is bounded by

$$\epsilon \leq \text{const}_k |\mathbf{t}|^k \|D^k f\|, \quad |\mathbf{t}| = \max_i (t_{i+1} - t_i), \quad \|f\| = \max_{x\in[a,b]} |f(x)| \tag{C.16}$$

Finally, the fact that each couple of different B-splines has a significant portion of their domain where they do not superpose gives rise to a strong linear independence.

C.2 Free knots optimization

Depending on the asymptotic behaviour of the wave function which is to be represented, different kinds of knot spacing are required. Indeed, for sufficiently regular functions f, the condition C.16 can be sharpened considerably by restricting to the optimal set of n-knots grids, in which case [82]

$$\epsilon \leq \text{const}_k n^{-k} \left(\int_a^b |D^k f|^{1/k} dx \right)^k. \tag{C.17}$$

In other terms, the convergence is still of order n^{-k} as stated in C.16 with a uniform grid, but if the largest values of $D^k f$ concentrate in small intervals, the last factor in C.17 can be substantially smaller than $\|D^k f\|$. Knot collocation is therefore a crucial issue in the use of B-splines.

In spherical coordinates the metric is r^2 so that basis functions are defined as

$$\chi_{n,l,m}(\vec{r}) = N_i \frac{B_i(r)}{r} Y_{lm}(\hat{r}) \tag{C.18}$$

For basis functions with orbital angular momentum l to be continuous, the first $l+1$ splines are to be rejected as long as origin adheres to their support. The first spline would introduce a negative divergence in hamiltonian matrix elements due to the electron-nucleus potential energy term and for non-zero angular momenta the first

$l+1$ B-splines, if adherent to the origin, give rise to positive divergences because of the repulsive centrifugal term in the kinetic energy. With Gauss-type integration algorithm, positive divergences turn out actually to be just very high numbers. Wave functions corresponding to irregular behaviour at origin have fictitious huge energies which somehow prevent their inclusion in the final wave functions. It is possible, and desirable, though, to get rid completely of such spurious behaviours rejecting all irregular functions. With B-splines of order k one would be limited in principle to orbital angular momenta lower than k. There are two ways to circumvent this problem. The first is to choose *a priori* a B-spline order higher than the orbital angular momenta that will actually be used. The other way, the one we adopted, is to add a knot near the origin (say at 10^{-3} au) and to reject always the first $min(l+1, k)$ B-splines. For angular momenta equal to or higher than k, wave functions are zero up to the first knot and therefore regular with respect to all operators with a singular kernel. For moderate energies this cutoff near the origin does not alter the results.

The second derivative of B-splines of order $k = 2$ (piecewise straight lines) is undefined at knots and zero elsewhere. They have thus zero kinetic energy and clearly cannot be used to represent wave functions. The B-spline with $k = 3$ have non zero but discontinuous kinetic energy, what make convergence with the number of knots awfully slow: in table C.1 the helium Hartree-Fock energies on fully optimized grids with n knots are reported.

n	E
3	-2.779 338 219
4	-2.843 069 934
5	-2.851 374 034
6	-2.857 303 447
7	-2.859 638 726
8	-2.860 414 302
9	-2.860 852 696
14	-2.861 529 370
∞	-2.861 679 995

Table C.1: Hartree-Fock energies of the Helium atom obtained on B-spline basis with order $k = 3$, defined by fully optimized grids with 3 to 9 knots.

B-splines of fourth order are therefore the first viable choice. Table C.2 shows the same convergence study as in table C.1 but with $k = 7$. More precisely, the SCF energy converges polynomially to the Hartree-Fock limit as a function of the number of knots.

$$\log(\Delta E) = a - b \log N \quad \text{where} \quad a = 6.8730 \pm 0.8213,\ b = -10.9805 \pm 0.4457 \tag{C.19}$$

A similar calculation reported in table C.3 shows that 16 knots are sufficient to reproduce the Hartree-Fock limit of SCF energy of Beryllium ground state up to ten digits.

n	E
3	-2.857 091 391
4	-2.861 502 991
5	-2.861 628 353
6	-2.861 678 169
7	-2.861 679 299
8	-2.861 679 879
9	-2.861 679 974
10	-2.861 679 984
11	-2.861 679 992
12	-2.861 679 993 4
13	-2.861 679 994 526
14	-2.861 679 995 332
∞	-2.861 679 995

Table C.2: Hartree-Fock energies of the Helium atom obtained on B-spline basis with order $k = 7$, defined by fully optimized grids with 3 to 14 knots.

n	E (au)
4	-14.434 395 620
5	-14.552 485 339
6	-14.572 440 224
7	-14.572 871 172
8	-14.572 987 929
9	-14.573 009 653
10	-14.573 020 704
11	-14.573 022 385
12	-14.573 022 844
15	-14.573 023 148
16	-14.573 023 158
18	-14.573 023 165
∞	-14.573 023 16

Table C.3: Hartree-Fock energies of the Beryllium atom obtained on fully optimized B-spline basis of order $k = 7$ with 4 through 18 knots.

There are atomic systems for which the Hartree-Fock approximation is inapplicable, like H^-. In such cases a configuration approach is required at the outset, and the optimization process is considerably slowed down. Such states as the fundamental states of H^- or He^- ($^4P^e$) do nevertheless greatly benefit from an optimization of the grid of knots as they are both very diffuse and highly correlated, therefore requiring large expansions on orbital angular momenta as shown for H^- in table C.4, where the CI energy of the fundamental state is reported as a function of both the radial and angular extension of the basis.

The quality of the results improves as the spline order rises, up to a point where the potentiality of the larger basis is counterbalanced by numerical loss

Table C.4: CI energies of the fundamental state of H^- as a function of the total number n of radial B-splines and the maximum orbital angular momentum ℓ. The accurate electrostatic limit is -0.527751016544306 au [225].

ℓ	n=26 R=19.62au	n=31 R=26.07au	n=34 R=29.93au	n=36 R=32.51au	n=38 R=35.09au
0	-0.5142638	-0.5144712	-0.5144896	-0.5144935	-0.5144952
1	-0.5265243	-0.5265816	-0.5265841	-0.5265844	-0.5265846
2	-0.5273831	-0.5274358	-0.5274380	-0.5274383	-0.5274384
3	-0.5275713	-0.5276229	-0.5276251	-0.5276254	-0.5276255
4	-0.5276347	-0.5276860	-0.5276881	-0.5276884	-0.5276885
5	-0.5276617	-0.5277128	-0.5277150	-0.5277153	-0.5277154
6	-0.5276751	-0.5277262	-0.5277284	-0.5277287	-0.5277287
7	-0.5276825	-0.5277336	-0.5277357	-0.5277360	-0.5277361
8	-	-	-0.5277401	-	-
9	-	-	-0.5277428	-	-
10	-	-	-0.5277446	-	-
11	-	-	-0.5277458	-	-
13	-	-	-0.5277473	-	-

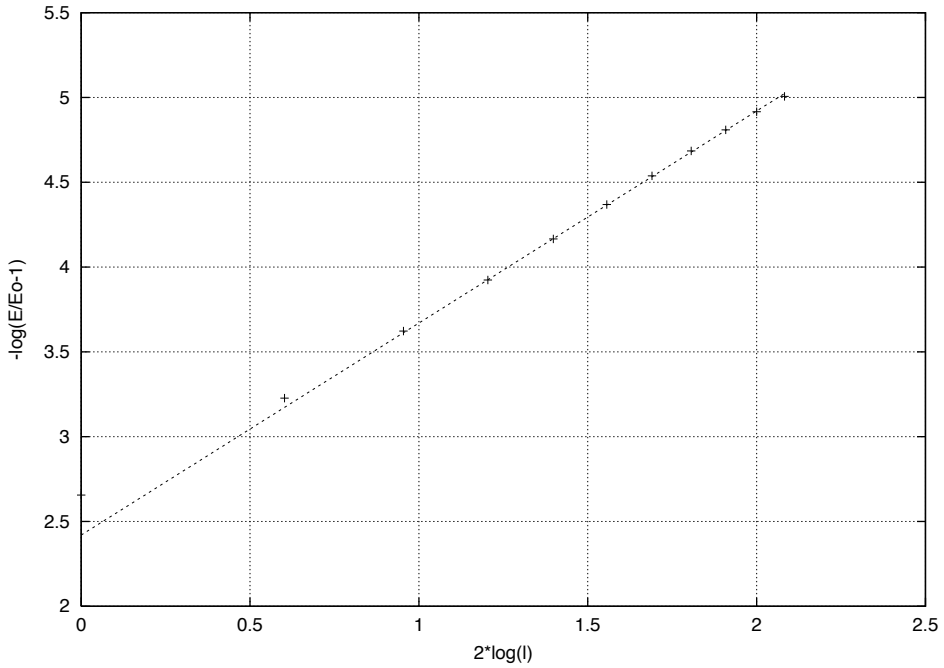

Figure C.2: For large values of the maximum orbital angular momentum ℓ the relative error on energy scales as $\ell^{-5/2}$.

of precision. In table C.5, the SCF helium energies on optimized grids with 14 knots and spline order from 3 to 8 are compared. In double precision arithmetic,

k	E (au)
3	-2.861 529 369 952
4	-2.861 677 544 736
5	-2.861 679 928 634
6	-2.861 679 992 042
7	-2.861 679 995 332
8	-2.861 679 995 554
∞	-2.861 679 995

Table C.5: Hartree-Fock energies of the Helium atom obtained on B-spline basis with 14 knots, defined by fully optimized grids with order $k = 3$ to 8.

$k \sim 8$ is a practical limit beyond which little advantages are gained. In this thesis anyway, all calculations were performed with $k = 5$ to keep the dimensions and computational time to a minimum.

C.3 Effective completeness

In numerical analysis the stability of the solution of a linear system

$$\mathbf{A}\mathbf{x} = \mathbf{b} \tag{C.20}$$

is characterized by the condition number $\mathcal{K}(\mathbf{A})$ of the matrix of the coefficients $\mathbf{A}$, given by $\|\mathbf{A}\| \cdot \|\mathbf{A}^{-1}\|$. $\log \mathcal{K}(\mathbf{A})$ is an indicative measure of the number of significant figures lost in the computation. The L^2 norm $\|\mathbf{A}\|_2$, defined as

$$\|\mathbf{A}\|_2 = \max_{\mathbf{x}\neq\mathbf{0}} \frac{\|\mathbf{A}\mathbf{x}\|_2}{\|\mathbf{x}\|_2}, \quad \text{where} \quad \|\mathbf{x}\|_2 = \sqrt{\sum_i |x_i|^2}, \tag{C.21}$$

is commonly chosen. In this case, $\|\mathbf{A}\|$ is given by its largest singular value, that is the largest eigenvalue $\max_i s_i$ of $\sqrt{\mathbf{A}^\dagger\mathbf{A}}$. For positive definite hermitian matrices, like the superposition matrix $\mathbf{S}$, the singular values s_i coincides with the eigenvalues λ_i and the condition number is consequently given by

$$\mathcal{K}_2(\mathbf{S}) = \frac{\max_i \lambda_i}{\min_i \lambda_i}. \tag{C.22}$$

If some eigenvalues of the superposition matrix of a certain basis used to project electronic wavefunctions are too large or too small, the accuracy of the results is seriously compromised.

A well known catastrophic example is given by the classical Gaussian and Slater basis, widely used before the attestation of B-splines for the lowest lying atomic bound states. In figure C.3 the eigenvalues of the superposition matrices for well

tempered Gauss and Slater basis [226] with dimensions $N = 10$, 100 and 1000 are plotted in decreasing order as a function of the eigenvalue fraction: $\lambda_i \, vs. \, i/N$. Already with 100 functions, roughly a fourth of the basis functions are numerically linearly dependent with the others. Larger basis does not add substantially to the linear independent set. Such situation leads to all sort of numerical problems.

This is at striking variance with the case of B-splines: with a basis of order 7 on as much as 10 000 equally spaced knots, all the eigenvalues lie above 10^{-2}.

The B-spline remarkable capability of approaching L^2 completeness in arbitrary, possibly unlimited, intervals without spoiling the well conditioning of the corresponding superposition matrix is known as effective completeness.

Effective completeness is largely the reason of B-spline success in atomic and molecular physics calculations [227]. In the following section the concept of effective completeness is precised and a general result is presented which demonstrate that for a large class of knot grids relevant to atomic calculations, the spectrum of the B-spline superposition matrix is well behaved and actually akin to a very specific functional form.

We shall investigate here what exactly one is to expect from a large B-spline basis in terms of the eigenvalues of its metric. It turns out that the extreme eigenvalues of the superposition matrix, and therefore its condition number, can be stringently localized around well defined finite values whenever reasonable limiting conditions on a sequence of grids apply.

Consider the following parametrization of an arbitrary grid of separated knots $\{t_i\}_{i \in I_N}$ $(t_0 < t_1)$:

$$t_{i+1} - t_i = e^{\delta_i}(t_i - t_{i-1}), \quad 2 \leq i \leq N-1, \quad t_0 < t_1. \tag{C.23}$$

The δ_i are convenient invariant parameters for the superposition integrals:

$$\langle B_i^k | B_j^k \rangle = s_{j-i}^k(\delta_{i+1}, \delta_{i+2}, \ldots, \delta_{j+k}) \tag{C.24}$$

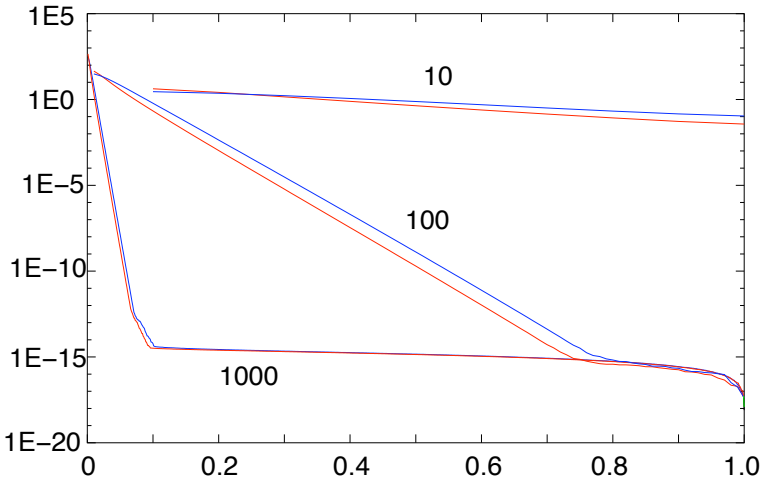

Figure C.3: Eigenvalue distributions λ_i *vs* i/N for even-tempered basis of slater (blue) and gaussian (red) functions of dimension 10, 100 and 1000. Recursion parameters are by Cooper *et al* [226]. See text for comments.

where, without loss of generality, we have assumed $j \geq i$. If the spacing between consecutive knots changes smoothly along a grid, then the matrix elements of the corresponding B-spline superposition matrix differ little from those defined by a uniform grid, even if the width ratio of far intervals may be substantially far from 1.

To precise this concept let introduce the following definition: a sequence of grids $\{\{t_i^1\}_{i\leq N_1}, \{t_i^2\}_{i\leq N_2}, \ldots\}$ with $N_s \to \infty$ is said locally uniform when

$$\lim_{s\to\infty} \Delta_s = 0, \quad \Delta_s = \max_i |\delta_i^s| \tag{C.25}$$

A relevant family of locally uniform sequences of grids can be the following

$$t_n^s = f[n \cdot g(N_s)], \quad f \in \mathcal{C}^2, \quad f'(0) > 0 \tag{C.26}$$

where $|f''/f'|$ is bounded, and g is a strictly positive infinitesimal function $\lim_{N\to\infty} g(N) = 0$. This family captures the idea of a set of knots with a knot density given by a well defined function f. If $g(N) = A/N$, the sequence of grids gets dense in $[f(0), f(A)]$, while if $\lim_{n\to\infty} g(N) * N = \infty$ and $\lim_{n\to\infty} f(n) = \infty$, the sequence of grids gets dense in $[f(0), +\infty)$. In the two cases the corresponding sequences of spline spaces get dense in $L^2[f(0), f(A)]$ and $L^2[f(0), +\infty]$.

The superposition between two splines can be approximated in the neighborhood of the evenly spaced knots in their support as

$$\langle B_i^k | B_j^k \rangle = s_{j-i}^k(\vec{0}) + \sum_{l=1}^{j-i+k} \partial_l \, s_{j-i}^k(\vec{0}) \; \delta_{i+l} + o(\delta_m). \tag{C.27}$$

In a locally uniform sequence of grids then, it eventually happens that

$$|\langle B_i^k | B_j^k \rangle - s_{j-i}^k(\vec{0})| \leq (2k-1)[1 + \max_l |\partial_l \, s_{j-i}^k(\vec{0})|] \; \Delta \tag{C.28}$$

Thanks to the fact that, by hypothesis, Δ in a locally uniform sequence is infinitesimal, the eigenvalues of the superposition matrix are equally distributed as in the case of a plainly uniform grid. Moreover, the eigenvalue distribution functions are known, as stated in the following theorem

Theorem C.3.1. *The sequence of spectra $\{\{\lambda_i^{(k),s}\}_{i\in I_{N_s}}\}_{s\in\mathbb{N}}$ of the superposition matrices among L^2 normalized B-splines of order k, defined by a locally uniform sequence of knot grids $\{\{t_i^s\}_{i\leq N_s}\}_{s=1,2,3,\ldots}$, is such that*

$$\lim_{s\to\infty} \lambda_{\lceil x\, N_s \rceil}^{(k),s} = f_k(x), \quad uniformly\ for \quad x \in (0,1] \tag{C.29}$$

where $\lceil x \rceil$ is the lowest integer greater than x, and $f_k(x)$ is a function which depends solely on the spline degree k and has the following analytical expression

$$f_k(x) = 1 + 2 \sum_{j=1}^{k-1} \; s_j^k \, \cos(\pi j x), \quad x \in [0,1], \quad s_j^k = s_j^k(\vec{0}). \tag{C.30}$$

In other terms, all the locally uniform sets of knots are equivalent in that they give rise to non-singular superposition matrices with the same distribution of eigenvalues, irrespective to their global character.

Proof.

First First we observe that the eigenvalues problem for a real symmetric banded circulant matrix $A_{ij} = a_{|i-j|}$ of total dimension N reads

$$\sum_{j=-k+1}^{k-1} a_{|j|} c_{i+j} = \lambda c_i \tag{C.31}$$

with the N solutions $n = 1, 2, \ldots, N$:

$$c_j^n = e^{2i\pi \frac{nj}{N}}, \quad \lambda_n = \sum_{j=-k+1}^{k-1} a_{|j|}\, e^{i\pi \frac{2nj}{N}} = a_0 + 2\sum_{j=1}^{k-1} a_j \cos \pi j \frac{2n}{N}. \tag{C.32}$$

The eigenvalues λ_n and λ_{N-n} are degenerate, each eigenvalue is therefore assumed twice with the exception of λ_N and of $\lambda_{N/2}$ if N is even. If the matrix elements of the circulant matrix are given by the superpositions between normalized B-splines on a uniform grid, $a_j \equiv s_j^k$ then, the eigenvalues are given by

$$\lambda_n = 1 + 2\sum_{j=1}^{k-1} s_j^k \cos \pi j \frac{2n}{N}, \quad n = 0, 1, \ldots, \lfloor N/2 \rfloor \tag{C.33}$$

As N approaches ∞, the set $\{x_n = 2n/N,\ n = 0, 1, \ldots, \lfloor N/2 \rfloor\}$ gets dense in $[0, 1]$, and we recover the analytic expression given in Eq.(C.30).

Incidentally, a uniform grid of knots on a circle gives rise to a superposition matrix which is circulant (see figure C.4). Indeed the iterative definition (C.1, C.2) of B-splines can be easily generalized to a circular domain for k greater than the number of knots.

Anyway, the superposition matrix of a set of B-splines defined on a uniform grid in the real axis is not circulant, as the first splines do not superpose to the last ones, but it is Toeplitz (constant on diagonals). It has long been known [228], though, that the spectra of a Toeplitz matrix is equally distributed to that of the corresponding circulant matrix, and, in the hermitian case, it is bounded both above and below by the extreme values of the discrete Fourier transform $f(\theta) = \sum_j a_j e^{ij\theta}$, $\theta \in [0, 2\pi]$. From this result it can be shown that the Toeplitz spectrum actually converges uniformly to that of the corresponding circulant matrix

$$\forall \epsilon \quad \exists N \quad | \quad \forall n > N \quad \forall n > N,\ i \leq n \quad |t_i^n - c_i^n| < \epsilon. \tag{C.34}$$

For hermitian banded Toeplitz matrices, the uniform convergence can be demonstrated more easily by means of a corollary of the min-max theorem [229], as reported at the end of this appendix. In the case of banded matrices, moreover, the uniform convergence can indeed be precised better [230]:

$$|t_i^{(k),n} - c_i^{(k),n}| < \pi \max_x |f(x)|(k-1)/(n+1). \tag{C.35}$$

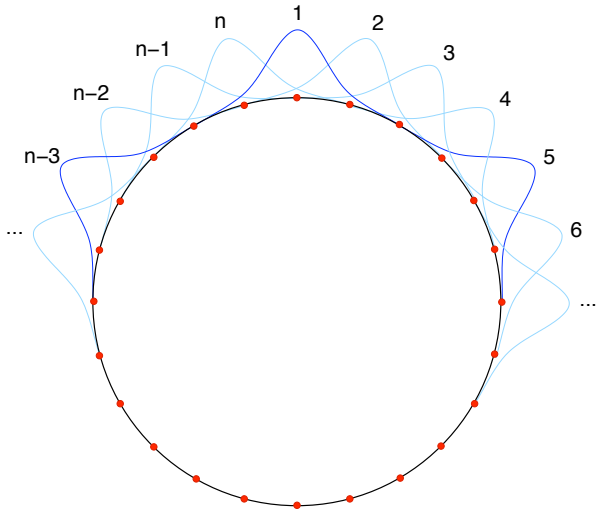

Figure C.4: B-splines (k=4) defined on a circular domain. If the knot spacing is uniform, they give rise to a circulant superposition matrix, since the "last" splines superpose to the "first" ones.

A still faster convergence is expected for the extreme eigenvalues. The two lowest errors vanish quadratically

$$e_1, e_2 \sim d(k)/n^2 \quad \text{with} \quad \forall m \lim_{k\to\infty} k^m d(k) = 0. \tag{C.36}$$

where n is the dimension of the B-spline basis and $d(k)$ a proportionality constant which converges to zero faster than any polynomials.

The errors on the highest even and odd eigenvalues obey instead the following conditions

$$e_e \sim k^{3/2}/n^2 \quad ; \quad e_o \sim k^2/n^3 \tag{C.37}$$

These properties on the extreme eigenvalues appear evident from a numerical example. In figure C.5 the functions for even i

$$f^e_{nk}(i/n) = (t^k_{in} - c^k_{in})\frac{n}{k^{3/2}}\left[(i-1)/n\right]^{-1}\left[1-(i-1/2)/n\right]^{-1} \tag{C.38}$$

and for odd i

$$f^o_{nk}(i/n) = (t^k_{in} - c^k_{in})\frac{n}{k^2}\left[(i-1/2)/n\right]^{-1}\left[1-(i-1)/n\right]^{-2} \tag{C.39}$$

are reported for $k = 7$ and for $n = ...$ as functions of the eigenvalue fraction. The functions clearly accumulate on the limiting functions.

$$f^{e/o}_k(x) = \lim_{\substack{n\to\infty \\ i/n=x}} f^{e/o}_{nk}(i/n) \tag{C.40}$$

To our purposes, the $f^{e/o}_k$ can be suitably approximated taking $n = 10000$. In figure C.6, $f^{e/o}_k$ for $k = 2$ to 20 are represented on a logarithmic scale. The terms in the two sets clearly share the same value at $x = 1$ and converge exponentially to zero at $x = 0$ as $k \to \infty$.

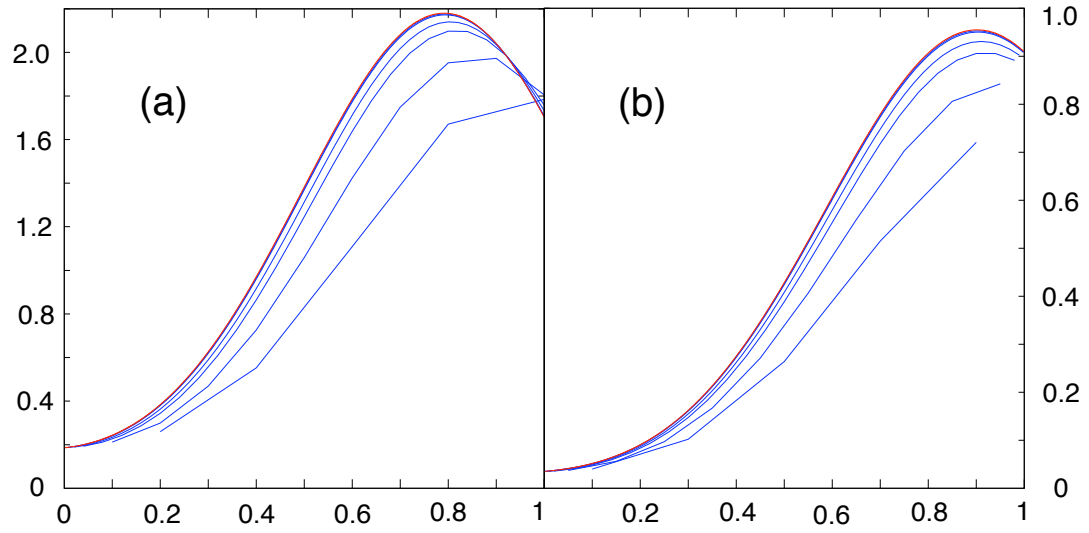

Figure C.5: $f^e_{nk}(x)$ (a) and $f^o_{nk}(x)$ (b) with $k = 7$ for $n = 10$, 20, 50, 100, 500, 1000 and 10000. See text for details.

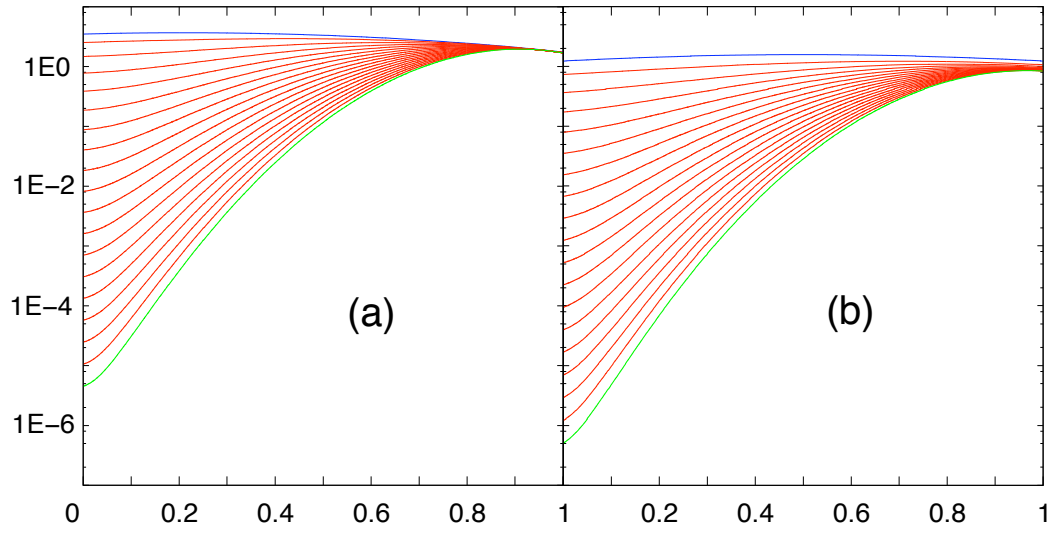

Figure C.6: $f^e_k(x)$ (a) and $f^o_k(x)$ (b), approximated with $f^{e/o}_{nk}$ with $n = 10000$, for k=2 (upper curves) through k=20 (lower curves). See text for definitions.

To conclude the demonstration, it is sufficent to show that the sequence of superposition spectra generated by locally uniform sequence of grids converges uniformly to that of the corresponding sequence of Toeplitz matrices.

Let define a sequence of perturbation matrices $\{V^1, V^2, \ldots\}$ as

$$V^s = S^s - T^s$$

The perturbation matrices are non zero on the $k-1$ upper and lower diagonals only.

For a complex matrix a_{ij}, the eigenvalues are contained within the circles with centers a_{ii} and radii $R_i = \sum_{j \neq i} |a_{ij}|$ (Gershgorin circle theorem). As a consequence, the spectral radius of V is limited by

$$\|V\| \leq \max_i \sum_j |V_{ij}|. \tag{C.41}$$

If we define $A = (2k-1)[1+\max_l |\partial_l \, s^k_{j-i}(\vec{0})|]$, then $|V_{ij}| < A\Delta_s$. Since the diagonal elements V_{ii} are zero

$$\|V\| < 2(k-1)A\Delta_s \tag{C.42}$$

Thanks to the last corollary of the min-max theorem reported at the end of this appendix (perturbations with small spectral radius) the distance between corresponding terms in equally ordered spectra of two hermitian matrices is at most equal to the spectral radius of their difference:

$$\forall i \leq N_s \quad |\lambda^s_i - t^s_i| \leq 2(k-1)A\Delta_s. \tag{C.43}$$

Since Δ_s is infinitesimal, the theorem is proven. □

What about the numerical value of the s^k_j? They can actually be computed analytically. To obtain their expression, we may adopt any set of splines defined on a uniform grid. Here it is expedient to choose the cardinal B-splines, those defined by the set of relative integers $\mathbb{Z}$ as an infinite grid of knots, since they have a simple non recursive expression [82]:

$$b^k_j(x) = \sum_{r=0}^{k} (-)^{k-r} \binom{k}{r} (r+j-x)^{k-1}_+ / (k-1)! \tag{C.44}$$

where

$$(x)^n_+ = \begin{cases} x^n & \text{if} \quad x \geq 0 \\ 0 & \text{otherwise.} \end{cases} \tag{C.45}$$

The characteristic superposition integrals between cardinal B-splines can then be computed straightforwardly:

$$(b^k_0, b^k_j) = \int_{-\infty}^{\infty} b^k_0(x) b^k_j(x) = \sum_{r,s=0}^{k} (-)^{r+s} \frac{\binom{k}{r}\binom{k}{s}}{[(k-1)!]^2} \sum_{\alpha,\beta=0}^{k-1} \binom{k-1}{\alpha}\binom{k-1}{\beta} \times$$

$$\times r^{k-1-\alpha} (s+j)^{k-1-\beta} \frac{(-)^{\alpha+\beta}}{\alpha+\beta+1} \left[\min(\max(r,j), s+j)^{\alpha+\beta+1} - j^{\alpha+\beta+1}\right] \tag{C.46}$$

This formula is not very telling, but when the cardinal b_j^k are normalized so to have unit L^2 norm, the reciprocals of their integrals happen to be integer numbers. Stated otherwise, the ratio between the largest and the smallest integrals between cardinal splines of the same order is an integer number, so they can be exactly tabulated. In the following we report $(b_0^k, b_j^k)/(b_0^k, b_{k-1}^k)$ for $k \leq 6$.

	j					
k	0	1	2	3	4	5
1	1					
2	4	1				
3	66	26	1			
4	2416	1191	120	1		
5	156190	88234	14608	502	1	
6	15724248	9738114	2203488	152637	2036	1

A line in this table can be read from right to left, in which case it gives $1/s_j^k$. Note in particular that the largest integral is $2(k-2)$ orders of magnitude larger than the smallest integral.

The theorem can be generalized to multidimensional B-splines. Let consider for definiteness the bi-dimensional case. The B-spline basis is given by

$$B_{ij}(x, y) = B_i(x)B_j(y) \tag{C.47}$$

and the superposition factorizes as

$$\langle B_{ij}|B_{nm}\rangle = S_{in}^{(x)} S_{jm}^{(y)} \tag{C.48}$$

The eigenvalues are given by

$$\lambda_{ij} = \lambda_i^{(x)} \lambda_j^{(y)}. \tag{C.49}$$

where $\lambda_i^{(x)}$ ($\lambda_i^{(y)}$) is the i-th eigenvalue of $S^{(x)}$ ($S^{(y)}$). For a sequence of locally uniform, possibly different, knot grids for both the x and y axis, the two set of eigenvalues separately converge uniformly to the corresponding sets of circulant eigenvalues, and since the two spectra are bounded, also their product converges uniformly to the product of circulant eigenvalues. The generalization to larger dimensions is straightforward.

In figure C.7 we have reported the difference between the eigenvalues on an exponential grid and the corresponding reference eigenvalues of the circulant matrix for $k = 7$ and $n = 10$, 20, 50, 100, 500, 1000 and 10000, times n. The exponential grid has been defined as

$$t_{in} = \exp\left[(i-1)/(n-1)^{3/4}\right]. \tag{C.50}$$

In the largest case, the intervals grows from $\sim 10^{-3}$ between the first and the second knot, to ~ 22 between the last two knots (around $t \sim 22000$). Still the convergence of the eigenvalues is similar to the case of the Toeplitz matrix, as it is uniform, more precisely the error is lower than C/n where C is a constant. For

any fixed number of extreme eigenvalues the convergence is even faster as for any fixed i: $|e_{i,n}|n \to 0$ and $|e_{n-i,n}|n \to 0$.

The set of knots of practical interest generally have a fixed number of intervals violating the condition on δ_i, typically an initial and a final set of $k-1$ zero-width intervals. This adds a finite number of non vanishing terms in the series of perturbation matrices. As a consequence of the second corollary to the min-max theorem reported at the end of this appendix (finite rank perturbations), only the extreme larger and lower $k-1$ eigenvalues may be seriously affected. In this case the uniform convergence claimed by the theorem applies only to the inner eigenvalues. As a matter of fact, though, no relevant deviations from the uniform case have been observed.

What happens if the requirement of local uniformity is relieved? To investigate that case we chose a random distribution of interval widths, uniform in $(0, 1]$. For a fixed number of knots and spline order there is a whole family of eigenvalue distributions which can be described with a mean function and a standard deviation function for each eigenvalue fraction value.

Both the mean and the standard deviation times $\sqrt{N}$ converge rapidly to a limiting function. This means that there is not a limiting distribution of eigenvalues but a limiting function of all distributions. Such limiting function is pretty similar to the limiting function of evenly spaced grid.

In figure C.8 a comparison of the limiting functions for both the uniform and the random case are shown from order 2 to order 10. The same plot is reproduced on a linear and on a logarithmic scale to emphasize the highest and the lowest

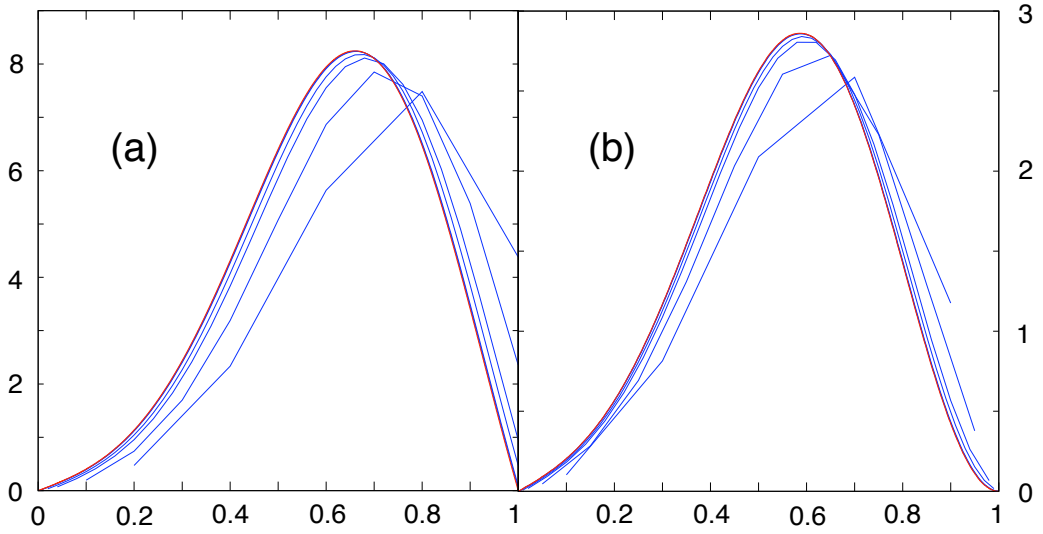

Figure C.7: Difference between the even (a) and odd (b) eigenvalues of the superposition matrix between B-splines of degree $k = 7$, built on a locally uniform sequence of exponential grids (see text for details), and the corresponding eigenvalues of the circulant matrix, multiplied by the basis dimension. Dimensions $n = 10$, 20, 50, 100, 500, 1000, 10000 are shown. Uniform convergence is apparent.

part of the spectrum respectively. The eigenvalue distribution depends primarily on the spline degree k and only marginally on the interval widths being constant or randomly distributed. The highest eigenvalues of the random case are slightly higher, and the lowest slightly lower, than in the uniform case.

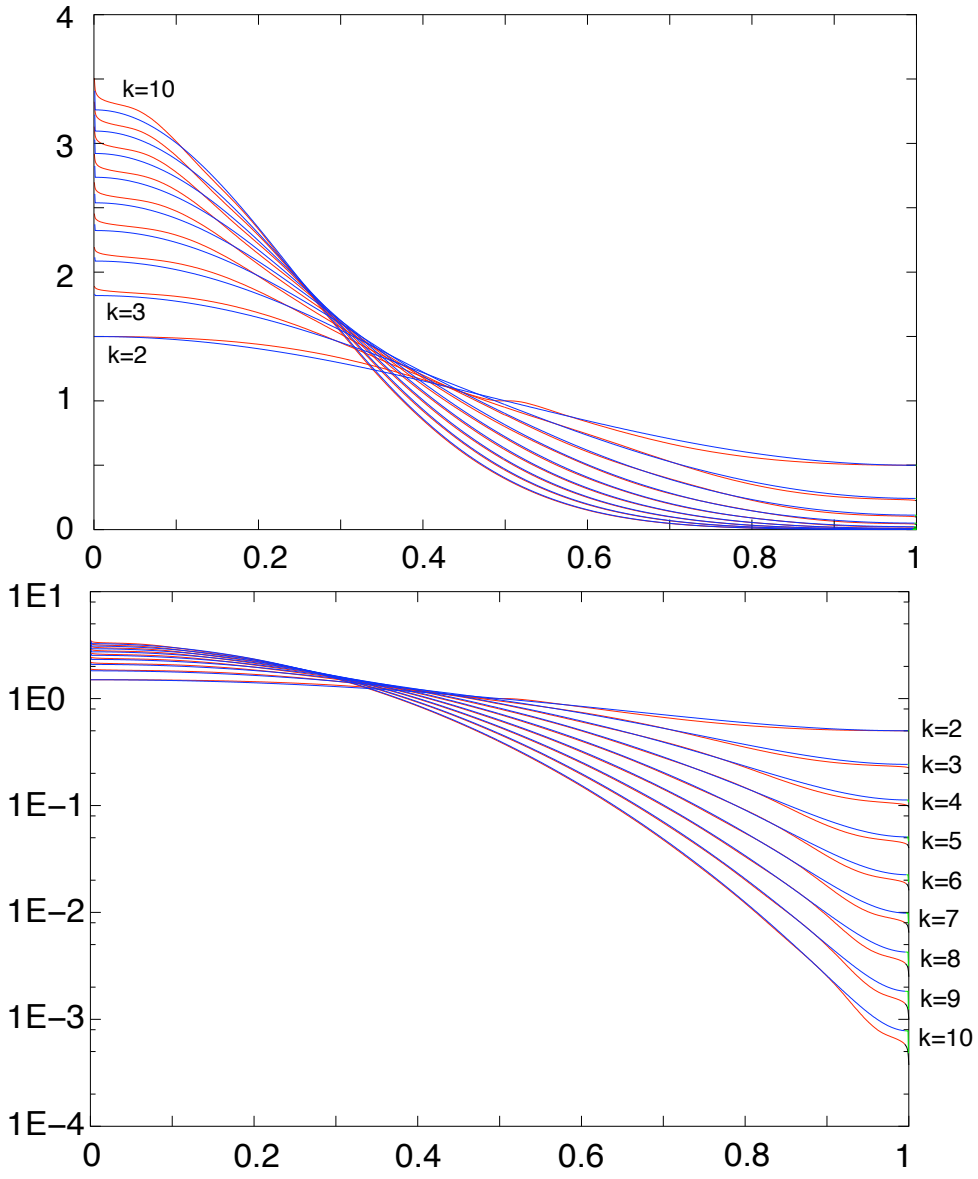

Figure C.8: Eigenvalues of the superposition matrices for large B-spline basis (dimension N=10000) of degree $k = 2$ to 10 on evenly spaced (blue) and randomly spaced (red) knots in decreasing order as functions of the eigenvalue fraction: λ_i *vs* i/N. In the top (bottom) panel a linear (logarithmic) scale emphasizes the region of highest (lowest) eigenvalues. The randomly distributed intervals do not cause the eigenvalue distribution to change significantly. This evidence exhibits the stability of the spectrum toward deviations from local uniformity.

C.4 Locally uniform grids and locally Toeplitz matrices

The superposition matrices between B-splines on a uniform sequence of grids are almost Toeplitz when the B-splines are L^2 normalized. With a different normalization, for example that of the native B-splines defined iteratively by C.1 and C.2, any term in the sequence of superposition matrices is no longer globally similar to a Toeplitz matrix but it is still locally so, in the sense that for any integer m, for any real $x \in (0,1)$, and for any $\epsilon > 0$ there exists an n_o such that for all $n > n_o$, $i,j = 1,2,\ldots,m$ $|A_{\lfloor nx \rfloor + i, \lfloor nx \rfloor + j} - A_{\lfloor nx \rfloor + 1, \lfloor nx \rfloor + |j-i|}| < \epsilon$. This concept of local Toeplitzness is different from that introduced a decade ago by Paolo Tilli [231]. If the sequence of B-spline grids is nevertheless defined by $t_i^n = t(i/n)$, the superposition matrix is indeed locally Toeplitz in the sense defined by Tilli. In this case Tilli has shown that the eigenvalue distribution is characterized by a generalized Szegö formula. The Tilli approach has been extended in 2003 by Serra Capizzano to the multilevel case of Generalized Locally Toeplitz (GLT) sequences of matrices [232, 233].

C.5 Min-max theorem and its consequences

For an hermitian matrix A, the range $(Ax,x)/\|x\|^2$ is a bounded real interval whose maximum and minimum are the largest and smallest eigenvalues of A, respectively. We have indicated with $(,)$ the standard hermitian form on $\mathbb{C}^n$, linear in the first and antilinear in the second argument, $(x,y) = \sum_{i=1}^n x_i y_i^*$, and $\|x\| = (x,x)$. The min-max theorem [1] [229] is a refinement of this proposition which provides a variational characterization of all the eigenvalues.

Let $\alpha_j^\uparrow$ be the eigenvalues of A in increasing order, $\alpha_1^\uparrow \leq \alpha_2^\uparrow \leq \ldots \leq \alpha_n^\uparrow$, $\alpha_j^\downarrow = \alpha_{n-j+1}^\uparrow$ those listed in decreasing order, and S_k an arbitrary $k \geq 1$ dimensional subspace of $\mathbb{C}^n$. The min-max theorem states that

$$\alpha_k^\uparrow = \min_{S_k} \max_{\substack{x \in S_k \\ \|x\|=1}} (Ax,x), \tag{C.51}$$

$$\alpha_k^\downarrow = \max_{S_k} \min_{\substack{x \in S_k \\ \|x\|=1}} (Ax,x). \tag{C.52}$$

In order to demonstrate the theorem we consider first the following lemma: for every S_k

1. there exists $x \in S_k$, $\|x\| = 1$ such that $(Ax,x) \geq \alpha_k^\uparrow$,
2. there exists $x \in S_k$, $\|x\| = 1$ such that $(Ax,x) \leq \alpha_k^\downarrow$.

To see this, consider the subspace $S' = span\{u_k \ldots u_n\}$, where u_i is the eigenvector corresponding to $\alpha_i^\uparrow$. S' has codimension $k-1$, therefore $S' \cap S_k \neq \emptyset$. Let $x \in S' \cap S_k$

[1] The min-max theorem is also known as variational theorem or Courant-Fischer-Weyl theorem.

with $\|x\| = 1$. $(Ax, x) \geq \alpha_k^{\uparrow}$ since $x \in S'$, so the first claim holds. The second result is obtained through analogous steps.
The first part of the lemma implies that

$$\inf_{S_k} \max_{\substack{x \in S_k \\ \|x\|=1}} (Ax, x) \geq \alpha_k^{\uparrow}.$$

Since the infimum is actually realized by choosing $S_k = span\{u_1 \dots u_k\}$, where it equals $\alpha_k^{\uparrow}$, the first equality holds. The second equality is demonstrated analogously, exploiting the second part of the lemma.

C.5.1 Interlace theorem

Consider the matrix $B = PAP$, where A is a $n \times n$ matrix and P is a $n \times (n-r)$ orthogonal projection onto a subspace of dimension $n - r$. If the eigenvalues α_j of A and β_j of B are listed in increasing order, then for all $j = 1, 2, \dots, n-r$

$$\alpha_j \leq \beta_j \leq \alpha_{j+r}. \tag{C.53}$$

Let β_i have corresponding eigenvector b_i and $S_j = span\{b_1 \dots b_j\}$, then

$$\beta_j = \max_{\substack{x \in S_j \\ \|x\|=1}} (Bx, x) = \max_{\substack{x \in S_j \\ \|x\|=1}} (PAPx, x) = \max_{\substack{x \in S_j \\ \|x\|=1}} (Ax, x) \geq \alpha_j$$

where in the last inequality we have applied the first part of the min-max theorem. On the other hand, if we define $S_{n-r-j+1} = span\{b_j \dots b_{n-r}\}$, then

$$\beta_j = \min_{\substack{x \in S_{n-r-j+1} \\ \|x\|=1}} (Bx, x) = \min_{\substack{x \in S_{n-r-j+1} \\ \|x\|=1}} (PAPx, x) = \min_{\substack{x \in S_{n-r-j+1} \\ \|x\|=1}} (Ax, x) \leq \alpha_{j+r},$$

where the last equality is given by the second part of the min-max theorem. In particular this corollary allows to demonstrate that the eigenvalues of a banded hermitian Toeplitz matrix $T_n(f)$ converge uniformly to those of the corresponding circulant matrix $C_n(f)$ as $n \to \infty$, since $T_n(f)$ is the principal submatrix of $C_{n+r}(f)$ obtained eliminating the last r rows and columns, where r is the number of upper diagonal elements of $T_n(f)$.

C.5.2 Finite rank perturbation

Let $B = A + E$ where A, E and B are all hermitian $n \times n$ matrices and E has finite rank r. Then for $k < j \leq n - k$

$$\alpha_{j-k} \leq \beta_j \leq \alpha_{j+k}. \tag{C.54}$$

Consider the projector P onto the orthogonal complement to the range of E. Then

$$PBP = PAP$$

let call q_j the eigenvalues of the projected operators. The interlace theorem assures that

$$\alpha_j, \beta_j \leq q_j \leq \alpha_{j+r}, \beta_{j+r}$$

from which the proposition follows immediately.

C.5.3 Perturbations with small spectral radius

Let $B = A + E$ where A, E and B are all hermitian $n \times n$ matrices and E has spectral radis ϵ, then

$$\forall j \qquad |\beta_j - \alpha_j| \leq \epsilon. \tag{C.55}$$

This can be seen by applying directly the min-max characterization of eigenvalues:

$$\beta_j^{\uparrow} = \min_{S_j} \max_{\substack{x \in S_j \\ \|x\|=1}} (Bx, x) = \min_{S_j} \max_{\substack{x \in S_j \\ \|x\|=1}} \big[(Ax, x) + (Ex, x)\big] \leq$$

$$\leq \min_{S_j} \max_{\substack{x \in S_j \\ \|x\|=1}} \big[(Ax, x) + \epsilon\big] = \alpha_j + \epsilon$$

and similarly

$$\beta_j^{\uparrow} = \max_{S_{j-1}^{\perp}} \min_{\substack{x \in S_{j-1}^{\perp} \\ \|x\|=1}} (Bx, x) = \max_{S_{j-1}^{\perp}} \min_{\substack{x \in S_{j-1}^{\perp} \\ \|x\|=1}} \big[(Ax, x) + (Ex, x)\big] \geq$$

$$\geq \max_{S_{j-1}^{\perp}} \min_{\substack{x \in S_{j-1}^{\perp} \\ \|x\|=1}} \big[(Ax, x) - \epsilon\big] = \alpha_j - \epsilon$$

Appendix D

Interpolation

In the K-matrix technique, interpolation is a crucial part of the algorithm. It is by means of interpolation that the set of integral equations can be discretized and on interpolation accuracy relies much of the eventual accuracy of results. We used two different kind of interpolation methods, which proved to be essentially equivalent: the cubic B-spline and the Lagrange interpolation method.

For the Lagrange interpolation the approximating function in every interval is computed with at most three points to the left and three points to the right of the given point. This is also the assumption to extrapolate matrix elements down to thresholds: the interpolation in the first interval, which usually is the smallest one, relies on the values on the first three points. The whole interpolating function can be written as

$$F(x) = \sum_{k=1}^{N} \varphi_k(x) \sum_{i \in I^N_{k,o}} \frac{\prod_{j \in I^N_{k,o} \setminus \{i\}} (x - x_j)}{\prod_{j \in I^N_{k,o} \setminus \{i\}} (x_i - x_j)} f(x_i) = \sum_i \Phi^N_{i,o}(x) f(x_i) \tag{D.1}$$

where φ_i is the characteristic function of the C_i interval[1]. F derivative is discontinuous at grid points. The matrix of a local operator between Lagrange characteristic functions $\Phi^N_{i,o}(x)$ is band diagonal with $2o-1$ non-zero elements above and below the diagonal. This is in particular the structure of $\mathsf{P}(E)$integration matrices:

$$\mathsf{P}(E)_{ij} = \int_{E_{th}}^{E_{cut}} d\epsilon \; \Phi_i(\epsilon) \frac{\mathcal{P}}{E - \epsilon} \Phi_j(\epsilon) \tag{D.3}$$

With cubic B-spline ($k = 4$), the interpolating function is $\mathcal{C}^2$. Given n grid points, threshold included, the $n + k - 2 = n + 2$ degrees of freedom need three conditions more than the $n-1$ values at points above threshold. The two common

[1] $C_i \equiv [x_{i-1}, x_i]$, depends on values at points $x_{i i \in I^N_{k,o}}$ where the index set is defined by

$$I^N_{k,o} \equiv \{\max(1, k-o), \ldots, \min(N, k+o-1)\} \tag{D.2}$$

where o is the prescribed maximum number of points to the left and to the right of the interval to be interpolated.

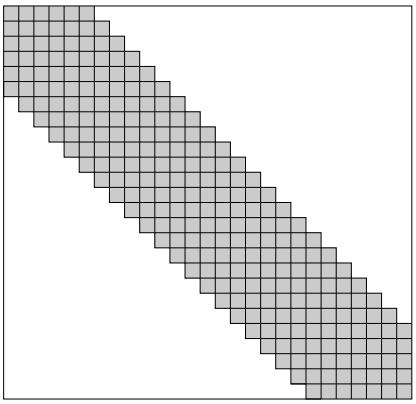

Figure D.1: The band structure of the integration matrix which results when Lagrange interpolation is used.

conditions of zero second derivative at boundaries define the set of *natural splines*. The last condition can be, for example, to set the first derivative at threshold to the same value at the first point after it. A characteristic feature of B-spline interpolation, which is a direct consequence of the requirement for differentiability, is that the value of the interpolating function depends on the values at all grid points. As a consequence the integration matrix is no more band diagonal.

As a matter of facts, the two methods did not give rise to appreciably different results.

Proper care must be paid for the signs of the PWC's states in the continuum in order to have matrix elements which can be correctly interpolated in the continuous index(es).

Appendix E

Radiative K-matrix, an example

In this appendix the full derivation of the radiative K-matrix equations is provided, along with the elementary application to the case of a single discrete state coupled both to an autoionizing and a fluorescence decay channel.

As anticipated in the first chapter, the close coupling autoionization wave functions are seeked as

$$|\Psi^{\mathcal{P}}_{\alpha E}\rangle = |\phi_{\alpha E}\rangle + \sum_{\gamma} \sum\!\!\!\!\!\!\int d\epsilon |\phi_{\gamma\epsilon}\rangle \frac{\mathcal{P}}{E-\epsilon} K_{\gamma\epsilon;\alpha E} + \sum_{d} \int^{\Omega_d} d\omega |d\otimes\omega\rangle \frac{\mathcal{P}}{E-E_d-\omega} K_{d\omega;\alpha E} \tag{E.1}$$

where in $|d\otimes\omega\rangle$ the bound state d is coupled to a dipole photon to form a state with the same symmetry of autoionization channels $|\phi_{\alpha E}\rangle$. The ultraviolet cutoffs Ω_d have been introduced for a reason that will become clear in the following. we shall consider for clarity only the case of dipole approximation, where the photons have only one discrete parameter: the polarization at the origin. The generalization to the interaction with general multipolar photons is straightforward. A similar expression holds for the fluorescence channels

$$|\Psi^{\mathcal{P}}_{a\omega}\rangle = |a\otimes\omega\rangle + \sum_{\gamma} \sum\!\!\!\!\!\!\int d\epsilon |\phi_{\gamma\epsilon}\rangle \frac{\mathcal{P}}{E-\epsilon} K_{\gamma\epsilon;a\omega} + \sum_{d} \int^{\Omega_d} d\omega' |d\otimes\omega'\rangle \frac{\mathcal{P}}{E-E_d-\omega'} K_{d\omega';a\omega} \tag{E.2}$$

where it is understood that $E = E_a + \omega$. This equations are transformed into a system of coupled integral equations through the action of the functionals

$$\langle\phi_{\beta E'}|(E-H), \qquad \langle b\otimes\omega'|(E-H)$$

To this purpose, we observe that

$$\langle a\otimes\omega|H|b\otimes\omega'\rangle = (E_b+\omega)\,\delta_{ab}\,\delta(\omega-\omega') \tag{E.3}$$

$$\langle\phi_{\alpha E}|H|a\otimes\omega\rangle = \sqrt{\frac{2\alpha^3}{3\pi(2L+1)}}\omega^{1/2}\langle\Phi_{\alpha E}\|\nabla_1\|a\rangle, \quad \nabla_1 = \sum_i \nabla_1(i) \tag{E.4}$$

We shall indicate with C the recurrent factor $\sqrt{\frac{2\alpha^3}{3\pi(2L+1)}}$. The reduced matrix element $\langle\phi_{\alpha E}\|\nabla_1\|a\rangle$ will be designated with $\nabla_{\alpha E,a}$ or $\nabla_{\bullet,a}$ wherever it is sensible to do so. For the effective interaction potential we adopt the shorthand notation

$$V(E)_{\beta E',\alpha E} = [H_{\beta E',\alpha E} - ES_{\beta E',\alpha E}](1-\delta_{\alpha\beta})$$

where also the dependence on energy will possibly be omitted. The four projected equation are

$$K_{\beta E',\alpha E} - \sum_{\gamma\neq\beta}\sum\!\!\!\!\!\!\int d\epsilon V(E)_{\beta E',\gamma\epsilon}\frac{\mathcal{P}}{E-\epsilon}K_{\gamma\epsilon,\alpha E} - \\ -C\sum_a \nabla_{\beta E',a}\int_0^{\Omega_a} d\omega\omega^{1/2}\frac{\mathcal{P}}{E-E_a-\omega}K_{a\omega,\alpha E} = V(E)_{\beta E';\alpha E} \tag{E.5}$$

$$K_{b\omega',\alpha E} = C\omega'^{1/2}\left\{\nabla_{b,\alpha E} + \sum_\gamma\sum\!\!\!\!\!\!\int d\epsilon\nabla_{b,\gamma\epsilon}\frac{\mathcal{P}}{E-\epsilon}K_{\gamma\epsilon,\alpha E}\right\} \tag{E.6}$$

$$K_{\beta E',a\omega} - \sum_{\gamma\neq\beta}\sum\!\!\!\!\!\!\int d\epsilon V(E)_{\beta E',\gamma E}\frac{\mathcal{P}}{E-\epsilon}K_{\gamma\epsilon,a\omega} - \\ -C\sum_d \nabla_{\beta E',d}\int_0^{\Omega_d} d\omega'\omega'^{1/2}\frac{\mathcal{P}}{E-E_d-\omega'}K_{d\omega',a\omega} = C\omega^{1/2}\nabla_{\beta E',a} \tag{E.7}$$

$$K_{b\omega',a\omega} = C\omega'^{1/2}\sum_\gamma\sum\!\!\!\!\!\!\int d\epsilon\nabla_{b,\gamma\epsilon}\frac{\mathcal{P}}{E-\epsilon}K_{\gamma\epsilon,a\omega} \tag{E.8}$$

It is immediate to see that, as it stands, the problem depends on the ultraviolet cutoffs Ω_d. For example when we replace $K_{d\omega',a\omega}$ in the last term in (E.7) with the expression in (E.8) we obtain

$$\sum_\gamma\sum\!\!\!\!\!\!\int d\epsilon\sum_d C^2\nabla_{\beta E',d}\left\{\int_0^{\Omega_d} d\omega'\frac{\omega'\mathcal{P}}{E-E_j-\omega'}\right\}\nabla_{d,\gamma\epsilon}\frac{\mathcal{P}}{E-\epsilon}K_{\gamma\epsilon,a\omega}$$

The integration in parenthesis is analytical:

$$I_a(\Omega_a) \equiv \int_0^{\Omega_a} d\omega'\frac{\omega'\mathcal{P}}{E-E_a-\omega'} = -\Omega_a + (E-E_a)\ln\left(\frac{E-E_a}{\Omega_a-E+E_a}\right)$$

$I_a(\Omega_a)$ diverges as Ω_a approaches ∞. If one is not interested in the radiative correction to the energy position of atomic levels or resonances, this trouble can be dealt with rather swiftly by choosing Ω_a in such a way to make all $I_a(\Omega_a)$ identically zero. This means in principle to choose a different set of cutoffs for each total

energy, but this aspects will not bother us at all, as with this assumption every reference to cutoffs graciously disappears and the whole problem gets hugely simpler. First of all only the electronic continuum needs to be discretized. Assuming the habitual discretization of the K-matrix system, equations (E.5) and (E.7) become very similar:

$$[1 - \mathsf{VP}(E)]\mathsf{K}_{\bullet,\alpha E} = \mathsf{V}(E)_{\bullet,\alpha E} \tag{E.9}$$

$$[1 - \mathsf{VP}(E)]\mathsf{K}_{\bullet,a\omega} = C\omega^{1/2}\nabla_{\bullet,a} \tag{E.10}$$

In particular, the K matrix between matter channels remains *unchanged* with respect to the case where the fluorescence channels are completely omitted. The other two equations, (E.6) and (E.8), allow to find the other matrix elements:

$$\mathsf{K}_{b\omega,\alpha E} = C\omega^{1/2}\left\{\nabla_{b,\alpha E} + \nabla_{b,\bullet}\mathsf{P}(E)\mathsf{K}_{\bullet,\alpha E}\right\} \tag{E.11}$$

$$\mathsf{K}_{b\omega',a\omega} = C\omega'^{1/2}\nabla_{b,\bullet}\mathsf{P}(E)\mathsf{K}_{\bullet,a\omega} \tag{E.12}$$

The on-shell K-matrix is manifestly symmetric. Simple manipulations shows that

$$\mathsf{K}_{a,b}(E) = C^2(E-E_a)^{1/2}(E-E_b)^{1/2}\nabla_{a,\bullet}\left\{\mathsf{P}(E)^{-1} - \mathsf{V}(E)\right\}^{-1}\nabla_{\bullet,b} \tag{E.13}$$

$$\mathsf{K}_{\alpha E,aE} = C(E-E_a)^{1/2}\mathsf{P}(E)^{-1}_{\alpha E,\bullet}\left\{\mathsf{P}(E)^{-1} - \mathsf{V}(E)\right\}^{-1}\nabla_{\bullet,a} \tag{E.14}$$

$$\mathsf{K}_{aE,\alpha E} = C(E-E_a)^{1/2}\nabla_{a,\bullet}\left\{\mathsf{P}(E)^{-1} - \mathsf{V}(E)\right\}^{-1}\mathsf{P}(E)^{-1}_{\bullet,\alpha E} \tag{E.15}$$

Even if the matter K-matrix is left unchanged, the transition matrices $\mathsf{T}^{\pm}$ *do* change, and so does the scattering matrix S as well as all the resonance widths.

Now we shall consider explicitly the case of one autoionization channel, one fluorescence channel and one discrete state. The unperturbed states are given by the autoionization channel functions $|\epsilon\rangle$ with a total energy ϵ above the autoionization threshold E_{th}, the fluorescence channel $|\omega\rangle$ where it is understood that the state is an atomic state $|a\rangle$ suitably coupled to a dipole photon γ_ω, and the discrete state $|\phi\rangle$:

$$\langle\epsilon|H|\epsilon'\rangle = (E_{th}+\epsilon)\delta(\epsilon-\epsilon'), \quad \langle\phi|H|\phi\rangle = E_\phi, \quad \langle\omega|H|\omega'\rangle = (E_a+\omega)\delta(\omega-\omega')$$

$$\langle\phi|H|\omega\rangle = C\omega^{1/2}\nabla_{\phi a}, \quad \langle\epsilon|H|\omega\rangle = C\omega^{1/2}\nabla_{\epsilon a}, \quad \langle\phi|E-H|\epsilon\rangle = -V_{\phi\epsilon}(E).$$

The two principal part Lippmann Schwinger equations are:

$$|\Psi_E^{\mathcal{P}}\rangle = |E\rangle + |\phi\rangle \frac{\mathcal{P}}{E-E_\phi} K_{\phi E} + \int d\epsilon |\epsilon\rangle \frac{\mathcal{P}}{E-\epsilon} K_{\epsilon E} + \int d\omega' |\omega'\rangle \frac{\mathcal{P}}{E-E_a-\omega'} K_{\omega' E}$$

$$|\Psi_\omega^{\mathcal{P}}\rangle = |\omega\rangle + |\phi\rangle \frac{\mathcal{P}}{E-E_\phi} K_{\phi \omega} + \int d\epsilon |\epsilon\rangle \frac{\mathcal{P}}{E-\epsilon} K_{\epsilon \omega} + \int d\omega' |\omega'\rangle \frac{\mathcal{P}}{E-E_a-\omega'} K_{\omega' \omega}$$

From the projection of the first equation on $(E-H)|E'\rangle$, $(E-H)|\phi\rangle$ and $(E-H)|\omega'\rangle$ we obtain the correspondent following three equations

$$-V_{\phi E} + K_{\phi E} - \int V_{\phi\epsilon} \frac{\mathcal{P}}{E-\epsilon} K_{\epsilon E} - C\nabla_{\phi a} \int \omega^{1/2} \frac{\mathcal{P}}{E-E_a-\omega} K_{\omega E} d\omega = 0$$

$$-V_{E'\phi} \frac{\mathcal{P}}{E-E_\phi} K_{\phi E} + K_{E'E} - C\nabla_{E'a} \int \omega^{1/2} \frac{\mathcal{P}}{E-E_a-\omega} K_{\omega E} d\omega = 0$$

$$-C\omega'^{1/2}\nabla_{aE} - C\omega'^{1/2}\nabla_{a\phi} \frac{\mathcal{P}}{E-E_\phi} K_{\phi E} - C\omega'^{1/2} \int \nabla_{a\epsilon} \frac{\mathcal{P}}{E-\epsilon} K_{\epsilon E} + K_{\omega' E} = 0$$

From the third of these equations we get

$$K_{\omega' E} = C\omega'^{1/2} \left\{ \nabla_{aE} + \nabla_{a\phi} \frac{\mathcal{P}}{E-E_\phi} K_{\phi E} + \int \nabla_{a\epsilon} \frac{\mathcal{P}}{E-\epsilon} K_{\epsilon E} \right\}$$

With the assumption on the cutoff regularization, we can replace $K_{\omega E}$ in the second projected equation to obtain the familiar expression

$$K_{E'E} = V_{E'\phi} \frac{\mathcal{P}}{E-E_\phi} K_{\phi E}$$

and finally, exploiting the first projected equation, we get

$$\frac{\mathcal{P}}{E-E_\phi} K_{\phi E} = \frac{V_{\phi E}}{E-E_\phi-\Delta_\phi}$$

where $\Delta_\phi = \Delta_\phi(E) \equiv \int d\epsilon V_{\phi\epsilon} \frac{\mathcal{P}}{E-\epsilon} V_{\epsilon\phi}$ Thus

$$K_{E'E} = \frac{V_{E'\phi} V_{\phi E}}{E-E_\phi-\Delta_\phi}$$

$$K_{\omega E} = C\omega^{1/2} \left\{ \nabla_{aE} + \left[\nabla_{a\phi} + \int \frac{\nabla_{a\epsilon} V_{\epsilon\phi}}{E-\epsilon} \right] \frac{V_{\phi E}}{E-E_\phi-\Delta_\phi} \right\}$$

We have obtained the autoionization-autoionization and fluorescence-autoionization elements of K-matrix. For the on-shell K-matrix, the autoionization-fluorescence matrix elements are also known since K is real and symmetric, but to obtain the general matrix elements as well as the fluorescence-fluorescence matrix elements we have to apply the same procedure to the second Lippmann-Schwinger equation. The three projected equations are

$$-C\omega^{1/2}\nabla_{\phi a} + K_{\phi\omega} - \int \frac{V_{\phi\epsilon}K_{\epsilon\omega}}{E-\epsilon} - C\nabla_{\phi a}\int \frac{\omega'^{1/2}K_{\omega'\omega}}{\omega-\omega'} = 0$$

$$-C\omega^{1/2}\nabla_{E'a} - V_{E'\phi}\frac{\mathcal{P}}{E-E_\phi}K_{\phi\omega} + K_{E'\omega} - C\nabla_{E'a}\int \frac{\omega'^{1/2}K_{\omega'\omega}}{\omega-\omega'} = 0$$

$$-C\omega'^{1/2}\nabla_{a\phi}\frac{\mathcal{P}}{E-E_\phi}K_{\phi\omega} - C\omega'^{1/2}\int \frac{\nabla_{a\epsilon}K_{\epsilon\omega}}{E-\epsilon} + K_{\omega'\omega} = 0$$

Therefore

$$K_{\omega'\omega} = C\omega'^{1/2}\left\{\nabla_{a\phi}\frac{\mathcal{P}}{E-E_\phi}K_{\phi\omega} + \int \frac{\nabla_{a\epsilon}K_{\epsilon\omega}}{E-\epsilon}\right\}$$

$$K_{E'\omega} = C\omega^{1/2}\nabla_{E'a} + V_{E'\phi}\frac{\mathcal{P}}{E-E_\phi}K_{\phi\omega}$$

$$\frac{\mathcal{P}}{E-E_\phi}K_{\phi\omega} = C\omega^{1/2}\frac{\nabla_{\phi a} + \int \frac{V_{\phi\epsilon}\nabla_{\epsilon a}}{E-\epsilon}}{E-E_\phi-\Delta_\phi}$$

and finally

$$K_{E'\omega} = C\omega^{1/2}\left\{\nabla_{E'a} + \frac{V_{E'\phi}}{E-E_\phi-\Delta_\phi}\left[\nabla_{\phi a} + \int \frac{V_{\phi\epsilon}\nabla_{\epsilon a}}{E-\epsilon}\right]\right\}$$

and

$$K_{\omega'\omega} = C^2(\omega'\omega)^{1/2}\left\{\int \frac{\nabla_{a\epsilon}\nabla_{\epsilon a}}{E-\epsilon} + \frac{\left(\nabla_{a\phi} + \int \frac{\nabla_{a\epsilon}V_{\epsilon\phi}}{E-\epsilon}\right)\left(\nabla_{\phi a} + \int \frac{V_{\phi\epsilon}\nabla_{\epsilon a}}{E-\epsilon}\right)}{E-E_\phi-\Delta_\phi}\right\}$$

Appendix F

Helium doubly excited states

Helium doubly excited states (DES) are those states where both the electrons ere excited out of the inner $1s$ shell. With the exception of unnatural states below N=2 threshold in electrostatic approximation, the DES give rise to autoionizing resonances as their energy is higher than the first He ionization threshold.

Since their observation in the photoionization spectrum of the pioneering experiment by Madden and Codling in 1963 [5] it was apparent that most of them could not be described in terms of a single electronic configuration. In a joint paper Cooper, Fano and Prats [234] proposed the first classification scheme for $^1P^o$ He DES below N=2 threshold in terms of symmetric and antisymmetric linear combinations of configurations $2snp \pm 2pns$, corresponding respectively to the strong and weak peaks in the photoionization spectrum. A third series, with a dominant single configuration $2pnd$, much narrower and weaker than the other two, was observed for the first time only in 1992 by Domke *et al* [16]. Doubly excited states in other symmetries and below higher thresholds cannot be easily reduced to expressions from independent particles approximation schemes. Still the effective principal quantum numbers and reduced widths of such resonances exhibit clear regularities which indicate the possible existence of approximate quantum numbers.

Many efforts were devoted to develop reliable approximated models for the correlated motion of the two electrons. After the pioneering work of Wulfman [235], Herrick, Kellman, Sinanoğlu and Poliak developed group theoretical methods which proved to be useful to interpret resonance widths and intensities. In the Doubly Excited State Basis (DESB), proposed by Herrick and Sinanoglu in 1975 [236], a DES is specified by four approximate quantum numbers, K, T, N, n, beyond the exact ones.

$$|Nn, KTLS\Pi\rangle = \sum_{ll'} |Nl, nl', LS\Pi\rangle D^{KTL\Pi}_{Nl,nl'} \tag{F.1}$$

where

$$\begin{aligned} D^{KTL\Pi}_{Nl,nl'} =& (-1)^{l'} g_\pi M_T \sqrt{(n+K+T)(n+K-T)(2l+1)(2l'+1)} \times \\ & \times \begin{Bmatrix} \frac{1}{2}(N-1) & \frac{1}{2}(n-1) & \frac{1}{2}(n-1+K+T) \\ \frac{1}{2}(N-1) & \frac{1}{2}(n-1) & \frac{1}{2}(n-1+K-T) \\ l & l' & L \end{Bmatrix} \end{aligned} \tag{F.2}$$

$g_\pi = 1$ if $l + l' \sim \Pi$ otherwise $g_\pi = 0$. $M_T = 1$ if $T = 0$ otherwise $M_T = \sqrt{2}$. Many other works on the same line followed [115, 187, 188, 237–240].

K is roughly proportional to $-\cos\theta_{12}$. The larger K, the larger the interelectronic angle, the smaller the energy. For an extensive investigation of this aspect, see Bürgers - 1999 [241]. T measures the angular momentum projection of the inner electron along the interelectronic axis. The problem with this approximation scheme is that yet many different principal quantum numbers n enter in a reliable description of the states.

C. D. Lin [189, 242, 243] proposed an hyperspherical adiabatic approximation where the wavefunction is written in the following form

$$\Psi = F_\mu^n(R)\Phi_\mu(R;\Omega) \tag{F.3}$$

where R and Ω are the hyper-radius and the hyper-angle respectively. The index μ defines a channel: $\mu \equiv \{N, (K,T)^A, L, S, \Pi\}$. K and T are the same as Herrick's. A is a "radial correlation" number, which is ± 1 according to the nodal/antinodal character of the wavefunction at $r_1 = r_2$. $A = 0$ is also allowed to label those states without a clear nodal character. See also the review [244].

In our opinion the clearest (and simplest) classification scheme is provided by the Stark model: when the external electron is very far away from the nucleus, the inner electron experiences an almost constant static field. Its eigenstates are therefore the Stark states, identified by three quantum numbers: N_1, N_2 and m which assign the number of nodes along ξ, η and ϕ coordinates in a parabolic system (see BETHE and SALPETER [107], sec. 6) in which hydrogenic atoms are still separable. In this last scheme the inner principal quantum number is $N = N_1+N_2+m+1$, $T = m$ and $K = N_2-N_1$. The series classification scheme based on Stark quantum numbers completed with the parity index $A = \pm 1$ which originates in the molecular approximation is also called the parabolic notation: $[N_1 N_2 m]^A$. A single term in a series is identified with a last index n for the principal quantum number of the outer electron: $[N_1 N_2 m]_n^A$.

Yet another classification scheme by Feagin and Briggs (1986) [245], maybe the most successful in accounting for the preservation of resonance series character down to very low excitation of the outer electron with respect to the inner one, is provided by the molecular model. In this model the states are expanded on the basis of molecular orbitals for the nucleus in the field of the two electrons, defining a molecular axis analogously as in the H_2^+ molecule.

For a detailed description of the classification schemes, autoionization and photoionization propensity rules see the topical review by Rost, Schulz, Domke and Kaindl [99] and references therein. Nicolaides *et al* - 2002 [246] gave a critical analysis of DES models. See also Bouri *et al* - 2006 [247] on the comparison between parabolic and spherical partial cross sections near He double ionization threshold.

Significant parallels can be drawn with the dynamics of the classical helium atom. Ostrovsky *et al* [248–253] dedicated many effort to the description of the so called planetary states [254]. In (quantum) planetary atoms, both the electrons are highly excited in a metastable state which is analogous to a stable classical

planetary atom configuration. For planetary states, the classification schemes examined above are inapplicable. For a review, see Richter *et al* - 1993 [255] and Tanner *et al* 2000 [256].

Appendix G

Matrix Elements

The celebrated series of papers by Racah on complex atomic spectra, appeared during the forties of the last century [257–260] opened the wide field of interaction between complex atomic configurations.

In particular the first derivation of three electron matrix elements between arbitrary configurations has been given algebraically by Fano, Prats and Goldschmidt [261]. In a later work, Fano introduced a standardized procedure to treat antisymmetrization of electrons in different shells and investigated satisfactorily most of the simplifications in the calculation of matrix elements [204].

Significant improvements may be obtained with the support of the graphical method, which has been used extensively by several authors from a general point of view. A general computer program to evaluate recoupling coefficients of arbitrary complexity has also been written more than 35 years ago by Burke [262]. Other relevant contributions came from Hibbert [263–265]. For a review on this topics see Briggs [266] and references therein. There are still improvements in this field, mainly in the production of efficient algorithms. See for example [267]

Even though, in the works cited thus far, recoupling coefficients and highly efficient methods have been developed, they rely heavily on subshell orthogonality and ordering. In the present work, where highly correlated systems of very few electrons are considered, it was found convenient to derive anew all formulas without the orthogonality restriction to fully take advantage of spline superposition properties and to treat on equal footing those configurations obtained through the coupling of an arbitrary spherical wave to a CI target. Matrix elements of monoelectronic tensor operators of arbitrary rank and electron-electron Coulomb repulsion are considered.

In what follows we shall consider explicitly the derivation of formulas in two and three electron systems for single particle operators of arbitrary rank and electron-electron coulomb repulsion. Prior to spin coupling and antisymmetrization, the

coupled spatial wavefunctions are written as

$$N=2 \;:\; \sum_{m_1 m_2} C^{LM}_{l_1 m_1, l_2 m_2} \phi_{n_1 l_1 m_1}(1) \phi_{n_2 l_2 m_2}(2) \tag{G.1}$$

$$N=3 \;:\; \sum_{m_1 m_2 m_3 M_\alpha} C^{LM}_{L_\alpha M_\alpha, l_3 m_3} C^{L_\alpha M_\alpha}_{l_1 m_1, l_2 m_2} \phi_{n_1 l_1 m_1}(1) \phi_{n_2 l_2 m_2}(2) \phi_{n_3 l_3 m_3}(3) \tag{G.2}$$

Contraction with configuration interaction coefficients, when present, will be considered separately. A prime to bra indexes will be added to distinguish them from ket indexes.

In the following it will appear that phase factors depends only on the naturality of some of the various subsystems or of the transition operator. Naturality[1] of subsystem α will be indicated with the symbol $\mathcal{N}_\alpha$.

G.1 Graphical rules for angular momentum theory

This section summarizes the basic graphical rules to deal with algebraic expressions in quantum angular momentum theory. The treatment will be limited to integer angular momenta (all phase factors of the form $(-)^{2j}$ are ignored) and to those relations strictly needed to follow diagram manipulations in this chapter. We adopt the conventions of Varshalovich, Moskalev and Khersonskii [216].

A $|jm\rangle$ state (ket) and the corresponding functional $\langle lm|$ (bra) are represented with the following two arrows:

the $3-jm$ symbol is represented with three $jm-$lines coming out from a common node:

$$\begin{pmatrix} a & b & c \\ \alpha & \beta & \gamma \end{pmatrix}$$

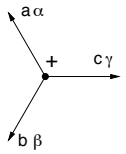

Direction of external $jm-$lines in a diagram can be inverted with the multiplication by the phase factor $(-1)^{j-m}$

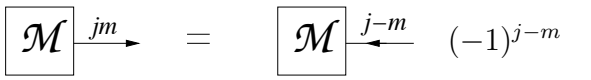

The sign of a node can be inverted with the multiplication by the phase factor $(-1)^{a+b+c}$ where a, b, c are the angular momenta connected to the node.

[1] An irreducible representation of $O(3)$ is called natural (naturality 0) if its parity is that of its angular momentum, otherwise it is called unnatural (naturality 1).

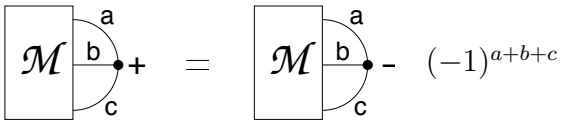

Summation over magnetic indexes of an outgoing bra (ket) and an ingoing ket (bra) jm lines is replaced with a continuous $j-$line:

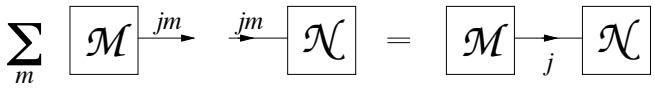

The orientations of internal lines (that is lines which connect two nodes) are irrelevant. Therefore they will be omitted unless they are thought to be useful to follow diagram manipulation. Moreover, lines with 0 angular momentum can be cancelled (residual nodes on a $j-$line are equivalent to a $1/\sqrt{2j+1}$ factor)

Summation over angular momenta J of internal lines multiplied by $(2J+1)$ are common and are indicated with a thicker internal line:

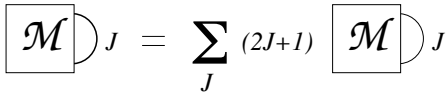

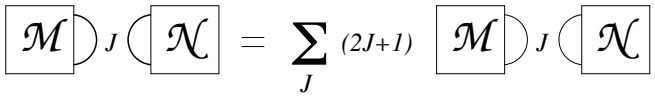

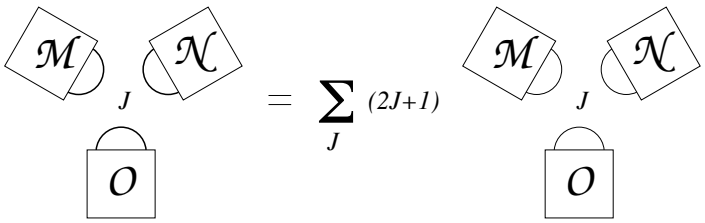

A summation over J in a single diagram can be eliminated when the couples of the other angular momenta which converge to the two nodes are identical

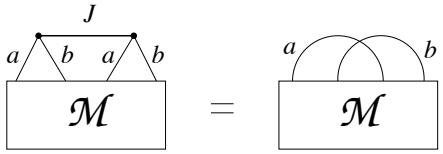

Given the previous rules some simple diagrams follow:

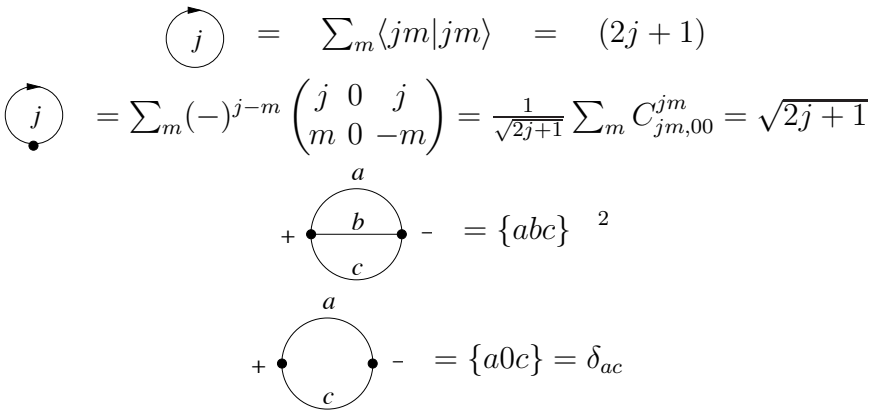

Clebsch Gordan coefficients, $6j$ symbols and $9j$ symbols have the following graphical representation:

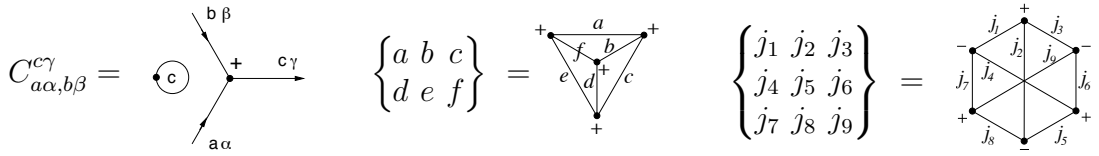

Connection and disconnection of diagrams Diagrams can be disconnected or recoupled according to the following rules, provided at least one of the subdiagrams have no external lines:

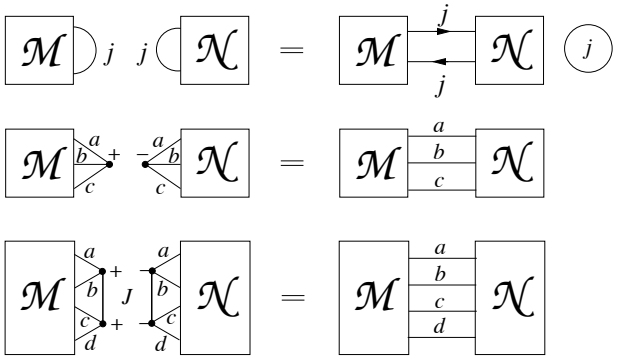

Coupling of more than two electrons The contracted product of two Clebsh Gordan coefficients in the three electron expression can be written down as a diagram (fig G.1).

$$\sum_{M_\alpha} C^{LM}_{L_\alpha M_\alpha, l_3 m_3} C^{L_\alpha M_\alpha}_{l_1 m_1, l_2 m_2} =$$

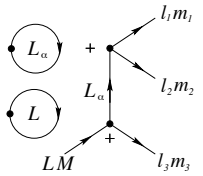

[2] $\{abc\} = 1$ if triangular inequalities are satisfied, $\{abc\} = 0$ otherwise.

G.2 Single particle operators

Let us consider a single particle operator of rank T:

$$\langle \phi_{\alpha,\ell' m'} | o_{T\tau} | \phi_{\beta,\ell m} \rangle = \frac{C^{\ell' m'}_{\ell m, T\tau}}{\sqrt{2\ell'+1}} \langle \phi_{\alpha,\ell'} \| o_T \| \phi_{\beta,\ell} \rangle \tag{G.3}$$

Zero particle (metric) and one particle zero-rank operators (electron kinetic energy and electron-nucleus attraction) are obtained easily setting to zero the parity and angular momentum of the transition operator. Examples of multipolar terms of higher rank (electric and magnetic dipole, electric quadrupole, ecc.) are examined in appendix B

G.2.1 Two-electron systems

The general expression to be computed can be written in a diagram as

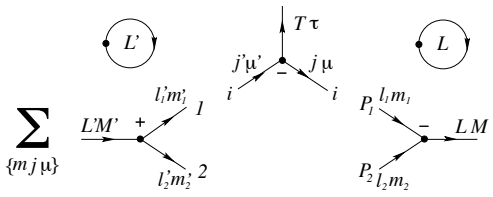

- $o(1)$

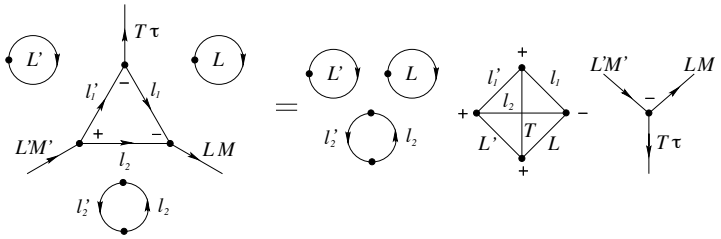

$$\langle [\phi'_1 \otimes \phi'_2] | o_{T\tau}(1) \hat{E} | [\phi_1 \otimes \phi_2] \rangle = \langle \phi'_1 \| o_T \| \phi_1 \rangle \langle \phi'_2 | \phi_2 \rangle \delta_{l_2 l'_2} \Pi_L (-)^{\mathcal{N}+\mathcal{N}_o} \begin{Bmatrix} L & T & L' \\ l'_1 & l_2 & l_1 \end{Bmatrix} C^{L'M'}_{LM,T\tau}$$

- $o(1)\mathcal{P}_{12}$

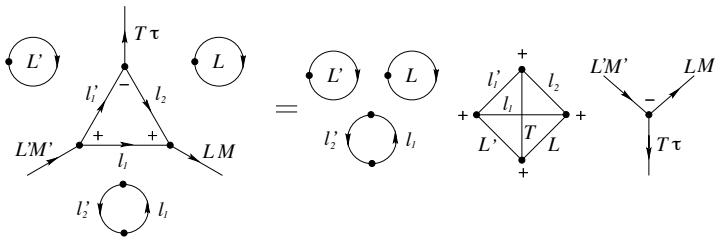

$$\langle [\phi'_1 \otimes \phi'_2] | o_{T\tau}(1) \mathcal{P}_{12} | [\phi_1 \otimes \phi_2] \rangle = \langle \phi'_1 \| o_T \| \phi_2 \rangle \langle \phi'_2 | \phi_1 \rangle \delta_{l_1 l'_2} \Pi_L (-)^{\mathcal{N}_o} \begin{Bmatrix} L & T & L' \\ l'_1 & l_1 & l_2 \end{Bmatrix} C^{L'M'}_{LM,T\tau}$$

- $o(2)$

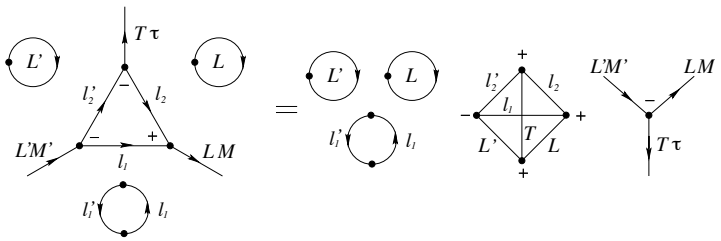

$$\langle[\phi_1'\otimes\phi_2']|o_{T\tau}(2)\hat{E}|[\phi_1\otimes\phi_2]\rangle = \langle\phi_1'|\phi_1\rangle\langle\phi_2'\|o_T\|\phi_2\rangle\delta_{l_1l_1'}\Pi_L(-)^{\mathcal{N}'+\mathcal{N}_o}\begin{Bmatrix} L & T & L' \\ l_2' & l_1 & l_2 \end{Bmatrix} C^{L'M'}_{LM,T\tau}$$

- $o(2)\mathcal{P}_{12}$

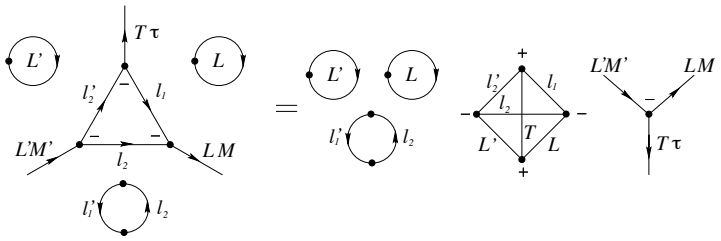

$$\langle[\phi_1'\otimes\phi_2']|o_{T\tau}(2)\mathcal{P}_{12}|[\phi_1\otimes\phi_2]\rangle = \langle\phi_1'|\phi_2\rangle\langle\phi_2'\|o_T\|\phi_1\rangle\delta_{l_2l_1'}\Pi_L(-)^{\mathcal{N}+\mathcal{N}'+\mathcal{N}_o}\begin{Bmatrix} L & T & L' \\ l_2' & l_2 & l_1 \end{Bmatrix} C^{L'M'}_{LM,T\tau}$$

G.2.2 Three-electron systems

The contraction to be performed is the following

$$\sum_{\substack{\{mj\mu\}\\ M_\alpha M_\beta}} C^{L_\alpha M_\alpha}_{l_1'm_1',l_2'm_2'} C^{L'M'}_{L_\alpha M_\alpha,l_3'm_3'} \delta_{m_i'\mu'}\delta_{l_ij'} \frac{C^{j'\mu'}_{j\mu,T\tau}}{\sqrt{2j'+1}} \delta_{\mu m_{\mathcal{P}_i}}\delta_{jl_{\mathcal{P}_i}} C^{L_\beta M_\beta}_{l_1m_1,l_2m_2} C^{LM}_{L_\beta M_\beta,l_3m_3} \delta_{m_{i'}',m_{\mathcal{P}_{i'}}}\delta_{m_{i''}',m_{\mathcal{P}_{i''}}} \tag{G.4}$$

where we have indicated with i' and i'' the two indexes other than that of the variable on which the transition operator acts. This expression can be reproduced in the following diagram where the bare numbers near edges of inner segments define the contraction scheme according to which operator and which permutation are considered.

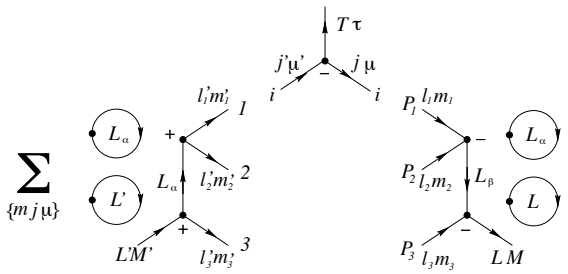

- $o(1)$

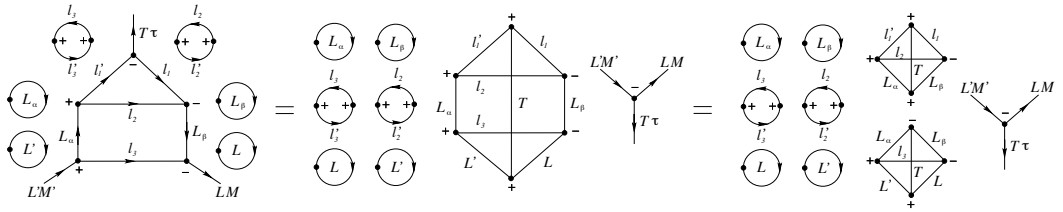

$$\langle[[\phi'_1\otimes\phi'_2]\otimes\phi'_3]|o_{T\tau}(1)\hat{E}|[[\phi_1\otimes\phi_2]\otimes\phi_3]\rangle=\langle\phi'_1\|o_T\|\phi_1\rangle\langle\phi'_2|\phi_2\rangle\langle\phi'_3|\phi_3\rangle\times$$
$$\times\delta_{l_2l'_2}\delta_{l_3l'_3}(-)^{\mathcal{N}_\alpha+\mathcal{N}_\beta+\mathcal{N}}\Pi_{L_\alpha L_\beta L}\begin{Bmatrix}L_\alpha & L_\beta & T\\ l_1 & l'_1 & l_2\end{Bmatrix}\begin{Bmatrix}L & T & L'\\ L_\alpha & l_3 & L_\beta\end{Bmatrix}C^{L'M'}_{LM,T\tau}$$

- $o(1)\mathcal{P}_{13}$

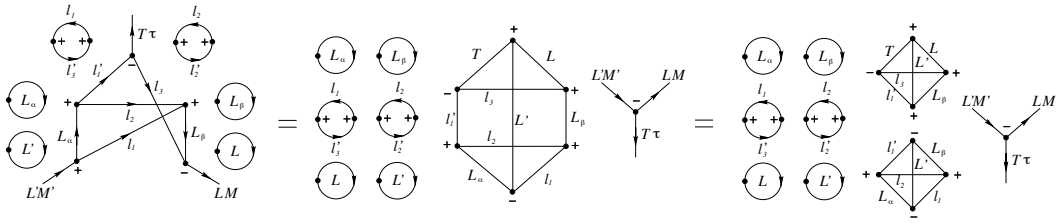

$$\langle[[\phi'_1\otimes\phi'_2]\otimes\phi'_3]|o_{T\tau}(1)\mathcal{P}_{13}|[[\phi_1\otimes\phi_2]\otimes\phi_3]\rangle=\langle\phi'_1\|o_T\|\phi_3\rangle\langle\phi'_2|\phi_2\rangle\langle\phi'_3|\phi_1\rangle\times$$
$$\times\delta_{l_2l'_2}\delta_{l_1l'_3}(-)^{\mathcal{N}_\beta+\mathcal{N}_o+\mathcal{N}'}\Pi_{L_\alpha L_\beta L}\begin{Bmatrix}l_1 & l_2 & L_\beta\\ l'_1 & L' & L_\alpha\end{Bmatrix}\begin{Bmatrix}L & T & L'\\ l'_1 & L_\beta & l_3\end{Bmatrix}C^{L'M'}_{LM,T\tau}$$

- $o(1)\mathcal{P}_{23}$

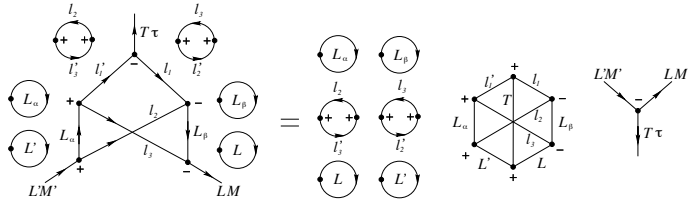

$$\langle[[\phi'_1\otimes\phi'_2]\otimes\phi'_3]|o_{T\tau}(1)\mathcal{P}_{23}|[[\phi_1\otimes\phi_2]\otimes\phi_3]\rangle=\langle\phi'_1\|o_T\|\phi_1\rangle\langle\phi'_2|\phi_3\rangle\langle\phi'_3|\phi_2\rangle\times$$
$$\times\delta_{l_2l'_3}\delta_{l_3l'_2}(-)^{\mathcal{N}_\alpha+\mathcal{N}_\beta+\mathcal{N}}\Pi_{L_\alpha L_\beta L}\begin{Bmatrix}L & T & L'\\ l_3 & l'_1 & L_\alpha\\ L_\beta & l_1 & l_2\end{Bmatrix}C^{L'M'}_{LM,T\tau}$$

- $o(1)\mathcal{P}_{12}$

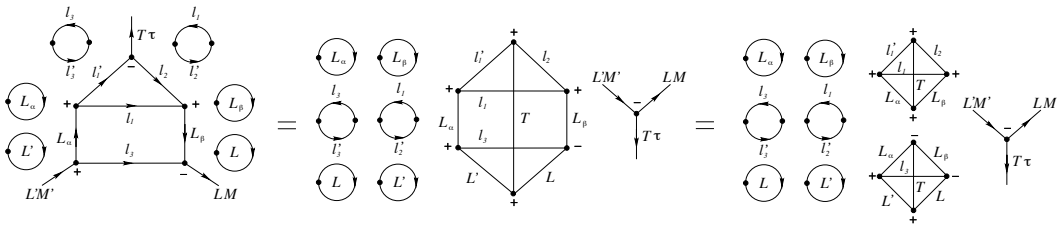

$$\langle[[\phi_1'\otimes\phi_2']\otimes\phi_3']|o_{T\tau}(1)\mathcal{P}_{12}|[[\phi_1\otimes\phi_2]\otimes\phi_3]\rangle = \langle\phi_1'\|o_T\|\phi_2\rangle\langle\phi_2'|\phi_1\rangle\langle\phi_3'|\phi_3\rangle\times$$
$$\times\delta_{l_3l_3'}\delta_{l_1l_2'}(-)^{\mathcal{N}_\alpha+\mathcal{N}}\Pi_{L_\alpha L_\beta L}\begin{Bmatrix}L_\alpha & T & L_\beta\\ l_2 & l_1 & l_1'\end{Bmatrix}\begin{Bmatrix}L & T & L'\\ L_\alpha & l_3 & L_\beta\end{Bmatrix}C^{L'M'}_{LM,T\tau}$$

- $o(1)\mathcal{P}_{123}$

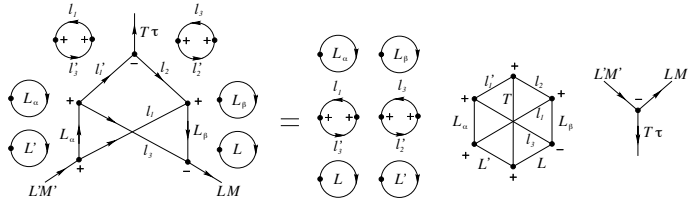

$$\langle[[\phi_1'\otimes\phi_2']\otimes\phi_3']|o_{T\tau}(1)\mathcal{P}_{123}|[[\phi_1\otimes\phi_2]\otimes\phi_3]\rangle = \langle\phi_1'\|o_T\|\phi_2\rangle\langle\phi_2'|\phi_3\rangle\langle\phi_3'|\phi_1\rangle\times$$
$$\times\delta_{l_1l_3'}\delta_{l_3l_2'}(-)^{\mathcal{N}+\mathcal{N}_\alpha}\Pi_{L_\alpha L_\beta L}\begin{Bmatrix}L & T & L'\\ l_3 & l_1' & L_\alpha\\ L_\beta & l_2 & l_1\end{Bmatrix}C^{L'M'}_{LM,T\tau}$$

- $o(1)\mathcal{P}_{321}$

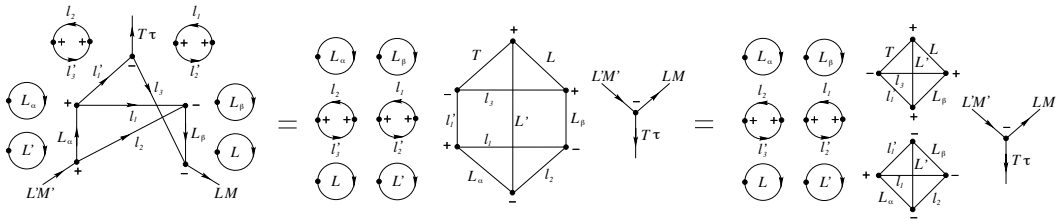

$$\langle[[\phi_1'\otimes\phi_2']\otimes\phi_3']|o_{T\tau}(1)\mathcal{P}_{321}|[[\phi_1\otimes\phi_2]\otimes\phi_3]\rangle = \langle\phi_1'\|o_T\|\phi_3\rangle\langle\phi_2'|\phi_1\rangle\langle\phi_3'|\phi_2\rangle\times$$
$$\times\delta_{l_2l_3'}\delta_{l_1l_2'}(-)^{\mathcal{N}_o+\mathcal{N}'}\Pi_{L_\alpha L_\beta L}\begin{Bmatrix}L_\alpha & l_1 & l_1'\\ L_\beta & L' & l_2\end{Bmatrix}\begin{Bmatrix}L & T & L'\\ l_1' & L_\beta & l_3\end{Bmatrix}C^{L'M'}_{LM,T\tau}$$

- $o(2)$

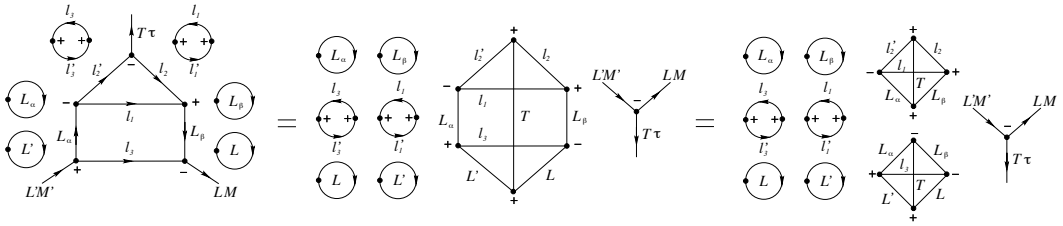

$$\langle[[\phi_1'\otimes\phi_2']\otimes\phi_3']|o_{T\tau}(2)\hat{E}|[[\phi_1\otimes\phi_2]\otimes\phi_3]\rangle = \langle\phi_1'|\phi_1\rangle\langle\phi_2'\|o_T\|\phi_2\rangle\langle\phi_3'|\phi_3\rangle\times$$
$$\times\delta_{l_1l_1'}\delta_{l_3l_3'}(-)^{\mathcal{N}}\Pi_{L_\alpha L_\beta L}\begin{Bmatrix}L_\alpha & L_\beta & T\\ l_2 & l_2' & l_1\end{Bmatrix}\begin{Bmatrix}L & T & L'\\ L_\alpha & l_3 & L_\beta\end{Bmatrix}C^{L'M'}_{LM,T\tau}$$

- $o(2)\mathcal{P}_{13}$

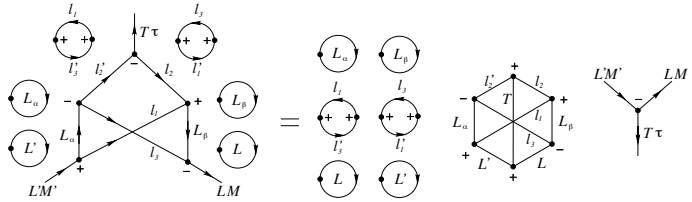

$$\langle[[\phi'_1\otimes\phi'_2]\otimes\phi'_3]|o_{T\tau}(2)\mathcal{P}_{13}|[[\phi_1\otimes\phi_2]\otimes\phi_3]\rangle=\langle\phi'_1|\phi_3\rangle\langle\phi'_2\|o_T\|\phi_2\rangle\langle\phi'_3|\phi_1\rangle\times$$
$$\times\delta_{l_1l'_3}\delta_{l_3l'_1}(-)^{\mathcal{N}}\Pi_{L_\alpha L_\beta L}\begin{Bmatrix}L & T & L'\\ l_3 & l'_2 & L_\alpha\\ L_\beta & l_2 & l_1\end{Bmatrix}C^{L'M'}_{LM,T\tau}$$

- $o(2)\mathcal{P}_{23}$

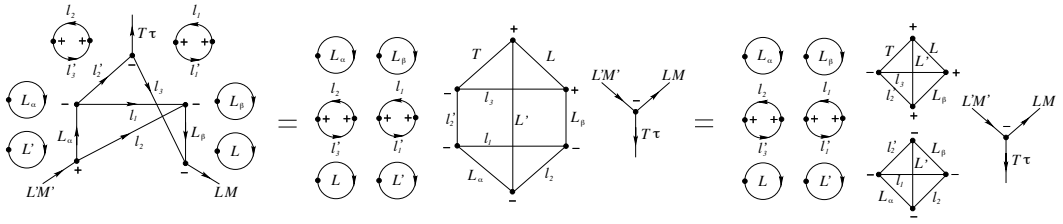

$$\langle[[\phi'_1\otimes\phi'_2]\otimes\phi'_3]|o_{T\tau}(2)\mathcal{P}_{23}|[[\phi_1\otimes\phi_2]\otimes\phi_3]\rangle=\langle\phi'_1|\phi_1\rangle\langle\phi'_2\|o_T\|\phi_3\rangle\langle\phi'_3|\phi_2\rangle\times$$
$$\times\delta_{l_2l'_3}\delta_{l_1l'_1}(-)^{\mathcal{N}'+\mathcal{N}_o+\mathcal{N}_\alpha}\Pi_{L_\alpha L_\beta L}\begin{Bmatrix}l_1 & l_2 & L_\beta\\ L' & l'_2 & L_\alpha\end{Bmatrix}\begin{Bmatrix}L & T & L'\\ l'_2 & L_\beta & l_3\end{Bmatrix}C^{L'M'}_{LM,T\tau}$$

- $o(2)\mathcal{P}_{12}$

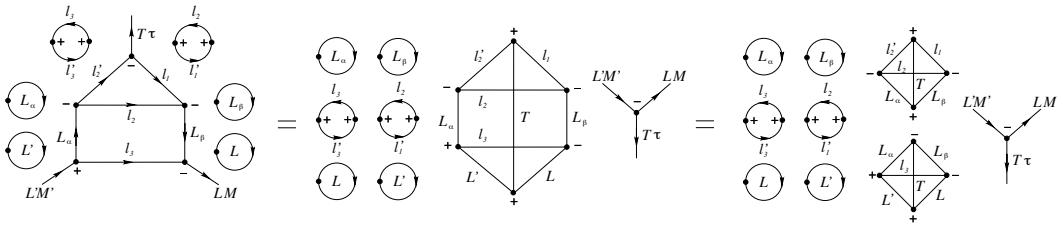

$$\langle[[\phi'_1\otimes\phi'_2]\otimes\phi'_3]|o_{T\tau}(2)\mathcal{P}_{12}|[[\phi_1\otimes\phi_2]\otimes\phi_3]\rangle=\langle\phi'_1|\phi_2\rangle\langle\phi'_2\|o_T\|\phi_1\rangle\langle\phi'_3|\phi_3\rangle\times$$
$$\times\delta_{l_3l'_3}\delta_{l_2l'_1}(-)^{\mathcal{N}+\mathcal{N}_\beta}\Pi_{L_\alpha L_\beta L}\begin{Bmatrix}L_\beta & T & L_\alpha\\ l'_2 & l_2 & l_1\end{Bmatrix}\begin{Bmatrix}L & T & L'\\ L_\alpha & l_3 & L_\beta\end{Bmatrix}C^{L'M'}_{LM,T\tau}$$

- $o(2)\mathcal{P}_{123}$

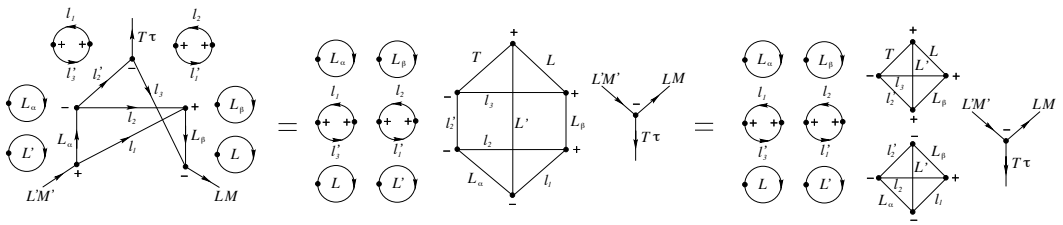

$$\langle[[\phi_1'\otimes\phi_2']\otimes\phi_3']|o_{T\tau}(2)\mathcal{P}_{123}|[[\phi_1\otimes\phi_2]\otimes\phi_3]\rangle = \langle\phi_1'|\phi_2\rangle\langle\phi_2'\|o_T\|\phi_3\rangle\langle\phi_3'|\phi_1\rangle\times$$
$$\times\delta_{l_1l_3'}\delta_{l_2l_1'}(-)^{\mathcal{N}_\alpha+\mathcal{N}_\beta+\mathcal{N}_o+\mathcal{N}'}\Pi_{L_\alpha L_\beta L}\begin{Bmatrix} l_1 & l_2 & L_\beta \\ l_2' & L' & L_\alpha\end{Bmatrix}\begin{Bmatrix} L & T & L' \\ l_2' & L_\beta & l_3\end{Bmatrix}C^{L'M'}_{LM,T\tau}$$

- $o(2)\mathcal{P}_{321}$

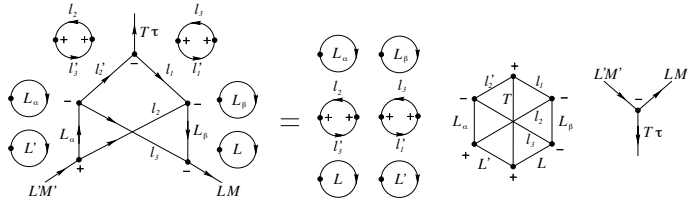

$$\langle[[\phi_1'\otimes\phi_2']\otimes\phi_3']|o_{T\tau}(2)\mathcal{P}_{321}|[[\phi_1\otimes\phi_2]\otimes\phi_3]\rangle = \langle\phi_1'|\phi_3\rangle\langle\phi_2'\|o_T\|\phi_1\rangle\langle\phi_3'|\phi_2\rangle\times$$
$$\times\delta_{l_2l_3'}\delta_{l_3l_1'}(-)^{\mathcal{N}+\mathcal{N}_\beta}\Pi_{L_\alpha L_\beta L}\begin{Bmatrix} L & T & L' \\ l_3 & l_2' & L_\alpha \\ L_\beta & l_1 & l_2\end{Bmatrix}C^{L'M'}_{LM,T\tau}$$

- $o(3)$

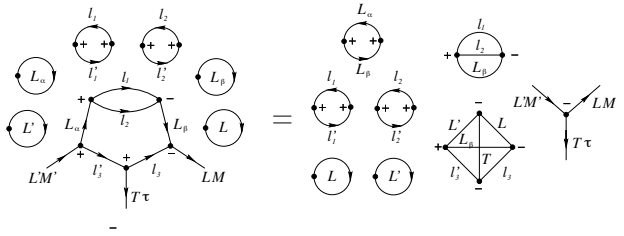

$$\langle[[\phi_1'\otimes\phi_2']\otimes\phi_3']|o_{T\tau}(3)\hat{E}|[[\phi_1\otimes\phi_2]\otimes\phi_3]\rangle = \langle\phi_1'|\phi_1\rangle\langle\phi_2'|\phi_2\rangle\langle\phi_3'\|o_T\|\phi_3\rangle\times$$
$$\times\delta_{l_1l_1'}\delta_{l_2l_2'}\delta_{L_\alpha L_\beta}(-)^{\mathcal{N}'+\mathcal{N}_\alpha+\mathcal{N}_o}\Pi_L\{l_1l_2L_\beta\}\begin{Bmatrix} L & T & L' \\ l_3' & L_\beta & l_3\end{Bmatrix}C^{L'M'}_{LM,T\tau}$$

- $o(3)\mathcal{P}_{13}$

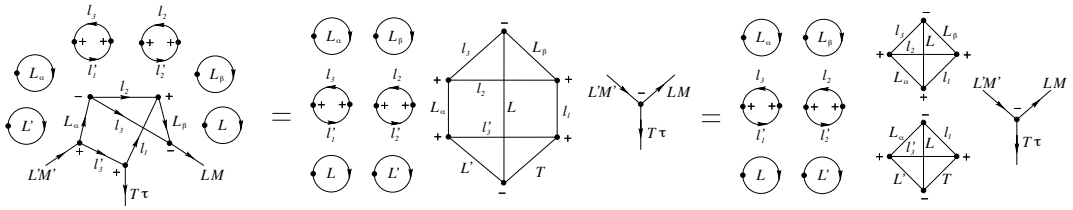

$$\langle[[\phi_1'\otimes\phi_2']\otimes\phi_3']|o_{T\tau}(3)\mathcal{P}_{13}|[[\phi_1\otimes\phi_2]\otimes\phi_3]\rangle = \langle\phi_1'|\phi_3\rangle\langle\phi_2'|\phi_2\rangle\langle\phi_3'\|o_T\|\phi_1\rangle\times$$
$$\times\delta_{l_2l_2'}\delta_{l_3l_1'}(-)^{\mathcal{N}_\alpha+\mathcal{N}'+\mathcal{N}_o}\Pi_{L_\alpha L_\beta L}\begin{Bmatrix} l_1 & l_2 & L_\beta \\ l_3 & L & L_\alpha\end{Bmatrix}\begin{Bmatrix} L & T & L' \\ l_3' & L_\alpha & l_1\end{Bmatrix}C^{L'M'}_{LM,T\tau}$$

- $o(3)\mathcal{P}_{23}$

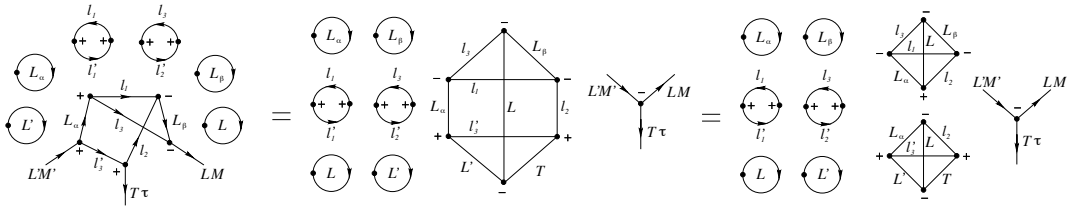

$$\langle[[\phi_1'\otimes\phi_2']\otimes\phi_3']|o_{T\tau}(3)\mathcal{P}_{23}|[[\phi_1\otimes\phi_2]\otimes\phi_3]\rangle=\langle\phi_1'|\phi_1\rangle\langle\phi_2'|\phi_3\rangle\langle\phi_3'\|o_T\|\phi_2\rangle\times$$
$$\times\delta_{l_1l_1'}\delta_{l_3l_2'}(-)^{\mathcal{N}_o+\mathcal{N}'+\mathcal{N}_\beta}\Pi_{L_\alpha L_\beta L}\begin{Bmatrix}l_1 & l_2 & L_\beta\\ L & l_3 & L_\alpha\end{Bmatrix}\begin{Bmatrix}L & T & L'\\ l_3' & L_\alpha & l_2\end{Bmatrix}C^{L'M'}_{LM,T\tau}$$

- $o(3)\mathcal{P}_{12}$

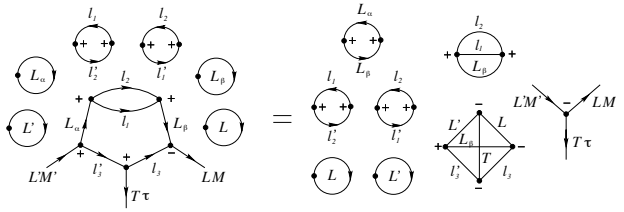

$$\langle[[\phi_1'\otimes\phi_2']\otimes\phi_3']|o_{T\tau}(3)\mathcal{P}_{12}|[[\phi_1\otimes\phi_2]\otimes\phi_3]\rangle=\langle\phi_1'|\phi_2\rangle\langle\phi_2'|\phi_1\rangle\langle\phi_3'\|o_T\|\phi_3\rangle\times$$
$$\times\delta_{l_1l_2'}\delta_{l_2l_1'}\delta_{L_\alpha L_\beta}(-)^{\mathcal{N}'}\Pi_L\{l_1l_2L_\beta\}\begin{Bmatrix}L & T & L'\\ l_3' & L_\beta & l_3\end{Bmatrix}C^{L'M'}_{LM,T\tau}$$

- $o(3)\mathcal{P}_{123}$

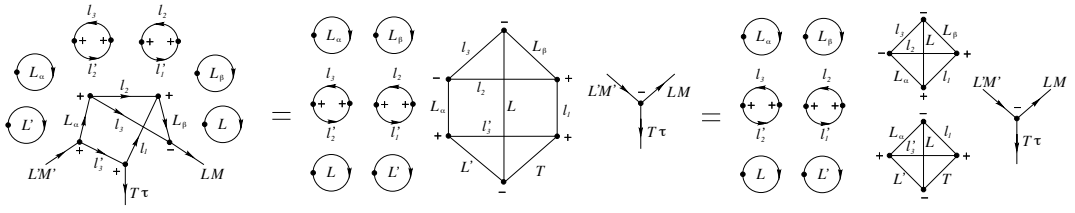

$$\langle[[\phi_1'\otimes\phi_2']\otimes\phi_3']|o_{T\tau}(3)\mathcal{P}_{123}|[[\phi_1\otimes\phi_2]\otimes\phi_3]\rangle=\langle\phi_1'|\phi_2\rangle\langle\phi_2'|\phi_3\rangle\langle\phi_3'\|o_T\|\phi_1\rangle\times$$
$$\times\delta_{l_2l_1'}\delta_{l_3l_2'}(-)^{\mathcal{N}_o+\mathcal{N}'}\Pi_{L_\alpha L_\beta L}\begin{Bmatrix}l_1 & l_2 & L_\beta\\ l_3 & L & L_\alpha\end{Bmatrix}\begin{Bmatrix}L & T & L'\\ l_3' & L_\alpha & l_1\end{Bmatrix}C^{L'M'}_{LM,T\tau}$$

- $o(3)\mathcal{P}_{321}$

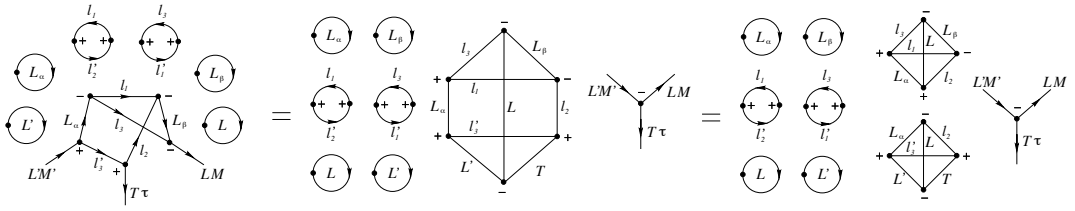

$$\langle[[\phi_1'\otimes\phi_2']\otimes\phi_3']|o_{T\tau}(3)\mathcal{P}_{321}|[[\phi_1\otimes\phi_2]\otimes\phi_3]\rangle=\langle\phi_1'|\phi_3\rangle\langle\phi_2'|\phi_1\rangle\langle\phi_3'\|o_T\|\phi_2\rangle\times$$
$$\times\delta_{l_3l_1'}\delta_{l_1l_2'}(-)^{\mathcal{N}_\alpha+\mathcal{N}_\beta+\mathcal{N}'+\mathcal{N}_o}\Pi_{L_\alpha L_\beta L}\begin{Bmatrix}l_1 & l_2 & L_\beta\\ L & l_3 & L_\alpha\end{Bmatrix}\begin{Bmatrix}L & T & L'\\ l_3' & L_\alpha & l_2\end{Bmatrix}C^{L'M'}_{LM,T\tau}$$

G.3 Two particle operators: e-e Coulomb repulsion

The diagrammatic representation of interelectronic repulsion multipolar expansion is readily derived

$$\frac{1}{r_{12}} = \sum_{l=0}^{\infty} g_l(1,2) \tag{G.5}$$

$$g_l(1,2) = \sum_{m=-l}^{l} \frac{4\pi}{2l+1} \frac{r_<^l}{r_>^{l+1}} Y_{lm}^*(\hat{r}_1) Y_{lm}(\hat{r}_2) \tag{G.6}$$

$$\langle \phi_1' \phi_2' | g_l(1,2) | \phi_1 \phi_2 \rangle = \sum_m \frac{4\pi}{2l+1} \langle Y_{l_1' m_1'} Y_{lm} | Y_{l_1 m_1} \rangle \langle Y_{l_2' m_2'} | Y_{lm} Y_{l_2 m_2} \rangle \langle \phi_1' \phi_2' | \phi_1 \phi_2 \rangle_l =$$

$$= (-)^{\Pi+l} \, \Pi_{l_1 l_2 l_1' l_2'} \begin{pmatrix} l & l_2 & l_2' \\ 0 & 0 & 0 \end{pmatrix} \begin{pmatrix} l_1' & l & l_1 \\ 0 & 0 & 0 \end{pmatrix} \langle \phi_1' \phi_2' | \phi_1 \phi_2 \rangle_l$$

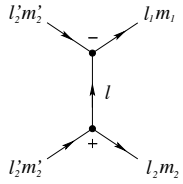

$$=$$

$$= \{ \phi_1' \phi_2' | \phi_1 \phi_2 \}_l$$

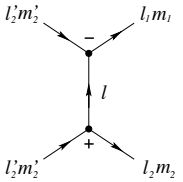

Please note that the sign at nodes are here irrelevant, since both l_1, l_1', l and l_2, l_2', l sum to even parity. Moreover, since either l_i or l_i' is incoming and the other is outgoing, also the direction of l-line is irrelevant. From the point of view of angular momenta, the bielectronic interaction is equivalent to the emission and reabsorption of a mock particle (once known with the unlucky name of "orbiton") with angular momentum l [261].

G.3.1 Two-electron systems

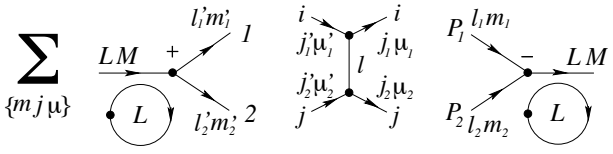

- $g(1,2)$

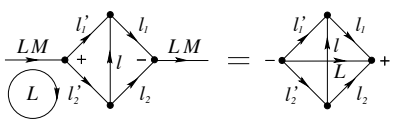

$$\langle[\phi_1'\otimes\phi_2']|g_l(1,2)\hat{E}|[\phi_1\otimes\phi_2]\rangle = \{\phi_1'\phi_2'|\phi_1\phi_2\}_l(-)^{\mathcal{N}}\begin{Bmatrix} l_1' & l_2' & L \\ l_2 & l_1 & l \end{Bmatrix}$$

- $g(1,2)\mathcal{P}_{12}$

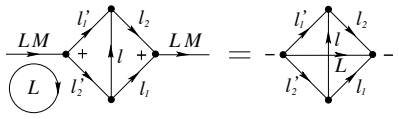

$$\langle[\phi_1'\otimes\phi_2']|g_l(1,2)\mathcal{P}_{12}|[\phi_1\otimes\phi_2]\rangle = \{\phi_1'\phi_2'|\phi_2\phi_1\}_l(-)^{\mathcal{N}}\begin{Bmatrix} l_1' & l_2' & L \\ l_1 & l_2 & l \end{Bmatrix}$$

G.3.2 Three-electron systems

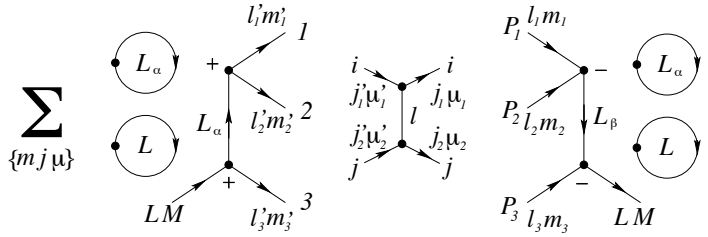

- $g(2,3)$

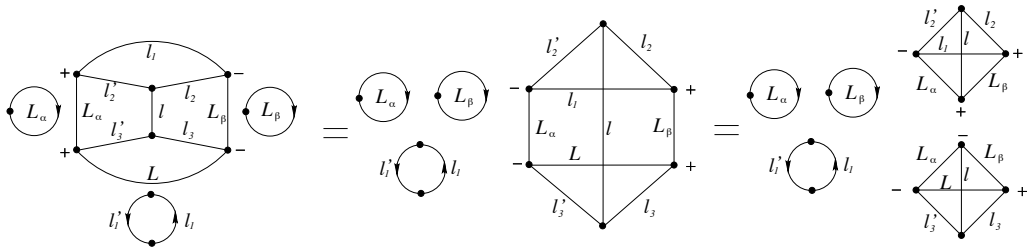

$$\langle[[\phi_1'\otimes\phi_2']\otimes\phi_3']|g_l(2,3)\hat{E}|[[\phi_1\otimes\phi_2]\otimes\phi_3]\rangle = \langle\phi_1'|\phi_1\rangle\{\phi_2'\phi_3'|\phi_2\phi_3\}_l\times$$
$$\times\delta_{l_1l_1'}(-)^{\mathcal{N}+\mathcal{N}_\alpha+\mathcal{N}_\beta}\Pi_{L_\alpha L_\beta}\begin{Bmatrix} L_\alpha & l & L_\beta \\ l_2 & l_1 & l_2' \end{Bmatrix}\begin{Bmatrix} L_\alpha & l & L_\beta \\ l_3 & L & l_3' \end{Bmatrix}$$

- $g(2,3)\mathcal{P}_{13}$

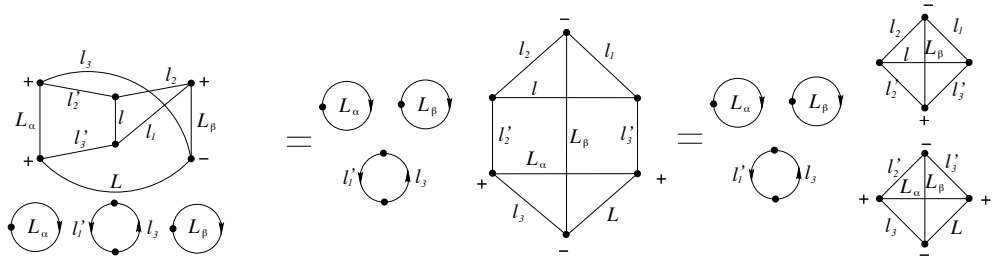

$$\langle[[\phi_1'\otimes\phi_2']\otimes\phi_3']|g_l(2,3)\mathcal{P}_{13}|[[\phi_1\otimes\phi_2]\otimes\phi_3]\rangle = \langle\phi_1'|\phi_3\rangle\{\phi_2'\phi_3'|\phi_2\phi_1\}_l\times$$
$$\times\delta_{l_3l_1'}(-)^{\mathcal{N}_\beta}\Pi_{L_\alpha L_\beta}\begin{Bmatrix} l_2' & l & l_2 \\ l_1 & L_\beta & l_3' \end{Bmatrix}\begin{Bmatrix} l_3' & L_\alpha & L \\ l_3 & L_\beta & l_2' \end{Bmatrix}$$

- $g(2,3)\mathcal{P}_{23}$

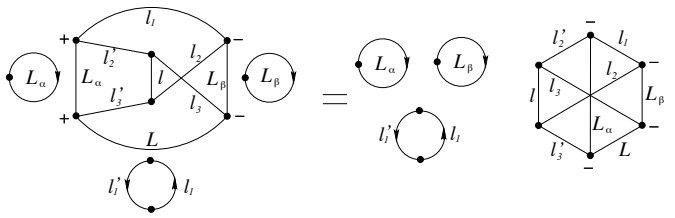

$$\langle[[\phi'_1\otimes\phi'_2]\otimes\phi'_3]|g_l(2,3)\mathcal{P}_{23}|[[\phi_1\otimes\phi_2]\otimes\phi_3]\rangle=\langle\phi'_1|\phi_1\rangle\{\phi'_2\phi'_3|\phi_3\phi_2\}_l\times$$
$$\times\delta_{l_1l'_1}(-)^{\mathcal{N}+\mathcal{N}_\alpha+\mathcal{N}_\beta}\Pi_{L_\alpha L_\beta}\begin{Bmatrix}L_\beta & l_3 & L\\ l_2 & l & l'_3\\ l_1 & l'_2 & L_\alpha\end{Bmatrix}$$

- $g(2,3)\mathcal{P}_{12}$

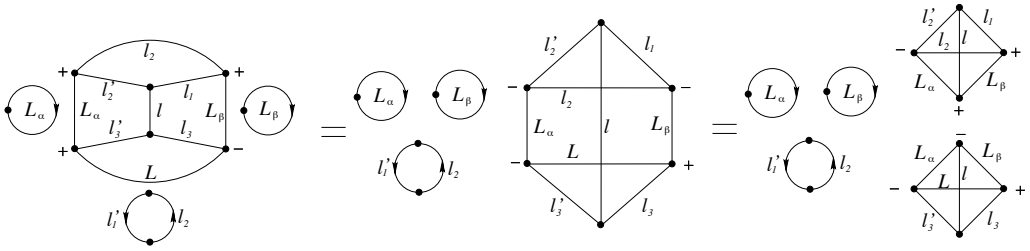

$$\langle[[\phi'_1\otimes\phi'_2]\otimes\phi'_3]|g_l(2,3)\mathcal{P}_{12}|[[\phi_1\otimes\phi_2]\otimes\phi_3]\rangle=\langle\phi'_1|\phi_2\rangle\{\phi'_2\phi'_3|\phi_1\phi_3\}_l\times$$
$$\times\delta_{l_2l'_1}(-)^{\mathcal{N}+\mathcal{N}_\alpha+\mathcal{N}_\beta}\Pi_{L_\alpha L_\beta}\begin{Bmatrix}l'_2 & l & l_1\\ L_\beta & l_2 & L_\alpha\end{Bmatrix}\begin{Bmatrix}L_\alpha & l & L_\beta\\ l_3 & L & l'_3\end{Bmatrix}$$

- $g(2,3)\mathcal{P}_{123}$

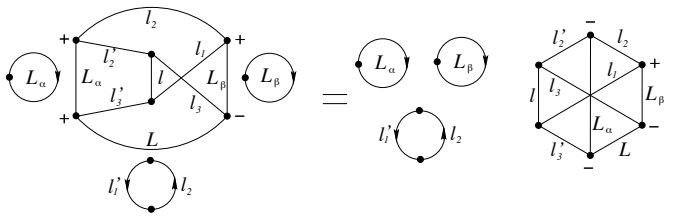

$$\langle[[\phi'_1\otimes\phi'_2]\otimes\phi'_3]|g_l(2,3)\mathcal{P}_{123}|[[\phi_1\otimes\phi_2]\otimes\phi_3]\rangle=\langle\phi'_1|\phi_2\rangle\{\phi'_2\phi'_3|\phi_3\phi_1\}_l\times$$
$$\times\delta_{l_2l'_1}(-)^{\mathcal{N}+\mathcal{N}_\alpha}\Pi_{L_\alpha L_\beta}\begin{Bmatrix}l'_2 & l & l_3\\ l_2 & l_1 & L_\beta\\ L_\alpha & l'_3 & L\end{Bmatrix}$$

- $g(2,3)\mathcal{P}_{321}$

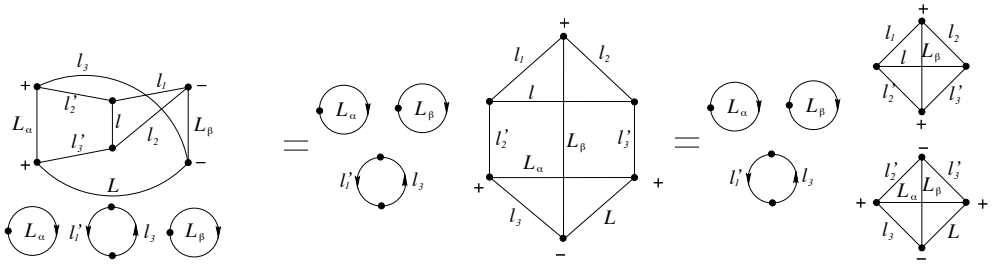

$$\langle[[\phi_1'\otimes\phi_2']\otimes\phi_3']|g_l(2,3)\mathcal{P}_{321}|[[\phi_1\otimes\phi_2]\otimes\phi_3]\rangle=\langle\phi_1'|\phi_3\rangle\{\phi_2'\phi_3'|\phi_1\phi_2\}_l\times$$
$$\times\delta_{l_3l_1'}\Pi_{L_\alpha L_\beta}\begin{Bmatrix}l_1 & L_\beta & l_2\\ l_3' & l & l_2'\end{Bmatrix}\begin{Bmatrix}l_2' & l_3' & L_\beta\\ L & l_3 & L_\alpha\end{Bmatrix}$$

- $g(1,3)$

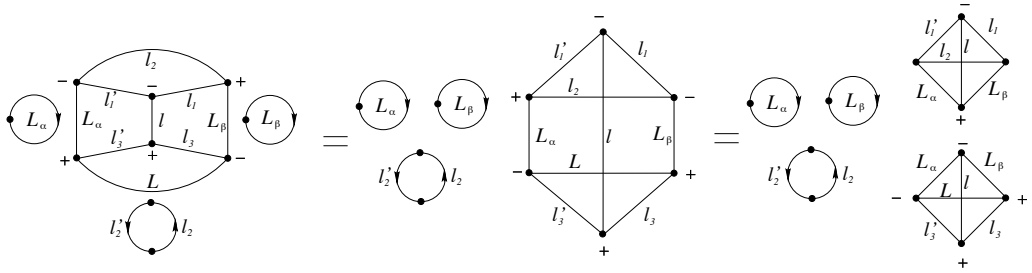

$$\langle[[\phi_1'\otimes\phi_2']\otimes\phi_3']|g_l(1,3)\hat{E}|[[\phi_1\otimes\phi_2]\otimes\phi_3]\rangle=\langle\phi_2'|\phi_2\rangle\{\phi_1'\phi_3'|\phi_1\phi_3\}_l\times$$
$$\times\delta_{l_2l_2'}(-)^{\mathcal{N}}\Pi_{L_\alpha L_\beta}\begin{Bmatrix}l_1 & l & l_1'\\ L_\alpha & l_2 & L_\beta\end{Bmatrix}\begin{Bmatrix}L_\alpha & l & L_\beta\\ l_3 & L & l_3'\end{Bmatrix}$$

- $g(1,3)\mathcal{P}_{13}$

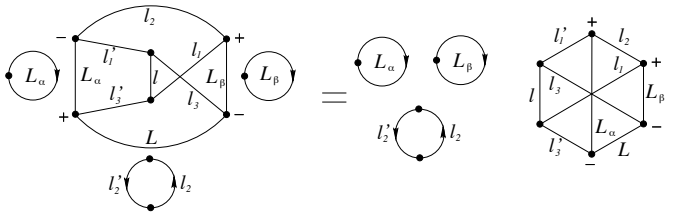

$$\langle[[\phi_1'\otimes\phi_2']\otimes\phi_3']|g_l(1,3)\mathcal{P}_{13}|[[\phi_1\otimes\phi_2]\otimes\phi_3]\rangle=\langle\phi_2'|\phi_2\rangle\{\phi_1'\phi_3'|\phi_3\phi_1\}_l\times$$
$$\times\delta_{l_2l_2'}(-)^{\mathcal{N}}\Pi_{L_\alpha L_\beta}\begin{Bmatrix}l_1' & L_\alpha & l_2\\ l_3 & L & L_\beta\\ l & l_3' & l_1\end{Bmatrix}$$

- $g(1,3)\mathcal{P}_{23}$

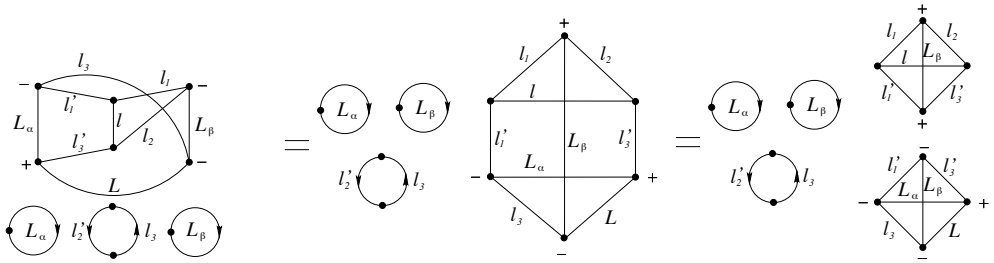

$$\langle[[\phi_1'\otimes\phi_2']\otimes\phi_3']|g_l(1,3)\mathcal{P}_{23}|[[\phi_1\otimes\phi_2]\otimes\phi_3]\rangle=\langle\phi_2'|\phi_3\rangle\{\phi_1'\phi_3'|\phi_1\phi_2\}_l\times$$
$$\times\delta_{l_3l_2'}(-)^{\mathcal{N}_\alpha}\Pi_{L_\alpha L_\beta}\begin{Bmatrix}l_1 & L_\beta & l_2\\ l_3' & l & l_1'\end{Bmatrix}\begin{Bmatrix}l_1' & L_\alpha & l_3\\ L & l_3' & L_\beta\end{Bmatrix}$$

- $g(1,3)\mathcal{P}_{12}$

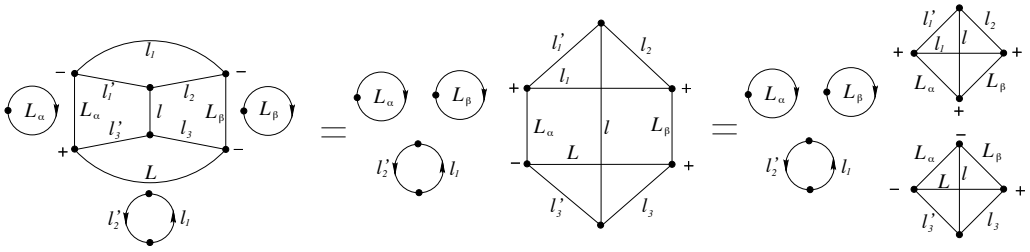

$$\langle[[\phi_1'\otimes\phi_2']\otimes\phi_3']|g_l(1,3)\mathcal{P}_{12}|[[\phi_1\otimes\phi_2]\otimes\phi_3]\rangle = \langle\phi_2'|\phi_1\rangle\{\phi_1'\phi_3'|\phi_2\phi_3\}_l\times$$
$$\times\delta_{l_1l_2'}(-)^{\mathcal{N}+\mathcal{N}_\beta}\Pi_{L_\alpha L_\beta}\begin{Bmatrix}L_\alpha & l_1 & l_1'\\ l_2 & l & L_\beta\end{Bmatrix}\begin{Bmatrix}L_\alpha & l & L_\beta\\ l_3 & L & l_3'\end{Bmatrix}$$

- $g(1,3)\mathcal{P}_{123}$

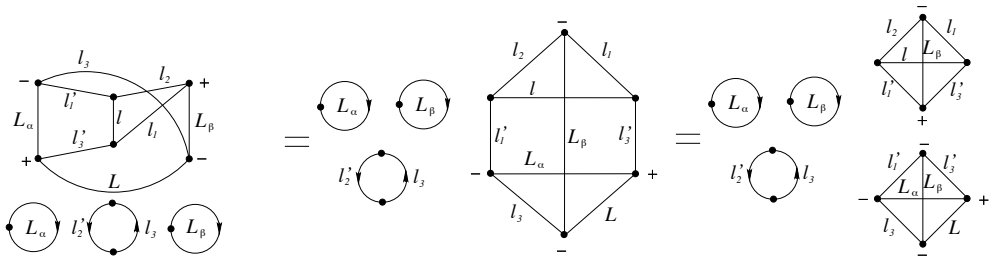

$$\langle[[\phi_1'\otimes\phi_2']\otimes\phi_3']|g_l(1,3)\mathcal{P}_{123}|[[\phi_1\otimes\phi_2]\otimes\phi_3]\rangle = \langle\phi_2'|\phi_3\rangle\{\phi_1'\phi_3'|\phi_2\phi_1\}_l\times$$
$$\times\delta_{l_3l_2'}(-)^{\mathcal{N}_\alpha+\mathcal{N}_\beta}\Pi_{L_\alpha L_\beta}\begin{Bmatrix}l_1 & L_\beta & l_2\\ l_1' & l & l_3'\end{Bmatrix}\begin{Bmatrix}l_3' & L_\beta & l_1'\\ l_3 & L_\alpha & L\end{Bmatrix}$$

- $g(1,3)\mathcal{P}_{321}$

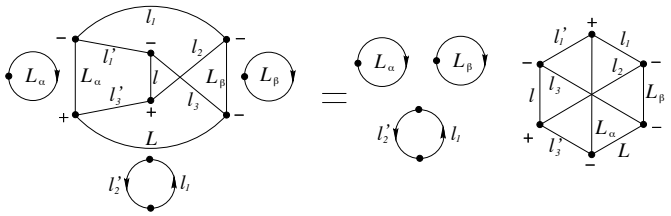

$$\langle[[\phi_1'\otimes\phi_2']\otimes\phi_3']|g_l(1,3)\mathcal{P}_{321}|[[\phi_1\otimes\phi_2]\otimes\phi_3]\rangle = \langle\phi_2'|\phi_1\rangle\{\phi_1'\phi_3'|\phi_3\phi_2\}_l\times$$
$$\times\delta_{l_1l_2'}(-)^{\mathcal{N}+\mathcal{N}_\beta}\Pi_{L_\alpha L_\beta}\begin{Bmatrix}l_1' & L_\alpha & l_1\\ l_3 & L & L_\beta\\ l & l_3' & l_2\end{Bmatrix}$$

- $g(1,2)$

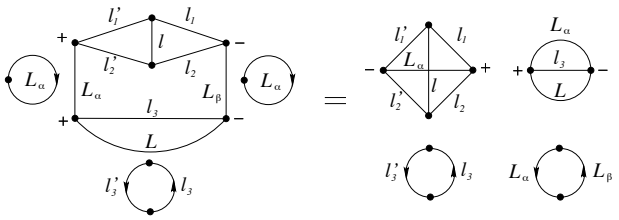

$$\langle[[\phi_1'\otimes\phi_2']\otimes\phi_3']|g_l(1,2)\hat{E}|[[\phi_1\otimes\phi_2]\otimes\phi_3]\rangle = \langle\phi_3'|\phi_3\rangle\{\phi_1'\phi_2'|\phi_1\phi_2\}_l\times$$
$$\times\delta_{l_3l_3'}\delta_{\mathcal{N}_\alpha}(-)^{l_1'+l+L_\alpha+l_2}\{Ll_3L_\alpha\}\begin{Bmatrix} l_1' & l & l_1\\ l_2 & L_\alpha & l_2'\end{Bmatrix}$$

- $g(1,2)\mathcal{P}_{13}$

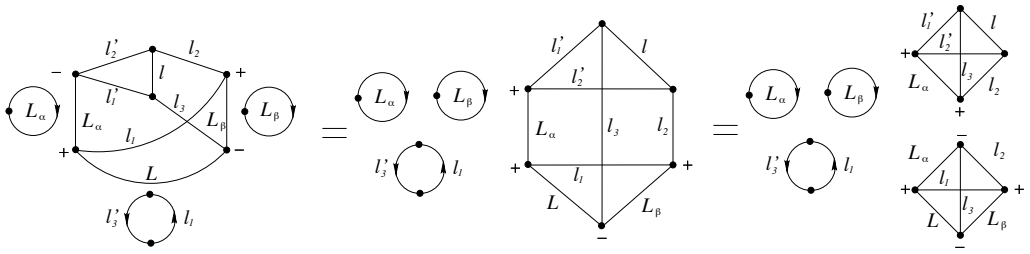

$$\langle[[\phi_1'\otimes\phi_2']\otimes\phi_3']|g_l(1,2)\mathcal{P}_{13}|[[\phi_1\otimes\phi_2]\otimes\phi_3]\rangle = \langle\phi_3'|\phi_1\rangle\{\phi_1'\phi_2'|\phi_3\phi_2\}_l\times$$
$$\times\delta_{l_1l_3'}(-)^{\mathcal{N}_\alpha}\Pi_{L_\alpha L_\beta}\begin{Bmatrix} l_1' & L_\alpha & l_2'\\ l_2 & l & l_3\end{Bmatrix}\begin{Bmatrix} L & l_1 & L_\alpha\\ l_2 & l_3 & L_\beta\end{Bmatrix}$$

- $g(1,2)\mathcal{P}_{23}$

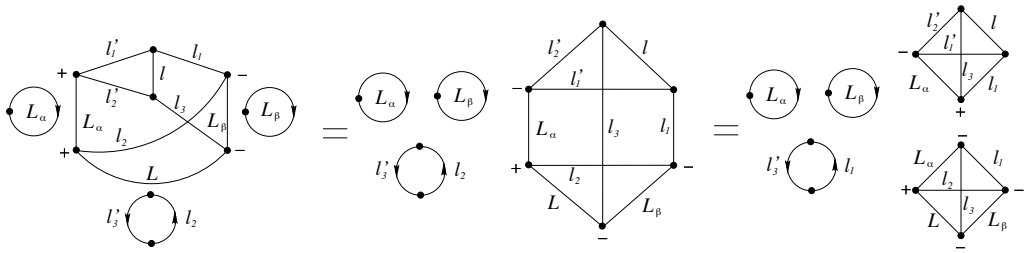

$$\langle[[\phi_1'\otimes\phi_2']\otimes\phi_3']|g_l(1,2)\mathcal{P}_{23}|[[\phi_1\otimes\phi_2]\otimes\phi_3]\rangle = \langle\phi_3'|\phi_2\rangle\{\phi_1'\phi_2'|\phi_1\phi_3\}_l\times$$
$$\times\delta_{l_2l_3'}(-)^{\mathcal{N}_\beta}\Pi_{L_\alpha L_\beta}\begin{Bmatrix} l_2' & l & l_3\\ l_2 & l_1' & L_\alpha\end{Bmatrix}\begin{Bmatrix} L & l_2 & L_\alpha\\ l_1 & l_3 & L_\beta\end{Bmatrix}$$

- $g(1,2)\mathcal{P}_{12}$

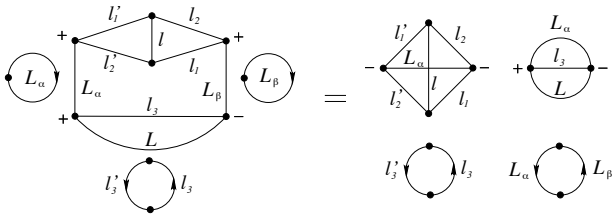

$$\langle[[\phi_1'\otimes\phi_2']\otimes\phi_3']|g_l(1,2)\mathcal{P}_{12}|[[\phi_1\otimes\phi_2]\otimes\phi_3]\rangle = \langle\phi_3'|\phi_3\rangle\{\phi_1'\phi_2'|\phi_2\phi_1\}_l\times$$
$$\times\delta_{l_3l_3'}\delta_{L_\alpha L_\beta}\{L_\alpha l_3 L\}\begin{Bmatrix} l_1' & l & l_2\\ l_1 & L_\alpha & l_2'\end{Bmatrix}$$

- $g(1,2)\mathcal{P}_{123}$

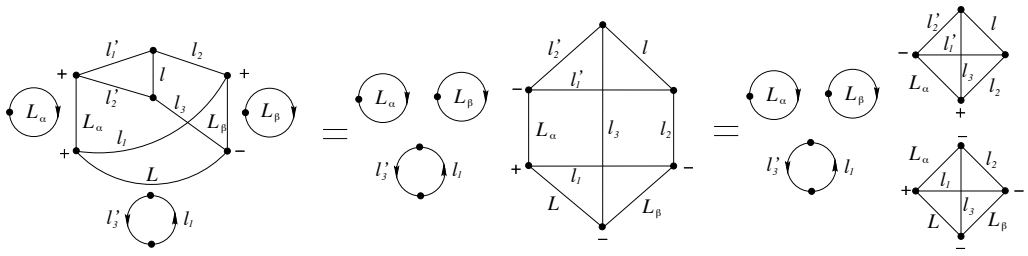

$$\langle[[\phi'_1\otimes\phi'_2]\otimes\phi'_3]|g_l(1,2)\mathcal{P}_{123}|[[\phi_1\otimes\phi_2]\otimes\phi_3]\rangle = \langle\phi'_3|\phi_1\rangle\{\phi'_1\phi'_2|\phi_2\phi_3\}_l\times$$
$$\times\delta_{l_1l'_3}\Pi_{L_\alpha L_\beta}\begin{Bmatrix} l'_2 & l_3 & l\\ l_2 & l'_1 & L_\alpha\end{Bmatrix}\begin{Bmatrix} L & l_1 & L_\alpha\\ l_2 & l_3 & L_\beta\end{Bmatrix}$$

- $g(1,2)\mathcal{P}_{321}$

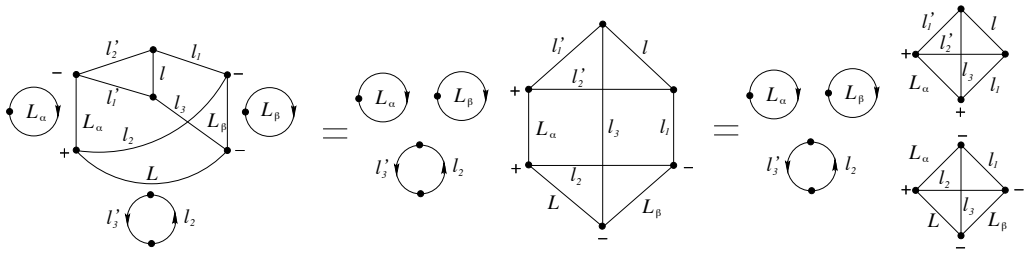

$$\langle[[\phi'_1\otimes\phi'_2]\otimes\phi'_3]|g_l(1,2)\mathcal{P}_{321}|[[\phi_1\otimes\phi_2]\otimes\phi_3]\rangle = \langle\phi'_3|\phi_2\rangle\{\phi'_1\phi'_2|\phi_3\phi_1\}_l\times$$
$$\times\delta_{l_2l'_3}(-)^{\mathcal{N}_\alpha+\mathcal{N}_\beta}\Pi_{L_\alpha L_\beta}\begin{Bmatrix} L_\alpha & l'_2 & l'_1\\ l & l_3 & l_1\end{Bmatrix}\begin{Bmatrix} L & l_2 & L_\alpha\\ l_1 & l_3 & L_\beta\end{Bmatrix}$$

G.4 Outline of a general recursive formula

As already stated in the introduction to this appendix, a completely different method suitable to deal with large systems with orthogonal, ordered shells has been described by Fano in the mid sixties [204]. The diagrams of angular and spin combination can be treated in a systematic way and reduced to few relevant cases of topologically different diagrams. This approach is heartily recommended in all standard cases.

In the present section, we nevertheless would like to take the opportunity of generalizing the approach of the previous sections to n-electron systems. The advantage is that the corresponding formulas are valid for any basis, in particular those which are not orthogonal. In some situations, like maybe the complete fragmentation of four electron systems, it may be more useful to have extensive summations over angular momenta but where almost all the radial matrix elements are zero, rather than very concise algebraic expressions with a huge number of non zero integrals.

In the general case we shall have to reduce the matrix element of a $p-$body operator times a permutation between multielectron states arbitrarily coupled:

$$\langle\Phi'|\mathcal{O}_{ij\cdots k}\mathcal{P}|\Phi\rangle \tag{G.7}$$

where indexes in the operator indicates the particle onto which it acts. With the relation

$$\mathcal{O}_{ij\cdots k} \;=\; \mathcal{P}_{k\,n}\cdots\mathcal{P}_{j\,n-p+2}\mathcal{P}_{i\,n-p+1}\;\mathcal{O}_{n-p+1\cdots n}\;\mathcal{P}_{i\,n-p+1}\mathcal{P}_{j\,n-p+2}\cdots\mathcal{P}_{k\,n} \tag{G.8}$$

the operator indexes in G.7 are reduced to the last n integers

$$\langle\Phi'|\mathcal{P}'\mathcal{O}_{n-p+1\cdots n}\mathcal{P}'^{\dagger}\mathcal{P}|\Phi\rangle \tag{G.9}$$

The angular part of G.9 can be dealt with separately. The operator $\mathcal{O}_{n-p+1\cdots n}$ and the two permutations $\mathcal{P}'$, $\mathcal{P}'' \equiv \mathcal{P}'^{\dagger}\mathcal{P}$ are separated with the help of the following identity

$$\prod_{i=1}^{n}\delta_{m'_i m_i} = \sum_{\substack{\{M_\gamma M'_\gamma\}\\ LM}} C^{L_\alpha M'_\alpha}_{l_1 m'_1, l_2 m'_2} C^{L_\beta M'_\beta}_{L_\alpha M'_\alpha, l_3 m'_3}\cdots C^{LM}_{L_\omega M'_\omega, l_n m'_n} C^{LM}_{L_\omega M_\omega, l_n m_n}\cdots C^{L_\beta M_\beta}_{L_\alpha M_\alpha, l_3 m_3} C^{L_\alpha M_\alpha}_{l_1 m_1, l_2 m_2}$$

The corresponding diagram can be represented schematically as

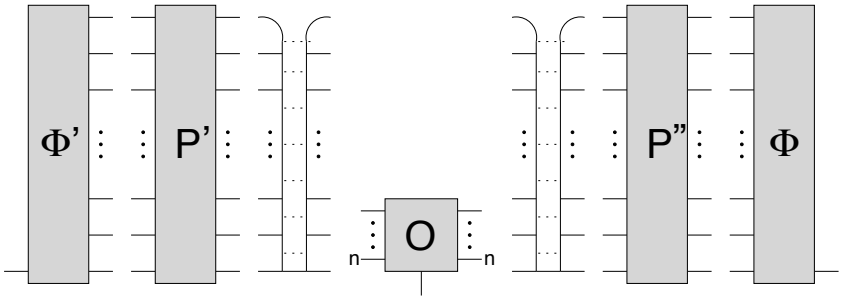

where dotted lines join contracted intermediate angular momenta. For the sake of clarity, many diagrammatic details are omitted. By means of the rules

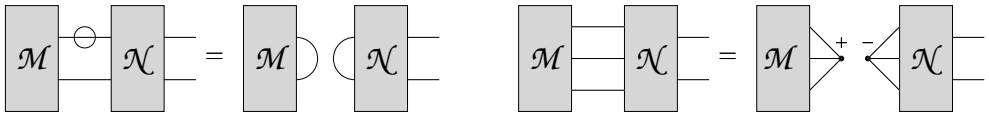

four main groups in each addendum of G.4 can be recognized and isolated as disconnected diagrams. The Y diagram represents the magnetic quantum number dependent Clebsh Gordan factor in the factorization of the whole matrix element according to Wigner Eckart theorem.

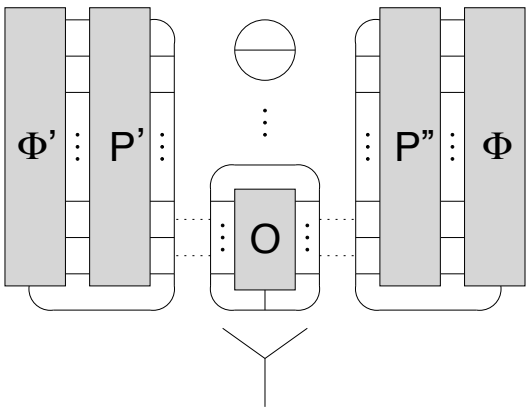

The diagram with the operator $\mathcal{O}$ is a reduced matrix element which can be computed once and for all. In the case of monoelectronic tensor and bielectronic scalar operators, the reduced matrix element factors are given by one and the product of two $6-j$ coefficients respectively

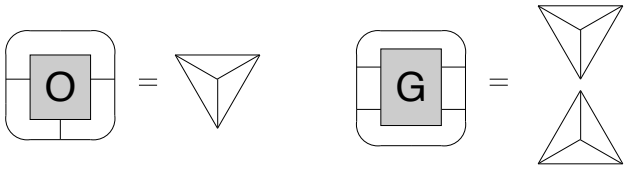

The two diagrams with a permutation are actually recoupling coefficients which can be dealt with recursively. To see this, consider the case in which the wave function is built coupling the i-th electron to an $i-1$-electron coupled wave function.

$$|\Phi\rangle \;=\; |\,[[\ldots[\phi_1\otimes\phi_2]\otimes\phi_3]\otimes\cdots]\otimes\phi_n]\,\rangle$$

Thanks to the elementary relation

$$\mathcal{S}_n = \bigcup_{i=1}^{n-1} \mathcal{P}_{in}\mathcal{S}_{n-1}$$

all permutations can be written uniquely as product of exchanges through the subduction chain

$$\mathcal{S}_n \supset \mathcal{S}_{n-1} \supset \mathcal{S}_{n-2} \supset \ldots \supset \mathcal{S}_2 \tag{G.10}$$

$$\mathcal{P} = \prod_j (j i_j), \qquad i_j \le j \tag{G.11}$$

Applying repeatedly the identity resolution between exchange factors, the general permutation term reduces to

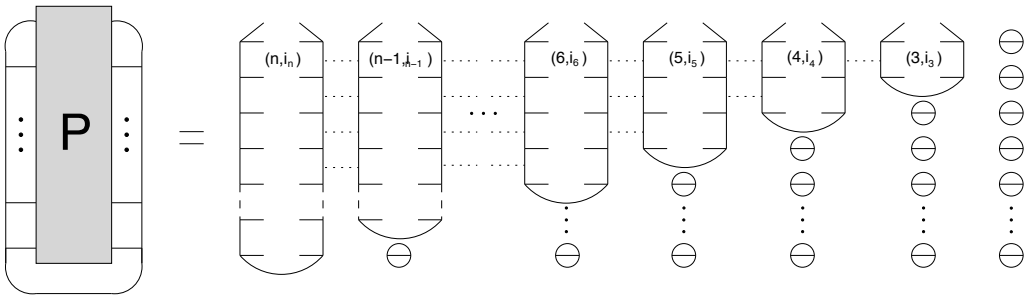

The matrix element of a general $\mathcal{P}_{in}$ exchange is known

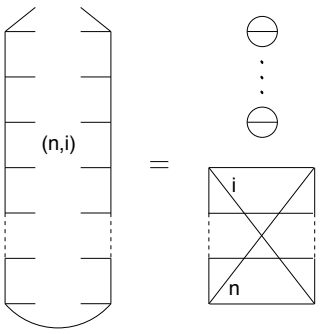

that is a product of $3j$ symbols and a $3(n-i+1)j$ symbol of the I kind.

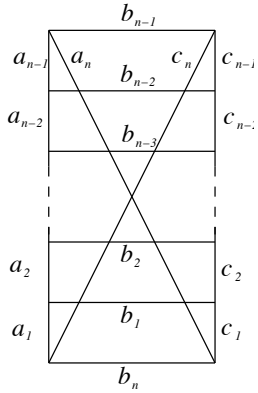

$$= \left\{ \begin{array}{ccccccccccc} a_1 & & a_2 & & \cdots & & a_{n-1} & & a_n & & \\ & b_1 & & b_2 & & \cdots & & b_{n-1} & & b_n & \\ c_1 & & c_2 & & \cdots & & c_{n-1} & & c_n & & \end{array} \right\}$$

The reduction procedure above is general and straightforward, but many summation over intermediate angular momenta are required, so it gets rapidly inefficient even in comparison with direct contraction of Clebsch-Gordan coefficients over magnetic quantum numbers. Efficient formulas are obtained with resummation of diagrams which often simplifies much the final expressions. In any case, the separation of matrix elements in permutation and operator part is convenient because the big work involves $n!$ formulas instead of $n \cdot n!$ or $\frac{1}{2}n(n+1) \cdot n!$ formulas for monoelectronic and bielectronic terms. The case of three electrons is somewhat a boundary situation since resummation of diagrams is not much easier than its direct computation.

Appendix H

Core-valence interaction

The normalized state of a frozen closed shell core coupled to a valence wave function is given by

$$\Psi = \sqrt{\frac{N!}{N_c!N_v!}}\mathscr{A}\Psi_c\Psi_v \tag{H.1}$$

The core function is trivially

$$\Psi_c = \sqrt{N_c!}\mathscr{A}_c\Theta\mathrm{F}_c \tag{H.2}$$

$$\Theta = \prod_{i=1}^{N_c/2}\alpha\beta, \quad \mathrm{F}_c = \prod_{i=1}^{N_c/2}\phi_i\phi_i = \prod_{n,l}\prod_{m=-l}^{l}\phi_{nl}^m\phi_{nl}^m \tag{H.3}$$

A basis function for the valence shell can be written as (see chapter 4)

$$\Psi_v = \sqrt{N_v!}\mathscr{A}_v\Theta_i^\alpha\mathrm{F}_v \tag{H.4}$$

Ψ can therefore be cast in the following form

$$\Psi = \sqrt{N!}\mathscr{A}\Theta\Theta_i^\alpha\mathrm{F}_c\mathrm{F}_v. \tag{H.5}$$

where the valence wavefunctions must be orthogonal to the core. The matrix elements of monoelectronic operators between such states is the sum of two contribution: the expectation value on the core times the superposition between valence shell, plus the matrix element between valence shells

$$\begin{aligned}
\langle\Psi|\mathcal{O}|\Psi'\rangle &= N_c!N_v!\langle\Theta\Theta_i^\alpha\mathrm{F}_c\mathrm{F}_v|(\mathcal{O}_c+\mathcal{O}_v)\mathscr{A}_c\mathscr{A}_v\Theta\Theta_j^\alpha\mathrm{F}_c\mathrm{F}'_v\rangle = \\
&= N_c!\langle\Theta\mathrm{F}_c|\mathcal{O}_c\mathscr{A}_c\Theta\mathrm{F}_c\rangle N_v!\langle\Theta_i^\alpha\mathrm{F}_v|\mathscr{A}_v\Theta_j^\alpha\mathrm{F}'_v\rangle + \\
&+N_c!\langle\Theta\mathrm{F}_c|\mathscr{A}_c\Theta\mathrm{F}_c\rangle N_v!\langle\Theta_i^\alpha\mathrm{F}_v|\mathcal{O}_v\mathscr{A}_v\Theta_j^\alpha\mathrm{F}'_v\rangle = \\
&= \left(\sum_{i=1}^{N_c/2}2\langle\phi_i|\hat{o}|\phi_i\rangle\right)\langle\mathrm{F}_v|w_{ij}^{\tilde{\alpha}}|\mathrm{F}'_v\rangle + \langle\mathrm{F}_v|\mathcal{O}_v w_{ij}^{\tilde{\alpha}}|\mathrm{F}'_v\rangle = \\
&= \langle\mathcal{O}\rangle_c\cdot\langle\mathrm{F}_v|w_{ij}^{\tilde{\alpha}}|\mathrm{F}'_v\rangle + \langle\mathrm{F}_v|\mathcal{O}_v w_{ij}^{\tilde{\alpha}}|\mathrm{F}'_v\rangle
\end{aligned} \tag{H.6}$$

where $\mathsf{W}^{\tilde{\alpha}}$ is the Wigner operator for the conjugate representation to α

$$\mathsf{W}^{\tilde{\alpha}}_{ij} \equiv \frac{n_\alpha}{N!} \sum_{\mathscr{P}\in\mathscr{S}_N} \epsilon_{\mathscr{P}} \mathsf{D}^{\alpha}_{ij}(\mathscr{P})\mathscr{P} = \frac{n_\alpha}{N!} w^{\tilde{\alpha}}_{ij}.$$

In particular the monoelectronic matrix is the same as if the core were absent in two cases: for the superposition matrix ($o_i = 1/N$)

$$\langle\Psi|\Psi'\rangle = \langle V|V'\rangle \tag{H.7}$$

and for non totally symmetric operators, where the first term in H.6 is zero.

For bielectronic operators instead

$$\mathcal{G} = \mathcal{G}^{cc} + \mathcal{G}^{vv} + \mathcal{G}^{cv} = \sum_{i_c>j_c} g_{i_c j_c} + \sum_{i_v>j_v} g_{i_v j_v} + \sum_{i_c j_v} g_{i_c j_v}$$

$$\begin{aligned}
\langle\Psi|\mathcal{G}|\Psi'\rangle &= N_c!N_v!\langle\Theta\Theta^\alpha_i \mathrm{F}_c\mathrm{F}_v|(\mathcal{G}^{cc}+\mathcal{G}^{vv}+\mathcal{G}^{cv})\mathscr{A}_c\mathscr{A}_v\Theta\Theta^\alpha_j\mathrm{F}_c\mathrm{F}'_v\rangle = \\
&= N_c!\langle\Theta\mathrm{F}_c|\mathcal{G}^{cc}\mathscr{A}_c\Theta\mathrm{F}_c\rangle N_v!\langle\Theta^\alpha_i\mathrm{F}_v|\mathscr{A}_v\Theta^\alpha_j\mathrm{F}'_v\rangle + \\
&+N_c!\langle\Theta\mathrm{F}_c|\mathscr{A}_c\Theta\mathrm{F}_c\rangle N_v!\langle\Theta^\alpha_i\mathrm{F}_v|\mathcal{G}^{vv}\mathscr{A}_v\Theta^\alpha_j\mathrm{F}'_v\rangle + \\
&+N_c!N_v!\langle\Theta\Theta^\alpha_i\mathrm{F}_c\mathrm{F}_v|\mathcal{G}^{cv}(1-\sum_{i_cj_v}\mathscr{P}_{i_cj_v})\mathscr{A}_c\mathscr{A}_v\Theta\Theta^\alpha_j\mathrm{F}_c\mathrm{F}'_v\rangle = \\
&= \langle\mathcal{G}\rangle_c\cdot\langle F_v|w^{\tilde{\alpha}}_{ij}|F'_v\rangle + \langle F_v|\mathcal{G}^{vv}w^{\tilde{\alpha}}_{ij}|F'_v\rangle + \\
&+N_c!N_v!\langle\Theta\Theta^\alpha_i\mathrm{F}_c\mathrm{F}_v|\mathcal{G}^{cv}\mathscr{A}_c\mathscr{A}_v\Theta\Theta^\alpha_j\mathrm{F}_c\mathrm{F}'_v\rangle - \\
&-N_c!N_v!\langle\Theta\Theta^\alpha_i\mathrm{F}_c\mathrm{F}_v|\mathcal{G}^{cv}\sum_{i_cj_v}\mathscr{P}_{i_cj_v}\mathscr{A}_c\mathscr{A}_v\Theta\Theta^\alpha_j\mathrm{F}_c\mathrm{F}'_v\rangle.
\end{aligned}$$

The first two terms are trivial. For the third term, coulomb repulsion,

$$\begin{aligned}
&N_c!N_v!\langle\Theta\Theta^\alpha_i\mathrm{F}_c\mathrm{F}_v|\mathcal{G}^{cv}\mathscr{A}_c\mathscr{A}_v\Theta\Theta^\alpha_j\mathrm{F}_c\mathrm{F}'_v\rangle = \\
&= N_v!\sum_{j_v}\langle\Theta^\alpha_i\mathrm{F}_v|\int d^3r\sum_{2i_c=2}^{N_c}\frac{|\phi_{i_c}(\vec{r})|^2}{|\vec{r}-\vec{r}_{j_v}|}|\mathscr{A}_v\Theta^\alpha_j\mathrm{F}'_v\rangle
\end{aligned}$$

the frozen core acts as a totally symmetric local effective potential on valence states.

The last term, which represents the exchange between core and valence electrons, is slightly more complicated

$$\begin{aligned}
&-N_c!N_v!\langle\Theta\Theta^\alpha_i\mathrm{F}_c\mathrm{F}_v|\mathcal{G}^{cv}\sum_{i_cj_v}\mathscr{P}_{i_cj_v}\mathscr{A}_c\mathscr{A}_v\Theta\Theta^\alpha_j\mathrm{F}_c\mathrm{F}'_v\rangle = \\
&= -N_c!N_v!\sum_{i_cj_v}\sum_{i'_cj'_v}\langle\Theta\Theta^\alpha_i\mathrm{F}_c\mathrm{F}_v|\frac{1}{r_{i'_cj'_v}}\mathscr{P}_{i_cj_v}\mathscr{A}_c\mathscr{A}_v\Theta\Theta^\alpha_j\mathrm{F}_c\mathrm{F}'_v\rangle = \\
&= -N_c!N_v!\sum_{i_cj_v}\langle\Theta\Theta^\alpha_i\mathrm{F}_c\mathrm{F}_v|\frac{1}{r_{i_cj_v}}\mathscr{P}_{i_cj_v}\mathscr{A}_c\mathscr{A}_v\Theta\Theta^\alpha_j\mathrm{F}_c\mathrm{F}'_v\rangle
\end{aligned}$$

Let integrate over the $N_c - 1$ core variables not included in the potential:

$$= -N_v! \sum_{j_v} \langle \Theta_i^\alpha \mathrm{F}_v | \sum_{i_c} \int dx_{i_c} \mathscr{P}_{i_c j_v} \left\{ N_c! \int \bigwedge_{j \neq i_c} dx_j \Theta' \mathrm{F}'_c \frac{1}{r_{i'_c j_v}} \mathscr{A}_c \Theta \mathrm{F}_c \right\} \mathscr{A}_v \Theta_j^\alpha \mathrm{F}'_v \rangle$$

where the prime means that the variable index of x_{i_c} is not altered by the permutation.

$$N_c! \int \bigwedge_{j \neq i_c} dx_j \Theta' \mathrm{F}'_c \frac{1}{r_{i'_c j_v}} \mathscr{A}_c \Theta \mathrm{F}_c = \frac{\phi^*_{i_c}(\vec{r}_{i'_c}) \phi_{i_c}(\vec{r}_{i_c})}{r_{i'_c j_v}} \zeta^*(\sigma_{i'_c}) \zeta(\sigma_{i_c})$$

ζ is α or β if i_c is odd or even respectively. We obtain

$$-N_v! \sum_{j_v} \langle \Theta_i^\alpha \mathrm{F}_v | \sum_{i_c} \int dx_{i_c} \frac{\phi^*_{i_c}(\vec{r}_{i_c}) \phi_{i_c}(\vec{r}_{j_v})}{r_{i_c j_v}} \zeta^*(\sigma_{i_c}) \zeta(\sigma_{j_v}) \mathscr{P}_{i_c j_v} \mathscr{A}_v \Theta_j^\alpha \mathrm{F}'_v \rangle =$$

$$= -\sum_{j_v} \sum_k \langle \Theta_i^\alpha \mathrm{F}_v | \sum_{i_c} \int dx_{i_c} \frac{\phi^*_{i_c}(\vec{r}_{i_c}) \phi_{i_c}(\vec{r}_{j_v})}{r_{i_c j_v}} \zeta^*(\sigma_{i_c}) \zeta(\sigma_{j_v}) \mathscr{P}_{i_c j_v} \Theta_k^\alpha w_{kj}^{\tilde{\alpha}} \mathrm{F}'_v \rangle =$$

$$= -\sum_{j_v} \sum_k \sum_{i_c} \langle \Theta_i^\alpha | \sum_{\sigma_{i_c}} \zeta^*(\sigma_{i_c}) \zeta(\sigma_{j_v}) \mathscr{P}_{i_c j_v} | \Theta_k^\alpha \rangle \times$$

$$\times \langle \mathrm{F}_v | \int d^3 r_{i_c} \frac{\phi^*_{i_c}(\vec{r}_{i_c}) \phi_{i_c}(\vec{r}_{j_v})}{r_{i_c j_v}} \mathscr{P}_{i_c j_v} w_{ij}^{\tilde{\alpha}} | \mathrm{F}'_v \rangle =$$

$$= \sum_{j_v} \langle \mathrm{F}_v | \left\{ \sum_{2i_c=2}^{N_c} \int d^3 r_{i_c} \frac{\phi^*_{i_c}(\vec{r}_{i_c}) \phi_{i_c}(\vec{r}_{j_v})}{r_{i_c j_v}} \mathscr{P}_{i_c j_v} \right\} w_{ij}^{\tilde{\alpha}} | \mathrm{F}'_v \rangle.$$

In this case the influence of the core is reduced to a totally symmetric non local potential.

If we define

$$\hat{f}^C \varphi(\vec{r}) \equiv \int d^3 r' \sum_{2i_c=2}^{N_c} \frac{|\phi_{i_c}(\vec{r}')|^2}{|\vec{r} - \vec{r}'|} \varphi(\vec{r}); \qquad \mathcal{F}^C \equiv \sum_j \hat{f}_j^C$$

$$\hat{f}^X \varphi(\vec{r}) \equiv \sum_{2i_c=2}^{N_c} \phi_{i_c}(\vec{r}) \int d^3 r' \frac{\phi^*_{i_c}(\vec{r}') \varphi(\vec{r}')}{|\vec{r} - \vec{r}'|}; \qquad \mathcal{F}^X \equiv \sum_j \hat{f}_j^X$$

we can write

$$\langle \Psi | \mathcal{G} | \Psi' \rangle = \langle \mathcal{G} \rangle_c \cdot \langle \mathrm{F}_v | w_{ij}^{\tilde{\alpha}} | \mathrm{F}'_v \rangle + \langle \mathrm{F}_v | \mathcal{G}^{vv} w_{ij}^{\tilde{\alpha}} | \mathrm{F}'_v \rangle + 2 \langle \mathrm{F}_v | \mathcal{F}^C w_{ij}^{\tilde{\alpha}} | \mathrm{F}'_v \rangle - \langle \mathrm{F}_v | \mathcal{F}^X w_{ij}^{\tilde{\alpha}} | \mathrm{F}'_v \rangle$$

Finally, the matrix elements between the monoelectronic coulomb and exchange operators can be expanded in multipolar components

$$\langle \varphi_a | f^C | \varphi_b \rangle = \delta_{\ell_a \ell_b} \delta_{m_a m_b} \sum_{\ell_c n_c} (2\ell_c + 1) \langle \phi_{\ell_c n_c} \varphi_a | \phi_{\ell_c n_c} \varphi_b \rangle_0$$

$$\langle \varphi_a | f^X | \varphi_b \rangle = \delta_{\ell_a \ell_b} \delta_{m_a m_b} \sum_{\ell \ell_c n_c} |C^{\ell_c 0}_{\ell_a 0 \ell 0}|^2 \langle \phi_{\ell_c n_c} \phi_{\ell_c n_c} | \varphi_a \varphi_b \rangle_\ell$$

Appendix I

Representation of effective potentials

The diagonal factor $V(r)$ of a local, spherical potential $V(r, r')$

$$\langle r|V|\psi\rangle = V(r)\psi(r), \quad V(r, r') = V(r)\frac{\delta(r - r')}{r^2} \tag{I.1}$$

can be written as

$$V(r) = \int_0^\infty V(r, r')r'^2 dr'. \tag{I.2}$$

When projected on a finite basis, the potential becomes

$$V_p = |\boldsymbol{\chi}\rangle\tilde{\mathsf{V}}\langle\boldsymbol{\chi}|, \qquad \tilde{\mathsf{V}} \equiv \mathsf{S}^{-1}\langle\boldsymbol{\chi}|V|\boldsymbol{\chi}\rangle\mathsf{S}^{-1}, \qquad \mathsf{S} = \langle\boldsymbol{\chi}|\boldsymbol{\chi}\rangle \tag{I.3}$$

where V_p is no more a diagonal operator: $\delta(r-r')$ in I.1 is replaced by a $\delta^\sigma(r-r'; r)$, centered at 0 integrating to 1, with width σ the smaller the richer the basis.

Let examine this is more detail. The projector kernel is given by

$$P(x, x') = \langle x|\boldsymbol{\chi}\rangle\mathbf{S}^{-1}\langle\boldsymbol{\chi}|x'\rangle, \qquad P(x', x) = P(x, x'); \tag{I.4}$$

the kernel of the projected diagonal operator therefore reads

$$V_p(x, x') = \int dy P(x, y)V(y)P(y, x') \tag{I.5}$$

or, more in general, for a non diagonal operator

$$O_p(x, x') = \int\int dy\, dy' P(x, y)O(y, y')P(y', x'). \tag{I.6}$$

As the basis approaches completeness, $P(x, y)$ and $P(x, y)P(x', y')$ are the kernel of operators converging to the mono and bidimensional identity. In figure I.1 a sequence of projector kernels for 7-th degree B-spline basis defined by uniform grids on the $[0, 1]$ interval with 10, 20, 50, 100 and 200 knots are reported. The dominant contribution comes from the diagonal band with a width $\sim 1/n$. $P(x, y)$

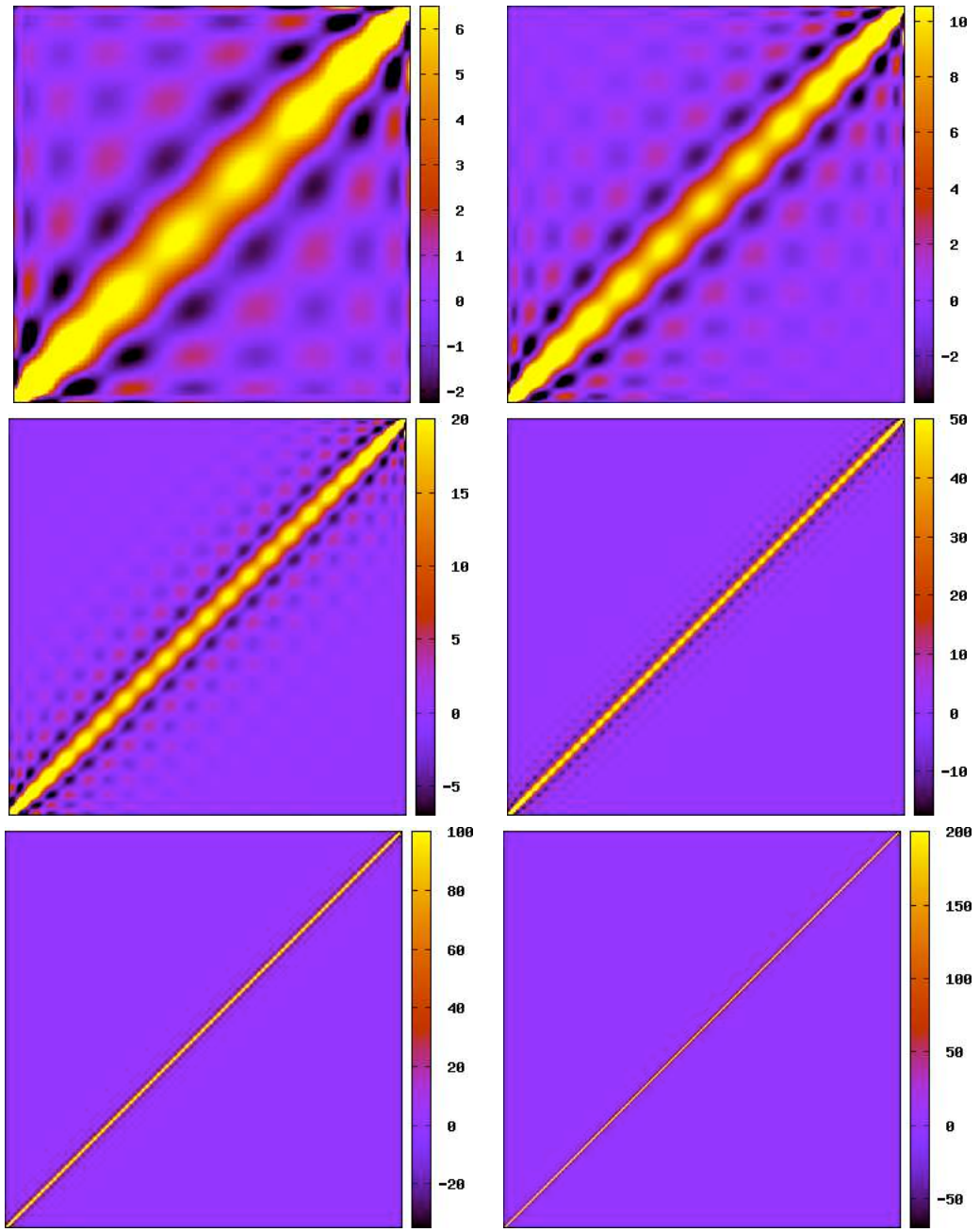

Figure I.1: Kernels of the projector operators $P(x, y)$ for B-spline basis with $k = 7$ defined by uniform grids on the $[0, 1]$ interval with 5, 10, 20, 50, 100 and 200 knots.

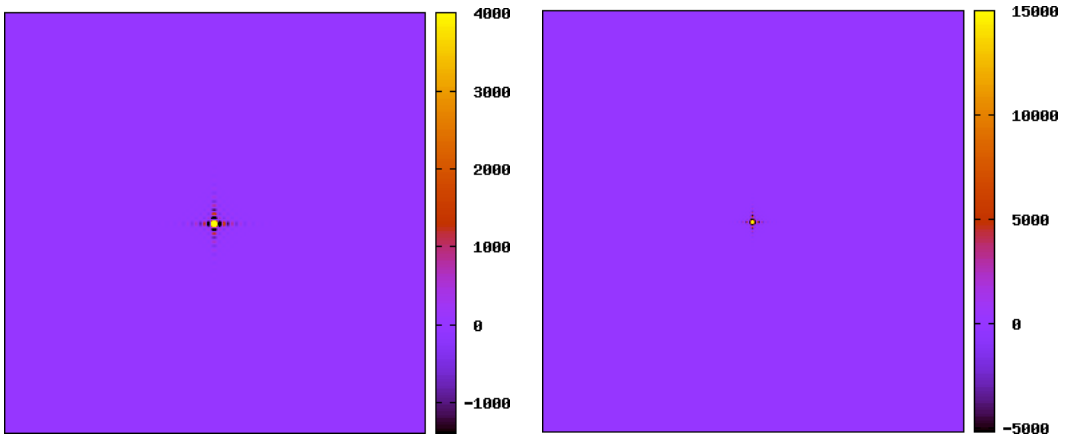

Figure I.2: $P(x,y)P(x',y')$ with $y = y' = 0.5$ for 7-th degree B-spline basis with 100 (left panel) and 200 (right panel) knots.

becomes negligible for $|x-y| \gtrsim k/n$. In figure I.2 the product $P(x,y)P(x',y)$ for $y = 0.5$ is reported for $k = 7$ and $n = 100$. This plot gives an idea of the resolution with which an operator is represented.

Equation I.3 can be exploited to extract a diagonal component $V_p^{(1)}$

$$V_p^{(1)}(r) = \frac{\langle r|\bar{\mathsf{B}}\rangle}{r}\,\tilde{\mathsf{V}}\int_0^\infty \langle \bar{\mathsf{B}}|r'\rangle r' dr' \tag{I.7}$$

$V_p^{(1)}(r)$ can now be compared to $V(r)$, but we must bear in mind that, for all functions f and g belonging to the basis space:

$$\langle f|V|g\rangle = \langle f|V_p|g\rangle \neq \langle f|V_p^{(1)}|g\rangle \qquad f,g \in \mathcal{S}_B. \tag{I.8}$$

Still the quality of this representation can be pretty good when a suitable B-spline basis is used. As an example, consider the following gaussian potential

$$V(r) \equiv V_0 e^{-\alpha r^2}, \qquad V_0 = 4\,\text{au}, \quad \alpha = 0.1\,\text{au} \tag{I.9}$$

projected on a B-spline basis with $k = 7$, defined on a grid with 50 knots thicker at the origin, and asymptotically evenly spaced by 0.5au intervals up to ~ 21.5 au. In figure I.3, the corresponding $V(r)$ and $V_p^{(1)}(r)$ are reported, along with their difference (the oscillating function) amplified by a factor of 10^5.

Non local potentials with diagonal predominance can still be approximated with local effective potentials by means of I.7. This technique has been applied to represent the effective potentials of one electron in the field of the boron parent ion in all the symmetries shown in chapter 4. On each plot, the corresponding single ionization branches are also reported.

The effective potentials are defined, on the line of the close coupling equations 1.8, as

$$V_i(r) = \frac{l(l+1)}{2r^2} - \frac{1}{r} - V_{ii}^\Gamma(r) - \int [K_{ii}^\Gamma(r,r') + X_{ii}^\Gamma(r,r')]dr' \tag{I.10}$$

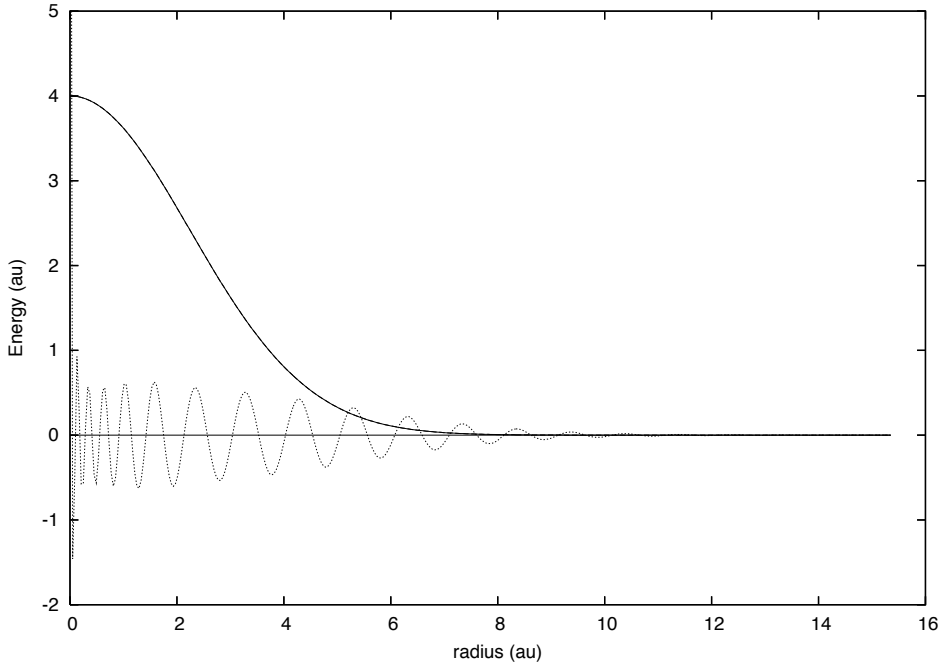

Figure I.3: Comparison between the diagonal approximating $V_p^{(1)}(r)$ of a projected diagonal gaussian potential V with its original kernel $V(r)$. The two functions are indistinguishable with the eye. Their difference, the oscillating function in the plot, has been multiplied by a factor of 10^5.

The reduction of nonlocal potentials adopted above gives a reliable idea of these potentials only if they have diagonal predominance, but actually is otherwise arbitrary. On the abscissas of effective potentials plots, $\log(r+1)$ is reported.

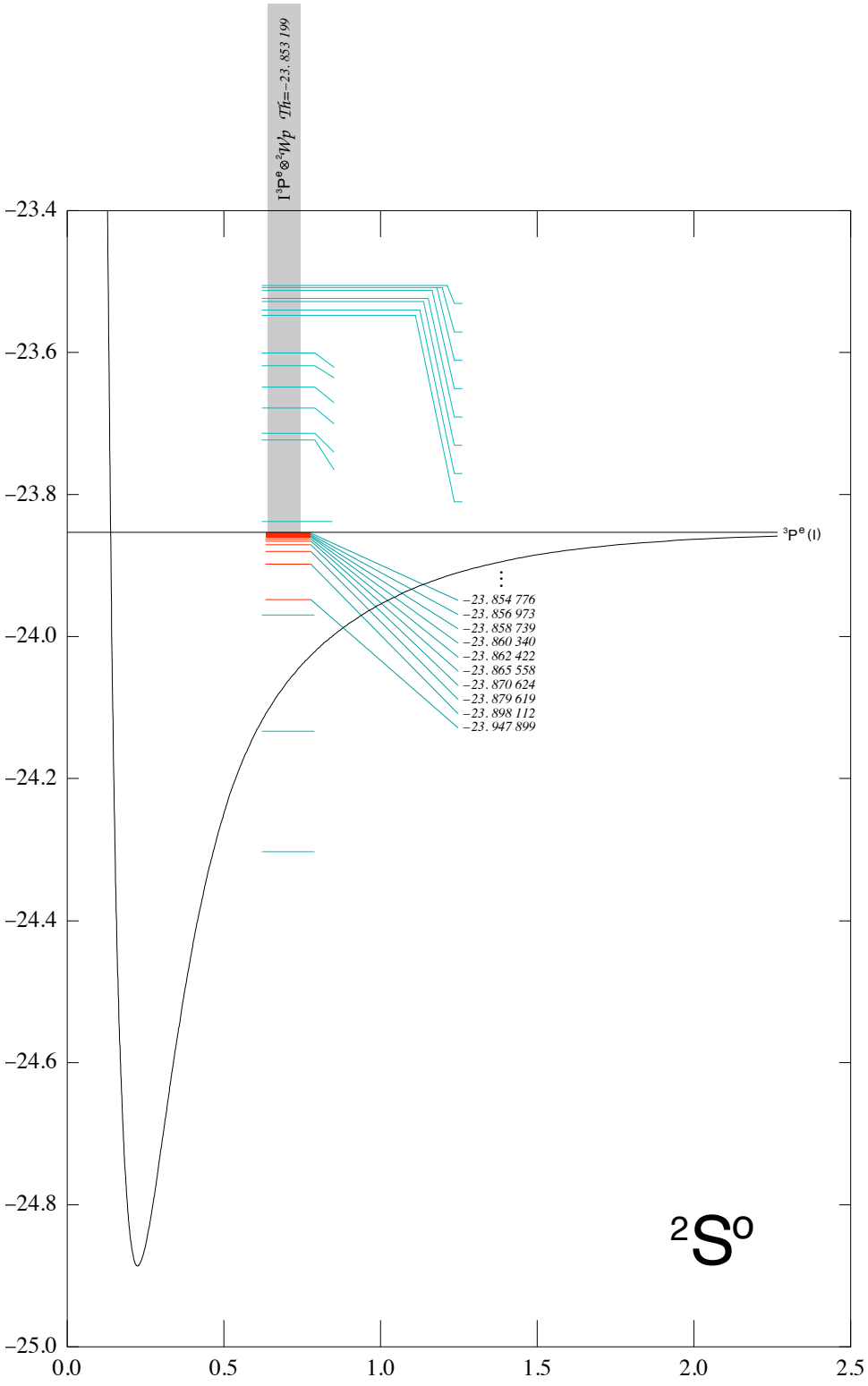
$1^3P^e \otimes {}^3\mathcal{W}p$ $\mathcal{T}h$=−23. 853 199
−23.4
−23.6
−23.8
−24.0
−24.2
−24.4
−24.6
−24.8
−25.0
0.0
0.5
1.0
1.5
2.0
2.5
$^3P^e$ (I)
−23. 854 776
−23. 856 973
−23. 858 739
−23. 860 340
−23. 862 422
−23. 865 558
−23. 870 624
−23. 879 619
−23. 898 112
−23. 947 899
$^2S^o$

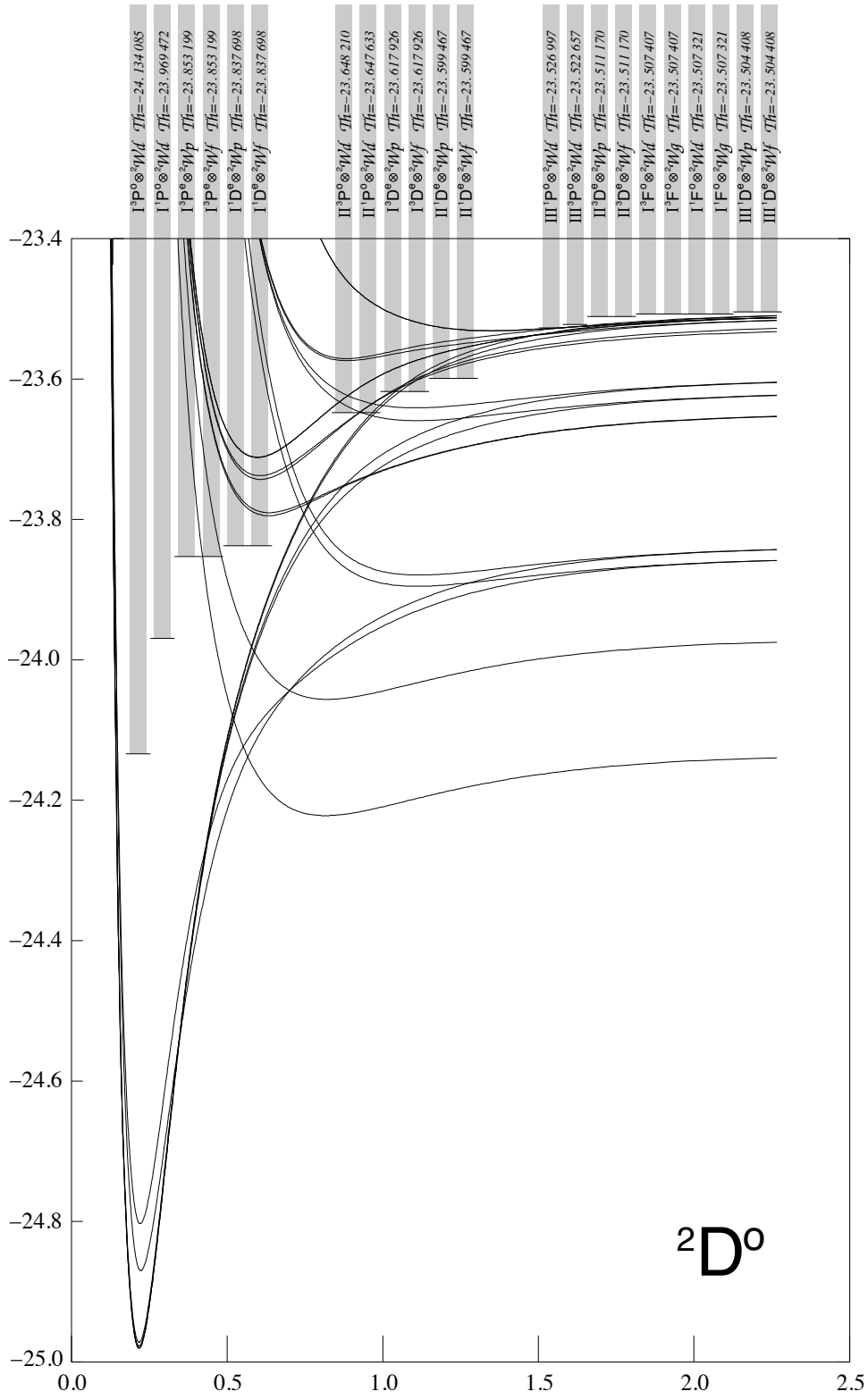
I 3P°⊗ 2Nd Th=-24.134085
I 1P°⊗ 2Nd Th=-23.969472
I 3P⊗ 2Np Th=-23.853199
I 3P⊗ 2Nf Th=-23.853199
I 1D⊗ 2Np Th=-23.837698
I 1D⊗ 2Nf Th=-23.837698
II 3P°⊗ 2Nd Th=-23.648210
II 1P°⊗ 2Nd Th=-23.647633
I 3D⊗ 2Np Th=-23.617926
I 3D⊗ 2Nf Th=-23.617926
II 1D⊗ 2Np Th=-23.599467
II 1D⊗ 2Nf Th=-23.599467
III 1P°⊗ 2Nd Th=-23.526997
III 3P°⊗ 2Nd Th=-23.522657
II 3D⊗ 2Np Th=-23.511170
II 3D⊗ 2Nf Th=-23.511170
I 3F°⊗ 2Nd Th=-23.507407
I 3F°⊗ 2Ng Th=-23.507407
I 1F°⊗ 2Nd Th=-23.507321
I 1F°⊗ 2Ng Th=-23.507321
III 1D⊗ 2Np Th=-23.504408
III 1D⊗ 2Nf Th=-23.504408
−23.4
−23.6
−23.8
−24.0
−24.2
−24.4
−24.6
−24.8
−25.0
0.0
0.5
1.0
1.5
2.0
2.5
2Do

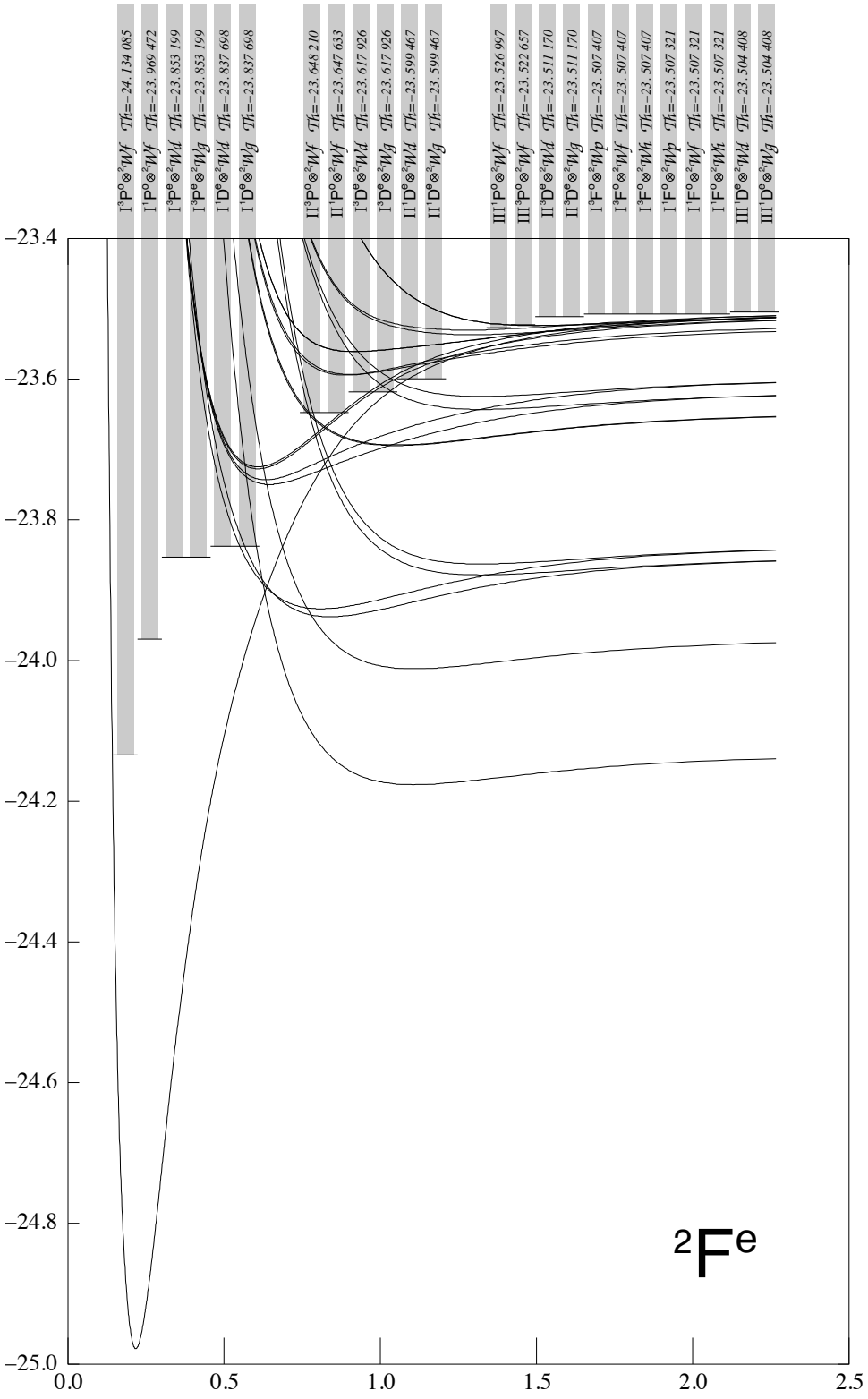
I 3P°⊗2Pf Th=−24.134 085
I 1P°⊗2Pf Th=−23.969 472
I 3Pe⊗2Pd Th=−23.853 199
I 3Pe⊗2Pg Th=−23.853 199
I 1De⊗2Pd Th=−23.837 698
I 1De⊗2Pg Th=−23.837 698
II 3P°⊗2Pf Th=−23.648 210
II 1P°⊗2Pf Th=−23.647 633
I 3De⊗2Pd Th=−23.617 926
I 3De⊗2Pg Th=−23.617 926
II 1De⊗2Pd Th=−23.599 467
II 1De⊗2Pg Th=−23.599 467
III 1P°⊗2Pf Th=−23.526 997
III 3P°⊗2Pf Th=−23.522 657
II 3De⊗2Pd Th=−23.511 170
II 3De⊗2Pg Th=−23.511 170
I 3F°⊗2Pp Th=−23.507 407
I 3F°⊗2Pf Th=−23.507 407
I 3F°⊗2Ph Th=−23.507 407
I 1F°⊗2Pp Th=−23.507 321
I 1F°⊗2Pf Th=−23.507 321
I 1F°⊗2Ph Th=−23.507 321
III 1De⊗2Pd Th=−23.504 408
III 1De⊗2Pg Th=−23.504 408
−23.4
−23.6
−23.8
−24.0
−24.2
−24.4
−24.6
−24.8
−25.0
0.0
0.5
1.0
1.5
2.0
2.5
2Fe

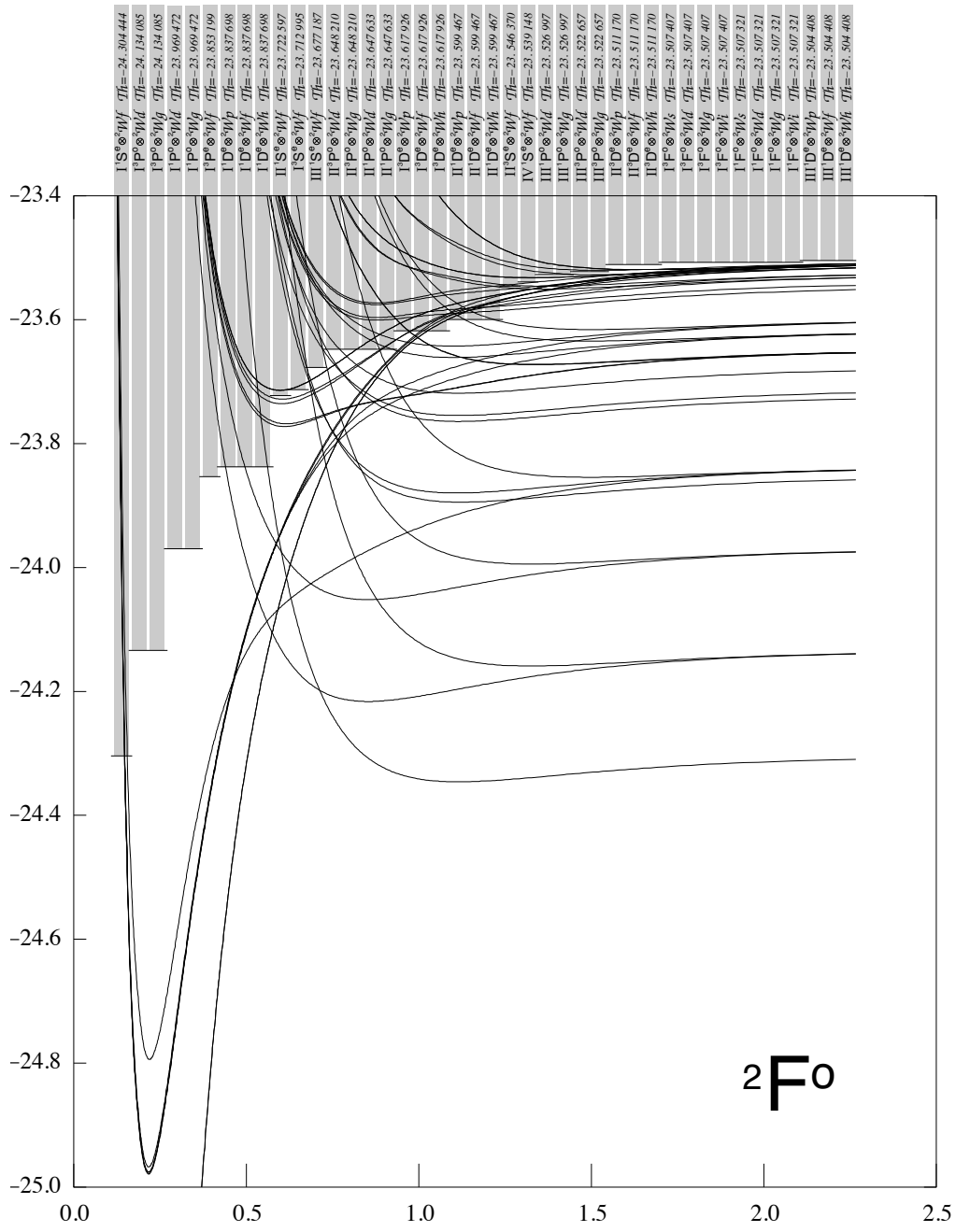
I¹S°⊗³Wf Tf= -24. 304 444
I³P°⊗³Wd Tf= -24. 134 085
I³P°⊗³We Tf= -24. 134 085
I¹P°⊗³Wd Tf= -23. 969 472
I¹P°⊗³Wg Tf= -23. 969 472
I³P°⊗³Wf Tf= -23. 853 199
I¹D°⊗³Wp Tf= -23. 837 698
I¹D°⊗³Wf Tf= -23. 837 698
I¹D°⊗³Wh Tf= -23. 837 698
II¹S°⊗³Wf Tf= -23. 722 597
I³S°⊗³Wf Tf= -23. 712 995
III¹S°⊗³Wf Tf= -23. 677 187
II³P°⊗³Wd Tf= -23. 648 210
II¹P°⊗³Wg Tf= -23. 648 210
II¹P°⊗³Wd Tf= -23. 647 633
II¹P°⊗³Wg Tf= -23. 647 633
I³D°⊗³Wp Tf= -23. 617 926
I³D°⊗³Wf Tf= -23. 617 926
I³D°⊗³Wh Tf= -23. 617 926
II¹D°⊗³Wp Tf= -23. 599 467
II¹D°⊗³Wf Tf= -23. 599 467
II¹D°⊗³Wh Tf= -23. 599 467
II³S°⊗³Wf Tf= -23. 546 370
IV¹S°⊗³Wf Tf= -23. 539 148
III³P°⊗³Wd Tf= -23. 526 997
III¹P°⊗³Wg Tf= -23. 526 997
III³P°⊗³Wd Tf= -23. 522 657
III³P°⊗³Wg Tf= -23. 522 657
II³D°⊗³Wp Tf= -23. 511 170
II¹D°⊗³Wf Tf= -23. 511 170
II¹D°⊗³Wh Tf= -23. 511 170
I³F°⊗³Wf Tf= -23. 507 407
I³F°⊗³Wd Tf= -23. 507 407
I³F°⊗³Wg Tf= -23. 507 407
I³F°⊗³We Tf= -23. 507 407
I¹F°⊗³Wd Tf= -23. 507 321
I¹F°⊗³We Tf= -23. 507 321
I¹F°⊗³Wg Tf= -23. 507 321
I¹F°⊗³Wi Tf= -23. 507 321
III¹D°⊗³Wp Tf= -23. 504 408
III¹D°⊗³Wf Tf= -23. 504 408
III¹D°⊗³Wh Tf= -23. 504 408
−23.4
−23.6
−23.8
−24.0
−24.2
−24.4
−24.6
−24.8
−25.0
0.0
0.5
1.0
1.5
2.0
2.5
2Fo

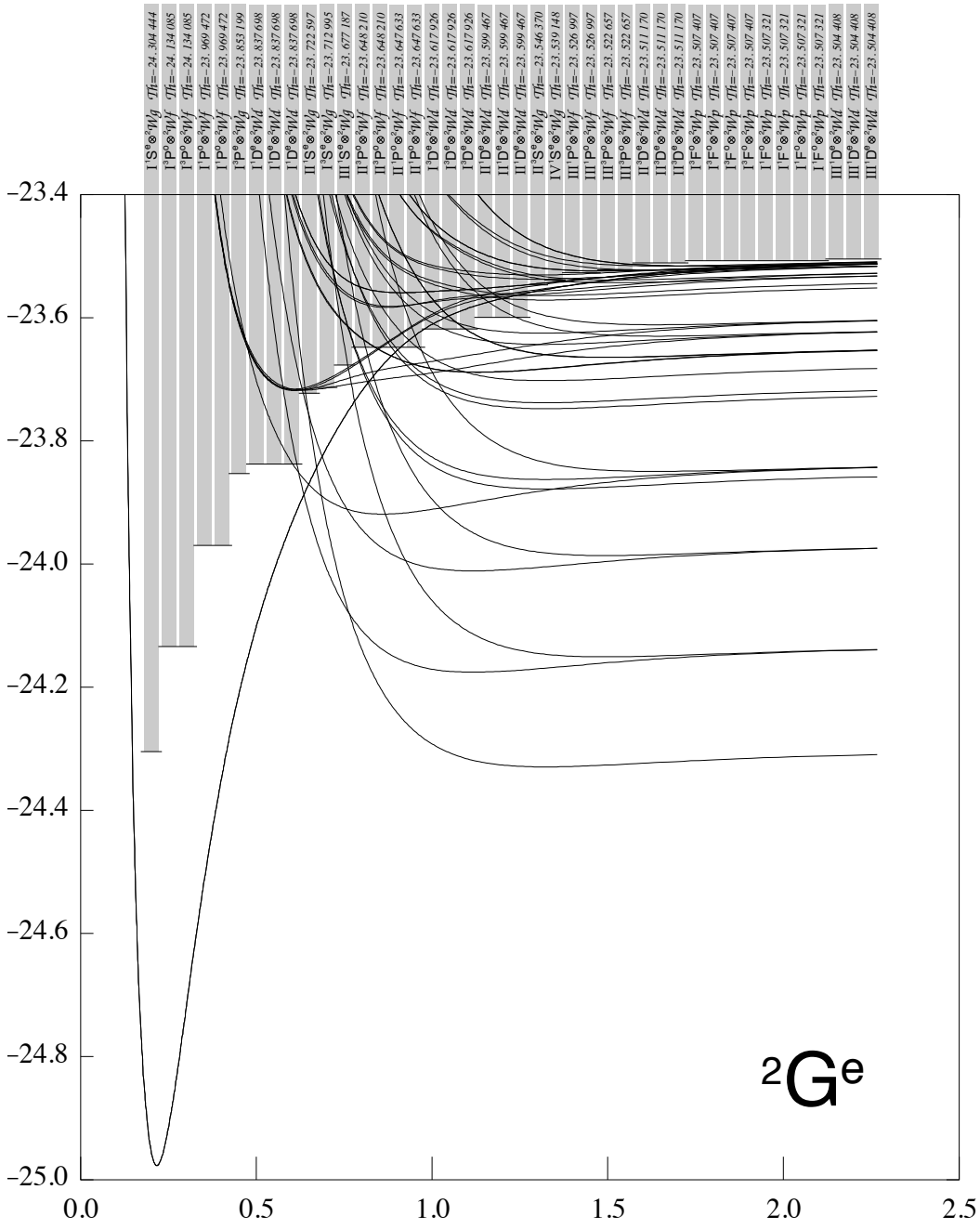
1 1S e ⊗ 2Ag Th= -24. 304 444
1 3P o ⊗ 2Af Th= -24. 134 085
1 3P o ⊗ 2Af Th= -24. 134 085
1 1P o ⊗ 2Af Th= -23. 969 472
1 1P o ⊗ 2Af Th= -23. 969 472
1 3P e ⊗ 2Ag Th= -23. 853 199
1 1D e ⊗ 2Ad Th= -23. 837 698
1 1D e ⊗ 2Ad Th= -23. 837 698
1 1D e ⊗ 2Ad Th= -23. 837 698
1 1S e ⊗ 2Ag Th= -23. 722 597
1 3S e ⊗ 2Ag Th= -23. 712 905
III 1S e ⊗ 2Ag Th= -23. 677 187
II 1P o ⊗ 2Af Th= -23. 648 210
II 3P o ⊗ 2Af Th= -23. 648 210
II 1P o ⊗ 2Af Th= -23. 647 633
II 1P o ⊗ 2Af Th= -23. 647 633
I 3D e ⊗ 2Ad Th= -23. 617 926
I 3D e ⊗ 2Ad Th= -23. 617 926
I 1D e ⊗ 2Ad Th= -23. 617 926
II 1D e ⊗ 2Ad Th= -23. 599 467
II 1D e ⊗ 2Ad Th= -23. 599 467
II 3S e ⊗ 2Ag Th= -23. 546 370
IV 1S e ⊗ 2Ag Th= -23. 539 148
III 1P o ⊗ 2Af Th= -23. 526 997
III 1P o ⊗ 2Af Th= -23. 526 997
III 3P o ⊗ 2Af Th= -23. 522 657
III 3P o ⊗ 2Af Th= -23. 522 657
II 3D e ⊗ 2Ad Th= -23. 511 170
II 1D e ⊗ 2Ad Th= -23. 511 170
II 3D e ⊗ 2Ad Th= -23. 511 170
I 3F o ⊗ 2Ap Th= -23. 507 407
I 3F o ⊗ 2Ap Th= -23. 507 407
I 3F o ⊗ 2Ap Th= -23. 507 407
I 1F o ⊗ 2Ap Th= -23. 507 321
I 1F o ⊗ 2Ap Th= -23. 507 321
I 1F o ⊗ 2Ap Th= -23. 507 321
III 1D e ⊗ 2Ad Th= -23. 504 408
III 1D e ⊗ 2Ad Th= -23. 504 408
III 1D e ⊗ 2Ad Th= -23. 504 408
-23.4
-23.6
-23.8
-24.0
-24.2
-24.4
-24.6
-24.8
-25.0
0.0
0.5
1.0
1.5
2.0
2.5
2Ge

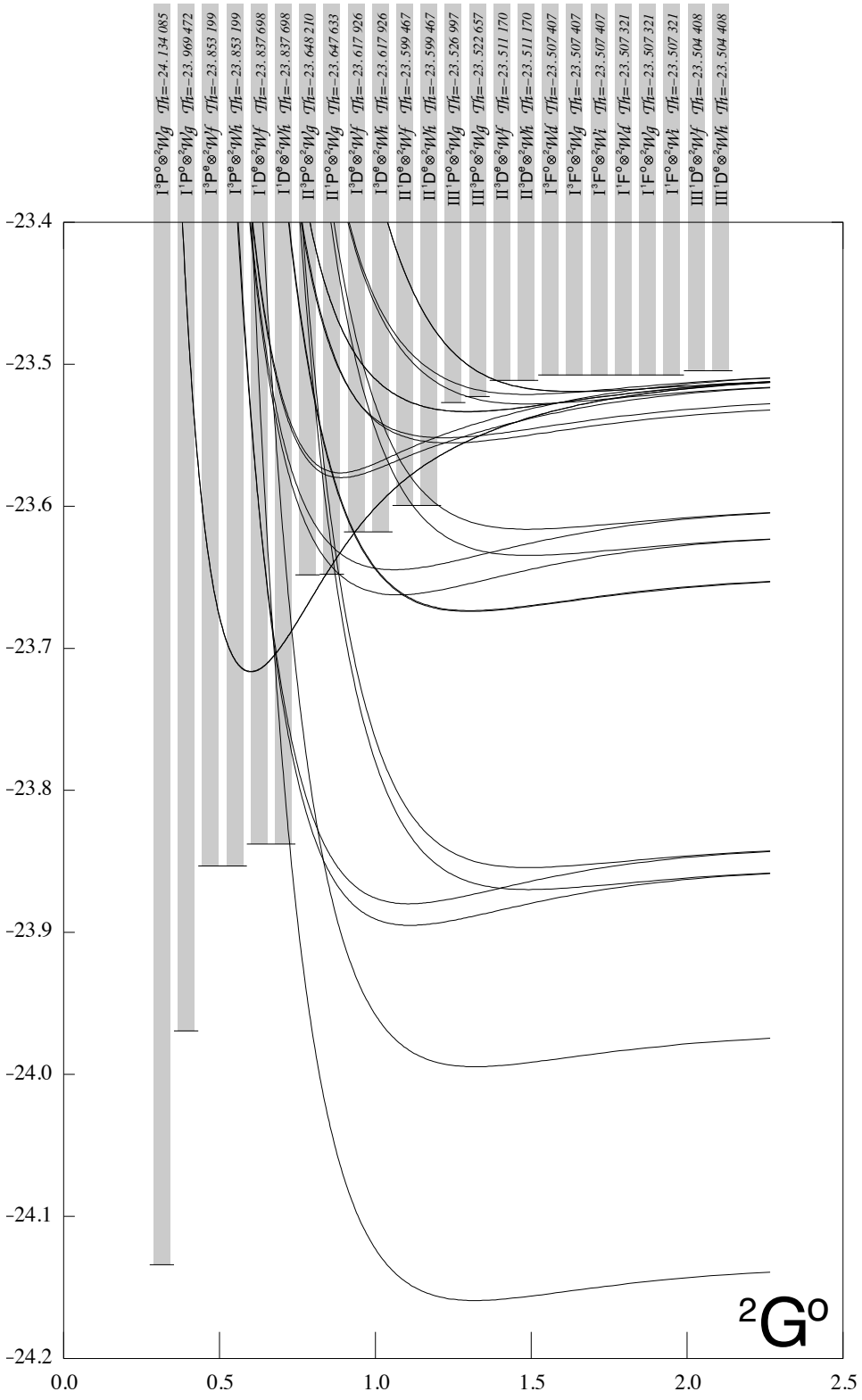
I 3P° ⊗ 2Wg Th=−24.134 085
I 1P° ⊗ 2Wg Th=−23.969 472
I 3P⊕ ⊗ 2Wf Th=−23.853 199
I 3P⊕ ⊗ 2Wh Th=−23.853 199
I 1D⊕ ⊗ 2Wf Th=−23.837 698
I 1D⊕ ⊗ 2Wh Th=−23.837 698
II 3P° ⊗ 2Wg Th=−23.648 210
II 1P° ⊗ 3Wg Th=−23.647 633
I 3D⊕ ⊗ 3Wf Th=−23.617 926
I 3D⊕ ⊗ 3Wh Th=−23.617 926
II 1D⊕ ⊗ 2Wf Th=−23.599 467
II 1D⊕ ⊗ 2Wh Th=−23.599 467
III 1P° ⊗ 2Wg Th=−23.526 997
III 3P° ⊗ 2Wg Th=−23.522 657
II 3D⊕ ⊗ 2Wf Th=−23.511 170
II 3D⊕ ⊗ 2Wh Th=−23.511 170
I 3F° ⊗ 2Wd Th=−23.507 407
I 3F° ⊗ 2Wg Th=−23.507 407
I 3F° ⊗ 2Wi Th=−23.507 407
I 1F° ⊗ 2Wd Th=−23.507 321
I 1F° ⊗ 2Wg Th=−23.507 321
I 1F° ⊗ 2Wi Th=−23.507 321
III 1D⊕ ⊗ 2Wf Th=−23.504 408
III 1D⊕ ⊗ 2Wh Th=−23.504 408
−23.4
−23.5
−23.6
−23.7
−23.8
−23.9
−24.0
−24.1
−24.2
0.0
0.5
1.0
1.5
2.0
2.5
2Go

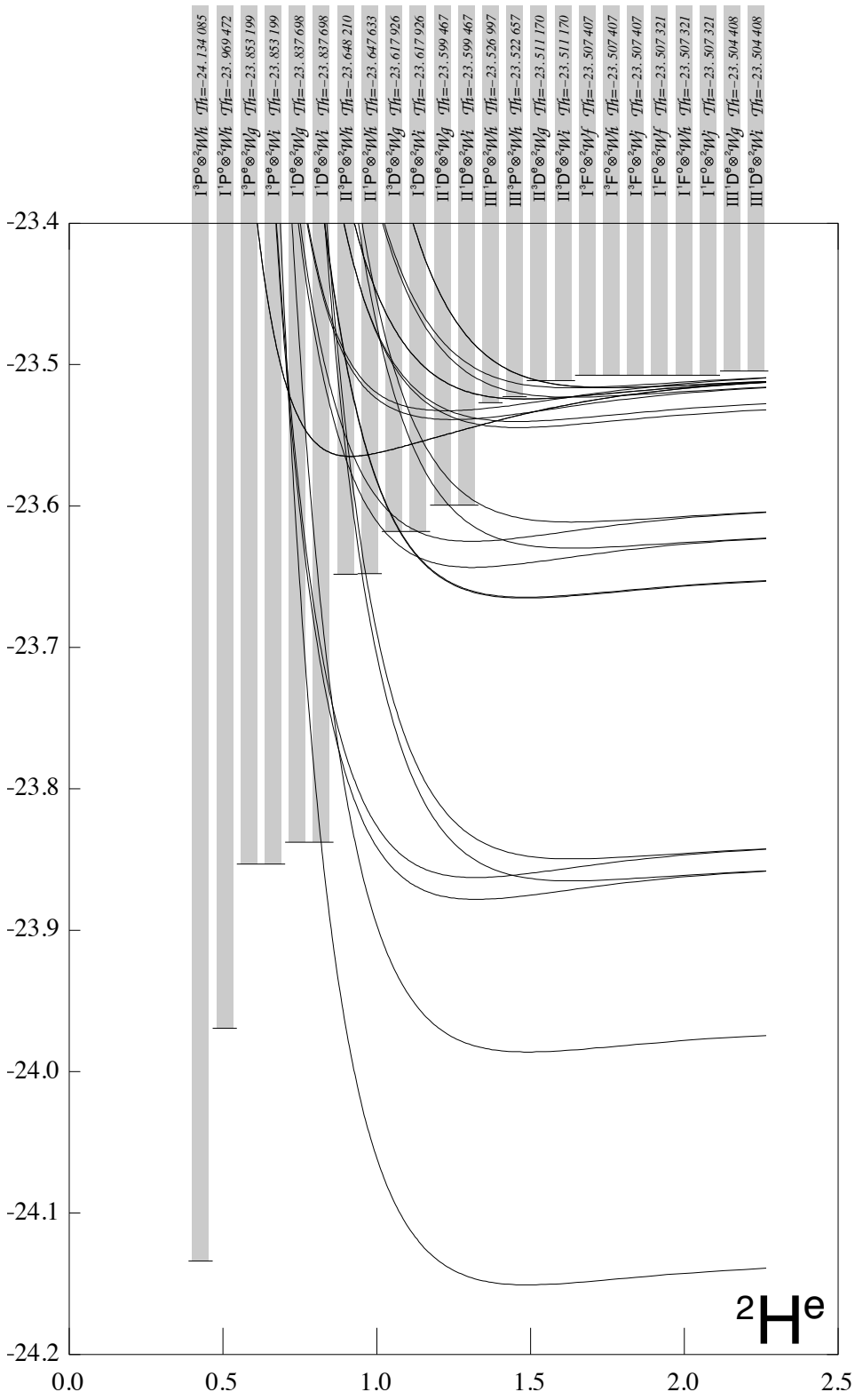
$^{1}P^{o}\otimes^{2}Wh$ Th=-24.134 085
$^{1}P^{o}\otimes^{2}Wh$ Th=-23.969 472
$^{1}P^{e}\otimes^{2}Wg$ Th=-23.853 199
$^{1}P^{e}\otimes^{2}Wi$ Th=-23.853 199
$^{1}D^{e}\otimes^{2}Wg$ Th=-23.837 698
$^{1}D^{e}\otimes^{2}Wi$ Th=-23.837 698
$^{3}P^{o}\otimes^{3}Wh$ Th=-23.648 210
$^{1}P^{o}\otimes^{3}Wh$ Th=-23.647 633
$^{3}D^{e}\otimes^{3}Wg$ Th=-23.617 926
$^{3}D^{e}\otimes^{3}Wi$ Th=-23.617 926
$^{1}D^{e}\otimes^{3}Wg$ Th=-23.599 467
$^{1}D^{e}\otimes^{3}Wi$ Th=-23.599 467
$^{1}P^{o}\otimes^{3}Wh$ Th=-23.526 997
$^{3}P^{o}\otimes^{3}Wh$ Th=-23.522 657
$^{3}D^{e}\otimes^{3}Wg$ Th=-23.511 170
$^{3}D^{e}\otimes^{3}Wi$ Th=-23.511 170
$^{3}F^{o}\otimes^{3}Wf$ Th=-23.507 407
$^{3}F^{o}\otimes^{2}Wh$ Th=-23.507 407
$^{3}F^{o}\otimes^{3}Wj$ Th=-23.507 407
$^{1}F^{o}\otimes^{3}Wf$ Th=-23.507 321
$^{1}F^{o}\otimes^{3}Wh$ Th=-23.507 321
$^{1}F^{o}\otimes^{3}Wj$ Th=-23.507 321
$^{1}D^{e}\otimes^{3}Wg$ Th=-23.504 408
$^{1}D^{e}\otimes^{3}Wi$ Th=-23.504 408
-23.4
-23.5
-23.6
-23.7
-23.8
-23.9
-24.0
-24.1
-24.2
0.0
0.5
1.0
1.5
2.0
2.5
^{2}He

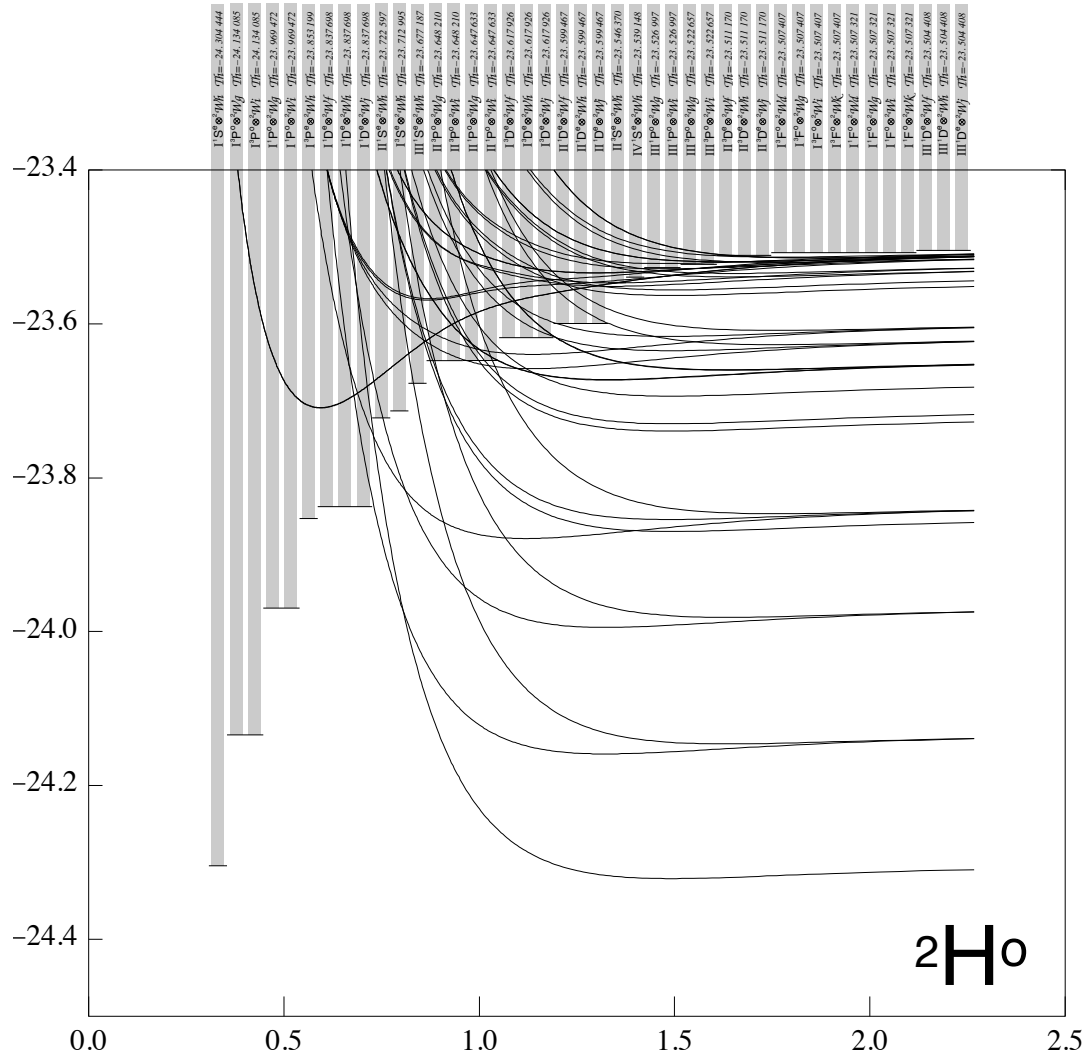
−23.4
−23.6
−23.8
−24.0
−24.2
−24.4
0.0
0.5
1.0
1.5
2.0
2.5
2Ho

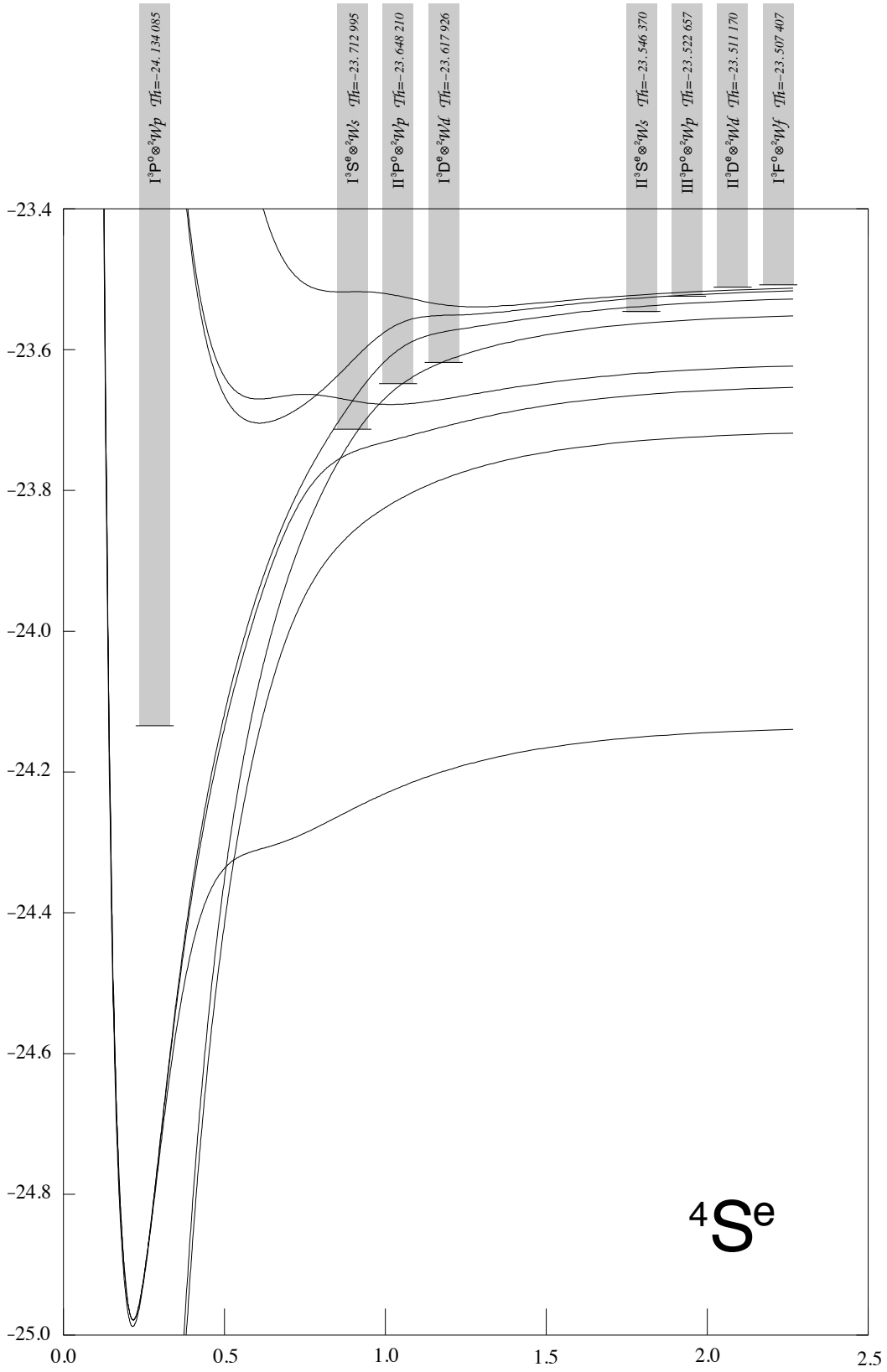
I 3P°⊗2Ψp Th=-24.134 085
I 3Se⊗2Ψs Th=-23.712 995
II 3P°⊗2Ψp Th=-23.648 210
I 3De⊗2Ψd Th=-23.617 926
II 3Se⊗2Ψs Th=-23.546 370
III 3P°⊗2Ψp Th=-23.522 657
II 3De⊗2Ψd Th=-23.511 170
I 3F°⊗2Ψf Th=-23.507 407
-23.4
-23.6
-23.8
-24.0
-24.2
-24.4
-24.6
-24.8
-25.0
0.0
0.5
1.0
1.5
2.0
2.5
4Se

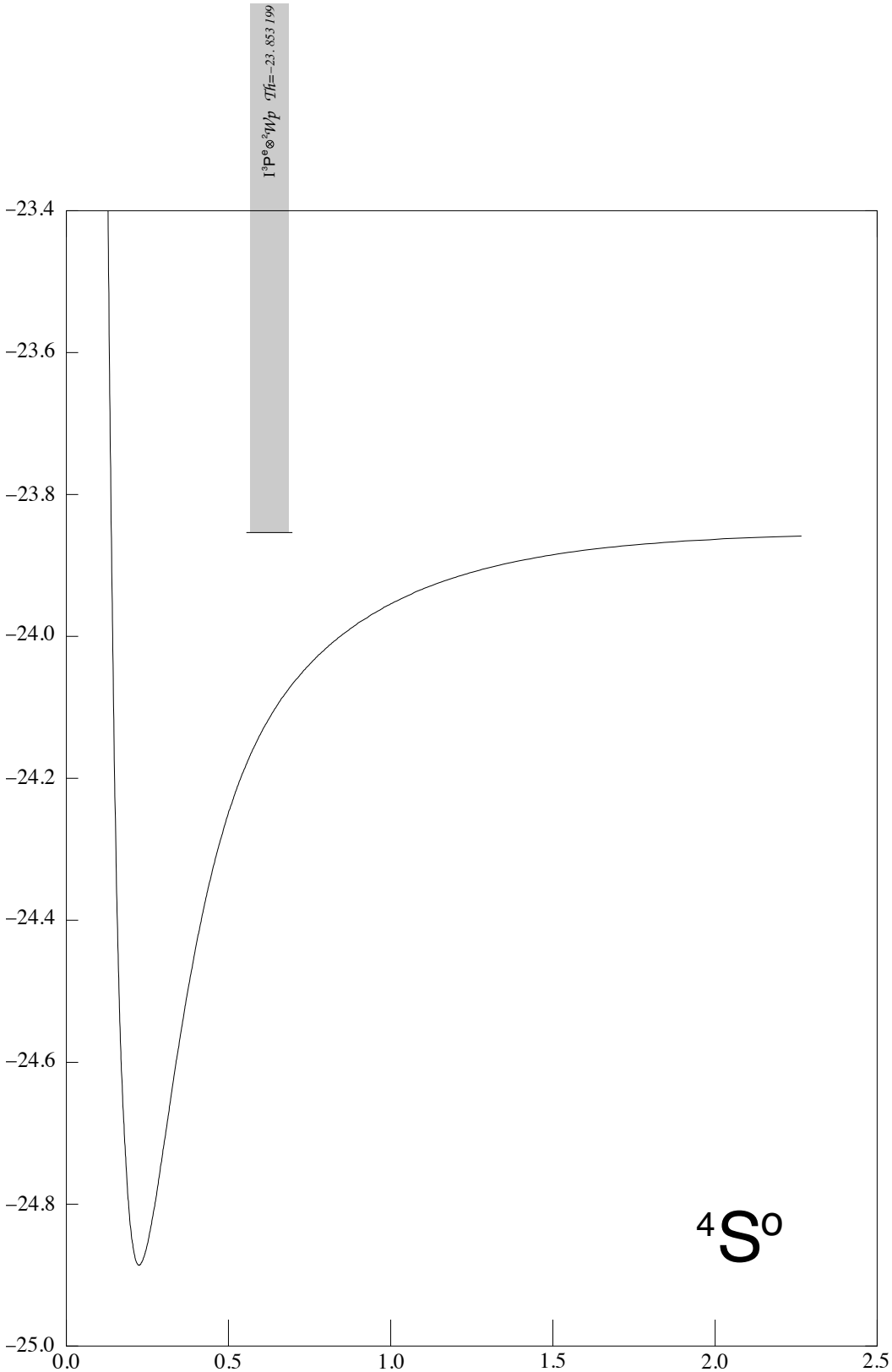
$1^3P^e \otimes {}^3\mathcal{W}p$ $\mathcal{T}k$=−23.853199
−23.4
−23.6
−23.8
−24.0
−24.2
−24.4
−24.6
−24.8
−25.0
0.0
0.5
1.0
1.5
2.0
2.5
$^4S^o$

Appendix J

Boron Data Tables

Table J.1: Boron Rydberg energies in atomic units.

	$^2S^e$		$^2P^o$		$^2P^e$		$^2D^e$
1	0.182 4573	1	0.000 3167	1	0.331 3216	1	0.218 6185
2	0.250 6678	2	0.221 5425	2	0.396 3435	2	0.249 6244
3	0.274 0805	3	0.263 3221	3	0.433 6333	3	0.273 3841
4	0.284 7712	4	0.279 9376	4	0.450 1606	4	0.284 7294
5	0.289 9053	5	0.288 2621	5	0.458 5667	5	0.290 9209
6	0.292 5248	6	0.293 0274	6	0.463 3916	6	0.294 6558
7	0.295 2722	7	0.296 0090	7	0.466 4104	7	0.297 0792
8	0.297 4263	8	0.298 0078	8	0.468 4312	8	0.298 7843
9	0.299 0569	9	0.299 5948	9	0.470 0199	9	0.300 3763
10	0.300 7387	10	0.301 4017	10	0.471 8115	10	0.302 3333
	$^4S^e$		$^4P^o$		$^4P^e$		$^4D^o$
1	0.3921041	1	0.3527474	1	0.1323976	1	0.4157530
2	0.4338456	2	0.4193579	2	0.3942320	2	0.4424892
3	0.4504494	3	0.4217358	3	0.4348490	3	0.4545794
4	0.4587647	4	0.4437658	4	0.4509637	4	0.4610572
5	0.4635235	5	0.4450997	5	0.4590581	5	0.4649272
6	0.4665008	6	0.4551778	6	0.4637053	6	0.4674226
7	0.4684967	7	0.4559372	7	0.4666208	7	0.4691614
8	0.4700837	8	0.4613865	8	0.4685822	8	0.4707420
9	0.4718933	9	0.4618497	9	0.4701677	9	0.4726726
10	0.4741371	10	0.4651281	10	0.4719998	10	0.4750248
		11	0.4654287				
	$^4S^o$	12	0.4675546				
		13	0.4677608				
1	0.4439246	14	0.4692623				
2	0.6788266	15	0.4694406				
3	0.7171957	16	0.4708579				
4	0.7326466	17	0.4711205				
5	0.7404728	18	0.4728185				
6	0.7449912	19	0.4732115				
7	0.7478371	20	0.4751973				
8	0.7497607						
9	0.7513459						
10	0.7532023						

Table J.2: $^2S^e$ resonances.

n	E (au)	Γ (au)	n	E (au)	Γ (au)
1	0.4085167	0.4701[-3]	25	0.7582243	0.2812[-4]
2	0.4396340	0.1669[-3]	26	0.7618414	0.1763[-4]
3	0.4631561	0.7754[-4]	27	0.7642023	0.1212[-4]
4	0.4602471	0.4212[-4]	28	0.7658792	0.9828[-5]
5	0.4644234	0.2536[-4]	29	0.7674785	0.1189[-4]
6	0.4670886	0.1638[-4]	30	0.7694511	0.1587[-4]
7	0.4689183	0.1184[-4]	31	0.7938887	0.1079[-3]
8	0.4705123	0.1439[-4]	32	0.8328874	0.2880[-2]
9	0.4724355	0.1484[-4]	33	0.8349317	0.2992[-3]
10	0.4748131	0.1501[-4]	34	0.8521379	0.3152[-2]
11	0.5574437	0.5890[-2]	35	0.8562010	0.2349[-2]
12	0.5989328	0.2182[-2]	36	0.8627778	0.4509[-4]
13	0.6153425	0.1028[-2]	37	0.8650121	0.4282[-3]
14	0.6235882	0.5533[-3]	38	0.8693540	0.5893[-3]
15	0.6283156	0.3097[-3]	39	0.8738883	0.4346[-3]
16	0.6332349	0.2202[-3]	40	0.8755017	0.8905[-4]
17	0.6348222	0.1958[-3]	41	0.8771874	0.2863[-3]
18	0.6366352	0.2465[-3]	42	0.8794310	0.1878[-3]
19	0.6388592	0.3579[-3]	43	0.8884221	0.1668[-4]
20	0.6399403	0.1931[-3]	44	0.8810801	0.1468[-3]
21	0.7186997	0.9090[-4]	45	0.8820231	0.4038[-4]
22	0.7320689	0.2438[-2]	46	0.8827513	0.1670[-3]
23	0.7414918	0.1343[-3]	47	0.8848185	0.1853[-3]
24	0.7522745	0.5169[-4]	48	0.8859145	0.2289[-4]

Table J.3: $^2P^e$ resonances.

n	E (au)	Γ (au)	n	E (au)	Γ (au)
1	0.5570265	0.1851[-2]	20	0.7381320	0.1294[-2]
2	0.5982813	0.2459[-3]	21	0.7405919	0.9893[-4]
3	0.6148892	0.3516[-4]	22	0.7435754	0.7151[-3]
4	0.6232668	0.3589[-5]	23	0.7469184	0.4595[-3]
5	0.6311194	0.1794[-5]	24	0.7484973	0.9509[-5]
6	0.6331782	0.2467[-5]	25	0.7491149	0.3291[-3]
7	0.6362453	0.3091[-4]	26	0.7507545	0.2814[-3]
8	0.6383349	0.5479[-4]	27	0.7516988	0.3889[-4]
9	0.6331783	0.2387[-5]	28	0.7524935	0.3439[-3]
10	0.6362460	0.3088[-4]	29	0.7546558	0.4109[-3]
11	0.6383373	0.5557[-4]	30	0.7580604	0.7357[-4]
12	0.6396474	0.1820[-4]	31	0.7617363	0.5400[-4]
13	0.6516653	0.1750[-1]	32	0.7641367	0.3726[-4]
14	0.6971973	0.1319[-3]	33	0.7658320	0.2862[-4]
15	0.7077438	0.5966[-2]	34	0.7674297	0.3072[-4]
16	0.7166435	0.1785[-3]	35	0.7694025	0.2328[-4]
17	0.7236946	0.4473[-4]	36	0.7717866	0.3246[-4]
18	0.7282782	0.2444[-2]	37	0.8311097	0.3341[-4]
19	0.7356274	0.4204[-4]	38	0.8333709	0.4169[-2]

Table J.4: $^2P^o$ resonances.

n	E (au)	Γ (au)	n	E (au)	Γ (au)
1	0.3662500	0.5717[-2]	38	0.7448724	0.1866[-3]
2	0.4202861	0.5517[-4]	39	0.7471779	0.3171[-4]
3	0.4252678	0.1581[-2]	40	0.7484641	0.1236[-3]
4	0.4465602	0.6660[-3]	41	0.7499643	0.1238[-3]
5	0.4441603	0.2709[-4]	42	0.7532036	0.1440[-3]
6	0.4566849	0.3412[-3]	43	0.7514527	0.1211[-3]
7	0.4553679	0.1427[-4]	44	0.7548838	0.7327[-4]
8	0.4622805	0.1977[-3]	45	0.7581126	0.6217[-2]
9	0.4657007	0.1248[-3]	46	0.7560947	0.4254[-4]
10	0.4679454	0.8370[-4]	47	0.7582333	0.2604[-5]
11	0.4712989	0.9264[-4]	48	0.7603598	0.3708[-3]
12	0.4722824	0.2963[-4]	49	0.7632153	0.2525[-3]
13	0.4734310	0.1146[-3]	50	0.7651462	0.1837[-3]
14	0.4742307	0.1101[-4]	51	0.7658869	0.1519[-5]
15	0.5185301	0.1465[-2]	52	0.7667207	0.1920[-3]
16	0.5840495	0.4886[-3]	53	0.7685493	0.2576[-3]
17	0.5859939	0.3513[-3]	54	0.7708091	0.3544[-3]
18	0.6085271	0.1553[-3]	55	0.7775986	0.2832[-2]
19	0.6097145	0.1511[-3]	56	0.7963371	0.3201[-2]
20	0.6199237	0.8200[-4]	57	0.8209828	0.2314[-2]
21	0.6206064	0.7893[-4]	58	0.8443360	0.1134[-2]
22	0.6261221	0.4920[-4]	59	0.8451241	0.6379[-3]
23	0.6265431	0.4626[-4]	60	0.8609688	0.4556[-3]
24	0.6298557	0.3249[-4]	61	0.8664348	0.1455[-3]
25	0.6324732	0.1970[-4]	62	0.8695517	0.2086[-3]
26	0.6341571	0.1590[-4]	63	0.8743638	0.1206[-3]
27	0.6355765	0.2162[-4]	64	0.8766954	0.4582[-4]
28	0.6358390	0.1819[-4]	65	0.8775667	0.7265[-4]
29	0.6375269	0.3004[-4]	66	0.8792887	0.1044[-3]
30	0.6379327	0.2143[-4]	67	0.8805970	0.1235[-3]
31	0.6398182	0.7341[-4]	68	0.8819173	0.1061[-3]
32	0.6552068	0.2865[-4]	69	0.8828981	0.1021[-3]
33	0.6969316	0.1532[-2]	70	0.8837028	0.1445[-3]
34	0.7185497	0.1008[-3]	71	0.8864086	0.1354[-3]
35	0.7309488	0.9077[-4]	72	0.8857342	0.1481[-3]
36	0.7346709	0.6104[-3]	73	0.8887093	0.2380[-4]
37	0.7412606	0.6684[-5]			

Table J.5: $^2D^e$ resonances.

n	E (au)	Γ (au)	n	E (au)	Γ (au)
1	0.3995875	0.1828[-2]	34	0.7504934	0.7840[-4]
2	0.4365075	0.5978[-3]	35	0.7515859	0.7552[-4]
3	0.4516772	0.2795[-3]	36	0.7529167	0.4186[-3]
4	0.4595050	0.1171[-3]	37	0.7540874	0.1046[-3]
5	0.4638626	0.1361[-3]	38	0.7561085	0.5180[-3]
6	0.4667373	0.7441[-4]	39	0.7564862	0.4526[-4]
7	0.4686638	0.5244[-4]	40	0.7578634	0.3323[-4]
8	0.4702448	0.5366[-4]	41	0.7586657	0.2262[-3]
9	0.4720836	0.7219[-4]	42	0.7616236	0.2313[-4]
10	0.4742650	0.1206[-3]	43	0.7621133	0.1734[-3]
11	0.4752254	0.4162[-4]	44	0.7640644	0.1603[-4]
12	0.5516936	0.1966[-2]	45	0.7644057	0.1137[-3]
13	0.5969892	0.7575[-3]	46	0.7660638	0.8842[-4]
14	0.6144544	0.3876[-3]	47	0.7673702	0.1548[-4]
15	0.6230958	0.2321[-3]	48	0.7677604	0.1078[-3]
16	0.6280092	0.1501[-3]	49	0.7693260	0.2149[-4]
17	0.6310685	0.1028[-3]	50	0.7698734	0.1240[-3]
18	0.6331093	0.7530[-4]	51	0.8215563	0.3930[-2]
19	0.6347004	0.7320[-4]	52	0.8448602	0.1117[-2]
20	0.6364783	0.9919[-4]	53	0.8533292	0.1291[-2]
21	0.6386839	0.1406[-3]	54	0.8591601	0.1175[-2]
22	0.6401475	0.3153[-4]	55	0.8650218	0.7528[-3]
23	0.6584581	0.7326[-2]	56	0.8673019	0.1144[-2]
24	0.7027311	0.8558[-3]	57	0.8724932	0.8772[-3]
25	0.7149138	0.2501[-3]	58	0.8739585	0.3336[-3]
26	0.7204269	0.2037[-2]	59	0.8764209	0.4760[-3]
27	0.7260017	0.4729[-3]	60	0.8804674	0.2440[-3]
28	0.7368871	0.2584[-3]	61	0.8805448	0.1534[-3]
29	0.7400100	0.1150[-3]	62	0.8821372	0.1127[-3]
30	0.7425337	0.8042[-3]	63	0.8841158	0.3608[-4]
31	0.7428409	0.1828[-3]	64	0.8850124	0.8763[-4]
32	0.7464490	0.9576[-4]	65	0.8865304	0.3881[-5]
33	0.7488002	0.5173[-4]	66	0.8877976	0.6798[-4]

Table J.6: $^4S^e$ resonances.

n	E (au)	Γ (au)	n	E (au)	Γ (au)
1	0.8264114	0.3424[-5]	10	0.9095645	0.1637[-4]
2	0.8602195	0.1386[-5]	11	0.9320126	0.1993[-4]
3	0.8741374	0.6771[-6]	12	0.9422872	0.1554[-4]
4	0.8812927	0.3815[-6]	13	0.9479202	0.1184[-4]
5	0.8854743	0.2341[-6]	14	0.9513283	0.9678[-5]
6	0.8881341	0.1560[-6]	15	0.9534721	0.9245[-5]
7	0.8915769	0.1256[-6]	16	0.9546266	0.4868[-5]
8	0.8935366	0.1573[-6]	17	0.9556120	0.5111[-6]
9	0.8959381	0.1830[-6]	18	0.9571654	0.2979[-5]

Table J.7: $^4D^e$ resonances.

n	E (au)	Γ (au)	n	E (au)	Γ (au)
1	0.6681220	0.1453[-3]	13	0.9411346	0.9563[-4]
2	0.7308407	0.1277[-4]	14	0.9451186	0.1164[-3]
3	0.7394823	0.5773[-5]	15	0.9540731	0.1482[-4]
4	0.7443904	0.3773[-5]	16	0.9556506	0.9659[-5]
5	0.7474455	0.2326[-5]	17	0.9519575	0.3473[-4]
6	0.7494838	0.2396[-5]	18	0.9594406	0.3630[-5]
7	0.7510761	0.1662[-5]	19	0.9608708	0.1849[-5]
8	0.7528633	0.2654[-5]	20	0.9573432	0.7858[-5]
9	0.7550831	0.1999[-5]	21	0.9633250	0.1557[-2]
10	0.8746223	0.7123[-3]	22	0.9730486	0.9298[-3]
11	0.9148657	0.1397[-3]	23	0.9785437	0.5160[-3]
12	0.9335134	0.4298[-5]			

Table J.8: $^4P^e$ resonances.

n	E (au)	Γ (au)	n	E (au)	Γ (au)
1	0.7518922	0.5993[-5]	16	0.9553243	0.4273[-4]
2	0.6390834	0.2761[-4]	17	0.9565486	0.4573[-5]
3	0.6984301	0.8873[-4]	18	0.9571508	0.5423[-4]
4	0.7242131	0.4843[-4]	19	0.9591768	0.7037[-4]
5	0.7266590	0.1726[-4]	20	0.9622455	0.2466[-3]
6	0.7039619	0.3064[-4]	21	0.9701114	0.9766[-4]
7	0.7359845	0.2395[-4]	22	0.9768570	0.6822[-4]
8	0.7372958	0.1492[-4]	23	0.9808329	0.4755[-4]
9	0.7485822	0.7589[-5]	24	0.9833816	0.3394[-4]
10	0.9089635	0.9307[-3]	25	0.9851458	0.2655[-4]
11	0.9192580	0.1850[-4]	26	0.9867167	0.2984[-4]
12	0.9318234	0.4271[-3]	27	0.9886223	0.3689[-4]
13	0.9422649	0.2227[-3]	28	0.9909531	0.3453[-4]
14	0.9479762	0.1300[-3]	29	1.0034642	0.1835[-2]
15	0.9536865	0.5425[-4]			

Table J.9: $^4P^o$ resonances.

n	E (au)	Γ (au)	n	E (au)	Γ (au)
1	0.4821355	0.1481[-4]	27	0.9444779	0.2020[-3]
2	0.6720436	0.2244[-3]	28	0.9461862	0.6323[-4]
3	0.7145667	0.9207[-4]	29	0.9458047	0.5436[-4]
4	0.7313744	0.4593[-4]	30	0.9498623	0.6145[-4]
5	0.7397652	0.2597[-4]	31	0.9503073	0.4817[-4]
6	0.7445586	0.1613[-4]	32	0.9526344	0.4522[-4]
7	0.7475537	0.1069[-4]	33	0.9529516	0.3367[-4]
8	0.7495593	0.7616[-5]	34	0.9578776	0.4982[-4]
9	0.7511474	0.7391[-5]	35	0.9583440	0.3059[-4]
10	0.7529520	0.9460[-5]	36	0.9600850	0.5794[-4]
11	0.7565282	0.1000[-5]	37	0.9607500	0.3557[-4]
12	0.7614152	0.9221[-3]	38	0.9628136	0.5777[-3]
13	0.8866690	0.1614[-4]	39	0.9645325	0.1284[-3]
14	0.8438639	0.1770[-3]	40	0.9725979	0.4423[-3]
15	0.8670089	0.7500[-4]	41	0.9737756	0.7223[-4]
16	0.8775105	0.3820[-4]	42	0.9781741	0.2947[-3]
17	0.8832101	0.2365[-4]	43	0.9789625	0.4741[-4]
18	0.8740513	0.4587[-3]	44	0.9816130	0.2008[-3]
19	0.8905752	0.1426[-4]	45	0.9821612	0.3644[-4]
20	0.8920938	0.1548[-3]	46	0.9838694	0.1368[-3]
21	0.8943948	0.5530[-5]	47	0.9842786	0.3475[-4]
22	0.9110294	0.2555[-4]	48	0.9854706	0.1049[-3]
23	0.9226133	0.3081[-3]	49	0.9858810	0.5399[-4]
24	0.9252411	0.1826[-3]	50	0.9869574	0.8852[-4]
25	0.9376533	0.2097[-3]	51	0.9875880	0.1640[-3]
26	0.9390302	0.1173[-3]	52	0.9890147	0.1583[-4]

Appendix K

Energy levels, resonances and oscillator strengths in triplet He

- **Table 1. Energies of bound triplet Rydberg states in Helium**
  n : Principal quantum number of the external electron in the dominant $1s\,n\ell$ and $2p\,n\ell$ configurations in natural n^3S, n^3P^o, n^3D^e and unnatural n^3P^e, n^3D^o states respectively.
  Energies are given in atomic units

- **Tables 2-54. Positions and widths of doubly excited states below N-th threshold**
  n : Principal quantum number of the external electron
  $E(au)$: Resonance position
  Γ : Resonance width
  n^* : Effective principal quantum number $1/\sqrt{2(E_{threshold}-E)}$
  $\bar{\Gamma}$: Reduced width: $\bar{\Gamma} \equiv (n^*)^3 \cdot \Gamma$
  Energies and widths are given in atomic units. Resonance series are labeled with a progressive letter. The corresponding (K,T) classification is specified when available in literature. The assignment of external principal quantum numbers is tentative. In some cases it is controversial because few states fall below N-1 threshold, or ill-defined because of intruder states from higher thresholds. ^{3}D^e resonances below N=5 threshold are particularly hard to be separated neatly in series at lower energies: the first table (labeled *Unclassified*) collects lower energy undifferentiated resonances and lacks numbering.

- **Tables 55-64. Oscillator strengths between triplet Helium Rydberg states**
  In atomic units the averaged oscillator strength is defined as:

$$\bar{f}_{n^3L'^{\pi'} \leftarrow m^3L^{\pi}} \equiv \frac{2}{(E'-E)(2L+1)} \sum_{M_{L'}M_L} |\langle n^3L'^{\pi'}, M_{L'}| \sum_i p_{z,i} |m^3L^{\pi}, M_L\rangle|^2 \tag{K.1}$$

  All oscillator strengths are reported in velocity gauge. *Inter-threshold* transitions (between natural and unnatural Rydberg states) are to be taken with

care. With an energy difference of roughly 1.5 au, the half wavelength of the emitted or absorbed photon is of the order of 250-300 au, thus fully comparable to or even much shorter than the characteristic dimension of most Rydberg states beyond the first four or five. The main contribution to oscillator strength comes from the decay of the inner $2p$ electron to the $1s$ fundamental shell in the dominant $2pn\ell$ configuration but the possible influence of the outlying external electron cannot be ruled out. Reported oscillator strengths for ${}^3D^o \leftarrow {}^3D^e$ transitions are computed in length gauge. Correction factors for finite-mass nucleus can be found in literature [185].

Table 1: Bound Rydberg states

n	^{3}S	^{3}P^o	^{3}D^e	n	^{3}P^e	^{3}D^o
2	-2. 175 229 311	-2. 133 164 081		2	-0. 710 499 239	
3	-2. 068 689 043	-2. 058 081 046	-2. 055 636 295	3	-0. 567 812 762	-0. 559 328 053
4	-2. 036 512 067	-2. 032 324 332	-2. 031 288 834	4	-0. 535 867 134	-0. 532 678 505
5	-2. 022 618 867	-2. 020 551 187	-2. 020 021 029	5	-0. 522 254 537	-0. 520 703 395
6	-2. 015 377 500	-2. 014 207 991	-2. 013 901 454	6	-0. 515 160 011	-0. 514 288 092
7	-2. 011 129 892	-2. 010 404 944	-2. 010 212 089	7	-0. 510 991 553	-0. 510 452 720
8	-2. 008 427 100	-2. 007 946 990	-2. 007 817 912	8	-0. 508 334 143	-0. 507 977 891
9	-2. 006 601 502	-2. 006 267 248	-2. 006 176 667	9	-0. 506 536 216	-0. 506 288 433
10	-2. 005 310 783	-2. 005 068 790	-2. 005 002 804	10	-0. 505 263 254	-0. 505 083 970
11	-2. 004 364 690	-2. 004 183 889	-2. 004 134 345	11	-0. 504 329 050	-0. 504 195 150
12	-2. 003 650 616	-2. 003 511 994	-2. 003 473 853	12	-0. 503 623 223	-0. 503 520 584
13	-2. 003 098 457	-2. 002 989 848	-2. 002 959 863	13	-0. 503 076 959	-0. 502 996 553
14	-2. 002 662 718	-2. 002 576 045	-2. 002 552 048	14	-0. 502 645 542	-0. 502 581 382
15	-2. 002 312 829	-2. 002 242 560	-2. 002 223 056	15	-0. 502 298 893	-0. 502 246 879
16	-2. 002 027 633	-2. 001 969 876	-2. 001 953 811	16	-0. 502 016 173	-0. 501 973 421
17	-2. 001 792 111	-2. 001 744 062	-2. 001 730 673	17	-0. 501 782 574	-0. 501 747 009
18	-2. 001 595 359	-2. 001 554 958	-2. 001 543 682	18	-0. 501 587 340	-0. 501 557 435
19	-2. 001 429 305	-2. 001 395 008	-2. 001 385 423	19	-0. 501 422 497	-0. 501 397 112
20	-2. 001 287 861	-2. 001 258 492	-2. 001 250 275	20	-0. 501 282 033	-0. 501 260 297
21	-2. 001 166 350	-2. 001 140 994	-2. 001 133 897	21	-0. 501 161 322	-0. 501 142 560
22	-2. 001 061 098	-2. 001 039 046	-2. 001 032 873	22	-0. 501 056 731	-0. 501 040 420
23	-2. 000 968 731	-2. 000 949 242	-2. 000 943 855	23	-0. 500 964 881	-0. 500 950 495
24	-2. 000 888 011	-2. 000 869 516	-2. 000 864 374	24	-0. 500 884 512	-0. 500 870 975
25	-2. 000 811 391	-2. 000 799 542	-2. 000 796 009	25	-0. 500 808 903	-0. 500 800 013

Table 2: $^3S^e$ resonances below N=2 threshold ($\ell_{max} = 8$).

A $(K,T) = (1,0)$					B $(K,T) = (-1,0)$				
n	E (au)	Γ (au)	n^*	$\bar{\Gamma}$	n	E (au)	Γ (au)	n^*	$\bar{\Gamma}$
3	-0. 602 577 486	6. 651 [-6]	2. 208	7. 157 [-5]	3	-0. 559 746 441	2. 606 [-7]	2. 893	6. 310 [-6]
4	-0. 548 840 846	3. 095 [-6]	3. 200	1. 014 [-4]	4	-0. 532 505 270	1. 431 [-7]	3. 922	8. 636 [-6]
5	-0. 528 413 960	1. 542 [-6]	4. 195	1. 138 [-4]	5	-0. 520 549 113	8. 202 [-8]	4. 933	9. 846 [-6]
6	-0. 518 546 252	8. 569 [-7]	5. 192	1. 199 [-4]	6	-0. 514 180 007	5. 038 [-8]	5. 938	1. 055 [-5]
7	-0. 513 046 289	5. 201 [-7]	6. 191	1. 234 [-4]	7	-0. 510 378 019	3. 284 [-8]	6. 941	1. 098 [-5]
8	-0. 509 672 670	3. 377 [-7]	7. 190	1. 255 [-4]	8	-0. 507 925 053	2. 249 [-8]	7. 943	1. 127 [-5]
9	-0. 507 455 981	2. 311 [-7]	8. 189	1. 269 [-4]	9	-0. 506 250 009	1. 603 [-8]	8. 944	1. 147 [-5]
10	-0. 505 922 102	1. 649 [-7]	9. 189	1. 279 [-4]	10	-0. 505 055 287	1. 181 [-8]	9. 945	1. 162 [-5]
11	-0. 504 816 981	1. 216 [-7]	10. 188	1. 286 [-4]	11	-0. 504 173 234	8. 940 [-9]	10. 946	1. 172 [-5]
12	-0. 503 994 567	9. 218 [-8]	11. 188	1. 291 [-4]	12	-0. 503 503 492	6. 925 [-9]	11. 946	1. 181 [-5]
13	-0. 503 366 074	7. 153 [-8]	12. 188	1. 295 [-4]	13	-0. 502 982 984	5. 470 [-9]	12. 947	1. 187 [-5]
14	-0. 502 875 011	5. 660 [-8]	13. 188	1. 298 [-4]	14	-0. 502 570 438	4. 394 [-9]	13. 947	1. 192 [-5]
15	-0. 502 484 051	4. 554 [-8]	14. 187	1. 301 [-4]	15	-0. 502 237 929	3. 582 [-9]	14. 947	1. 196 [-5]
16	-0. 502 167 730	3. 718 [-8]	15. 187	1. 303 [-4]	16	-0. 502 237 929	3. 582 [-9]	14. 947	1. 196 [-5]
17	-0. 502 167 730	3. 718 [-8]	15. 187	1. 303 [-4]	17	-0. 501 966 012	2. 958 [-9]	15. 947	1. 200 [-5]
18	-0. 501 908 191	3. 075 [-8]	16. 187	1. 304 [-4]	18	-0. 501 740 808	2. 470 [-9]	16. 948	1. 202 [-5]
19	-0. 501 692 614	2. 572 [-8]	17. 187	1. 306 [-4]	19	-0. 501 552 195	2. 083 [-9]	17. 948	1. 204 [-5]
20	-0. 501 511 599	2. 172 [-8]	18. 187	1. 307 [-4]	20	-0. 501 392 643	1. 773 [-9]	18. 948	1. 206 [-5]
21	-0. 501 358 122	1. 852 [-8]	19. 187	1. 308 [-4]	21	-0. 501 256 453	1. 522 [-9]	19. 949	1. 208 [-5]
22	-0. 501 226 840	1. 592 [-8]	20. 188	1. 310 [-4]	22	-0. 501 139 226	1. 317 [-9]	20. 950	1. 211 [-5]
23	-0. 501 113 599	1. 380 [-8]	21. 189	1. 313 [-4]	23	-0. 501 037 505	1. 147 [-9]	21. 953	1. 213 [-5]
24	-0. 501 015 108	1. 210 [-8]	22. 194	1. 323 [-4]					

Table 3: $^3P^o$ resonances below N=2 threshold

A $(K,T)=(1,0)$					B $(K,T)=(0,1)$				
n	E (au)	Γ (au)	n^*	$\bar{\Gamma}$	n	E (au)	Γ (au)	n^*	$\bar{\Gamma}$
2	-0. 760 490 639	2. 989 [-4]	1. 385	7. 948 [-4]	3	-0. 579 030 867	1. 895 [-6]	2. 515	3. 016 [-5]
3	-0. 584 671 760	8. 230 [-5]	2. 430	1. 181 [-3]	4	-0. 539 558 730	7. 979 [-7]	3. 555	3. 585 [-5]
4	-0. 542 837 034	3. 157 [-5]	3. 416	1. 259 [-3]	5	-0. 523 946 606	4. 126 [-7]	4. 569	3. 937 [-5]
5	-0. 525 711 793	1. 491 [-5]	4. 410	1. 278 [-3]	6	-0. 516 079 530	2. 385 [-7]	5. 576	4. 135 [-5]
6	-0. 517 107 078	8. 134 [-6]	5. 406	1. 285 [-3]	7	-0. 511 547 658	1. 494 [-7]	6. 580	4. 257 [-5]
7	-0. 512 191 135	4. 904 [-6]	6. 404	1. 288 [-3]	8	-0. 508 696 339	9. 947 [-8]	7. 583	4. 336 [-5]
8	-0. 509 123 755	3. 178 [-6]	7. 403	1. 289 [-3]	9	-0. 506 785 384	6. 942 [-8]	8. 584	4. 391 [-5]
9	-0. 507 082 906	2. 175 [-6]	8. 402	1. 290 [-3]	10	-0. 505 442 041	5. 030 [-8]	9. 585	4. 430 [-5]
10	-0. 505 657 109	1. 553 [-6]	9. 401	1. 291 [-3]	11	-0. 504 461 704	3. 758 [-8]	10. 586	4. 459 [-5]
11	-0. 504 622 042	1. 147 [-6]	10. 401	1. 291 [-3]	12	-0. 503 724 371	2. 880 [-8]	11. 587	4. 481 [-5]
12	-0. 503 847 012	8. 715 [-7]	11. 400	1. 291 [-3]	13	-0. 503 155 851	2. 255 [-8]	12. 587	4. 498 [-5]
13	-0. 503 251 709	6. 771 [-7]	12. 400	1. 291 [-3]	14	-0. 502 708 265	1. 799 [-8]	13. 587	4. 512 [-5]
14	-0. 502 784 582	5. 367 [-7]	13. 400	1. 291 [-3]	15	-0. 502 349 585	1. 457 [-8]	14. 588	4. 523 [-5]
15	-0. 502 411 319	4. 325 [-7]	14. 400	1. 291 [-3]	16	-0. 502 057 727	1. 197 [-8]	15. 588	4. 532 [-5]
16	-0. 502 108 362	3. 536 [-7]	15. 400	1. 291 [-3]	17	-0. 501 817 063	9. 946 [-9]	16. 588	4. 540 [-5]
17	-0. 501 859 103	2. 928 [-7]	16. 400	1. 291 [-3]	18	-0. 501 616 280	8. 356 [-9]	17. 588	4. 547 [-5]
18	-0. 501 651 563	2. 452 [-7]	17. 400	1. 291 [-3]	19	-0. 501 447 022	7. 089 [-9]	18. 589	4. 553 [-5]
19	-0. 501 476 920	2. 074 [-7]	18. 400	1. 292 [-3]	20	-0. 501 303 000	6. 065 [-9]	19. 589	4. 559 [-5]
20	-0. 501 328 557	1. 769 [-7]	19. 400	1. 292 [-3]	21	-0. 501 179 398	5. 230 [-9]	20. 590	4. 565 [-5]
21	-0. 501 201 422	1. 523 [-7]	20. 400	1. 293 [-3]	22	-0. 501 072 436	4. 542 [-9]	21. 592	4. 573 [-5]
22	-0. 501 091 563	1. 322 [-7]	21. 402	1. 296 [-3]					

Table 4: $^3P^o$ resonances below N=2 threshold ($\ell_{max} = 8$).

C $(K,T) = (-1,0)$				
n	E (au)	Γ (au)	n^*	$\bar{\Gamma}$
3	-0. 548 844 002	1. 253 [-8]	3. 199	4. 104 [-7]
4	-0. 528 638 225	5. 777 [-9]	4. 178	4. 215 [-7]
5	-0. 518 709 909	3. 006 [-9]	5. 170	4. 152 [-7]
6	-0. 513 155 641	1. 745 [-9]	6. 165	4. 088 [-7]
7	-0. 509 747 145	1. 108 [-9]	7. 162	4. 070 [-7]
8	-0. 507 508 309	7. 472 [-10]	8. 160	4. 060 [-7]
9	-0. 505 960 038	5. 276 [-10]	9. 159	4. 054 [-7]
10	-0. 504 845 264	3. 863 [-10]	10. 158	4. 050 [-7]
11	-0. 504 016 174	2. 915 [-10]	11. 158	4. 049 [-7]
12	-0. 503 382 930	2. 253 [-10]	12. 157	4. 049 [-7]
13	-0. 502 888 404	1. 778 [-10]	13. 157	4. 050 [-7]
14	-0. 502 494 862	1. 429 [-10]	14. 157	4. 053 [-7]
15	-0. 502 176 579	1. 165 [-10]	15. 156	4. 057 [-7]
16	-0. 501 915 524	9. 635 [-11]	16. 156	4. 063 [-7]
17	-0. 501 698 757	8. 060 [-11]	17. 156	4. 070 [-7]
18	-0. 501 516 797	6. 816 [-11]	18. 156	4. 079 [-7]
19	-0. 501 362 561	5. 818 [-11]	19. 156	4. 090 [-7]
20	-0. 501 230 668	5. 012 [-11]	20. 156	4. 104 [-7]
21	-0. 501 116 939	4. 356 [-11]	21. 158	4. 126 [-7]
22	-0. 501 018 079	3. 825 [-11]	22. 161	4. 163 [-7]

Table 5: $^3D^e$ resonances below N=2 threshold ($\ell_{max} = 8$).

	A				B				
n	E (au)	Γ (au)	n^*	$\bar{\Gamma}$	n	E (au)	Γ (au)	n^*	$\bar{\Gamma}$
3	-0. 560 686 118	7. 520 [-6]	2. 870	1. 778 [-4]	3	-0. 583 784 086	2. 838 [-8]	2. 443	4. 137 [-7]
4	-0. 533 463 037	3. 821 [-6]	3. 865	2. 207 [-4]	4	-0. 541 678 920	9. 778 [-9]	3. 464	4. 063 [-7]
5	-0. 521 131 058	2. 063 [-6]	4. 864	2. 374 [-4]	5	-0. 525 018 569	4. 184 [-9]	4. 470	3. 738 [-7]
6	-0. 514 540 681	1. 219 [-6]	5. 864	2. 458 [-4]	6	-0. 516 688 308	2. 151 [-9]	5. 474	3. 528 [-7]
7	-0. 510 613 111	7. 753 [-7]	6. 864	2. 507 [-4]	7	-0. 511 924 352	1. 249 [-9]	6. 475	3. 390 [-7]
8	-0. 508 085 701	5. 218 [-7]	7. 864	2. 538 [-4]	8	-0. 508 944 928	7. 898 [-10]	7. 476	3. 301 [-7]
9	-0. 506 364 245	3. 674 [-7]	8. 864	2. 558 [-4]	9	-0. 506 957 765	5. 316 [-10]	8. 477	3. 239 [-7]
10	-0. 505 139 251	2. 681 [-7]	9. 864	2. 573 [-4]	10	-0. 505 566 353	3. 752 [-10]	9. 478	3. 194 [-7]
11	-0. 504 236 675	2. 015 [-7]	10. 864	2. 584 [-4]	11	-0. 504 554 240	2. 747 [-10]	10. 478	3. 160 [-7]
12	-0. 503 552 554	1. 552 [-7]	11. 864	2. 592 [-4]	12	-0. 503 795 079	2. 073 [-10]	11. 478	3. 135 [-7]
13	-0. 503 021 685	1. 221 [-7]	12. 864	2. 598 [-4]	13	-0. 503 211 079	1. 603 [-10]	12. 478	3. 114 [-7]
14	-0. 502 601 491	9. 768 [-8]	13. 864	2. 603 [-4]	14	-0. 502 752 215	1. 265 [-10]	13. 479	3. 098 [-7]
15	-0. 502 263 218	7. 939 [-8]	14. 864	2. 607 [-4]	15	-0. 502 385 125	1. 016 [-10]	14. 479	3. 084 [-7]
16	-0. 501 986 875	6. 538 [-8]	15. 864	2. 610 [-4]	16	-0. 502 086 871	8. 285 [-11]	15. 479	3. 073 [-7]
17	-0. 501 758 219	5. 448 [-8]	16. 864	2. 613 [-4]	17	-0. 501 841 257	6. 844 [-11]	16. 479	3. 062 [-7]
18	-0. 501 566 873	4. 588 [-8]	17. 864	2. 615 [-4]	18	-0. 501 636 583	5. 718 [-11]	17. 479	3. 053 [-7]
19	-0. 501 405 133	3. 899 [-8]	18. 864	2. 617 [-4]	19	-0. 501 464 226	4. 828 [-11]	18. 479	3. 046 [-7]
20	-0. 501 267 172	3. 343 [-8]	19. 864	2. 620 [-4]	20	-0. 501 317 707	4. 115 [-11]	19. 479	3. 042 [-7]
21	-0. 501 148 501	2. 889 [-8]	20. 865	2. 624 [-4]	21	-0. 501 192 073	3. 543 [-11]	20. 480	3. 043 [-7]
22	-0. 501 045 592	2. 515 [-8]	21. 868	2. 630 [-4]	22	-0. 501 083 446	3. 086 [-11]	21. 482	3. 059 [-7]

Table 6: $^3D^e$ resonances below N=2 threshold ($\ell_{max} = 8$).

	C			
n	E (au)	Γ (au)	n^*	$\bar{\Gamma}$
4	-0. 529 312 204	7. 062 [-11]	4. 130	4. 975 [-9]
5	-0. 519 016 757	1. 196 [-11]	5. 128	1. 613 [-9]
6	-0. 513 321 957	1. 023 [-12]	6. 126	2. 352 [-10]
7	-0. 509 847 831	1. 200 [-14]	7. 125	4. 341 [-12]
8	-0. 507 574 056	3. 870 [-13]	8. 125	2. 076 [-10]
9	-0. 506 005 427	7. 180 [-13]	9. 125	5. 455 [-10]
10	-0. 504 877 961	8. 680 [-13]	10. 124	9. 008 [-10]
11	-0. 504 040 531	8. 970 [-13]	11. 124	1. 235 [-9]
12	-0. 503 401 574	8. 580 [-13]	12. 124	1. 529 [-9]
13	-0. 502 902 999	7. 920 [-13]	13. 124	1. 790 [-9]
14	-0. 502 506 507	7. 160 [-13]	14. 124	2. 017 [-9]
15	-0. 502 186 021	6. 410 [-13]	15. 124	2. 217 [-9]
16	-0. 501 923 287	5. 710 [-13]	16. 124	2. 393 [-9]
17	-0. 501 705 219	5. 080 [-13]	17. 124	2. 551 [-9]
18	-0. 501 522 234	4. 530 [-13]	18. 124	2. 697 [-9]
19	-0. 501 367 182	4. 060 [-13]	19. 124	2. 839 [-9]
20	-0. 501 234 633	3. 680 [-13]	20. 124	2. 999 [-9]
21	-0. 501 120 377	3. 410 [-13]	21. 125	3. 215 [-9]
22	-0. 501 021 103	3. 320 [-13]	22. 128	3. 597 [-9]

Table 7: $^3S^e$ resonances below N=3 threshold ($\ell_{max} = 8$).

A ($K = 0$)					B ($K = 2$)				
n	E (au)	Γ (au)	n^*	$\bar{\Gamma}$	n	E (au)	Γ (au)	n^*	$\bar{\Gamma}$
4	-0. 270 283 422	4. 683 [-5]	3. 225	1. 571 [-3]	4	-0. 287 277 011	2. 963 [-5]	2. 772	6. 313 [-4]
5	-0. 249 000 355	1. 371 [-5]	4. 321	1. 106 [-3]	5	-0. 258 133 940	1. 953 [-5]	3. 731	1. 014 [-3]
6	-0. 239 695 136	9. 167 [-6]	5. 349	1. 403 [-3]	6	-0. 244 807 143	1. 163 [-5]	4. 705	1. 212 [-3]
7	-0. 234 565 599	6. 102 [-6]	6. 365	1. 573 [-3]	7	-0. 237 670 165	7. 124 [-6]	5. 689	1. 312 [-3]
8	-0. 231 419 790	4. 201 [-6]	7. 373	1. 684 [-3]	8	-0. 233 432 364	4. 651 [-6]	6. 679	1. 385 [-3]
9	-0. 229 344 766	2. 977 [-6]	8. 379	1. 751 [-3]	9	-0. 230 718 511	3. 168 [-6]	7. 671	1. 430 [-3]
10	-0. 227 902 299	2. 175 [-6]	9. 382	1. 796 [-3]	10	-0. 228 879 603	2. 239 [-6]	8. 666	1. 457 [-3]
11	-0. 226 858 396	1. 633 [-6]	10. 385	1. 829 [-3]	11	-0. 227 577 458	1. 634 [-6]	9. 663	1. 474 [-3]
12	-0. 226 078 366	1. 256 [-6]	11. 387	1. 854 [-3]	12	-0. 226 622 327	1. 227 [-6]	10. 660	1. 486 [-3]
13	-0. 225 480 077	9. 862 [-7]	12. 389	1. 875 [-3]	13	-0. 225 901 269	9. 436 [-7]	11. 658	1. 495 [-3]
14	-0. 225 011 086	7. 885 [-7]	13. 390	1. 893 [-3]	14	-0. 225 343 728	7. 409 [-7]	12. 656	1. 502 [-3]
15	-0. 224 636 614	6. 399 [-7]	14. 391	1. 907 [-3]	15	-0. 224 903 819	5. 925 [-7]	13. 655	1. 509 [-3]
16	-0. 224 332 846	5. 262 [-7]	15. 391	1. 919 [-3]	16	-0. 224 550 671	4. 812 [-7]	14. 654	1. 514 [-3]
17	-0. 224 083 028	4. 378 [-7]	16. 392	1. 928 [-3]	17	-0. 224 262 904	3. 960 [-7]	15. 653	1. 519 [-3]
18	-0. 223 875 093	3. 680 [-7]	17. 393	1. 936 [-3]	18	-0. 224 025 331	3. 298 [-7]	16. 652	1. 523 [-3]
19	-0. 223 700 165	3. 123 [-7]	18. 393	1. 943 [-3]	19	-0. 223 826 928	2. 775 [-7]	17. 652	1. 526 [-3]
20	-0. 223 551 596	2. 673 [-7]	19. 394	1. 950 [-3]	20	-0. 223 659 530	2. 357 [-7]	18. 651	1. 529 [-3]
21	-0. 223 424 310	2. 307 [-7]	20. 395	1. 957 [-3]	21	-0. 223 516 983	2. 019 [-7]	19. 651	1. 532 [-3]
22	-0. 223 314 348	2. 008 [-7]	21. 397	1. 967 [-3]	22	-0. 223 394 557	1. 744 [-7]	20. 652	1. 536 [-3]
23	-0. 223 218 488	1. 780 [-7]	22. 403	2. 001 [-3]	23	-0. 223 288 534	1. 517 [-7]	21. 654	1. 540 [-3]

Table 8: $^3S^e$ resonances below N=3 threshold ($\ell_{max} = 8$).

C ($K = -2$)				
n	E (au)	Γ (au)	n^*	$\bar{\Gamma}$
4	-0. 249 964 424	1. 358 [-5]	4. 245	1. 039 [-3]
5	-0. 240 313 501	6. 965 [-6]	5. 257	1. 012 [-3]
6	-0. 234 966 464	4. 133 [-6]	6. 264	1. 016 [-3]
7	-0. 231 690 681	2. 624 [-6]	7. 267	1. 007 [-3]
8	-0. 229 534 909	1. 768 [-6]	8. 269	9. 993 [-4]
9	-0. 228 040 350	1. 248 [-6]	9. 270	9. 946 [-4]
10	-0. 226 961 568	9. 153 [-7]	10. 271	9. 919 [-4]
11	-0. 226 157 388	6. 915 [-7]	11. 272	9. 904 [-4]
12	-0. 225 541 884	5. 356 [-7]	12. 273	9. 900 [-4]
13	-0. 225 060 309	4. 236 [-7]	13. 273	9. 904 [-4]
14	-0. 224 676 433	3. 408 [-7]	14. 273	9. 909 [-4]
15	-0. 224 365 502	2. 782 [-7]	15. 274	9. 912 [-4]
16	-0. 224 110 135	2. 300 [-7]	16. 274	9. 915 [-4]
17	-0. 223 897 835	1. 924 [-7]	17. 274	9. 916 [-4]
18	-0. 223 719 431	1. 625 [-7]	18. 274	9. 917 [-4]
19	-0. 223 568 059	1. 385 [-7]	19. 275	9. 917 [-4]
20	-0. 223 438 494	1. 190 [-7]	20. 275	9. 916 [-4]
21	-0. 223 326 673	1. 029 [-7]	21. 277	9. 914 [-4]
22	-0. 223 229 358	8. 977 [-8]	22. 281	9. 930 [-4]

Table 9: $^3P^o$ resonances below N=3 threshold ($\ell_{max} = 8$).

A $(K,T) = (2,0)$					B $(K,T) = (0,0)$				
n	E (au)	Γ (au)	n^*	$\bar{\Gamma}$	n	E (au)	Γ (au)	n^*	$\bar{\Gamma}$
3	-0. 350 370 393	2. 982 [-3]	1. 975	2. 299 [-2]	3	-0. 309 374 900	1. 121 [-3]	2. 395	1. 540 [-2]
4	-0. 279 476 095	1. 379 [-3]	2. 955	3. 560 [-2]	4	-0. 260 232 139	3. 111 [-4]	3. 627	1. 484 [-2]
5	-0. 255 161 062	6. 489 [-4]	3. 896	3. 838 [-2]	5	-0. 245 233 699	1. 556 [-4]	4. 661	1. 576 [-2]
6	-0. 243 373 653	3. 354 [-4]	4. 862	3. 855 [-2]	6	-0. 237 754 303	8. 867 [-5]	5. 674	1. 620 [-2]
7	-0. 236 874 557	1. 904 [-4]	5. 842	3. 796 [-2]	7	-0. 233 430 257	5. 514 [-5]	6. 679	1. 643 [-2]
8	-0. 232 946 601	1. 185 [-4]	6. 828	3. 772 [-2]	8	-0. 230 694 989	3. 637 [-5]	7. 682	1. 649 [-2]
9	-0. 230 400 641	7. 849 [-5]	7. 819	3. 752 [-2]	9	-0. 228 853 181	2. 523 [-5]	8. 684	1. 652 [-2]
10	-0. 228 660 387	5. 443 [-5]	8. 813	3. 725 [-2]	10	-0. 227 553 324	1. 822 [-5]	9. 684	1. 655 [-2]
11	-0. 227 419 970	3. 920 [-5]	9. 808	3. 698 [-2]	11	-0. 226 601 612	1. 360 [-5]	10. 685	1. 659 [-2]
12	-0. 226 505 419	2. 913 [-5]	10. 804	3. 675 [-2]	12	-0. 225 883 856	1. 043 [-5]	11. 686	1. 664 [-2]
13	-0. 225 812 117	2. 224 [-5]	11. 802	3. 656 [-2]	13	-0. 225 329 170	8. 164 [-6]	12. 686	1. 667 [-2]
14	-0. 225 274 195	1. 737 [-5]	12. 800	3. 642 [-2]	14	-0. 224 891 631	6. 512 [-6]	13. 686	1. 669 [-2]
15	-0. 224 848 542	1. 382 [-5]	13. 798	3. 631 [-2]	15	-0. 224 540 423	5. 276 [-6]	14. 686	1. 671 [-2]
16	-0. 224 506 002	1. 118 [-5]	14. 796	3. 623 [-2]	16	-0. 224 254 238	4. 333 [-6]	15. 686	1. 673 [-2]
17	-0. 224 226 291	9. 177 [-6]	15. 795	3. 616 [-2]	17	-0. 224 017 957	3. 602 [-6]	16. 686	1. 674 [-2]
18	-0. 223 994 947	7. 623 [-6]	16. 794	3. 611 [-2]	18	-0. 223 820 614	3. 026 [-6]	17. 687	1. 674 [-2]
19	-0. 223 801 434	6. 402 [-6]	17. 794	3. 607 [-2]	19	-0. 223 654 092	2. 567 [-6]	18. 687	1. 675 [-2]
20	-0. 223 637 928	5. 429 [-6]	18. 793	3. 603 [-2]	20	-0. 223 512 275	2. 197 [-6]	19. 687	1. 676 [-2]
21	-0. 223 498 515	4. 645 [-6]	19. 793	3. 602 [-2]	21	-0. 223 390 467	1. 895 [-6]	20. 688	1. 678 [-2]
22	-0. 223 378 636	4. 008 [-6]	20. 794	3. 603 [-2]	22	-0. 223 284 979	1. 648 [-6]	21. 690	1. 681 [-2]
23	-0. 223 274 706	3. 484 [-6]	21. 796	3. 607 [-2]					

Table 10: $^3P^o$ resonances below N=3 threshold ($\ell_{max} = 8$).

C $(K,T) = (1,1)$					D $(K,T) = (-1,1)$				
n	E (au)	Γ (au)	n^*	$\bar{\Gamma}$	n	E (au)	Γ (au)	n^*	$\bar{\Gamma}$
4	-0. 278 816 984	6. 261 [-5]	2. 972	1. 644 [-3]	4	-0. 258 524 589	5. 367 [-6]	3. 711	2. 743 [-4]
5	-0. 253 552 863	3. 343 [-5]	3. 995	2. 131 [-3]	5	-0. 244 036 412	3. 571 [-6]	4. 788	3. 919 [-4]
6	-0. 242 189 451	1. 964 [-5]	5. 004	2. 461 [-3]	6	-0. 237 010 671	2. 532 [-6]	5. 815	4. 977 [-4]
7	-0. 236 068 109	1. 217 [-5]	6. 009	2. 642 [-3]	7	-0. 232 945 981	1. 963 [-6]	6. 828	6. 249 [-4]
8	-0. 232 391 212	7. 999 [-6]	7. 012	2. 758 [-3]	8	-0. 230 364 271	1. 275 [-6]	7. 836	6. 136 [-4]
9	-0. 230 007 776	5. 495 [-6]	8. 013	2. 828 [-3]	9	-0. 228 618 146	8. 816 [-7]	8. 842	6. 094 [-4]
10	-0. 228 374 471	3. 923 [-6]	9. 015	2. 874 [-3]	10	-0. 227 380 666	6. 444 [-7]	9. 845	6. 149 [-4]
11	-0. 227 206 338	2. 893 [-6]	10. 016	2. 906 [-3]	11	-0. 226 471 229	4. 872 [-7]	10. 848	6. 219 [-4]
12	-0. 226 342 032	2. 192 [-6]	11. 017	2. 931 [-3]	12	-0. 225 783 086	3. 776 [-7]	11. 850	6. 283 [-4]
13	-0. 225 684 590	1. 701 [-6]	12. 017	2. 951 [-3]	13	-0. 225 249 730	2. 987 [-7]	12. 851	6. 339 [-4]
14	-0. 225 172 875	1. 345 [-6]	13. 017	2. 968 [-3]	14	-0. 224 827 930	2. 402 [-7]	13. 852	6. 385 [-4]
15	-0. 224 766 783	1. 082 [-6]	14. 018	2. 981 [-3]	15	-0. 224 488 580	1. 960 [-7]	14. 853	6. 423 [-4]
16	-0. 224 439 118	8. 834 [-7]	15. 018	2. 992 [-3]	16	-0. 224 211 493	1. 620 [-7]	15. 854	6. 456 [-4]
17	-0. 224 170 908	7. 301 [-7]	16. 018	3. 001 [-3]	17	-0. 223 982 307	1. 354 [-7]	16. 855	6. 483 [-4]
18	-0. 223 948 588	6. 103 [-7]	17. 018	3. 008 [-3]	18	-0. 223 790 576	1. 143 [-7]	17. 855	6. 506 [-4]
19	-0. 223 762 251	5. 153 [-7]	18. 019	3. 015 [-3]	19	-0. 223 628 549	9. 734 [-8]	18. 856	6. 526 [-4]
20	-0. 223 604 519	4. 390 [-7]	19. 019	3. 020 [-3]	20	-0. 223 490 372	8. 358 [-8]	19. 856	6. 544 [-4]
21	-0. 223 469 800	3. 772 [-7]	20. 019	3. 026 [-3]	21	-0. 223 371 539	7. 229 [-8]	20. 858	6. 559 [-4]
22	-0. 223 353 765	3. 267 [-7]	21. 021	3. 034 [-3]	22	-0. 223 268 507	6. 291 [-8]	21. 860	6. 572 [-4]
23	-0. 223 253 015	2. 853 [-7]	22. 024	3. 048 [-3]					

Table 11: $^3P^o$ resonances below N=3 threshold ($\ell_{max} = 8$).

E $(K,T) = (-2,0)$				
n	E (au)	Γ (au)	n^*	$\bar{\Gamma}$
4	-0. 246 059 262	3. 523 [-7]	4. 580	3. 384 [-5]
5	-0. 238 511 037	2. 223 [-7]	5. 540	3. 781 [-5]
6	-0. 233 987 640	1. 454 [-7]	6. 519	4. 028 [-5]
7	-0. 231 098 360	9. 793 [-8]	7. 505	4. 140 [-5]
8	-0. 229 148 368	6. 819 [-8]	8. 496	4. 183 [-5]
9	-0. 227 773 587	4. 904 [-8]	9. 490	4. 192 [-5]
10	-0. 226 769 408	3. 632 [-8]	10. 486	4. 188 [-5]
11	-0. 226 014 207	2. 761 [-8]	11. 483	4. 180 [-5]
12	-0. 225 432 239	2. 146 [-8]	12. 480	4. 172 [-5]
13	-0. 224 974 426	1. 701 [-8]	13. 479	4. 165 [-5]
14	-0. 224 607 872	1. 370 [-8]	14. 477	4. 158 [-5]
15	-0. 224 309 876	1. 120 [-8]	15. 476	4. 153 [-5]
16	-0. 224 064 367	9. 276 [-9]	16. 475	4. 148 [-5]
17	-0. 223 859 717	7. 767 [-9]	17. 474	4. 144 [-5]
18	-0. 223 687 340	6. 570 [-9]	18. 473	4. 142 [-5]
19	-0. 223 540 781	5. 608 [-9]	19. 473	4. 141 [-5]
20	-0. 223 415 105	4. 828 [-9]	20. 473	4. 143 [-5]
21	-0. 223 306 450	4. 190 [-9]	21. 475	4. 149 [-5]

Table 12: $^3P^e$ resonances below N=3 threshold ($\ell_{max} = 8$).

A					B				
n	E (au)	Γ (au)	n^*	$\bar{\Gamma}$	n	E (au)	Γ (au)	n^*	$\bar{\Gamma}$
3	-0. 336 083 896	4. 487 [-3]	2. 096	4. 129 [-2]	3	-0. 291 155 340	7. 399 [-5]	2. 693	1. 445 [-3]
4	-0. 271 555 941	1. 788 [-3]	3. 184	5. 770 [-2]	4	-0. 253 574 102	2. 350 [-5]	3. 993	1. 497 [-3]
5	-0. 250 930 988	8. 553 [-4]	4. 173	6. 216 [-2]	5	-0. 241 957 507	1. 444 [-5]	5. 033	1. 841 [-3]
6	-0. 240 959 065	4. 552 [-4]	5. 166	6. 275 [-2]	6	-0. 235 890 571	9. 539 [-6]	6. 048	2. 110 [-3]
7	-0. 235 394 228	2. 668 [-4]	6. 161	6. 240 [-2]	7	-0. 232 269 422	6. 441 [-6]	7. 054	2. 261 [-3]
8	-0. 231 981 606	1. 691 [-4]	7. 158	6. 202 [-2]	8	-0. 229 922 900	4. 533 [-6]	8. 058	2. 371 [-3]
9	-0. 229 740 071	1. 136 [-4]	8. 154	6. 163 [-2]	9	-0. 228 313 631	3. 301 [-6]	9. 060	2. 455 [-3]
10	-0. 228 189 764	7. 992 [-5]	9. 154	6. 129 [-2]	10	-0. 227 161 481	2. 473 [-6]	10. 061	2. 518 [-3]
11	-0. 227 073 437	5. 831 [-5]	10. 152	6. 102 [-2]	11	-0. 226 308 106	1. 896 [-6]	11. 062	2. 567 [-3]
12	-0. 226 243 160	4. 384 [-5]	11. 151	6. 079 [-2]	12	-0. 225 658 351	1. 484 [-6]	12. 063	2. 605 [-3]
13	-0. 225 609 008	3. 378 [-5]	12. 150	6. 060 [-2]	13	-0. 225 152 183	1. 182 [-6]	13. 063	2. 636 [-3]
14	-0. 225 113 778	2. 658 [-5]	13. 150	6. 045 [-2]	14	-0. 224 750 188	9. 563 [-7]	14. 064	2. 660 [-3]
15	-0. 224 719 689	2. 129 [-5]	14. 149	6. 032 [-2]	15	-0. 224 425 610	7. 840 [-7]	15. 064	2. 680 [-3]
16	-0. 224 400 973	1. 732 [-5]	15. 149	6. 021 [-2]	16	-0. 224 159 768	6. 504 [-7]	16. 064	2. 696 [-3]
17	-0. 224 139 574	1. 428 [-5]	16. 149	6. 013 [-2]	17	-0. 223 939 295	5. 453 [-7]	17. 064	2. 709 [-3]
18	-0. 223 922 530	1. 191 [-5]	17. 148	6. 005 [-2]	18	-0. 223 754 420	4. 615 [-7]	18. 065	2. 720 [-3]
19	-0. 223 740 345	1. 004 [-5]	18. 148	5. 999 [-2]	19	-0. 223 597 861	3. 939 [-7]	19. 065	2. 729 [-3]
20	-0. 223 585 923	8. 539 [-6]	19. 148	5. 995 [-2]	20	-0. 223 464 094	3. 386 [-7]	20. 065	2. 736 [-3]
21	-0. 223 453 871	7. 330 [-6]	20. 148	5. 996 [-2]	21	-0. 223 348 846	2. 930 [-7]	21. 067	2. 739 [-3]
22	-0. 223 340 003	6. 345 [-6]	21. 150	6. 003 [-2]	22	-0. 223 248 756	2. 547 [-7]	22. 070	2. 738 [-3]
23	-0. 223 241 011	5. 552 [-6]	22. 154	6. 037 [-2]					

Table 13: $^3D^e$ resonances below N=3 threshold ($\ell_{max} = 8$).

	A				B				
n	E (au)	Γ (au)	n^*	$\bar{\Gamma}$	n	E (au)	Γ (au)	n^*	$\bar{\Gamma}$
4	-0. 269 760 137	3. 740 [-5]	3. 243	1. 276 [-3]	4	-0. 283 046 467	4. 890 [-5]	2. 867	1. 152 [-3]
5	-0. 249 134 456	6. 642 [-5]	4. 310	5. 319 [-3]	5	-0. 255 929 620	3. 056 [-5]	3. 851	1. 746 [-3]
6	-0. 239 877 256	7. 315 [-5]	5. 322	1. 102 [-2]	6	-0. 243 573 485	1. 799 [-5]	4. 839	2. 038 [-3]
7	-0. 234 733 927	4. 658 [-5]	6. 322	1. 177 [-2]	7	-0. 236 925 074	1. 103 [-5]	5. 832	2. 188 [-3]
8	-0. 231 552 835	3. 018 [-5]	7. 320	1. 184 [-2]	8	-0. 232 952 736	7. 204 [-6]	6. 826	2. 291 [-3]
9	-0. 229 446 909	2. 049 [-5]	8. 319	1. 180 [-2]	9	-0. 230 393 417	4. 910 [-6]	7. 822	2. 350 [-3]
10	-0. 227 980 843	1. 453 [-5]	9. 318	1. 175 [-2]	10	-0. 228 649 822	3. 478 [-6]	8. 820	2. 386 [-3]
11	-0. 226 919 446	1. 068 [-5]	10. 317	1. 173 [-2]	11	-0. 227 409 378	2. 547 [-6]	9. 818	2. 410 [-3]
12	-0. 226 126 461	8. 079 [-6]	11. 317	1. 171 [-2]	12	-0. 226 495 835	1. 919 [-6]	10. 817	2. 429 [-3]
13	-0. 225 518 490	6. 259 [-6]	12. 316	1. 169 [-2]	13	-0. 225 803 776	1. 481 [-6]	11. 815	2. 443 [-3]
14	-0. 225 042 173	4. 947 [-6]	13. 316	1. 168 [-2]	14	-0. 225 267 046	1. 167 [-6]	12. 815	2. 455 [-3]
15	-0. 224 662 079	3. 978 [-6]	14. 315	1. 167 [-2]	15	-0. 224 842 446	9. 350 [-7]	13. 814	2. 465 [-3]
16	-0. 224 353 942	3. 246 [-6]	15. 315	1. 166 [-2]	16	-0. 224 500 802	7. 607 [-7]	14. 813	2. 473 [-3]
17	-0. 224 100 683	2. 683 [-6]	16. 315	1. 165 [-2]	17	-0. 224 221 844	6. 270 [-7]	15. 813	2. 479 [-3]
18	-0. 223 890 005	2. 244 [-6]	17. 315	1. 165 [-2]	18	-0. 223 991 127	5. 229 [-7]	16. 813	2. 485 [-3]
19	-0. 223 712 869	1. 895 [-6]	18. 315	1. 164 [-2]	19	-0. 223 798 137	4. 405 [-7]	17. 812	2. 489 [-3]
20	-0. 223 562 500	1. 615 [-6]	19. 315	1. 164 [-2]	20	-0. 223 635 070	3. 746 [-7]	18. 812	2. 494 [-3]
21	-0. 223 433 738	1. 389 [-6]	20. 315	1. 164 [-2]	21	-0. 223 496 025	3. 212 [-7]	19. 812	2. 498 [-3]
22	-0. 223 322 554	1. 204 [-6]	21. 317	1. 166 [-2]	22	-0. 223 376 456	2. 778 [-7]	20. 813	2. 504 [-3]
23	-0. 223 225 711	1. 059 [-6]	22. 322	1. 178 [-2]	23	-0. 223 272 791	2. 419 [-7]	21. 816	2. 512 [-3]

Table 14: $^3D^e$ resonances below N=3 threshold ($\ell_{max} = 8$).

	C				D				
n	E (au)	Γ (au)	n^*	$\bar{\Gamma}$	n	E (au)	Γ (au)	n^*	$\bar{\Gamma}$
4	-0. 250 840 023	9. 559 [-6]	4. 180	6. 981 [-4]					
5	-0. 241 043 908	7. 768 [-6]	5. 154	1. 064 [-3]	5	-0. 239 589 052	6. 263 [-7]	5. 366	9. 676 [-5]
6	-0. 235 469 950	5. 395 [-6]	6. 143	1. 251 [-3]	6	-0. 234 560 282	1. 499 [-6]	6. 366	3. 867 [-4]
7	-0. 232 037 765	3. 726 [-6]	7. 137	1. 355 [-3]	7	-0. 231 424 007	1. 263 [-6]	7. 371	5. 058 [-4]
8	-0. 229 780 289	2. 648 [-6]	8. 134	1. 425 [-3]	8	-0. 229 349 245	9. 646 [-7]	8. 375	5. 668 [-4]
9	-0. 228 218 965	1. 935 [-6]	9. 131	1. 473 [-3]	9	-0. 227 906 081	7. 433 [-7]	9. 379	6. 133 [-4]
10	-0. 227 095 132	1. 449 [-6]	10. 130	1. 506 [-3]	10	-0. 226 861 459	5. 799 [-7]	10. 382	6. 489 [-4]
11	-0. 226 259 654	1. 109 [-6]	11. 128	1. 529 [-3]	11	-0. 226 080 832	4. 585 [-7]	11. 383	6. 763 [-4]
12	-0. 225 621 812	8. 667 [-7]	12. 128	1. 546 [-3]	12	-0. 225 482 072	3. 673 [-7]	12. 385	6. 977 [-4]
13	-0. 225 123 904	6. 892 [-7]	13. 127	1. 559 [-3]	13	-0. 225 012 715	2. 979 [-7]	13. 386	7. 145 [-4]
14	-0. 224 727 827	5. 566 [-7]	14. 126	1. 569 [-3]	14	-0. 224 637 956	2. 445 [-7]	14. 387	7. 280 [-4]
15	-0. 224 407 609	4. 557 [-7]	15. 126	1. 577 [-3]	15	-0. 224 333 963	2. 028 [-7]	15. 387	7. 390 [-4]
16	-0. 224 145 053	3. 777 [-7]	16. 126	1. 584 [-3]	16	-0. 224 083 966	1. 700 [-7]	16. 388	7. 480 [-4]
17	-0. 223 927 107	3. 164 [-7]	17. 125	1. 589 [-3]	17	-0. 223 875 887	1. 437 [-7]	17. 388	7. 556 [-4]
18	-0. 223 744 206	2. 676 [-7]	18. 125	1. 593 [-3]	18	-0. 223 700 844	1. 225 [-7]	18. 389	7. 620 [-4]
19	-0. 223 589 215	2. 283 [-7]	19. 125	1. 597 [-3]	19	-0. 223 552 179	1. 053 [-7]	19. 389	7. 674 [-4]
20	-0. 223 456 709	1. 964 [-7]	20. 125	1. 601 [-3]	20	-0. 223 424 814	9. 106 [-8]	20. 390	7. 720 [-4]
21	-0. 223 342 485	1. 703 [-7]	21. 126	1. 606 [-3]	21	-0. 223 314 785	7. 926 [-8]	21. 393	7. 760 [-4]
22	-0. 223 243 234	1. 490 [-7]	22. 129	1. 615 [-3]	22	-0. 223 218 865	6. 960 [-8]	22. 398	7. 821 [-4]

Table 15: $^3D^e$ resonances below N=3 threshold ($\ell_{max} = 8$).

E					F				
n	E (au)	Γ (au)	n^*	$\bar{\Gamma}$	n	E (au)	Γ (au)	n^*	$\bar{\Gamma}$
					3	-0. 325 326 889	7. 271 [-4]	2. 202	7. 765 [-3]
4	-0. 261 601 751	1. 684 [-6]	3. 563	7. 620 [-5]	4	-0. 267 315 659	2. 458 [-4]	3. 330	9. 077 [-3]
5	-0. 245 602 301	9. 169 [-7]	4. 624	9. 068 [-5]	5	-0. 248 816 197	7. 765 [-5]	4. 336	6. 330 [-3]
6	-0. 237 888 092	5. 529 [-7]	5. 649	9. 970 [-5]	6	-0. 239 707 057	6. 273 [-6]	5. 348	9. 593 [-4]
7	-0. 233 486 842	3. 574 [-7]	6. 662	1. 057 [-4]	7	-0. 234 610 957	5. 804 [-7]	6. 353	1. 488 [-4]
8	-0. 230 721 570	2. 436 [-7]	7. 670	1. 099 [-4]	8	-0. 231 477 641	1. 092 [-7]	7. 350	4. 336 [-5]
9	-0. 228 866 542	1. 730 [-7]	8. 675	1. 129 [-4]	9	-0. 229 398 012	5. 972 [-8]	8. 347	3. 474 [-5]
10	-0. 227 560 337	1. 270 [-7]	9. 678	1. 152 [-4]	10	-0. 227 947 171	4. 265 [-8]	9. 345	3. 481 [-5]
11	-0. 226 605 381	9. 590 [-8]	10. 680	1. 168 [-4]	11	-0. 226 895 233	3. 258 [-8]	10. 344	3. 606 [-5]
12	-0. 225 885 892	7. 409 [-8]	11. 682	1. 181 [-4]	12	-0. 226 108 445	2. 557 [-8]	11. 343	3. 732 [-5]
13	-0. 225 330 247	5. 839 [-8]	12. 684	1. 191 [-4]	13	-0. 225 504 710	2. 041 [-8]	12. 342	3. 837 [-5]
14	-0. 224 892 164	4. 680 [-8]	13. 685	1. 199 [-4]	14	-0. 225 031 389	1. 651 [-8]	13. 341	3. 921 [-5]
15	-0. 224 540 643	3. 808 [-8]	14. 686	1. 206 [-4]	15	-0. 224 653 477	1. 352 [-8]	14. 341	3. 987 [-5]
16	-0. 224 254 276	3. 138 [-8]	15. 686	1. 211 [-4]	16	-0. 224 346 966	1. 119 [-8]	15. 340	4. 039 [-5]
17	-0. 224 017 890	2. 616 [-8]	16. 687	1. 215 [-4]	17	-0. 224 094 947	9. 350 [-9]	16. 340	4. 079 [-5]
18	-0. 223 820 490	2. 203 [-8]	17. 687	1. 219 [-4]	18	-0. 223 885 231	7. 883 [-9]	17. 340	4. 110 [-5]
19	-0. 223 653 938	1. 872 [-8]	18. 688	1. 222 [-4]	19	-0. 223 708 854	6. 699 [-9]	18. 339	4. 132 [-5]
20	-0. 223 512 109	1. 604 [-8]	19. 688	1. 224 [-4]	20	-0. 223 559 096	5. 734 [-9]	19. 339	4. 147 [-5]
21	-0. 223 390 301	1. 385 [-8]	20. 689	1. 226 [-4]	21	-0. 223 430 838	4. 937 [-9]	20. 340	4. 154 [-5]
22	-0. 223 284 822	1. 203 [-8]	21. 692	1. 228 [-4]	22	-0. 223 320 091	4. 271 [-9]	21. 341	4. 151 [-5]
					23	-0. 223 223 678	3. 703 [-9]	22. 344	4. 131 [-5]

Table 16: $^3D^o$ resonances below N=3 threshold ($\ell_{max} = 8$).

	A				B				
n	E (au)	Γ (au)	n^*	$\bar{\Gamma}$	n	E (au)	Γ (au)	n^*	$\bar{\Gamma}$
3	-0. 315 573 897	2. 086 [-3]	2. 314	2. 586 [-2]					
4	-0. 262 441 854	6. 947 [-4]	3. 526	3. 045 [-2]	4	-0. 275 260 068	1. 923 [-5]	3. 070	5. 567 [-4]
5	-0. 246 320 252	3. 529 [-4]	4. 555	3. 335 [-2]	5	-0. 251 926 336	9. 134 [-6]	4. 103	6. 308 [-4]
6	-0. 238 364 509	2. 004 [-4]	5. 565	3. 455 [-2]	6	-0. 241 327 835	4. 799 [-6]	5. 116	6. 425 [-4]
7	-0. 233 805 536	1. 237 [-4]	6. 570	3. 508 [-2]	7	-0. 235 561 924	2. 708 [-6]	6. 122	6. 214 [-4]
8	-0. 230 941 919	8. 149 [-5]	7. 572	3. 538 [-2]	8	-0. 232 069 708	1. 634 [-6]	7. 126	5. 911 [-4]
9	-0. 229 024 130	5. 642 [-5]	8. 574	3. 556 [-2]	9	-0. 229 791 339	1. 050 [-6]	8. 128	5. 638 [-4]
10	-0. 227 676 482	4. 064 [-5]	9. 575	3. 567 [-2]	10	-0. 228 222 005	7. 106 [-7]	9. 129	5. 406 [-4]
11	-0. 226 693 242	3. 022 [-5]	10. 575	3. 574 [-2]	11	-0. 227 094 970	5. 016 [-7]	10. 130	5. 214 [-4]
12	-0. 225 953 860	2. 308 [-5]	11. 575	3. 579 [-2]	12	-0. 226 258 242	3. 667 [-7]	11. 130	5. 057 [-4]
13	-0. 225 383 849	1. 801 [-5]	12. 576	3. 583 [-2]	13	-0. 225 619 981	2. 761 [-7]	12. 131	4. 929 [-4]
14	-0. 224 935 152	1. 433 [-5]	13. 576	3. 585 [-2]	14	-0. 225 122 015	2. 130 [-7]	13. 131	4. 824 [-4]
15	-0. 224 575 626	1. 158 [-5]	14. 576	3. 586 [-2]	15	-0. 224 726 034	1. 679 [-7]	14. 131	4. 737 [-4]
16	-0. 224 283 113	9. 495 [-6]	15. 576	3. 588 [-2]	16	-0. 224 405 968	1. 347 [-7]	15. 132	4. 665 [-4]
17	-0. 224 041 936	7. 879 [-6]	16. 576	3. 589 [-2]	17	-0. 224 143 578	1. 097 [-7]	16. 132	4. 606 [-4]
18	-0. 223 840 744	6. 612 [-6]	17. 576	3. 590 [-2]	18	-0. 223 925 793	9. 058 [-8]	17. 132	4. 554 [-4]
19	-0. 223 671 156	5. 602 [-6]	18. 576	3. 591 [-2]	19	-0. 223 743 040	7. 565 [-8]	18. 132	4. 509 [-4]
20	-0. 223 526 867	4. 789 [-6]	19. 577	3. 593 [-2]	20	-0. 223 588 178	6. 380 [-8]	19. 132	4. 468 [-4]
21	-0. 223 403 048	4. 127 [-6]	20. 577	3. 596 [-2]	21	-0. 223 455 783	5. 422 [-8]	20. 133	4. 425 [-4]
22	-0. 223 295 910	3. 585 [-6]	21. 580	3. 603 [-2]	22	-0. 223 341 648	4. 625 [-8]	21. 134	4. 366 [-4]
23	-0. 223 202 186	3. 179 [-6]	22. 588	3. 664 [-2]	23	-0. 223 242 458	3. 936 [-8]	22. 138	4. 270 [-4]

Table 17: $^3D^o$ resonances below N=3 threshold ($\ell_{max} = 8$).

	C			
n	E (au)	Γ (au)	n^*	$\bar{\Gamma}$
4	-0. 251 185 409	3. 821 [-6]	4. 155	2. 741 [-4]
5	-0. 241 008 676	2. 781 [-6]	5. 159	3. 819 [-4]
6	-0. 235 395 634	1. 965 [-6]	6. 161	4. 595 [-4]
7	-0. 231 972 876	1. 421 [-6]	7. 161	5. 218 [-4]
8	-0. 229 729 343	1. 046 [-6]	8. 161	5. 687 [-4]
9	-0. 228 179 660	7. 851 [-7]	9. 161	6. 036 [-4]
10	-0. 227 064 651	6. 020 [-7]	10. 161	6. 316 [-4]
11	-0. 226 235 735	4. 702 [-7]	11. 162	6. 537 [-4]
12	-0. 225 602 787	3. 733 [-7]	12. 162	6. 715 [-4]
13	-0. 225 108 570	3. 008 [-7]	13. 162	6. 857 [-4]
14	-0. 224 715 313	2. 455 [-7]	14. 162	6. 974 [-4]
15	-0. 224 397 277	2. 029 [-7]	15. 162	7. 071 [-4]
16	-0. 224 136 433	1. 697 [-7]	16. 162	7. 163 [-4]
17	-0. 223 919 846	1. 428 [-7]	17. 162	7. 218 [-4]
18	-0. 223 738 036	1. 215 [-7]	18. 162	7. 277 [-4]
19	-0. 223 583 929	1. 042 [-7]	19. 162	7. 334 [-4]
20	-0. 223 452 144	9. 028 [-8]	20. 163	7. 400 [-4]
21	-0. 223 338 511	7. 910 [-8]	21. 164	7. 498 [-4]
22	-0. 223 239 736	7. 069 [-8]	22. 167	7. 700 [-4]

Table 18: $^3S^e$ resonances below N=4 threshold ($\ell_{max} = 8$).

A ($K = 3$)					B ($K = 1$)				
n	E (au)	Γ (au)	n^*	$\bar{\Gamma}$	n	E (au)	Γ (au)	n^*	$\bar{\Gamma}$
5	-0. 169 307 049	4. 174 [-5]	3. 359	1. 582 [-3]	5	-0. 161 480 677	1. 041 [-4]	3. 702	5. 280 [-3]
6	-0. 152 122 239	3. 366 [-5]	4. 294	2. 664 [-3]	6	-0. 147 168 474	7. 429 [-5]	4. 749	7. 958 [-3]
7	-0. 143 174 471	2. 302 [-5]	5. 245	3. 322 [-3]	7	-0. 139 996 316	4. 045 [-5]	5. 774	7. 788 [-3]
8	-0. 137 960 487	1. 551 [-5]	6. 211	3. 716 [-3]	8	-0. 135 856 441	3. 005 [-5]	6. 786	9. 393 [-3]
9	-0. 134 678 824	1. 039 [-5]	7. 187	3. 857 [-3]	9	-0. 133 229 823	2. 097 [-5]	7. 795	9. 929 [-3]
10	-0. 132 490 263	7. 421 [-6]	8. 170	4. 047 [-3]	10	-0. 131 456 612	1. 505 [-5]	8. 800	1. 026 [-2]
11	-0. 130 962 077	5. 505 [-6]	9. 157	4. 228 [-3]	11	-0. 130 202 034	1. 116 [-5]	9. 804	1. 051 [-2]
12	-0. 129 854 995	4. 124 [-6]	10. 148	4. 310 [-3]	12	-0. 129 281 338	8. 476 [-6]	10. 807	1. 070 [-2]
13	-0. 129 028 328	3. 140 [-6]	11. 141	4. 342 [-3]	13	-0. 128 585 499	6. 575 [-6]	11. 809	1. 083 [-2]
14	-0. 128 395 254	2. 438 [-6]	12. 135	4. 356 [-3]	14	-0. 128 046 710	5. 195 [-6]	12. 811	1. 092 [-2]
15	-0. 127 899 972	1. 928 [-6]	13. 131	4. 364 [-3]	15	-0. 127 620 966	4. 171 [-6]	13. 812	1. 099 [-2]
16	-0. 127 505 349	1. 550 [-6]	14. 127	4. 371 [-3]	16	-0. 127 278 685	3. 397 [-6]	14. 813	1. 104 [-2]
17	-0. 127 185 926	1. 266 [-6]	15. 124	4. 379 [-3]	17	-0. 126 999 373	2. 802 [-6]	15. 814	1. 108 [-2]
18	-0. 126 923 789	1. 047 [-6]	16. 122	4. 386 [-3]	18	-0. 126 768 468	2. 337 [-6]	16. 815	1. 111 [-2]
19	-0. 126 706 042	8. 759 [-7]	17. 119	4. 395 [-3]	19	-0. 126 575 387	1. 969 [-6]	17. 815	1. 113 [-2]
20	-0. 126 523 214	7. 405 [-7]	18. 118	4. 404 [-3]	20	-0. 126 412 286	1. 675 [-6]	18. 816	1. 116 [-2]
21	-0. 126 368 215	6. 320 [-7]	19. 116	4. 415 [-3]	21	-0. 126 273 241	1. 437 [-6]	19. 817	1. 118 [-2]
22	-0. 126 235 649	5. 442 [-7]	20. 116	4. 430 [-3]	22	-0. 126 153 696	1. 243 [-6]	20. 818	1. 122 [-2]
23	-0. 126 121 313	4. 726 [-7]	21. 116	4. 450 [-3]	23	-0. 126 050 072	1. 085 [-6]	21. 821	1. 127 [-2]
24	-0. 126 021 880	4. 151 [-7]	22. 120	4. 493 [-3]					

Table 19: $^3S^e$ resonances below N=4 threshold ($\ell_{max} = 8$).

C $(K=-1)$					D $(K=-3)$				
n	E (au)	Γ (au)	n^*	$\bar{\Gamma}$	n	E (au)	Γ (au)	n^*	$\bar{\Gamma}$
5	-0. 151 176 483	4. 434 [-5]	4. 370	3. 701 [-3]	5	-0. 140 087 265	8. 689 [-6]	5. 757	1. 658 [-3]
6	-0. 141 690 357	2. 983 [-5]	5. 473	4. 891 [-3]	6	-0. 135 972 645	3. 585 [-6]	6. 750	1. 103 [-3]
7	-0. 136 785 394	1. 932 [-5]	6. 513	5. 338 [-3]	7	-0. 133 327 916	2. 701 [-6]	7. 748	1. 257 [-3]
8	-0. 133 810 627	1. 304 [-5]	7. 533	5. 576 [-3]	8	-0. 131 533 055	2. 183 [-6]	8. 747	1. 462 [-3]
9	-0. 131 848 665	8. 995 [-6]	8. 544	5. 611 [-3]	9	-0. 130 260 957	1. 779 [-6]	9. 749	1. 648 [-3]
10	-0. 130 480 659	6. 559 [-6]	9. 551	5. 716 [-3]	10	-0. 129 327 109	1. 453 [-6]	10. 749	1. 804 [-3]
11	-0. 129 487 004	4. 923 [-6]	10. 556	5. 791 [-3]	11	-0. 128 621 517	1. 191 [-6]	11. 750	1. 932 [-3]
12	-0. 128 741 865	3. 775 [-6]	11. 560	5. 831 [-3]	12	-0. 128 075 454	9. 825 [-7]	12. 751	2. 037 [-3]
13	-0. 128 168 473	2. 949 [-6]	12. 562	5. 847 [-3]	13	-0. 127 644 217	8. 160 [-7]	13. 751	2. 122 [-3]
14	-0. 127 717 686	2. 344 [-6]	13. 564	5. 848 [-3]	14	-0. 127 297 730	6. 829 [-7]	14. 751	2. 192 [-3]
15	-0. 127 356 814	1. 890 [-6]	14. 565	5. 842 [-3]	15	-0. 127 015 153	5. 758 [-7]	15. 752	2. 250 [-3]
16	-0. 127 063 403	1. 546 [-6]	15. 567	5. 831 [-3]	16	-0. 126 781 680	4. 890 [-7]	16. 752	2. 299 [-3]
17	-0. 126 821 607	1. 280 [-6]	16. 568	5. 819 [-3]	17	-0. 126 586 555	4. 182 [-7]	17. 752	2. 340 [-3]
18	-0. 126 619 978	1. 071 [-6]	17. 568	5. 807 [-3]	18	-0. 126 421 810	3. 600 [-7]	18. 753	2. 374 [-3]
19	-0. 126 450 076	9. 048 [-7]	18. 569	5. 794 [-3]	19	-0. 126 281 434	3. 116 [-7]	19. 753	2. 402 [-3]
20	-0. 126 305 558	7. 714 [-7]	19. 570	5. 781 [-3]	20	-0. 126 160 813	2. 710 [-7]	20. 754	2. 423 [-3]
21	-0. 126 181 573	6. 632 [-7]	20. 571	5. 773 [-3]	21	-0. 126 056 320	2. 365 [-7]	21. 756	2. 436 [-3]
22	-0. 126 074 322	5. 746 [-7]	21. 573	5. 769 [-3]					

Table 20: $^3P^o$ resonances below N=4 threshold ($\ell_{max} = 8$).

	A				B				
n	E (au)	Γ (au)	n^*	$\bar{\Gamma}$	n	E (au)	Γ (au)	n^*	$\bar{\Gamma}$
4	-0. 200 081 541	2. 106 [-3]	2. 581	3. 620 [-2]	4	-0. 185 761 841	5. 077 [-3]	2. 869	1. 198 [-1]
5	-0. 165 151 518	1. 285 [-3]	3. 529	5. 645 [-2]	5	-0. 155 787 599	2. 286 [-3]	4. 030	1. 496 [-1]
6	-0. 150 478 122	6. 840 [-4]	4. 430	5. 947 [-2]	6	-0. 144 776 317	1. 382 [-3]	5. 028	1. 756 [-1]
7	-0. 142 387 206	3. 667 [-4]	5. 363	5. 654 [-2]	7	-0. 138 834 123	8. 359 [-4]	6. 012	1. 816 [-1]
8	-0. 137 549 478	2. 006 [-4]	6. 312	5. 046 [-2]	8	-0. 135 208 703	5. 484 [-4]	6. 998	1. 880 [-1]
9	-0. 134 457 654	1. 073 [-4]	7. 271	4. 124 [-2]	9	-0. 132 839 700	3. 591 [-4]	7. 986	1. 829 [-1]
10	-0. 132 384 105	5. 254 [-5]	8. 229	2. 927 [-2]	10	-0. 131 208 917	2. 435 [-4]	8. 974	1. 759 [-1]
11	-0. 130 940 194	1. 713 [-5]	9. 175	1. 323 [-2]	11	-0. 130 037 416	1. 674 [-4]	9. 963	1. 655 [-1]
12	-0. 129 919 873	1. 243 [-6]	10. 081	1. 274 [-3]	12	-0. 129 161 459	1. 179 [-4]	10. 961	1. 553 [-1]
13	-0. 129 213 969	3. 343 [-5]	10. 893	4. 320 [-2]	13	-0. 128 502 092	9. 101 [-5]	11. 949	1. 553 [-1]
14	-0. 128 676 383	8. 933 [-5]	11. 662	1. 417 [-2]	14	-0. 127 986 169	6. 784 [-5]	12. 940	1. 470 [-1]
15	-0. 128 202 268	8. 869 [-5]	12. 496	1. 730 [-1]	15	-0. 127 576 042	5. 128 [-5]	13. 932	1. 387 [-1]
16	-0. 127 779 332	6. 455 [-5]	13. 413	1. 556 [-1]	16	-0. 127 244 642	3. 979 [-5]	14. 925	1. 323 [-1]
17	-0. 127 421 103	4. 715 [-5]	14. 371	1. 399 [-1]	17	-0. 126 973 123	3. 133 [-5]	15. 919	1. 264 [-1]
18	-0. 127 123 084	3. 529 [-5]	15. 346	1. 275 [-1]	18	-0. 126 747 905	2. 498 [-5]	16. 913	1. 209 [-1]
19	-0. 126 874 974	2. 744 [-5]	16. 330	1. 195 [-1]	19	-0. 126 559 034	2. 018 [-5]	17. 908	1. 159 [-1]
20	-0. 126 667 015	2. 191 [-5]	17. 319	1. 138 [-1]	20	-0. 126 399 155	1. 646 [-5]	18. 904	1. 112 [-1]
21	-0. 126 491 369	1. 784 [-5]	18. 310	1. 095 [-1]	21	-0. 126 262 555	1. 366 [-5]	19. 900	1. 077 [-1]
22	-0. 126 341 794	1. 482 [-5]	19. 304	1. 066 [-1]	22	-0. 126 144 920	1. 141 [-5]	20. 898	1. 041 [-1]
23	-0. 126 213 409	1. 242 [-5]	20. 299	1. 039 [-1]					
24	-0. 126 102 365	1. 060 [-5]	21. 297	1. 024 [-1]					

Table 21: $^3P^o$ resonances below N=4 threshold ($\ell_{max} = 8$).

C					D				
n	E (au)	Γ (au)	n^*	$\bar{\Gamma}$	n	E (au)	Γ (au)	n^*	$\bar{\Gamma}$
4	-0. 163 688 665	1. 380 [-3]	3. 595	6. 410 [-2]	4	-0. 165 479 474	7. 553 [-5]	3. 515	3. 279 [-3]
5	-0. 145 650 088	3. 968 [-4]	4. 921	4. 727 [-2]	5	-0. 144 084 127	4. 346 [-5]	5. 119	5. 828 [-3]
6	-0. 138 960 557	1. 422 [-4]	5. 985	3. 049 [-2]	6	-0. 138 430 789	2. 661 [-5]	6. 101	6. 044 [-3]
7	-0. 135 150 368	1. 150 [-4]	7. 018	3. 975 [-2]	7	-0. 134 869 692	2. 057 [-5]	7. 118	7. 417 [-3]
8	-0. 132 760 403	7. 206 [-5]	8. 027	3. 727 [-2]	8	-0. 132 567 565	1. 481 [-5]	8. 128	7. 952 [-3]
9	-0. 131 131 495	5. 130 [-5]	9. 029	3. 778 [-2]	9	-0. 130 990 772	1. 092 [-5]	9. 136	8. 327 [-3]
10	-0. 129 968 543	3. 838 [-5]	10. 032	3. 874 [-2]	10	-0. 129 862 043	8. 207 [-6]	10. 141	8. 558 [-3]
11	-0. 129 107 596	2. 965 [-5]	11. 033	3. 982 [-2]	11	-0. 129 025 684	6. 288 [-6]	11. 145	8. 704 [-3]
12	-0. 128 453 250	2. 349 [-5]	12. 033	4. 093 [-2]	12	-0. 128 388 452	4. 909 [-6]	12. 147	8. 798 [-3]
13	-0. 127 943 722	1. 888 [-5]	13. 033	4. 179 [-2]	13	-0. 127 891 651	3. 897 [-6]	13. 150	8. 859 [-3]
14	-0. 127 539 228	1. 537 [-5]	14. 032	4. 246 [-2]	14	-0. 127 496 771	3. 143 [-6]	14. 151	8. 906 [-3]
15	-0. 127 212 741	1. 272 [-5]	15. 032	4. 322 [-2]	15	-0. 127 177 675	2. 571 [-6]	15. 153	8. 943 [-3]
16	-0. 126 945 396	1. 064 [-5]	16. 032	4. 384 [-2]	16	-0. 126 916 122	2. 128 [-6]	16. 154	8. 968 [-3]
17	-0. 126 723 728	8. 978 [-6]	17. 031	4. 435 [-2]	17	-0. 126 699 045	1. 781 [-6]	17. 155	8. 992 [-3]
18	-0. 126 537 886	7. 637 [-6]	18. 031	4. 477 [-2]	18	-0. 126 516 892	1. 505 [-6]	18. 155	9. 009 [-3]
19	-0. 126 380 547	6. 547 [-6]	19. 031	4. 513 [-2]	19	-0. 126 362 539	1. 284 [-6]	19. 156	9. 025 [-3]
20	-0. 126 246 136	5. 673 [-6]	20. 031	4. 560 [-2]	20	-0. 126 230 576	1. 103 [-6]	20. 157	9. 037 [-3]
21	-0. 126 130 365	4. 943 [-6]	21. 032	4. 598 [-2]	21	-0. 126 116 816	9. 552 [-7]	21. 159	9. 048 [-3]

Table 22: $^3P^o$ resonances below N=4 threshold ($\ell_{max} = 8$).

E					F				
n	E (au)	Γ (au)	n^*	$\bar{\Gamma}$	n	E (au)	Γ (au)	n^*	$\bar{\Gamma}$
5	-0. 149 636 646	5. 621 [-5]	4. 505	5. 139 [-3]	5	-0. 156 237 035	9. 798 [-5]	4. 001	6. 275 [-3]
6	-0. 141 563 473	3. 718 [-5]	5. 494	6. 166 [-3]	6	-0. 144 826 007	4. 023 [-5]	5. 022	5. 095 [-3]
7	-0. 136 884 498	2. 513 [-5]	6. 486	6. 857 [-3]	7	-0. 138 098 092	2. 081 [-5]	6. 178	4. 909 [-3]
8	-0. 133 934 773	1. 711 [-5]	7. 481	7. 162 [-3]	8	-0. 134 630 888	1. 495 [-5]	7. 205	5. 592 [-3]
9	-0. 131 958 526	1. 225 [-5]	8. 477	7. 460 [-3]	9	-0. 132 397 985	1. 074 [-5]	8. 221	5. 965 [-3]
10	-0. 130 570 899	9. 055 [-6]	9. 474	7. 699 [-3]	10	-0. 130 867 370	8. 105 [-6]	9. 231	6. 376 [-3]
11	-0. 129 559 837	6. 851 [-6]	10. 472	7. 867 [-3]	11	-0. 129 769 849	6. 235 [-6]	10. 238	6. 691 [-3]
12	-0. 128 800 687	5. 386 [-6]	11. 470	8. 127 [-3]	12	-0. 128 955 139	4. 866 [-6]	11. 244	6. 916 [-3]
13	-0. 128 216 179	4. 620 [-6]	12. 469	8. 955 [-3]	13	-0. 128 333 344	3. 848 [-6]	12. 247	7. 068 [-3]
14	-0. 127 756 596	3. 556 [-6]	13. 468	8. 686 [-3]	14	-0. 127 847 817	3. 086 [-6]	13. 250	7. 180 [-3]
15	-0. 127 388 981	2. 777 [-6]	14. 467	8. 407 [-3]	15	-0. 127 461 350	2. 510 [-6]	14. 253	7. 266 [-3]
16	-0. 127 090 249	2. 245 [-6]	15. 466	8. 305 [-3]	16	-0. 127 148 660	2. 062 [-6]	15. 255	7. 320 [-3]
17	-0. 126 844 209	1. 853 [-6]	16. 466	8. 270 [-3]	17	-0. 126 892 062	1. 715 [-6]	16. 256	7. 367 [-3]
18	-0. 126 639 163	1. 550 [-6]	17. 465	8. 255 [-3]	18	-0. 126 678 877	1. 441 [-6]	17. 257	7. 404 [-3]
19	-0. 126 466 484	1. 311 [-6]	18. 465	8. 256 [-3]	19	-0. 126 499 822	1. 222 [-6]	18. 258	7. 436 [-3]
20	-0. 126 319 686	1. 121 [-6]	19. 465	8. 265 [-3]	20	-0. 126 347 963	1. 045 [-6]	19. 260	7. 465 [-3]
21	-0. 126 193 809	9. 654 [-7]	20. 465	8. 274 [-3]	21	-0. 126 218 030	9. 007 [-7]	20. 261	7. 491 [-3]
22	-0. 126 084 962	8. 388 [-7]	21. 467	8. 298 [-3]	22	-0. 126 105 929	7. 837 [-7]	21. 263	7. 533 [-3]

Table 23: $^3P^o$ resonances below N=4 threshold ($\ell_{max} = 8$).

	G			
n	E (au)	Γ (au)	n^*	$\bar{\Gamma}$
5	-0. 138 880 613	8. 298 [-5]	6. 002	1. 794 [-2]
6	-0. 135 337 061	6. 429 [-6]	6. 955	2. 163 [-3]
7	-0. 132 956 168	1. 891 [-6]	7. 927	9. 420 [-4]
8	-0. 131 301 711	9. 109 [-7]	8. 907	6. 439 [-4]
9	-0. 130 108 771	5. 353 [-7]	9. 893	5. 182 [-4]
10	-0. 129 222 192	3. 559 [-7]	10. 882	4. 586 [-4]
11	-0. 128 546 317	2. 453 [-7]	11. 874	4. 106 [-4]
12	-0. 128 019 771	1. 813 [-7]	12. 868	3. 862 [-4]
13	-0. 127 601 846	1. 386 [-7]	13. 863	3. 692 [-4]
14	-0. 127 264 736	1. 088 [-7]	14. 859	3. 569 [-4]
15	-0. 126 988 950	8. 723 [-8]	15. 855	3. 477 [-4]
16	-0. 126 760 514	7. 114 [-8]	16. 853	3. 405 [-4]
17	-0. 126 569 204	5. 884 [-8]	17. 850	3. 346 [-4]
18	-0. 126 407 403	4. 928 [-8]	18. 848	3. 300 [-4]
19	-0. 126 269 334	4. 170 [-8]	19. 847	3. 260 [-4]
20	-0. 126 150 546	3. 559 [-8]	20. 846	3. 225 [-4]

Table 24: $^3P^e$ resonances below N=4 threshold ($\ell_{max} = 8$).

A					B				
n	E (au)	Γ (au)	n^*	$\bar{\Gamma}$	n	E (au)	Γ (au)	n^*	$\bar{\Gamma}$
4	-0. 178 240 156	4. 775 [-3]	3. 065	1. 374 [-1]	4	-0. 194 440 707	3. 296 [-3]	2. 683	6. 368 [-2]
5	-0. 151 544 472	1. 776 [-3]	4. 340	1. 452 [-1]	5	-0. 161 234 044	1. 888 [-3]	3. 715	9. 678 [-2]
6	-0. 142 327 804	8. 540 [-4]	5. 372	1. 324 [-1]	6	-0. 148 031 683	1. 053 [-3]	4. 659	1. 065 [-1]
7	-0. 137 292 634	6. 339 [-4]	6. 378	1. 644 [-1]	7	-0. 140 836 221	5. 758 [-4]	5. 619	1. 021 [-1]
8	-0. 134 179 265	4. 267 [-4]	7. 380	1. 715 [-1]	8	-0. 136 521 989	3. 301 [-4]	6. 588	9. 436 [-2]
9	-0. 132 127 835	3. 020 [-4]	8. 375	1. 774 [-1]	9	-0. 133 743 207	1. 919 [-4]	7. 562	8. 298 [-2]
10	-0. 130 693 384	2. 214 [-4]	9. 371	1. 822 [-1]	10	-0. 131 858 396	1. 137 [-4]	8. 538	7. 076 [-2]
11	-0. 129 652 096	1. 643 [-4]	10. 367	1. 830 [-1]	11	-0. 130 522 511	6. 775 [-5]	9. 515	5. 837 [-2]
12	-0. 128 872 765	1. 238 [-4]	11. 363	1. 816 [-1]	12	-0. 129 542 748	3. 901 [-5]	10. 491	4. 505 [-2]
13	-0. 128 273 976	9. 486 [-5]	12. 358	1. 790 [-1]	13	-0. 128 803 502	2. 095 [-5]	11. 466	3. 157 [-2]
14	-0. 127 803 898	7. 317 [-5]	13. 354	1. 742 [-1]	14	-0. 128 229 619	8. 190 [-6]	12. 443	1. 578 [-2]
15	-0. 127 427 781	5. 686 [-5]	14. 351	1. 681 [-1]	15	-0. 127 783 551	4. 410 [-6]	13. 402	1. 062 [-2]
16	-0. 127 121 890	4. 517 [-5]	15. 351	1. 634 [-1]	16	-0. 127 422 681	2. 565 [-6]	14. 366	7. 605 [-3]
17	-0. 126 870 307	3. 732 [-5]	16. 350	1. 631 [-1]	17	-0. 127 129 027	2. 415 [-6]	15. 325	8. 691 [-3]
18	-0. 126 661 128	3. 150 [-5]	17. 349	1. 645 [-1]	18	-0. 126 886 020	2. 782 [-6]	16. 282	1. 201 [-2]
19	-0. 126 485 236	2. 681 [-5]	18. 348	1. 656 [-1]	19	-0. 126 682 052	4. 042 [-6]	17. 241	2. 071 [-2]
20	-0. 126 335 892	2. 295 [-5]	19. 346	1. 662 [-1]	20	-0. 126 509 042	5. 847 [-6]	18. 203	3. 526 [-2]
21	-0. 126 207 926	1. 978 [-5]	20. 345	1. 666 [-1]	21	-0. 126 360 951	7. 638 [-6]	19. 167	5. 379 [-2]
22	-0. 126 097 365	1. 717 [-5]	21. 346	1. 670 [-1]	22	-0. 126 233 172	9. 079 [-6]	20. 136	7. 412 [-2]
					23	-0. 126 122 111	1. 007 [-5]	21. 109	9. 467 [-2]

Table 25: $^3P^e$ resonances below N=4 threshold ($\ell_{max} = 8$).

C				
n	E (au)	Γ (au)	n^*	$\bar{\Gamma}$
4	-0. 155 172 439	2. 582 [-4]	4. 071	1. 742 [-2]
5	-0. 142 343 805	3. 229 [-4]	5. 369	4. 998 [-2]
6	-0. 137 150 797	1. 117 [-4]	6. 415	2. 949 [-2]
7	-0. 134 060 121	5. 730 [-5]	7. 429	2. 349 [-2]
8	-0. 132 027 930	3. 218 [-5]	8. 435	1. 931 [-2]
9	-0. 130 614 028	1. 986 [-5]	9. 436	1. 669 [-2]
10	-0. 129 588 829	1. 303 [-5]	10. 438	1. 482 [-2]
11	-0. 128 821 476	8. 965 [-6]	11. 439	1. 342 [-2]
12	-0. 128 234 759	8. 305 [-6]	12. 433	1. 596 [-2]
13	-0. 127 767 941	4. 722 [-6]	13. 440	1. 146 [-2]
14	-0. 127 397 997	3. 465 [-6]	14. 440	1. 043 [-2]
15	-0. 127 097 511	2. 630 [-6]	15. 439	9. 681 [-3]
16	-0. 126 850 151	2. 041 [-6]	16. 439	9. 066 [-3]
17	-0. 126 644 095	1. 613 [-6]	17. 439	8. 555 [-3]
18	-0. 126 470 631	1. 296 [-6]	18. 439	8. 122 [-3]
19	-0. 126 323 218	1. 056 [-6]	19. 439	7. 757 [-3]
20	-0. 126 196 864	8. 725 [-7]	20. 439	7. 450 [-3]
21	-0. 126 087 670	7. 309 [-7]	21. 441	7. 204 [-3]

Table 26: $^3D^e$ resonances below N=4 threshold ($\ell_{max} = 8$).

	A				B				
n	E (au)	Γ (au)	n^*	$\bar{\Gamma}$	n	E (au)	Γ (au)	n^*	$\bar{\Gamma}$
4	-0. 191 597 213	3. 850 [-3]	2. 740	7. 920 [-2]					
5	-0. 159 583 226	2. 088 [-3]	3. 802	1. 148 [-1]	5	-0. 167 875 236	5. 697 [-5]	3. 415	2. 269 [-3]
6	-0. 147 072 448	1. 114 [-3]	4. 759	1. 201 [-1]	6	-0. 151 230 011	4. 479 [-5]	4. 366	3. 728 [-3]
7	-0. 140 266 870	6. 351 [-4]	5. 723	1. 190 [-1]	7	-0. 142 610 135	3. 004 [-5]	5. 328	4. 545 [-3]
8	-0. 136 159 977	3. 864 [-4]	6. 694	1. 159 [-1]	8	-0. 137 589 749	2. 035 [-5]	6. 302	5. 093 [-3]
9	-0. 133 502 142	2. 379 [-4]	7. 669	1. 073 [-1]	9	-0. 134 425 494	1. 369 [-5]	7. 283	5. 289 [-3]
10	-0. 131 687 970	1. 537 [-4]	8. 646	9. 938 [-2]	10	-0. 132 310 841	9. 832 [-6]	8. 270	5. 561 [-3]
11	-0. 130 396 140	1. 001 [-4]	9. 625	8. 931 [-2]	11	-0. 130 831 000	7. 272 [-6]	9. 260	5. 774 [-3]
12	-0. 129 445 644	6. 584 [-5]	10. 605	7. 853 [-2]	12	-0. 129 756 643	5. 455 [-6]	10. 253	5. 879 [-3]
13	-0. 128 724 493	4. 535 [-5]	11. 586	7. 055 [-2]	13	-0. 128 952 809	4. 168 [-6]	11. 247	5. 929 [-3]
14	-0. 128 165 175	2. 544 [-5]	12. 569	5. 051 [-2]	14	-0. 128 336 102	3. 245 [-6]	12. 242	5. 954 [-3]
15	-0. 127 725 319	1. 482 [-5]	13. 545	3. 682 [-2]	15	-0. 127 852 830	2. 573 [-6]	13. 239	5. 970 [-3]
16	-0. 127 370 675	8. 763 [-6]	14. 523	2. 684 [-2]	16	-0. 127 467 205	2. 074 [-6]	14. 236	5. 982 [-3]
17	-0. 127 080 855	4. 955 [-6]	15. 501	1. 845 [-2]	17	-0. 127 154 649	1. 696 [-6]	15. 233	5. 996 [-3]
18	-0. 126 840 985	2. 611 [-6]	16. 480	1. 169 [-2]	18	-0. 126 897 838	1. 407 [-6]	16. 231	6. 015 [-3]
19	-0. 126 640 190	1. 242 [-6]	17. 460	6. 610 [-3]	19	-0. 126 684 282	1. 181 [-6]	17. 230	6. 040 [-3]
20	-0. 126 470 385	5. 307 [-7]	18. 440	3. 328 [-3]	20	-0. 126 504 795	1. 002 [-6]	18. 228	6. 067 [-3]
21	-0. 126 325 562	1. 223 [-7]	19. 422	8. 957 [-4]	21	-0. 126 352 490	8. 583 [-7]	19. 227	6. 101 [-3]
22	-0. 126 200 875	5. 500 [-8]	20. 405	4. 673 [-4]	22	-0. 126 222 118	7. 422 [-7]	20. 227	6. 142 [-3]
23	-0. 126 092 746	1. 121 [-7]	21. 391	1. 097 [-3]	23	-0. 126 109 578	6. 480 [-7]	21. 228	6. 198 [-3]
					24	-0. 126 011 585	5. 745 [-7]	22. 232	6. 313 [-3]

Table 27: $^3D^e$ resonances below N=4 threshold ($\ell_{max} = 8$).

	C				D				
n	E (au)	Γ (au)	n^*	$\bar{\Gamma}$	n	E (au)	Γ (au)	n^*	$\bar{\Gamma}$
5	-0. 141 685 015	3. 595 [-5]	5. 474	5. 898 [-3]	5	-0. 171 555 467	1. 328 [-3]	3. 277	4. 675 [-2]
6	-0. 136 897 004	1. 485 [-5]	6. 483	4. 047 [-3]	6	-0. 149 126 704	4. 083 [-4]	4. 552	3. 852 [-2]
7	-0. 133 958 099	7. 949 [-6]	7. 471	3. 315 [-3]	7	-0. 140 996 582	1. 243 [-4]	5. 591	2. 173 [-2]
8	-0. 131 985 475	5. 476 [-6]	8. 460	3. 316 [-3]	8	-0. 136 562 238	5. 885 [-5]	6. 576	1. 674 [-2]
9	-0. 130 595 928	4. 037 [-6]	9. 452	3. 410 [-3]	9	-0. 133 700 991	4. 976 [-5]	7. 581	2. 168 [-2]
10	-0. 129 581 377	3. 079 [-6]	10. 447	3. 510 [-3]	10	-0. 131 783 629	4. 140 [-5]	8. 585	2. 620 [-2]
11	-0. 128 818 692	2. 407 [-6]	11. 443	3. 606 [-3]	11	-0. 130 438 746	3. 330 [-5]	9. 588	2. 936 [-2]
12	-0. 128 231 216	1. 922 [-6]	12. 439	3. 699 [-3]	12	-0. 129 458 766	2. 504 [-5]	10. 590	2. 974 [-2]
13	-0. 127 769 277	1. 558 [-6]	13. 437	3. 780 [-3]	13	-0. 128 724 066	1. 733 [-5]	11. 587	2. 696 [-2]
14	-0. 127 399 582	1. 279 [-6]	14. 435	3. 848 [-3]	14	-0. 128 157 897	1. 837 [-5]	12. 583	3. 659 [-2]
15	-0. 127 099 159	1. 062 [-6]	15. 433	3. 904 [-3]	15	-0. 127 709 496	1. 620 [-5]	13. 584	4. 062 [-2]
16	-0. 126 851 751	8. 882 [-7]	16. 432	3. 941 [-3]	16	-0. 127 350 736	1. 348 [-5]	14. 584	4. 182 [-2]
17	-0. 126 645 596	7. 452 [-7]	17. 431	3. 947 [-3]	17	-0. 127 058 888	1. 128 [-5]	15. 584	4. 267 [-2]
18	-0. 126 472 024	6. 062 [-7]	18. 430	3. 795 [-3]	18	-0. 126 818 224	9. 503 [-6]	16. 583	4. 334 [-2]
19	-0. 126 324 425	5. 903 [-7]	19. 430	4. 330 [-3]	19	-0. 126 617 418	8. 073 [-6]	17. 582	4. 388 [-2]
20	-0. 126 197 976	4. 955 [-7]	20. 430	4. 225 [-3]	20	-0. 126 448 118	6. 909 [-6]	18. 582	4. 433 [-2]
21	-0. 126 088 680	4. 287 [-7]	21. 431	4. 220 [-3]	21	-0. 126 304 045	5. 955 [-6]	19. 581	4. 471 [-2]
					22	-0. 126 180 392	5. 168 [-6]	20. 581	4. 505 [-2]
					23	-0. 126 073 390	4. 513 [-6]	21. 583	4. 537 [-2]

Table 28: $^3D^e$ resonances below N=4 threshold ($\ell_{max} = 8$).

E					F				
n	E (au)	Γ (au)	n^*	$\bar{\Gamma}$	n	E (au)	Γ (au)	n^*	$\bar{\Gamma}$
5	-0. 150 986 983	5. 089 [-5]	4. 386	4. 295 [-3]					
6	-0. 140 871 148	1. 111 [-4]	5. 613	1. 964 [-2]	6	-0. 136 205 239	2. 519 [-6]	6. 680	7. 510 [-4]
7	-0. 136 383 776	9. 679 [-5]	6. 627	2. 817 [-2]	7	-0. 133 496 577	5. 063 [-6]	7. 671	2. 286 [-3]
8	-0. 133 581 476	5. 093 [-5]	7. 633	2. 265 [-2]	8	-0. 131 656 836	6. 779 [-6]	8. 667	4. 413 [-3]
9	-0. 131 708 763	2. 467 [-5]	8. 633	1. 587 [-2]	9	-0. 130 352 756	7. 188 [-6]	9. 665	6. 489 [-3]
10	-0. 130 391 390	1. 257 [-5]	9. 630	1. 122 [-2]	10	-0. 129 396 176	6. 547 [-6]	10. 665	7. 942 [-3]
11	-0. 129 427 295	7. 568 [-6]	10. 627	9. 084 [-3]	11	-0. 128 674 450	5. 444 [-6]	11. 665	8. 641 [-3]
12	-0. 128 700 015	4. 927 [-6]	11. 625	7. 741 [-3]	12	-0. 128 116 812	4. 367 [-6]	12. 666	8. 872 [-3]
13	-0. 128 138 049	3. 235 [-6]	12. 623	6. 506 [-3]	13	-0. 127 677 116	3. 478 [-6]	13. 666	8. 878 [-3]
14	-0. 127 694 915	2. 171 [-6]	13. 621	5. 487 [-3]	14	-0. 127 324 321	2. 786 [-6]	14. 667	8. 791 [-3]
15	-0. 127 339 342	1. 504 [-6]	14. 620	4. 699 [-3]	15	-0. 127 036 948	2. 255 [-6]	15. 667	8. 673 [-3]
16	-0. 127 049 708	1. 075 [-6]	15. 618	4. 097 [-3]	16	-0. 126 799 767	1. 846 [-6]	16. 668	8. 548 [-3]
17	-0. 126 810 672	7. 916 [-7]	16. 617	3. 632 [-3]	17	-0. 126 601 729	1. 528 [-6]	17. 668	8. 429 [-3]
18	-0. 126 611 107	5. 979 [-7]	17. 617	3. 269 [-3]	18	-0. 126 434 666	1. 278 [-6]	18. 669	8. 318 [-3]
19	-0. 126 442 779	4. 620 [-7]	18. 616	2. 980 [-3]	19	-0. 126 292 424	1. 081 [-6]	19. 669	8. 223 [-3]
20	-0. 126 299 486	3. 642 [-7]	19. 615	2. 749 [-3]	20	-0. 126 170 282	9. 230 [-7]	20. 670	8. 151 [-3]
21	-0. 126 176 474	2. 923 [-7]	20. 616	2. 561 [-3]	21	-0. 126 064 541	7. 975 [-7]	21. 672	8. 118 [-3]
22	-0. 126 070 019	2. 383 [-7]	21. 617	2. 407 [-3]					

Table 29: $^3D^e$ resonances below N=4 threshold ($\ell_{max} = 8$).

	G				H				
n	E (au)	Γ (au)	n^*	$\bar{\Gamma}$	n	E (au)	Γ (au)	n^*	$\bar{\Gamma}$
5	-0. 161 297 966	8. 979 [-5]	3. 711	4. 590 [-3]	5	-0. 146 691 679	8. 190 [-6]	4. 801	9. 064 [-4]
6	-0. 147 085 559	6. 478 [-5]	4. 758	6. 978 [-3]	6	-0. 139 516 430	1. 038 [-5]	5. 869	2. 098 [-3]
7	-0. 139 965 954	4. 302 [-5]	5. 780	8. 308 [-3]	7	-0. 135 510 705	9. 692 [-6]	6. 897	3. 180 [-3]
8	-0. 135 837 446	2. 892 [-5]	6. 792	9. 061 [-3]	8	-0. 132 987 010	7. 866 [-6]	7. 912	3. 896 [-3]
9	-0. 133 218 041	1. 998 [-5]	7. 800	9. 481 [-3]	9	-0. 131 282 291	6. 193 [-6]	8. 920	4. 397 [-3]
10	-0. 131 448 817	1. 435 [-5]	8. 805	9. 798 [-3]	10	-0. 130 073 476	4. 825 [-6]	9. 927	4. 721 [-3]
11	-0. 130 196 618	1. 060 [-5]	9. 809	1. 001 [-2]	11	-0. 129 184 112	3. 777 [-6]	10. 932	4. 934 [-3]
12	-0. 129 277 434	8. 028 [-6]	10. 812	1. 015 [-2]	12	-0. 128 510 316	2. 987 [-6]	11. 935	5. 077 [-3]
13	-0. 128 582 592	6. 211 [-6]	11. 814	1. 024 [-2]	13	-0. 127 987 434	2. 393 [-6]	12. 937	5. 181 [-3]
14	-0. 128 044 488	4. 900 [-6]	12. 815	1. 031 [-2]	14	-0. 127 573 437	1. 943 [-6]	13. 939	5. 262 [-3]
15	-0. 127 619 230	3. 931 [-6]	13. 817	1. 037 [-2]	15	-0. 127 240 006	1. 598 [-6]	14. 940	5. 328 [-3]
16	-0. 127 277 302	3. 200 [-6]	14. 817	1. 041 [-2]	16	-0. 126 967 486	1. 329 [-6]	15. 942	5. 384 [-3]
17	-0. 126 998 253	2. 639 [-6]	15. 818	1. 045 [-2]	17	-0. 126 741 876	1. 117 [-6]	16. 942	5. 431 [-3]
18	-0. 126 767 548	2. 202 [-6]	16. 819	1. 048 [-2]	18	-0. 126 552 982	9. 473 [-7]	17. 943	5. 473 [-3]
19	-0. 126 574 622	1. 856 [-6]	17. 820	1. 050 [-2]	19	-0. 126 393 235	8. 103 [-7]	18. 944	5. 509 [-3]
20	-0. 126 411 642	1. 579 [-6]	18. 820	1. 052 [-2]	20	-0. 126 256 909	6. 979 [-7]	19. 945	5. 537 [-3]
21	-0. 126 272 694	1. 354 [-6]	19. 821	1. 055 [-2]	21	-0. 126 139 591	6. 041 [-7]	20. 946	5. 552 [-3]
22	-0. 126 153 226	1. 171 [-6]	20. 822	1. 058 [-2]	22	-0. 126 037 814	5. 243 [-7]	21. 950	5. 544 [-3]
23	-0. 126 049 663	1. 021 [-6]	21. 825	1. 061 [-2]					

Table 30: $^3D^e$ resonances below N=4 threshold ($\ell_{max} = 8$).

	I			
n	E (au)	Γ (au)	n^*	$\bar{\Gamma}$
5	-0. 158 979 138	1. 181 [-4]	3. 836	6. 665 [-3]
6	-0. 145 793 423	7. 089 [-5]	4. 904	8. 359 [-3]
7	-0. 139 183 201	4. 106 [-5]	5. 937	8. 595 [-3]
8	-0. 135 331 005	2. 488 [-5]	6. 957	8. 377 [-3]
9	-0. 132 873 466	1. 613 [-5]	7. 969	8. 162 [-3]
10	-0. 131 204 519	1. 120 [-5]	8. 977	8. 100 [-3]
11	-0. 130 017 483	8. 083 [-6]	9. 983	8. 040 [-3]
12	-0. 129 142 338	6. 019 [-6]	10. 987	7. 981 [-3]
13	-0. 128 478 282	4. 604 [-6]	11. 990	7. 936 [-3]
14	-0. 127 962 317	3. 603 [-6]	12. 992	7. 900 [-3]
15	-0. 127 553 373	2. 876 [-6]	13. 994	7. 881 [-3]
16	-0. 127 223 724	2. 335 [-6]	14. 995	7. 873 [-3]
17	-0. 126 954 090	1. 924 [-6]	15. 996	7. 876 [-3]
18	-0. 126 730 722	1. 605 [-6]	16. 997	7. 883 [-3]
19	-0. 126 543 597	1. 355 [-6]	17. 998	7. 897 [-3]
20	-0. 126 385 262	1. 155 [-6]	18. 998	7. 918 [-3]
21	-0. 126 250 077	9. 940 [-7]	19. 999	7. 951 [-3]
22	-0. 126 133 686	8. 648 [-7]	21. 001	8. 010 [-3]
23	-0. 126 032 668	7. 610 [-7]	22. 004	8. 106 [-3]

Table 31: $^3D^o$ resonances below N=4 threshold ($\ell_{max} = 8$).

A					B				
n	E (au)	Γ (au)	n^*	$\bar{\Gamma}$	n	E (au)	Γ (au)	n^*	$\bar{\Gamma}$
4	-0. 187 045 545	5. 048 [-3]	2. 839	1. 155 [-1]	4	-0. 167 096 649	1. 700 [-3]	3. 446	6. 958 [-2]
5	-0. 156 561 142	2. 204 [-3]	3. 980	1. 390 [-1]	5	-0. 146 855 777	5. 431 [-4]	4. 783	5. 943 [-2]
6	-0. 145 205 569	1. 252 [-3]	4. 975	1. 541 [-1]	6	-0. 139 625 842	3. 335 [-4]	5. 847	6. 666 [-2]
7	-0. 139 077 366	7. 352 [-4]	5. 960	1. 556 [-1]	7	-0. 135 588 221	2. 195 [-4]	6. 872	7. 123 [-2]
8	-0. 135 369 120	4. 516 [-4]	6. 944	1. 512 [-1]	8	-0. 133 045 656	1. 528 [-4]	7. 883	7. 488 [-2]
9	-0. 132 954 415	2. 860 [-4]	7. 928	1. 425 [-1]	9	-0. 131 324 757	1. 087 [-4]	8. 891	7. 640 [-2]
10	-0. 131 294 620	1. 927 [-4]	8. 913	1. 364 [-1]	10	-0. 130 105 005	7. 291 [-5]	9. 897	7. 067 [-2]
11	-0. 130 103 673	1. 399 [-4]	9. 898	1. 357 [-1]	11	-0. 129 210 462	4. 846 [-5]	10. 897	6. 271 [-2]
12	-0. 129 218 001	1. 059 [-4]	10. 888	1. 366 [-1]	12	-0. 128 533 308	3. 397 [-5]	11. 896	5. 719 [-2]
13	-0. 128 542 964	8. 067 [-5]	11. 880	1. 352 [-1]	13	-0. 128 007 657	2. 509 [-5]	12. 894	5. 378 [-2]
14	-0. 128 017 327	6. 194 [-5]	12. 873	1. 321 [-1]	14	-0. 127 591 238	1. 940 [-5]	13. 891	5. 201 [-2]
15	-0. 127 600 201	4. 794 [-5]	13. 867	1. 278 [-1]	15	-0. 127 255 668	1. 560 [-5]	14. 888	5. 148 [-2]
16	-0. 127 263 764	3. 745 [-5]	14. 862	1. 229 [-1]	16	-0. 126 981 252	1. 296 [-5]	15. 886	5. 197 [-2]
17	-0. 126 988 513	2. 946 [-5]	15. 857	1. 175 [-1]	17	-0. 126 753 963	1. 105 [-5]	16. 884	5. 319 [-2]
18	-0. 126 760 513	2. 336 [-5]	16. 853	1. 118 [-1]	18	-0. 126 563 589	9. 598 [-6]	17. 882	5. 488 [-2]
19	-0. 126 569 547	1. 868 [-5]	17. 848	1. 062 [-1]	19	-0. 126 402 544	8. 456 [-6]	18. 881	5. 692 [-2]
20	-0. 126 407 984	1. 507 [-5]	18. 845	1. 008 [-1]	20	-0. 126 265 080	7. 482 [-6]	19. 880	5. 879 [-2]
21	-0. 126 270 119	1. 225 [-5]	19. 841	9. 571 [-2]	21	-0. 126 146 782	6. 649 [-6]	20. 881	6. 054 [-2]
22	-0. 126 151 453	1. 008 [-5]	20. 838	9. 119 [-2]	22	-0. 126 044 163	5. 923 [-6]	21. 883	6. 207 [-2]
23	-0. 126 048 487	8. 374 [-6]	21. 838	8. 721 [-2]					

Table 32: $^3D^o$ resonances below N=4 threshold ($\ell_{max} = 8$).

	C				D				
n	E (au)	Γ (au)	n^*	$\bar{\Gamma}$	n	E (au)	Γ (au)	n^*	$\bar{\Gamma}$
5	-0. 164 329 806	7. 335 [-5]	3. 566	3. 325 [-3]	5	-0. 154 365 919	3. 739 [-5]	4. 126	2. 627 [-3]
6	-0. 148 964 520	5. 496 [-5]	4. 568	5. 238 [-3]	6	-0. 143 332 157	2. 488 [-5]	5. 222	3. 544 [-3]
7	-0. 141 151 991	3. 603 [-5]	5. 564	6. 205 [-3]	7	-0. 137 738 916	1. 651 [-5]	6. 265	4. 059 [-3]
8	-0. 136 618 682	2. 431 [-5]	6. 560	6. 863 [-3]	8	-0. 134 414 550	1. 109 [-5]	7. 288	4. 292 [-3]
9	-0. 133 754 681	1. 655 [-5]	7. 557	7. 143 [-3]	9	-0. 132 255 660	7. 920 [-6]	8. 301	4. 530 [-3]
10	-0. 131 831 412	1. 187 [-5]	8. 555	7. 432 [-3]	10	-0. 130 768 236	5. 775 [-6]	9. 310	4. 660 [-3]
11	-0. 130 478 097	8. 766 [-6]	9. 554	7. 643 [-3]	11	-0. 129 697 910	4. 299 [-6]	10. 317	4. 720 [-3]
12	-0. 129 490 122	6. 617 [-6]	10. 553	7. 775 [-3]	12	-0. 128 901 238	3. 274 [-6]	11. 321	4. 751 [-3]
13	-0. 128 747 006	5. 097 [-6]	11. 552	7. 856 [-3]	13	-0. 128 291 894	2. 548 [-6]	12. 324	4. 770 [-3]
14	-0. 128 174 093	4. 001 [-6]	12. 551	7. 910 [-3]	14	-0. 127 815 244	2. 021 [-6]	13. 327	4. 784 [-3]
15	-0. 127 723 139	3. 194 [-6]	13. 550	7. 947 [-3]	15	-0. 127 435 282	1. 631 [-6]	14. 329	4. 798 [-3]
16	-0. 127 361 846	2. 589 [-6]	14. 550	7. 975 [-3]	16	-0. 127 127 468	1. 335 [-6]	15. 330	4. 812 [-3]
17	-0. 127 067 940	2. 127 [-6]	15. 549	7. 996 [-3]	17	-0. 126 874 598	1. 108 [-6]	16. 332	4. 827 [-3]
18	-0. 126 825 651	1. 769 [-6]	16. 549	8. 018 [-3]	18	-0. 126 664 313	9. 300 [-7]	17. 333	4. 843 [-3]
19	-0. 126 623 563	1. 488 [-6]	17. 549	8. 040 [-3]	19	-0. 126 487 547	7. 883 [-7]	18. 334	4. 858 [-3]
20	-0. 126 453 247	1. 263 [-6]	18. 549	8. 058 [-3]	20	-0. 126 337 517	6. 738 [-7]	19. 335	4. 870 [-3]
21	-0. 126 308 358	1. 082 [-6]	19. 549	8. 081 [-3]	21	-0. 126 209 062	5. 809 [-7]	20. 336	4. 885 [-3]
22	-0. 126 184 038	9. 339 [-7]	20. 550	8. 104 [-3]	22	-0. 126 098 159	5. 048 [-7]	21. 338	4. 904 [-3]
23	-0. 126 076 472	8. 127 [-7]	21. 552	8. 135 [-3]	23	-0. 126 001 592	4. 445 [-7]	22. 343	4. 958 [-3]

Table 33: $^3D^o$ resonances below N=4 threshold ($\ell_{max} = 8$).

	E			
n	E (au)	Γ (au)	n^*	$\bar{\Gamma}$
5	-0. 141 527 687	9. 099 [-7]	5. 500	1. 514 [-4]
6	-0. 136 888 980	1. 151 [-6]	6. 485	3. 139 [-4]
7	-0. 133 946 445	1. 009 [-6]	7. 476	4. 216 [-4]
8	-0. 131 969 393	8. 361 [-7]	8. 470	5. 081 [-4]
9	-0. 130 579 836	6. 727 [-7]	9. 466	5. 706 [-4]
10	-0. 129 566 960	5. 392 [-7]	10. 463	6. 177 [-4]
11	-0. 128 806 305	4. 351 [-7]	11. 461	6. 551 [-4]
12	-0. 128 220 739	3. 547 [-7]	12. 460	6. 860 [-4]
13	-0. 127 760 452	2. 922 [-7]	13. 458	7. 123 [-4]
14	-0. 127 392 138	2. 432 [-7]	14. 457	7. 349 [-4]
15	-0. 127 092 854	2. 044 [-7]	15. 457	7. 546 [-4]
16	-0. 126 846 382	1. 734 [-7]	16. 456	7. 726 [-4]
17	-0. 126 640 995	1. 483 [-7]	17. 455	7. 885 [-4]
18	-0. 126 468 045	1. 277 [-7]	18. 455	8. 028 [-4]
19	-0. 126 321 037	1. 108 [-7]	19. 455	8. 154 [-4]
20	-0. 126 195 008	9. 677 [-8]	20. 455	8. 282 [-4]
21	-0. 126 086 081	8. 536 [-8]	21. 456	8. 431 [-4]

Table 34: $^3S^e$ resonances below N=5 threshold ($\ell_{max} = 8$).

A					B				
n	E (au)	Γ (au)	n^*	$\bar{\Gamma}$	n	E (au)	Γ (au)	n^*	$\bar{\Gamma}$
6	-0. 102 439 250	1. 413 [-4]	4. 720	1. 486 [-2]	6	-0. 107 784 412	1. 016 [-4]	4. 242	7. 756 [-3]
7	-0. 094 541 259	9. 539 [-5]	5. 864	1. 923 [-2]	7	-0. 098 051 314	9. 015 [-5]	5. 263	1. 314 [-2]
8	-0. 090 412 669	5. 881 [-5]	6. 930	1. 957 [-2]	8	-0. 092 734 234	6. 652 [-5]	6. 266	1. 637 [-2]
9	-0. 087 881 120	4. 072 [-5]	7. 965	2. 058 [-2]	9	-0. 089 470 988	4. 674 [-5]	7. 266	1. 793 [-2]
10	-0. 086 192 030	3. 062 [-5]	8. 986	2. 222 [-2]	10	-0. 087 319 733	3. 319 [-5]	8. 265	1. 874 [-2]
11	-0. 085 000 091	2. 308 [-5]	10. 000	2. 308 [-2]	11	-0. 085 826 359	2. 422 [-5]	9. 263	1. 925 [-2]
12	-0. 084 125 179	1. 770 [-5]	11. 009	2. 363 [-2]	12	-0. 084 747 075	1. 883 [-5]	10. 263	2. 036 [-2]
13	-0. 083 462 857	1. 393 [-5]	12. 016	2. 416 [-2]	13	-0. 083 942 107	1. 445 [-5]	11. 262	2. 064 [-2]
14	-0. 082 948 899	1. 118 [-5]	13. 021	2. 469 [-2]	14	-0. 083 325 763	1. 126 [-5]	12. 261	2. 075 [-2]
15	-0. 082 541 838	9. 138 [-6]	14. 025	2. 521 [-2]	15	-0. 082 843 398	8. 942 [-6]	13. 261	2. 085 [-2]
16	-0. 082 213 814	7. 569 [-6]	15. 028	2. 569 [-2]	16	-0. 082 458 817	7. 260 [-6]	14. 260	2. 105 [-2]
17	-0. 081 945 571	6. 306 [-6]	16. 031	2. 598 [-2]	17	-0. 082 147 250	6. 006 [-6]	15. 260	2. 134 [-2]
18	-0. 081 723 377	5. 300 [-6]	17. 033	2. 619 [-2]	18	-0. 081 891 333	5. 010 [-6]	16. 259	2. 154 [-2]
19	-0. 081 537 240	4. 493 [-6]	18. 035	2. 636 [-2]	19	-0. 081 678 569	4. 220 [-6]	17. 259	2. 170 [-2]
20	-0. 081 379 737	3. 840 [-6]	19. 036	2. 649 [-2]	20	-0. 081 499 772	3. 584 [-6]	18. 259	2. 182 [-2]
21	-0. 081 245 252	3. 308 [-6]	20. 038	2. 661 [-2]	21	-0. 081 348 065	3. 068 [-6]	19. 259	2. 191 [-2]
22	-0. 081 129 452	2. 871 [-6]	21. 040	2. 674 [-2]	22	-0. 081 218 210	2. 646 [-6]	20. 259	2. 200 [-2]
23	-0. 081 028 939	2. 513 [-6]	22. 044	2. 692 [-2]	23	-0. 081 106 124	2. 301 [-6]	21. 261	2. 212 [-2]
					24	-0. 081 008 533	2. 031 [-6]	22. 266	2. 241 [-2]

Table 35: $^3S^e$ resonances below N=5 threshold ($\ell_{max} = 8$).

C					D				
n	E (au)	Γ (au)	n^*	$\bar{\Gamma}$	n	E (au)	Γ (au)	n^*	$\bar{\Gamma}$
6	-0. 095 762 093	3. 403 [-5]	5. 632	6. 080 [-3]	6	-0. 111 941 116	4. 680 [-5]	3. 956	2. 899 [-3]
7	-0. 090 929 197	3. 359 [-5]	6. 764	1. 039 [-2]	7	-0. 101 026 980	4. 209 [-5]	4. 876	4. 880 [-3]
8	-0. 088 214 284	2. 576 [-5]	7. 802	1. 224 [-2]	8	-0. 094 815 296	3. 075 [-5]	5. 809	6. 029 [-3]
9	-0. 086 424 462	1. 898 [-5]	8. 822	1. 303 [-2]	9	-0. 090 947 129	2. 246 [-5]	6. 758	6. 933 [-3]
10	-0. 085 169 303	1. 426 [-5]	9. 835	1. 357 [-2]	10	-0. 088 389 792	1. 610 [-5]	7. 720	7. 407 [-3]
11	-0. 084 252 247	1. 076 [-5]	10. 844	1. 372 [-2]	11	-0. 086 620 785	1. 232 [-5]	8. 690	8. 086 [-3]
12	-0. 083 560 753	8. 298 [-6]	11. 850	1. 381 [-2]	12	-0. 085 349 455	9. 281 [-6]	9. 668	8. 387 [-3]
13	-0. 083 025 950	6. 561 [-6]	12. 854	1. 394 [-2]	13	-0. 084 408 108	6. 807 [-6]	10. 650	8. 223 [-3]
14	-0. 082 603 574	5. 298 [-6]	13. 858	1. 410 [-2]	14	-0. 083 692 762	5. 200 [-6]	11. 636	8. 192 [-3]
15	-0. 082 264 065	4. 346 [-6]	14. 861	1. 426 [-2]	15	-0. 083 137 035	4. 142 [-6]	12. 625	8. 335 [-3]
16	-0. 081 987 015	3. 603 [-6]	15. 863	1. 438 [-2]	16	-0. 082 697 072	3. 408 [-6]	13. 616	8. 603 [-3]
17	-0. 081 757 957	3. 017 [-6]	16. 865	1. 447 [-2]	17	-0. 082 343 025	2. 849 [-6]	14. 608	8. 881 [-3]
18	-0. 081 566 392	2. 548 [-6]	17. 866	1. 453 [-2]	18	-0. 082 054 030	2. 375 [-6]	15. 602	9. 018 [-3]
19	-0. 081 404 541	2. 170 [-6]	18. 868	1. 458 [-2]	19	-0. 081 815 164	1. 986 [-6]	16. 597	9. 081 [-3]
20	-0. 081 266 539	1. 863 [-6]	19. 869	1. 461 [-2]	20	-0. 081 615 515	1. 672 [-6]	17. 593	9. 106 [-3]
21	-0. 081 147 876	1. 610 [-6]	20. 871	1. 463 [-2]	21	-0. 081 446 967	1. 418 [-6]	18. 589	9. 109 [-3]
22	-0. 081 045 016	1. 399 [-6]	21. 874	1. 464 [-2]	22	-0. 081 303 377	1. 212 [-6]	19. 586	9. 104 [-3]
					23	-0. 081 180 011	1. 043 [-6]	20. 585	9. 098 [-3]
					24	-0. 081 073 135	9. 044 [-7]	21. 585	9. 096 [-3]

Table 36: $^3S^e$ resonances below N=5 threshold ($\ell_{max} = 8$).

	E			
n	E (au)	Γ (au)	n^*	$\bar{\Gamma}$
6	-0. 089 235 499	1. 387 [-7]	7. 358	5. 523 [-5]
7	-0. 087 273 786	4. 338 [-7]	8. 291	2. 472 [-4]
8	-0. 085 830 657	1. 309 [-6]	9. 260	1. 039 [-3]
9	-0. 084 762 455	7. 230 [-7]	10. 246	7. 778 [-4]
10	-0. 083 958 095	6. 148 [-7]	11. 239	8. 729 [-4]
11	-0. 083 339 868	5. 589 [-7]	12. 235	1. 024 [-3]
12	-0. 082 855 272	5. 082 [-7]	13. 233	1. 178 [-3]
13	-0. 082 468 685	4. 543 [-7]	14. 232	1. 309 [-3]
14	-0. 082 155 470	3. 990 [-7]	15. 230	1. 409 [-3]
15	-0. 081 898 224	3. 485 [-7]	16. 230	1. 490 [-3]
16	-0. 081 684 385	3. 047 [-7]	17. 229	1. 558 [-3]
17	-0. 081 504 721	2. 670 [-7]	18. 229	1. 617 [-3]
18	-0. 081 352 316	2. 346 [-7]	19. 229	1. 668 [-3]
19	-0. 081 221 910	2. 067 [-7]	20. 229	1. 711 [-3]
20	-0. 081 109 418	1. 823 [-7]	21. 229	1. 744 [-3]
21	-0. 081 011 622	1. 605 [-7]	22. 232	1. 763 [-3]

Table 37: $^3P^o$ resonances below N=5 threshold ($\ell_{max} = 8$).

A					B				
n	E (au)	Γ (au)	n^*	$\bar{\Gamma}$	n	E (au)	Γ (au)	n^*	$\bar{\Gamma}$
5	-0. 122 504 611	3. 565 [-3]	3. 430	1. 438 [-1]	5	-0. 100 038 925	6. 111 [-4]	4. 995	7. 617 [-2]
6	-0. 104 893 779	2. 953 [-3]	4. 482	2. 658 [-1]	6	-0. 092 489 093	3. 354 [-4]	6. 327	8. 496 [-2]
7	-0. 096 766 510	1. 347 [-3]	5. 461	2. 194 [-1]	7	-0. 089 284 754	3. 098 [-4]	7. 338	1. 224 [-1]
8	-0. 092 190 082	7. 055 [-4]	6. 404	1. 853 [-1]	8	-0. 087 076 041	1. 241 [-4]	8. 406	7. 369 [-2]
9	-0. 089 172 890	1. 776 [-4]	7. 383	7. 148 [-2]	9	-0. 085 636 109	7. 678 [-5]	9. 419	6. 416 [-2]
10	-0. 087 404 546	3. 638 [-5]	8. 217	2. 019 [-2]	10	-0. 084 600 472	5. 881 [-5]	10. 425	6. 664 [-2]
11	-0. 086 180 865	9. 278 [-5]	8. 994	6. 750 [-2]	11	-0. 083 829 274	5. 284 [-5]	11. 427	7. 885 [-2]
12	-0. 085 213 111	3. 189 [-4]	9. 793	2. 995 [-1]	12	-0. 083 238 172	4. 737 [-5]	12. 426	9. 088 [-2]
13	-0. 084 399 277	3. 460 [-4]	10. 661	4. 193 [-1]	13	-0. 082 774 246	4. 190 [-5]	13. 425	1. 014 [-1]
14	-0. 083 734 810	2. 806 [-4]	11. 570	4. 347 [-1]	14	-0. 082 403 421	3. 656 [-5]	14. 423	1. 097 [-1]
15	-0. 083 194 653	2. 096 [-4]	12. 510	4. 105 [-1]	15	-0. 082 102 457	3. 207 [-5]	15. 421	1. 176 [-1]
16	-0. 082 751 112	1. 544 [-4]	13. 481	3. 782 [-1]	16	-0. 081 854 713	2. 835 [-5]	16. 419	1. 255 [-1]
17	-0. 082 390 405	1. 205 [-4]	14. 463	3. 656 [-1]	17	-0. 081 648 194	2. 525 [-5]	17. 417	1. 334 [-1]
18	-0. 082 094 914	9. 455 [-5]	15. 449	3. 487 [-1]	18	-0. 081 474 251	2. 255 [-5]	18. 416	1. 408 [-1]
19	-0. 081 849 662	7. 564 [-5]	16. 441	3. 362 [-1]	19	-0. 081 326 408	2. 025 [-5]	19. 415	1. 482 [-1]
20	-0. 081 645 141	6. 196 [-5]	17. 433	3. 283 [-1]	20	-0. 081 199 735	1. 804 [-5]	20. 415	1. 535 [-1]
21	-0. 081 472 732	5. 148 [-5]	18. 426	3. 220 [-1]	21	-0. 081 090 207	1. 617 [-5]	21. 416	1. 588 [-1]
22	-0. 081 325 855	4. 255 [-5]	19. 419	3. 116 [-1]					
23	-0. 081 199 120	3. 670 [-5]	20. 420	3. 125 [-1]					
24	-0. 081 089 974	3. 168 [-5]	21. 418	3. 112 [-1]					

Table 38: $^3P^o$ resonances below N=5 threshold ($\ell_{max} = 8$).

	C				D				
n	E (au)	Γ (au)	n^*	$\bar{\Gamma}$	n	E (au)	Γ (au)	n^*	$\bar{\Gamma}$
6	-0. 109 415 996	1. 054 [-3]	4. 123	7. 390 [-2]	6	-0. 089 539 098	2. 456 [-4]	7. 240	9. 320 [-2]
7	-0. 098 946 585	1. 743 [-3]	5. 137	2. 364 [-1]	7	-0. 088 018 854	2. 637 [-4]	7. 896	1. 298 [-1]
8	-0. 093 173 436	1. 515 [-3]	6. 161	3. 543 [-1]	8	-0. 086 432 116	1. 491 [-4]	8. 817	1. 022 [-1]
9	-0. 089 755 148	1. 117 [-3]	7. 159	4. 098 [-1]	9	-0. 085 230 213	9. 901 [-5]	9. 777	9. 254 [-2]
10	-0. 087 488 661	1. 006 [-3]	8. 170	5. 488 [-1]	10	-0. 084 324 273	6. 933 [-5]	10. 753	8. 621 [-2]
11	-0. 086 054 358	4. 083 [-4]	9. 088	3. 064 [-1]	11	-0. 083 631 830	4. 930 [-5]	11. 733	7. 964 [-2]
12	-0. 084 948 647	2. 544 [-4]	10. 052	2. 584 [-1]	12	-0. 083 091 515	3. 677 [-5]	12. 717	7. 562 [-2]
13	-0. 084 116 639	1. 348 [-4]	11. 021	1. 804 [-1]	13	-0. 082 662 169	2. 858 [-5]	13. 705	7. 358 [-2]
14	-0. 083 479 224	6. 434 [-5]	11. 988	1. 109 [-1]	14	-0. 082 315 543	2. 286 [-5]	14. 695	7. 254 [-2]
15	-0. 082 981 581	2. 498 [-5]	12. 950	5. 424 [-2]	15	-0. 082 031 945	1. 853 [-5]	15. 687	7. 154 [-2]
16	-0. 082 584 525	6. 875 [-6]	13. 909	1. 850 [-2]	16	-0. 081 797 115	1. 518 [-5]	16. 680	7. 046 [-2]
17	-0. 082 261 296	1. 280 [-6]	14. 870	4. 210 [-3]	17	-0. 081 600 568	1. 258 [-5]	17. 675	6. 948 [-2]
18	-0. 081 993 818	1. 633 [-6]	15. 836	6. 483 [-3]	18	-0. 081 434 445	1. 055 [-5]	18. 670	6. 867 [-2]
19	-0. 081 769 795	3. 876 [-6]	16. 808	1. 841 [-2]	19	-0. 081 292 776	8. 923 [-6]	19. 666	6. 787 [-2]
20	-0. 081 580 466	6. 132 [-6]	17. 787	3. 451 [-2]	20	-0. 081 170 946	7. 594 [-6]	20. 664	6. 700 [-2]
21	-0. 081 419 245	7. 796 [-6]	18. 770	5. 155 [-2]	21	-0. 081 065 321	6. 531 [-6]	21. 664	6. 641 [-2]
22	-0. 081 281 004	8. 808 [-6]	19. 756	6. 792 [-2]					
23	-0. 081 161 666	9. 279 [-6]	20. 746	8. 287 [-2]					
24	-0. 081 057 925	9. 396 [-6]	21. 740	9. 654 [-2]					

Table 39: $^3P^o$ resonances below N=5 threshold ($\ell_{max} = 8$).

	E				F				
n	E (au)	Γ (au)	n^*	$\bar{\Gamma}$	n	E (au)	Γ (au)	n^*	$\bar{\Gamma}$
6	-0. 114 321 608	3. 554 [-3]	3. 817	1. 976 [-1]	6	-0. 091 745 806	5. 923 [-6]	6. 524	1. 645 [-3]
7	-0. 100 430 772	1. 609 [-3]	4. 947	1. 948 [-1]	7	-0. 088 886 152	3. 844 [-6]	7. 501	1. 622 [-3]
8	-0. 094 417 779	2. 737 [-4]	5. 889	5. 589 [-2]	8	-0. 086 966 377	8. 538 [-6]	8. 472	5. 192 [-3]
9	-0. 090 981 826	3. 111 [-5]	6. 748	9. 557 [-3]	9	-0. 085 599 815	1. 610 [-5]	9. 449	1. 358 [-2]
10	-0. 088 553 313	2. 920 [-6]	7. 646	1. 305 [-3]	10	-0. 084 590 021	1. 479 [-5]	10. 437	1. 682 [-2]
11	-0. 086 713 599	1. 381 [-5]	8. 630	8. 875 [-3]	11	-0. 083 824 941	9. 529 [-6]	11. 433	1. 424 [-2]
12	-0. 085 387 039	1. 762 [-5]	9. 634	1. 576 [-2]	12	-0. 083 234 445	6. 879 [-6]	12. 433	1. 322 [-2]
13	-0. 084 416 737	1. 525 [-5]	10. 640	1. 837 [-2]	13	-0. 082 770 404	5. 529 [-6]	13. 434	1. 340 [-2]
14	-0. 083 687 470	1. 231 [-5]	11. 644	1. 943 [-2]	14	-0. 082 399 409	4. 675 [-6]	14. 436	1. 406 [-2]
15	-0. 083 125 491	9. 849 [-6]	12. 648	1. 993 [-2]	15	-0. 082 098 210	4. 027 [-6]	15. 437	1. 481 [-2]
16	-0. 082 683 155	7. 913 [-6]	13. 651	2. 013 [-2]	16	-0. 081 850 374	3. 467 [-6]	16. 438	1. 540 [-2]
17	-0. 082 328 680	6. 435 [-6]	14. 653	2. 025 [-2]	17	-0. 081 644 013	2. 986 [-6]	17. 439	1. 584 [-2]
18	-0. 082 040 198	5. 286 [-6]	15. 655	2. 028 [-2]	18	-0. 081 470 360	2. 577 [-6]	18. 441	1. 616 [-2]
19	-0. 081 802 264	4. 386 [-6]	16. 656	2. 027 [-2]	19	-0. 081 322 837	2. 232 [-6]	19. 442	1. 640 [-2]
20	-0. 081 603 702	3. 692 [-6]	17. 657	2. 033 [-2]	20	-0. 081 196 424	1. 941 [-6]	20. 443	1. 658 [-2]
21	-0. 081 436 260	3. 153 [-6]	18. 658	2. 048 [-2]	21	-0. 081 087 207	1. 699 [-6]	21. 445	1. 675 [-2]
22	-0. 081 293 735	2. 736 [-6]	19. 659	2. 079 [-2]					
23	-0. 081 171 375	2. 416 [-6]	20. 660	2. 131 [-2]					
24	-0. 081 065 453	2. 171 [-6]	21. 663	2. 207 [-2]					

Table 40: $^3P^o$ resonances below N=5 threshold ($\ell_{max} = 8$).

G					H				
n	E (au)	Γ (au)	n^*	$\bar{\Gamma}$	n	E (au)	Γ (au)	n^*	$\bar{\Gamma}$
5	-0. 109 915 045	7. 560 [-5]	4. 088	5. 166 [-3]					
6	-0. 099 551 889	6. 794 [-5]	5. 057	8. 786 [-3]	6	-0. 105 129 575	1. 361 [-4]	4. 461	1. 208 [-2]
7	-0. 093 773 001	4. 905 [-5]	6. 025	1. 073 [-2]	7	-0. 096 279 433	1. 107 [-4]	5. 542	1. 885 [-2]
8	-0. 090 201 671	3. 495 [-5]	7. 001	1. 199 [-2]	8	-0. 091 545 167	7. 292 [-5]	6. 581	2. 078 [-2]
9	-0. 087 846 220	2. 479 [-5]	7. 983	1. 261 [-2]	9	-0. 088 655 432	5. 299 [-5]	7. 600	2. 327 [-2]
10	-0. 086 216 331	1. 979 [-5]	8. 968	1. 427 [-2]	10	-0. 086 748 820	2. 919 [-5]	8. 606	1. 862 [-2]
11	-0. 085 041 815	1. 427 [-5]	9. 958	1. 409 [-2]	11	-0. 085 415 998	1. 563 [-5]	9. 608	1. 386 [-2]
12	-0. 084 169 852	1. 068 [-5]	10. 950	1. 402 [-2]	12	-0. 084 441 638	1. 059 [-5]	10. 610	1. 265 [-2]
13	-0. 083 505 023	8. 213 [-6]	11. 944	1. 399 [-2]	13	-0. 083 708 215	7. 867 [-6]	11. 612	1. 232 [-2]
14	-0. 082 986 811	6. 520 [-6]	12. 938	1. 412 [-2]	14	-0. 083 142 596	6. 140 [-6]	12. 614	1. 232 [-2]
15	-0. 082 575 190	5. 314 [-6]	13. 934	1. 438 [-2]	15	-0. 082 697 254	4. 942 [-6]	13. 615	1. 247 [-2]
16	-0. 082 242 900	4. 401 [-6]	14. 931	1. 465 [-2]	16	-0. 082 340 357	4. 052 [-6]	14. 617	1. 265 [-2]
17	-0. 081 970 854	3. 674 [-6]	15. 928	1. 485 [-2]	17	-0. 082 049 930	3. 370 [-6]	15. 618	1. 284 [-2]
18	-0. 081 745 361	3. 091 [-6]	16. 926	1. 499 [-2]	18	-0. 081 810 428	2. 833 [-6]	16. 619	1. 300 [-2]
19	-0. 081 556 394	2. 618 [-6]	17. 924	1. 507 [-2]	19	-0. 081 610 596	2. 406 [-6]	17. 619	1. 316 [-2]
20	-0. 081 396 474	2. 232 [-6]	18. 922	1. 512 [-2]	20	-0. 081 442 123	2. 061 [-6]	18. 620	1. 331 [-2]
21	-0. 081 259 919	1. 918 [-6]	19. 921	1. 517 [-2]	21	-0. 081 298 758	1. 777 [-6]	19. 621	1. 342 [-2]
22	-0. 081 142 334	1. 662 [-6]	20. 921	1. 522 [-2]	22	-0. 081 175 717	1. 535 [-6]	20. 622	1. 347 [-2]
23	-0. 081 040 261	1. 450 [-6]	21. 924	1. 528 [-2]	23	-0. 081 069 254	1. 323 [-6]	21. 624	1. 338 [-2]

Table 41: $^3P^o$ resonances below N=5 threshold ($\ell_{max} = 8$).

	I			
n	E (au)	Γ (au)	n^*	$\bar{\Gamma}$
6	-0. 098 954 598	7. 344 [-5]	5. 136	9. 950 [-3]
7	-0. 092 686 179	6. 125 [-5]	6. 278	1. 516 [-2]
8	-0. 089 316 349	3. 526 [-5]	7. 326	1. 386 [-2]
9	-0. 087 179 312	2. 147 [-5]	8. 345	1. 248 [-2]
10	-0. 085 723 957	1. 253 [-5]	9. 346	1. 023 [-2]
11	-0. 084 679 125	7. 329 [-6]	10. 337	8. 096 [-3]
12	-0. 083 897 921	4. 491 [-6]	11. 326	6. 524 [-3]
13	-0. 083 296 721	2. 986 [-6]	12. 315	5. 577 [-3]
14	-0. 082 823 925	2. 131 [-6]	13. 306	5. 020 [-3]
15	-0. 082 445 488	1. 598 [-6]	14. 299	4. 670 [-3]
16	-0. 082 137 969	1. 244 [-6]	15. 293	4. 448 [-3]
17	-0. 081 884 772	9. 842 [-7]	16. 288	4. 252 [-3]
18	-0. 081 673 870	7. 890 [-7]	17. 283	4. 073 [-3]
19	-0. 081 496 373	6. 404 [-7]	18. 280	3. 911 [-3]
20	-0. 081 345 595	5. 258 [-7]	19. 276	3. 766 [-3]
21	-0. 081 216 427	4. 366 [-7]	20. 274	3. 638 [-3]
22	-0. 081 104 889	3. 659 [-7]	21. 273	3. 522 [-3]

Table 42: $^3P^e$ resonances below N=5 threshold ($\ell_{max} = 8$).

	A					B			
n	E (au)	Γ (au)	n^*	$\bar{\Gamma}$	n	E (au)	Γ (au)	n^*	$\bar{\Gamma}$
6	-0. 109 477 030	3. 223 [-3]	4. 119	2. 252 [-1]	6	-0. 107 285 286	1. 547 [-3]	4. 281	1. 214 [-1]
7	-0. 098 555 228	9. 301 [-4]	5. 191	1. 301 [-1]	7	-0. 096 589 412	1. 275 [-3]	5. 490	2. 110 [-1]
8	-0. 093 427 266	4. 458 [-4]	6. 102	1. 013 [-1]	8	-0. 091 458 956	9. 695 [-4]	6. 606	2. 794 [-1]
9	-0. 090 200 787	1. 159 [-4]	7. 001	3. 976 [-2]	9	-0. 088 618 911	6. 630 [-4]	7. 617	2. 930 [-1]
10	-0. 088 392 302	9. 024 [-5]	7. 719	4. 150 [-2]	10	-0. 086 699 650	4. 896 [-4]	8. 638	3. 157 [-1]
11	-0. 086 747 214	2. 096 [-4]	8. 608	1. 337 [-1]	11	-0. 085 410 433	3. 552 [-4]	9. 613	3. 156 [-1]
12	-0. 085 525 841	3. 936 [-5]	9. 512	3. 387 [-2]	12	-0. 084 460 092	2. 817 [-4]	10. 588	3. 344 [-1]
13	-0. 084 637 149	1. 513 [-5]	10. 384	1. 694 [-2]	13	-0. 083 743 322	2. 191 [-4]	11. 557	3. 383 [-1]
14	-0. 083 934 386	7. 807 [-5]	11. 273	1. 118 [-1]	14	-0. 083 182 566	1. 628 [-4]	12. 534	3. 206 [-1]
15	-0. 083 356 729	1. 273 [-4]	12. 205	2. 314 [-1]	15	-0. 082 732 839	1. 286 [-4]	13. 526	3. 183 [-1]
16	-0. 082 889 074	1. 390 [-4]	13. 155	3. 165 [-1]	16	-0. 082 373 966	9. 257 [-5]	14. 513	2. 829 [-1]
17	-0. 082 496 142	2. 166 [-4]	14. 153	6. 139 [-1]	17	-0. 082 085 624	7. 564 [-5]	15. 483	2. 808 [-1]
18	-0. 082 212 410	1. 308 [-4]	15. 033	4. 445 [-1]	18	-0. 081 844 315	5. 113 [-5]	16. 465	2. 282 [-1]
19	-0. 081 930 946	1. 106 [-4]	16. 092	4. 610 [-1]	19	-0. 081 640 361	3. 864 [-5]	17. 459	2. 056 [-1]
20	-0. 081 710 201	1. 381 [-4]	17. 099	6. 903 [-1]	20	-0. 081 470 133	3. 186 [-5]	18. 442	1. 998 [-1]
21	-0. 081 552 979	8. 932 [-5]	17. 943	5. 160 [-1]	21	-0. 081 324 210	2. 332 [-5]	19. 432	1. 711 [-1]
22	-0. 081 399 209	9. 861 [-5]	18. 904	6. 661 [-1]	22	-0. 081 198 959	1. 838 [-5]	20. 421	1. 565 [-1]
23	-0. 081 257 792	6. 920 [-5]	19. 938	5. 485 [-1]	23	-0. 081 090 396	1. 442 [-5]	21. 414	1. 416 [-1]

Table 43: $^3P^e$ resonances below N=5 threshold ($\ell_{max} = 8$).

C					D				
n	E (au)	Γ (au)	n^*	$\bar{\Gamma}$	n	E (au)	Γ (au)	n^*	$\bar{\Gamma}$
6	-0. 119 403 711	3. 458 [-3]	3. 562	1. 563 [-1]					
7	-0. 102 137 324	2. 260 [-3]	4. 753	2. 426 [-1]	7	-0. 095 235 803	9. 778 [-5]	5. 729	1. 838 [-2]
8	-0. 095 081 244	1. 525 [-3]	5. 758	2. 912 [-1]	8	-0. 090 562 004	3. 545 [-5]	6. 880	1. 155 [-2]
9	-0. 091 069 404	8. 713 [-4]	6. 721	2. 645 [-1]	9	-0. 088 066 201	3. 613 [-5]	7. 873	1. 763 [-2]
10	-0. 088 485 771	4. 349 [-4]	7. 676	1. 967 [-1]	10	-0. 086 353 189	2. 685 [-5]	8. 871	1. 875 [-2]
11	-0. 087 230 498	4. 127 [-4]	8. 316	2. 373 [-1]	11	-0. 085 133 500	1. 738 [-5]	9. 869	1. 670 [-2]
12	-0. 085 974 791	2. 923 [-4]	9. 148	2. 238 [-1]	12	-0. 084 234 503	1. 180 [-5]	10. 866	1. 514 [-2]
13	-0. 084 903 979	1. 909 [-4]	10. 097	1. 966 [-1]	13	-0. 083 552 605	8. 134 [-6]	11. 863	1. 358 [-2]
14	-0. 084 078 457	1. 355 [-4]	11. 072	1. 839 [-1]	14	-0. 083 023 081	5. 476 [-6]	12. 861	1. 165 [-2]
15	-0. 083 441 663	9. 010 [-5]	12. 053	1. 578 [-1]	15	-0. 082 603 726	3. 678 [-6]	13. 858	9. 787 [-3]
16	-0. 082 940 957	6. 619 [-5]	13. 039	1. 467 [-1]	16	-0. 082 265 940	2. 416 [-6]	14. 855	7. 918 [-3]
17	-0. 082 539 278	5. 307 [-5]	14. 032	1. 466 [-1]	17	-0. 081 989 830	1. 573 [-6]	15. 852	6. 265 [-3]
18	-0. 082 216 212	4. 211 [-5]	15. 020	1. 427 [-1]	18	-0. 081 761 257	1. 033 [-6]	16. 849	4. 943 [-3]
19	-0. 081 950 826	3. 238 [-5]	16. 009	1. 328 [-1]	19	-0. 081 569 886	6. 868 [-7]	17. 846	3. 904 [-3]
20	-0. 081 728 822	2. 607 [-5]	17. 006	1. 282 [-1]	20	-0. 081 408 056	4. 700 [-7]	18. 844	3. 145 [-3]
21	-0. 081 542 576	2. 237 [-5]	18. 004	1. 306 [-1]	21	-0. 081 269 972	3. 352 [-7]	19. 842	2. 619 [-3]
22	-0. 081 385 195	1. 905 [-5]	18. 999	1. 307 [-1]	22	-0. 081 151 175	2. 515 [-7]	20. 841	2. 277 [-3]
23	-0. 081 250 495	1. 614 [-5]	19. 996	1. 291 [-1]	23	-0. 081 048 160	2. 001 [-7]	21. 841	2. 085 [-3]

Table 44: $^3D^e$ resonances below N=5 threshold ($\ell_{max} = 8$).

Unclassified

E (au)	Γ (au)	n^*	$\bar{\Gamma}$
-0. 117 715 602	4. 123 [-3]	3. 641	1. 990 [-1]
-0. 111 330 752	5. 495 [-5]	3. 995	3. 503 [-3]
-0. 107 712 032	1. 009 [-4]	4. 248	7. 735 [-3]
-0. 106 827 700	1. 212 [-4]	4. 317	9. 753 [-3]
-0. 106 581 329	1. 636 [-3]	4. 337	1. 334 [-1]
-0. 104 738 968	1. 506 [-3]	4. 496	1. 369 [-1]
-0. 102 328 077	1. 133 [-4]	4. 732	1. 201 [-2]
-0. 100 853 697	1. 166 [-4]	4. 897	1. 369 [-2]
-0. 100 600 324	5. 283 [-5]	4. 927	6. 318 [-3]
-0. 101 246 709	2. 469 [-3]	4. 851	2. 818 [-1]
-0. 098 013 778	8. 497 [-5]	5. 268	1. 243 [-2]
-0. 098 155 272	1. 032 [-3]	5. 248	1. 492 [-1]
-0. 097 440 508	9. 808 [-5]	5. 354	1. 506 [-2]
-0. 095 715 874	4. 831 [-5]	5. 640	8. 669 [-3]
-0. 094 500 088	4. 310 [-4]	5. 872	8. 726 [-2]
-0. 094 497 924	7. 628 [-5]	5. 873	1. 545 [-2]
-0. 094 521 981	3. 765 [-5]	5. 868	7. 607 [-3]
-0. 094 555 491	2. 171 [-3]	5. 861	4. 371 [-1]
-0. 093 770 735	8. 113 [-5]	6. 026	1. 775 [-2]
-0. 093 164 077	5. 239 [-4]	6. 163	1. 226 [-1]
-0. 092 712 898	6. 245 [-5]	6. 271	1. 540 [-2]
-0. 092 338 387	7. 061 [-5]	6. 366	1. 822 [-2]
-0. 090 937 583	4. 327 [-5]	6. 761	1. 337 [-2]
-0. 090 741 139	2. 744 [-5]	6. 823	8. 714 [-3]
-0. 090 394 489	5. 032 [-5]	6. 936	1. 679 [-2]
-0. 090 013 284	1. 526 [-4]	7. 066	5. 386 [-2]
-0. 090 669 392	1. 293 [-3]	6. 846	4. 147 [-1]
-0. 088 160 095	3. 710 [-5]	7. 828	1. 779 [-2]
-0. 088 247 148	7. 036 [-4]	7. 786	3. 321 [-1]
-0. 085 832 564	3. 730 [-4]	9. 259	2. 961 [-1]
-0. 085 363 373	9. 818 [-5]	9. 654	8. 837 [-2]

Table 45: $^3D^e$ resonances below N=5 threshold ($\ell_{max} = 8$).

A					B				
n	E (au)	Γ (au)	n^*	$\bar{\Gamma}$	n	E (au)	Γ (au)	n^*	$\bar{\Gamma}$
10	-0. 084 481 832	6. 709 [-6]	10. 562	7. 906 [-3]	10	-0. 084 823 660	2. 310 [-4]	10. 181	2. 438 [-1]
11	-0. 083 803 278	1. 286 [-5]	11. 466	1. 938 [-2]	11	-0. 084 018 174	1. 650 [-4]	11. 155	2. 290 [-1]
12	-0. 083 253 818	4. 417 [-5]	12. 396	8. 414 [-2]	12	-0. 083 395 450	1. 172 [-4]	12. 135	2. 094 [-1]
13	-0. 082 806 283	7. 169 [-5]	13. 348	1. 705 [-1]	13	-0. 082 904 641	8. 660 [-5]	13. 120	1. 956 [-1]
14	—	—	—	—	14	-0. 082 513 890	6. 256 [-5]	14. 103	1. 755 [-1]
15	—	—	—	—	15	-0. 082 194 143	5. 305 [-5]	15. 096	1. 825 [-1]
16	-0. 081 885 959	8. 928 [-5]	16. 282	3. 854 [-1]	16	-0. 081 930 529	4. 198 [-5]	16. 093	1. 750 [-1]
17	—	—	—	—	17	-0. 081 712 865	3. 517 [-5]	17. 085	1. 754 [-1]
18	—	—	—	—	18	-0. 081 529 229	2. 853 [-5]	18. 082	1. 687 [-1]
19	-0. 081 348 991	7. 505 [-5]	19. 252	5. 356 [-1]	19	-0. 081 373 492	2. 379 [-5]	19. 080	1. 653 [-1]
					20	-0. 081 240 383	2. 022 [-5]	20. 077	1. 637 [-1]
					21	-0. 081 125 650	1. 743 [-5]	21. 076	1. 632 [-1]

Table 46: $^3D^e$ resonances below N=5 threshold ($\ell_{max} = 8$).

	C				D				
n	E (au)	Γ (au)	n^*	$\bar{\Gamma}$	n	E (au)	Γ (au)	n^*	$\bar{\Gamma}$
					7	-0. 090 365 551	2. 145 [-4]	6. 945	7. 185 [-2]
8	-0. 087 804 960	1. 435 [-5]	8. 004	7. 358 [-3]	8	-0. 087 869 804	1. 658 [-4]	7. 971	8. 395 [-2]
9	-0. 086 258 666	1. 886 [-5]	8. 938	1. 347 [-2]	9	-0. 086 198 385	1. 354 [-4]	8. 981	9. 813 [-2]
10	-0. 085 074 641	2. 112 [-5]	9. 926	2. 065 [-2]	10	-0. 085 017 914	1. 056 [-4]	9. 982	1. 051 [-1]
11	-0. 084 193 087	2. 073 [-5]	10. 920	2. 699 [-2]	11	-0. 084 141 017	9. 450 [-5]	10. 988	1. 254 [-1]
12	-0. 083 521 190	1. 907 [-5]	11. 916	3. 227 [-2]	12	-0. 083 478 888	7. 536 [-5]	11. 988	1. 298 [-1]
13	-0. 082 998 173	1. 735 [-5]	12. 914	3. 736 [-2]	13	-0. 082 964 679	5. 900 [-5]	12. 987	1. 292 [-1]
14	-0. 082 583 328	1. 611 [-5]	13. 912	4. 338 [-2]	14	-0. 082 556 701	4. 383 [-5]	13. 984	1. 199 [-1]
15	-0. 082 248 961	1. 524 [-5]	14. 911	5. 050 [-2]	15	-0. 082 229 123	3. 415 [-5]	14. 977	1. 147 [-1]
16	-0. 081 975 467	1. 488 [-5]	15. 909	5. 994 [-2]	16	-0. 081 960 338	2. 611 [-5]	15. 971	1. 064 [-1]
17	-0. 081 749 024	1. 480 [-5]	16. 908	7. 154 [-2]	17	-0. 081 737 754	1. 886 [-5]	16. 963	9. 207 [-2]
18	-0. 081 559 525	1. 501 [-5]	17. 906	8. 615 [-2]	18	-0. 081 550 707	1. 326 [-5]	17. 956	7. 674 [-2]
19	-0. 081 399 704	1. 516 [-5]	18. 900	1. 023 [-1]	19	-0. 081 392 122	9. 200 [-6]	18. 952	6. 262 [-2]
20	-0. 081 263 350	1. 455 [-5]	19. 894	1. 145 [-1]	20	-0. 081 256 403	6. 499 [-6]	19. 949	5. 159 [-2]
21	-0. 081 146 026	1. 363 [-5]	20. 888	1. 242 [-1]	21	-0. 081 139 470	4. 750 [-6]	20. 948	4. 366 [-2]

Table 47: $^3D^e$ resonances below N=5 threshold ($\ell_{max} = 8$).

E					F				
n	E (au)	Γ (au)	n^*	$\bar{\Gamma}$	n	E (au)	Γ (au)	n^*	$\bar{\Gamma}$
					7	-0. 089 968 373	4. 926 [-5]	7. 082	1. 750 [-2]
8	-0. 087 904 397	2. 107 [-5]	7. 953	1. 060 [-2]	8	-0. 087 602 143	3. 786 [-5]	8. 109	2. 020 [-2]
9	-0. 086 163 611	1. 497 [-5]	9. 007	1. 094 [-2]	9	-0. 085 994 447	2. 797 [-5]	9. 133	2. 130 [-2]
10	-0. 084 986 435	1. 096 [-5]	10. 014	1. 100 [-2]	10	-0. 084 858 297	2. 212 [-5]	10. 145	2. 309 [-2]
11	-0. 084 120 093	7. 848 [-6]	11. 016	1. 049 [-2]	11	-0. 084 019 303	1. 740 [-5]	11. 153	2. 414 [-2]
12	-0. 083 463 752	6. 044 [-6]	12. 015	1. 048 [-2]	12	-0. 083 381 569	1. 411 [-5]	12. 160	2. 538 [-2]
13	-0. 082 953 686	5. 573 [-6]	13. 011	1. 228 [-2]	13	-0. 082 884 970	1. 178 [-5]	13. 165	2. 688 [-2]
14	-0. 082 548 660	5. 738 [-6]	14. 006	1. 577 [-2]	14	-0. 082 490 549	9. 825 [-6]	14. 169	2. 795 [-2]
15	-0. 082 221 413	5. 995 [-6]	15. 003	2. 025 [-2]	15	-0. 082 171 984	8. 240 [-6]	15. 172	2. 878 [-2]
16	-0. 081 953 131	6. 210 [-6]	16. 000	2. 544 [-2]	16	-0. 081 910 999	6. 823 [-6]	16. 175	2. 888 [-2]
17	-0. 081 730 431	6. 199 [-6]	16. 998	3. 045 [-2]	17	-0. 081 694 492	5. 720 [-6]	17. 178	2. 899 [-2]
18	-0. 081 543 556	5. 933 [-6]	17. 998	3. 459 [-2]	18	-0. 081 512 864	4. 803 [-6]	18. 180	2. 886 [-2]
19	-0. 081 385 308	5. 430 [-6]	18. 998	3. 724 [-2]	19	-0. 081 358 980	4. 076 [-6]	19. 181	2. 877 [-2]
20	-0. 081 250 161	4. 827 [-6]	19. 999	3. 861 [-2]	20	-0. 081 227 428	3. 489 [-6]	20. 183	2. 868 [-2]
21	-0. 081 133 815	4. 252 [-6]	21. 000	3. 938 [-2]	21	-0. 081 114 026	3. 017 [-6]	21. 185	2. 869 [-2]

Table 48: $^3D^e$ resonances below N=5 threshold ($\ell_{max} = 8$).

G					H				
n	E (au)	Γ (au)	n^*	$\bar{\Gamma}$	n	E (au)	Γ (au)	n^*	$\bar{\Gamma}$
7	-0. 089 202 998	5. 032 [-5]	7. 371	2. 015 [-2]	7	-0. 089 456 704	4. 448 [-5]	7. 271	1. 710 [-2]
8	-0. 087 131 691	3. 806 [-5]	8. 372	2. 234 [-2]	8	-0. 087 309 593	3. 105 [-5]	8. 271	1. 756 [-2]
9	-0. 085 688 634	2. 819 [-5]	9. 375	2. 323 [-2]	9	-0. 085 819 309	2. 368 [-5]	9. 269	1. 886 [-2]
10	-0. 084 644 260	2. 084 [-5]	10. 376	2. 328 [-2]	10	-0. 084 741 887	1. 801 [-5]	10. 269	1. 950 [-2]
11	-0. 083 863 827	1. 603 [-5]	11. 376	2. 360 [-2]	11	-0. 083 938 170	1. 379 [-5]	11. 268	1. 972 [-2]
12	-0. 083 264 612	1. 611 [-5]	12. 376	3. 053 [-2]	12	-0. 083 322 740	1. 088 [-5]	12. 267	2. 008 [-2]
13	-0. 082 793 562	1. 134 [-5]	13. 378	2. 716 [-2]	13	-0. 082 840 963	8. 878 [-6]	13. 266	2. 073 [-2]
14	-0. 082 418 482	8. 902 [-6]	14. 378	2. 646 [-2]	14	-0. 082 456 730	7. 250 [-6]	14. 266	2. 105 [-2]
15	-0. 082 114 177	7. 161 [-6]	15. 379	2. 604 [-2]	15	-0. 082 145 514	5. 937 [-6]	15. 266	2. 112 [-2]
16	-0. 081 863 899	5. 875 [-6]	16. 378	2. 581 [-2]	16	-0. 081 889 887	4. 951 [-6]	16. 265	2. 131 [-2]
17	-0. 081 655 554	4. 930 [-6]	17. 379	2. 587 [-2]	17	-0. 081 677 349	4. 141 [-6]	17. 265	2. 131 [-2]
18	-0. 081 480 273	4. 163 [-6]	18. 379	2. 584 [-2]	18	-0. 081 498 739	3. 515 [-6]	18. 265	2. 142 [-2]
19	-0. 081 331 406	3. 550 [-6]	19. 379	2. 583 [-2]	19	-0. 081 347 182	3. 006 [-6]	19. 265	2. 149 [-2]
20	-0. 081 203 859	3. 051 [-6]	20. 380	2. 582 [-2]	20	-0. 081 217 453	2. 589 [-6]	20. 266	2. 155 [-2]
21	-0. 081 093 671	2. 653 [-6]	21. 382	2. 593 [-2]	21	-0. 081 105 466	2. 246 [-6]	21. 267	2. 160 [-2]

Table 49: $^3D^e$ resonances below N=5 threshold ($\ell_{max} = 8$).

	I				J				
n	E (au)	Γ (au)	n^*	$\bar{\Gamma}$	n	E (au)	Γ (au)	n^*	$\bar{\Gamma}$
7	-0. 089 993 413	1. 389 [-5]	7. 073	4. 917 [-3]					
8	-0. 087 558 930	5. 048 [-6]	8. 133	2. 715 [-3]	8	-0. 088 242 318	1. 954 [-5]	7. 789	9. 231 [-3]
9	-0. 086 038 645	3. 871 [-6]	9. 099	2. 916 [-3]	9	-0. 086 511 521	1. 489 [-5]	8. 763	1. 002 [-2]
10	-0. 084 923 156	4. 001 [-6]	10. 078	4. 095 [-3]	10	-0. 085 267 208	1. 116 [-5]	9. 743	1. 032 [-2]
11	-0. 084 083 871	5. 453 [-6]	11. 065	7. 387 [-3]	11	-0. 084 344 847	8. 259 [-6]	10. 727	1. 020 [-2]
12	-0. 083 437 932	6. 268 [-6]	12. 060	1. 099 [-2]	12	-0. 083 643 202	6. 323 [-6]	11. 715	1. 017 [-2]
13	-0. 082 931 974	5. 978 [-6]	13. 059	1. 331 [-2]	13	-0. 083 097 575	5. 049 [-6]	12. 705	1. 035 [-2]
14	-0. 082 529 382	5. 173 [-6]	14. 060	1. 438 [-2]	14	-0. 082 665 168	4. 164 [-6]	13. 697	1. 070 [-2]
15	-0. 082 204 192	4. 318 [-6]	15. 061	1. 475 [-2]	15	-0. 082 316 897	3. 445 [-6]	14. 690	1. 092 [-2]
16	-0. 081 937 916	3. 537 [-6]	16. 063	1. 466 [-2]	16	-0. 082 032 391	2. 863 [-6]	15. 685	1. 105 [-2]
17	-0. 081 717 159	2. 917 [-6]	17. 064	1. 449 [-2]	17	-0. 081 797 051	2. 400 [-6]	16. 680	1. 114 [-2]
18	-0. 081 532 112	2. 421 [-6]	18. 065	1. 427 [-2]	18	-0. 081 600 209	2. 026 [-6]	17. 677	1. 119 [-2]
19	-0. 081 375 452	2. 034 [-6]	19. 066	1. 409 [-2]	19	-0. 081 433 921	1. 719 [-6]	18. 673	1. 119 [-2]
20	-0. 081 241 635	1. 729 [-6]	20. 067	1. 397 [-2]	20	-0. 081 292 168	1. 470 [-6]	19. 671	1. 119 [-2]
21	-0. 081 126 373	1. 489 [-6]	21. 069	1. 392 [-2]	21	-0. 081 170 312	1. 271 [-6]	20. 670	1. 123 [-2]

Table 50: $^3D^e$ resonances below N=5 threshold ($\ell_{max} = 8$).

K					L				
n	E (au)	Γ (au)	n^*	$\bar{\Gamma}$	n	E (au)	Γ (au)	n^*	$\bar{\Gamma}$
					6	-0. 093 124 168	9. 109 [-6]	6. 172	2. 142 [-3]
					7	-0. 089 531 866	7. 416 [-6]	7. 243	2. 817 [-3]
8	-0. 088 244 478	3. 146 [-5]	7. 788	1. 486 [-2]	8	-0. 087 311 923	6. 979 [-6]	8. 269	3. 946 [-3]
9	-0. 086 463 223	2. 159 [-5]	8. 795	1. 469 [-2]	9	-0. 085 800 905	5. 582 [-6]	9. 284	4. 467 [-3]
10	-0. 085 209 979	1. 519 [-5]	9. 795	1. 428 [-2]	10	-0. 084 719 111	4. 678 [-6]	10. 293	5. 102 [-3]
11	-0. 084 291 266	1. 047 [-5]	10. 794	1. 316 [-2]	11	-0. 083 916 105	4. 102 [-6]	11. 299	5. 919 [-3]
12	-0. 083 596 540	7. 440 [-6]	11. 791	1. 220 [-2]	12	-0. 083 302 802	4. 330 [-6]	12. 304	8. 065 [-3]
13	-0. 083 057 902	5. 579 [-6]	12. 787	1. 166 [-2]	13	-0. 082 822 987	4. 058 [-6]	13. 309	9. 566 [-3]
14	-0. 082 631 688	4. 347 [-6]	13. 784	1. 138 [-2]	14	-0. 082 441 079	2. 992 [-6]	14. 312	8. 772 [-3]
15	-0. 082 288 622	3. 476 [-6]	14. 781	1. 122 [-2]	15	-0. 082 132 034	2. 328 [-6]	15. 314	8. 359 [-3]
16	-0. 082 008 412	2. 836 [-6]	15. 778	1. 114 [-2]	16	-0. 081 878 281	1. 889 [-6]	16. 316	8. 206 [-3]
17	-0. 081 776 606	2. 348 [-6]	16. 776	1. 108 [-2]	17	-0. 081 667 342	1. 569 [-6]	17. 317	8. 149 [-3]
18	-0. 081 582 674	1. 974 [-6]	17. 774	1. 108 [-2]	18	-0. 081 490 071	1. 330 [-6]	18. 318	8. 176 [-3]
19	-0. 081 418 797	1. 671 [-6]	18. 773	1. 106 [-2]	19	-0. 081 339 652	1. 138 [-6]	19. 319	8. 206 [-3]
20	-0. 081 279 068	1. 434 [-6]	19. 771	1. 108 [-2]	20	-0. 081 210 898	9. 843 [-7]	20. 320	8. 260 [-3]
21	-0. 081 158 935	1. 240 [-6]	20. 771	1. 111 [-2]	21	-0. 081 099 779	8. 557 [-7]	21. 322	8. 295 [-3]

Table 51: $^3D^o$ resonances below N=5 threshold ($\ell_{max} = 8$).

A					B				
n	E (au)	Γ (au)	n^*	$\bar{\Gamma}$	n	E (au)	Γ (au)	n^*	$\bar{\Gamma}$
5	-0. 114 815 858	3. 673 [-3]	3. 790	1. 999 [-1]	5	-0. 123 430 808	3. 580 [-3]	3. 393	1. 398 [-1]
6	-0. 104 775 280	1. 829 [-3]	4. 492	1. 658 [-1]	6	-0. 102 424 520	1. 248 [-3]	4. 722	1. 314 [-1]
7	-0. 096 909 400	1. 235 [-3]	5. 438	1. 986 [-1]	7	-0. 093 205 035	4. 873 [-4]	6. 153	1. 135 [-1]
8	-0. 092 297 331	6. 511 [-4]	6. 376	1. 688 [-1]	8	-0. 089 364 490	2. 539 [-4]	7. 307	9. 907 [-2]
9	-0. 089 593 698	2. 121 [-4]	7. 219	7. 981 [-2]	9	-0. 087 355 518	1. 358 [-4]	8. 245	7. 610 [-2]
10	-0. 087 476 365	2. 355 [-5]	8. 178	1. 288 [-2]	10	-0. 085 845 013	1. 019 [-4]	9. 249	8. 065 [-2]
11	-0. 086 265 812	1. 155 [-4]	8. 933	8. 234 [-2]	11	-0. 084 760 100	8. 395 [-5]	10. 249	9. 037 [-2]
12	-0. 085 305 092	3. 496 [-4]	9. 708	3. 199 [-1]	12	-0. 083 952 900	7. 219 [-5]	11. 247	1. 027 [-1]
13	-0. 084 472 986	3. 602 [-4]	10. 573	4. 257 [-1]	13	-0. 083 335 786	6. 133 [-5]	12. 243	1. 126 [-1]
14	-0. 083 787 935	2. 453 [-4]	11. 489	3. 719 [-1]	14	-0. 082 852 808	5. 460 [-5]	13. 239	1. 267 [-1]
15	-0. 083 224 077	1. 760 [-4]	12. 453	3. 398 [-1]	15	-0. 082 467 360	4. 643 [-5]	14. 235	1. 340 [-1]
16	-0. 082 767 604	1. 256 [-4]	13. 441	3. 050 [-1]	16	-0. 082 154 688	4. 118 [-5]	15. 233	1. 456 [-1]
17	-0. 082 405 589	9. 946 [-5]	14. 417	2. 980 [-1]	17	-0. 081 898 244	3. 696 [-5]	16. 230	1. 580 [-1]
18	-0. 082 105 539	7. 768 [-5]	15. 410	2. 843 [-1]	18	-0. 081 684 264	3. 145 [-5]	17. 230	1. 609 [-1]
19	-0. 081 858 219	6. 634 [-5]	16. 404	2. 928 [-1]	19	-0. 081 505 043	2. 726 [-5]	18. 227	1. 650 [-1]
20	-0. 081 651 571	5. 301 [-5]	17. 399	2. 792 [-1]	20	-0. 081 352 702	2. 401 [-5]	19. 226	1. 706 [-1]
21	-0. 081 478 859	4. 322 [-5]	18. 387	2. 687 [-1]	21	-0. 081 222 379	2. 115 [-5]	20. 225	1. 750 [-1]
22	-0. 081 330 593	3. 640 [-5]	19. 385	2. 651 [-1]	22	-0. 081 109 922	1. 860 [-5]	21. 225	1. 778 [-1]
23	-0. 081 203 545	3. 098 [-5]	20. 382	2. 623 [-1]					
24	-0. 081 093 735	2. 650 [-5]	21. 381	2. 590 [-1]					

Table 52: $^3D^o$ resonances below N=5 threshold ($\ell_{max} = 8$).

	C				D				
n	E (au)	Γ (au)	n^*	$\bar{\Gamma}$	n	E (au)	Γ (au)	n^*	$\bar{\Gamma}$
					5	-0. 104 423 685	1. 234 [-4]	4. 525	1. 143 [-2]
6	-0. 099 232 218	1. 769 [-3]	5. 099	2. 346 [-1]	6	-0. 095 858 954	9. 516 [-5]	5. 615	1. 685 [-2]
7	-0. 093 451 285	1. 261 [-3]	6. 097	2. 857 [-1]	7	-0. 091 287 153	6. 418 [-5]	6. 656	1. 892 [-2]
8	-0. 089 926 001	9. 717 [-4]	7. 097	3. 474 [-1]	8	-0. 088 478 716	4. 564 [-5]	7. 679	2. 067 [-2]
9	-0. 087 675 831	6. 499 [-4]	8. 071	3. 417 [-1]	9	-0. 086 615 605	3. 311 [-5]	8. 694	2. 176 [-2]
10	-0. 086 117 065	3. 748 [-4]	9. 041	2. 770 [-1]	10	-0. 085 309 885	2. 646 [-5]	9. 704	2. 418 [-2]
11	-0. 085 000 624	2. 519 [-4]	9. 999	2. 518 [-1]	11	-0. 084 358 142	1. 956 [-5]	10. 711	2. 403 [-2]
12	-0. 084 158 461	1. 136 [-4]	10. 965	1. 498 [-1]	12	-0. 083 642 518	1. 486 [-5]	11. 716	2. 390 [-2]
13	-0. 083 516 551	4. 785 [-5]	11. 924	8. 113 [-2]	13	-0. 083 090 346	1. 165 [-5]	12. 720	2. 397 [-2]
14	-0. 083 015 945	1. 370 [-5]	12. 876	2. 925 [-2]	14	-0. 082 655 196	9. 361 [-6]	13. 723	2. 419 [-2]
15	-0. 082 617 993	1. 779 [-6]	13. 820	4. 697 [-3]	15	-0. 082 306 041	7. 652 [-6]	14. 725	2. 443 [-2]
16	-0. 082 289 650	1. 509 [-6]	14. 777	4. 871 [-3]	16	-0. 082 021 610	6. 435 [-6]	15. 727	2. 503 [-2]
17	-0. 082 017 973	4. 801 [-6]	15. 741	1. 872 [-2]	17	-0. 081 786 749	5. 168 [-6]	16. 728	2. 419 [-2]
18	-0. 081 790 310	8. 628 [-6]	16. 712	4. 027 [-2]	18	-0. 081 590 651	4. 378 [-6]	17. 730	2. 440 [-2]
19	-0. 081 597 913	1. 117 [-5]	17. 689	6. 184 [-2]	19	-0. 081 425 166	3. 757 [-6]	18. 731	2. 469 [-2]
20	-0. 081 434 166	1. 285 [-5]	18. 672	8. 365 [-2]	20	-0. 081 284 214	3. 224 [-6]	19. 732	2. 476 [-2]
21	-0. 081 293 936	1. 354 [-5]	19. 658	1. 028 [-1]	21	-0. 081 163 133	2. 788 [-6]	20. 733	2. 485 [-2]
22	-0. 081 172 976	1. 369 [-5]	20. 646	1. 204 [-1]	22	-0. 081 058 261	2. 429 [-6]	21. 736	2. 494 [-2]
23	-0. 081 067 896	1. 354 [-5]	21. 638	1. 372 [-1]					

Table 53: $^3D^o$ resonances below N=5 threshold ($\ell_{max} = 8$).

E					F				
n	E (au)	Γ (au)	n^*	$\bar{\Gamma}$	n	E (au)	Γ (au)	n^*	$\bar{\Gamma}$
5	-0. 109 437 520	8. 015 [-5]	4. 121	5. 610 [-3]					
6	-0. 099 233 768	7. 152 [-5]	5. 099	9. 479 [-3]	6	-0. 097 904 669	3. 442 [-5]	5. 284	5. 080 [-3]
7	-0. 093 559 127	5. 156 [-5]	6. 073	1. 155 [-2]	7	-0. 092 069 192	3. 157 [-5]	6. 436	8. 417 [-3]
8	-0. 090 053 875	3. 671 [-5]	7. 052	1. 287 [-2]	8	-0. 088 917 656	2. 343 [-5]	7. 488	9. 838 [-3]
9	-0. 087 741 280	2. 576 [-5]	8. 037	1. 337 [-2]	9	-0. 086 892 803	1. 679 [-5]	8. 516	1. 038 [-2]
10	-0. 086 139 046	1. 962 [-5]	9. 025	1. 442 [-2]	10	-0. 085 499 429	1. 293 [-5]	9. 535	1. 121 [-2]
11	-0. 084 984 148	1. 477 [-5]	10. 016	1. 484 [-2]	11	-0. 084 494 413	1. 017 [-5]	10. 547	1. 193 [-2]
12	-0. 084 125 553	1. 108 [-5]	11. 009	1. 478 [-2]	12	-0. 083 744 081	7. 997 [-6]	11. 556	1. 234 [-2]
13	-0. 083 470 346	8. 585 [-6]	12. 003	1. 485 [-2]	13	-0. 083 168 332	6. 338 [-6]	12. 562	1. 256 [-2]
14	-0. 082 959 181	6. 844 [-6]	12. 999	1. 503 [-2]	14	-0. 082 716 547	5. 156 [-6]	13. 567	1. 287 [-2]
15	-0. 082 552 848	5. 589 [-6]	13. 995	1. 532 [-2]	15	-0. 082 355 319	4. 379 [-6]	14. 570	1. 354 [-2]
16	-0. 082 224 576	4. 621 [-6]	14. 992	1. 557 [-2]	16	-0. 082 061 829	3. 843 [-6]	15. 573	1. 451 [-2]
17	-0. 081 955 663	3. 854 [-6]	15. 990	1. 576 [-2]	17	-0. 081 820 073	3. 491 [-6]	16. 575	1. 589 [-2]
18	-0. 081 732 634	3. 241 [-6]	16. 988	1. 589 [-2]	18	-0. 081 618 524	3. 243 [-6]	17. 576	1. 761 [-2]
19	-0. 081 545 613	2. 745 [-6]	17. 986	1. 597 [-2]	19	-0. 081 448 698	3. 076 [-6]	18. 578	1. 972 [-2]
20	-0. 081 387 281	2. 343 [-6]	18. 985	1. 603 [-2]	20	-0. 081 304 226	2. 897 [-6]	19. 580	2. 175 [-2]
21	-0. 081 252 012	2. 012 [-6]	19. 984	1. 606 [-2]	21	-0. 081 180 273	2. 680 [-6]	20. 582	2. 337 [-2]
22	-0. 081 135 481	1. 744 [-6]	20. 984	1. 611 [-2]	22	-0. 081 073 064	2. 415 [-6]	21. 586	2. 429 [-2]
23	-0. 081 034 277	1. 526 [-6]	21. 987	1. 622 [-2]					

Table 54: $^3D^o$ resonances below N=5 threshold ($\ell_{max} = 8$).

	G			
n	E (au)	Γ (au)	n^*	$\bar{\Gamma}$
6	-0. 090 330 278	7. 261 [-7]	6. 957	2. 445 [-4]
7	-0. 088 013 809	2. 244 [-7]	7. 899	1. 106 [-4]
8	-0. 086 343 451	2. 995 [-7]	8. 878	2. 096 [-4]
9	-0. 085 138 136	3. 781 [-7]	9. 865	3. 629 [-4]
10	-0. 084 243 952	4. 597 [-7]	10. 854	5. 878 [-4]
11	-0. 083 563 161	5. 387 [-7]	11. 846	8. 955 [-4]
12	-0. 083 033 463	7. 700 [-7]	12. 839	1. 629 [-3]
13	-0. 082 610 676	6. 295 [-7]	13. 839	1. 669 [-3]
14	-0. 082 272 848	2. 395 [-7]	14. 832	7. 815 [-4]
15	-0. 081 995 765	2. 509 [-7]	15. 828	9. 950 [-4]
16	-0. 081 766 239	2. 464 [-7]	16. 825	1. 174 [-3]
17	-0. 081 574 046	2. 339 [-7]	17. 823	1. 324 [-3]
18	-0. 081 411 529	2. 180 [-7]	18. 821	1. 453 [-3]
19	-0. 081 272 882	2. 014 [-7]	19. 819	1. 568 [-3]
20	-0. 081 153 629	1. 857 [-7]	20. 819	1. 676 [-3]
21	-0. 081 050 249	1. 718 [-7]	21. 819	1. 784 [-3]

Table 55: $\bar{f}_{n^3P^o \leftarrow m^3S^e}$ oscillator strenghts

	2^3S^e	3^3S^e	4^3S^e	5^3S^e	6^3S^e
2^3P^o	5. 390 870 [-1]	-2. 085 364 [-1]	-3. 172 093 [-2]	-1. 134 088 [-2]	-5. 488 485 [-3]
3^3P^o	6. 446 082 [-2]	8. 908 526 [-1]	-4. 356 720 [-1]	-6. 760 725 [-2]	-2. 469 796 [-2]
4^3P^o	2. 576 876 [-2]	5. 008 293 [-2]	1. 215 265 [0]	-6. 683 002 [-1]	-1. 039 430 [-1]
5^3P^o	1. 249 044 [-2]	2. 291 382 [-2]	4. 422 977 [-2]	1. 530 632 [0]	-9. 032 396 [-1]
6^3P^o	6. 982 294 [-3]	1. 199 357 [-2]	2. 163 046 [-2]	4. 151 815 [-2]	1. 841 771 [0]
7^3P^o	4. 298 887 [-3]	7. 076 979 [-3]	1. 177 503 [-2]	2. 109 924 [-2]	4. 030 463 [-2]
8^3P^o	2. 835 977 [-3]	4. 540 376 [-3]	7. 160 886 [-3]	1. 174 240 [-2]	2. 099 341 [-2]
9^3P^o	1. 970 048 [-3]	3. 094 438 [-3]	4. 708 194 [-3]	7. 269 737 [-3]	1. 183 710 [-2]
10^3P^o	1. 424 514 [-3]	2. 207 348 [-3]	3. 275 235 [-3]	4. 853 676 [-3]	7. 409 636 [-3]
11^3P^o	1. 063 610 [-3]	1. 631 697 [-3]	2. 377 428 [-3]	3. 422 112 [-3]	4. 996 548 [-3]
12^3P^o	8. 152 543 [-4]	1. 241 246 [-3]	1. 784 071 [-3]	2. 513 719 [-3]	3. 554 955 [-3]
13^3P^o	6. 387 118 [-4]	9. 667 541 [-4]	1. 375 086 [-3]	1. 906 390 [-3]	2. 633 046 [-3]
14^3P^o	5. 097 559 [-4]	7. 679 861 [-4]	1. 083 436 [-3]	1. 483 332 [-3]	2. 012 099 [-3]
15^3P^o	4. 133 538 [-4]	6. 204 226 [-4]	8. 695 367 [-4]	1. 178 717 [-3]	1. 576 510 [-3]
16^3P^o	3. 398 366 [-4]	5. 085 207 [-4]	7. 089 147 [-4]	9. 533 192 [-4]	1. 260 788 [-3]
17^3P^o	2. 827 917 [-4]	4. 220 920 [-4]	5. 858 492 [-4]	7. 826 806 [-4]	1. 025 715 [-3]
18^3P^o	2. 378 532 [-4]	3. 542 671 [-4]	4. 899 143 [-4]	6. 509 675 [-4]	8. 467 210 [-4]
19^3P^o	2. 019 826 [-4]	3. 003 029 [-4]	4. 140 089 [-4]	5. 476 077 [-4]	7. 078 347 [-4]
20^3P^o	1. 730 262 [-4]	2. 568 593 [-4]	3. 531 882 [-4]	4. 653 597 [-4]	5. 983 549 [-4]
21^3P^o	1. 494 691 [-4]	2. 215 978 [-4]	3. 040 175 [-4]	3. 992 512 [-4]	5. 110 508 [-4]

	7^3S^e	8^3S^e	9^3S^e	10^3S^e	11^3S^e
2^3P^o	-3. 112 866 [-3]	-1. 949 215 [-3]	-1. 306 611 [-3]	-9. 208 172 [-4]	-6. 743 981 [-4]
3^3P^o	-1. 221 412 [-2]	-7. 068 684 [-3]	-4. 507 166 [-3]	-3. 070 399 [-3]	-2. 195 052 [-3]
4^3P^o	-3. 825 320 [-2]	-1. 910 391 [-2]	-1. 117 088 [-2]	-7. 195 678 [-3]	-4. 949 538 [-3]
5^3P^o	-1. 401 713 [-1]	-5. 170 765 [-2]	-2. 594 122 [-2]	-1. 525 452 [-2]	-9. 885 609 [-3]
6^3P^o	-1. 139 311 [0]	-1. 762 544 [-1]	-6. 502 975 [-2]	-3. 269 262 [-2]	-1. 928 491 [-2]
7^3P^o	2. 150 535 [0]	-1. 376 077 [0]	-2. 121 576 [-1]	-7. 821 826 [-2]	-3. 935 459 [-2]
8^3P^o	3. 991 693 [-2]	2. 457 900 [0]	-1. 613 283 [0]	-2. 479 425 [-1]	-9. 131 034 [-2]
9^3P^o	2. 114 163 [-2]	4. 003 155 [-2]	2. 764 313 [0]	-1. 850 759 [0]	-2. 836 295 [-1]
10^3P^o	1. 201 600 [-2]	2. 145 931 [-2]	4. 047 614 [-2]	3. 070 055 [0]	-2. 088 424 [0]
11^3P^o	7. 574 310 [-3]	1. 225 736 [-2]	2. 189 341 [-2]	4. 114 807 [-2]	3. 375 313 [0]
12^3P^o	5. 141 444 [-3]	7. 761 118 [-3]	1. 254 400 [-2]	2. 241 090 [-2]	4. 198 275 [-2]
13^3P^o	3. 681 048 [-3]	5. 291 702 [-3]	7. 965 312 [-3]	1. 286 458 [-2]	2. 299 005 [-2]
14^3P^o	2. 742 615 [-3]	3. 805 280 [-3]	5. 447 202 [-3]	8. 183 394 [-3]	1. 321 118 [-2]
15^3P^o	2. 107 508 [-3]	2. 847 316 [-3]	3. 929 221 [-3]	5. 607 548 [-3]	8. 412 677 [-3]
16^3P^o	1. 659 886 [-3]	2. 196 996 [-3]	2. 949 227 [-3]	4. 053 706 [-3]	5. 772 216 [-3]
17^3P^o	1. 333 959 [-3]	1. 737 213 [-3]	2. 282 669 [-3]	3. 049 625 [-3]	4. 179 138 [-3]
18^3P^o	1. 090 231 [-3]	1. 401 394 [-3]	1. 810 453 [-3]	2. 365 926 [-3]	3. 149 324 [-3]
19^3P^o	9. 039 050 [-4]	1. 149 540 [-3]	1. 464 878 [-3]	1. 881 007 [-3]	2. 447 767 [-3]
20^3P^o	7. 588 325 [-4]	9. 565 205 [-4]	1. 205 271 [-3]	1. 525 786 [-3]	1. 949 987 [-3]
21^3P^o	6. 443 287 [-4]	8. 061 515 [-4]	1. 006 318 [-3]	1. 259 076 [-3]	1. 585 683 [-3]

Table 56: $\bar{f}_{n^3P^o \leftarrow m^3S^e}$ oscillator strenghts

	12^3S^e	13^3S^e	14^3S^e	15^3S^e	16^3S^e
2^3P^o	-5. 092 690 [-4]	-3. 942 896 [-4]	-3. 116 759 [-4]	-2. 507 400 [-4]	-2. 047 820 [-4]
3^3P^o	-1. 628 252 [-3]	-1. 243 623 [-3]	-9. 726 950 [-4]	-7. 759 596 [-4]	-6. 294 322 [-4]
4^3P^o	-3. 570 586 [-3]	-2. 670 859 [-3]	-2. 055 751 [-3]	-1. 619 374 [-3]	-1. 300 335 [-3]
5^3P^o	-6. 841 291 [-3]	-4. 964 696 [-3]	-3. 734 905 [-3]	-2. 890 350 [-3]	-2. 288 483 [-3]
6^3P^o	-1. 254 358 [-2]	-8. 714 971 [-3]	-6. 349 842 [-3]	-4. 795 990 [-3]	-3. 725 944 [-3]
7^3P^o	-2. 325 502 [-2]	-1. 516 057 [-2]	-1. 056 070 [-2]	-7. 716 047 [-3]	-5. 844 470 [-3]
8^3P^o	-4. 594 726 [-2]	-2. 717 534 [-2]	-1. 774 143 [-2]	-1. 238 003 [-2]	-9. 062 893 [-3]
9^3P^o	-1. 043 233 [-1]	-5. 248 181 [-2]	-3. 105 266 [-2]	-2. 029 003 [-2]	-1. 417 490 [-2]
10^3P^o	-3. 192 369 [-1]	-1. 172 719 [-1]	-5. 896 843 [-2]	-3. 489 378 [-2]	-2. 281 087 [-2]
11^3P^o	-2. 326 226 [0]	-3. 547 801 [-1]	-1. 301 687 [-1]	-6. 541 574 [-2]	-3. 870 474 [-2]
12^3P^o	3. 680 209 [0]	-2. 564 134 [0]	-3. 902 716 [-1]	-1. 430 232 [-1]	-7. 183 075 [-2]
13^3P^o	4. 293 780 [-2]	3. 984 830 [0]	-2. 802 123 [0]	-4. 257 207 [-1]	-1. 558 431 [-1]
14^3P^o	2. 361 600 [-2]	4. 398 430 [-2]	4. 289 237 [0]	-3. 040 176 [0]	-4. 611 352 [-1]
15^3P^o	1. 357 812 [-2]	2. 427 832 [-2]	4. 510 190 [-2]	4. 593 471 [0]	-3. 278 280 [0]
16^3P^o	8. 651 085 [-3]	1. 396 129 [-2]	2. 496 944 [-2]	4. 627 572 [-2]	4. 897 560 [0]
17^3P^o	5. 940 694 [-3]	8. 897 043 [-3]	1. 435 764 [-2]	2. 568 381 [-2]	4. 749 397 [-2]
18^3P^o	4. 305 749 [-3]	6. 112 600 [-3]	9. 149 462 [-3]	1. 476 514 [-2]	2. 641 714 [-2]
19^3P^o	3. 248 949 [-3]	4. 433 801 [-3]	6. 287 834 [-3]	9. 407 915 [-3]	1. 518 274 [-2]
20^3P^o	2. 529 074 [-3]	3. 349 177 [-3]	4. 563 795 [-3]	6. 466 852 [-3]	9. 673 056 [-3]
21^3P^o	2. 018 925 [-3]	2. 611 416 [-3]	3. 451 694 [-3]	4. 697 747 [-3]	6. 652 629 [-3]

	17^3S^e	18^3S^e	19^3S^e	20^3S^e	21^3S^e
2^3P^o	-1. 694 512 [-4]	-1. 418 365 [-4]	-1. 199 407 [-4]	-1. 023 634 [-4]	-8. 811 931 [-5]
3^3P^o	-5. 179 336 [-4]	-4. 315 194 [-4]	-3. 634 829 [-4]	-3. 091 886 [-4]	-2. 654 104 [-4]
4^3P^o	-1. 061 188 [-3]	-8. 781 167 [-4]	-7. 354 524 [-4]	-6. 225 815 [-4]	-5. 322 307 [-4]
5^3P^o	-1. 846 495 [-3]	-1. 513 766 [-3]	-1. 258 041 [-3]	-1. 058 048 [-3]	-8. 995 034 [-4]
6^3P^o	-2. 961 184 [-3]	-2. 397 948 [-3]	-1. 972 771 [-3]	-1. 645 178 [-3]	-1. 388 693 [-3]
7^3P^o	-4. 553 461 [-3]	-3. 629 111 [-3]	-2. 947 119 [-3]	-2. 431 454 [-3]	-2. 033 973 [-3]
8^3P^o	-6. 878 788 [-3]	-5. 370 754 [-3]	-4. 289 913 [-3]	-3. 491 711 [-3]	-2. 888 247 [-3]
9^3P^o	-1. 039 107 [-2]	-7. 898 900 [-3]	-6. 177 426 [-3]	-4. 943 112 [-3]	-4. 032 043 [-3]
10^3P^o	-1. 594 823 [-2]	-1. 170 254 [-2]	-8. 906 229 [-3]	-6. 974 687 [-3]	-5. 590 868 [-3]
11^3P^o	-2. 530 823 [-2]	-1. 770 325 [-2]	-1. 299 994 [-2]	-9. 903 193 [-3]	-7. 766 243 [-3]
12^3P^o	-4. 249 071 [-2]	-2. 778 620 [-2]	-1. 944 351 [-2]	-1. 428 665 [-2]	-1. 089 499 [-2]
13^3P^o	-7. 821 923 [-2]	-4. 625 641 [-2]	-3. 024 909 [-2]	-2. 117 323 [-2]	-1. 556 953 [-2]
14^3P^o	-1. 686 348 [-1]	-8. 458 670 [-2]	-5. 000 705 [-2]	-3. 270 206 [-2]	-2. 290 138 [-2]
15^3P^o	-4. 965 220 [-1]	-1. 814 055 [-1]	-9. 093 997 [-2]	-5. 374 912 [-2]	-3. 515 692 [-2]
16^3P^o	-3. 516 412 [0]	-5. 318 904 [-1]	-1. 941 662 [-1]	-9. 728 932 [-2]	-5. 750 032 [-2]
17^3P^o	5. 201 499 [0]	-3. 754 497 [0]	-5. 672 513 [-1]	-2. 069 353 [-1]	-1. 036 674 [-1]
18^3P^o	4. 874 391 [-2]	5. 505 165 [0]	-3. 992 254 [0]	-6. 026 013 [-1]	-2. 197 699 [-1]
19^3P^o	2. 716 442 [-2]	5. 000 257 [-2]	5. 808 082 [0]	-4. 228 795 [0]	-6. 379 516 [-1]
20^3P^o	1. 560 991 [-2]	2. 791 425 [-2]	5. 121 893 [-2]	6. 108 796 [0]	-4. 461 919 [0]
21^3P^o	9. 949 054 [-3]	1. 604 712 [-2]	2. 864 408 [-2]	5. 229 285 [-2]	6. 403 537 [0]

Table 57: $\bar{f}_{n^3P^e \leftarrow m^3P^o}$ oscillator strenghts

	2^3P^o	3^3P^o	4^3P^o	5^3P^o	6^3P^o
2^3P^e	1. 804 802 [-1]	9. 553 117 [-3]	2. 629 933 [-3]	1. 123 997 [-3]	5. 916 040 [-4]
3^3P^e	9. 365 622 [-4]	1. 354 211 [-1]	4. 584 980 [-3]	1. 343 901 [-3]	6. 070 773 [-4]
4^3P^e	3. 608 874 [-5]	4. 972 619 [-3]	1. 279 345 [-1]	3. 703 022 [-3]	1. 096 768 [-3]
5^3P^e	7. 873 424 [-5]	6. 627 902 [-4]	5. 870 988 [-3]	1. 257 285 [-1]	3. 378 988 [-3]
6^3P^e	6. 737 636 [-5]	2. 123 772 [-4]	9. 889 155 [-4]	6. 135 274 [-3]	1. 248 796 [-1]
7^3P^e	5. 059 275 [-5]	9. 593 597 [-5]	3. 635 423 [-4]	1. 116 776 [-3]	6. 228 770 [-3]
8^3P^e	3. 731 143 [-5]	5. 213 897 [-5]	1. 797 696 [-4]	4. 302 796 [-4]	1. 177 017 [-3]
9^3P^e	2. 778 198 [-5]	3. 178 990 [-5]	1. 041 067 [-4]	2. 198 109 [-4]	4. 645 388 [-4]
10^3P^e	2. 104 025 [-5]	2. 095 804 [-5]	6. 652 118 [-5]	1. 304 309 [-4]	2. 415 625 [-4]
11^3P^e	1. 622 687 [-5]	1. 461 901 [-5]	4. 546 120 [-5]	8. 495 229 [-5]	1. 453 621 [-4]
12^3P^e	1. 273 398 [-5]	1. 064 134 [-5]	3. 262 670 [-5]	5. 897 062 [-5]	9. 577 945 [-5]
13^3P^e	1. 015 354 [-5]	8. 008 447 [-6]	2. 430 463 [-5]	4. 287 923 [-5]	6. 714 399 [-5]
14^3P^e	8. 213 451 [-6]	6. 190 583 [-6]	1. 864 489 [-5]	3. 230 115 [-5]	4. 924 141 [-5]
15^3P^e	6. 730 594 [-6]	4. 891 827 [-6]	1. 464 729 [-5]	2. 502 109 [-5]	3. 737 456 [-5]
16^3P^e	5. 579 909 [-6]	3. 937 381 [-6]	1. 173 538 [-5]	1. 982 503 [-5]	2. 914 659 [-5]
17^3P^e	4. 674 563 [-6]	3. 219 142 [-6]	9. 559 421 [-6]	1. 600 492 [-5]	2. 323 439 [-5]
18^3P^e	3. 953 281 [-6]	2. 667 663 [-6]	7. 898 087 [-6]	1. 312 668 [-5]	1. 886 132 [-5]
19^3P^e	3. 372 175 [-6]	2. 236 885 [-6]	6. 606 346 [-6]	1. 091 307 [-5]	1. 554 853 [-5]
20^3P^e	2. 899 374 [-6]	1. 895 427 [-6]	5. 586 346 [-6]	9. 181 004 [-6]	1. 298 866 [-5]
21^3P^e	2. 511 902 [-6]	1. 621 703 [-6]	4. 771 273 [-6]	7. 807 450 [-6]	1. 097 974 [-5]

	7^3P^o	8^3P^o	9^3P^o	10^3P^o	11^3P^o
2^3P^e	3. 520 748 [-4]	2. 273 955 [-4]	1. 557 443 [-4]	1. 115 031 [-4]	8. 265 172 [-5]
3^3P^e	3. 335 979 [-4]	2. 054 586 [-4]	1. 364 427 [-4]	9. 562 882 [-5]	6. 980 731 [-5]
4^3P^e	5. 054 562 [-4]	2. 833 698 [-4]	1. 777 123 [-4]	1. 199 276 [-4]	8. 525 600 [-5]
5^3P^e	9. 993 733 [-4]	4. 640 391 [-4]	2. 626 882 [-4]	1. 664 009 [-4]	1. 133 839 [-4]
6^3P^e	3. 227 605 [-3]	9. 526 448 [-4]	4. 438 982 [-4]	2. 526 763 [-4]	1. 610 567 [-4]
7^3P^e	1. 244 948 [-1]	3. 145 656 [-3]	9. 267 833 [-4]	4. 326 844 [-4]	2. 471 603 [-4]
8^3P^e	6. 264 124 [-3]	1. 243 013 [-1]	3. 097 033 [-3]	9. 113 201 [-4]	4. 259 950 [-4]
9^3P^e	1. 208 283 [-3]	6. 277 573 [-3]	1. 241 966 [-1]	3. 066 031 [-3]	9. 014 530 [-4]
10^3P^e	4. 837 161 [-4]	1. 226 198 [-3]	6. 281 769 [-3]	1. 241 369 [-1]	3. 045 161 [-3]
11^3P^e	2. 543 574 [-4]	4. 954 219 [-4]	1. 237 162 [-3]	6. 281 885 [-3]	1. 241 016 [-1]
12^3P^e	1. 544 843 [-4]	2. 624 854 [-4]	5. 030 073 [-4]	1. 244 214 [-3]	6. 280 211 [-3]
13^3P^e	1. 026 013 [-4]	1. 604 589 [-4]	2. 679 366 [-4]	5. 081 532 [-4]	1. 248 930 [-3]
14^3P^e	7. 242 918 [-5]	1. 071 827 [-4]	1. 645 717 [-4]	2. 717 493 [-4]	5. 117 752 [-4]
15^3P^e	5. 344 842 [-5]	7. 605 505 [-5]	1. 104 045 [-4]	1. 675 145 [-4]	2. 745 079 [-4]
16^3P^e	4. 079 572 [-5]	5. 638 866 [-5]	7. 865 177 [-5]	1. 127 532 [-4]	1. 696 874 [-4]
17^3P^e	3. 197 738 [-5]	4. 322 636 [-5]	5. 852 831 [-5]	8. 057 533 [-5]	1. 145 165 [-4]
18^3P^e	2. 561 093 [-5]	3. 401 887 [-5]	4. 502 110 [-5]	6. 013 643 [-5]	8. 204 112 [-5]
19^3P^e	2. 088 174 [-5]	2. 734 908 [-5]	3. 554 729 [-5]	4. 638 902 [-5]	6. 137 983 [-5]
20^3P^e	1. 728 581 [-5]	2. 237 999 [-5]	2. 866 869 [-5]	3. 672 922 [-5]	4. 746 313 [-5]
21^3P^e	1. 450 121 [-5]	1. 859 589 [-5]	2. 353 864 [-5]	2. 971 068 [-5]	3. 768 010 [-5]

Table 58: $\bar{f}_{n^3P^e \leftarrow m^3P^o}$ oscillator strenghts

	12^3P^o	13^3P^o	14^3P^o	15^3P^o	16^3P^o
2^3P^e	6. 300 721 [-5]	4. 915 529 [-5]	3. 910 055 [-5]	3. 162 153 [-5]	2. 594 095 [-5]
3^3P^e	5. 261 136 [-5]	4. 068 724 [-5]	3. 214 333 [-5]	2. 585 293 [-5]	2. 111 443 [-5]
4^3P^e	6. 302 317 [-5]	4. 803 272 [-5]	3. 751 946 [-5]	2. 990 792 [-5]	2. 425 053 [-5]
5^3P^e	8. 133 708 [-5]	6. 063 237 [-5]	4. 656 886 [-5]	3. 663 532 [-5]	2. 939 466 [-5]
6^3P^e	1. 104 402 [-4]	7. 971 766 [-5]	5. 977 843 [-5]	4. 617 117 [-5]	3. 651 460 [-5]
7^3P^e	1. 582 046 [-4]	1. 089 694 [-4]	7. 901 012 [-5]	5. 950 923 [-5]	4. 615 903 [-5]
8^3P^e	2. 439 281 [-4]	1. 566 050 [-4]	1. 082 214 [-4]	7. 873 282 [-5]	5. 950 050 [-5]
9^3P^e	4. 217 579 [-4]	2. 419 282 [-4]	1. 556 691 [-4]	1. 078 430 [-4]	7. 866 255 [-5]
10^3P^e	8. 948 311 [-4]	4. 189 452 [-4]	2. 406 377 [-4]	1. 551 065 [-4]	1. 076 629 [-4]
11^3P^e	3. 030 502 [-3]	8. 902 057 [-4]	4. 170 069 [-4]	2. 397 773 [-4]	1. 547 637 [-4]
12^3P^e	1. 240 803 [-1]	3. 019 847 [-3]	8. 868 675 [-4]	4. 156 295 [-4]	2. 391 889 [-4]
13^3P^e	6. 277 812 [-3]	1. 240 673 [-1]	3. 011 880 [-3]	8. 843 921 [-4]	4. 146 259 [-4]
14^3P^e	1. 252 187 [-3]	6. 275 196 [-3]	1. 240 594 [-1]	3. 005 781 [-3]	8. 825 146 [-4]
15^3P^e	5. 144 030 [-4]	1. 254 497 [-3]	6. 272 605 [-3]	1. 240 546 [-1]	3. 001 018 [-3]
16^3P^e	2. 765 606 [-4]	5. 163 589 [-4]	1. 256 172 [-3]	6. 270 153 [-3]	1. 240 519 [-1]
17^3P^e	1. 713 345 [-4]	2. 781 253 [-4]	5. 178 481 [-4]	1. 257 412 [-3]	6. 267 886 [-3]
18^3P^e	1. 158 746 [-4]	1. 726 134 [-4]	2. 793 464 [-4]	5. 190 096 [-4]	1. 258 356 [-3]
19^3P^e	8. 318 800 [-5]	1. 169 481 [-4]	1. 736 331 [-4]	2. 803 271 [-4]	5. 199 464 [-4]
20^3P^e	6. 236 934 [-5]	8. 411 209 [-5]	1. 178 236 [-4]	1. 744 751 [-4]	2. 811 473 [-4]
21^3P^e	4. 834 305 [-5]	6. 319 533 [-5]	8. 489 975 [-5]	1. 185 883 [-4]	1. 752 332 [-4]

	17^3P^o	18^3P^o	19^3P^o	20^3P^o	21^3P^o
2^3P^e	2. 154 773 [-5]	1. 809 637 [-5]	1. 534 778 [-5]	1. 313 331 [-5]	1. 133 471 [-5]
3^3P^e	1. 747 444 [-5]	1. 463 074 [-5]	1. 237 663 [-5]	1. 056 769 [-5]	9. 103 326 [-6]
4^3P^e	1. 995 168 [-5]	1. 662 321 [-5]	1. 400 445 [-5]	1. 191 601 [-5]	1. 023 426 [-5]
5^3P^e	2. 397 843 [-5]	1. 983 827 [-5]	1. 661 533 [-5]	1. 406 779 [-5]	1. 203 155 [-5]
6^3P^e	2. 944 326 [-5]	2. 413 028 [-5]	2. 005 249 [-5]	1. 686 692 [-5]	1. 434 553 [-5]
7^3P^e	3. 665 399 [-5]	2. 967 113 [-5]	2. 440 869 [-5]	2. 035 911 [-5]	1. 719 351 [-5]
8^3P^e	4. 630 535 [-5]	3. 688 934 [-5]	2. 995 674 [-5]	2. 472 233 [-5]	2. 069 387 [-5]
9^3P^e	5. 960 524 [-5]	4. 651 029 [-5]	3. 715 163 [-5]	3. 025 232 [-5]	2. 504 458 [-5]
10^3P^e	7. 869 436 [-5]	5. 975 765 [-5]	4. 673 277 [-5]	3. 741 642 [-5]	3. 055 231 [-5]
11^3P^e	1. 075 934 [-4]	7. 877 734 [-5]	5. 992 945 [-5]	4. 695 946 [-5]	3. 768 954 [-5]
12^3P^e	1. 545 559 [-4]	1. 075 885 [-4]	7. 888 855 [-5]	6. 011 267 [-5]	4. 720 357 [-5]
13^3P^e	2. 387 794 [-4]	1. 544 356 [-4]	1. 076 265 [-4]	7. 902 260 [-5]	6. 032 659 [-5]
14^3P^e	4. 138 804 [-4]	2. 384 943 [-4]	1. 543 799 [-4]	1. 077 031 [-4]	7. 920 519 [-5]
15^3P^e	8. 810 654 [-4]	4. 133 230 [-4]	2. 383 063 [-4]	1. 543 848 [-4]	1. 078 522 [-4]
16^3P^e	2. 997 238 [-3]	8. 799 372 [-4]	4. 129 168 [-4]	2. 382 104 [-4]	1. 544 951 [-4]
17^3P^e	1. 240 506 [-1]	2. 994 206 [-3]	8. 790 698 [-4]	4. 126 531 [-4]	2. 382 688 [-4]
18^3P^e	6. 265 829 [-3]	1. 240 501 [-1]	2. 991 780 [-3]	8. 784 435 [-4]	4. 126 239 [-4]
19^3P^e	1. 259 107 [-3]	6. 264 011 [-3]	1. 240 502 [-1]	2. 989 901 [-3]	8. 782 095 [-4]
20^3P^e	5. 207 390 [-4]	1. 259 745 [-3]	6. 262 452 [-3]	1. 240 512 [-1]	2. 988 783 [-3]
21^3P^e	2. 819 150 [-4]	5. 215 240 [-4]	1. 260 470 [-3]	6. 261 267 [-3]	1. 240 542 [-1]

Table 59: $\bar{f}_{n^3D^e \leftarrow m^3P^o}$ oscillator strenghts

	2^3P^o	3^3P^o	4^3P^o	5^3P^o	6^3P^o
2^3D^e	6. 102 259 [-1]	1. 120 993 [-1]	-3. 695 898 [-2]	-6. 900 863 [-3]	-2. 584 814 [-3]
3^3D^e	1. 228 469 [-1]	4. 775 950 [-1]	2. 009 481 [-1]	-8. 830 098 [-2]	-1. 704 275 [-2]
4^3D^e	4. 700 679 [-2]	1. 245 527 [-1]	4. 383 880 [-1]	2. 800 567 [-1]	-1. 469 889 [-1]
5^3D^e	2. 346 969 [-2]	5. 300 995 [-2]	1. 239 445 [-1]	4. 294 506 [-1]	3. 542 957 [-1]
6^3D^e	1. 356 347 [-2]	2. 815 799 [-2]	5. 523 185 [-2]	1. 252 336 [-1]	4. 337 845 [-1]
7^3D^e	8. 604 610 [-3]	1. 698 097 [-2]	3. 028 522 [-2]	5. 705 751 [-2]	1. 280 701 [-1]
8^3D^e	5. 824 755 [-3]	1. 112 123 [-2]	1. 870 916 [-2]	3. 183 414 [-2]	5. 899 588 [-2]
9^3D^e	4. 136 846 [-3]	7. 719 978 [-3]	1. 249 261 [-2]	1. 995 069 [-2]	3. 324 077 [-2]
10^3D^e	3. 049 010 [-3]	5. 596 721 [-3]	8. 812 869 [-3]	1. 348 629 [-2]	2. 101 735 [-2]
11^3D^e	2. 314 650 [-3]	4. 196 640 [-3]	6. 477 417 [-3]	9. 616 324 [-3]	1. 432 163 [-2]
12^3D^e	1. 800 146 [-3]	3. 233 031 [-3]	4. 915 195 [-3]	7. 135 192 [-3]	1. 028 673 [-2]
13^3D^e	1. 428 508 [-3]	2. 546 566 [-3]	3. 826 365 [-3]	5. 460 281 [-3]	7. 683 693 [-3]
14^3D^e	1. 153 127 [-3]	2. 043 455 [-3]	3. 041 959 [-3]	4. 283 143 [-3]	5. 916 110 [-3]
15^3D^e	9. 445 950 [-4]	1. 665 840 [-3]	2. 461 264 [-3]	3. 428 619 [-3]	4. 666 913 [-3]
16^3D^e	7. 837 111 [-4]	1. 376 614 [-3]	2. 021 452 [-3]	2. 791 566 [-3]	3. 755 318 [-3]
17^3D^e	6. 575 660 [-4]	1. 151 202 [-3]	1. 681 834 [-3]	2. 305 971 [-3]	3. 072 398 [-3]
18^3D^e	5. 572 678 [-4]	9. 728 788 [-4]	1. 415 229 [-3]	1. 928 847 [-3]	2. 549 541 [-3]
19^3D^e	4. 765 691 [-4]	8. 300 120 [-4]	1. 203 016 [-3]	1. 631 353 [-3]	2. 141 956 [-3]
20^3D^e	4. 111 103 [-4]	7. 145 407 [-4]	1. 032 429 [-3]	1. 394 009 [-3]	1. 819 983 [-3]
21^3D^e	3. 575 769 [-4]	6. 203 939 [-4]	8. 939 876 [-4]	1. 202 614 [-3]	1. 562 498 [-3]

	7^3P^o	8^3P^o	9^3P^o	10^3P^o	11^3P^o
2^3D^e	-1. 284 485 [-3]	-7. 441 310 [-4]	-4. 746 506 [-4]	-3. 234 682 [-4]	-2. 313 692 [-4]
3^3D^e	-6. 502 642 [-3]	-3. 276 617 [-3]	-1. 920 573 [-3]	-1. 237 839 [-3]	-8. 515 285 [-4]
4^3D^e	-2. 892 647 [-2]	-1. 116 387 [-2]	-5. 674 118 [-3]	-3. 350 706 [-3]	-2. 174 278 [-3]
5^3D^e	-2. 099 351 [-1]	-4. 184 509 [-2]	-1. 627 192 [-2]	-8. 317 852 [-3]	-4. 936 537 [-3]
6^3D^e	4. 258 068 [-1]	-2. 755 882 [-1]	-5. 541 025 [-2]	-2. 165 917 [-2]	-1. 111 576 [-2]
7^3D^e	4. 450 908 [-1]	4. 955 852 [-1]	-3. 430 590 [-1]	-6. 941 267 [-2]	-2. 723 541 [-2]
8^3D^e	1. 319 365 [-1]	4. 604 954 [-1]	5. 642 297 [-1]	-4. 118 100 [-1]	-8. 372 020 [-2]
9^3D^e	6. 110 108 [-2]	1. 365 229 [-1]	4. 784 968 [-1]	6. 320 891 [-1]	-4. 814 981 [-1]
10^3D^e	3. 462 022 [-2]	6. 336 823 [-2]	1. 416 136 [-1]	4. 982 490 [-1]	6. 993 802 [-1]
11^3D^e	2. 201 086 [-2]	3. 601 651 [-2]	6. 576 632 [-2]	1. 470 696 [-1]	5. 192 377 [-1]
12^3D^e	1. 507 860 [-2]	2. 297 765 [-2]	3. 743 856 [-2]	6. 826 880 [-2]	1. 527 982 [-1]
13^3D^e	1. 088 533 [-2]	1. 579 692 [-2]	2. 393 509 [-2]	3. 888 720 [-2]	7. 085 478 [-2]
14^3D^e	8. 169 762 [-3]	1. 144 430 [-2]	1. 649 407 [-2]	2. 489 128 [-2]	4. 036 055 [-2]
15^3D^e	6. 318 746 [-3]	8. 619 059 [-3]	1. 197 909 [-2]	1. 717 952 [-2]	2. 585 006 [-2]
16^3D^e	5. 005 714 [-3]	6. 688 639 [-3]	9. 044 645 [-3]	1. 249 866 [-2]	1. 785 870 [-2]
17^3D^e	4. 044 125 [-3]	5. 315 967 [-3]	7. 036 724 [-3]	9. 454 573 [-3]	1. 300 870 [-2]
18^3D^e	3. 321 393 [-3]	4. 308 407 [-3]	5. 606 904 [-3]	7. 370 171 [-3]	9. 854 391 [-3]
19^3D^e	2. 766 525 [-3]	3. 549 674 [-3]	4. 556 150 [-3]	5. 885 050 [-3]	7. 694 429 [-3]
20^3D^e	2. 333 707 [-3]	2. 967 156 [-3]	3. 765 282 [-3]	4. 794 643 [-3]	6. 157 348 [-3]
21^3D^e	1. 991 221 [-3]	2. 512 266 [-3]	3. 157 719 [-3]	3. 973 756 [-3]	5. 028 926 [-3]

Table 60: $\bar{f}_{n^3D^e \leftarrow m^3P^o}$ oscillator strenghts

	12^3P^o	13^3P^o	14^3P^o	15^3P^o	16^3P^o
2^3D^e	-1. 717 349 [-4]	-1. 312 617 [-4]	-1. 027 448 [-4]	-8. 202 861 [-5]	-6. 659 168 [-5]
3^3D^e	-6. 143 119 [-4]	-4. 595 590 [-4]	-3. 537 841 [-4]	-2. 787 571 [-4]	-2. 239 094 [-4]
4^3D^e	-1. 505 171 [-3]	-1. 092 277 [-3]	-8. 216 370 [-4]	-6. 358 003 [-4]	-5. 033 975 [-4]
5^3D^e	-3. 218 217 [-3]	-2. 237 660 [-3]	-1. 630 650 [-3]	-1. 231 530 [-3]	-9. 566 269 [-4]
6^3D^e	-6. 620 183 [-3]	-4. 330 028 [-3]	-3. 020 261 [-3]	-2. 207 723 [-3]	-1. 672 334 [-3]
7^3D^e	-1. 401 778 [-2]	-8. 369 678 [-3]	-5. 487 440 [-3]	-3. 836 520 [-3]	-2. 810 834 [-3]
8^3D^e	-3. 294 260 [-2]	-1. 699 143 [-2]	-1. 016 419 [-2]	-6. 675 874 [-3]	-4. 675 612 [-3]
9^3D^e	-9. 824 852 [-2]	-3. 874 372 [-2]	-2. 001 599 [-2]	-1. 199 043 [-2]	-7. 885 998 [-3]
10^3D^e	-5. 518 927 [-1]	-1. 129 416 [-1]	-4. 461 424 [-2]	-2. 307 779 [-2]	-1. 383 962 [-2]
11^3D^e	7. 662 463 [-1]	-6. 228 332 [-1]	-1. 277 606 [-1]	-5. 053 734 [-2]	-2. 616 752 [-2]
12^3D^e	5. 411 316 [-1]	8. 327 862 [-1]	-6. 942 039 [-1]	-1. 426 780 [-1]	-5. 650 119 [-2]
13^3D^e	1. 587 351 [-1]	5. 637 078 [-1]	8. 990 703 [-1]	-7. 659 198 [-1]	-1. 576 739 [-1]
14^3D^e	7. 350 805 [-2]	1. 648 346 [-1]	5. 868 110 [-1]	9. 651 500 [-1]	-8. 379 160 [-1]
15^3D^e	4. 185 593 [-2]	7. 621 616 [-2]	1. 710 634 [-1]	6. 103 290 [-1]	1. 031 063 [0]
16^3D^e	2. 681 326 [-2]	4. 337 075 [-2]	7. 896 970 [-2]	1. 773 972 [-1]	6. 341 761 [-1]
17^3D^e	1. 853 507 [-2]	2. 778 200 [-2]	4. 490 325 [-2]	8. 176 243 [-2]	1. 838 182 [-1]
18^3D^e	1. 351 335 [-2]	1. 921 147 [-2]	2. 875 777 [-2]	4. 645 351 [-2]	8. 459 213 [-2]
19^3D^e	1. 024 870 [-2]	1. 401 655 [-2]	1. 989 127 [-2]	2. 974 376 [-2]	4. 802 542 [-2]
20^3D^e	8. 016 426 [-3]	1. 064 478 [-2]	1. 452 637 [-2]	2. 058 419 [-2]	3. 075 343 [-2]
21^3D^e	6. 428 505 [-3]	8. 340 667 [-3]	1. 104 700 [-2]	1. 504 703 [-2]	2. 129 506 [-2]

	17^3P^o	18^3P^o	19^3P^o	20^3P^o	21^3P^o
2^3D^e	-5. 483 864 [-5]	-4. 572 452 [-5]	-3. 854 487 [-5]	-3. 281 337 [-5]	-2. 819 421 [-5]
3^3D^e	-1. 827 964 [-4]	-1. 513 222 [-4]	-1. 267 933 [-4]	-1. 073 882 [-4]	-9. 186 773 [-5]
4^3D^e	-4. 061 916 [-4]	-3. 330 326 [-4]	-2. 768 184 [-4]	-2. 328 711 [-4]	-1. 980 694 [-4]
5^3D^e	-7. 601 749 [-4]	-6. 155 263 [-4]	-5. 063 698 [-4]	-4. 223 074 [-4]	-3. 565 699 [-4]
6^3D^e	-1. 302 796 [-3]	-1. 038 174 [-3]	-8. 429 617 [-4]	-6. 954 200 [-4]	-5. 818 230 [-4]
7^3D^e	-2. 134 016 [-3]	-1. 666 196 [-3]	-1. 330 758 [-3]	-1. 083 055 [-3]	-8. 959 517 [-4]
8^3D^e	-3. 431 608 [-3]	-2. 609 924 [-3]	-2. 041 476 [-3]	-1. 633 630 [-3]	-1. 332 709 [-3]
9^3D^e	-5. 530 596 [-3]	-4. 064 699 [-3]	-3. 095 886 [-3]	-2. 425 413 [-3]	-1. 944 830 [-3]
10^3D^e	-9. 111 709 [-3]	-6. 397 008 [-3]	-4. 706 806 [-3]	-3. 589 534 [-3]	-2. 817 085 [-3]
11^3D^e	-1. 570 591 [-2]	-1. 034 904 [-2]	-7. 272 165 [-3]	-5. 356 248 [-3]	-4. 090 959 [-3]
12^3D^e	-2. 927 877 [-2]	-1. 758 543 [-2]	-1. 159 573 [-2]	-8. 154 972 [-3]	-6. 014 227 [-3]
13^3D^e	-6. 249 743 [-2]	-3. 240 735 [-2]	-1. 947 619 [-2]	-1. 285 121 [-2]	-9. 047 960 [-3]
14^3D^e	-1. 727 336 [-1]	-6. 852 079 [-2]	-3. 555 153 [-2]	-2. 137 834 [-2]	-1. 411 990 [-2]
15^3D^e	-9. 101 377 [-1]	-1. 878 470 [-1]	-7. 456 988 [-2]	-3. 871 322 [-2]	-2. 330 004 [-2]
16^3D^e	1. 096 831 [0]	-9. 825 168 [-1]	-2. 030 051 [-1]	-8. 064 819 [-2]	-4. 190 815 [-2]
17^3D^e	6. 582 713 [-1]	1. 162 451 [0]	-1. 054 908 [0]	-2. 181 884 [-1]	-8. 677 749 [-2]
18^3D^e	1. 903 109 [-1]	6. 824 946 [-1]	1. 227 854 [0]	-1. 126 944 [0]	-2. 333 738 [-1]
19^3D^e	8. 746 145 [-2]	1. 968 501 [-1]	7. 065 983 [-1]	1. 292 800 [0]	-1. 197 809 [0]
20^3D^e	4. 963 931 [-2]	9. 039 217 [-2]	2. 034 089 [-1]	7. 301 070 [-1]	1. 356 573 [0]
21^3D^e	3. 179 446 [-2]	5. 130 280 [-2]	9. 336 629 [-2]	2. 097 605 [-1]	7. 510 367 [-1]

Table 61: $\bar{f}_{n^3D^o \leftarrow m^3D^e}$ oscillator strenghts

	2^3D^e	3^3D^e	4^3D^e	5^3D^e	6^3D^e
2^3D^o	1. 361 319 [-1]	6. 428 315 [-4]	1. 422 915 [-4]	5. 678 995 [-5]	2. 916 436 [-5]
3^3D^o	8. 591 110 [-4]	1. 359 747 [-1]	7. 232 721 [-4]	1. 772 140 [-4]	7. 480 955 [-5]
4^3D^o	1. 598 625 [-4]	9. 792 620 [-4]	1. 359 142 [-1]	7. 402 188 [-4]	1. 889 217 [-4]
5^3D^o	6. 082 717 [-5]	2. 025 723 [-4]	1. 007 712 [-3]	1. 358 905 [-1]	7. 436 671 [-4]
6^3D^o	3. 062 022 [-5]	8. 120 352 [-5]	2. 174 563 [-4]	1. 015 623 [-3]	1. 358 794 [-1]
7^3D^o	1. 790 740 [-5]	4. 226 462 [-5]	8. 940 906 [-5]	2. 240 658 [-4]	1. 017 550 [-3]
8^3D^o	1. 150 144 [-5]	2. 532 592 [-5]	4. 740 011 [-5]	9. 350 049 [-5]	2. 271 933 [-4]
9^3D^o	7. 878 286 [-6]	1. 658 042 [-5]	2. 882 291 [-5]	5. 014 460 [-5]	9. 566 739 [-5]
10^3D^o	5. 657 002 [-6]	1. 153 769 [-5]	1. 910 321 [-5]	3. 078 834 [-5]	5. 170 148 [-5]
11^3D^o	4. 211 485 [-6]	8. 396 047 [-6]	1. 343 493 [-5]	2. 057 864 [-5]	3. 196 033 [-5]
12^3D^o	3. 226 497 [-6]	6. 323 232 [-6]	9. 868 230 [-6]	1. 458 159 [-5]	2. 149 341 [-5]
13^3D^o	2. 530 247 [-6]	4. 893 652 [-6]	7. 493 869 [-6]	1. 078 319 [-5]	1. 531 545 [-5]
14^3D^o	2. 023 126 [-6]	3. 872 251 [-6]	5. 843 004 [-6]	8. 239 235 [-6]	1. 138 458 [-5]
15^3D^o	1. 644 420 [-6]	3. 121 120 [-6]	4. 654 736 [-6]	6. 460 466 [-6]	8. 740 469 [-6]
16^3D^o	1. 355 570 [-6]	2. 555 307 [-6]	3. 774 936 [-6]	5. 173 392 [-6]	6. 884 058 [-6]
17^3D^o	1. 131 235 [-6]	2. 120 359 [-6]	3. 108 074 [-6]	4. 215 792 [-6]	5. 535 614 [-6]
18^3D^o	9. 542 849 [-7]	1. 780 201 [-6]	2. 592 586 [-6]	3. 486 762 [-6]	4. 528 818 [-6]
19^3D^o	8. 128 598 [-7]	1. 510 281 [-6]	2. 187 502 [-6]	2. 921 079 [-6]	3. 760 013 [-6]
20^3D^o	6. 987 420 [-7]	1. 293 790 [-6]	1. 865 240 [-6]	2. 475 776 [-6]	3. 162 774 [-6]
21^3D^o	6. 056 099 [-7]	1. 118 022 [-6]	1. 605 409 [-6]	2. 119 939 [-6]	2. 690 827 [-6]

	7^3D^e	8^3D^e	9^3D^e	10^3D^e	11^3D^e
2^3D^o	1. 723 363 [-5]	1. 113 724 [-5]	7. 659 875 [-6]	5. 516 041 [-6]	4. 115 425 [-6]
3^3D^o	3. 986 958 [-5]	2. 420 658 [-5]	1. 597 818 [-5]	1. 118 066 [-5]	8. 168 919 [-6]
4^3D^o	8. 197 830 [-5]	4. 459 299 [-5]	2. 751 848 [-5]	1. 841 134 [-5]	1. 303 270 [-5]
5^3D^o	1. 937 191 [-4]	8. 536 492 [-5]	4. 701 580 [-5]	2. 931 961 [-5]	1. 979 592 [-5]
6^3D^o	7. 436 163 [-4]	1. 957 952 [-4]	8. 707 741 [-5]	4. 834 677 [-5]	3. 036 686 [-5]
7^3D^o	1. 358 746 [-1]	7. 427 342 [-4]	1. 968 155 [-4]	8. 805 134 [-5]	4. 915 614 [-5]
8^3D^o	1. 017 644 [-3]	1. 358 727 [-1]	7. 417 425 [-4]	1. 973 588 [-4]	8. 865 137 [-5]
9^3D^o	2. 288 987 [-4]	1. 017 163 [-3]	1. 358 720 [-1]	7. 408 322 [-4]	1. 976 634 [-4]
10^3D^o	9. 696 372 [-5]	2. 299 117 [-4]	1. 016 526 [-3]	1. 358 719 [-1]	7. 400 444 [-4]
11^3D^o	5. 268 187 [-5]	9. 779 968 [-5]	2. 305 502 [-4]	1. 015 881 [-3]	1. 358 722 [-1]
12^3D^o	3. 272 603 [-5]	5. 334 136 [-5]	9. 836 836 [-5]	2. 309 708 [-4]	1. 015 281 [-3]
13^3D^o	2. 210 866 [-5]	3. 325 668 [-5]	5. 380 665 [-5]	9. 877 144 [-5]	2. 312 576 [-4]
14^3D^o	1. 582 103 [-5]	2. 254 518 [-5]	3. 364 062 [-5]	5. 414 721 [-5]	9. 906 658 [-5]
15^3D^o	1. 180 745 [-5]	1. 618 681 [-5]	2. 286 732 [-5]	3. 392 786 [-5]	5. 440 395 [-5]
16^3D^o	9. 099 287 [-6]	1. 211 862 [-5]	1. 646 128 [-5]	2. 311 253 [-5]	3. 414 870 [-5]
17^3D^o	7. 192 235 [-6]	9. 367 388 [-6]	1. 235 565 [-5]	1. 667 345 [-5]	2. 330 426 [-5]
18^3D^o	5. 803 210 [-6]	7. 425 943 [-6]	9. 574 691 [-6]	1. 254 177 [-5]	1. 684 224 [-5]
19^3D^o	4. 763 675 [-6]	6. 009 328 [-6]	7. 609 621 [-6]	9. 740 380 [-6]	1. 269 282 [-5]
20^3D^o	3. 969 345 [-6]	4. 948 854 [-6]	6. 175 781 [-6]	7. 761 271 [-6]	9. 880 293 [-6]
21^3D^o	3. 350 258 [-6]	4. 136 264 [-6]	5. 099 857 [-6]	6. 314 242 [-6]	7. 889 838 [-6]

Table 62: $\bar{f}_{n^3D^o \leftarrow m^3D^e}$ oscillator strenghts

	12^3D^e	13^3D^e	14^3D^e	15^3D^e	16^3D^e
2^3D^o	3. 158 239 [-6]	2. 480 109 [-6]	1. 985 290 [-6]	1. 615 221 [-6]	1. 332 605 [-6]
3^3D^o	6. 170 804 [-6]	4. 786 978 [-6]	3. 795 039 [-6]	3. 063 665 [-6]	2. 511 555 [-6]
4^3D^o	9. 618 110 [-6]	7. 330 136 [-6]	5. 731 395 [-6]	4. 576 131 [-6]	3. 718 070 [-6]
5^3D^o	1. 412 614 [-5]	1. 050 056 [-5]	8. 055 006 [-6]	6. 335 648 [-6]	5. 086 158 [-6]
6^3D^o	2. 063 635 [-5]	1. 481 311 [-5]	1. 107 101 [-5]	8. 535 108 [-6]	6. 744 393 [-6]
7^3D^o	3. 103 273 [-5]	2. 118 908 [-5]	1. 527 736 [-5]	1. 146 541 [-5]	8. 873 643 [-6]
8^3D^o	4. 968 433 [-5]	3. 148 363 [-5]	2. 157 387 [-5]	1. 560 788 [-5]	1. 175 158 [-5]
9^3D^o	8. 904 350 [-5]	5. 004 761 [-5]	3. 180 369 [-5]	2. 185 348 [-5]	1. 585 269 [-5]
10^3D^o	1. 978 400 [-4]	8. 931 187 [-5]	5. 030 802 [-5]	3. 203 950 [-5]	2. 206 375 [-5]
11^3D^o	7. 393 760 [-4]	1. 979 443 [-4]	8. 950 253 [-5]	5. 050 103 [-5]	3. 221 866 [-5]
12^3D^o	1. 358 726 [-1]	7. 388 113 [-4]	1. 980 062 [-4]	8. 964 232 [-5]	5. 064 832 [-5]
13^3D^o	1. 014 742 [-3]	1. 358 731 [-1]	7. 383 336 [-4]	1. 980 427 [-4]	8. 974 793 [-5]
14^3D^o	2. 314 588 [-4]	1. 014 263 [-3]	1. 358 735 [-1]	7. 379 284 [-4]	1. 980 640 [-4]
15^3D^o	9. 928 863 [-5]	2. 316 031 [-4]	1. 013 842 [-3]	1. 358 740 [-1]	7. 375 839 [-4]
16^3D^o	5. 460 243 [-5]	9. 945 983 [-5]	2. 317 093 [-4]	1. 013 473 [-3]	1. 358 745 [-1]
17^3D^o	3. 432 291 [-5]	5. 475 994 [-5]	9. 959 573 [-5]	2. 317 909 [-4]	1. 013 151 [-3]
18^3D^o	2. 345 856 [-5]	3. 446 467 [-5]	5. 488 956 [-5]	9. 970 891 [-5]	2. 318 595 [-4]
19^3D^o	1. 698 128 [-5]	2. 358 773 [-5]	3. 458 559 [-5]	5. 500 277 [-5]	9. 981 112 [-5]
20^3D^o	1. 282 359 [-5]	1. 710 530 [-5]	2. 370 738 [-5]	3. 470 335 [-5]	5. 512 116 [-5]
21^3D^o	1. 000 120 [-5]	1. 293 885 [-5]	1. 721 680 [-5]	2. 381 686 [-5]	3. 481 197 [-5]

	17^3D^e	18^3D^e	19^3D^e	20^3D^e	21^3D^e
2^3D^o	1. 112 880 [-6]	9. 394 114 [-7]	8. 006 743 [-7]	6. 887 045 [-7]	5. 975 258 [-7]
3^3D^o	2. 086 384 [-6]	1. 753 380 [-6]	1. 488 825 [-6]	1. 276 510 [-6]	1. 104 440 [-6]
4^3D^o	3. 066 006 [-6]	2. 560 883 [-6]	2. 163 267 [-6]	1. 846 612 [-6]	1. 591 647 [-6]
5^3D^o	4. 153 258 [-6]	3. 440 998 [-6]	2. 887 053 [-6]	2. 450 310 [-6]	2. 101 612 [-6]
6^3D^o	5. 437 710 [-6]	4. 458 487 [-6]	3. 708 519 [-6]	3. 124 687 [-6]	2. 663 480 [-6]
7^3D^o	7. 037 727 [-6]	5. 694 214 [-6]	4. 684 966 [-6]	3. 911 663 [-6]	3. 308 784 [-6]
8^3D^o	9. 123 477 [-6]	7. 257 762 [-6]	5. 889 962 [-6]	4. 862 428 [-6]	4. 074 271 [-6]
9^3D^o	1. 196 717 [-5]	9. 314 844 [-6]	7. 429 411 [-6]	6. 047 499 [-6]	5. 008 572 [-6]
10^3D^o	1. 604 008 [-5]	1. 213 512 [-5]	9. 466 960 [-6]	7. 571 109 [-6]	6. 180 820 [-6]
11^3D^o	2. 222 671 [-5]	1. 618 818 [-5]	1. 227 097 [-5]	9. 595 915 [-6]	7. 694 463 [-6]
12^3D^o	3. 235 883 [-5]	2. 235 723 [-5]	1. 631 013 [-5]	1. 238 969 [-5]	9. 711 729 [-6]
13^3D^o	5. 076 426 [-5]	3. 247 262 [-5]	2. 246 690 [-5]	1. 642 080 [-5]	1. 250 021 [-5]
14^3D^o	8. 983 091 [-5]	5. 085 988 [-5]	3. 257 075 [-5]	2. 257 150 [-5]	1. 652 823 [-5]
15^3D^o	1. 980 779 [-4]	8. 990 097 [-5]	5. 094 553 [-5]	3. 267 116 [-5]	2. 267 821 [-5]
16^3D^o	7. 372 915 [-4]	1. 980 921 [-4]	8. 996 853 [-5]	5. 104 329 [-5]	3. 277 959 [-5]
17^3D^o	1. 358 749 [-1]	7. 370 502 [-4]	1. 981 174 [-4]	9. 006 361 [-5]	5. 115 561 [-5]
18^3D^o	1. 012 878 [-3]	1. 358 754 [-1]	7. 368 727 [-4]	1. 982 009 [-4]	9. 017 948 [-5]
19^3D^o	2. 319 274 [-4]	1. 012 667 [-3]	1. 358 758 [-1]	7. 368 291 [-4]	1. 983 001 [-4]
20^3D^o	9. 993 146 [-5]	2. 320 404 [-4]	1. 012 576 [-3]	1. 358 766 [-1]	7. 368 743 [-4]
21^3D^o	5. 522 794 [-5]	1. 000 266 [-4]	2. 320 636 [-4]	1. 012 217 [-3]	1. 358 849 [-1]

Table 63: $\bar{f}_{n^3D^o \leftarrow m^3P^e}$ oscillator strenghts

	2^3P^e	3^3P^e	4^3P^e	5^3P^e	6^3P^e
2^3D^o	4. 534 587 [-1]	2. 564 256 [-1]	-6. 172 021 [-2]	-9. 991 978 [-3]	-3. 645 926 [-3]
3^3D^o	1. 390 282 [-1]	1. 905 040 [-1]	4. 173 455 [-1]	-1. 373 267 [-1]	-2. 252 117 [-2]
4^3D^o	6. 213 692 [-2]	6. 467 311 [-2]	1. 523 745 [-1]	5. 589 664 [-1]	-2. 200 451 [-1]
5^3D^o	3. 346 545 [-2]	3. 030 973 [-2]	5. 634 632 [-2]	1. 354 188 [-1]	6. 922 934 [-1]
6^3D^o	2. 018 362 [-2]	1. 689 115 [-2]	2. 779 125 [-2]	5. 194 725 [-2]	1. 271 106 [-1]
7^3D^o	1. 314 637 [-2]	1. 047 204 [-2]	1. 606 101 [-2]	2. 629 648 [-2]	4. 960 924 [-2]
8^3D^o	9. 055 103 [-3]	6. 979 138 [-3]	1. 023 901 [-2]	1. 551 321 [-2]	2. 546 616 [-2]
9^3D^o	6. 508 706 [-3]	4. 901 732 [-3]	6. 978 578 [-3]	1. 005 982 [-2]	1. 520 808 [-2]
10^3D^o	4. 838 562 [-3]	3. 582 886 [-3]	4. 993 300 [-3]	6. 956 562 [-3]	9. 969 348 [-3]
11^3D^o	3. 696 544 [-3]	2. 702 641 [-3]	3. 707 734 [-3]	5. 040 379 [-3]	6. 961 010 [-3]
12^3D^o	2. 888 666 [-3]	2. 091 342 [-3]	2. 834 972 [-3]	3. 784 068 [-3]	5. 087 631 [-3]
13^3D^o	2. 300 775 [-3]	1. 652 873 [-3]	2. 219 803 [-3]	2. 921 635 [-3]	3. 849 648 [-3]
14^3D^o	1. 862 614 [-3]	1. 329 810 [-3]	1. 772 742 [-3]	2. 307 619 [-3]	2. 993 525 [-3]
15^3D^o	1. 529 283 [-3]	1. 086 313 [-3]	1. 439 487 [-3]	1. 857 316 [-3]	2. 379 812 [-3]
16^3D^o	1. 271 156 [-3]	8. 991 867 [-4]	1. 185 676 [-3]	1. 518 853 [-3]	1. 926 855 [-3]
17^3D^o	1. 068 148 [-3]	7. 529 483 [-4]	9. 887 932 [-4]	1. 259 131 [-3]	1. 584 390 [-3]
18^3D^o	9. 063 278 [-4]	6. 369 978 [-4]	8. 336 535 [-4]	1. 056 307 [-3]	1. 320 200 [-3]
19^3D^o	7. 758 425 [-4]	5. 439 195 [-4]	7. 097 659 [-4]	8. 955 575 [-4]	1. 112 937 [-3]
20^3D^o	6. 697 616 [-4]	4. 685 363 [-4]	6. 098 712 [-4]	7. 667 565 [-4]	9. 482 753 [-4]
21^3D^o	5. 826 308 [-4]	4. 068 211 [-4]	5. 283 967 [-4]	6. 622 722 [-4]	8. 156 651 [-4]

	7^3P^e	8^3P^e	9^3P^e	10^3P^e	11^3P^e
2^3D^o	-1. 797 851 [-3]	-1. 038 340 [-3]	-6. 612 182 [-4]	-4. 500 823 [-4]	-3. 216 132 [-4]
3^3D^o	-8. 260 298 [-3]	-4. 097 290 [-3]	-2. 382 311 [-3]	-1. 527 948 [-3]	-1. 047 590 [-3]
4^3D^o	-3. 656 559 [-2]	-1. 350 867 [-2]	-6. 741 595 [-3]	-3. 943 074 [-3]	-2. 543 808 [-3]
5^3D^o	-3. 064 774 [-1]	-5. 138 789 [-2]	-1. 908 801 [-2]	-9. 569 368 [-3]	-5. 621 176 [-3]
6^3D^o	8. 211 473 [-1]	-3. 951 323 [-1]	-6. 661 134 [-2]	-2. 482 701 [-2]	-1. 248 349 [-2]
7^3D^o	1. 231 422 [-1]	9. 473 490 [-1]	-4. 852 354 [-1]	-8. 209 061 [-2]	-3. 066 670 [-2]
8^3D^o	4. 842 455 [-2]	1. 216 373 [-1]	1. 071 828 [0]	-5. 763 221 [-1]	-9. 773 063 [-2]
9^3D^o	2. 503 873 [-2]	4. 797 169 [-2]	1. 216 524 [-1]	1. 195 123 [0]	-6. 681 093 [-1]
10^3D^o	1. 506 112 [-2]	2. 489 475 [-2]	4. 799 675 [-2]	1. 226 702 [-1]	1. 317 565 [0]
11^3D^o	9. 941 763 [-3]	1. 503 844 [-2]	2. 494 538 [-2]	4. 835 044 [-2]	1. 243 837 [-1]
12^3D^o	6. 987 364 [-3]	9. 971 332 [-3]	1. 510 539 [-2]	2. 513 490 [-2]	4. 893 977 [-2]
13^3D^o	5. 138 280 [-3]	7. 039 561 [-3]	1. 004 447 [-2]	1. 523 869 [-2]	2. 542 702 [-2]
14^3D^o	3. 910 236 [-3]	5. 199 263 [-3]	7. 112 949 [-3]	1. 015 113 [-2]	1. 542 245 [-2]
15^3D^o	3. 056 841 [-3]	3. 973 243 [-3]	5. 269 888 [-3]	7. 203 466 [-3]	1. 028 411 [-2]
16^3D^o	2. 442 209 [-3]	3. 118 536 [-3]	4. 039 726 [-3]	5. 348 925 [-3]	7. 307 969 [-3]
17^3D^o	1. 986 555 [-3]	2. 501 022 [-3]	3. 180 409 [-3]	4. 109 856 [-3]	5. 435 293 [-3]
18^3D^o	1. 640 646 [-3]	2. 041 877 [-3]	2. 558 339 [-3]	3. 243 360 [-3]	4. 183 680 [-3]
19^3D^o	1. 372 853 [-3]	1. 692 418 [-3]	2. 095 002 [-3]	2. 615 462 [-3]	3. 308 100 [-3]
20^3D^o	1. 162 436 [-3]	1. 421 657 [-3]	1. 742 287 [-3]	2. 147 946 [-3]	2. 674 119 [-3]
21^3D^o	9. 945 513 [-4]	1. 208 155 [-3]	1. 468 221 [-3]	1. 791 249 [-3]	2. 201 267 [-3]

Table 64: $\bar{f}_{n^3D^o \leftarrow m^3P^e}$ oscillator strenghts

	12^3P^e	13^3P^e	14^3P^e	15^3P^e	16^3P^e
2^3D^o	-2. 385 007 [-4]	-1. 821 343 [-4]	-1. 424 465 [-4]	-1. 136 346 [-4]	-9. 217 921 [-5]
3^3D^o	-7. 538 720 [-4]	-5. 628 461 [-4]	-4. 325 864 [-4]	-3. 403 683 [-4]	-2. 730 613 [-4]
4^3D^o	-1. 754 087 [-3]	-1. 269 282 [-3]	-9. 526 821 [-4]	-7. 358 959 [-4]	-5. 817 842 [-4]
5^3D^o	-3. 641 768 [-3]	-2. 521 638 [-3]	-1. 832 106 [-3]	-1. 380 536 [-3]	-1. 070 437 [-3]
6^3D^o	-7. 354 461 [-3]	-4. 778 836 [-3]	-3. 318 864 [-3]	-2. 418 530 [-3]	-1. 827 796 [-3]
7^3D^o	-1. 545 100 [-2]	-9. 121 163 [-3]	-5. 939 224 [-3]	-4. 133 639 [-3]	-3. 018 892 [-3]
8^3D^o	-3. 656 652 [-2]	-1. 844 919 [-2]	-1. 090 655 [-2]	-7. 112 433 [-3]	-4. 958 005 [-3]
9^3D^o	-1. 134 758 [-1]	-4. 250 299 [-2]	-2. 146 493 [-2]	-1. 270 207 [-2]	-8. 292 327 [-3]
10^3D^o	-7. 604 145 [-1]	-1. 292 928 [-1]	-4. 846 243 [-2]	-2. 449 068 [-2]	-1. 450 281 [-2]
11^3D^o	1. 439 375 [0]	-8. 531 141 [-1]	-1. 451 604 [-1]	-5. 443 654 [-2]	-2. 752 198 [-2]
12^3D^o	1. 265 993 [-1]	1. 560 702 [0]	-9. 461 210 [-1]	-1. 610 649 [-1]	-6. 042 019 [-2]
13^3D^o	4. 970 369 [-2]	1. 291 889 [-1]	1. 681 652 [0]	-1. 039 372 [0]	-1. 769 970 [-1]
14^3D^o	2. 579 702 [-2]	5. 060 053 [-2]	1. 320 645 [-1]	1. 802 301 [0]	-1. 132 820 [0]
15^3D^o	1. 564 546 [-2]	2. 622 756 [-2]	5. 160 087 [-2]	1. 351 634 [-1]	1. 922 704 [0]
16^3D^o	1. 043 815 [-2]	1. 589 966 [-2]	2. 670 616 [-2]	5. 268 348 [-2]	1. 384 391 [-1]
17^3D^o	7. 424 118 [-3]	1. 060 943 [-2]	1. 617 929 [-2]	2. 722 396 [-2]	5. 383 274 [-2]
18^3D^o	5. 528 248 [-3]	7. 550 339 [-3]	1. 079 541 [-2]	1. 648 057 [-2]	2. 777 512 [-2]
19^3D^o	4. 261 407 [-3]	5. 627 526 [-3]	7. 685 875 [-3]	1. 099 486 [-2]	1. 680 191 [-2]
20^3D^o	3. 376 194 [-3]	4. 344 547 [-3]	5. 734 682 [-3]	7. 832 542 [-3]	1. 121 052 [-2]
21^3D^o	2. 734 459 [-3]	3. 447 368 [-3]	4. 432 303 [-3]	5. 848 249 [-3]	7. 988 293 [-3]

	17^3P^e	18^3P^e	19^3P^e	20^3P^e	21^3P^e
2^3D^o	-7. 585 457 [-5]	-6. 320 316 [-5]	-5. 324 250 [-5]	-4. 529 379 [-5]	-3. 888 509 [-5]
3^3D^o	-2. 226 786 [-4]	-1. 841 540 [-4]	-1. 541 610 [-4]	-1. 304 508 [-4]	-1. 114 857 [-4]
4^3D^o	-4. 688 444 [-4]	-3. 839 715 [-4]	-3. 188 373 [-4]	-2. 679 630 [-4]	-2. 276 793 [-4]
5^3D^o	-8. 493 504 [-4]	-6. 868 666 [-4]	-5. 644 344 [-4]	-4. 702 527 [-4]	-3. 966 209 [-4]
6^3D^o	-1. 421 334 [-3]	-1. 130 970 [-3]	-9. 171 692 [-4]	-7. 558 000 [-4]	-6. 316 179 [-4]
7^3D^o	-2. 286 567 [-3]	-1. 782 037 [-3]	-1. 421 167 [-3]	-1. 155 164 [-3]	-9. 544 077 [-4]
8^3D^o	-3. 626 902 [-3]	-2. 751 760 [-3]	-2. 148 377 [-3]	-1. 716 527 [-3]	-1. 398 326 [-3]
9^3D^o	-5. 787 284 [-3]	-4. 238 876 [-3]	-3. 220 441 [-3]	-2. 518 040 [-3]	-2. 015 622 [-3]
10^3D^o	-9. 475 413 [-3]	-6. 618 864 [-3]	-4. 852 857 [-3]	-3. 691 190 [-3]	-2. 890 575 [-3]
11^3D^o	-1. 630 600 [-2]	-1. 065 981 [-2]	-7. 451 520 [-3]	-5. 468 136 [-3]	-4. 164 460 [-3]
12^3D^o	-3. 055 626 [-2]	-1. 811 021 [-2]	-1. 184 487 [-2]	-8. 285 146 [-3]	-6. 086 104 [-3]
13^3D^o	-6. 641 026 [-2]	-3. 359 234 [-2]	-1. 991 525 [-2]	-1. 303 102 [-2]	-9. 122 198 [-3]
14^3D^o	-1. 929 503 [-1]	-7. 240 554 [-2]	-3. 663 060 [-2]	-2. 172 221 [-2]	-1. 422 211 [-2]
15^3D^o	-1. 226 425 [0]	-2. 089 220 [-1]	-7. 840 757 [-2]	-3. 967 366 [-2]	-2. 353 764 [-2]
16^3D^o	2. 042 895 [0]	-1. 320 131 [0]	-2. 249 105 [-1]	-8. 442 147 [-2]	-4. 273 429 [-2]
17^3D^o	1. 418 521 [-1]	2. 162 857 [0]	-1. 413 808 [0]	-2. 409 069 [-1]	-9. 046 825 [-2]
18^3D^o	5. 503 564 [-2]	1. 453 555 [-1]	2. 282 442 [0]	-1. 507 092 [0]	-2. 569 035 [-1]
19^3D^o	2. 835 611 [-2]	5. 627 551 [-2]	1. 488 682 [-1]	2. 401 152 [0]	-1. 599 105 [0]
20^3D^o	1. 714 748 [-2]	2. 896 853 [-2]	5. 753 017 [-2]	1. 522 453 [-1]	2. 517 624 [0]
21^3D^o	1. 144 008 [-2]	1. 751 182 [-2]	2. 958 867 [-2]	5. 868 594 [-2]	1. 549 252 [-1]

Appendix L

Additional helium tables and spectra

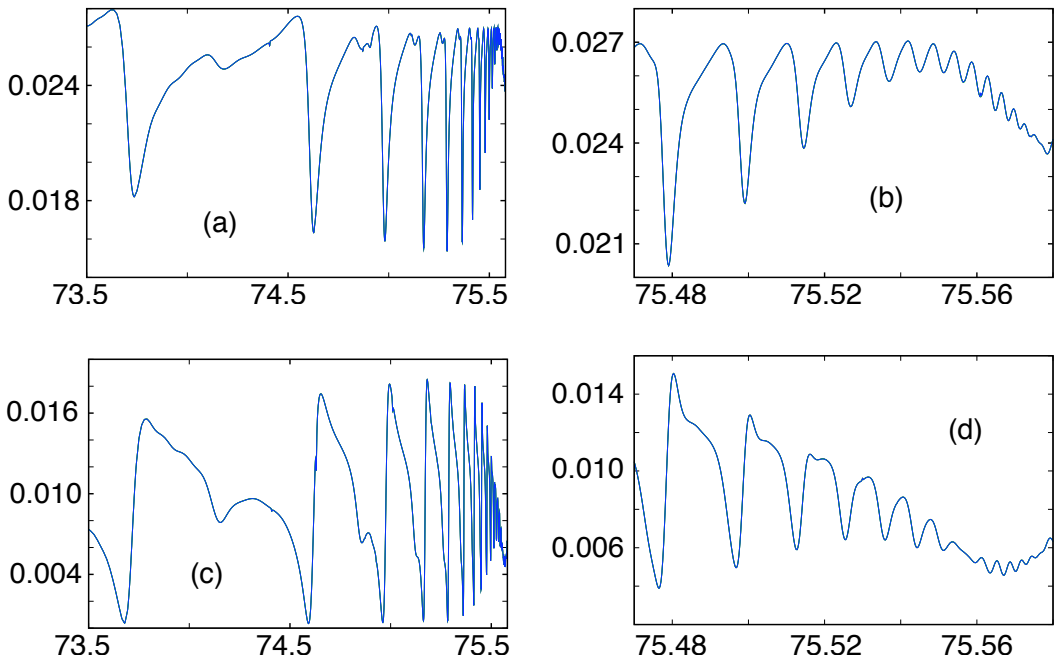

Figure L.1: ℓ resolved partial cross sections for $n = 2$ in 1^1S helium photoionization spectrum below N= 4 threshold. Cross sections are given in Mb. On the x axis the photon energy in eV is reported. (a) σ_{2s}, (b) detail of σ_{2s} close to threshold; (c) σ_{2p}, (d) detail of σ_{2p} close to threshold.

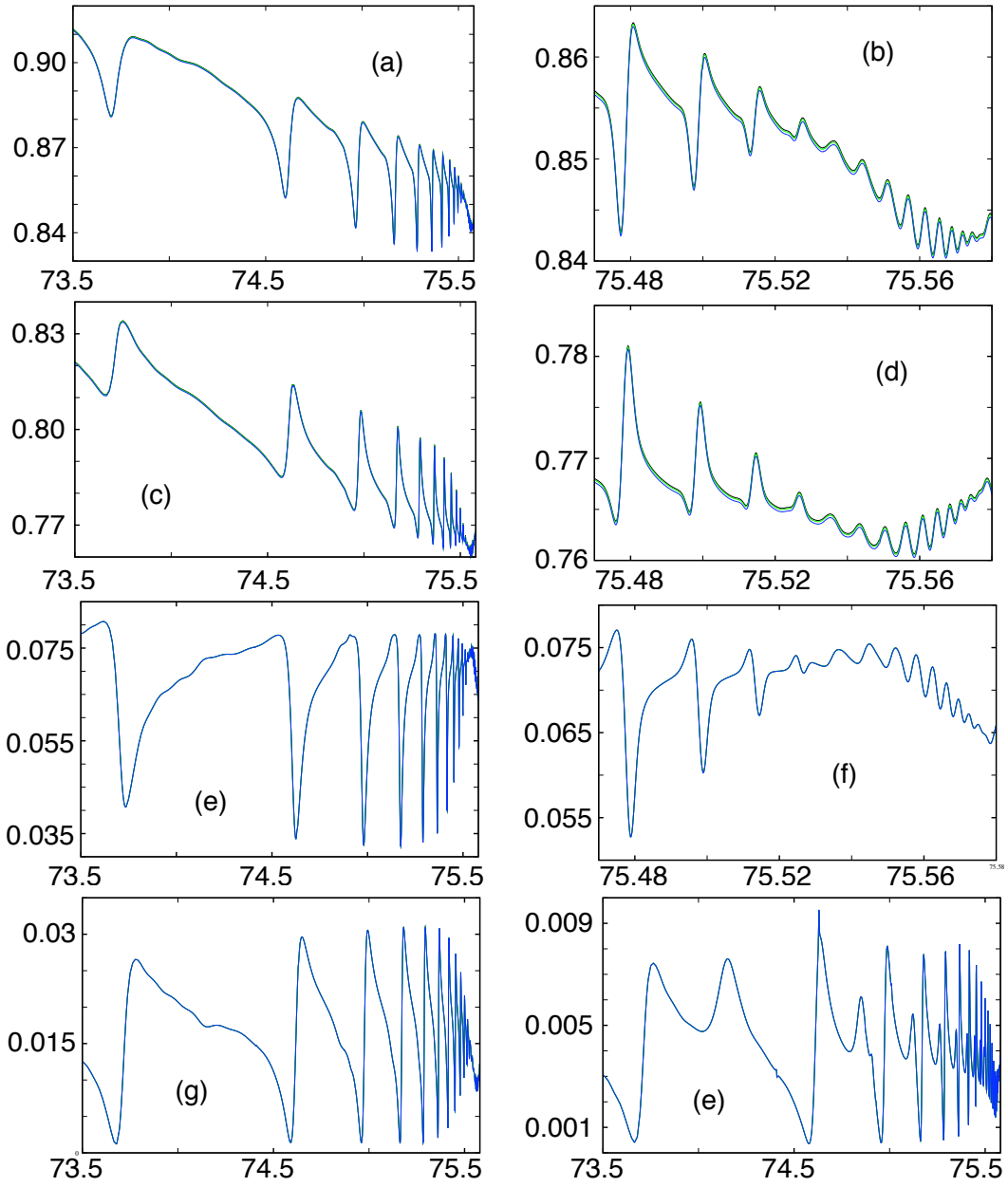

Figure L.2: Total and N resolved partial photoionization cross sections of 1^1S helium below N= 4 threshold, convoluted with a gaussian resolution function, FWHM= 2.08 meV. Cross sections are given in Mb. On the x axis the photon energy in eV is reported. (a) σ_{tot}, (b) σ_{tot} detail, (c) $\sigma_{N=1}$, (d) $\sigma_{N=1}$ detail, (e) $\sigma_{N=2}$, (f) $\sigma_{N=2}$ detail, (g) $\sigma_{N=3}$, (h) $\sigma_{N=3}$ detail.

Table 1: $^1P^o$ $[021]^+$ (upper values) and $[030]^-$ (lower values) resonance parameters below N=4 threshold for $n \geq 12$. For $n = 12, 13$ the highest values in Rost *et al* classification [99] are reported for comparison. The notation $[-n]$ is to be read $\times 10^{-n}$.

n	-E (au)	Γ (au)	E (eV)	Γ (eV)	μ	$\bar{\Gamma}(au)$
Rost *et al*	0.1295425	4.78[-5]				
12	0.1295400	4.72[-5]	75.47825	1.28[-3]	1.506	5.46[-2]
	0.1298115	4.58[-6]	75.47087	1.25[-4]	1.806	4.86[-3]
Rost *et al*	0.1298231	4.46[-6]				
Rost *et al*	0.1288034	2.62[-5]				
13	0.1288005	2.63[-5]	75.49837	7.15[-4]	1.530	3.97[-2]
	0.1289940	3.51[-6]	75.49311	9.56[-5]	1.811	4.92[-3]
Rost *et al*	0.1290039	4.2 [-6]				
14	0.1282294	1.34[-5]	75.51391	3.65[-4]	1.557	2.58[-2]
	0.1283677	2.75[-6]	75.51015	7.48[-5]	1.815	4.97[-3]
15	0.1277794	5.99[-6]	75.52615	1.63[-4]	1.588	1.44[-2]
	0.1278775	2.19[-6]	75.52348	5.96[-5]	1.818	5.02[-3]
16	0.1274186	2.59[-6]	75.53597	7.05[-5]	1.622	7.70[-3]
	0.1274868	1.78[-6]	75.53411	4.84[-5]	1.821	5.07[-3]
17	0.1271247	2.11[-6]	75.54397	5.73[-5]	1.660	7.60[-3]
	0.1271705	1.47[-6]	75.54272	3.99[-5]	1.822	5.13[-3]
18	0.1268819	3.42[-6]	75.55057	9.31[-5]	1.700	1.48[-2]
	0.1269109	1.24[-6]	75.54979	3.37[-5]	1.824	5.24[-3]
19	0.1266787	5.37[-6]	75.55610	1.46[-4]	1.742	2.76[-2]
	0.1266951	1.10[-6]	75.55565	2.99[-5]	1.826	5.56[-3]
20	0.1265063	7.24[-6]	75.56079	1.97[-4]	1.781	4.38[-2]
	0.1265140	1.15[-6]	75.56058	3.14[-5]	1.827	6.93[-3]
21	0.1263589	8.56[-6]	75.56480	2.33[-4]	1.818	6.04[-2]
	0.1263601	1.72[-6]	75.56477	4.70[-5]	1.827	1.22[-2]
22	0.1262318	1.08[-6]	75.56826	2.93[-4]	1.853	8.81[-2]
	0.1262284	1.08[-6]	75.56835	2.93[-5]	1.825	8.86[-3]
23	0.1261211	1.22[-6]	75.57127	3.31[-4]	1.881	1.14[-1]
	0.1261150	7.70[-7]	75.57144	2.09[-5]	1.824	7.31[-3]
24	0.1260243	1.35[-5]	75.57391	3.68[-4]	1.906	1.46[-1]
	0.1260163	6.31[-7]	75.57412	1.72[-5]	1.820	6.89[-3]

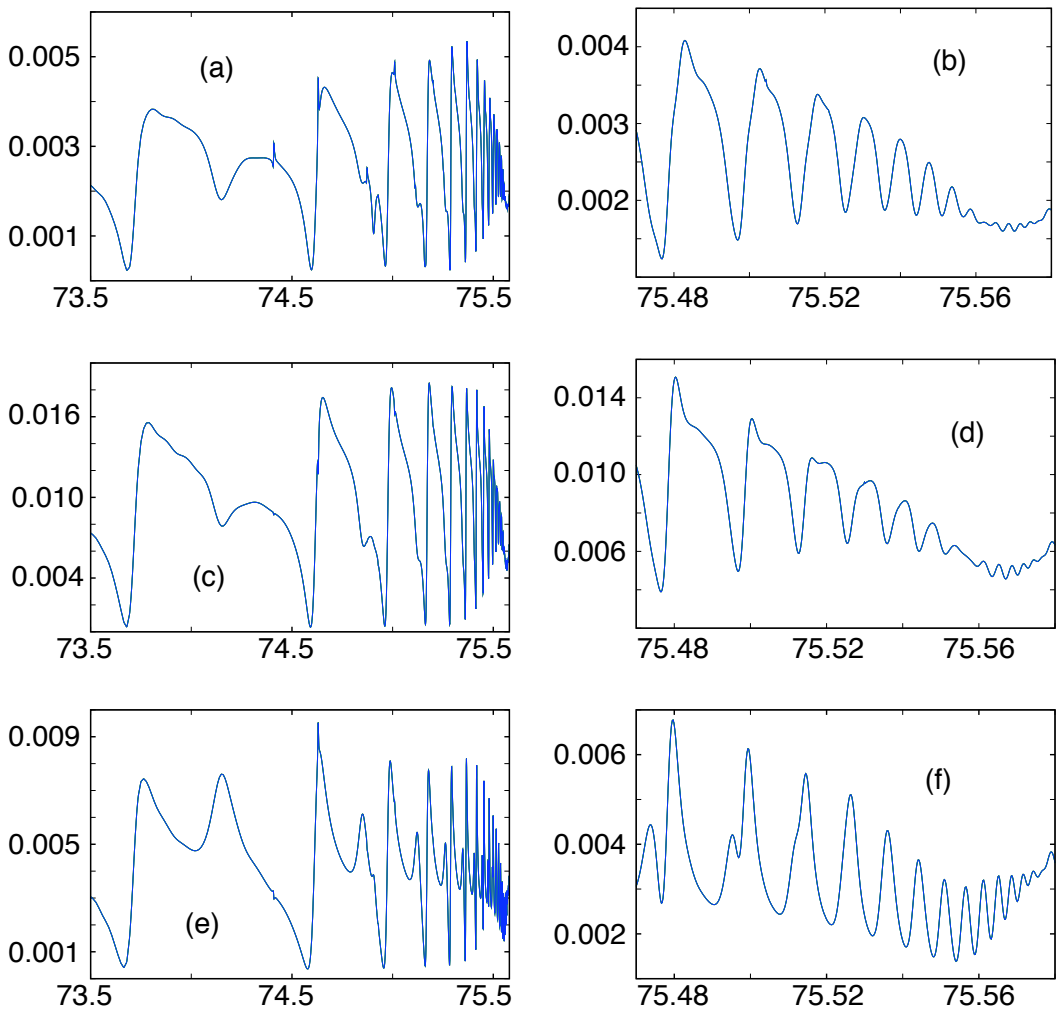

Figure L.3: ℓ resolved partial cross sections for $n = 3$ in 1^1Shelium photoionization spectrum below N= 4 threshold. Cross sections are given in Mb. On the x axis the photon energy in eV is reported. (a) σ_{3s}, (b) detail of σ_{3s} close to threshold; (c) σ_{3p}, (d) detail of σ_{3p} close to threshold; (e) σ_{3d}, (f) detail of σ_{3d} close to threshold.

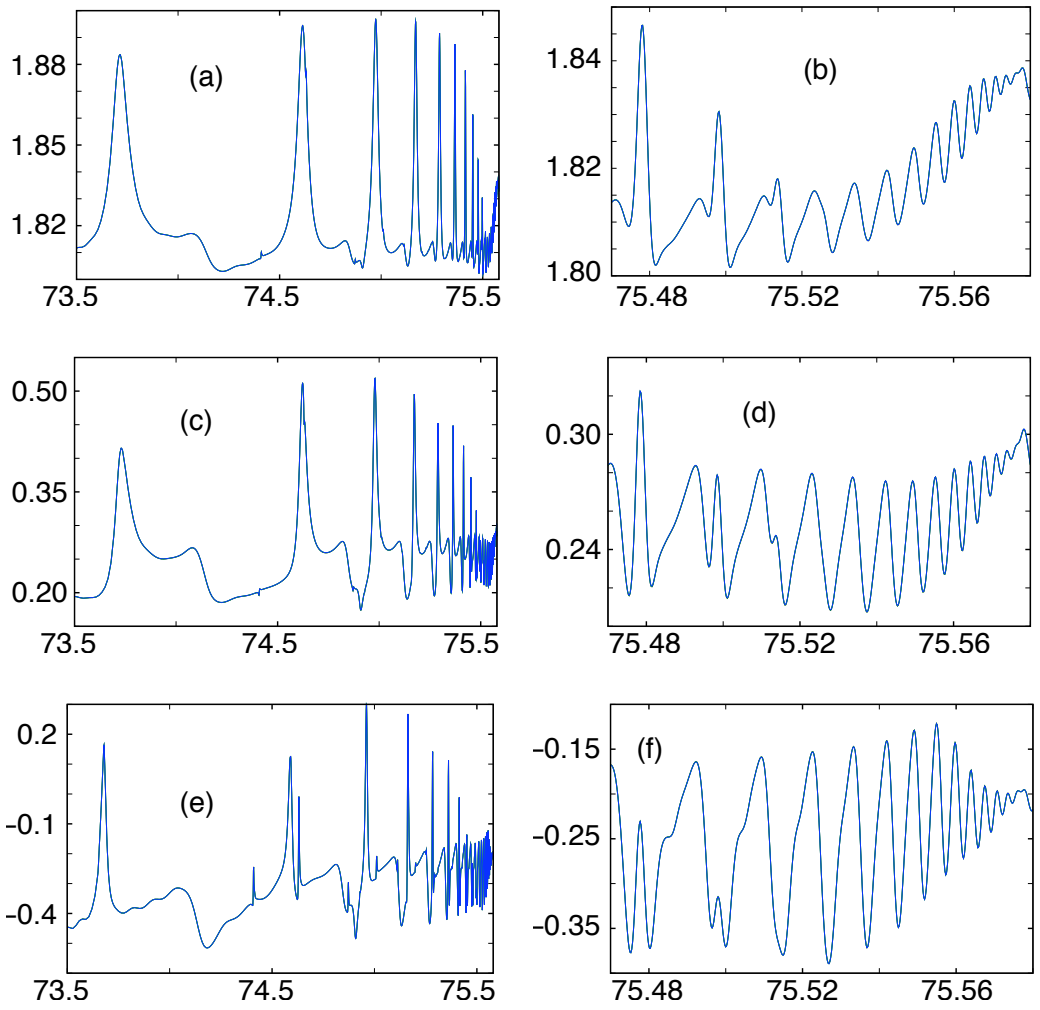

Figure L.4: Total and N resolved dipole asymmetry parameter β in the photoionization of 1^1S helium. On the x axis the photon energy in eV is reported. (a) β_{tot}, (b) β_{tot} detail; (c) β_2, (d) β_2 detail; (e) β_3, (f) β_3 detail. $\beta_1 = 2$ identically. The clearest features near threshold at this resolution are the disappearance of the narrowest structure which is almost complete at 75.52 eV, and a slight drift at higher values of the asymmetry parameter. In the unconvoluted version, which is not shown here, the narrow structure appears again beyond 75.55 eV.

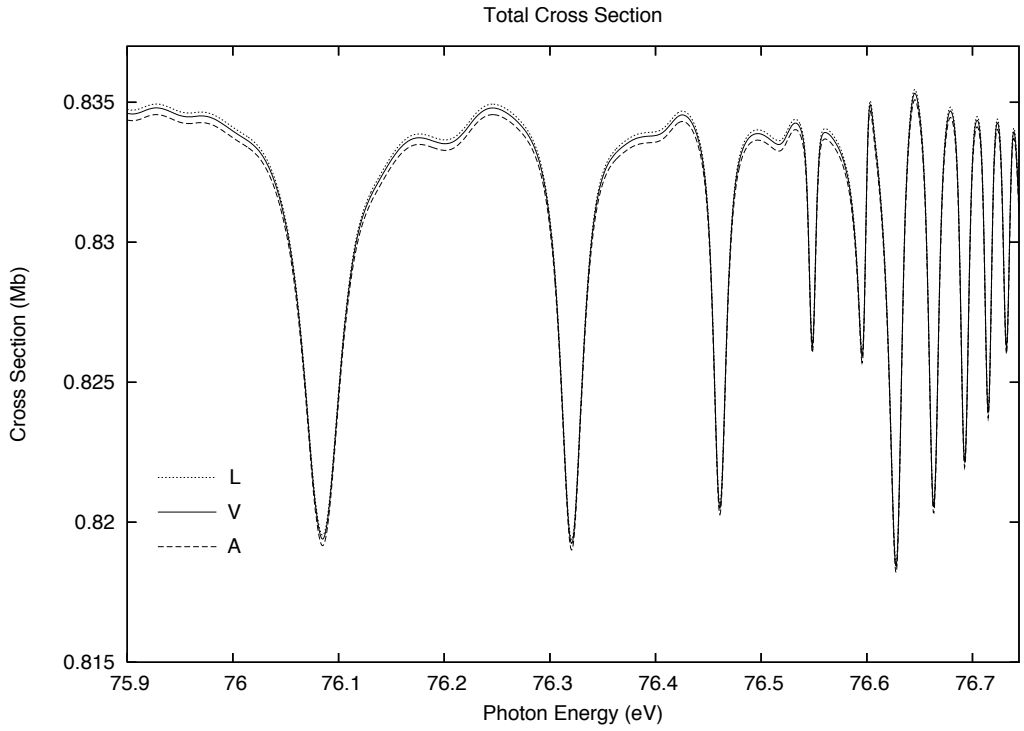

Figure L.5: Total cross section of 1^1S helium below N=5 threshold, convoluted with a gaussian profile with FWHM = 5.4 meV. A linear baseline ($-0.026 Mb/eV(E - 76.3eV)$) has been subtracted for closer comparison with measurements by Domke *et al* [20]. All three gauges, length, velocity and acceleration, are reported.

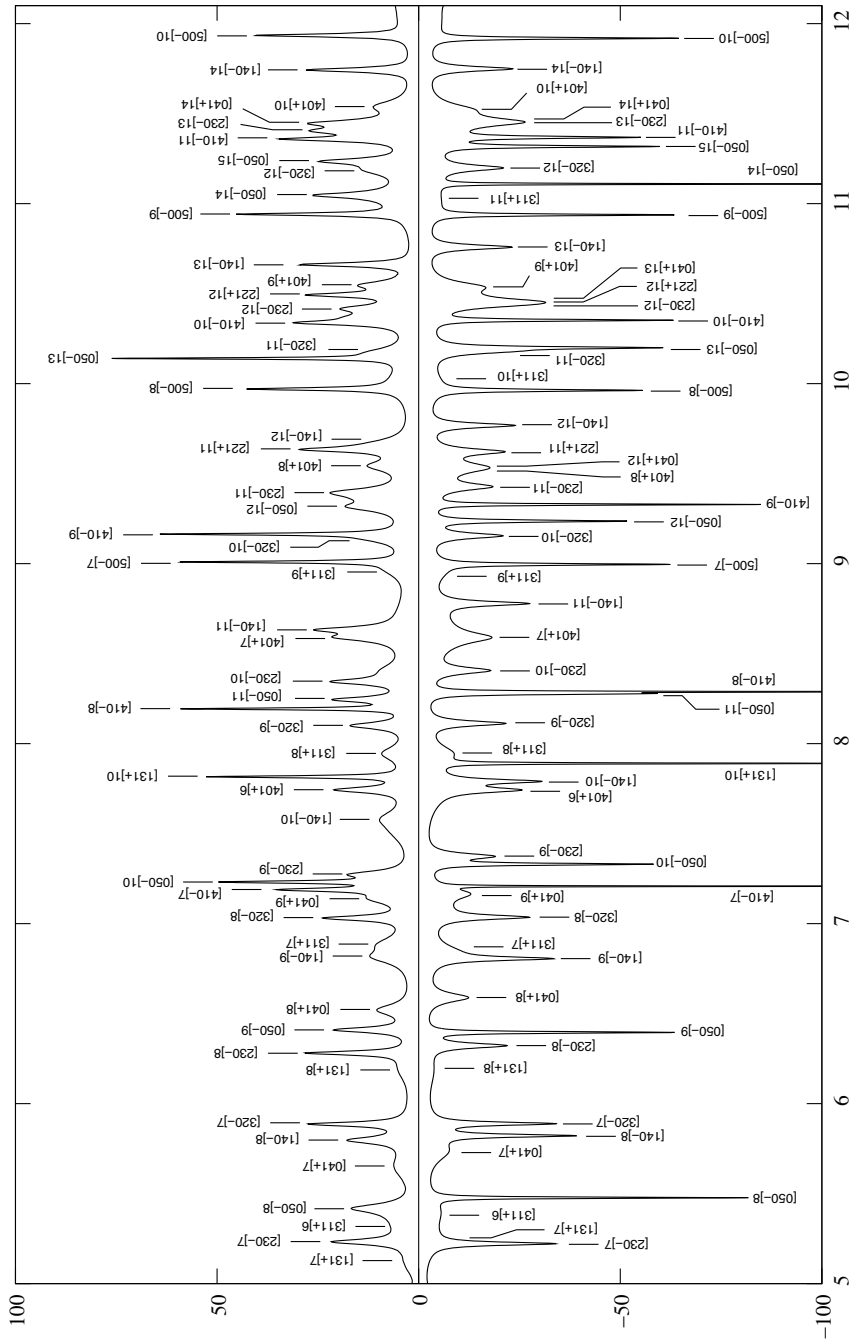

Figure L.6: Below N=6 threshold, complete ^{1}P^o multiplets have 11 resonances each, which should be found in an energy interval corresponding to $\Delta n^* = 1$. Considering that among so many resonances, some terms, mainly in $[131]^+$, $[221]^+$ and $[041]^+$ series, have widths greater than or comparable to the whole span of the corresponding multiplet, it is no surprise that it is quite difficult to characterize them with the fitting method. It is nevertheless possible to compare the density of states determined numerically (upper panel) with the same quantity reconstructed from resonance parameters found in [99] (lower panel). Even though a rather clear correspondence can be seen for many peaks, particularly those belonging to $[401]^+$, $[500]^-$, $[311]^+$ and $[320]^-$ series, the other assignments are more arbitrary. Differences are manifold and probably due to a bad representation of the intruder states from higher thresholds.

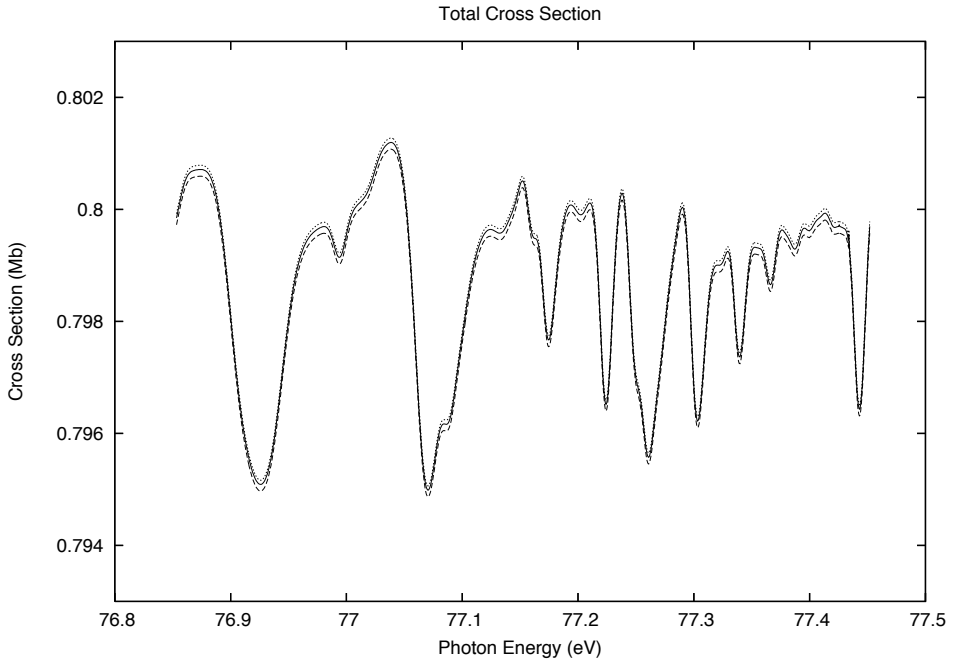

Figure L.7: Total photoionization cross sections of 1^1S helium below N=6 threshold. Baseline has been subtracted for a better comparison with experimental data by Domke *et al* [20].

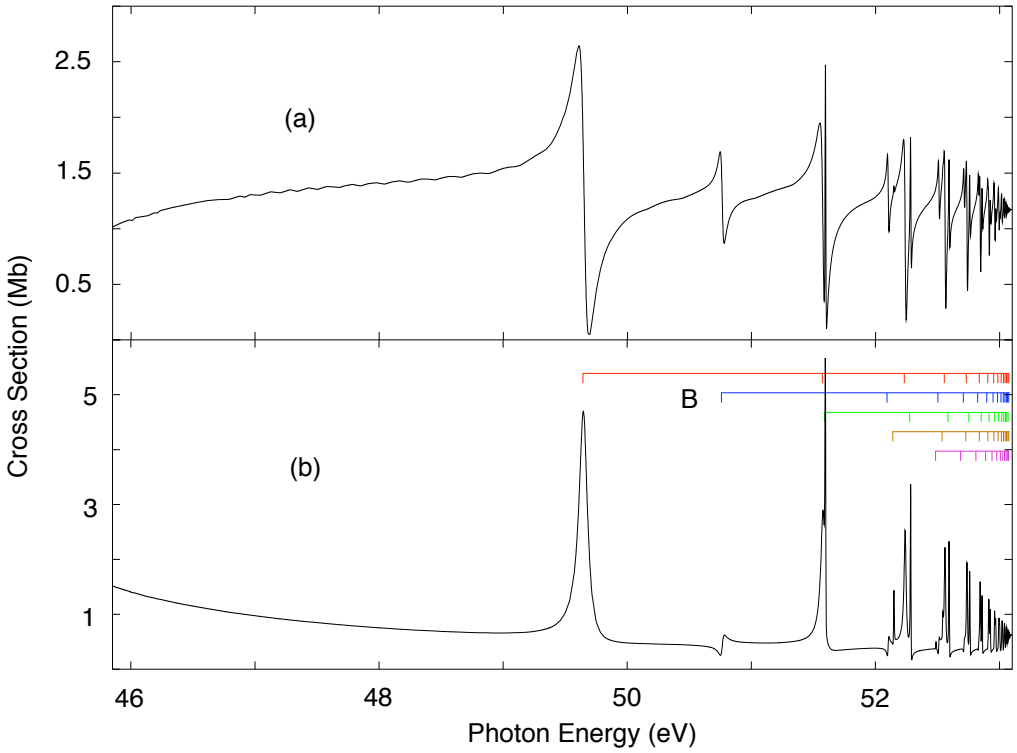

Figure L.8: 2^3S helium partial photoionization cross sections σ_{2s} (a) and σ_{2p} (b) below N=3 threshold. See chapter 3 for the definition of labels.

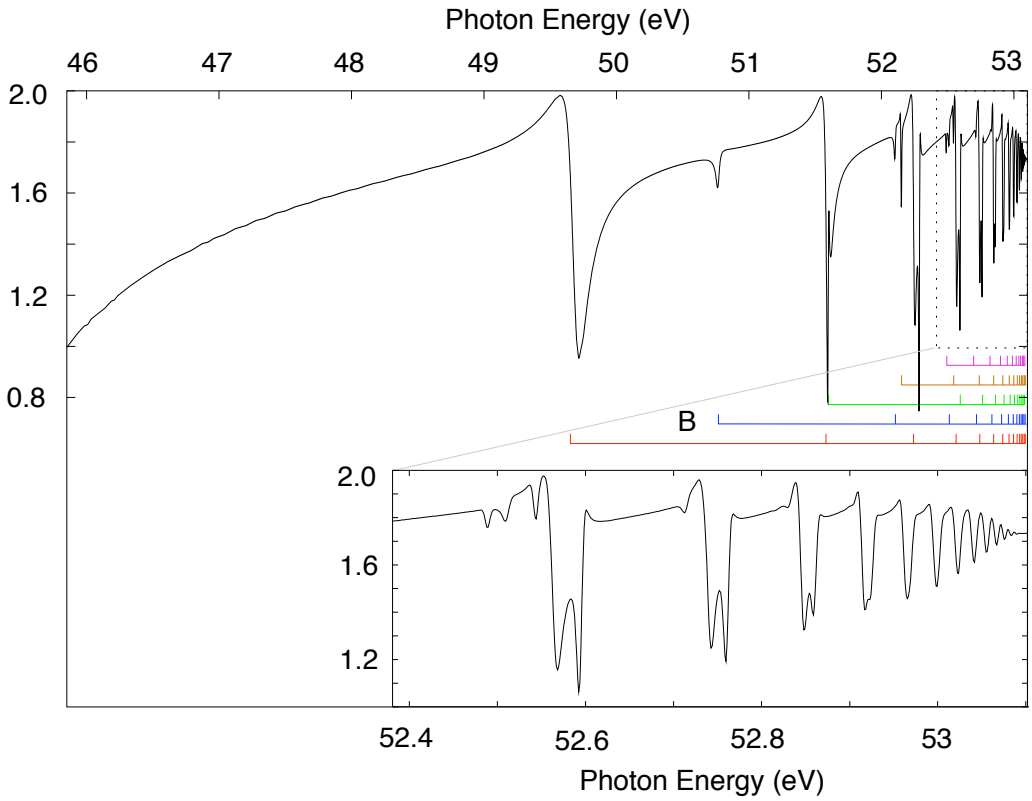

Figure L.9: Asymmetry parameter β_{tot} of 2^3S helium total cross section below N=3 threshold. β_2 is not shown since it differs from β_{tot} for only a small structureless baseline. See chapter 3 for the definition of labels.

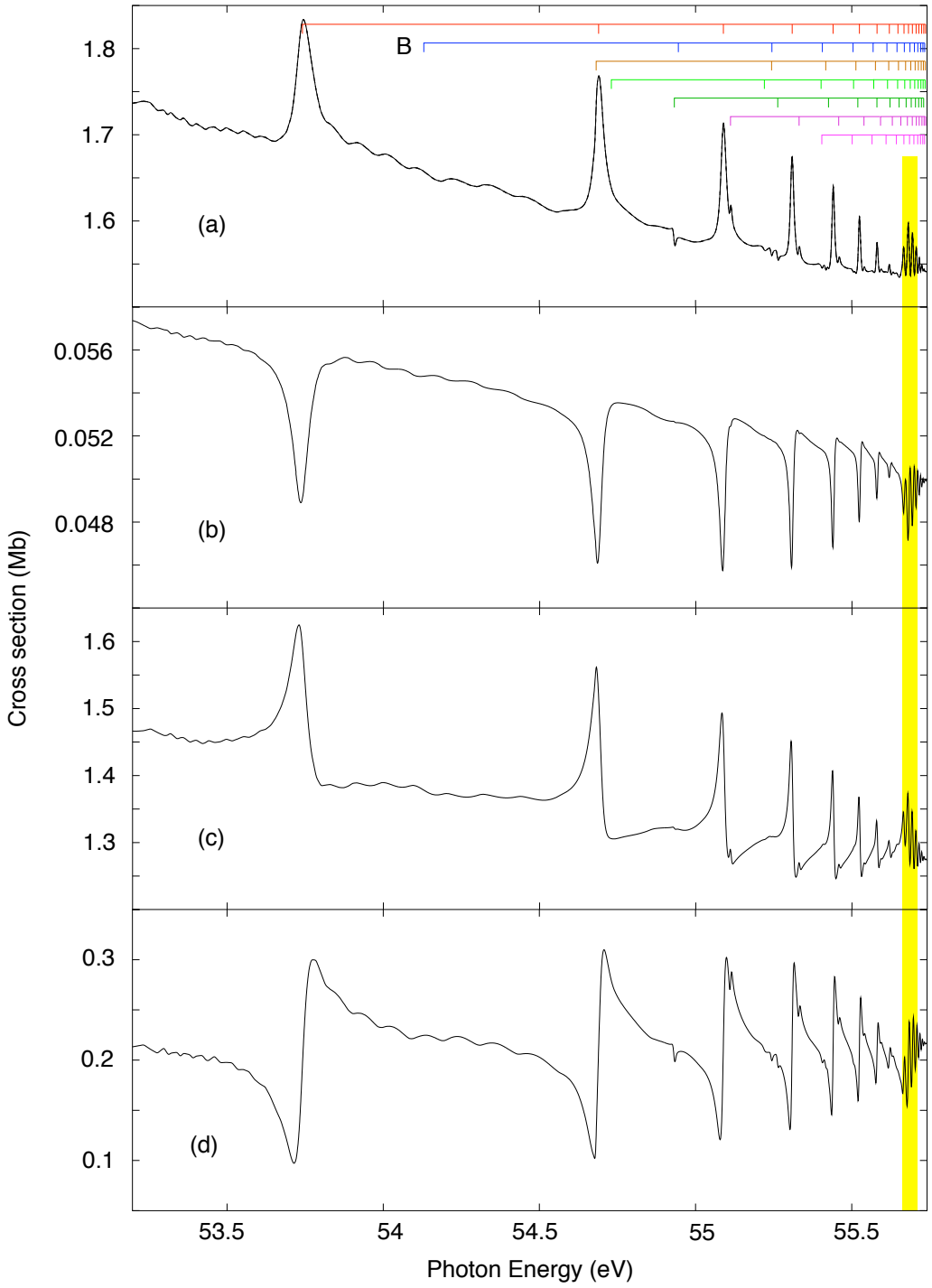

Figure L.10: 2^3S helium total and partial photoionization cross sections below N=4 threshold. σ_{tot} (a), σ_1 (b), σ_2 (c), σ_3 (d). A) $[030]^+$, B) $[120]^+$, C) $[210]^+$, D) $[021]^-$, E) $[111]^-$, F) $[201]^-$, G) $[300]^0$. The assignment is tentative, see chapter 3 for more details.

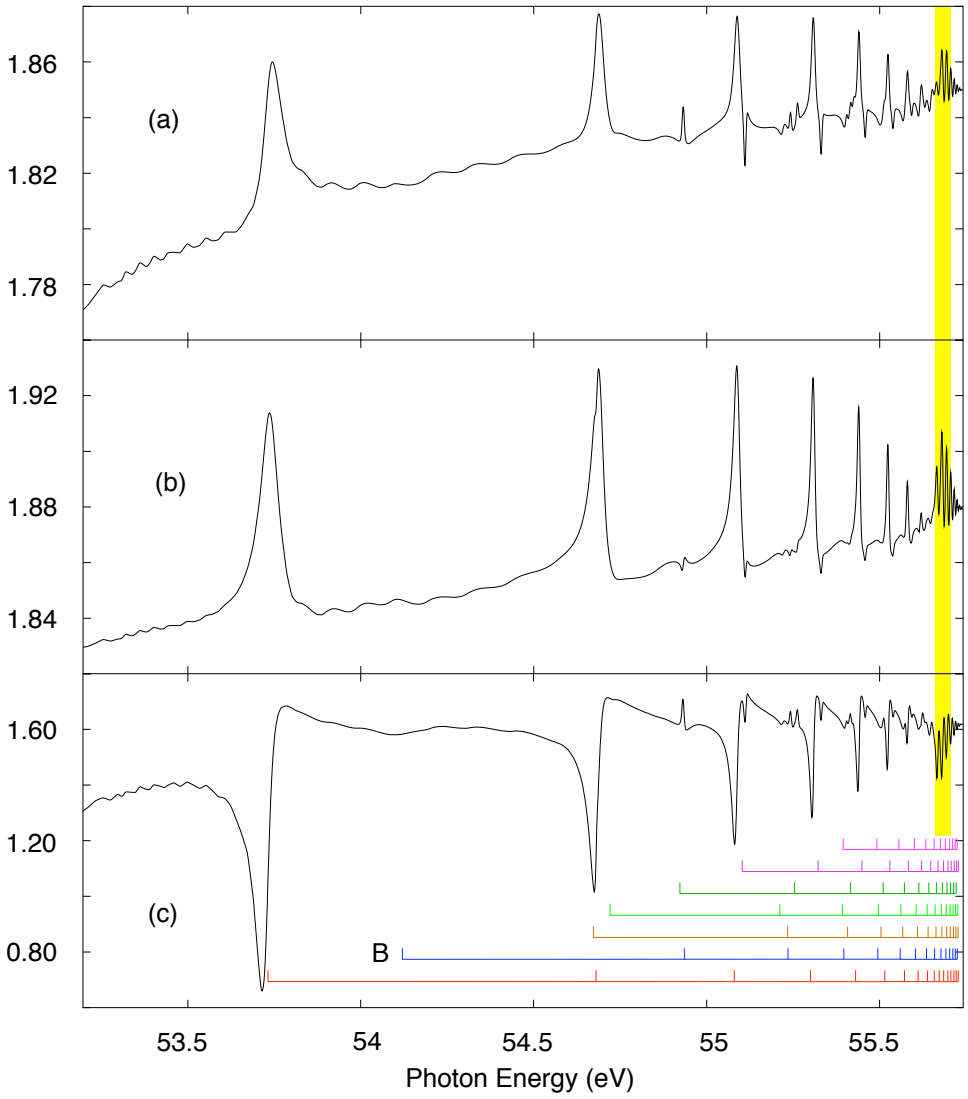

Figure L.11: 2^3S helium asymmetry parameters of total and partial cross sections below N=4 threshold. β_{tot} (a), β_2, β_3.

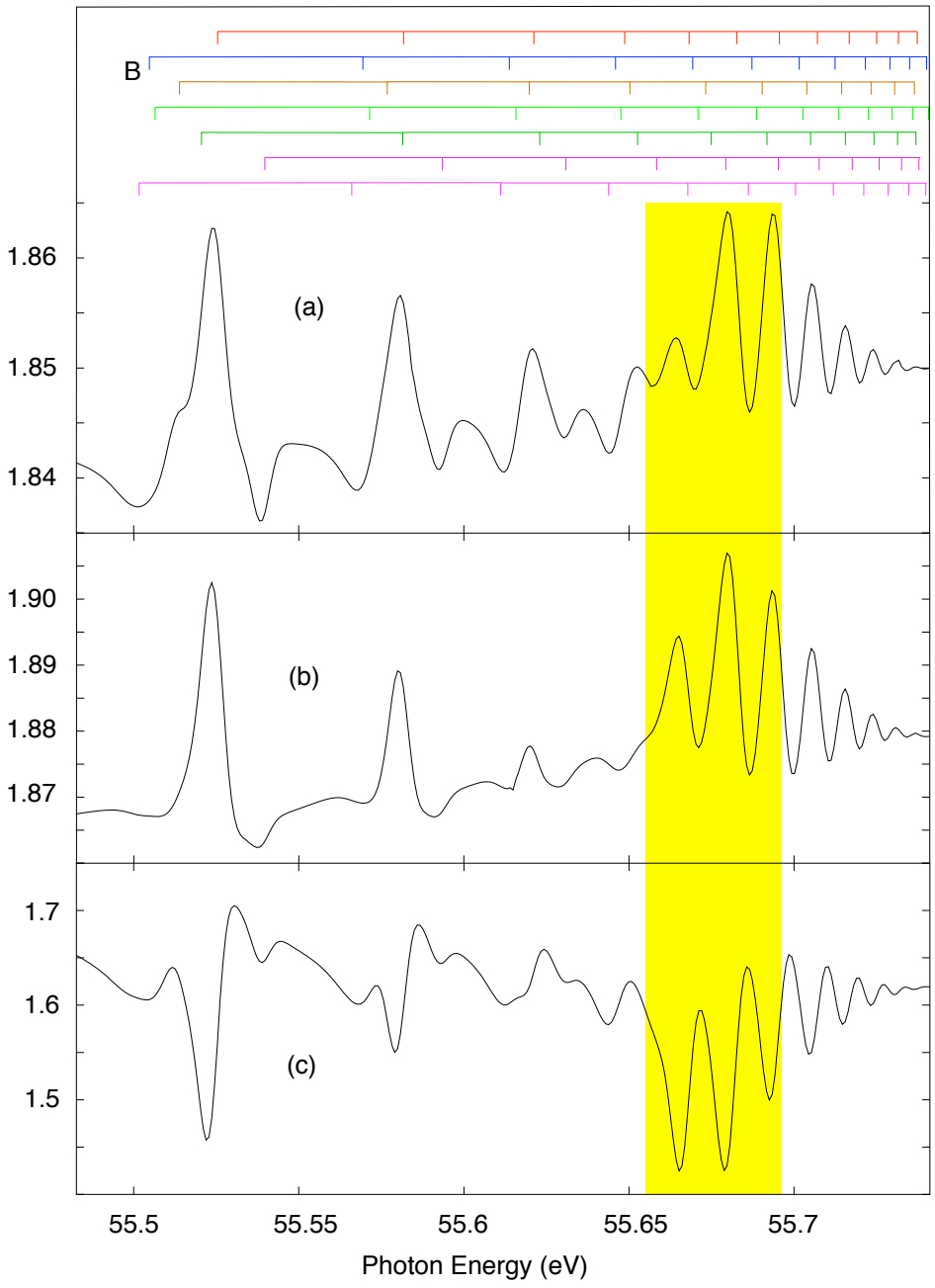

Figure L.12: Details of the 2^3S helium photoionization asymmetry parameters of total and partial cross sections below N=4 threshold. β_{tot} (a), β_2, β_3.

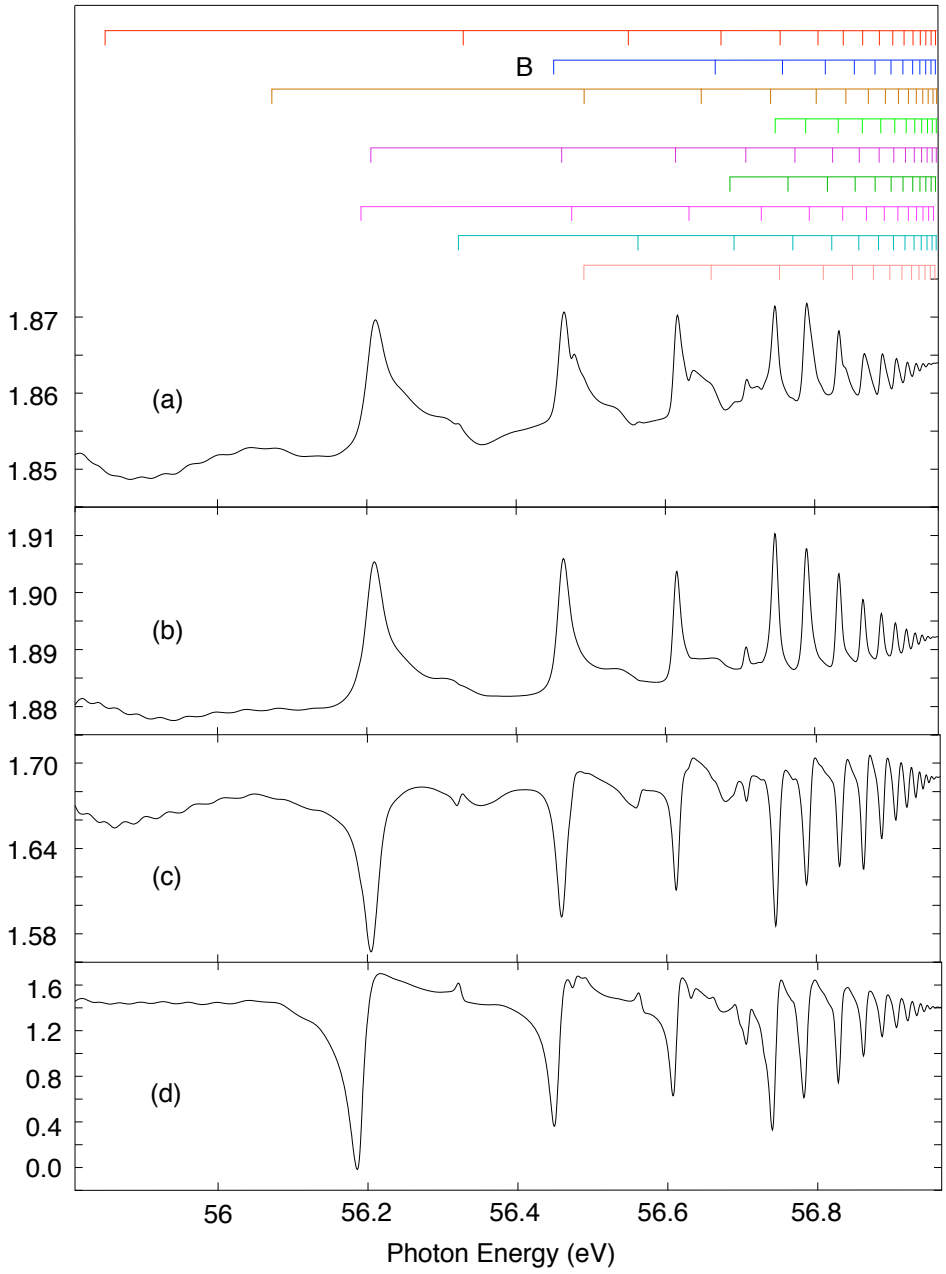

Figure L.13: 2^3S helium photoionization asymmetry parameters of total and partial cross sections below N=5 threshold. β_{tot} (a), β_2 (b), β_3 (c), β_4 (d).

Bibliography

[1] H. Hertz, *Über den Einfluß des ultravioletten Lichtes auf die elektrische Entladung*, Wiedemann Annalen **31** 982 (1887)

[2] A. Einstein, *Über einen die Erzeugung und Verwandlung des Lichtes betreffenden heuristischen Gesichtspunkt*, Annalen del Physik **17** 132 (1905)

[3] K. T. Compton and J. C. Boyce, *Extreme ultraviolet spectra excited by controlled electron impacts*, J. Frank. Inst. **205** 497 (1928)

[4] P. G. Kruger, *New lines in the arc and spark spectrum of helium*, Phys. Rev. **36** 855 (1930)

[5] R. P. Madden and K. Codling, *New Autoionizing Atomic Energy Levels in He, Ne, and Ar*, Phys. Rev. Lett. **10** 516 (1963)

[6] ALS - Advanced Light Source - Berkeley URL http://www-als.lbl.gov/als/

[7] ELETTRA - Trieste URL http://www.elettra.trieste.it

[8] BESSY - Berlin URL http://www.bessy.de

[9] PF - Photon Factory - Tsukuba URL http://pfwww.kek.jp

[10] SOLEIL - Gif sur Yvette URL http://www.synchrotron-soleil.fr

[11] APS - Advanced Photon Source - Chicago URL http://www.aps.anl.gov

[12] SRS - Synchrotron Radiation Source - Daresbury URL http://www.srs.ac.uk

[13] Max-Lab - Lund URL http://www.maxlab.lu.se

[14] P. R. Woodruff and J. A. R. Samson, *Measurements of partial cross sections and autoionization in the photoionization of helium to $He^+(N = 2)$*, Phys. Rev. A **25** 848 (1982)

[15] M. Domke, C. Xue, A. Puschmann, T. Mandel, E. Hudson, D. A. Shirley, G. Kaindl, C. H. Greene, H. R. Sadeghpour and H. Petersen, *Extensive double-excitation states in atomic helium*, Phys. Rev. Lett. **66** 1306 (1991)

[16] M. Domke, G. Remmers and G. Kaindl, *Observation of the $(2p, nd)\ ^1P^o$ double-excitation rydberg series of helium*, Phys. Rev. Lett. **69** 1171 (1992)

[17] M. Zubek, G. Dawber, R. I. Hall, L. Avaldi, K. Ellis and G. C. King, *Angular distribution of photoelectrons from ionization of helium into the He^+ $(N = 2)$ states, between 69 and 77 eV*, J. Phys. B: At. Mol. Opt. Phys. **24** L337 (1991)

[18] K. Schulz, G. Kaindl, M. Domke, J. D. Bozek, P. A. Heimann, A. S. Schlachter and J. M. Rost, *Observation of New Rydberg Series and Resonances in Doubly Excited Helium at Ultrahigh Resolution*, Phys. Rev. Lett. **77** 3086 (1996)

[19] M. Domke, K. Schulz, G. Remmers, G. Kaindl and D. Wintgen, *High-resolution study of $^1P^o$ double-excitation states in helium*, Phys. Rev. A **53** 1424 (1996)

[20] M. Domke, K. Schulz, G. Remmers, A. Gutiérrez, G. Kaindl and D. Wintgen, *Interferences in photoexcited double-excitation series of He*, Phys. Rev. A **51** 4309(R) (1995)

[21] R. Püttner, M. Domke, B. Gremaud, M. Martins, A. S. Schlachter and G. Kaindl, *New interseries interferences in doubly-excited helium*, J. Electron Spectros. **101-103** 27 (1999)

[22] H. W. van der Hart and C. H. Greene, *Regularities and irregularities in partial photoionization cross sections of He*, Phys. Rev. A **66** 022710 (2002)

[23] R. Püttner, B. Grémaud, D. Delande, M. Domke, M. Martins, A. S. Schlachter, and G. Kaindl, *Statistical Properties of Inter-Series Mixing in Helium: From Integrability to Chaos*, Phys. Rev. Lett. **86** 3747 (2001)

[24] B. Grémaud and D. Delande, *Photo-ionization of the helium atom close to the double-ionization threshold: Towards the Ericson regime*, Europhys. Lett. **40** 403 (1997)

[25] A. Czasch *et al.*, *Partial Photoionization Cross Sections and Angular Distributions for Double Excitation of Helium up to the $N = 13$ Threshold*, Phys. Rev. Lett. **95** 243003 (2005)

[26] A.-T. Le, T. Morishita, X.-M. Tong and C. D. Lin, *Signature of chaos in high-lying doubly excited states of the helium atom*, Phys. Rev. A **72** 032511 (2005)

[27] C. W. Byun, N. N. Choi, M.-H. Lee and G. Tanner, *Scaling Laws for the Photoionization Cross Section of Two-Electron Atoms*, Phys. Rev. Lett. **98** 113001 (2007)

[28] G. Tanner, N. N. Choi, M.-H. Lee, A. Czasch and R. Dörner, *Evidence of triple collision dynamics in partial photo-ionization cross sections of helium*, J. Phys. B: At. Mol. Opt. Phys. **40** F157 (2007)

[29] T. W. Gorczyca, J.-E. Rubensson, C. Såthe, M. Ström, M. Agøaker, D. Ding, S. Stranges, R. Richter and M. Alagia, *Radiative and Relativistic Effects in the Decay of Highly Excited States in Helium*, Phys. Rev. Lett. **85** 1202 (2000)

[30] F. Penent, P. Lablanquie, R. I. Hall, M. Žitnik, K. Bučar, S. Stranges, R. Richter, M. Alagia, P. Hammond and J. G. Lambourne, *Observation of Triplet Doubly Excited States in Single Photon Excitation from Ground State Helium*, Phys. Rev. Lett. **86** 2758 (2001)

[31] M. Coreno, K. C. Prince, R. Richter, M. de Simone, K. Bučar and M. Žitnik, *Branching ratios in the radiative decay of helium doubly excited states*, Phys. Rev. A **72** 052512 (2005)

[32] R. Richter, M. Alagia, M. Coreno, H. Farrokhpour, P. Franceschi, K. C. Prince, J. Söderström and S. Stranges, *High resolution study of doubly excited states of Helium: excitation of $^{1,3}S$ He metastable atoms.*, in *Int. Symp. on $(e, 2e)$, $(\gamma, 2e)$ and Related Topics, 1-4 Aug. 2007, Königstein im Taunus, Germany.* (2007)

[33] R. Richter, private communication (2008)

[34] R. Püttner, private communication (2008)

[35] J. R. Harries, J. P. Sullivan, J. B. Sternberg, S. Obara, T. Suzuki, P. Hammond, J. Bozek, N. Berrah, M. Halka and Y. Azuma, *Double Photoexcitation of Helium in a Strong dc Electric Field*, Phys. Rev. Lett. **90** 133002 (2003)

[36] K. C. Prince, M. Coreno, R. Richter, M. de Simone, V. Feyer, A. Kivimäki, A. Mihelič and M. Žitnik, *Detection of the* $^1P^e$ *Series of Doubly Excited Helium States below* $N = 2$ *via the Stark Effect*, Phys. Rev. Lett. **96** 093001 (2006)

[37] A. Mihelič and M. Žitnik, Ab Initio *Calculation of Photoionization and Inelastic Photon Scattering Spectra of He below the N=2 Threshold in a dc Electric Field*, Phys. Rev. Lett. **98** 243002 (2007)

[38] M. Ström, C. Såthe, M. Agåker, J. Söderström, J.-E. Rubensson, S. Stranges, R. Richter, M. Alagia, T. W. Gorczyca and F. Robicheaux, *Magnetic-Field Induced Enhancement in the Fluorescence Yield Spectrum of Doubly Excited States in Helium*, Phys. Rev. Lett. **97** 253002 (2006)

[39] A. Lühr, O.-A. Al-Hujaj and P. Schmelcher, *Resonances of the helium atom in a strong magnetic field*, Phys. Rev. A **75** 013403 (2007)

[40] E. P. Kanter, B. Krässig, S. H. Southworth, R. Guillemin, O. Hemmers, D. W. Lindle, R. Wehlitz, M. Y. Amusia, L. V. Chernysheva and N. L. S. Martin, $E1-E2$ *interference in the vuv photoionization of He*, Phys. Rev. A **68** 012714 (2003)

[41] U. Fano, *Effects of configuration interaction on intensities and phase shifts*, Phys. Rev. **124** 1866 (1961)

[42] M. Domke, T. Mandel, A. Puschmann, C. Xue, D. A. Shirley, G. Kaindl, H. Petersen and P. Kuske, *Performance of the high-resolution SX700/II monochromator*, Rev. Sci. Instrum. **63** 80 (1992)

[43] U. Becker, D. Szostak, H. G. Kerkhoff, M. Kupsch, B. Langer, R. Wehlitz, A. Yagishita and T. Hayaishi, *Subshell photoionization of Xe between 40 and 1000 eV*, Phys. Rev. A **39** 8 3902 (1989)

[44] R. K. Nesbet, *Variational methods in electron-atom scattering theory* (Plenum, New York) (1980)

[45] E. Gerjuoy, A. R. P. Rau and L. Spruch, *A unified formulation of the construction of variational principles*, Rev. Mod. Phys. **55** 725 (1983)

[46] J. Callaway, *The variational method in atomic scattering*, Phys. Rep. **45** 89 (1978)

[47] B. I. Schneider and T. N. Rescigno, *Complex Kohn variational method: Application to low-energy electron-molecule collisions*, Phys. Rev. A **37** 10 3749 (1988)

[48] K. Takatsuka and V. McKoy, *Variational scattering theory using a functional of fractional form. I. General theory*, Phys. Rev. A **23** 5 2352 (1981)

[49] E. P. Wigner, *Resonance Reactions and Anomalous Scattering*, Phys. Rev. **70** 1-2 15 (1946)

[50] E. P. Wigner, *Resonance Reactions*, Phys. Rev. **70** 9-10 606 (1946)

[51] E. P. Wigner and L. Eisenbud, *Higher Angular Momenta and Long Range Interaction in Resonance Reactions*, Phys. Rev. **72** 1 29 (1947)

[52] P. G. Burke and K. A. Berrington, *Atomic and molecular processes: an R-matrix approach* (Institute of Physics, Bristol) (1993)

[53] C. Bloch, *Une formulation unifiée de la théorie des réactions nucléaires*, Nucl. Phys. **4** 503 (1957)

[54] W. Reinhardt, *Complex coordinates in the theory of atomic and molecular structure and dynamics*, Annu. Rev. Phys. Chem. **33** 223 (1982)

[55] B. Simon, *The definition of molecular resonance curves by the method of exterior complex scaling*, Phys. Lett. A **71** 211 (1979)

[56] C. A. Nicolaides and D. R. Beck, *The variational calculation of energies and widths of resonances*, Phys. Lett. A **65** 11 (1978)

[57] D. A. Horner, J. Colgan, F. Martín, C. W. McCurdy, M. S. Pindzola and T. N. Rescigno, *Symmetrized complex amplitudes for He double photoionization from the time-dependent close-coupling and exterior complex scaling methods*, Phys. Rev. A **70** 06401 (2004)

[58] M. S. Pindzola and D. R. Schultz, *Time-dependent close-coupling method for electron-impact ionization of hydrogen*, Phys. Rev. A **53** 3 1525 (1996)

[59] L. B. Madsen, L. A. A. Nikolopoulos, T. K. Kjeldsen and J. Fernández, *Extracting continuum information from $\Psi(t)$ in time-dependent wave-packet calculations*, Phys. Rev. A **76** 063407 (2007)

[60] I. Cacelli, V. Carravetta and R. Moccia, *Molecular photoionization cross sections and asymmetry parameters by L^2 basis functions calculations: H_2O*, J. Chem. Phys. **85** 7038 (1986)

[61] I. Cacelli, V. Carravetta, A. Rizzo and R. Moccia, *The calculation of photoionisation cross sections of simple polyatomic molecules by L^2 methods*, Phys. Rep. **205** 283 (1991)

[62] R. G. Newton, *Scattering Theory of Waves and Particles, 2nd edition* (Dover Publications, Inc., Mineola, New York) (2002)

[63] W. P. Reinhardt and A. Szabo, *Fredholm Method. I. A Numerical Procedure for Elastic Scattering*, Phys. Rev. A **1** 1162 (1970)

[64] W. P. Reinhardt, *Fredholm Method. II. A Numerical Procedure for Inelastic Scattering*, Phys. Rev. A **2** 1767 (1970)

[65] W. P. Reinhardt, *Erratum "Fredholm Method. II. A Numerical Procedure for Inelastic Scattering"*, Phys. Rev. A **4** 429 (1971)

[66] J. T. Broad and W. P. Reinhardt, *One- and two-electron photoejection from H^-: A multichannel $J-$matrix calculation*, Phys. Rev. A **14** 2159 (1976)

[67] J. T. Broad and W. P. Reinhardt, *J-matrix method: multichannel scattering and photoionization*, J. Phys. B: At. Mol. Opt. Phys. **9** 1491 (1976)

[68] B. H. Bransdent and A. T. Stelbovics, *An L^2 approach to the solution of coupled-channel scattering equations*, J. Phys. B: At. Mol. Opt. Phys. **17** 1877 (1984)

[69] H. A. Slim and A. T. Stelbovics, *The L^2 method and finite-basis expansions in coupled channels*, J. Phys. B: At. Mol. Opt. Phys. **22** 475 (1989)

[70] M. L. Du and A. Dalgarno, *Artificial-channel method for multichannel-decay-resonance energies and widths*, Phys. Rev. A **43** 3474 (1991)

[71] D. H. Madison and J. Callaway, *Accuracy of pseudostates for the electron-hydrogen scattering problem*, J. Phys. B: At. Mol. Opt. Phys. **20** 4197 (1987)

[72] I. Bray, D. A. Konovalov and I. E. McCarthy, *Convergence of an L^2 approach in the coupled-channel optical-potential method for $e-H$ scattering*, Phys. Rev. A **43** 1301 (1991)

[73] R. Moccia and P. Spizzo, *Lithium anion photodetachment up to the 3s threshold: a K-matrix L^2 basis calculation*, J. Phys. B: At. Mol. Opt. Phys. **23** 3557 (1990)

[74] R. Moccia and P. Spizzo, *Helium photoionization between the $N = 2$ and $N = 3$ thresholds including angular distribution and resonance properties: A K-matrix L^2 basis-set calculation*, Phys. Rev. A **43** 2199 (1991)

[75] I. Sánchez and F. Martín, *L^2 calculation of multichannel photoionization parameters in the neighborhood of the $3s3p\ ^1P^o$ resonance of He*, Phys. Rev. A **44** 13(R) (1992)

[76] S. Mengali and R. Moccia, *Non-empirical core polarization effects on the optical properties of Mg(I): I. Discrete and continuum energy spectrum up to the third ionization threshold*, J. Phys. B: At. Mol. Opt. Phys. **29** 1597 (1996)

[77] T. K. Fang and T. N. Chang, *B-spline-based multichannel K-matrix method for atomic photoionization*, Phys. Rev. A **61** 062704 (2000)

[78] Y. Jiang, J. Yan, J. Li, J. Sun and L. Wan, *Photoionization of helium between the $N = 2$ and $N = 5$ thresholds of He^+: Partial differential cross sections*, Phys. Rev. A **61** 032721 (2000)

[79] J.-Z. Tang and I. Shimamura, *Mechanism of the enhancement of some high-lying resonace series in the photoionization spectra of excited helium*, Phys. Rev. A **50** 1321 (1994)

[80] G. S. Ezra, K. Richter, G. Tanner and D. Wintgen, *Semiclassical cycle expansion for the helium atom*, J. Phys. B: At. Mol. Opt. Phys. **24** L413 (1991)

[81] H. R. Fiebig, *A spline function approach to the numerical treatment of scattering and bound-state problems for nonlocal potentials*, CPC **20** 181 (1980)

[82] C. deBoor, *A Practical Guide to Splines* (Springer, New York) (1985)

[83] J. Sapirstein and W. R. Johnson, *The use of basis splines in theoretical atomic physics*, J. Phys. B: At. Mol. Opt. Phys. **29** 5213 (1996)

[84] C. F. Froese Fischer and M. Indrees, *Spline algorithms for continuum functions*, CP **3** 53 (1989)

[85] C. F. Fischer and M. Idrees, *Spline methods for resonances in photoionisation cross sections*, J. Phys. B: At. Mol. Opt. Phys. **23** 679 (1990)

[86] C. F. Fischer and W. Guo, *Spline algorithms for the hartree-fock equation for the helium ground state*, J. Comp. Phys. **90** 486 (1990)

[87] O. Zatsarinny, *B-spline atomic R-matrix codes*, CPC **174** 273 (2006)

[88] L. A. A. Nikolopoulos, *A package for the ab-initio calculation of one- and two-photon cross sections of two-electron atoms, using a CI B-splines method*, CPC **150** 140 (2003)

[89] R. Montuoro and R. Moccia, *Photoionization cross sections calculation with mixed L^2 basis set: STOs plus B-splines. Results for N_2 and C_2H_2 by KM-RPA method*, Chem. Phys. **293** 281 (2003)

[90] F. Martín, *Ionization and dissociation using B-splines: photoionization of the hydrogen molecule*, J. Phys. B: At. Mol. Opt. Phys. **32** R197 (1999)

[91] I. Sánchez and F. Martín, *Representation of the electronic continuum of H_2 with B-spline basis*, J. Phys. B: At. Mol. Opt. Phys. **30** 679 (1997)

[92] H. Bachau, E. Cormier, P. Decleva, J. E. Hansen and F. Mart 'in, *Applications of B-splines in atomic and molecular physics*, Rep. Prog. Phys. **64** 1815 (2001)

[93] C. T. F. Fischer, *B-splines in variational atomic structure calculations*, Adv. At. Mol. Opt. Phys. **55** 235 (2008)

[94] H. S. Friedrich, *Theoretical Atomic Physics* (Springer, New York) (1994)

[95] G. Breit and E. Wigner, *Capture of slow neutrons*, Phys. Rev. **49** 519 (1936)

[96] H. Feshbach, *Unified theory of nuclear reactions*, Ann. Phys. **5** 357 (1958)

[97] H. Feshbach, *A unified theory of nuclear reactions. II*, Ann. Phys. **19** 287 (1962)

[98] A. U. Hazi, *Behavior of the eigenphase sum near a resonance*, Phys. Rev. A **19** 2 920 (1979)

[99] J. M. Rost, K. Schulz, M. Domke and G. Kaindl, *Resonance parameters of photo doubly excited helium*, J. Phys. B: At. Mol. Opt. Phys. **30** 4663 (1997)

[100] L. Eisenbud, *Dissertation (*unpublished*)* (June 1948)

[101] E. P. Wigner, *Lower Limit for the Energy Derivative of the Scattering Phase Shift*, Phys. Rev. **98** 1 145 (1955)

[102] C. A. A. de Carvalho and H. M. Nussenzveig, *Time delay*, Phys. Rep. **364** 83 (2002)

[103] P. C. W. Davies and M. J. Seaton, *Radiation damping in the optical continuum*, J. Phys. B: At. Mol. Opt. Phys. **2** 757 (1969)

[104] K. J. LaGattuta, *Interference effects in electron-ion recombination. II. Resonance and direct channels*, Phys. Rev. A **38** 1820 (1988)

[105] S. L. Haan and V. L. Jacobs, *Projection-operator approach to the unified treatment of radiative and dielectronic recombination*, Phys. Rev. A **40** 80 (1989)

[106] K. Sakimoto, M. Terao and K. A. Berrington, *Effects of radiative decay on the bound-continuum transition of highly charged atomic ions*, Phys. Rev. A **42** 291 (1990)

[107] H. A. Bethe and E. E. Salpeter, *Quantum mechanics of one and two electron atoms* (Springer-Verlag, Berlin, Göttingen, Heidelberg) (1957)

[108] T. Schneider, C.-N. Liu and J.-M. Rost, *Intermanifold similarities in partial photoionization cross sections of helium*, Phys. Rev. A **65** 042715 (2002)

[109] Y. H. Jiang, R. Püttner, R. Hentges, J. Viefhaus, M. Poygin, C. Cacho, U. Becker, J. M. Rost and G. Kaindl, *Partial photoionization cross sections of doubly excited helium below the ionization thresholds I_8 and I_9*, J. Phys. B: At. Mol. Opt. Phys. **39** L9 (2006)

[110] Y. H. Jiang, R. Püttner, R. Hentges, J. Viefhaus, M. Poiguine, U. Becker, J. M. Rost and G. Kaindl, *Partial cross sections of doubly excited helium below the ionization threshold I_7*, Phys. Rev. A **69** 042706 (2004)

[111] L. Argenti and R. Moccia, *K-matrix method with B-splines: $\sigma_{n\ell}$, β_n and resonances in He photoionization below $N = 4$ threshold*, J. Phys. B: At. Mol. Opt. Phys. **39** 2773 (2006)

[112] Y. Jiang, *Doubly excited helium: from strong correlation to chaos*, http://www.diss.fu-berlin.de/2006/269 (2006)

[113] L. Argenti and R. Moccia, *He photoionization: β_N and σ_N below N=5 and 6 thresholds*, Th. Chem. Acc. **118** 485 (2007)

[114] B. Krässig, E. P. Kanter, S. H. Southworth, R. Guillemin, O. Hemmers, D. W. Lindle, R. Wehlitz and N. L. S. Martin, *Photoexcitation of a Dipole-Forbidden Resonance in Helium*, Phys. Rev. Lett. **88** 203002 (2002)

[115] D. R. Herrick and M. E. Kellman, *Novel supermultiplet energy levels for doubly excited He*, Phys. Rev. A **21** 418 (1980)

[116] C. E. U and S. G. H, *The Theory of Atomic Spectra* (The Press Syndacate of The University of Cambridge, Cambridge University Press) (1935)

[117] J.-E. Rubensson, C. Søathe, S. Cramm, B. Kessler, S. Stranges, R. Richter, M. Alagia and M. Coreno, *Influence of the Radiative Decay on the Cross Section for Double Excitations in Helium*, Phys. Rev. Lett. **83** 947 (1999)

[118] C.-N. Liu, M.-K. Chen and C. D. Lin, *Radiative decay of helium doubly excited states*, Phys. Rev. A **64** 010501(R) (2001)

[119] M. Žitnik, K. Bučar, M. Štuhec, F. Penent, R. I. Hall and P. Lablanquie, *Fluorescence of low-lying doubly photoexcited states in helium*, Phys. Rev. A **65** 032520 (2002)

[120] J. G. Lambourne *et al.*, *Experimental Determination of the Lifetime for the* $2p3d\ ^1P^o$ *Helium Doubly Excited State*, Phys. Rev. Lett. **90** 153004 (2003)

[121] K. T. Lu and U. Fano, *Graphic analysis of perturbed rydberg series*, Phys. Rev. A **2** 81 (1970)

[122] A. Bürgers and D. Wintgen, *Inhibited autoionization of planetary atom states*, J. Phys. B: At. Mol. Opt. Phys. **27** L131 (1994)

[123] A. Bürgers, D. Wintgen and J.-M. Rost, *Highly doubly excited S states of the helium atom*, J. Phys. B: At. Mol. Opt. Phys. **28** 3163 (1995)

[124] M. Zubek, G. C. King, P. M. Rutter and F. H. Read, *Photoionisation studies of autoionising states of helium between 69 and 77 eV*, J. Phys. B: At. Mol. Opt. Phys. **22** 3411 (1989)

[125] A. Menzel, S. P. Frigo, S. B. Whitfield, C. D. Caldwell and M. O. Krause, *Partial photoionization cross sections and photoelectron angular distributions for double excitations up to the $N = 5$ threshold in helium*, Phys. Rev. A **54** 2080 (1996)

[126] J. R. Harries, J. P. Sullivan, S. Obara, P. Hammond and Y. Azuma, *Doubly excited states of helium observed in $N-$ and $l-$specific partial photoionization cross-sections using lifetime-resolved fluorescence spectroscopy*, J. Phys. B: At. Mol. Opt. Phys. **36** L319 (2003)

[127] M. A. Hayes and M. P. Scott, *Resonances in the simultaneous photoionisation and excitation of He*, J. Phys. B: At. Mol. Opt. Phys. **21** 1499 (1988)

[128] F. Martín, *Completely L^2 integrable method for strong-coupling multichannel photoionization: Photoelectron emission of He between the $N = 3$ and 4 threshold*, Phys. Rev. A **48** 331 (1993)

[129] I. Sánchez and F. Martín, *Extensive L^2 calculation of partial photoionization cross sections of He in the $4lnl'$ resonance region*, Phys. Rev. A **48** 1243 (1993)

[130] Y. H. Jiang, R. Püttner and G. Kaindl, *Theoretical photoionization partial cross sections and angular distribution parameters of doubly excited helium*, J. Phys. B: At. Mol. Opt. Phys. **38** 2157 (2005)

[131] A. Menzel, S. P. Frigo, S. B. Whitfield, C. D. Caldwell, M. O. Krause, J.-Z. Tang and I. Shimamura, *Decay Paths of Interfering Two-Electron Excitations in Helium*, Phys. Rev. Lett. **75** 1479 (1995)

[132] E. Sokell, A. A. Wills, J. Comer and P. Hammond, *A study of autoionizing decay routes of doubly excited states in helium using two-dimensional photoelectron spectroscopy*, J. Phys. B: At. Mol. Opt. Phys. **29** L83 (1996)

[133] D. E. Freund, B. D. Huxtable and J. D. Morgan, III, *Variational calculations on the helium isoelectronic sequence*, Phys. Rev. A **29** 980 (1984)

[134] D. P. Carroll, H. J. Silverstone and R. M. Metzger, *Piecewise polynomial configuration interaction natural orbital study of $1\,s^2$ helium*, J. Chem. Phys. **71** 4142 (1979)

[135] C. N. Yang, *On the Angular Distribution in Nuclear Reactions and Coincidence Measurements*, Phys. Rev. **79** 764 (1948)

[136] M. O. Krause, *Photo-Ionization of Krypton Between 300 and 1500 eV. Relatwe Subshell Cross Sections and Angular Distributions of Photoelectrons*, Phys. Rev. **177** 151 (1968)

[137] M. Y. Amusia, P. U. Arifov, A. S. Baltenkov, A. A. Grinberg and S. G. Shapiro, *Calculation of current induced by photon momentum in gaseous argon*, Phys. Lett. A **47** 66 (1974)

[138] M. Y. Amusia, A. S. Baltenkov, L. V. Chernysheva, Z. Felfli, A. Z. Msezane and J. Nordgren, *Directed motion of electrons in gases under the action of photon flux*, Phys. Rev. A **63** 052512 (2001)

[139] M. J. Seaton, *Momentum transfer in photo-ionization processes*, J. Phys. B: At. Mol. Opt. Phys. **28** 3185 (1995)

[140] G. Leuchs, S. J. Smith, S. N. Dixit and P. Lambropoulos, *Observation of Interferece between Quadrupole and Dipole Transitions in Low-Energy (2eV) Photoionization from a Sodium Rydberg State*, Phys. Rev. Lett. **56** 708 (1986)

[141] N. L. S. Martin, D. B. Thompson, R. P. Bauman, C. D. Caldwell, M. O. Krause, S. P. Frigo and M. Wilson, *Electric-Dipole Quadrupole Interference of Overlapping Autoionizing Levels in Photoelectron Energy Spectra*, Phys. Rev. Lett. **81** 1199 (1998)

[142] B. Krässig, M. Jung, D. S. Gemmell, E. P. Kanter, T. LeBrun, S. H. Southworth and L. Young, *Nondipolar Asymmetries of Photoelectron Angular Distributions*, Phys. Rev. Lett. **75** 4736 (1995)

[143] O. Hemmers *et al.*, *Beyond the dipole approximation: angular-distribution effects in valence photoemission*, J. Phys. B: At. Mol. Opt. Phys. **30** L727 (1997)

[144] V. K. Dolmatov and S. T. Manson, *Enhanced Nondipole Effects in Low Energy Photoionization*, Phys. Rev. Lett. **83** 939 (1999)

[145] N. A. Cherepkov and S. K. Semenov, *On quadrupole resonances in atomic photoionization*, J. Phys. B: At. Mol. Opt. Phys. **34** L495 (2001)

[146] T. Khalil, B. Schmidtke, M. Drescher, N. Müller and U. Heinzmann, *Experimental Verification of Quadrupole-Dipole Interference in Spin-Resolved Photoionization*, Phys. Rev. Lett. **89** 053001 (2002)

[147] S. Ricz, R. Sankari, Á. Kövér, M. Jurvansuu, D. Varga, J. Nikkinen, T. Ricsoka, H. Aksela and S. Aksela, *Strong nondipole effect created by multielectron correlation in 5s photoionization of xenon*, Phys. Rev. A **67** 012712 (2003)

[148] F. Lépine, S. Zamith, A. de Snaijer, C. Bordas and M. J. J.Vrakking, *Observation of Large Quadrupolar Effects in a Slow Photoelectron Imaging Experiment*, Phys. Rev. Lett. **93** 233003 (2004)

[149] O. Hemmers *et al.*, *Dramatic Nondipole Effects in Low-Energy Photoionization: Experimental and Theoretical Study of Xe* $5s$, Phys. Rev. Lett. **91** 053002 (2003)

[150] O. Hemmers, R. Guillemin, D. Rolles, A. Wolska, D. W. Lindle, K. T. Cheng, W. R. Johnson, H. L. Zhou, and S. Manson, *Nondipole Effects in the Photoionization of Xe* $4d_{5/2}$ *and* $4d_{3/2}$*: Evidence for Quadrupole Satellites*, Phys. Rev. Lett. **93** 113001 (2004)

[151] B. Krässig, J.-C. Bilheux, R. W. Dunford, D. S. Gemmell, S. Hasegawa, E. P. Kanter, S. H. Southworth, L. Young, L. A. LaJohn and R. H. Pratt, *Nondipole asymmetries of Kr 1s photoelectrons*, Phys. Rev. A **67** 022707 (2003)

[152] R. Bruch, P. L. Altick, E. Träbert and P. H. Heckmann, *High-resolution EUV satellite spectra of doubly excited He I* $(nln'l')$*,* $n = 2$ *to* 5, J. Phys. B: At. Mol. Opt. Phys. **17** L655 (1984)

[153] N. Oda, S. Tahira, F. Nishimura and F. Koike, *Energy and angular distribution of electrons ejected from autoionization states in helium by electron impact*, Phys. Rev. A **15** 574 (1977)

[154] J. J. Quéméner, C. Paquet and P. Marmet, *Natural line shapes resolved in the ionization yield of* He^+ *below the N=2 threshold*, Phys. Rev. A **4** 494 (1971)

[155] R. L. Brooks and E. H. Pinnington, *Spectrum and polarization of helium doubly excited triplet states*, Phys. Rev. A **22** 529 (1980)

[156] J. G. Lambourne *et al.*, *Detailed observations of photo-accessible triplet doubly excited states in helium*, J. Phys. B: At. Mol. Opt. Phys. **36** 4339 (2003)

[157] J. G. Lambourne *et al.*, *Angular distribution of the fluorescence of helium doubly photo-excited states converging on the* He^+ $(N = 2)$ *ionization threshold*, J. Phys. B: At. Mol. Opt. Phys. **36** 4351 (2003)

[158] S. Mickat, K.-H. Schartner, S. Kammer, R. Schill, L. Werner, S. Klumpp, A. Ehresmann, H. Schmoranzer and V. L. Sukhorukov, *Absolute cross sections and branching ratios for the radiative decay of doubly excited helium determined by photon-induced fluorescence spectroscopy*, J. Phys. B: At. Mol. Opt. Phys. **38** 2613 (2005)

[159] M. Coreno, M. de Simone, M. Danailov, R. Richter, A. Kivimäki, M. Zitnik and K. Prince, *A new system for photon induced fluorescence spectroscopy applied to the study of doubly excited states of helium*, J. Electron Spectros. **147** 39 (2005)

[160] G. W. F. Drake, *Theory of relativistic magnetic dipole transitions: lifetime of the metastable 2^3S state of the heliumlike ions*, Phys. Rev. A **3** 908 (1971)

[161] R. F. Stebbings, F. B. Dunning, F. K. Tittel and R. D. Rundel, *Photoionization of Helium Metastable Atoms near Threshold*, Phys. Rev. Lett. **30** 815 (1973)

[162] L. Argenti and R. Moccia, *Helium 2^3S photoionization up to the N=5 threshold*, J. Phys. B: At. Mol. Opt. Phys. **41** 035002 (2008)

[163] D. W. Norcross, *Photoionization of the He metastable states*, J. Phys. B: At. Mol. Opt. Phys. **4** 652 (1971)

[164] H. Doyle, M. Oppenheimer and A. Dalgarno, *Bound-state expansion method for calculating resonance and nonresonance contributions to continuum processes: theoretical development and application to the photoionization of helium and the hydrogen negative ion*, Phys. Rev. A **11** 909 (1975)

[165] U. I. Safranova, V. S. Senashenko and S. V. Khristenko, Title unavailable, Opt. Spectrosc. (USSR) **45** 333 (1978)

[166] B. Zhou, C. D. Lin, J.-Z. Tang, S. Watanabe and M. Matsuzawa, *Enhancement of narrow resonances in photoabsorption from the He atom in metastable states*, J. Phys. B: At. Mol. Opt. Phys. **26** L337 (1993)

[167] T. N. Chang and M. Zhen, *Photoionization from $1sns\ ^{1,3}S^e$ states of helium*, Phys. Rev. A **47** 4849 (1993)

[168] T. K. Fang and T. N. Chang, *Doubly excited resonance structures in He photoionization from $1s2s\ ^{1,3}S$ metastable states*, Phys. Rev. A **56** 1650 (1997)

[169] V. L. Jacobs and P. G. Burke, *Photoionization of the helium metastable states above the $n = 2$ threshold*, J. Phys. B: At. Mol. Opt. Phys. **5** 2272 (1972)

[170] K. L. Bell, A. E. Kingston and I. R. Taylor, *Photoionization of the 2^1S and 2^3S states of helium*, J. Phys. B: At. Mol. Opt. Phys. **6** 2271 (1973)

[171] I. Sánchez and F. Martin, *Multichannel photoionization of metastable He(2^3S^e): A complete study of the $^3P^o$ resonances between the $N = 2$ and 3 thresholds*, Phys. Rev. A **47** 1878 (1993)

[172] B. Zhou and C. D. Lin, *Photoionization from metastable (1s2s) $^1S^e$ and $^3S^e$ states of the He atom for energies between the $N = 2$ and 3 thresholds of He^+*, Phys. Rev. A **49** 1057 (1994)

[173] R. E. S. Clegg and J. P. Harrington, *The photo-ionization of He I (2^3S) in nebulae*, Mon. Not. R. astr. Soc. **239** 869 (1989)

[174] R. L. Porter, G. J. Ferland and K. B. MacAdam, *He I emission in the orion nebula and implications for primordial helium abundance*, Astrophys. J. **657** 327 (2007)

[175] R. P. Bauman, R. L. Porter, G. J. Ferland and K. B. MacAdam, *J-resolved He I emission predictions in the low-density limit*, Astrophys. J. **628** 541 (2005)

[176] L. Argenti and R. Moccia, *^3S, $^3P^{o,e}$, $^3D^{e,o}$ resonance series in helium*, J. Phys. B: At. Mol. Opt. Phys. **40** 3655 (2007)

[177] R. S. Oberoi, *Auto-ionization states of two electron atoms*, J. Phys. B: At. Mol. Opt. Phys. **5** 1120 (1972)

[178] E. Lindroth, *Calculation of doubly excited states of helium with a finite discrete spectrum*, Phys. Rev. A **49** 4473 (1994)

[179] S. Kar and Y. K. Ho, *Doubly excited* $2s2p\ ^{1,3}P^o$ *resonance states of helium in dense plasmas*, Phys. Rev. A **72** 010703(R) (2005)

[180] S. Kar and Y. K. Ho, *Doubly excited inter-shell P-wave resonances of helium in weakly coupled plasmas*, J. Phys. B: At. Mol. Opt. Phys. **39** 2445 (2006)

[181] Y. K. Ho, *P-wave doubly excited resonances in He*, J. Phys. B: At. Mol. Opt. Phys. **15** L691 (1982)

[182] Y. K. Ho and A. K. Bhatia, *Doubly excited* $^{1,3}P^e$ *states in heliumlike systems*, Phys. Rev. A **47** 2628 (1993)

[183] Y. K. Ho, *Doubly excited* $^3P^o$ *resonance states of He below the* $N = 2$ *and* $N = 3$ He^+ *thresholds*, Phys. Rev. A **48** 3598 (1993)

[184] M.-K. Chen, *Doubly excited* $^{1,3}S^e$, $^{1,3}P^o$, *and* $^{1,3}D^e$ *resonances in He below the* $n = 2$ He^+ *threshold*, Phys. Rev. A **56** 4537 (1997)

[185] G. W. F. Drake, *Handbook of Atomic, Molecular, and Optical Physics* (Springer, New York) (2006)

[186] L. Argenti, *Rydberg and Autoionizing Triplet States in Helium up to N=5 threshold*, In press (2007)

[187] M. E. Kellman and D. R. Herrick, *Rotor-like spectra for some doubly excited two-electron states*, J. Phys. B: At. Mol. Opt. Phys. **11** L755 (1978)

[188] M. E. Kellman and D. R. Herrick, *Ro-vibrational collective interpretation of supermultiplet classifications of intrashell levels of two-electron atoms*, Phys. Rev. A **22** 1536 (1980)

[189] C. D. Lin, *Classification and supermultiplet structure of doubly excited states*, Phys. Rev. A **29** 1019 (1984)

[190] G. W. F. Drake and Z.-C. Yan, *Energies and relativistic corrections for the Rydberg states of helium: Variational results and asymptotic analysis*, Phys. Rev. A **46** 2378 (1992)

[191] D. Z. Goodson, D. K. Watson, J. G. Loeser and D. R. Herschbach, *Energies of doubly excited two-electron atoms from interdimensional degeneracies*, Phys. Rev. A **44** 97 (1992)

[192] L. W. Manning and F. C. Sanders, *Complex rotation method applied to Z-dependent perturbation theory: The* $2s2p$ *autoionizing states of two-electron atoms*, Phys. Rev. A **44** 7206 (1992)

[193] L. Wu and J. Xi, *The autoionization widths of He I below the N=3* He^+ *threshold*, J. Phys. B: At. Mol. Opt. Phys. **23** 727 (1990)

[194] J. zhi Tang, S. Watanabe and M. Matsuzawa, *General computational method for two-electron systems*, Phys. Rev. A **46** 2437 (1992)

[195] T. Braget, C. F. Fischer and N. Vaeck, *MCHF calculations of autoionization widths in two- and three-electron systems*, J. Phys. B: At. Mol. Opt. Phys. **26** 621 (1993)

[196] T. T. Gien, *The series of doubly-excited resonances* $^3P^o$ *of He below the* $N = 2$ He^+ *threshold*, J. Phys. B: At. Mol. Opt. Phys. **39** 939 (2006)

[197] D. H. Oza, *Phase shifts and resonances for electron scattering by* He^+ *below the* $N = 2$ *threshold*, Phys. Rev. A **33** 824 (1986)

[198] I. Sánchez and F. Martín, *Enhancement of resonant structure in the photoelectron spectra of excited He* $(2\,^1S^e)$ *above the* $n = 2$ *threshold*, Phys. Rev. A **47** 1520 (1993)

[199] A. Vollweiter, J. M. Rost and J. S. Briggs, *Saddle dynamics of intrashell resonances: propensity rules for radiative transitions*, J. Phys. B: At. Mol. Opt. Phys. **24** L155 (1991)

[200] J. M. Rost and J. S. Briggs, *Saddle structure of the three-body Coulomb problem; symmetry of doubly-excited states and propensity rules for transitions*, J. Phys. B: At. Mol. Opt. Phys. **24** 4293 (1991)

[201] Y. K. Ho and J. Callaway, *Doubly excited states of helium atoms between the* $N = 2$ *and* $N = 3$ He^+ *thresholds*, J. Phys. B: At. Mol. Opt. Phys. **18** 3481 (1985)

[202] M. Hamermesh, *Group theory and its application to physical problems* (Dover, New York) (1989)

[203] R. McWeeny and B. T. Sutcliffe, *Methods of molecular quantum mechanics* (Academic Press Inc., U.S.) (1989)

[204] U. Fano, *Interaction between Configurations with Several Open Shells*, Phys. Rev. **140** A67 (1965)

[205] P. Kristensen, U. V. Pedersen, V. V. Petrunin, T. Andersen and K. T. Chung, *Binding energy of the metastable* $He-$ *ion*, Phys. Rev. A **55** 2 978 (1997)

[206] A. Kupliauskiene, *Simultaneous ionization and excitation of B and Al atoms in the ground and excited states by photons*, Physica Scripta **55** 445 (1997)

[207] R. Moccia and P. Spizzo, *Atomic magnesium: Discrete and continuum spectrum properties from a valence-shell* L^2 *configuration-interaction calculation with polarization potential*, Phys. Rev. A **39** 3855 (1989)

[208] H. W. van der Hart, C. Laughlin and J. E. Hansen, *Influence of core polarization on the electron affinity of Ca*, Phys. Rev. Lett. **71** 10 1506 (1993)

[209] A. N. Ryabtsev, I. Kink, Y. Awaya, J. O. Ekberg, S. Mannervik, A. Ölme and I. Martinson, *Additions to the spectrum and energy levels and a critical compiilation of singly-ionized boron, B II*, Physica Scripta **71** 489 (2005)

[210] A. E. Kramida and A. N. Ryabtsev, *A critical compilation of energy levels ans spectral lines of neutral boron*, Physica Scripta **76** 544 (2007)

[211] *NIST Atomic Spectra Database*, http://physics.nist.gov/PhysRefData/ASD

[212] A. Messiah, *Quantum Mechanics* (Dover Publications, Inc., Mineola, New York) (1999)

[213] J. R. Taylor, *Scattering Theory: The Quantum Theory of Nonrelativistic Collisions* (John Wiley & Sons, Inc., New York) (1972)

[214] E. Prugovečki, *Quantum mechanics in Hilbert space* (Academic Press, New York, London, Toronto, Sydney, San Francisco) (1981)

[215] B. A. Lippmann and J. Schwinger, *Variational principles for scattering processes I*, Phys. Rev. **79** 469 (1950)

[216] D. A. Varshalovich, A. N. Moskalev and V. K. Khersonskiĭ, *Quantum Theory of Angular Momentum* (World Scientific) (1988)

[217] J. W. Cooper, *Photoelectron-angular-distribution parameters for rare-gas subshells*, Phys. Rev. A **47** 1841 (1993)

[218] J. W. Cooper, *Multipole corrections to the angular distribution of photoelectrons at low energies*, Phys. Rev. A **42** 6942 (1990)

[219] J. W. Cooper, *Erratum: Multipole corrections to the angular distribution of photoelectrons at low energies [Phsy. Rev. A. 42, 6942 (1990)]*, Phys. Rev. A **45** 3362 (1992)

[220] A. N. Grum-Grzhimailo, *Non-dipole effects in magnetic dichroism in atomic photoionization*, J. Phys. B: At. Mol. Opt. Phys. **34** L359 (2001)

[221] H. Bachau, P. Lambropoulos and X. Tang, *Method for the calculation of multiphoton and above-threshold ionization with discretized bases in two-electron atoms*, Phys. Rev. A **42** 5801 (1990)

[222] L. A. A. Nikolopoulos, *Electromagnetic transitions between states satisfying free-boundary conditions*, Phys. Rev. A **73** 043408 (2006)

[223] I. J. Schoenberg, *Contributions to the problem of approximation of equdistant data by analytic functions, Part A: On the problem of smoothing or graduation, a first class of analytic approximation formulas*, Quart. Appl. Math. **4** 45 (1946)

[224] I. J. Schoenberg, *Contributions to the problem of approximation of equdistant data by analytic functions, Part B: On the problem of osculatory interpolation, a second class of analytic approximation formulae*, Quart. Appl. Math. **4** 112 (1946)

[225] G. W. F. Drake, *High precision variational calculations for the* $1s^2\ ^1S$ *state of* H^- *and the* $1s^2\ ^1S$*,* $1s2s\ ^1S$ *and* $1s2s\ ^3S$ *states of helium*, Nucl. Instrum. Methods B **31** 7 (1988)

[226] D. L. Cooper and J. Gerratt, *The use of universal even-tempered basis sets in spin-coupled wavefunctions; the electron affinity of Li(*^2S*)*, J. Phys. B: At. Mol. Opt. Phys. **16** 3703 (1983)

[227] J. E. Hansen, M. Bentley, H. W. van der Hart, M. Landtman, G. M. S. Lister, Y. T. Shen and N. Vaeck, *The introduction of B-spline basis sets in atomic structure calculations*, Physica Scripta **T47** 7 (1993)

[228] U. Grenander and G. Szegö, *Toeplitz Forms and Their Applications* (University of California Press, Berkeley and Los Angeles) (1958)

[229] R. Courant and D. Hilbert, *Methods of mathematical physics* (Interscience publisher, Inc., New York) (1966)

[230] S. Serra Capizzano, private communication (20008)

[231] P. Tilli, *Locally Toeplitz matrices: spectral theory and applications*, Linear Algebra App. **278** 91 (1998)

[232] S. S. Capizzano, *Generalized Locally Toeplitz sequences: spectral analysis and applications to discretized Partial Differential equations*, Linear Algebra App. **366** 371 (2003)

[233] S. S. Capizzano, *The GLT class as a generalized Fourier analysis and applications*, Linear Algebra App. **419** 180 (2006)

[234] J. W. Cooper, U. Fano and F. Prats, *Classification of two-electron excitation levels of helium*, Phys. Rev. Lett. **10** 518 (1963)

[235] C. Wulfman, *Approximated dynamical symmetry of two-electron atoms*, Chem. Phys. Lett. **23** 370 (1973)

[236] D. R. Herrick and O. Sinanoğlu, *Comparison of doubly-excited helium energy levels, isoelectronic series, autoionization lifetimes, and group-theoretical configuration-mixing predictions with large-configuration-interaction calculations and experimental spectra*, Phys. Rev. A **11** 97 (1975)

[237] D. R. Herrick, *Resonance-channel quantum numbers in electron-hydrogen and proton-hydrogen scattering from group theory of the long-range dipole interaction*, Phys. Rev. A **12** 413 (1975)

[238] D. R. Herrick, *Channel invariants and SU(3) classification for two-electron atoms*, Phys. Rev. A **17** 1 (1978)

[239] D. R. Herrick, *Pairing model for doubly excited atoms*, Phys. Rev. A **22** 1346 (1980)

[240] D. R. Herrick, M. E. Kellman and R. D. Poliak, *Supermultiplet classification of higher intrashell doubly excited states of H^- and He*, Phys. Rev. A **22** 1517 (1980)

[241] A. Bürgers, *The interelectronic angle in doubly excited states: towards higher N*, J. Phys. B: At. Mol. Opt. Phys. **32** 845 (1999)

[242] C. D. Lin, *Correlations of excited electrons. The study of channels in hyperspherical coordinates*, Phys. Rev. A **10** 1986 (1974)

[243] C. D. Lin, *Analytical channel functions for two-electron atoms in hyperspherical coordinates*, Phys. Rev. A **24** 1585 (1981)

[244] U. Fano, *Correlations of two excited electrons*, Rep. Prog. Phys. **46** 97 (1983)

[245] J. M. Feagin and J. S. Briggs, *Molecular description of two-electron atoms*, Phys. Rev. Lett. **60** 984 (1988)

[246] C. A. Nicolaides, S. I. Themelis and Y. Komninos, *Degrees of validity of models for the description of doubly excited states of H^- and He*, J. Phys. B: At. Mol. Opt. Phys. **35** 1831 (2002)

[247] C. Bouri, P. Selles, L. Malegat and M. G. K. Njock, *Parabolic versus spherical partial cross sections for photoionization excitation of He near threshold*, Phys. Rev. A **74** 032704 (2006)

[248] D. Janby, L. B. Madsen and V. N. Ostrovsky, *Control of autoionization widths: Doubly excited coherent elliptic states*, Phys. Rev. A **73** 062708 (2006)

[249] N. V. Prudov and V. N. Ostrovsky, *Vibrorotational structure in asymmetric doubly excited states*, Phys. Rev. Lett. **81** 285 (1998)

[250] V. N. Ostrovsky and N. V. Prudov, *Adiabatic theory for the doubly excited asymmetric states of the helium atom*, Phys. Rev. A **51** 1936 (1995)

[251] A. K. Kazansky and V. N. Ostrovsky, *Classical unstable equilibrium configurations of helium atom and Wannier resonances*, Physica Scripta **49** 166 (1994)

[252] V. N. Ostrovsky and N. V. Prudov, *Rydberg series of the planetary atom states*, J. Phys. B: At. Mol. Opt. Phys. **26** L263 (1993)

[253] V. N. Ostrovsky, *Dinamic dipole nature of the planetary atom states*, Phys. Rev. A **46** R5309 (1992)

[254] K. Richter and D. Wintgen, *Calculations of planetary atom states*, J. Phys. B: At. Mol. Opt. Phys. **24** L565 (1991)

[255] K. Richter, G. Tanner and D. Wintgen, *Classical mechanics of two-electron atoms*, Phys. Rev. A **48** 4182 (1993)

[256] G. Tanner, K. Richter and J.-M. Rost, *The theory of two-electron atoms: between ground state and compl ete fragmentation*, Rev. Mod. Phys. **72** 497 (2000)

[257] G. Racah, *Theory of Complex Spectra. I*, Phys. Rev. **61** 186 (1942)

[258] G. Racah, *Theory of Complex Spectra. II*, Phys. Rev. **62** 438 (1942)

[259] G. Racah, *Theory of Complex Spectra. III*, Phys. Rev. **63** 367 (1943)

[260] G. Racah, *Theory of Complex Spectra. IV*, Phys. Rev. **76** 1352 (1949)

[261] U. Fano, F. Prats and Z. Goldschmidt, *Interaction Matrix Element in a Shell Model*, Phys. Rev. **129** 2643 (1962)

[262] P. G. Burke, *A program to calculate a general recoupling coefficient*, CPC **1** 241 (1970)

[263] A. Hibbert, *A general program for calculating angular momentum integrals in atomic structure*, CPC **1** 359 (1970)

[264] A. Hibbert, *A new version of a general program to calculate angular momentum integrals in atomic structure*, CPC **2** 180 (1971)

[265] A. Hibbert, *CIV3 A general program to calculate configuration interaction wave functions and electric-dipole oscillator strengths*, CPC **9** 141 (1975)

[266] J. S. Briggs, *Evaluation of Matrix Elements from a Graphical Representation of the Angular Integral*, Rev. Mod. Phys. **43** 189 (1971)

[267] P. M. Lima, *A new program for calculating matrix elements in atomic structure*, CPC **66** 99 (1991)